N-Heterocyclic Carbene Complexes: Mechanisms in Catalysis and Electrochemical Reactivity

Frances Natasha Singer

Submitted in accordance with the requirements for the degree of
Doctor of Philosophy

The University of Leeds
School of Chemistry

May 2019

The candidate confirms that the work submitted is his/her own and that appropriate credit has been given where reference has been made to the work of others.

This copy has been supplied on the understanding that it is copyright material and that no quotation from the thesis may be published without proper acknowledgement.

The right of Frances Natasha Singer to be identified as Author of this work has been asserted by her in accordance with the Copyright, Designs and Patents Act 1988.

© 2019 The University of Leeds and Frances Natasha Singer

For Grandpa K.

Acknowledgements

First, I would like to thank my supervisor, Dr Charlotte Willans for all the advice and support over the years. I will always be grateful for the many wonderful opportunities you provided me with, which have inspired me and allowed me to develop as a researcher. Thanks too for your unwavering support in the final months of my PhD, and the truly superhuman speed with which you have read my thesis chapters – the effort has been above and beyond.

Thanks are also due to Dr John Slattery, for his assistance with DFT calculations, without which this thesis would be one chapter shorter. John, you gave me my first taste of research when I was still an undergraduate, allowed me back into your lab as an MChem, and then offered your support during my PhD. Undoubtedly your influence on this thesis extends beyond a single chapter.

The chapter on reaction monitoring was made possible with the assistance of Dr Ulrich Hintermair and the team at the DReaM Facility (University of Bath). I would like to personally thank Dr John Lowe and Dr Catherine Lyall for being such welcoming hosts during my visit to Bath.

This has it seems, been a project of many supervisors, so I must also now thank Michaele and Paddy, for signing innumerable COSHH forms while Charlotte was away, and for always being able to provide me with a useful nugget of advice. Finally, I want to thank my unofficial second supervisor: Dr Mike Chapman. Thanks for always making time for me, even long after your official duties as a member of the Willans group had been discharged. I'm also eternally grateful that you gave me the triazoliums…

There are additionally a number of practical scientific contributions to this thesis which must be acknowledged. Thanks to Dr Chris Pask, for not only taking on any crystallographic task great or small, but also for always ensuring we stop at the best services on the way to Diamond. You have provided me with many much needed kind words over the years, and your patience is an example to us all. A huge thank you to Dr Mark Howard for assisting my quest for hydrides across multiple spectrometers, humouring my vague NMR questions, and most importantly, always being up for a coffee and a chat. Thanks must also go to Dr Stuart Warriner, for running direct injection experiments on the HRMS, and for never failing to greet me in the corridor.

To all the members of offices 1.25 and 1.32, past and present, know that you have all in some way contributed to this work. I am grateful for every smile, chat or biscuit that I have received. I would also like to thank the SLUGs in York, for always welcoming me when I visited the department.

Office 1.32 18/19 cohort, thank you for tolerating me during my writing period, for proof-reading my chapters, and most importantly of all, for committing to the office bake-off which such skill and enthusiasm. Chrissi, thanks for all the smuggled food, I would surely have starved without your heroic efforts. Abi, you've also provided me with plenty of nourishment, physical and emotional. Hamish, you were everything a PhD student could want in an MChem, and your crag beta isn't bad either. Tom, you really crack me up, so thanks for the laughs. Lastly Ed, even though you're a year behind, it feels as though you've been through the whole thing with me. I will miss your unique blend of cynicism and joy when I am gone. I consider you my academic brother, and it's been a pleasure working alongside you.

Of all the past students, Jordan, you certainly stand apart from the rest, and carborane corner hasn't been the same since you left it. Thanks for providing the ground work for half of this thesis. Sam and Jonny – what can I say, you made quite a pair. Jonny, I have never known a person to be so cheerful in the face of catastrophe, and Sam, I have never known someone so miserable in the face of success. Together you taught me a lot about resilience, as well as providing me with useful chemistry advice more often than you realised. Laura, you really made me believe in the 18 month PhD, and proved to me that it was possible. For that I will always be indebted to you. Pablo, thanks for being generally Pabulous and for keeping me company in Florence, I will miss not understanding anything you say. Kay, I can't imagine how this PhD would have gone without you next door. I am thankful for all that you have done for me, from the smallest biscuit break, to picking me up off the floor when everything was going wrong. Thank you for being my advisor, sounding board, and friend.

This PhD would have been a hell of a lot harder without a one hour lunch break every day, so thanks Emma, Kevin, Kay, Chris, Tom, Becky and Ben for providing distraction, advice and quality conversation. Kev, I already miss our climbing trips and conversations about life, the universe, and demonstrating. I owe you a great deal more than petrol money. Tom, if I end up on any committees in future I don't know how I'll do it without you by my side. Lucy, Lucy and Lewis, your invaluable Facebook chat support group has kept us close, even when we are far apart.

Finally I need to thank my family. Ted, thank you for being the best excuse not to do lab work at weekends a girl could ask for. You always have my back (in climbing and chemistry!), and I look forward to many more adventures together when we're on the other side. Patrick, you've been a great ear to have throughout this process; it's been nice to have someone on the outside to talk to. Lastly, I want to thank my parents, without whom, of course, none of this would have been possible. You gave me a great start in life, and have always been able to push me just the right amount. It is because of you that I have achieved this. Thank you.

Abstract

This thesis is concerned with the chemistry of N-heterocyclic carbene complexes. There are two parts to this work, the first describes the synthesis and catalytic activity of Ir-NHC complexes, the second part details the electrochemical synthesis of Cu-NHC complexes derived from triazolium salts.

Iridium complexes bearing NHC-carborane ligands are active in the catalytic transfer hydrogenation of acetophenone. These complexes were synthesised and characterised. The known catalytic activity was probed by studying the chemical reactivity of these complexes under a range of conditions. This led to the characterisation of a hydride species by various analytical techniques. The proposed mechanism of catalysis has been investigated using computational methods (DFT). No evidence to support the previously proposed mechanism was found, but there was some evidence for the operation of an unprecedented alternative. The catalytic reaction was monitored using on-line NMR spectroscopy. This confirmed the presence of hydridic species under catalytic conditions, however their exact identity could not be determined. Combined mass spectroscopic data indicates the presence of both monomeric and dimeric species.

Transition metal NHC complexes can be synthesised electrochemically, by reduction of the NHC precursor and concomitant oxidation of a sacrificial metal anode. Triazolium salts, which are known precursors to NHCs, have not previously been applied to this method. Triazolium salts were prepared and fully characterised. Several copper-NHC complexes bearing triazolium derived NHCs have been prepared both chemically and electrochemically, and characterised by a range of analytical techniques. An unexpected ring-opening reaction was observed under electrochemical conditions in one case, and various factors affecting this reaction have been investigated.

List of Abbreviations

bipy	Bipyridine
CM	Cross Metathesis
COD	1,5-Cyclooctadiene
Cp	Cyclopentadienyl
Cp*	Pentamethylcyclopentadienyl
Cy	Cyclohexyl
DCM	Dichloromethane
DFT	Density Functional Theory
DMSO	Dimethylsulfoxide
DReaM	Dynamic Reaction Monitoring
EtOH	Ethanol
HRMS	High Resolution Mass Spectrometry
ICy	1,3-Dicyclohexyl-imidazol-2-ylidene
IMes	1,3-Dimesityl-imidazol-2-ylidene
IPA	2-Propanol
IPr	1,3-Diisopropyl-imidazol-2-ylidene
MAO	Methylalumoxane
MeCN	Acetonitrile
MeOH	Methanol
MPV	Meerwein-Ponndorf-Verley
NHC	N-Heterocyclic Carbene
NMR	Nuclear Magnetic Resonance
Phen	1,10-phenanthroline
py	Pyridine
RCM	Ring Closing Metathesis
ROMP	Ring-Opening Metathesis Polymerisation
RPKA	Reaction Progress Kinetic Analysis
r.t.	Room Temperature

SCF	Self-Consistent Field
SCXRD	Single Crystal X-Ray Diffraction
SEP	Skeletal Electron Pair
SICy	1,3-Dicyclohexyl-imidazolin-2-ylidene
TBAF	Tetrabutylammonium fluoride
TEP	Tolman Electronic Parameter
TH	Transfer Hydrogenation
THF	Tetrahydrofuran
TOF	Turnover Frequency
TON	Turnover Number
VTNA	Variable Time Normalisation Analysis
XRD	X-Ray Diffraction

Table of Contents

Acknowledgements iv

Abstract vi

List of Abbreviations vii

Table of Contents 1

List of Tables 4

List of Figures 6

Preface – An Introduction to N-Heterocyclic Carbenes 18

1 Carbenes – A Quest for Stability 18

2 Carbene Multiplicity 20

3 Properties of NHCs 21

4 Synthesis of NHCs and NHC Complexes 24

List of References 28

Part I31

Catalytic Activity of Iridium NHC-Carborane Complexes for Transfer Hydrogenation 31

Chapter 1 Introduction 32

1.1 Carboranes 32

1.2 Transfer Hydrogenation Catalysis 41

1.3 Previous Work 49

1.4 Aims 54

List of References 55

Chapter 2 A chemical investigation into the role of the carboranyl moiety in NHC-carborane containing catalysts. 60

2.1 Attempted Synthesis of Carbonyl Complexes 60

2.2 Synthesis of Catalytically Active Iridium Complexes 68

2.3 Stoichiometric Reactions 75

2.4 Investigation of Hydride Complexes 82

2.5 Conclusions and Future Work 97

2.6 Experimental 99

List of References 106

Chapter 3 Computational Investigation into NHC-Carborane Complexes 108

3.1 Introduction 108

3.2 Carbonyl complexes 110

3.3 Investigation of Cyclometallation Effect ... 115
3.4 Investigation of the Proposed Catalytic Cycle ... 119
3.6 Conclusions and Future Work ... 133
3.7 Experimental ... 134
Appendix ... 135
List of References ... 136
Chapter 4 On-line Monitoring of a Transfer Hydrogenation Reaction Catalysed by NHC-Carborane Iridium Complexes ... 138
4.1 Introduction ... 138
4.2 Preparation for use of the DReaM Facility ... 143
4.3 Investigation into Transfer Hydrogenation using the DReaM Facility ... 147
4.4 Conclusions and Future Work ... 173
4.6 Summary and Possible Mechanisms ... 174
4.5. Experimental ... 177
Appendix ... 180
List of References ... 181
Part II ... 183
Electrochemical Synthesis of Copper N-Heterocyclic Carbene Complexes ... 183
Chapter 1 Introduction to Electrochemical Synthesis of NHC Complexes ... 184
1.1 Principals of Electrochemical Synthesis ... 184
1.2 Unusual NHC Architectures ... 191
1.3 Methods for Electrochemical Synthesis ... 193
1.4 Aims ... 197
List of References ... 198
Chapter 2 Investigation into the electrochemical synthesis of copper-NHC complexes derived from triazolium salts ... 200
2.1 Introduction ... 200
2.2 Reactions of Copper with Triazolium 1 ... 200
2.3 Scope of the Ring-Opening Reaction ... 212
2.4 Chemical Synthesis of bis-NHC Copper Complexes ... 222
2.5 Investigation of Related Ring-opening Species ... 226
2.6 Conclusions and Future Work ... 238
2.7 Experimental ... 240

2.8 Appendix 254

List of References.. 257

Chapter 3 Investigation into the mechanism of triazolium ring-opening reaction under standard conditions 259

3.1 Introduction 259

3.2 Investigation into the Effect of Current on the Ring-Opening Reaction 259

3.3 Investigation into the Effect of Q on Reaction Progress........................ 262

3.4 Effect of Voltage.. 264

3.5 Deuterium Labelling Studies... 267

3.6 Effect of Water 269

3.7 Conclusions and Future Work 275

3.8 Experimental 279

List of References.. 283

List of Tables

Table 1. Catalytic activity of Ir complexes for TH 53

Table 1. Selected bond lengths for the halide mixed molecular structures of **C1** and **C2**. 68

Table 2. Comparison of conversions obtained with two alkoxide bases. 84

Table 3. Comparison of selected structural parameters in **C6.H** and **C6**.[18] 91

Table 4. Comparison of key signals in the ^{1}H NMR spectra for attempted synthesis of hydride complexes for **C3** and **C6**.. 97

Table 1. Calculated carbonyl stretching frequencies and CO bond lengths. 113

Table 2. Interplanar angles and CH-CO distances.. 114

Table 3. Comparison of solid state bond lengths with calculated lengths at different levels of theory.[15].. 116

Table 4. Relative energies for cyclometallated and non-cyclometallated complexes.. 118

Table 5. Intermediates, molecules used for correction and relative Gibbs free energies. 122

Table 6. Relative Gibbs free energies using alternative corrections. 123

Table 7. Bond distances at various PES scan optimised geometries. 130

Table 1. Summary of experiments performed using the DReaM Facility. 148

Table 2. Comparison of catalytic activity for batch and continuous flow reactions. 151

Table 3. Stokes-Einstein equation, with calculated diffusion constants and hydrodynamic radii for 3 hydride signals observed at the end of 2 mol% **C3** reaction.. 165

Table 4. T_1 values for the 3 hydride signals observed at the end of 2 mol% **C3** reaction. 165

Table 1. Selected bond lengths and angles for **Cu1a.BF$_4$**. 203

Table 2. Selected bond lengths and angles for **Cu1b.BF$_4$**. 206

Table 3. Selected bond lengths and angles for **Cu1b’.BF$_4$** 207

Table 4. Selected bond lengths for the molecular structure of **Tz2.BF$_4$**.............. 213

Table 5. Selected bond lengths and angles for **Cu5a.Br**. 225

Table 6. Selected bond lengths for **Cu9a.BF$_4$**.. 235

Table 7. Comparison of phenyl twist angles for **Cu9a.BF$_4$** and **2.2**.[50]................. 236

Table 8. Selected bond distances for **Tz9.BF$_4$**. 237

Table 1. Conversions obtained after 1 and 2Q for various triazoliums. 262

Table 2. Results for electrochemical reactions run at a range of applied voltages. 265

Table 3. Reaction progress as a function of Q 281

Table 4. Reaction progress as a function of Q, with water added. **...................... 282**

List of Figures

Figure 1. Early carbene complexes.[4–7] 18

Figure 2. Synthesis of Bertrand's carbene and resonance forms.[9,10] 19

Figure 3. Synthesis of Arduengo's carbene.[11] 19

Figure 4. Recent examples of stable carbenes. 20

Figure 5. Top: Four possible electronic states for a carbene. Bottom: Orbital diagram for linear (left) and bent (right) carbene geometries. 21

Figure 6. Estimated singlet-triplet energy gaps for carbenes. 21

Figure 7. Push-pull stabilisation of NHCs. 22

Figure 8. Orbital basis for TEP. 23

Figure 9. Second generation Grubbs catalyst and Pd-PEPPSI complex. 24

Figure 10. Synthetic strategies for the synthesis of imidazolium salts. 25

Figure 11. Common routes to NHC complexes: reaction with the free carbene, *in situ* deprotonation, and transmetallation using Ag_2O. 27

Figure 12. Examples of more unusual synthesis of NHC complexes.[68,71] 27

Figure 13. *Closo*, *nido*, and *arachno* borane clusters. 33

Figure 14. Orbital diagram indicating p_x, p_y and p_z orbital positions in a $[B_6H_6]^{2-}$ borane cluster.[25] 34

Figure 15. Structures of *ortho*, *meta*, and *para* 1,2-dicarbadodecaborane. 34

Figure 16. Synthetic routes to substituted 12 vertex carboranes. 35

Figure 17. Top: Three binding modes available to carboranes. Bottom: Bonding orbital diagram for Cp (left) and *nido*-carborane (right). 36

Figure 18. Structures of carboranyl catalysts for alkene polymerisation. 37

Figure 19. Carboranyl complexes for hydrogenation. 38

Figure 20. Carboranyl catalysts with complementary solubilities for ring-closing metathesis.[56] 39

Figure 21. Pincer complexes for the reductive Aldol reaction (**1.11** and **1.12**) and Suzuki-Miyaura cross coupling (**1.13** and **1.14**). 40

Figure 22. Pincer complexes for Buchwald-Hartwig amination (**1.15** and **1.16**) and imine formation (**1.17**). 41

Figure 23. General scheme for transfer hydrogenation reaction using IPA as the proton source. 41

Figure 24. Mechanism for MPV reduction using an Al catalyst. 42

Figure 25. Crabtree's hydrogenation catalyst **1.18** and the dihydride species **1.19** postulated to be active in catalysis.[86] 43

Figure 26. Reactions of Noyori's bifunctional catalyst. **1.20** - precatalyst, **1.21** – reactive intermediate, **1.22** – catalyst resting state. 43

Figure 27. Active catalytic species for Cp*M (M = Rh, Ir) complexes. Left: 16-electron complex **1.23**. Right: Hydride complex **1.24**. **44**

Figure 28. Example catalysts based on the [IrCp*(NHC)] fragment.[95–97] **44**

Figure 29. Monohydride (top) *vs* dihydride (bottom) mechanism. A dihydride mechanism leads to poor retention of deuterium in the α-position.[99] **45**

Figure 30. Racemisation of deuterium labelled 1-phenylethanol catalysed by Ru catalysts **1.28** and **1.29**.[99] **45**

Figure 31. Top: Catalysts for TH **1.30**-**1.33**. Bottom: Proposed catalytic cycle featuring 7-coordinate Ir species. **46**

Figure 32. General mechanism for inner-sphere TH reaction. **47**

Figure 33. General mechanism for outer-sphere TH reaction. **47**

Figure 34. Left: Ir catalysts **1.34** and **1.35**. Middle: Proposed hydrogen-bond ordered transition state. Right: Ir catalysts **1.36** and **1.37**.[70,95] **48**

Figure 35. Literature examples of NHC-carborane compounds.[109–113] **50**

Figure 36. Top: Synthetic route to imidazolium carborane tethers **1.43** and **1.44**. Bottom: Diverse Rh complexes prepared from these tethers **1.45**-**1.47**. **50**

Figure 37. Top left: Range of ligand precursors **1.43**-**1.50**. Top right: Non-cyclometallated complexes **1.51**-**1.53**. Bottom: Range of Ir complexes prepared **1.54**-**1.59**. **51**

Figure 38. Proposed catalytic cycle for TH by complexes **1.54**-**1.57**.[116] **53**

Figure 39. Generalised route to dicarbonyl complexes. M = Rh or Ir. **61**

Figure 40. Route to Rh(COD) complex bearing NHC-carborane tethered ligand published by Holmes *et al.*[8] **61**

Figure 41. Synthesis of Ir complexes **C1** and **C2**. **61**

Figure 42. ^{1}H NMR spectra (400 MHz, $CDCl_3$). Top: **L2**. Bottom: **C2**. **62**

Figure 43. ^{1}H NMR spectrum (400 MHz, $CDCl_3$) of **C1**. **63**

Figure 44. ^{11}B{^{1}H} NMR spectra (96 MHz, d$_6$-DMSO [above] and $CDCl_3$ [below]). Top: **L1**. Bottom: **C1**. **63**

Figure 45. HRMS spectrum of **C2**. Inset: above: molecular ion peak [**C2**-Cl]$^+$, below: calculated molecular ion peak for [**C2**-Cl]$^+$. **64**

Figure 46. HRMS spectrum of **C1**. Inset: above: molecular ion peak [**C1**-Cl]$^+$, below: calculated molecular ion peak for [**C1**-Cl]$^+$. **65**

Figure 47. Molecular structure for the asymmetric unit of **C1**. Ellipsoids shown at the 50% probability level. Hydrogen atoms omitted for clarity. **66**

Figure 48. Partial asymmetric unit of **C1**, showing halide mixing. Ellipsoids are shown at the 50% probability level. **67**

Figure 49. Molecular structure of **C2**, showing halide mixing. Ellipsoids are shown at the 50% probability level. **67**

Figure 50. Complexes prepared by Holmes with conversions for the TH of acetophenone to 1-phenylethanol.[18] **69**

Figure 51. Synthetic route to **C6**. Use of *n*-BuLi allows for the selective deprotonation of a carbon atom in the carborane cage. **69**

Figure 52. ^{1}H NMR spectrum (300 MHz, d_6-DMSO) of *nido* contaminated **L1**. Inset: ^{11}B{^{1}H} NMR spectrum (96 MHz, d_6-DMSO) showing characteristic signals of a *nido*-cage. Green stars denote *nido* product signals. **70**

Figure 53. Example HRMS of impure product isolated during attempted synthesis of **C6** using the literature method. Green star denotes non-cyclometallated impurity (**C3**). Purple star denotes **C6**. **71**

Figure 54. ^{1}H NMR spectrum (300 MHz, CD_2Cl_2) of impure product isolated during attempted synthesis of **C6** using the literature method. Green stars indicate impurities. **71**

Figure 55. HRMS of reaction mixture during attempted synthesis of **C6**, after addition of 2.2 equivalents of *n*-BuLi. Purple star denotes **C6**, green star denotes **C3**. **72**

Figure 56. HRMS of reaction mixture during attempted synthesis of **C6**, after addition of 4.4 equivalents of *n*-BuLi. Purple star denotes **C6**, green star denotes **C3**. **72**

Figure 57. HRMS of reaction mixture during attempted synthesis of **C6**, after addition of 7.7 equivalents of *n*-BuLi. Purple star denotes **C6**, green star denotes **C3**, blue stars denote carborane containing side products. **72**

Figure 58. ^{1}H NMR spectrum (300 MHz, CD_2Cl_2) of **C6**. **73**

Figure 59. HRMS of **C6**. Inset: above: molecular ion peak [**C6**-Cl]$^+$, below: calculated molecular ion peak for [**C6**-Cl]$^+$. **73**

Figure 60. Literature synthesis of C3 from L1 *via* silver oxide route.[18] **74**

Figure 61. Literature synthesis of **C4**/**C5** from **C3** *via* silver oxide route.[18] **74**

Figure 62. Schematic of substituted carborane showing possible sites of BH activation by a metal centre, B3 or B6. **75**

Figure 63. Top: Formal loss of HCl from **C3** generates **C6**. Bottom: Reaction of **C6** with HCl in a stoichiometric reaction in CD_3CN. **76**

Figure 64. ^{1}H NMR spectra (300 MHz, CD_3CN). Top: **C6** Middle: **C6** + 5 equivalents HCl, heated for 72 hours. Bottom: **C3**. **77**

Figure 65. ^{11}B{^{1}H} NMR Spectra (96 MHz, CD_3CN). Top: **C6**. Middle: **C6** + 5 equivalents HCl, heated to 80 °C for 72 hours. Bottom: **C3**. **78**

Figure 66. HRMS obtained following the reaction of **C6** + 5 equivalents of HCl, heated to 80 °C for 72 hours. **78**

Figure 67. Comparison of ^{1}H NMR shifts for coordinated alkoxides versus parent alcohols (ppm).[20,21] **79**

Figure 68. ^{1}H NMR spectra (CD_3CN, 300 MHz) recorded for reaction of **C6** with K^{t}BuO and IPA. Green stars denote IPA, purple stars denote K^{t}BuO, blue stars denote acetone. **1. C6** + IPA, **2.** 5 minutes after K^{t}BuO addition. **3.** 1 hour after K^{t}BuO addition. **4.** 18 hours after K^{t}BuO addition. Inset: enlarged images of NHC-backbone region. **81**

Figure 69. $^{11}B\{^{1}H\}$ NMR Spectra (96 MHz, CD_3CN). Top: **C4**. Bottom: **C4** + K^{t}BuO + IPA, heated 80 °C for 18 hours. **82**

Figure 70. Hydride complexes and proposed formation mechanism reported by Yamaguchi.[24] **83**

Figure 71. Above: HRMS data obtained from catalytic run using **C3**. Below: calculated values. (**1**) [**C6**–Cl+O]$^{+}$. (**2**) [**C6**–Cl+O+MeCN]$^{+}$. Structures indicate possible sites of oxygen incorporation. **85**

Figure 72. Oxidation of a Cp* methyl group in the presence of oxygen as reported by Rauchfuss *et al.*[25] **85**

Figure 73. Scheme showing conditions for the reaction of **C3** with $NaBH_4$. **86**

Figure 74. Scheme showing conditions for the reaction of **C6** with $NaBH_4$. **87**

Figure 75. ^{1}H NMR Spectra (400 MHz, d_8-THF). **1**. **C6**. **2**. **C6** + 1.4 equivs $NaBH_4$ after 27 hours. **3**. **C6** + 8.6 equivs $NaBH_4$ after 7 days. **4**. **C6** + 16.2 equivs $NaBH_4$ after 13 days. Green and purple stars identify the shift in peak position for NCH_2 signals. Note: hydride region not to scale. **88**

Figure 76. ^{1}H NMR Spectra (400 MHz, d_8-THF) taken throughout reaction of **C6** with $NaBH_4$ (top - prior to $NaBH_4$ addition, bottom -after 13 days), showing changes to the signals in the NHC-backbone region (left), NMe group (centre) and Cp* (right). **89**

Figure 77. Possible structure for hydridic species derived from **C6**. **89**

Figure 78. Above: HRMS data obtained from reaction of **C6** with $NaBH_4$. Below: Calculated molecular ion peak for $[C_8H_{20}B_{10}IrN_2]^{+}$ with structure inset. **90**

Figure 79. Molecular structure for **C6.H**. Ellipsoids shown at the 50% probability level, hydrogen atoms omitted for clarity. **91**

Figure 80. ^{1}H NMR spectra (400 MHz, C_6D_6). Top: **C3**. Bottom: crude product of **C3** and Na^{i}PrO, with partial hydride region inset. Green star denotes IPA. **92**

Figure 81. $^{1}H^{13}C$ HMQC spectrum (400 MHz, C_6D_6) of the product of **C3** and Na^{i}PrO. Green box – NHC backbone region, purple box – NMe region, blue box – Cp* region. **93**

Figure 82. ^{1}H NMR spectra (400 MHz, C_6D_6). Above: **C6**. Below: crude product of **C6** and Na^{i}PrO, with partial hydride region inset. Green star denotes IPA, purple star denotes Et_2O. **94**

Figure 83. Above: HRMS data from the reaction of **C6** with Na^{i}PrO. Below: calculated data for $[C_{36}H_{67}B_{20}Ir_2N_4]^{+}$, with possible structures inset. **95**

Figure 84. TH of acetophenone catalysed by NHC-carborane Ir complexes. Percentages show conversions to 1-phenyl ethanol determined by ^{1}H NMR spectroscopy. **109**

Figure 85. Ligands and complexes which are precursors to Ir carbonyl complexes. **110**

Figure 86. Model complex proposed by Gusev for CO stretching frequency calculation, and range of ligands investigated. **111**

Figure 87. Correlation of calculated CO stretching frequency with CO bond length. **112**

Figure 88. Correlation of calculated CO stretching frequency with CO bond length (averages). **112**

Figure 89. Optimised geometry for [IrCp(CO)**L2**] with NHC ring plane and CO-Ir-$C_{carbene}$ plane shown. **114**

Figure 90. Cyclometallated and non-cyclometallated complexes. **115**

Figure 91. Proposed cycle and intermediate species **I-VI** considered in initial optimisations. **120**

Figure 92. Optimised structures for intermediates **I**-**VI**. **121**

Figure 93. Schematic indicating transition state search process. Initial guess structure (1) is optimised (2). An eigenvector following routine follows the imaginary frequency to locate the energy maximum (3). **124**

Figure 94. Proposed mechanisms for step **A** and **B** in the catalytic cycle. **125**

Figure 95. Imaginary vibrational mode (-1055 cm^{-1}) for transition state calculation. **125**

Figure 96. Left: Geometry optimised structure for DRC calculation in the minus direction. Middle: Geometry optimised transition state structure. Right: Geometry optimised structure for DRC calculation in the plus direction. **126**

Figure 97. Example fulvene complexes.[22,23,25,26] **126**

Figure 98. Top: Schematic showing mechanism for TH by Shvo catalyst. Bottom: Potential mechanistic pathway for TH observed computationally. **127**

Figure 99. Schematic diagram of a potential energy surface scan. Input structures designed to be at various degrees of progress along the reaction coordinate are optimised (orange circles). The highest energy structure (filled circle) has the geometry closest to that at the energy maximum and can be used for subsequent transition state calculations. **128**

Figure 100. C-H distances versus calculated SCF energy. **129**

Figure 101. Left: Optimised constrained structure with a 1.4 Å C-H distance. structure. Right: Optimised constrained structure with a 1.3 Å C-H distance. **130**

Figure 102. Ir-O distances versus calculated SCF energy. **131**

Figure 103. Left: Optimised constrained geometry structures for 3.0 Å Ir-O distance. Right: Optimised constrained geometry structures for 2.1 Å Ir-O distance. **131**

Figure 104. Ir-H distances versus calculated SCF energy. **132**

Figure 105. Optimised constrained geometry structures for 1.98 Å Ir-H distance (left) and 1.93 Å Ir-H distance (right). **132**

Figure 106. Palladium catalysed amine arylation reaction and structure of phosphine ligands **4.1** and **4.2**.[15] **141**

Figure 107. Variable time normalisation analysis enables the determination of the order in substrate A (a), substrate B (b), and catalyst (c). The sequential normalisation of the time scale in A, B, and catalyst leads to the overlay of all reaction profiles in a straight line with a slope that corresponds to k_{obs} (d). Figure reproduced with permission from John Wiley and Sons (License number: 4557830043329).[17] **142**

Figure 108. The correct order in catalyst is the one that causes all the curves to overlay (in this case first order). Figure reproduced under Creative Commons Licensing.[22] **143**

Figure 109. Reaction scheme for catalytic reaction with structures of catalysts **C3** and **C4**/**C5**. 1 mmol acetophenone, 1 mol% catalyst, 10 mol% Na^{i}PrO, 0.33 mmol 1,3,5-trimethyoxybenzene (internal standard), 2.3 mL IPA........ **144**

Figure 110. Reaction progress over time for TH catalysed by **C3** and **C4**/**C5**..... **145**

Figure 111. Mixture of Na^{i}PrO (0.10 mmol), and 1,3,5-trimethoxybenzene (0.33 mmol) in IPA (2.3 mL). Left: prior to heating. Right: after heating at 75 °C for 20 minutes and cooling to room temperature for 10 minutes. **145**

Figure 112. Labelled diagram of tubing used to check for blockages. **146**

Figure 113. Example ^{1}H NMR spectrum (500 MHz, IPA) showing integral regions used for determination of conversion. Purple stars denote acetophenone, green stars denote 1-phenylethanol, blue star denotes internal standard. **149**

Figure 114. Plot of concentration versus time. **149**

Figure 115. Plot of conversion versus time for all catalysts. **150**

Figure 116. Reaction profile for **C4**/**C5** at 1 mol% catalyst loading. Change in concentration of acetophenone (red circle) and 1-phenylethanol (green triangle) over time **152**

Figure 117. Graph shoing time vs ln[acetophenone], for reaction catalysed by **C4**/**C5** at 1 mol% catalyst loading. **152**

Figure 118. Graph showing time vs 1/[acetophenone] for reaction catalysed by **C4**/**C5** at 1 mol% catalyst loading. **153**

Figure 119. Reaction profile for **C3** at 1 mol% catalyst loading. Change in concentration of acetophenone (red circle) and 1-phenylethanol (green triangle) over time. **154**

Figure 120. Reaction profile for $[IrCp^*Cl_2]_2$ at 0.5 mol% catalyst loading. Change in concentration of acetophenone (red circle) and 1-phenylethanol (green triangle) over time. **154**

Figure 121. Top: ^{1}H NMR spectrum (400 MHz, d_8-THF) for product of **C6** and $NaBH_4$. Middle: ^{1}H NMR spectrum (400 MHz, d_6-benzene) for product of **C6** and Na^{i}PrO. Bottom: ^{1}H NMR spectrum (500 MHz, IPA) for reaction using **C4**/**C5** at 1 mol% catalyst loading prior to base addition (i.e. **C4**/**C5**, acetophenone, 1,3,5-trimethoxybenzene, IPA). **155**

Figure 122. Superimposed ^{1}H NMR spectra (500 MHz, IPA) for reaction using **C4**/**C5** at 1 mol% loading. Blue spectra: prior to base addition, red spectra: evolution over first 20 min, green spectrum: final spectrum at 14.4 hours. **156**

Figure 123. Raw data showing concentration of hydride signals over time. **157**

Figure 124. Concentration of hydride signals over time with moving average trendlines applied. **158**

Figure 125. Superimposed ^{1}H NMR spectra (500 MHz, IPA). Blue trace: 1 mol% **C4**/**C5** after 297 min. Red trace: 0.5 mol% **C4**/**C5** after 297 min. **159**

Figure 126. Superimposed ^{1}H NMR spectra (500 MHz, IPA) for reaction using **C3** at 2 mol% loading. Blue spectrum prior to base addition, red spectra: evolution over first 20 min, green spectrum: final spectrum at 3 hours. **160**

Figure 127. Concentration of hydride signals over time. **161**

Figure 128. Superimposed ^{1}H NMR spectra (500 MHz, IPA) for reaction using $[IrCp^*Cl_2]_2$ at 0.5 mol% loading. Blue spectra: prior to base addition, red spectra: evolution over first 20 min, green spectrum: final spectrum at 13.7 hours **162**

Figure 129. ^{1}H NMR spectra (500 MHz, IPA) for reaction using $[IrCp^*Cl_2]_2$ at 0.5 mol% loading. Top: After base addition. Middle spectra: approximate hourly intervals. Bottom: reaction end after 13.7 hours. **163**

Figure 130. Plot of hydride concentration over time **163**

Figure 131. ^{1}H-^{13}C HMBC spectrum (500 MHz, IPA). Inset: enlarged region showing cross-peaks. **166**

Figure 132. HRMS obtained for catalytic reaction using **C4**/**C5** (1 mol%) prior to base addition. **167**

Figure 133. HRMS obtained for catalytic reaction using **C3** (2 mol%) after 17 minutes. **168**

Figure 134. HRMS obtained for catalytic reaction using **C3** (2 mol%) after 32 minutes. **168**

Figure 135. Top: Partial HRMS for reaction using **C3** (2 mol%). Bottom: Simulated pattern for $[C_{36}H_{73}B_{20}ClIr_2N_4+H]^+$. Inset: potential structure for dimer of this formula. **169**

Figure 136. Top: Partial HRMS for reaction using **C3** (2 mol%). Bottom: Simulated pattern for $[C_{18}H_{36}B_{10}ClIrN_2+H]^+$. Inset: potential structure for complex of this formula. **169**

Figure 137. HRMS obtained for catalytic reaction using $[IrCp^*Cl_2]_2$ (0.5 mol%) after 35 minutes. **170**

Figure 138. Analyses to determine order in catalyst for **C3**. Concentration of 1-phenylethanol vs. $t[cat]^{n.}$ **171**

Figure 139. Analyses to determine order in catalyst for **C4/C5**. Concentration of 1-phenylethanol vs. $t[cat]^{n.}$ **172**

Figure 140. Analyses to determine order in catalyst for $[IrCp^*Cl_2]_2$. Concentration of 1-phenylethanol vs. $t[cat]^{n.}$ **172**

Figure 141. Possible mechanistic scenario to explain difference in reactivity of **C3** and **C6**. 175

Figure 142. Possible Shvo-type equilibria for monohydride species derived from **C3** (top) and **C6** (bottom). 176

Figure 143. Transition states for Shvo-type mechanism for computational investigation. 176

Figure 144. Generalised scheme for anodic oxidation followed by subsequent reaction. 184

Figure 145. Scope of inorganic electrochemical reactions described by Tuck *et al.* Top: Periodic table indicating elements used. Bottom: Ligand precursors and associated reduced products. 185

Figure 146. General scheme for electrochemical synthesis of metal complexes. 186

Figure 147. Complexes prepared electrochemically, showing full and partial reduction of reducible groups. 186

Figure 148. Organometallic complexes prepared electrochemically. 189

Figure 149. Organometallic Ni complexes prepared by generation of a reactive Ni(0) species. 189

Figure 150. NHC complexes prepared electrochemically reported by Chen and Willans. 191

Figure 151. Synthesis of non-classical NHCs (**1.17**, and **1.18**) and acylic diamino carbene (**1.19**).[38,40,41] 192

Figure 152. First example of abnormal carbene complex (**1.20**) and isolated free abnormal carbene (**1.21**). 192

Figure 153. Examples of various NHCs.[44,49] 193

Figure 154. Power supply set-up for electrochemical reactions. 194

Figure 155. a. ElectraSyn set-up for electrochemical reactions, b. electrode fittings in vial cap, c. electrical contacts on vial cap, d. septum on vial cap. 195

Figure 156. Structure of triazolium salts **Tz1.BF$_4$** and **Tz1.Cl**. 200

Figure 157. Chemical synthesis of **Cu1a.BF$_4$** from **Tz1.BF$_4$**. 201

Figure 158. ^{1}H NMR spectra (400 MHz, CD$_3$CN). Top: **Tz1.BF$_4$**. Bottom: **Cu1a.BF$_4$**, purple stars denote presence of **Tz1.BF$_4$**, green stars denote residual solvent (DCM and Et$_2$O). 201

Figure 159. Molecular structure for **Cu1a.BF$_4$**. Ellipsoids are shown at the 50% probability level. One $[BF_4]^-$ counter-ion is omitted for clarity. Hydrogen atoms added in calculated positions and refined using the riding model. 203

Figure 160. Scheme showing electrochemical reaction with **Tz1.BF$_4$**. 203

Figure 161. ^{1}H NMR spectra (400 MHz, CD$_3$CN). Top: **Tz1.BF$_4$**. Middle: **Cu1a.BF$_4$**. Bottom: product of electrochemical reaction using **Tz1.BF$_4$**. Purple stars denote new CH$_2$ and aromatic signals, blue stars denote new signals, green stars denote residual solvent (DCM and Et$_2$O). 204

Figure 162. Molecular structure of **Cu1b.BF$_4$**. Ellipsoids are shown at the 50% probability level. One $[BF_4]^-$ counter-ion is omitted for clarity. Hydrogen atoms added in calculated positions and refined using the riding model. Inset: a. nitrogen-nitrogen bond cleavage resulting in diimine ligand; b. structure of **Cu1b.BF$_4$**. **205**

Figure 163. Molecular structure for **Cu1b'.BF$_4$**. Ellipsoids are shown at the 40% probability level. Left: Unit cell structure showing Cu_4O_4 cube. Hydrogen atoms and four $[BF_4]^-$ counter ions have been omitted for clarity. Right: Asymmetric unit. One $[BF_4]^-$ counter-ion omitted for clarity. Hydrogen atoms added in calculated positions and refined using the riding model. **206**

Figure 164. Space-filled model showing crystal packing of **Cu1b'.BF$_4$** viewed along the crystallographic C-axis. **207**

Figure 165. Structure of **Cu1b.BF$_4$** and complex **Cu1c.BF$_4$** with associated molecular ion peaks. **208**

Figure 166. ^{1}H NMR spectrum (400 MHz, CD_3CN) for **Cu1a.BF$_4$/Cu1b.BF$_4$**. Integrals shown relative to 2 for CH_2 signal labelled “m”. **209**

Figure 167. Comparison of simulated XRD powder pattern for **Cu1a.BF$_4$** and **Cu1b.BF$_4$** with measured sample of **Cu1a.BF$_4$/Cu1b.BF$_4$** mixture. **209**

Figure 168. Schematic indicating formal reactivity of **Tz1.BF$_4$** or the NHC derived from **Tz1.BF$_4$** to form the diimine. **210**

Figure 169. Examples of chemical reductive N-N bond cleavage.[21,24] **211**

Figure 170. Examples of electrochemical reductive N-N bond cleavage.[23,25,26] **211**

Figure 171. Structure of **Tz1.BF$_4$** and **Tz2.BF$_4$**. **212**

Figure 172. Synthetic route to **Tz2.BF$_4$**. **212**

Figure 173. Molecular structure for **Tz2.BF$_4$**. Ellipsoids shown at the 50% probability level. Hydrogen atoms added in calculated positions and refined using the riding model. **213**

Figure 174. Electrochemical reaction of **Tz2.BF$_4$**. **214**

Figure 175. HRMS for the product of electrochemical reaction using **Tz2.BF$_4$**. Inset: structures corresponding to observed peaks. **214**

Figure 176. Structural variation of triazolium salts **Tz1.BF$_4$**, **Tz2.BF$_4$** and new targets **Tz3.BF$_4$** and **Tz4.BF$_4$**. **215**

Figure 177. Reaction scheme for the synthesis of 1-phenyl-1,2,4-triazole. **216**

Figure 178. Reaction scheme for the synthesis of **Tz4.I** and **Tz4.BF$_4$**. **216**

Figure 179. Left: molecular structure of **Tz4.BF$_4$** obtained from block crystal. Ellipsoids shown at the 50% probability level. Hydrogen atoms added in calculated positions and refined using the riding model. Right: asymmetric unit cell obtained from needle crystal. Ellipsoids shown at the 50% probability level, one triazolium cation, and all hydrogen atoms omitted for clarity. **217**

Figure 180. Preparation of triazolium bromide salts **Tz5.Br**, **Tz6.Br**, and **Tz7.Br** using bromoalkanes. **218**

Figure 181. Left: molecular structure for **Tz6.Br**. Right: molecular structure for **Tz7.Br**. 218

Figure 182. Reaction scheme for the electrochemical synthesis of **Cu5a.BF$_4$**. 219

Figure 183. Structural similarity between **Tz1.BF$_4$**, **Tz5.BF$_4$** and **Tz8.BF$_4$**. 220

Figure 184. Products and starting materials for **Tz1.BF$_4$** and proposed target **Tz8.BF$_4$**. 220

Figure 185. Synthetic route used for attempted preparation of **Tz8.BF$_4$**. 220

Figure 186. Molecular structure of **Tz8'.BF$_4$**. Ellipsoids shown at the 50% probability level. One $[BF_4]^-$ counter-ion omitted for clarity. Hydrogen atoms added in calculated positions and refined using the riding model. 221

Figure 187. ^{1}H NMR spectra (400 MHz, d_6-DMSO). Top: **Tz8'.BF$_4$**. Bottom: D_2O shake on sample of **Tz8'.BF$_4$**, showing disappearance of NH and H_a signals. 222

Figure 188. Reaction scheme for the chemical synthesis of **Cu5a**. 223

Figure 189. Reaction scheme for the synthesis of **Cu5a***. 223

Figure 190. ^{1}H NMR spectra (400 MHz, CD_3CN). Top: **Cu5a.BF$_4$** prepared electrochemically. Middle: **Cu5a** prepared chemically. Bottom: **Cu5a*** prepared chemically. Purple stars denote solvent peaks (top: Et_2O, middle: THF). 224

Figure 191. Molecular structure for **Cu5a.Br**. Ellipsoids shown at 50% probability level. Hydrogen atoms added in calculated positions and refined using the riding model. 225

Figure 192. Reaction scheme for the chemical synthesis of **Cu1a.BF$_4$**. 226

Figure 193. Reduction of yellow coloured tetrazolium salt MTT to purple coloured formazan by NADH. 226

Figure 194. Reaction scheme for electrochemical reaction using MTT. 227

Figure 195. Left: solution of MTT in MeCN prior to electrode insertion. Right: solution of MTT in MeCN after 10 minutes in contact with Cu electrodes. 227

Figure 196. IR spectrum for MTT. 228

Figure 197. IR spectrum for product of electrochemical reaction of MTT with Cu electrodes. 228

Figure 198. Molecular structure for MTT.$CuBr_2$. Ellipsoids shown at 50% probability level. Hydrogen atoms added in calculated positions and refined using the riding model. 229

Figure 199. Reaction schemes for reaction of MTT with Cu powder. 229

Figure 200. IR spectrum of product from chemical reaction of MTT with Cu powder in MeCN. 231

Figure 201. IR spectrum of product from chemical reaction of MTT with Cu powder in MeOH. 231

Figure 202. Comparison of simulated XRD powder pattern for MTT.$CuBr_2$ with measured sample of MeCN reaction product and MeOH reaction product. 232

Figure 203. Tautomerism between zwitterion and carbenic forms displayed by nitron and example complexes reported by Siemeling *et al.*[50] 233

Figure 204. Rearrangement reaction of nitron reported by O'Donoghue *et al.*[51] 233

Figure 205. Reaction scheme for the synthesis of **Cu9a.BF_4**. 234

Figure 206. Molecular structure of **Cu9a.BF_4**. Ellipsoids shown at the 50% probability level. Hydrogen atoms added in calculated positions and refined using the riding model. 235

Figure 207. Molecular structure of **Tz9.BF_4**. Ellipsoids shown at 50% probability level. Hydrogen atoms added in calculated positions and refined using the riding model. 236

Figure 208. Reaction scheme for electrochemical reaction using **Tz9.BF_4.** 237

Figure 209. Comparison of simulated XRD powder pattern for **Cu9a.BF_4** and $[Cu(MeCN)_4][BF_4]$ with that measured for the product of electrochemical reaction of **Tz9.BF_4** with Cu electrodes.[52] 238

Figure 210. Possible alternative triazolium salts. 238

Figure 211. ^1H NMR spectra (400 MHz, CD_3CN). Top: **Cu1a**/**Cu1b** with NH and CH imine signals labelled. Middle: **Tz1.BF_4**. Bottom: product of electrolysis of **Tz1.BF_4** using glassy carbon electrodes. 260

Figure 212. Comparison of simulated powder XRD pattern for **Cu1a.BF_4** and **Cu1b.BF_4** with that measured for reaction product. 261

Figure 213. Reaction progress as a function of Q during the electrochemical synthesis of **Cu1a**/**Cu1b** mixture. 263

Figure 214. Scatter plot showing fraction **Cu1a**/**Cu1b** for all electrochemical reactions using **Tz1.BF_4** as a function of Q. 264

Figure 215. Above: Product mixture from the electrochemical reactions performed at 2, 5 and 10 V. Below: Electrodes after reactions performed at 2, 5 and 10 V showing differing degrees of fouling. 266

Figure 216. ^1H NMR spectra (400 MHz, CD_3CN) of crude product from electrochemical reactions at fixed voltages of: Top: 2 V; Middle: 5 V; bottom: 10 V. Green stars denote **Tz2.BF_4**, purple stars denote **Cu2a.BF_4**. 266

Figure 217. Possible sources of hydrogen atoms and their corresponding position in the imine product. Inset: structure of **Tz1.D**. 267

Figure 218. Reaction scheme showing preparation of deuterated triazoliums, and back-reaction. 268

Figure 219. Scatter plot showing fraction **Cu1a**/**Cu1b** for all electrochemical reactions using **Tz1.BF_4** as a function of Q, including reaction using d_3-MeCN. 269

Figure 220. Scatter plot showing fraction **Cu1a**/**Cu1b** for all electrochemical reactions using **Tz1.BF$_4$** as a function of Q, including water doped reactions. **270**

Figure 221. ^{1}H NMR spectra (400 MHz, CD_3CN). **1. Cu1a.BF$_4$**; **2a-e.** Reaction progress after addition of H_2O from 20 min – 8 days [green stars denote new product peaks]; **3. Cu1a**/**Cu1b** mixture [purple stars denote key peaks indicative of **Cu1b**]; **4. Tz1.BF$_4$**. **271**

Figure 222. Reaction scheme showing deuteration experiments. Top: Electrochemical reaction doped with D_2O. Middle: D_2O shake on **Cu1a**/**Cu1b** mixture (**Cu1a** omitted for clarity). Bottom: D_2O shake on **Tz1.BF$_4$**. **272**

Figure 223. ^{1}H NMR (400 MHz, CD_3CN) spectrum obtained from the electrochemical reaction of **Tz1.BF$_4$** with Cu electrodes and D_2O dopant, with integral values shown below peaks. CH_2 peak used as reference, CH and NH peaks show lower integral values than predicted. **273**

Figure 224. Possible route to deuterated **Cu1b.BF$_4$** *via* deuterium hydrogen exchange, before and after electrochemical reaction. **273**

Figure 225. Reaction progress as a function of Q during the electrochemical synthesis of **Cu1a**/**Cu1b** mixture. **274**

Figure 226. Two possible mechanistic pathways for the formation of **Cu1b.BF$_4$**. **276**

Figure 227. Possible route to the formation of the diimine ligand from either **Tz1.BF$_4$** (top) or NHC (bottom), assisted by adventitious water. **277**

Figure 228. Possible products from electrochemical reaction of **Tz1.BF$_4$** with Fe. **278**

Preface – An Introduction to N-Heterocyclic Carbenes

This chapter serves to provide an introduction to N-heterocyclic carbenes. A historical background to the isolation of stable carbenes is provided, followed by a discussion of the various factors influencing carbene stability. The use of NHCs as ligands for transition metal complexes is the main concern of this thesis and thus a description of their ligand properties is provided, along with an overview of applications. The most common synthetic strategies for preparing NHC complexes are described.

1 Carbenes – A Quest for Stability

The quest for the isolation of persistent carbenes began in 1895, when J. U. Nef declared that “It will now be my next task to prepare methylene, or derivatives of it which are free of nitrogen..”.[1,2] The rest of the community clearly lacked the resolve of Nef, and progress in this area has been limited; methylene remains unisolated, and even nitrogen containing aminomethylene requires trapping in an inert argon matrix at 12 K to be observed.[3]

The 1960s and 70s brought the publication of seminal examples of metal carbene complexes. In 1964, Fischer reported the preparation of tungsten carbene complex **1**, and hence gave his name to all carbenes in this class (Figure 1).[4] Four years later Öfele and Wanzlick independently reported the preparation of what would later become known as the first N-heterocyclic carbene (NHC) complexes (**2**, **3** - Figure 1).[5,6] In 1974, Schrock developed a new family of carbene ligands: those which are not stabilised by a π-donor substituent (**4** - Figure 1).[7] While carbenes as ligands became an established part of organometallic chemistry, the isolation of a free carbene remained remote.[8]

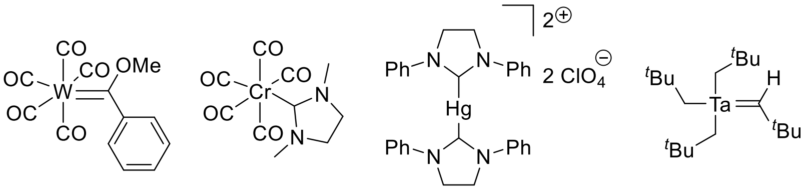

1 **2** **3** **4**

Figure 1. Early carbene complexes.[4–7]

Bertrand *et al.* arguably have a claim to the synthesis of the first stable carbene. In 1988, the preparation of compound **6** *via* either photolysis or thermolysis of the diazo-compound **5** was reported (Figure 2). The resulting product could exist in any of three canonical structures, one of which (**6a**) is a carbene. Although the NMR spectroscopic data appeared to indicate the existence of **6** in the form of **6c**, subsequent reactivity studies demonstrated the likelihood of form **6a** being the dominant species.[9,10]

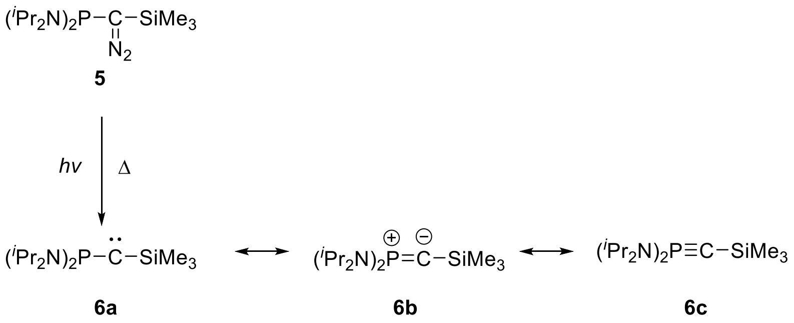

Figure 2. Synthesis of Bertrand's carbene and resonance forms.[9,10]

A few years later, Arduengo reported on the preparation of a stable, crystalline carbene (**7** - Figure 3). This was the first unambiguous example of a persistent carbene, stable enough to be bottled (in the absence of air and moisture), heated to 240 °C, and perhaps most excitingly, characterised crystallographically. In the end, the preparation of such a species was relatively straightforward, being achieved by deprotonation of an imidazolium salt using NaH in THF, with a catalytic quantity of DMSO (Figure 3).[11] The resulting carbene is stabilised by the two neighbouring nitrogen atoms and exists in the singlet state (*vide infra* - 3.1). The isolation of the first NHC heralded a brave new world in organometallic chemistry, with NHCs now near ubiquitous in this area.[12]

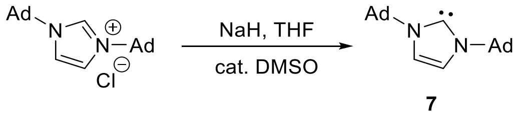

Figure 3. Synthesis of Arduengo's carbene.[11]

Air stable NHCs have also been reported. Analogues of the well-known IPr and IMes NHCs, in which the hydrogen atoms on the backbone are replaced by bromine, are reported to be stable in air in the presence of a dessicant (**8**, **9** - Figure 4). The reasons for the increased air stability are not clear. The geometry of **8** in the solid state is such that there is greater steric protection of the carbene centre than in IPr. However, the structure of ClIPr reveals even greater steric protection, and yet ClIPr is less air tolerant than **8**. It is suggested by the authors that increased hydrophobicity may be the main contributing factor to the air tolerance of these species.[13]

Recently, another breakthrough was made in the synthesis of stable carbenes, with the report by Bertrand *et al.* of the isolation of a stable monosubstituted carbene (**10** - Figure 4). A series of iminium-type carbene precursors were prepared with increasingly bulky aryl substituents. These were deprotonated using KHDMS at -78 °C in an attempt to prepare the free carbene derivatives. The use of 3,5-diphenylphenyl substituents led to the observation of a carbenic species by ^{1}H NMR spectroscopy which could not be isolated. Addition of further bulk in the form of CF_3 groups allowed for the crystallisation of the free monosubstituted carbene at -40 °C.

10 exists in the singlet state and calculations indicate that this is among the most π-accepting carbenes known.[14]

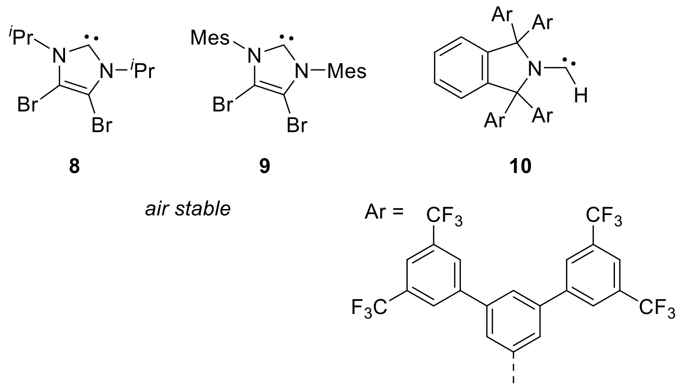

Figure 4. Recent examples of stable carbenes.

2 Carbene Multiplicity

Key to understanding the properties of carbenes is the spin state they exist in. A carbene is defined as a divalent species with 6 valence electrons, and thus has two electrons which are not involved in bonding, and two orbitals in which to put them. As a consequence there are four possible spin states, depending on the arrangement of the electrons (Figure 5). The natural ground state for a carbene is dependent on the energy gap between the two orbitals, and the pairing energy of the electrons.[15,16] This gap is influenced by a number of factors.

The nature of the orbitals is dependent on the geometry at the carbene centre. For a linear geometry, the carbon is sp hybridised, with two degenerate p-orbitals (Figure 5). As the carbene substituents move closer together (from a linear to a bent geometry) the orbital hybridisation changes to sp^2 and hence the two orbitals are no longer degenerate. There is now one lower energy orbital with significant s-orbital character (termed σ), and a higher energy orbital, which is essentially the unchanged p_y orbital (now termed p_π) (Figure 5). Given the additional stabilisation afforded to the σ-orbital as a consequence of sp mixing, the singlet ground state tends to be favoured in carbenes with a bent geometry.[15,16]

The singlet-triplet gap is also influenced by the substituents of the carbene. Computational investigations on the substituent effect have found an increase in singlet state stability when the carbene has adjacent electron withdrawing groups (Figure 6). For example, a triplet state is predicted for CLi_2 and CH_2, whilst CHF and CF_2 are predicted to have a singlet ground state.[17,18] Electron withdrawing groups are able to stabilise the “lone pair” of the carbene in a singlet state, by lowering the energy of the sigma orbital.

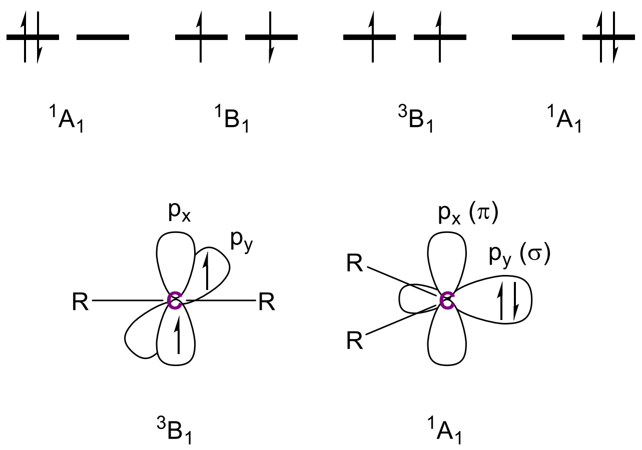

Figure 5. Top: Four possible electronic states for a carbene. Bottom: Orbital diagram for linear (left) and bent (right) carbene geometries.

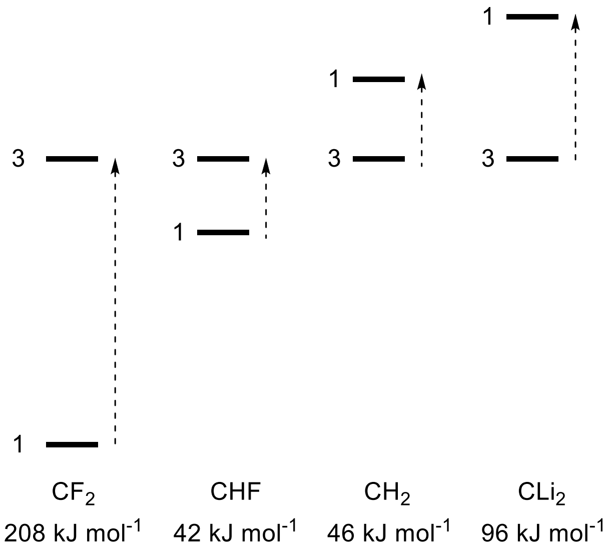

Figure 6. Estimated singlet-triplet energy gaps for carbenes.

3 Properties of NHCs

3.1 Structure and Stability

Arduengo's carbene was the first example of an N-heterocyclic carbene, that is, a stable carbene within a nitrogen heterocycle. NHCs are singlet carbenes, as would be expected based on their geometry and electronic environment (*vide supra* - 2).[12] X-ray photoelectron spectroscopy has confirmed that the HOMO of an NHC with ^{t}Bu nitrogen substituents is indeed a lone pair centred on the carbene carbon.[19] A crystallographic investigation using X-ray and neutron diffraction also found evidence for a lone pair at this position for 1,3,4,5-tetramethylimidazol-2-ylidene.[20]

The electronic argument for the stability of NHCs arises chiefly from the nitrogen atoms adjacent to the carbenic carbon. The nitrogen atoms not only withdraw electrons inductively and provide stability to the lone pair, they additionally stabilise the vacant p_π orbital through mesomeric electron donation.[12] This is often termed push-pull stabilisation (Figure 7).

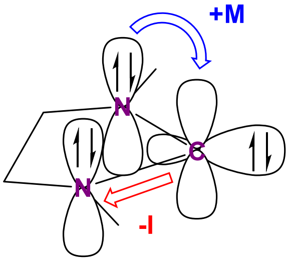

Figure 7. Push-pull stabilisation of NHCs.

The stability of Arduengo's carbene was initially purported to arise not only from the adjacent nitrogen atoms, but also the steric protection afforded by adamantyl substituents, and aromatic stabilisation within the ring. The role that π-delocalisation plays in the stability of NHCs has been the subject of much debate.

A range of methods have been used to investigate the importance of aromatic stabilisation. Computational studies suggest that NHCs exhibit significant π-delocalisation, though to a lesser extent quantified as 55.8%, than standard aromatic systems (e.g. benzene, imidazolium cation). This was confirmed by analysis of magnetic properties, although the bond lengths and charge density analysis pointed to a smaller contribution. The carbon-carbon double bond is believed to provide ~105 kJ mol^{-1} of stabilisation relative to the saturated equivalent, which explains the increased stability of imidazolylidenes over imidazolinylidenes.[21,22]

Steric protection can prevent dimerization into enetetraamine species. It is generally accepted that the tendency of an NHC to dimerise is a subtle blend of steric and electronic effects; an increase in electronic stabilisation makes an NHC less likely to dimerise, whilst bulky substituents may provide kinetic stabilisation. Thus less electronically stable NHCs (e.g. saturated rings) may be prevented from dimerisation by application of steric bulk.[16]

3.2 NHCs as Ligands

NHCs are often compared with phosphines in terms of their ability to act as ligands for transition metal complexes. Phosphines are known to be σ-donor/π-acceptor ligands, but with NHCs the picture is more complex, and the subject of much debate.[23] The reason for the debate likely stems from the fact that the extent to which an NHC-metal bond has a π component is very dependent on the metal centre. While NHCs can form complexes in situations where π-bonding is an impossibility, in electron rich metal centres a π component may be invoked.[23–27] Nonetheless, in most cases the bond between an NHC and a metal is considered to be single, in accordance with the free rotation about it that is generally observed.[12]

The enhanced σ-donor ability of NHCs as compared to phosphines is often given as a reason for their success as supporting ligands, particularly in catalysis.[28,29] Quantification of this effect is generally achieved through use of the Tolman Electronic Parameter (TEP). This compares CO stretching frequencies in metal-carbonyl complexes substituted with the relevant phosphine or NHC ligand. Traditionally $[Ni(CO)_3L]$ is used, with the A_1 stretching mode being examined.[30] Greater net electron donation from the ligand will result in more electron density at the metal centre, leading to a weaker C-O bond due to increased back-donation from a metal d-orbital into the π* orbital (Figure 8).

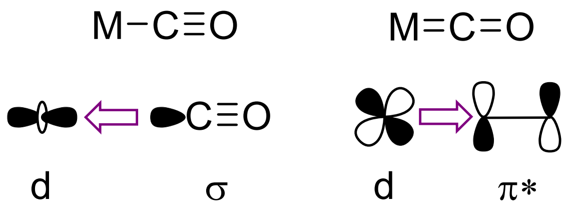

Figure 8. Orbital basis for TEP.

TEP values obtained using the nickel complex for tertiary phosphine ligands vary from 2060-2110 cm^{-1}, whilst for NHCs the values are 2048-2058 cm^{-1}, clearly indicating the increase in electron donation from NHCs.[23,31] It is important to note that the TEP is an indirect measure of σ-donation; in fact TEPs report on the quantity of electron density at the metal centre, which is a product of σ-donation and π-donor/acceptor effects.

The steric stress exerted on a metal centre by an NHC is also an important property to be considered. The size of phosphine ligands can be measured by their cone angle; NHCs fill a different space and are classified according the measure % buried volume ($\%V_{bur}$), a measure which has also been applied to other ligand classes. A sphere of radius 3 Å centred on a metal at a distance of 2 Å from the carbene carbon is visualised, and the percentage of space occupied by the NHC ligand is calculated, thus NHCs with different substituents can be compared. It has been noted that a greater $\%V_{bur}$ correlates with a lower bond dissociation energy.[32]

3.3 Applications of NHC Complexes

NHC complexes have found innumerable applications in diverse fields over the past 3 decades. Their application in materials and medicinal chemistry is well documented.[33–36] The most notable application of NHCs has been in the field of catalysis, with the most famous examples being Ru-NHC complexes for alkene metathesis (e.g. 2nd generation Grubbs catalyst - **11** - Figure 9), and Pd-PEPPSI complexes for cross-coupling (**12** - Figure 9).[37,38] In the case of the Grubbs catalyst, the enhanced σ-donor properties of the NHC vs. the previously employed phosphine confers enhanced activity and improved air and moisture stability.[39–41] The Pd-PEPPSI catalysts owe their activity to the steric bulk around the metal centre, which facilitates reductive elimination of the coupled products.[42]

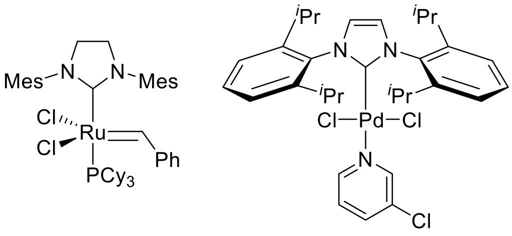

11 **12**

Figure 9. Second generation Grubbs catalyst and Pd-PEPPSI complex.

The wide range of the application of NHCs in catalytic reactions has been described in numerous review articles.[28,29,43–50] A description of the application of NHC complexes to transfer hydrogenation catalysis is provided in Part 1 Chapter 1.

4 Synthesis of NHCs and NHC Complexes

4.1 Preparation of NHC precursors

An attractive feature of NHCs as ligands, is the ease with which their steric and electronic properties can be tuned by variation of the nitrogen substituents. A wide variety of functional groups can be introduced at these positions, with the most common being aryl, alkyl, pyridyl, ester, ketone, ether or phosphine.[51]

NHCs have been prepared which demonstrate a wide variety of different ring architectures, with 5-membered rings being the most common.[2,8,52–54] Of these, imidazolium salts are the most frequently used precursors, due to their ease of synthesis and the greater stability of the subsequently formed carbene.[2,55] There are two main methods used for the preparation of imidazolium salts: a one-pot condensation reaction, or alkylation of an already formed imidazole ring.[2,55]

If starting from imidazole, this must first be deprotonated before reaction with an alkyl halide to effect either mono or disubstitution, depending on the stoichiometry used (Figure 10). This therefore allows access to both symmetrically and unsymmetrically substituted imidazolium salts.[2] This method is generally limited to primary alkyl halides, although Ullman-type coupling reactions can in some cases be used to prepare 1-aryl-imidazoles.[2,56]

The one-pot acid-catalysed condensation reaction proceeds *via* reaction of 2 equivalents of primary amine with glyoxal and formaldehyde, to generate a diamine species *in situ* which undergoes a cyclisation reaction (Figure 10).[8] This allows access to symmetrically substituted imidazolium rings that bear substituents that cannot be introduced using the substitution method.[2] This method does however become unfavourable for bulky systems, and has been noted to produce impure material.[8,57] Performing the reaction in two steps can lead to purer product, as can modifications to the solvent system or acid catalyst. In general, it has been observed that this chemistry can be capricious and optimisation of reaction conditions for each substrate may be necessary.[57]

A combination of the two methods can be used to prepare unsymmetrical imidazoliums, for example, with one aryl and one alkyl substituent. In this case glyoxal and formaldehyde are reacted with one equivalent of a relevant ammonium chloride (Figure 10).[58] The N-substituted imidazole obtained can then be reacted with a further alkylating agent.

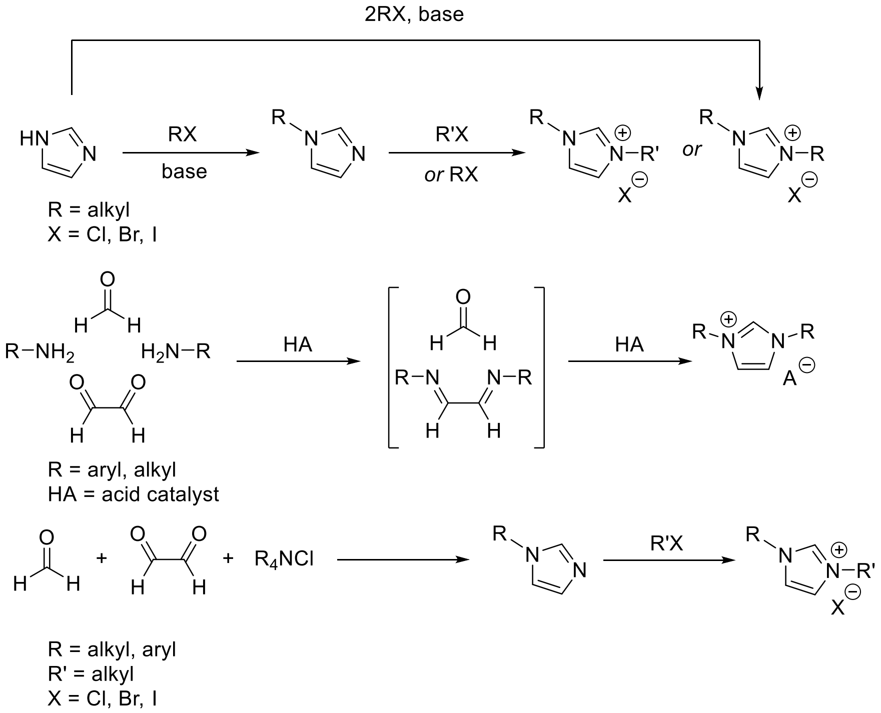

Figure 10. Synthetic strategies for the synthesis of imidazolium salts.

Imidazoliniums, benzimidazoliums, and triazoliums can all be prepared using similar methods.[2,54] Imidazoliniums are often prepared *via* a cyclisation reaction using a 1,2-diaminoethane and a trialkylorthoformate which supplies the proto-carbene carbon. The cyclisation step is generally tolerant and high yielding, thus the range of architectures is limited only by the ease with which the necessary diamine is prepared.[54] Modification of the diamine species allows triazolium and 6 or 7-membered heterocycles to be prepared in this way. Benzimidazoliums can be prepared by cyclisation of phenylene diamines; alkylation of the preformed benzimidazole is also possible.[54,59,60]

4.2 Preparation of Free Carbenes

As with Arduengo's carbene, the preparation of NHCs from their precursor structures is generally achieved through deprotonation with a strong base, in an aprotic solvent under anhydrous conditions (Figure 3). Many bases are appropriate including NaH, KH, n-BuLi, KHMDS, $LiAlH_4$, K^tBuO, although NaH and KH have been found to require addition of catalytic ^tBuO anion to progress quickly.[2,8]

An extremely efficient method of deprotonation was developed by Herrmann *et al.* using NaH in liquid ammonia. An approximate 5:1 ratio of ammonia:THF was used as the solvent for the reaction. On addition of NaH, deprotonation is achieved in minutes with yields typically in excess of 95%. This method was applied to a range of NHC precursors, and was also used to isolate the first example of a persistent dicarbene.[61,62] Although the reaction improves on existing methods in which deprotonation might take several hours, the use of liquid ammonia, and the requirement for the reaction to be cooled using cryogens makes this method considerably less attractive.

4.3 Preparation of NHC complexes

An isolated free carbene can be used to prepare metal-NHC complexes, for example by a ligand exchange reaction (known for CO, PR_3 and py) or by cleavage of a dimeric structure bridged by halides, CO, or MeCN (Figure 11).[63] Although pleasing in its simplicity, the difficulty associated with the handling of the free carbene presents a significant drawback. Thus, a more common method is the *in situ* deprotonation of the proto-carbene using an external base in the presence of a metal precursor (Figure 11).[12,63] One benefit of this route is that weaker bases such as NEt_3, NaOAc and Cs_2CO_3 are also competent. These bases have pKa values well below that of a typical NHC precursor; the reasons for their effectiveness are not clear, but it is likely that the complexation reaction provides a driving force for the equilibrium process.[63,64]

In situ deprotonation can also be achieved by using a basic metal, for example one bearing alkoxide, acetate or hydride ligands.[2] This was the method used by Wanzlick and Öfele in the preparation of the first NHC complexes.[5,6] Since then, this has been demonstrated for a range of transition metals including Pd, Ni, Rh, Ir, Ru, Cr, Mo, and W.[63]

A related and widely applied method makes use of Ag_2O as a basic metal. The reaction, which can be performed step-wise or in one pot, relies on the synthesis of a Ag-NHC complex which subsequently acts as a carbene transfer agent to move the NHC ligand onto another metal (Figure 11). The method utilises the labile nature of the Ag-NHC bond, with the precipitation of a highly insoluble silver halide salt acting as a driving force. The preparation of the Ag complexes is achieved in DCM at room temperature, often in air, thus the method benefits from extremely mild conditions. Subsequent transmetallation has been demonstrated for many metals including Au, Cu, Ni, Pd, Pt, Rh, Ir, and Ru, and the method is found to have broad applicability.[2,63,65] More recently, copper-NHC complexes have been demonstrated to be efficient carbene transfer agents to metals including Pd, Au, Ni, Ru, Cr and Rh.[66,67]

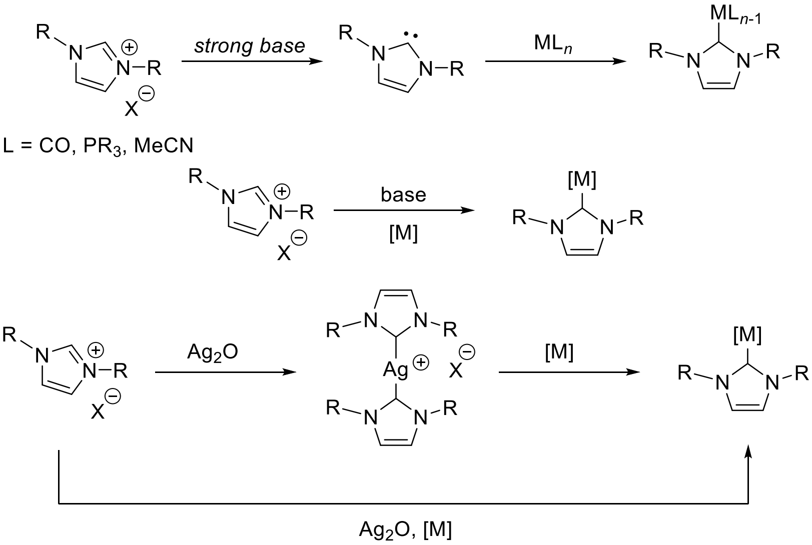

Figure 11. Common routes to NHC complexes: reaction with the free carbene, *in situ* deprotonation, and transmetallation using Ag_2O.

The above constitute the most common routes to NHC complexes, however there are other methods. Group 10 metals in the 0 oxidation state may undergo an oxidative addition reaction on a C-H or C-I proto-carbene bond to form NHC complexes (Figure 12).[8,63] In a similar vein, neutral NHC dimers (enetetraamines) can be reacted directly with metals of groups 6, 8, 9 or 10 to form complexes (Figure 12). The reactions occur *via* the cleavage of a halide bridged dimer, or by displacement of a neutral or anionic ligand.[68–70]

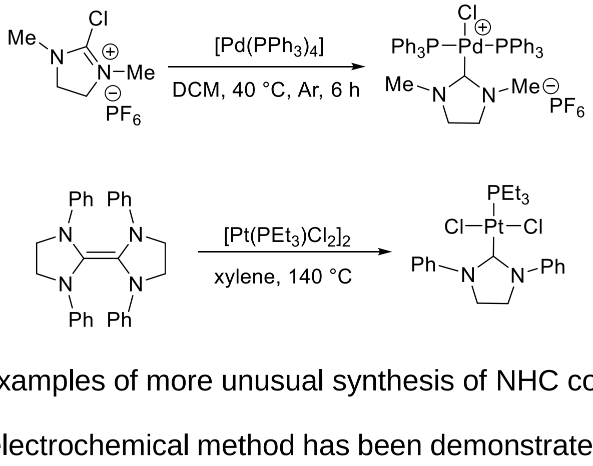

Figure 12. Examples of more unusual synthesis of NHC complexes.[68,71]

More recently, an electrochemical method has been demonstrated to be effective for the preparation of NHC complexes - this is described in Part 2 Chapter 1.

List of References

1 J. U. Nef, *Justus Liebigs Ann. Chem.*, 1895, **287**, 265–359.

2 F. E. Hahn and M. C. Jahnke, *Angew. Chemie Int. Ed.*, 2008, **47**, 3122–3172.

3 A. K. Eckhardt and P. R. Schreiner, *Angew. Chemie Int. Ed.*, 2018, **57**, 5248–5252.

4 E. O. Fischer and A. Maasböl, *Angew. Chemie Int. Ed.*, 1964, **3**, 580–581.

5 H.-W. Wanzlick and H.-J. Schönherr, *Angew. Chemie Int. Ed.*, 1968, **7**, 141–142.

6 K. Öfele, *J. Organomet. Chem.*, 1968, **12**, 42–43.

7 R. R. Schrock, *J. Am. Chem. Soc.*, 1974, **96**, 6796–6797.

8 P. de Frémont, N. Marion and S. P. Nolan, *Coord. Chem. Rev.*, 2009, **253**, 862–892.

9 A. Igau, H. Grutzmacher, A. Baceiredo and G. Bertrand, *J. Am. Chem. Soc.*, 1988, **110**, 6463–6466.

10 A. Igau, A. Baceiredo, G. Trinquier and G. Bertrand, *Angew. Chemie Int. Ed.*, 1989, **28**, 621–622.

11 A. J. Arduengo, R. L. Harlow and M. Kline, *J. Am. Chem. Soc.*, 1991, **113**, 361–363.

12 M. N. Hopkinson, C. Richter, M. Schedler and F. Glorius, *Nature*, 2014, **510**, 485–96.

13 S. K. Furfari, M. R. Gyton, D. Twycross and M. L. Cole, *Chem. Commun.*, 2015, **51**, 74–76.

14 R. Nakano, R. Jazzar and G. Bertrand, *Nat. Chem.*, 2018, **10**, 1196–1200.

15 D. Bourissou, O. Guerret, F. P. Gabbaï and G. Bertrand, *Chem. Rev.*, 2000, **100**, 39–91.

16 H. Jacobsen, A. Correa, A. Poater, C. Costabile and L. Cavallo, *Coord. Chem. Rev.*, 2009, **253**, 687–703.

17 J. F. Harrison, *J. Am. Chem. Soc.*, 1971, **93**, 4112–4119.

18 J. F. Harrison, R. C. Liedtke and J. F. Liebman, *J. Am. Chem. Soc.*, 1979, **101**, 7162–7168.

19 A. J. Arduengo, H. Bock, H. Chen, M. Denk, D. A. Dixon, J. C. Green, W. A. Herrmann, N. L. Jones, M. Wagner and R. West, *J. Am. Chem. Soc.*, 1994, **116**, 6641–6649.

20 A. J. Arduengo, H. V. R. Dias, D. A. Dixon, R. L. Harlow, W. T. Klooster and T. F. Koetzle, *J. Am. Chem. Soc.*, 1994, **116**, 6812–6822.

21 C. Heinemann, T. Müller, Y. Apeloig and H. Schwarz, *J. Am. Chem. Soc.*, 1996, **118**, 2023–2038.

22 C. Boehme and G. Frenking, *J. Am. Chem. Soc.*, 1996, **118**, 2039–2046.

23 D. J. Nelson and S. P. Nolan, *Chem. Soc. Rev.*, 2013, **42**, 6723–6753.

24 X. Hu, I. Castro-Rodriguez, K. Olsen and K. Meyer, *Organometallics*, 2004, **23**, 755–764.

25 D. Nemcsok, K. Wichmann, Gernot Frenking, D. Nemcsok, K. Wichmann and G. Frenking, *Organometallics*, 2004, **23**, 3640–3646.

26 H. Jacobsen, A. Correa, C. Costabile and L. Cavallo, *J. Organomet. Chem.*, 2006, **691**, 4350–4358.

27 A. Comas-Vives and J. N. Harvey, *Eur. J. Inorg. Chem.*, 2011, **2011**, 5025–5035.

28 S. Díez-González, N. Marion and S. P. Nolan, *Chem. Rev.*, 2009, **109**, 3612–3676.

29 T. N. Tekavec and J. Louie, *Top. Organomet. Chem.*, 2006, **21**, 159–192.

30 C. A. Tolman, *Chem. Rev.*, 1977, **77**, 313–348.

31 D. G. Gusev, *Organometallics*, 2009, **28**, 6458–6461.

32 A. C. Hillier, W. J. Sommer, B. S. Yong, J. L. Petersen, L. Cavallo and S. P. Nolan, *Organometallics*, 2003, **22**, 4322–4326.

33 L. Mercs and M. Albrecht, *Chem. Soc. Rev.*, 2010, **39**, 1903–1912.

34 R. Visbal and M. C. Gimeno, *Chem. Soc. Rev.*, 2014, **43**, 3551–3574.

35 W. Liu and R. Gust, *Coord. Chem. Rev.*, 2016, 329, 191–213.

36 S. B. Aher, P. N. Muskawar, K. Thenmozhi and P. R. Bhagat, *Eur. J. Med. Chem.*, 2014, 81, 408–419.

37 C. Samojłowicz, M. Bieniek and K. Grela, *Chem. Rev.*, 2009, **109**, 3708–42.

38 N. Marion and S. P. Nolan, *Acc. Chem. Res.*, 2008, **41**, 1440–1449.

39 J. Huang, E. D. Stevens, S. P. Nolan and J. L. Petersen, *J. Am. Chem. Soc.*, 1999, **121**, 2674–2678.

40 M. Scholl, T. M. Trnka, J. P. Morgan and R. H. Grubbs, *Tetrahedron Lett.*, 1999, **40**, 2247–2250.

41 M. Scholl, S. Ding, C. W. Lee and R. H. Grubbs, *Org. Lett.*, 1999, **1**, 953–956.

42 C. J. O'Brien, E. A. B. Kantchev, C. Valente, N. Hadei, G. A. Chass, A. Lough, A. C. Hopkinson and M. G. Organ, *Chem. Eur. J.*, 2006, **12**, 4743–4748.

43 F. Glorius, *Top. Organomet. Chem.*, 2006, 21, 1–20.

44 E. Peris, *Chem. Rev.*, 2018, 118, 9988–10031.

45 A. T. Normand and K. J. Cavell, *Eur. J. Inorg. Chem.*, 2008, **2008**, 2781–2800.

46 D. Gnanamgari, E. L. O. Sauer, N. D. Schley, C. Butler, C. D. Incarvito and R. H. Crabtree, *Organometallics*, 2009, **28**, 321–325.

47 F. Lazreg, F. Nahra and C. S. J. Cazin, *Coord. Chem. Rev.*, 2015, **293**–**294**, 48–79.

48 A. Nasr, A. Winkler and M. Tamm, *Coord. Chem. Rev.*, 2016, **316**, 68–124.

49 B. Ramasamy and P. Ghosh, *Eur. J. Inorg. Chem.*, 2016, **2016**, 1448–1465.

50 V. Charra, P. de Frémont and P. Braunstein, *Coord. Chem. Rev.*, 2017, 341, 53–176.

51 O. Kühl, *Chem. Soc. Rev.*, 2007, **36**, 592–607.

52 O. Schuster, L. Yang, H. G. Raubenheimer and M. Albrecht, *Chem. Rev.*, 2009, **109**, 3445–3478.

53 R. H. Crabtree, *Coord. Chem. Rev.*, 2013, 257, 755–766.

54 L. Benhamou, E. Chardon, G. Lavigne, S. Bellemin-Laponnaz and V. César, *Chem. Rev.*, 2011, **111**, 2705–2733.

55 W. A. Herrmann, *Angew. Chemie Int. Ed.*, 2002, **41**, 1290–1309b.

56 A. Kiyomori, J.-F. Marcoux and S. L. Buchwald, *Tetrahedron Lett.*, 1999, **40**, 2657–2660.

57 L. Hintermann, *Beilstein J. Org. Chem.*, 2007, 3, 22: DOI:10.1186/1860-5397-3-22.

58 A. A. Gridnev and I. M. Mihaltseva, *Synth. Commun.*, 1994, **24**, 1547–1555.

59 B. Bildstein, M. Malaun, H. Kopacka, K.-H. Ongania and K. Wurst, *J. Organomet. Chem.*, 1999, **572**, 177–187.

60 F. E. Hahn, C. Holtgrewe, T. Pape, M. Martin, E. Sola and L. A. Oro, *Organometallics*, 2005, **24**, 2203–2209.

61 W. A. Herrmann, M. Elison, J. Fischer, C. Köcher and G. R. J. Artus, *Chem. Eur. J.*, 1996, **2**, 772–780.

62 W. A. Herrmann, C. Köcher, L. J. Gooßen and G. R. J. Artus, *Chem. Eur. J.*, 1996, **2**, 1627–1636.

63 E. Peris, *Top. Organomet. Chem.*, 2006, **21**, 83–116.

64 D. J. Nelson, *Eur. J. Inorg. Chem.*, 2015, 2015, 2012–2027.

65 Z. Hou, A. Fujita, T. Koizumi, H. Yamazaki and Y. Wakatsuki, *Organometallics*, 1999, **18**, 1979–1985.

66 M. R. L. Furst and C. S. J. Cazin, *Chem. Commun.*, 2010, **46**, 6924–6925.

67 F. Nahra, A. Gómez-Herrera and C. S. J. Cazin, *Dalton Trans.*, 2017, 46, 628–631.

68 D. J. Cardin, B. Cetinkaya, M. F. Lappert, L. Manojlović-Muir and K. W. Muir, *J. Chem. Soc. D*, 1971, **0**, 400–401.

69 M. F. Lappert, *J. Organomet. Chem.*, 1988, **358**, 185–213.

70 M. F. Lappert, *J. Organomet. Chem.*, 2005, **690**, 5467–5473.

71 A. Fürstner, G. Seidel, D. Kremzow and C. W. Lehmann, *Organometallics*, 2003, **22**, 907–909.

Part I

Catalytic Activity of Iridium NHC-Carborane Complexes for Transfer Hydrogenation

Chapter 1
Introduction

This chapter provides background information that is pertinent to all chapters in Part 1 of this thesis. Where necessary, subsequent chapters contain introductory text on topics of peculiar relevance. Part 1 describes investigations into the catalytic activity of iridium complexes bearing NHC-carborane ligands, building on work of a previous group member. NHCs having been discussed in the preface, what follows is a description of carboranes, transfer hydrogenation catalysis, and work previously carried out in this area. The aims of the project are summarised at the end of the chapter.

1.1 Carboranes

1.1.1 History

Carboranes were first synthesised by industrial chemists in the 1950s. It was anticipated that organic borane compounds could be used to provide an efficient fuel source for aircraft and rockets. However, due to the detrimental effect of formed boron oxides and nitrides on the engines, efforts in this area were abandoned and attention turned to converting the boron hydride reserves into useful polymers.[1,2] This led to the discovery of novel organoborane compounds, including *ortho*-carborane ([1,2-$C_2B_{10}H_{12}$]) and *meta*-carborane ([1,7-$C_2B_{10}H_{12}$]), that would not be reported in the literature until the early 1960s.[3–13]

Meanwhile in the academic world, carboranes existed only in the minds of theoreticians. In 1955, it was calculated that dodecaborane $[B_{12}H_{12}]^{2-}$ should exist as a dianion.[14] The successful isolation of its salts in 1960 fuelled speculation that *ortho*-carborane should exist as a stable, neutral species.[15,16] A variety of small carboranes with three or four boron atoms were synthesised over the next few years, followed by the publication of previous industrial work in this area, in 1962 and 1963.[3–13] Two years later, the synthesis of the first metallacarborane complexes allowed a whole new field of inorganic chemistry to be born.[17,18] Since then, carboranes and carborane complexes have seen various applications including homogeneous catalysis, and in the areas of medicinal and materials chemistry.[1,19–21]

1.1.2 Structure and Bonding

The structure and bonding exhibited by carboranes is analogous to that seen in borane clusters. Borane clusters exist as deltahedra - structures that feature equilateral triangles as faces. For example, $[B_6H_6]^{2-}$ exists as an octahedron – with 8 triangular faces defined by boron vertices, whilst the largest known borane cluster,

$[B_{12}H_{12}]^{2-}$, exists as an icosahedron with 20 triangular faces. Clusters with the general formula $[B_nH_n]^{2-}$ are described as *closo*, whilst those in which one or two vertices have been removed are called *nido* and *arachno* respectively (Figure 13). For carboranes, a *closo* compound will have the formula $[C_xB_yH_{x+y}]$; *nido* and *arachno* clusters are likewise formed by removal of one or two vertices.

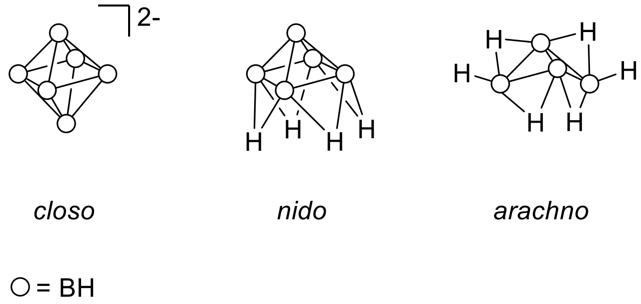

Figure 13. *Closo*, *nido*, and *arachno* borane clusters.

The bonding displayed by borane clusters is not easy to describe using classical bonding models. This is largely due to the boron atoms typically having 4 - 6 nearest neighbours, while having only 3 electrons available for bonding. In some simple cases the bonding can be described using a localised bonding approach, in which the cluster is considered to contain a combination of 2c2e and 3c2e bonds that is suitable to the number of electrons and molecular orbitals present.[1] However, with large cluster sizes and the presence of heteroatoms, this model quickly becomes too complex to be practically useful. Instead, clusters are generally considered to feature bonding that is delocalised over the whole cluster, often described as 3D aromaticity.[1] Calculations of the resonance energies of *closo*-borane clusters where $n \geq 6$ using molecular orbital methods give a strong indication of aromatic bonding, with $[B_{12}H_{12}]^{2-}$ and $[B_6H_6]^{2-}$ showing the greatest aromaticity.[22] Nuclear independent chemical shift values (a measure of ring currents), and magnetic susceptibilities also lend weight to the aromatic argument; these have been calculated for carbon substituted boranes, with $[CB_5H_6]^-$, $[C_2B_4H_6]$, $[CB_{11}H_{12}]^-$, and $[C_2B_{10}H_{12}]$ having the greatest aromatic stabilisation.[23]

Previously, borane clusters had been described as being electron deficient, due to having insufficient electrons to form 2c2e bonds. This is now considered to be bad practice, given that extra electrons confer no greater stability on these structures, in fact, $[B_{12}H_{12}]^{2-}$ is the most stable compound known to science.[1]

1.1.3 Wade's Rules

Whether a given cluster composition will adopt a *closo*, *nido*, or *arachno* structure can be predicted using Wade's rules.[24,25] Under these rules, the structure of the cluster is given by calculating the number of skeletal electrons, i.e. those that are involved in delocalised cluster bonding. Each boron vertex is viewed as a BH unit, which contributes 2 electrons spread over 3 bonding MOs. This is derived from each unit having 4 electrons (3 from boron, 1 from hydrogen), 2 of which are removed from consideration due to forming the 2c2e B-H bond. Hence each BH unit contributes 1 skeletal electron pair (SEP). In a boron cluster of *n* vertices, a *closo* cluster will have *n*+1 SEPs, a *nido* *n*+2, and an arachno *n*+3. The total number of skeletal electrons is found by considering the BH units, plus additional electrons from any hydrogens not contained within a BH unit and the charge on the cluster. Wade's rules are easily adapted for carboranes or other heteroatom containing clusters. For example a CH unit contributes 3 electrons, while an NH unit contributes 4.

The findings of Wade's rules are supported by molecular orbital theory. An *n* vertex cluster will have 3*n* cluster bonding MOs – for each vertex a p_x and p_y orbital which are tangential to the surface of the cluster, and a p_z directed towards the centre (Figure 14). Thus there will be *n* $\sigma p_{x/y}$ bonding MOs in addition to a bonding combination of all the p_z orbitals, yielding *n*+1 bonding MOs.[1,24,25]

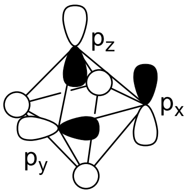

Figure 14. Orbital diagram indicating p_x, p_y and p_z orbital positions in a $[B_6H_6]^{2-}$ borane cluster.[25]

1.1.4 Synthesis and Reactivity

The $[C_2B_{10}H_{12}]$ cluster exists as one of three isomers: 1,2 (*ortho*), 1,7 (*meta*) or 1,12 (*para*), depending upon the relative positions of the two carbon atoms (Figure 15). The stability of the cluster increases with increasing distance between the carbon vertices. Thus *meta*-carborane can be formed by heating *ortho*-carborane to 465-500 °C, with *para*-carborane formed at 615 °C.[5,26]

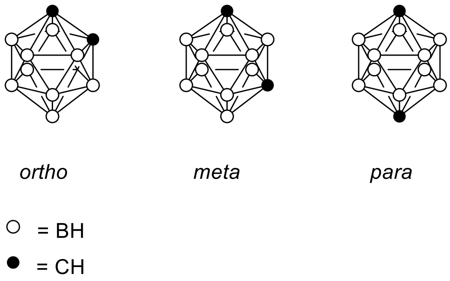

Figure 15. Structures of *ortho*, *meta*, and *para* 1,2-dicarbadodecaborane.

Ortho-carboranes can be formed from Lewis-base adducts of the parent borane cluster decaborane, by reaction with alkynes. The adduct may be pre-formed or generated *in situ*, allowing for a convenient one-pot reaction with MeCN acting as both the base and the solvent. Reactions of this type have been known for over 50 years, and are effective with a wide variety of substituted alkynes including aryls, alkyls, alkyl halides, and esters (Figure 16). However, reactions with di-substituted alkynes, or those containing acid or alcohol groups are ineffective.[9,10] More recently, reactions using internal alkynes have been shown to be effective when performed in ionic liquid solvent, or with the addition of a silver salt as a catalyst (Figure 16).[27–29] Preparation of *ortho*-carborane itself can be effected by reaction of decaborane and acetylene, however a more convenient route is reaction of decaborane with propiolic acid *tert*-butyl ester.[30] The ester group is unstable under the reaction conditions and is eliminated as CO_2 and *iso*-butene to produce *ortho*-carborane as the product (Figure 16).[31]

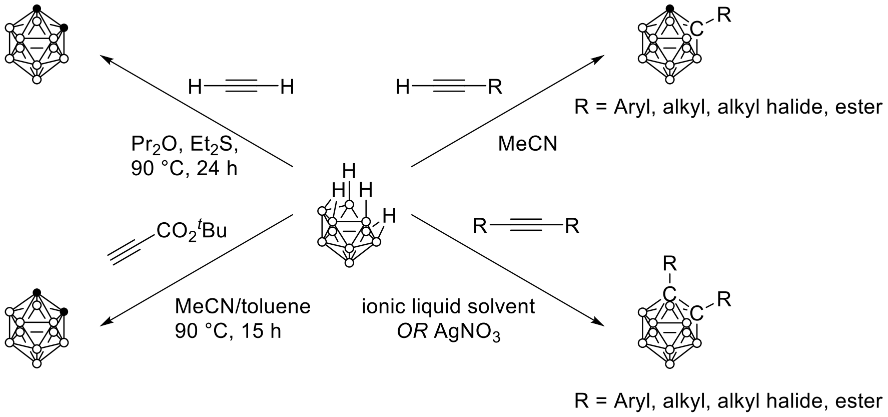

Figure 16. Synthetic routes to substituted 12 vertex carboranes.

If the desired alkyne is unavailable, or features a reactive group, then there are other possible routes to substituted carboranes. The CH protons in *ortho*-carborane are more acidic than those at boron, and therefore may be deprotonated using a strong base, such as *n*-BuLi. The lithiated carborane can then be substituted by an appropriate reagent, for example bromobutane or ethylene oxide.[7] Once obtained, the carborane cage is stable to oxidation, hydrolysis, and acid attack, but may form *nido*-caboranes on reaction with strong bases.[11,32] Carboranes are therefore often stable to subsequent manipulations of the carbon substituents, for example nucleophilic substitution or preparation of a Grignard at bromine.[7,11,33]

1.1.5 Transition Metal Bonding

Carboranes are unusual ligands, given that they can bind metals in three different ways: through a boron atom (B-H activation), carbon atom (C-H activation) or through the open face of a *nido*-cluster (Figure 17).[17,34,35] The open face binding mode is the most widely reported in the literature, with examples of complexes with many transition metals including Fe, Co, Mn, Re, Ni, Mo, W, Cu and Pd.[17,18,32,36,37] In this binding mode, 5 sp^3 hybridised orbitals from carbon and boron atoms in the framework combine to produce 3 bonding molecular orbitals. This can be compared to the bonding exhibited by the cyclopentadienyl anion (Cp), however due the hybridisation of the carborane orbitals, they are angled inwards towards the centre of the open face instead of perpendicular to the plane of the ring (Figure 17).[18] This gives the orbitals σ-bonding character and means *nido*-carboranes bind more strongly to metal centres than the Cp ligand. A wider variety of metal complexes can therefore be formed, for example with Cu.[1,38] Other important differences between the bonding of the *nido*-carborane anion and Cp are that the C_2B_3 ring is not planar and that the metal does not always sit above the centroid of the carborane. A "slip" toward the central boron atom of the C_2B_3 ring is often observed, being most significant in d^8 and d^9 species.[39]

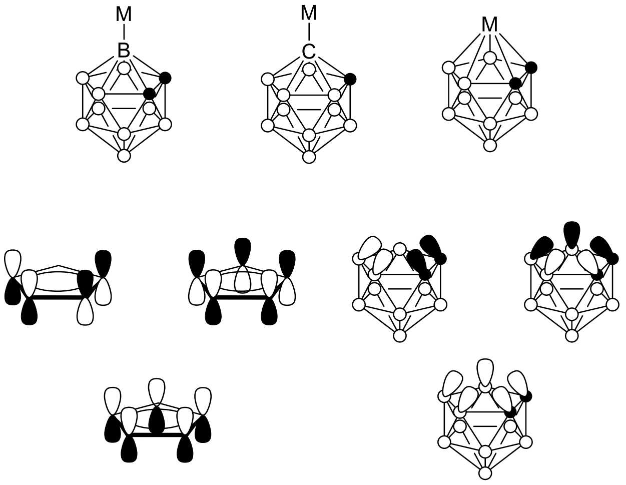

Figure 17. Top: Three binding modes available to carboranes. Bottom: Bonding orbital diagram for Cp (left) and *nido*-carborane (right).

Transition metal complexes featuring σ-bonds between the metal centre and a cage carbon or boron atom are less well studied.[1] Metal-carbon bonds can be formed from a lithiated carborane precursor, and have been demonstrated for various metals including Fe, Mn, Pd and Pt.[40,41] B-H activated complexes are known for transition metals including, Ir, Pd, Rh, Ru and Hg. The activation of the boron at the B3/6 vertices are usually the most favoured; these are adjacent to both carbon atoms, which being more electronegative than boron, polarise the C-B bonds and make the B-H protons more acidic.[42–45]

1.1.6 Applications in Catalysis

The vast majority of catalytic applications for carboranes can be found in the area of homogeneous transition metal catalysis. Transition metal carborane complexes and metallacarboranes are ideal for this, given their tunability through substituent groups, their chemical and thermal stability, and wide-ranging solubilities.[1,46] A selection of representative examples from the literature are given below. These have been selected for being either particularly prominent areas of carborane catalysis, or for featuring elegant exploitation of the unique properties of carboranes.

1.1.6.1 Alkene Polymerisation

A variety of *closo*-*ortho*-carborane complexes of mid-late transition metals have been applied to alkene polymerisation reactions, using methylalumoxane (MAO) as a cocatalyst. These mostly feature an exo-metallated carborane, in which both carbon atoms are bound to the metal or ligand architecture to form a complex with constrained geometry. Many examples use a pendant coordinating ligand on the carborane to form the chelate ring.[47–49] This type of architecture, featuring one strong donor ligand site and one labile one, is potentially useful for catalysis because the labile part of the ligand allows for facile generation of an active site. Jin *et al*. applied this principle in the synthesis of **1.1** which features a strongly binding carborane ligand and a labile picolyl group (Figure 18).

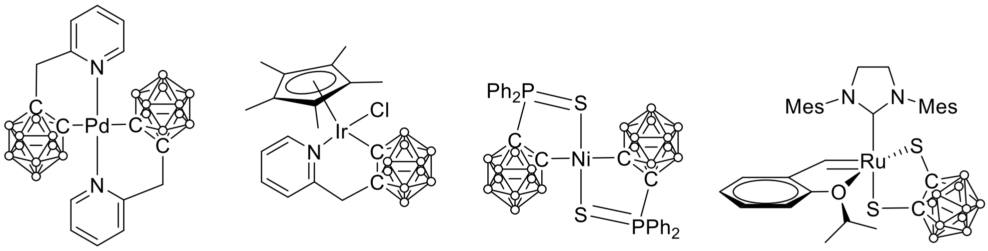

1.1 **1.2** **1.3** **1.4**

Figure 18. Structures of carboranyl catalysts for alkene polymerisation.

1.1 was found to be moderately active in the polymerisation of norbornene, producing a high molecular weight polymer in 30 minutes at 60 °C.[47] **1.2** uses a related architecture and was similarly active in the polymerisation of ethene, producing a very high molecular weight polymer in 30 minutes at only 30 °C (Figure 18).[48] A computational investigation into the activity of **1.2** found that the presence of the carborane facilitates the ethylene insertion step, by a transfer of charge from the carborane to the Ir centre. Additionally, a stabilisation effect due to hydrogen bonding interactions with the carborane BH bonds was observed for one of the intermediates. Interestingly, computational results also indicated that the boron coordinated complex ought to be more effective than carbon coordinated **1.2**.[50] Carborane-sulfur donor complex **1.3** was designed with the expectation that the stability of metal intermediates would be enhanced if coordinated by an inflexible ligand architecture; the chelating structure and the rigidity of the carborane are key in promoting this. **1.3** was found to have moderately high activity towards the polymerisation of norbornene, giving high molecular weight polynorbornene in 30 minutes at 30 °C.[49]

An alternative Ru catalyst structure was reported by Wang *et al.* for ring-opening metathesis polymerisation (ROMP), ring-opening cross-metathesis (ROCM) and cross-metathesis (CM). **1.4** showed excellent Z/E selectivity (98:2) for the ROMP of norbornene, and for the ROCM of norbornene and styrene (Figure 18). CM between terminal alkenes and (Z)-but-2-ene-1,4-diol was also investigated with generally good Z/E selectivity observed (85:15 – 97:3). A computational study was carried out to investigate the catalytic cycle, and compare the performance of **1.4** with the analogous catecholthiolate complex, in order to determine the effect of the carborane. It was noted that for **1.4** the transition state for the decomposition pathway had a higher barrier than that for formation of the Z-alkene product. Furthermore the Z-alkene product was at a lower thermodynamic minimum than that of the decomposition product. However the catecholdithiolate complex had energy barriers that were similar for the desired reaction and the decomposition pathway.[51]

1.1.6.2 Hydrogenation Reactions

Nido-ortho-carborane complexes have been shown to have activity towards the hydrogenation of alkenes. Many of these catalysts feature an *exo-nido* bound metal, that is the metal bound to the outside of the cage system, through a bridging hydrogen atom. This can be formed *via* tautomerisation from a parent metallocarborane.[1] The first example of a carborane containing Rh catalyst for hydrogenation of alkenes was complex **1.5** (Figure 19). Under a pressure of H_2 (1 atm) at 35 °C with 0.1 mol % catalyst loading, **1.5** was found to hydrogenate 1-hexene.[52] A more recent catalyst is complex **1.6**, which was also found to hydrogenate 1-hexene at 25 °C under a H_2 atmosphere (Figure 19). It was found to be 8 times more active than the well-known Wilkinson's catalyst $[RhCl(PPh_3)_3]$.[53]

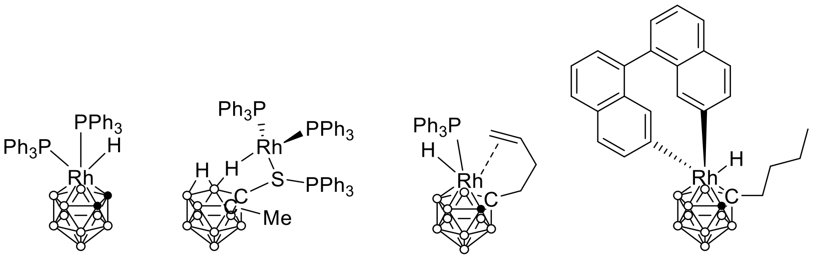

1.5 **1.6** **1.7** **1.8**

Figure 19. Carboranyl complexes for hydrogenation.

One of the most successful examples of a *nido*-carborane catalyst is complex **1.7** (Figure 19).[54] It was known that for complex **1.5** the rate of the hydrogenation reaction was inverse to the concentration of $PsPh_3$, strongly indicating that dissociation of a PPh_3 ligand is crucial for hydrogenation to occur. Hawthorne *et al.* reasoned that the ease of functionalisation of the carborane could be harnessed to improve catalytic activity. By substituting the carborane with a coordinating alkene, which subsequently undergoes hydrogenation and therefore ceases to be coordinated, a permanent active site can be generated. The initial rate of reaction for 3,3-dimethyl-butene was found to be 4 times faster than the best previously reported hydrogenation catalyst, at a lower catalyst loading. This represents not just one of the best carborane based catalysts, but at the time, was the most effective hydrogenation catalyst reported.[54] The BINAP derivative **1.8** was also highly successful, being capable of hydrogenating ketones with 100% conversions and enantiomeric excesses of more than 97% in ionic liquid solvents.[55]

1.1.6.3 Exploitation of Carborane Properties

One particularly interesting example of the unusual properties of carboranes being exploited can be found in catalysts **1.9** and **1.10** for ring-closing metathesis (RCM) (Figure 20). The same precursor ligand was used in the synthesis of both compounds; treated with TBAF in a THF/water solvent, the ligand undergoes deboronation, generating the *nido*-species, which can then be used to form complex **1.10**. The two complexes have opposite solubilities, with **1.9** being soluble in non-polar solvents and **1.10** being soluble in polar solvents. Furthermore, **1.10** was found to be reusable 10 times in ionic liquid media for RCM, demonstrating its robustness as a catalyst.[56]

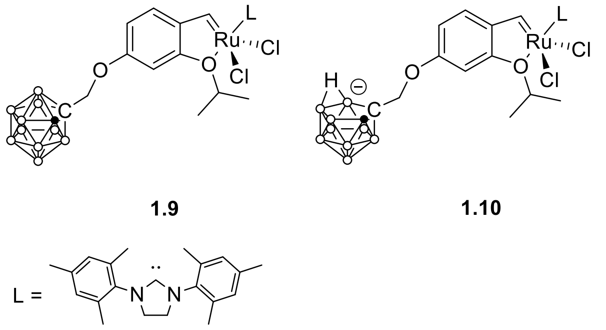

1.9 **1.10**

Figure 20. Carboranyl catalysts with complementary solubilities for ring-closing metathesis.[56]

Carboranes are often used for their rigid, 3D structure. Pincer ligands are often particularly effective for catalytic reactions due to the high stability they confer on complexes.[57] One member of this class of ligands is Phebox, which coordinates through one carbon and two nitrogen atoms as in **1.11** (Figure 21). **1.11** has been found to catalyse the asymmetric reductive Aldol reaction between benzaldehyde and *tert*-butyl-acetate with a 93% yield and a 94% ee, and also the asymmetric conjugate reduction of (E)-ethyl 3-phenylbut-2-enoate with a 99% yield and 98% ee.[58] Nakamura *et al.* have synthesised the analogous carborane ligand Carbox, and used it to form Rh complex **1.12** (Figure 21). It was anticipated that the enhanced rigidity of the pincer ligand due to the presence of the carborane would improve the catalytic performance of the complex.[57] The electronic properties of the carborane were also believed to be potentially beneficial for catalysis. It has been shown that the use of a carborane substituted phosphine ligand for a coupled Sonogashira/hydride transfer reaction is effective. Electron deficient phosphine ligands were also found to work well, so the authors propose that the reason for the success of the carborane is its electron deficiency.[59] Studies on complexes using Phebox-type ligands found that those which were electron withdrawing were better at promoting catalysis, therefore Carbox should be well placed to function as an efficient ligand for supporting catalytic processes. The results showed that complex **1.12** performed similarly to the analogous complex **1.11** for the asymmetric reduction of α-β unsaturated esters, but was more effective for the asymmetric reductive Aldol reaction.[57]

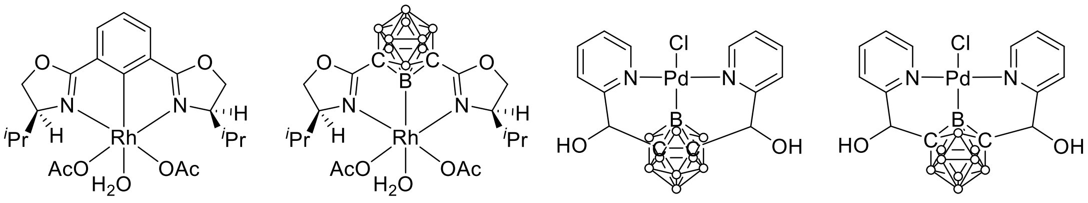

1.11 **1.12** **1.13** **1.14**

Figure 21. Pincer complexes for the reductive Aldol reaction (**1.11** and **1.12**) and Suzuki-Miyaura cross coupling (**1.13** and **1.14**).

Another example of rational design in carborane pincer complexes can be seen with Pd complexes **1.13** and **1.14**.[60] These feature an *ortho-* and *meta*-carborane pincer ligand respectively. In *ortho*-carborane, the B3/6 position is the most δ+ boron due to the proximity of the two more electronegative carbon atoms. In *meta*-carborane, the B2/3 position is the most δ+ boron, but this is not as electropositive as B3/6 in *ortho*-carborane. Therefore, the authors expected to see these electronic differences conferred on the metal centre, and thus a difference in catalytic activity between **1.13** and **1.14**. As the sterics are so similar between the two complexes, it should be possible to examine electronic effects in isolation. The study was moderately successful, and found the *ortho-* complexes to be more successful catalysts for Suzuki-Miyaura cross-couplings, although not by a large margin. In addition to offering mechanistic insight, the complexes were highly useful catalysts in their own right, due to requiring extremely low loadings, and the reactions being performed in water.[60]

A more unusual example of a carborane pincer complex featuring chelating N-heterocyclic silylenes (NHSi) was recently reported (Figure 22 - **1.15**). As with other pincer complexes, the carborane moiety provides a rigid structure to support the chelating ligands. Analysis of carbonyl stretching frequencies indicated the ligand to have extremely high σ-donor properties, higher indeed than many phosphines or NHCs. **1.15** was compared with the ferrocenyl analogue **1.16** for activity in a

Buchwald-Hartwig amination reaction and was found to be more active (93% vs 78%), which was attributed to electronic effects.[61]

Carborane pincer complex **1.17** featuring two carboranes was reported by Islam *et al*. This highly sterically encumbered catalyst was found to catalyse the imine formation reaction between piperidine and MeCN with a moderately high TON of 80.[62]

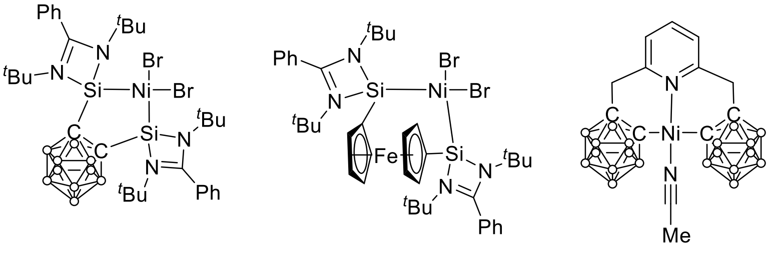

1.15 **1.16** **1.17**

Figure 22. Pincer complexes for Buchwald-Hartwig amination (**1.15** and **1.16**) and imine formation (**1.17**).

1.2 Transfer Hydrogenation Catalysis

Hydrogenation reactions are an extremely important class of transformation with applications in both the academic lab and in industries including pharmaceuticals, petrochemicals and fine chemicals.[63–67] Whilst the traditional approach to hydrogenation applies a pressure of hydrogen gas to a reaction mixture, there are many limitations to this approach. These include the necessity of handling hazardous H_2 gas, and the use of complex reaction set-ups. Therefore, in recent times a great deal of emphasis has been placed on hydrogen transfer reactions, in which hydrogen is transferred directly from one substrate to another (Figure 23). The method of transfer hydrogenation (TH) uses a donor hydrogen source, and a hydrogen acceptor, which could be an aldehyde, ketone, alkene, or imine. TH is a mild technique, using reagents that are easy to handle and environmentally benign.[63,65,68] Reactions typically use either IPA or formic acid as the proton source, in combination with an auxiliary base (e.g. KOH, K^{t}BuO), although base-free catalysis is known.[63,65,69,70]

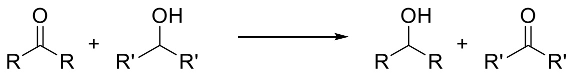

Figure 23. General scheme for transfer hydrogenation reaction using IPA as the proton source.

1.2.1 History

The first example of TH is generally considered to be Meerwein-Ponndorf-Verley (MPV) reduction. In 1925, Verley and, independently, Meerwein and Schmidt reported the reduction of aldehydes to alcohols using $[Al(OEt)_3]$.[71,72] This was followed in 1926 by a report from Ponndorf, extending the reaction scope to include ketone substrates, using [Al(^{i}PrO)$_3$].[73] These traditional Al catalysts suffer from the need for stoichiometric quantities and their extreme air and moisture sensitivity.[63] More recent developments have focussed on the use of lanthanide complexes in order to overcome these issues. Okano *et al.* have reported the use of a range of lanthanide alkoxide complexes for MPV reduction of ketones, with catalyst loadings as low as 0.15 mol%.[74] Success in this area has also been achieved using Cp complexes of Zr and Hf.[75] Whilst the catalysts were originally homogeneous, MPV reduction has also been performed heterogeneously.[76]

The mechanism of MPV reduction using Al catalysts is understood to proceed *via* a direct mechanism, in which both alcohol and carbonyl are coordinated to the Al.[63,77] The metal templates the substrates, allowing direct transfer of the hydrogen from alkoxide to carbonyl *via* a planar 6-membered transition state (Figure 24).[77]

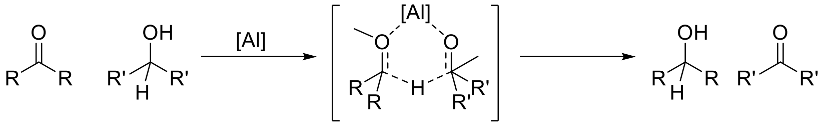

Figure 24. Mechanism for MPV reduction using an Al catalyst.

Ir catalysed TH was first reported in 1964. Haddad *et al.* described the use of $H_2[IrCl_6]$ and various derivatives to reduce cyclohexanones in the presence of IPA. The noted formation of acetone as a by-product led to the conclusion that the IPA acts as a hydrogen source, which was confirmed by deuterium labelling.[78] Subsequently, an Ir-H species was, for the first time, invoked to explain TH. It was reported that heating $H[IrCl_4(DMSO)_2].2DMSO$ in IPA produced the hydride species $[IrHCl_2(DMSO)_3]$. This was found to catalyse the reduction of 4-^{t}Bu-cyclohexanone, and thus was assumed to be an intermediate in the catalytic cycle starting from the parent complex.[79]

The first examples of asymmetric TH using an Ir catalyst were reported in the 1980s using chelating chiral N-donor ligands. Although the conversions were good, the enantiomeric excesses were between 15 and 50% depending on the substrate and catalyst used.[80,81] From these modest beginnings, Ir complexes have become some the most widely used catalysts for asymmetric TH in recent times.[63,82]

1.2.2 Notable Examples

Crabtree's catalyst is arguably the archetypal Ir hydrogenation catalyst (**1.18** -Figure 25).[83–86] First reported in the 1970s for hydrogenation, it has since been applied to TH reactions.[87] In the presence of molecular hydrogen the complex forms the active catalytic species, the dihydride complex **1.19** (Figure 25). The process is reversible, when a solution containing **1.19** is purged with nitrogen the original complex is recovered, albeit with partial hydrogenation of the COD ligand.[83,84]

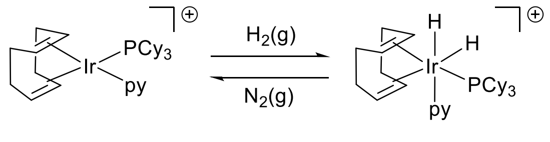

1.18 **1.19**

Figure 25. Crabtree's hydrogenation catalyst **1.18** and the dihydride species **1.19** postulated to be active in catalysis.[86]

An early example of an Ir catalyst bearing an NHC ligand for TH was a modification of Crabtree's catalyst. NHC complexes were prepared from the precursor $[Ir(COD)(py)_2][PF_6]$, using IMes, IPr, ICy, with the ICy complex giving the highest conversion in the shortest time for a TH reaction. It was noted that this ligand is the most electron donating, and hence the SICy analogue was prepared – although this was found to be less effective. A monohydride was proposed to be a key intermediate; heating a mixture of $[Ir(COD)(ICy)(py)][PF_6]$, IPA and KOH resulted in a product with a signal characteristic of a hydride species in the ^{1}H NMR spectrum, although the product itself could not be isolated.[87]

The concept of bifunctional TH catalysis was first invoked by the group of Noyori in 1997.[88] Asymmetric TH using chiral TsDPEN ligands and Ru-arene precursor complexes had already been demonstrated to give excellent enantioselectivities.[89] In this seminal paper however, Noyori was able to isolate the precatalyst, true catalyst and the reactive intermediate. The catalyst precursor is the expected product from reaction of S,S-TsDPEN with $[Ru(p\text{-cymene})Cl_2]_2$ and KOH (**1.20** - Figure 26).

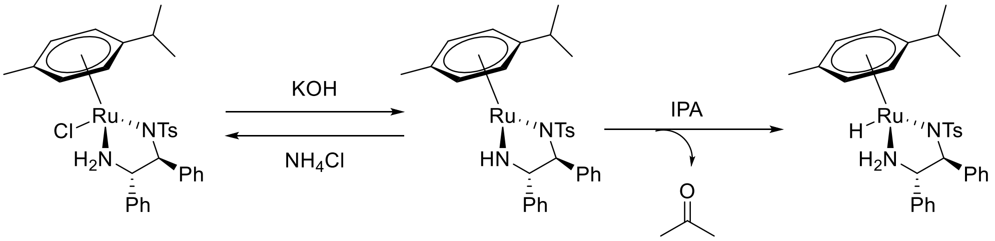

1.20 **1.21** **1.22**

Figure 26. Reactions of Noyori's bifunctional catalyst. **1.20** - precatalyst, **1.21** – reactive intermediate, **1.22** – catalyst resting state.

Treatment of **1.20** with one equivalent of KOH generates a 16 electron, coordinatively unsaturated complex (Figure 26 - **1.21**). This reaction may be reversed by application of ammonium chloride. Reaction of **1.21** with IPA generates the hydride complex **1.22** and eliminates acetone (Figure 26). The reaction also proceeds with MeOH and EtOH, but not ^{t}BuOH. Both **1.21** and **1.22** can be used as catalysts for the asymmetric TH of acetophenone, without the need for a base. The fact that both the metal and the ligand play a role during the catalysis led to it being termed bifunctional catalysis.

The 'winning formula' for Noyori's catalyst has also been applied to Ir complexes. These were reported independently by the groups of Noyori and Tani.[90–92] Mashima *et al.* note that the MCp* fragment (M = Rh, Ir) is isolobal with the Ru(arene) fragment of Noyori's successful complexes.[88,90] Both groups report the Ir and Rh complexes to be efficient but less competent than the original Ru complex. Mashima *et al.* were able to isolate both the 16 electron and hydride complexes **1.23** and **1.24** (Figure 27). Although attempts were made to repeat this with the Rh complex these were unsuccessful. Based on the colours seen during the catalytic reaction it was observed that the equilibrium for Ir seems to favour the hydride complex, whilst for Rh the 16 electron species is favoured.[91] This is interesting as although Rh complexes were more effective catalysts than the Ir complexes, this was not by a particularly large margin, so it would be surprising if a different mechanism was in play.

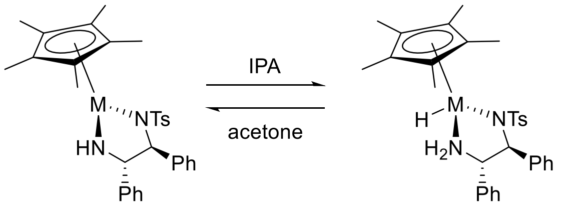

1.23 **1.24**

favoured for M = Rh *favoured for M = Ir*

Figure 27. Active catalytic species for Cp*M (M = Rh, Ir) complexes. Left: 16-electron complex **1.23**. Right: Hydride complex **1.24**.

Following on from these reports, there are numerous examples of complexes of the form [IrCp*(NHC)] which may be supplemented by a neutral or anionic ligand to give a cationic or neutral complex respectively (Figure 28).[63,93–97]

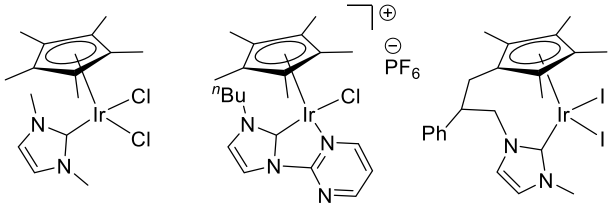

1.25 **1.26** **1.27**

Figure 28. Example catalysts based on the [IrCp*(NHC)] fragment.[95–97]

A variation on the standard IrCp*NHC fragment was reported by Pontes da Costa *et al.* (**1.27** - Figure 28).[97] Applying the principles that chelating ligands offer higher catalyst stability, whilst also noting that an [IrCp*] complex with a chelating bis-NHC ligand would bear just one potential vacant site, led to the rational design of a Cp*-NHC tethered catalyst for TH. Good conversions were achieved with **1.27** at low catalyst loadings.

1.2.3 Proposed Mechanisms

Whilst MPV reduction is understood to operate *via* a direct mechanism (*vide supra* - 1.2.1), transition metals are generally understood to operate by formation of a hydride species.[68,98] The species formed during catalysis may be either a monohydride or a polyhydride. In the case of the monohydride, the reaction may proceed through either an inner-sphere or outer-sphere mechanism.

1.2.3.1 Monohydride or Dihydride?

Bäckvall *et al.* carried out mechanistic studies into the origin of the metal hydride.[99,100] It is argued that the hydride may come either from the α-CH of the donor alcohol, or from both the CH and the OH. In the case of the latter, a dihydride species is invoked. Therefore, by using an α-deuterium labelled alcohol donor, and by monitoring the degree of deuterium incorporation in the product, a monohydride or dihydride mechanism can be proposed for a given catalyst (Figure 29).

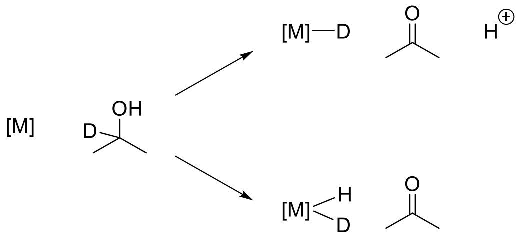

Figure 29. Monohydride (top) *vs* dihydride (bottom) mechanism. A dihydride mechanism leads to poor retention of deuterium in the α-position.[99]

Those catalysts which lead to a high degree of deuterium retention at the α-carbon proceed *via* a monohydride; those which provide a low degree of retention proceed *via* a dihydride (or polyhydride). Bäckvall initially examined the racemisation of (*S*)-α-deuterated 1-phenylethanol by two Ru catalysts (Figure 30).[99] The product from racemisation by catalyst **1.28** showed 37% deuterium retention, indicative of a dihydride intermediate. By contrast, catalyst **1.29** gave product with 95% deuterium retention, indicative of a monohydride intermediate.

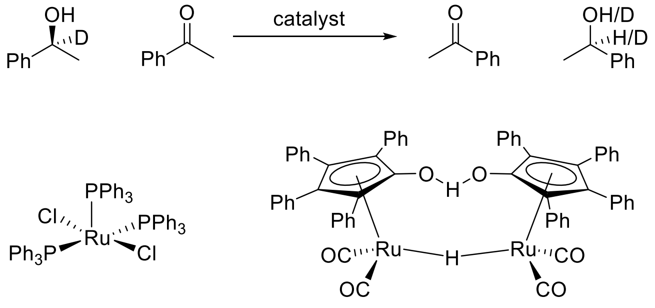

1.28 **1.29**

Figure 30. Racemisation of deuterium labelled 1-phenylethanol catalysed by Ru catalysts **1.28** and **1.29**.[99]

A subsequent study investigated 21 Ru, Rh and Ir catalysts. It was found that Rh and Ir catalysts all proceeded through a monohydride mechanism. The Ru catalysts tested gave mixed results, some proceeding *via* a monohydride and others *via* a dihydride.[100]

One example where a dihydride is invoked comes from Corberán *et al.*[69] It was suggested that the complexes **1.30**-**1.33** catalysed TH by an “O-H” activation to generate a 7-coordinate cationic monohydride Ir(V) species (Figure 31). β-hydride elimination generates the dihydride species, which hydrogenates the substrate. It is unclear how a 7-coordinate Ir centre can undergo β-hydride elimination, likely this would have to involve ring-slippage from the Cp*, or the triflate anion acting in a non-coordinating manner. The evidence for this mechanism stems from the observed production of hydrogen; additionally, the reaction proceeds without the need for an external base which does favour the direct O-H activation theory. In any case, the catalysts proved to be highly active at room temperature, achieving full conversion of the cyclohexanone in 15 minutes using a moderate catalyst loading (2 mol%).

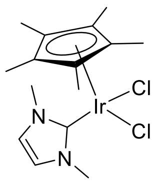

1.30

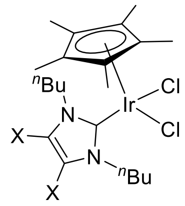

1.31 X = H
1.32 X = Cl
1.33 X = Me

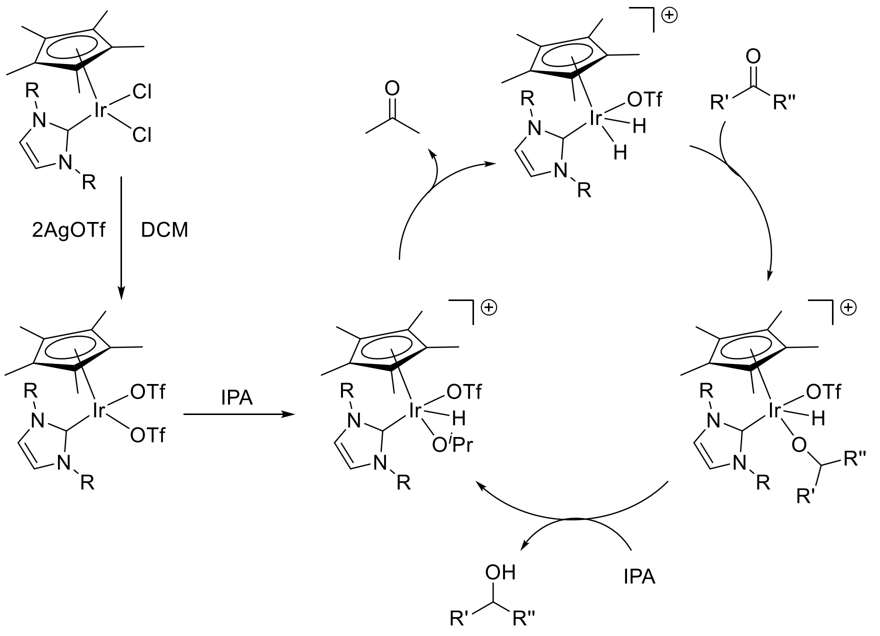

Figure 31. Top: Catalysts for TH **1.30**-**1.33**. Bottom: Proposed catalytic cycle featuring 7-coordinate Ir species.

The monohydride mechanism can be further divided into inner-sphere or outer-sphere routes. This classification refers to whether the substrate is coordinated directly to the metal centre (inner-sphere) or not (outer-sphere).[64] In the inner sphere process a hydride is formed *via* β-hydride elimination from a coordinated alkoxide. The hydride is transferred to a coordinated ketone, which is then substituted by the donor alkoxide, and re-protonated to form the alcohol product (Figure 32). Outer-sphere mechanisms usually involve the assistance of a ligand, termed bifunctional catalysis (*vide supra* - 1.2.2). The metal hydride is formed concurrently with the deprotonation of the OH group in the donor species by a neighbouring ligand. The incoming ketone is held in a 6-membered transition state during which the hydride attacks the carbonyl carbon and the oxygen is protonated by the neighbouring ligand (Figure 33).[100]

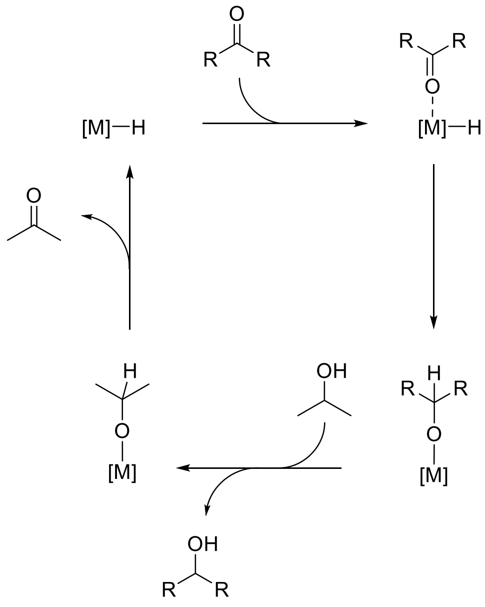

Figure 32. General mechanism for inner-sphere TH reaction.

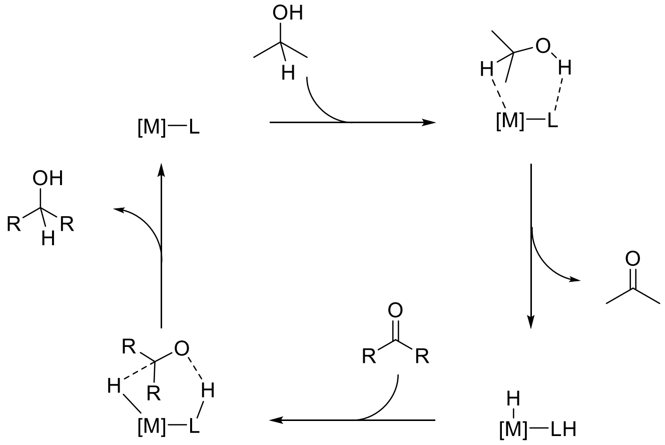

Figure 33. General mechanism for outer-sphere TH reaction.

1.2.3.2 Alternative Mechanisms

Although the monohydride mechanism is generally assumed to be in operation for transition metal catalysts, some studies paint a more complex picture. Computational work by Handgraaf *et al.* compared the mechanism for TH for Ru arene and Ir COD complexes. Whilst their findings agreed with those of Noyori for the Ru arene - indicating a monohydride mechanism, for the Ir complex the most favourable pathway was determined to be a direct mechanism, in which both the alkoxide and ketone are coordinated to the metal centre.[101,102] Similarly, a combined experimental and theoretical study on $[Ir(COD)(NHC)_2]^+$ complexes with functionalised NHCs, found that the energetics of the direct and hydride mechanisms were similar enough to conclude both could be in operation.[103]

An outer-sphere variant on the direct mechanism has been proposed for complexes **1.34** and **1.35** reported by Sabater *et al.* (Figure 34).[70] Cationic IrCp* complexes bearing an NHC and a chelating C-NH_2 donor were prepared and tested for TH activity using a range of ketones. These complexes are chiral at metal and also at the benzylic carbon. With both the racemic and enantiopure ligands a single diastereomer was produced, which computational evidence indicated might be slightly more thermodynamically favoured. The enantioselectivities achieved were poor to moderate, with the bulkier ^{n}Bu NHC complex giving better results. A mechanism was proposed based on computational evidence, featuring a hydrogen-bonding organised transition state (Figure 34). The propoxide interacts with one N-H bond with the substrate interacting with the other simultaneously. The hydride can then be transferred directly, along with the proton from the NH group. Thus, after initial activation, no base is required for the catalyst to turn over. The computational results agree well with the experimental data as they indicate similar energy barriers to the formation of the two enantiomers of the product - thus accounting for the low selectivities observed. This interesting new mechanism shows that in some cases catalysis can proceed without any vacant coordination sites, which is potentially advantageous, as it should provide higher stability catalysts.

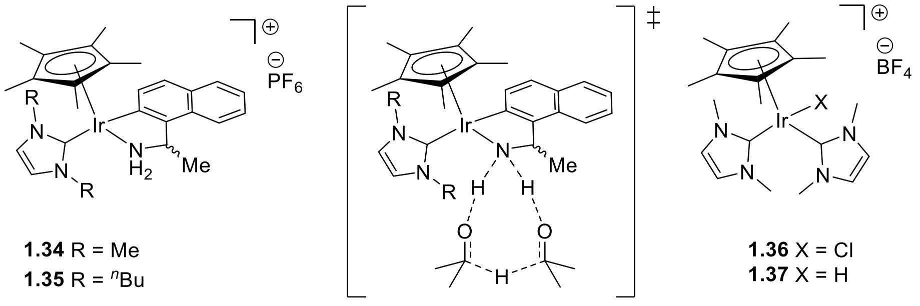

1.34 R = Me
1.35 R = ^{n}Bu

1.36 X = Cl
1.37 X = H

Figure 34. Left: Ir catalysts **1.34** and **1.35**. Middle: Proposed hydrogen-bond ordered transition state. Right: Ir catalysts **1.36** and **1.37**.[70,95]

Crabtree *et al.* report on a detailed study of the catalytic activity of a range of directly comparable complexes based on the IrCp* motif, with varying ligands.[95] It was noted that no overall conclusions could be drawn about the impact of, for example, denticity or ligand type. The most active of the complexes, **1.36**, was investigated further. A hydride species derived from this complex, **1.37**, could be generated by reaction with $NaBH_4$. Whilst this was found to be competent in catalysis, its activity was lower than that of the parent complex, albeit with no induction period observed or base required. The results of Bäckvall's test gave further evidence that there was not a simple relationship between the two complexes. Whilst **1.37** gave 95% incorporation at the alpha carbon (indicating a monohydride mechanism), incorporation was only 75% for **1.36**. This was strong evidence that the catalytic cycle starting from **1.36**, must have intermediates other than **1.37** in play. The authors also note that both the β-hydride elimination step to generate the hydride, and the subsequent hydrogen transfer, requires two adjacent vacant sites, a criterion not met by either **1.36** or **1.37**. A further study on these complexes found that the reaction probably proceeded *via* loss of the Cp* ligand, and that this process corresponds to the observed induction period.[104] Dissociation of a Cp* ligand is unusual, but has been reported in Ir complexes previously.[105] Concordant with this supposition, it was found that complexes featuring a bulkier NHC ligand had a shorter induction period, whilst a comparable complex featuring the less bulky Cp ligand a much longer one. The authors therefore propose that in cases where the system is sterically congested, and where the ligands are not labile - catalysis may proceed *via* loss of a Cp* ligand; whilst in cases where the ligands are labile a classical monohydride mechanism prevails.

1.3 Previous Work

1.3.1 Fusing NHCs and Carboranes

NHCs and carboranes are each important ligand classes which have been applied to complexes used for catalytic reactions (Preface - *3.3*, *vide supra* - *1.1.7*). Whilst there have been reports of NHCs and carboranes co-existing in the same complex, it was not until recently that reports of carborane appended NHCs emerged.[106–108] In 2010, Willans *et al.* reported the formation of 2:1 NHC-carborane adducts in which the *closo* structure of the carborane is lost, and two NHCs coordinate to an *exo*-boron atom (**1.38** - Figure 35).[109] Two years later Zheng and Xie reported 1:1 adducts, prepared selectively by use of a sterically encumbered NHC (**1.39** - Figure 35).[110] This was followed by work from Lavallo *et al.* who reported the synthesis of NHCs which are both di- and mono-substituted with carboranes at the N positions (**1.40** - Figure 35).[111,112] The same group later reported the first complex bearing a fused NHC-carborane ligand, **1.41**, based on the same motif (Figure 35).[113] More recently Selg *et al.* have reported the appending of a carborane to a triazolium-based organocatalyst (**1.42** - Figure 35). The use of a *nido*-carborane as an aryl mimetic is reported, and the compound found to be active in the organocatalysis of Umpolung-type reactions, as well as being more widely applicable than the phenyl analogue.[114]

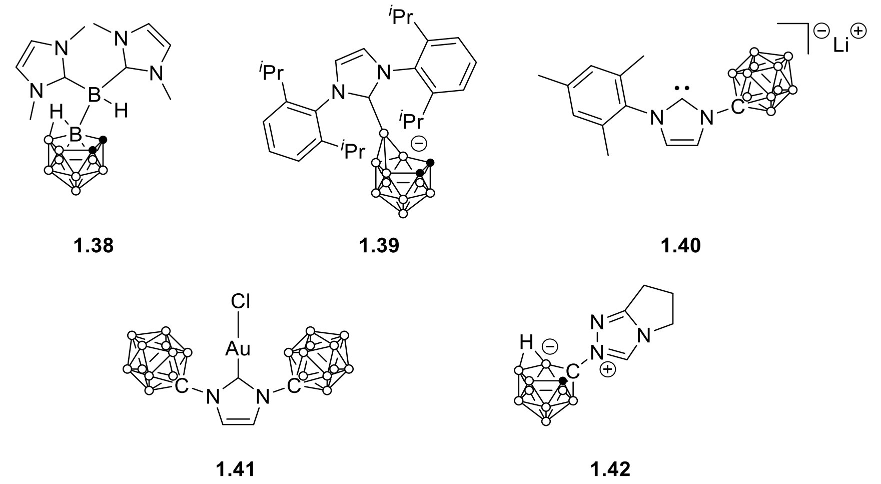

1.38 **1.39** **1.40**

1.41 **1.42**

Figure 35. Literature examples of NHC-carborane compounds.[109–113]

Concurrent work in the Willans group established a synthetic methodology for the preparation of NHCs connected to a carborane *via* a flexible linker.[115–117] Holmes *et al.* note that reaction of bromoethylcarborane with one equivalent of ^{t}Bu-imidazole produces the *closo*-carborane tether **1.43**. Reaction with a second equivalent results in deboronation (due to the basic properties of the imidazole) to form **1.44**. These imidazolium salts are precursors to NHC-carborane tethers, and as such can be used in complexation reactions. This was demonstrated with Rh initially, with a structurally diverse range of complexes prepared and characterised (Figure 36).

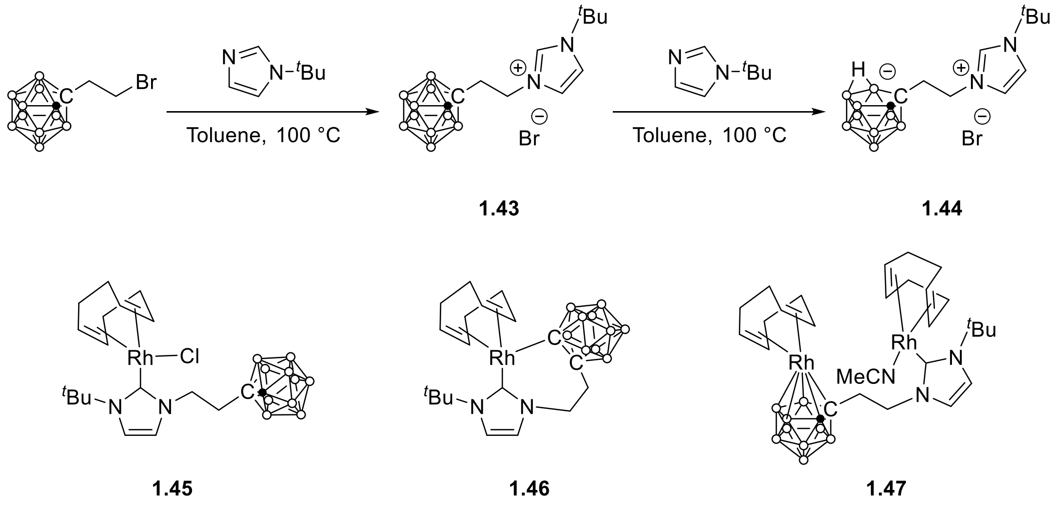

1.43 **1.44**

1.45 **1.46** **1.47**

Figure 36. Top: Synthetic route to imidazolium carborane tethers **1.43** and **1.44**. Bottom: Diverse Rh complexes prepared from these tethers **1.45**-**1.47**.

It is possible to vary the N-substituent on the NHC to some degree, and various *closo*-carborane imidazolium salts were also prepared (Figure 37).[117] The methyl-substituted precursor was used for further study on complexation to Ru, Rh and Ir. For each metal the [M(arene)(NHC)Cl_2] type complex was prepared and fully characterised; in the case of Ir, a range of cyclometallated complexes were also synthesised (Figure 37).[116] As discussed previously, metal-carborane coordination can occur through activation of either a CH or a BH vertex (1.1.6). The CH protons are more acidic than the BH protons so in some cases it is possible to selectively activate at this position. In case of BH activation this occurs at either of the two boron atoms directly adjacent to both carbon atoms; carbon is more electronegative than boron and hence the more electron poor boron atoms are the most susceptible to proton loss.[118]

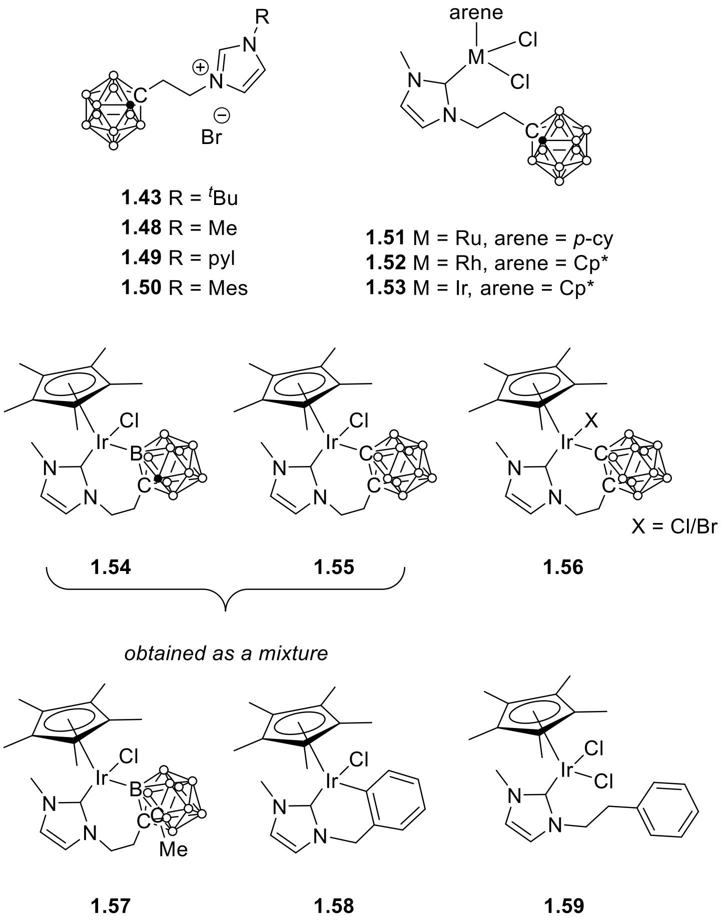
R
N
N
C
Br
1.43 R = ^{t}Bu
1.48 R = Me
1.49 R = pyl
1.50 R = Mes
arene
M
Cl
Cl
N
N
C
1.51 M = Ru, arene = *p*-cy
1.52 M = Rh, arene = Cp*
1.53 M = Ir, arene = Cp*
Ir
Cl
B
C
N
N
C
X
X = Cl/Br
1.54
1.55
1.56
obtained as a mixture
Me
1.57
1.58
1.59

Figure 37. Top left: Range of ligand precursors **1.43**-**1.50**. Top right: Non-cyclometallated complexes **1.51**-**1.53**. Bottom: Range of Ir complexes prepared **1.54**-**1.59**.

Holmes *et al.* note that when cyclometallation of **1.53** is achieved by reaction with Ag_2O the product obtained is a mixture of **1.54** and **1.55**, i.e. both CH and BH activation occur. It was possible to selectively prepare only the carbon cyclometallated complex **1.56** by deprotonating both the imidazolium and the carborane using *n*-BuLi. In this case, a mixed halide product is obtained. Achieving boron only cyclometallation is more complex - this requires synthesis of the methyl substituted carborane precursor, thus physically blocking the possibility of CH activation, and furnishing **1.57**. Phenyl containing analogues **1.58** and **1.59** were also prepared for comparison; it has been noted that a phenyl ring rotating in solution has an equivalent steric effect to that of a 12 vertex carborane.[119]

1.3.2 Transfer Hydrogenation Catalysis

The prepared Ir complexes were tested for activity in the catalytic TH of acetophenone (Table 1 – entries 2-7).[116] Compared to the complex precursor $[IrCp^*Cl_2]_2$, addition of an NHC ligand reduces catalytic activity (*cf.* entries 1 and 2). However, when in addition to an NHC ligand the Ir centre is cyclometallated by a carborane, an increase in catalytic activity is seen (*cf.* entries 1-5). There is no clear indication in the data about whether boron or carbon cyclometallation produces a greater enhancement in reactivity, in fact, the mixture of carbon and boron cyclometallation gave better conversion than either isolated complex (*cf*. entries 3-5). In general, the carboranyl complexes outperform their phenyl analogues (*cf.* entries 2 and 7; 3-5 and 6). This effect is particularly marked in the case of the cyclometallated phenyl complex. Given that cyclometallation only increases the activity for carboranyl complexes, a mechanism was proposed in which the carborane is involved in the catalytic cycle (Figure 38). The first step (**A**) involves coordination of a propoxide and concomitant carborane protonation. The second step (**B**) is the formation of a monohydride species. The third step (**C**) is the hydride transfer to the product - which is envisioned as occurring *via* either the standard inner- or outer-sphere mechanism (*vide supra* - *1.2.3*). The cycle is completed (**D**) by transfer of a proton from the pendant carborane to the product, the deprotonated carborane re-coordinating to the metal centre, thus regenerating the cyclometallated complex.

This straightforward cycle masks many potential complexities. The starting complex might feature a chloride or a bromide ligand - or be rapidly substituted by a ^{t}BuO (or ^{i}PrO) ligand upon base addition. Furthermore, the cyclometallation may occur through a carbon, boron, or a mixture of both. It is unclear which form of coordination would be favoured during cyclometallation step **D** that occurs to complete the cycle. Given the competency of the carborane-methylated complex **1.57** in catalysis, for the proposed mechanism to be in operation, it must be possible for a BH to supply the proton for the product (**D**). Another point of interest is that **1.53** was found to be relatively inactive in catalysis, even though the propoxide coordinated species formed in step **A** should ostensibly be easily accessible from this complex.

Table 1. Catalytic activity of Ir complexes for TH

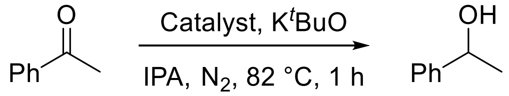
O
Ph
Catalyst, K^{t}BuO
IPA, N$_2$, 82 °C, 1 h
OH
Ph

Entry	Catalyst	Catalyst loading / mol%	Conversion / %
1	[IrCp*Cl$_2$]$_2$	1	68
2	**1.53**	1	33
3	**1.54/1.55**	1	>99
		0.5	91
4	**1.56**	1	75
5	**1.57**	1	>99
		0.5	82
6	**1.58**	1	39
7	**1.59**	1	25

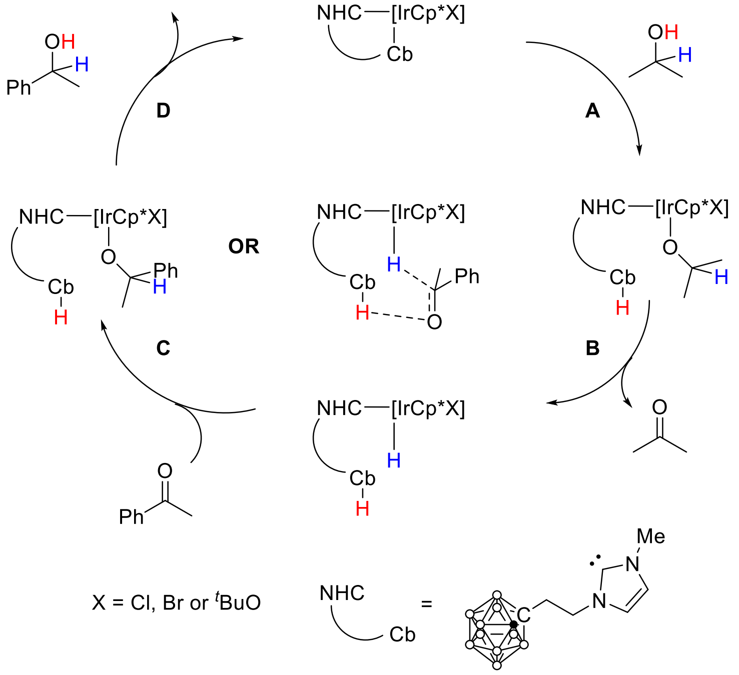
NHC—[IrCp*X]
Cb
OH
H
Ph
D
A
OR
B
C
O
Ph
H
X = Cl, Br or ^{t}BuO
NHC
Cb
=
Me
N
N
C

Figure 38. Proposed catalytic cycle for TH by complexes **1.54-1.57**.[116]

1.4 Aims

The key question that arises from the work conducted previously by Holmes is what role carborane cyclometallation has catalytic activity. The cyclometallation of the carborane moiety has a larger effect on the activity than any other change between complexes, which suggests that the carborane is involved in catalysis. However the nature of this involvement is as yet unclear. If, as suggested, the role is similar to the amine group in Noyori's bifunctional catalysts, this would represent the first example of this behaviour with a carborane. It is also possible that the carborane influences the sterics, electronics, or both, of the metal centre in a crucial way.

A central aim, therefore, was the determination of the mechanism of catalytic TH for the complexes synthesised by Holmes, with a particular emphasis on the cyclometallated complexes. A number of approaches were used to investigate the mechanism (*vide infra*).

Another aim was to understand more about the fundamental behaviour and properties of carboranyl-NHC ligands. The determination of TEPs for both carborane and phenyl containing ligands is desirable, so that the electronic properties of the ligands can be compared with other standard NHCs. It was also hoped than any great difference in electron donating properties seen between the phenyl and carborane ligands, might provide an insight into the difference in catalytic activity.

Additionally, it is desirable to probe the cyclometallation reaction further. The reasons why the use of silver oxide lead to a mixture of carbon and boron cyclometallation in the case of the Ir complexes are unclear. In a related vein, it was noted that the analogous Ru (*p*-cy) complexes were resistant to cyclometallation under these conditions, and there is no clear explanation for this. Another objective was therefore to probe the reaction products for these complexes computationally.

The work presented in the following chapters describes the progress made towards answering these questions. Experimental studies can be performed to gain an insight into catalyst speciation, for example by employing stoichiometric reactions. Work of this kind is described in Chapter 2. Computational chemistry is also a valuable tool, particularly with regard to assessing the feasibility of reaction mechanisms. Details of the computational study that was performed are given in Chapter 3. Lastly, kinetic analysis can provide vital insight into the way a catalytic reaction works. This can be through determination of the order of the reaction in substrate or catalyst, or through the observation of an induction period, or catalyst deactivation or saturation over time. The use of on-line reaction monitoring to this end is described in Chapter 4.

List of References

1 R. N. Grimes, *Carboranes*, Elsevier, 2011.

2 R. P. Alexander and H. Schroeder, *Inorg. Chem.*, 1963, **2**, 1107–1110.

3 T. P. Onak, R. E. Williams and H. G. Weiss, *J. Am. Chem. Soc.*, 1962, **84**, 2830–2831.

4 I. Shapiro, C. D. Good and R. E. Williams, *J. Am. Chem. Soc.*, 1962, **84**, 3837–3840.

5 D. Grafstein and J. Dvorak, *Inorg. Chem.*, 1963, **2**, 1128–1133.

6 H. Schroeder, T. L. Heying and J. R. Reiner, *Inorg. Chem.*, 1963, **2**, 1092–1096.

7 T. L. Heying, J. W. Ager, S. L. Clark, R. P. Alexander, S. Papetti, J. A. Reid and S. I. Trotz, *Inorg. Chem.*, 1963, **2**, 1097–1105.

8 S. Papetti and T. L. Heying, *Inorg. Chem.*, 1963, **2**, 1105–1107.

9 M. M. Fein, J. Bobinski, N. Mayes, N. Schwartz and M. S. Cohen, *Inorg. Chem.*, 1963, **2**, 1111–1115.

10 M. M. Fein, D. Grafstein, J. E. Paustian, J. Bobinski, B. M. Lichstein, N. Mayes, N. N. Schwartz and M. S. Cohen, *Inorg. Chem.*, 1963, **2**, 1115–1119.

11 D. Grafstein, J. Bobinski, J. Dvorak, H. Smith, N. Schwartz, M. S. Cohen and M. M. Fein, *Inorg. Chem.*, 1963, **2**, 1120–1125.

12 D. Grafstein, J. Bobinski, J. Dvorak, J. E. Paustian, H. F. Smith, S. Karlan, C. Vogel and M. M. Fein, *Inorg. Chem.*, 1963, **2**, 1125–1128.

13 H. Schroeder and G. D. Vickers, *Inorg. Chem.*, 1963, **2**, 1317–1319.

14 H. C. Longuet-Higgins and M. de V. Roberts, *Proc. R. Soc. A Math. Phys. Eng. Sci.*, 1955, **230**, 110–119.

15 A. R. Pitochelli and F. M. Hawthorne, *J. Am. Chem. Soc.*, 1960, **82**, 3228–3229.

16 R. Hoffmann and W. N. Lipscomb, *J. Chem. Phys.*, 1962, **36**, 3489–3493.

17 M. F. Hawthorne, D. C. Young and P. A. Wegner, *J. Am. Chem. Soc.*, 1965, **87**, 1818–1819.

18 M. F. Hawthorne and R. L. Pilling, *J. Am. Chem. Soc.*, 1965, **87**, 3987–3988.

19 R. N. Grimes, *Dalton Trans.*, 2015, **44**, 5939–5956.

20 A. F. Armstrong and J. F. Valliant, *Dalton Trans.*, 2007, 4240–4251.

21 Y. Zhu and N. S. Hosmane, *J. Organomet. Chem.*, 2017, **849–850**, 286–292.

22 J. Aihara, *J. Am. Chem. Soc.*, 1978, **100**, 3339–3342.

23 P. von R. Schleyer and K. Najafian, *Inorg. Chem.*, 1998, **37**, 3454–3470.

24 K. Wade, *J. Chem. Soc. D Chem. Commun.*, 1971, 792–793.

25 P. Atkins, T. Overton, J. Rourke, M. Weller and F. Armstrong, *Inorganic Chemistry*, Oxford University Press, Oxford, 5th edn., 2010.

26 S. Papetti and T. L. Heying, *J. Am. Chem. Soc.*, 1964, **86**, 2295–2295.

27 U. Kusari, Y. Li, M. G. Bradley and L. G. Sneddon, *J. Am. Chem. Soc.*, 2004, **126**, 8662–8663.

28 A. Toppino, A. R. Genady, M. E. El-Zaria, J. Reeve, F. Mostofian, J. Kent and J. F. Valliant, *Inorg. Chem.*, 2013, **52**, 8743–8749.

29 M. E. El-Zaria, K. Keskar, A. R. Genady, J. A. Ioppolo, J. McNulty and J. F. Valliant, *Angew. Chemie Int. Ed.*, 2014, **53**, 5156–5160.

30 T. L. Heying, J. W. Ager, S. L. Clark, D. J. Mangold, H. L. Goldstein, M. Hillman, R. J. Polak and J. W. Szymanski, *Inorg. Chem.*, 1963, **2**, 1089–1092.

31 L. F. Tietze, U. Griesbach and O. Elsner, *Synlett*, 2002, **2002**, 1109–1110.

32 L. F. Warren and M. F. Hawthorne, *J. Am. Chem. Soc.*, 1967, **89**, 470–471.

33 K. Li, Y. Wang, G. Yang, S. Byun, G. Rao, C. Shoen, H. Yang, A. Gulati, D. C. Crick, M. Cynamon, G. Huang, R. Docampo, J. H. No and E. Oldfield, *ACS Infect. Dis.*, 2015, **1**, 215–221.

34 E. L. Hoel and M. F. Hawthorne, *J. Am. Chem. Soc.*, 1973, **95**, 2712–2713.

35 Z.-J. Yao and G.-X. Jin, *Organometallics*, 2011, **30**, 5365–5373.

36 M. F. Hawthorne and T. D. Andrews, *Chem. Commun.*, 1965, 443–444.

37 M. F. Hawthorne, D. C. Young, T. D. Andrews, D. V. Howe, R. L. Pilling, A. D. Pitts, M. Reintjes, L. F. Warren and P. A. Wegner, *J. Am. Chem. Soc.*, 1968, **90**, 879–896.

38 L. F. Warren and M. F. Hawthorne, *J. Am. Chem. Soc.*, 1968, **90**, 4823–4828.

39 D. M. P. Mingos, M. I. Forsyth and A. J. Welch, *J. Chem. Soc., Dalton Trans.*, 1978, 1363–1374.

40 M. F. Hawthorne, D. A. Owen, J. C. Smart and P. M. Garrett, *J. Am. Chem. Soc.*, 1971, **93**, 1362–1368.

41 S. Bresadola, A. Frigo, B. Longato and G. Rigatti, *Inorg. Chem.*, 1973, **12**, 2788–2793.

42 E. L. Hoel and M. F. Hawthorne, *J. Am. Chem. Soc.*, 1975, **97**, 6388–6395.

43 N. Fey, M. F. Haddow, R. Mistry, N. C. Norman, A. G. Orpen, T. J. Reynolds and P. G. Pringle, *Organometallics*, 2012, **31**, 2907–2913.

44 L. E. Riley, A. P. Y. Chan, J. Taylor, W. Y. Man, D. Ellis, G. M. Rosair, A. J. Welch and I. B. Sivaev, *Dalton Trans.*, 2016, **45**, 1127–1137.

45 Z. Zheng, C. B. Knobler, C. E. Curtis and M. F. Hawthorne, *Inorg. Chem.*, 1995, **34**, 432–435.

46 R. N. Grimes, *Coord. Chem. Rev.*, 2000, **200–202**, 773–811.

47 X. Wang and G.-X. Jin, *Organometallics*, 2004, **23**, 6319–6322.

48 X. Wang and G.-X. Jin, *Chem. Eur. J.*, 2005, **11**, 5758–5764.

49 P. Hu, Z.-J. Yao, J.-Q. Wang and G.-X. Jin, *Organometallics*, 2011, **30**, 4935–4940.

50 N. Ma, C. Wei, S. Li and G. Zhang, *Dalton Trans.*, 2018, **47**, 14421–14425.

51 T. Wang, B. Wu, W. Guo, S. Wu, H. Zhang, Y. Dang and J. Wang, *Dalton Trans.*, 2019, **48**, 2646–2656.

52 T. E. Paxson and M. F. Hawthorne, *J. Am. Chem. Soc.*, 1974, **96**, 4674–4676.

53 F. Teixidor, M. A. Flores, C. Viñas, R. Kivekäs and R. Sillanpää, *Angew. Chemie Int. Ed.*, 1996, **35**, 2251–2253.

54 M. S. Delaney, C. B. Knobler and M. F. Hawthorne, *Inorg. Chem.*, 1981, **20**, 1341–1347.

55 Y. Zhu, K. Carpenter, C. B. Ching, S. Bahnmueller, P. K. Chan, V. S. Srid, W. K. Leong and M. F. Hawthorne, *Angew. Chemie Int. Ed.*, 2003, **42**, 3792–3795.

56 G. Liu, J. Zhang, B. Wu and J. Wang, *Org. Lett.*, 2007, **9**, 4263–4266.

57 M. E. El-Zaria, H. Arii and H. Nakamura, *Inorg. Chem.*, 2011, **50**, 4149–4161.

58 H. Nishiyama, *Chem. Soc. Rev.*, 2007, **36**, 1133–1141.

59 H. Nakamura, T. Kamakura and S. Onagi, *Org. Lett.*, 2006, **8**, 2095–2098.

60 M. Y. Tsang, C. Viñas, F. Teixidor, J. G. Planas, N. Conde, R. SanMartin, M. T. Herrero, E. Domínguez, A. Lledós, P. Vidossich and D. Choquesillo-Lazarte, *Inorg. Chem.*, 2014, **53**, 9284–9295.

61 Y.-P. Zhou, S. Raoufmoghaddam, T. Szilvási and M. Driess, *Angew. Chemie Int. Ed.*, 2016, **55**, 12868–12872.

62 M. J. Islam, M. D. Smith and D. V. Peryshkov, *J. Organomet. Chem.*, 2018, **867**, 208–213.

63 D. Wang and D. Astruc, *Chem. Rev.*, 2015, **115**, 6621–6686.

64 S. E. Clapham, A. Hadzovic and R. H. Morris, *Coord. Chem. Rev.*, 2004, **248**, 2201–2237.

65 D. A. Hey, R. M. Reich, W. Baratta and F. E. Kühn, *Coord. Chem. Rev.*, 2018, **374**, 114–132.

66 J. Ito and H. Nishiyama, *Tetrahedron Lett.*, 2014, **55**, 3133–3146.

67 J. Magano and J. R. Dunetz, *Org. Process Res. Dev.*, 2012, **16**, 1156–1184.

68 J. S. M. Samec, J.-E. Bäckvall, P. G. Andersson and P. Brandt, *Chem. Soc. Rev.*, 2006, **35**, 237–348.

69 R. Corberán and E. Peris, *Organometallics*, 2008, **27**, 1954–1958.

70 S. Sabater, M. Baya and J. A. Mata, *Organometallics*, 2014, **33**, 6830–6839.

71 A. Verley, *Bull. Soc. Chim. Fr.*, 1925, **37**, 537–542.

72 H. Meerwein and R. Schmidt, *Justus Liebigs Ann. Chem.*, 1925, **444**, 221–238.

73 W. Ponndorf, *Zeitschrift für Angew. Chemie*, 1926, **39**, 138–143.

74 T. Okano, M. Matsuoka, H. Konishi and J. Kiji, *Chem. Lett.*, 1987, **16**, 181–184.

75 Y. Ishii, T. Nakano, A. Inada, Y. Kishigami, K. Sakurai and M. Ogawa, *J. Org. Chem.*, 1986, **51**, 240–242.

76 G. Chuah, S. Jaenicke, Y. Zhu and S. Liu, *Curr. Org. Chem.*, 2006, **10**, 1639–1654.

77 R. Cohen, C. R. Graves, S. T. Nguyen, J. M. L. Martin and M. A. Ratner, *J. Am. Chem. Soc.*, 2004, **126**, 14796–14803.

78 Y. M. Y. Haddad, H. B. Henbest, J. Husbands and T. R. B. Mitchell, *Proc. Chem. Soc.*, 1964, 349–349.

79 J. Trocha-Grimshaw and H. B. Henbest, *Chem. Commun. (London)*, 1967, **0**, 544–544.

80 G. Zassinovich, C. del Bianco and G. Mestroni, *J. Organomet. Chem.*, 1981, **222**, 323–329.

81 G. Zassinovich and G. Mestroni, *J. Mol. Catal.*, 1987, **42**, 81–90.

82 A. Bartoszewicz, N. Ahlsten and B. Martín-Matute, *Chem. Eur. J.*, 2013, **19**, 7274–7302.

83 R. H. Crabtree, H. Felkin, T. Fillebeen-Khan and G. E. Morris, *J. Organomet. Chem.*, 1979, **168**, 183–195.

84 R. H. Crabtree, H. Felkin and G. E. Morris, *J. Chem. Soc. Chem. Commun.*, 1976, **0**, 716.

85 R. H. Crabtree and G. E. Morris, *J. Organomet. Chem.*, 1977, **135**, 395–403.

86 R. Crabtree, *Acc. Chem. Res.*, 1979, **12**, 331–337.

87 A. C. Hillier, H. M. Lee, E. D. Stevens and S. P. Nolan, *Organometallics*, 2001, **20**, 4246–4252.

88 K.-J. Haack, S. Hashiguchi, A. Fujii, T. Ikariya and R. Noyori, *Angew. Chemie Int. Ed.*, 1997, **36**, 285–288.

89 S. Hashiguchi, A. Fujii, J. Takehara, T. Ikariya and R. Noyori, *J. Am. Chem. Soc.*, 1995, **117**, 7562–7563.

90 K. Mashima, T. Abe and K. Tani, *Chem. Lett.*, 1998, **27**, 1199–1200.

91 K. Mashima, T. Abe and K. Tani, *Chem. Lett.*, 1998, **27**, 1201–1202.

92 K. Murata, T. Ikariya and R. Noyori, *J. Org. Chem.*, 1999, **64**, 2186–2187.

93 M. Iglesias and L. A. Oro, *Chem. Soc. Rev.*, 2018, **47**, 2772–2808.

94 G. Sipos and R. Dorta, *Coord. Chem. Rev.*, 2018, **375**, 13–68.

95 U. Hintermair, J. Campos, T. P. Brewster, L. M. Pratt, N. D. Schley and R. H. Crabtree, *ACS Catal.*, 2014, **4**, 99–108.

96 D. Gnanamgari, E. L. O. Sauer, N. D. Schley, C. Butler, C. D. Incarvito and R. H. Crabtree, *Organometallics*, 2009, **28**, 321–325.

97 A. Pontes da Costa, M. Viciano, M. Sanaú, S. Merino, J. Tejeda, E. Peris and B. Royo, *Organometallics*, 2008, **27**, 1305–1309.

98 A. Comas-Vives, G. Ujaque and A. Lledós, *J. Mol. Struct. THEOCHEM*, 2009, **903**, 123–132.

99 Y. R. S. Laxmi and J.-E. Bäckvall, *Chem. Commun.*, 2000, **0**, 611–612.

100 O. Pàmies and J.-E. Bäckvall, *Chem. Eur. J.*, 2001, **7**, 5052–5058.

101 J.-W. Handgraaf, J. N. H. Reek and E. J. Meijer, *Organometallics*, 2003, **22**, 3150–3157.

102 M. Yamakawa, H. Ito and R. Noyori, *J. Am. Chem. Soc.*, 2000, **122**, 1466–1478.

103 M. V. Jiménez, J. Fernández-Tornos, J. J. Pérez-Torrente, F. J. Modrego, P. García-Orduña and L. A. Oro, *Organometallics*, 2015, **34**, 926–940.

104 J. Campos, U. Hintermair, T. P. Brewster, M. K. Takase and R. H. Crabtree, *ACS Catal.*, 2014, **4**, 973–985.

105 W. J. Oldham Jr., A. S. Amber S. Hinkle and D. M. Heinekey, *J. Am. Chem. Soc.*, 1997, **119**, 11028–11036.

106 Y. Sun, H.-S. Chan, P. H. Dixneuf and Z. Xie, *J. Organomet. Chem.*, 2006, **691**, 3071–3082.

107 X. Wang, S. Liu, L.-H. Weng and G.-X. Jin, *Chem. Eur. J.*, 2007, **13**, 188–195.

108 X.-Q. Xiao and G.-X. Jin, *J. Organomet. Chem.*, 2008, **693**, 316–320.

109 C. E. Willans, C. A. Kilner and M. A. Fox, *Chem. Eur. J.*, 2010, **16**, 10644–10648.

110 F. Zheng and Z. Xie, *Dalton Trans.*, 2012, **41**, 12907–12914.

111 A. El-Hellani and V. Lavallo, *Angew. Chemie Int. Ed.*, 2014, **53**, 4489–4493.

112 M. J. Asay, S. P. Fisher, S. E. Lee, F. S. Tham, D. Borchardt and V. Lavallo, *Chem. Commun.*, 2015, **51**, 5359–5362.

113 S. P. Fisher, A. El-Hellani, F. S. Tham and V. Lavallo, *Dalton Trans.*, 2016, **45**, 9762–9765.

114 C. Selg, W. Neumann, P. Lönnecke, E. Hey-Hawkins and K. Zeitler, *Chem. Eur. J.*, 2017, **23**, 7932–7937.

115 J. Holmes, C. M. Pask, M. A. Fox and C. E. Willans, *Chem. Commun.*, 2016, **52**, 6443–6446.

116 J. Holmes, C. M. Pask and C. E. Willans, *Dalton Trans.*, 2016, **45**, 15818–15827.

117 J. Holmes, *Preparation of Brand New Ligand Architectures Incorporating N-Heterocyclic Carbene Complexes with Carboranyl Substituents: Coordination Chemistry, Catalytic Evaluation and Anticancer Properties,* University of Leeds, 2017.

118 W. M. Haynes, *CRC Handbook of Chemistry and Physics 97th Edition*, CRC Press/Taylor & Francis, Boca Raton, FL., 97th edn., 2017.

119 O. Leukart, M. Caviezel, A. Eberle, E. Escher, A. Tun-Kyi and R. Schwyzer, *Helv. Chim. Acta*, 1976, **59**, 2184–2187.

Chapter 2

A Chemical Investigation into the Role of the Carboranyl Moiety in NHC-Carborane Containing Catalysts.

This chapter describes reactivity studies performed on Ir complexes bearing NHC-carborane ligands that have previously been found to be active in TH catalysis. The synthesis and characterisation of relevant complexes is described. These have been used in a variety of stoichiometric reactions, as well as catalytic screening reactions, in an attempt to gain an insight into catalyst speciation. Additionally, efforts towards the preparation of Ir carbonyl complexes are described.

2.1 Attempted Synthesis of Carbonyl Complexes

As described in Chapter 1, the coordination chemistry of NHC-carborane ligands has been previously investigated. Ir complexes bearing these ligands were found to be active in TH catalysis. Prior to these results being obtained however, efforts were made to determine which catalytic transformations the novel NHC-carborane ligands would be well suited to. To this end, it was desirable to probe the electronic differences between ligands bearing a carborane, compared to those bearing a phenyl group. Determination of a given ligands' electron donating properties is generally achieved with reference to the Tolman Electronic Parameter (TEP) (Preface - *3.2*). Traditionally, the model complex with the general formula $[Ni(CO)_3L]$ has been used, and the frequency of the A_1 carbonyl stretching mode is compared with that for other ligands.[1] Due to the toxicity of $[Ni(CO)_4]$, attempts have been made in recent years to introduce alternative carbonyl complexes as model complexes.[2–4] The most commonly used model complex is $[Ir(CO)_2ClL]$ with the average of the two carbonyl stretching frequencies being comparable with traditional TEP values using the following equation.

$$TEP = 0.847v_{av}(CO)[Ir] + 336\ cm^{-1}$$

These complexes can be prepared in a straightforward manner by displacement of the COD ligand in the relevant [Ir(COD)ClL] complex by bubbling through carbon monoxide.[2,5,6] Preparation of such complexes will allow the comparison of the NHC-carborane ligands with already known NHCs, for with TEPs have been reported. It was additionally envisaged that the prepared COD complexes could be applied to catalytic reactions. NHC complexes of the type [M(COD)Cl(NHC)] (M = Ir, Rh) can be prepared *via* the silver oxide route as reported by Crabtree *et al.* (Figure 39).[7]

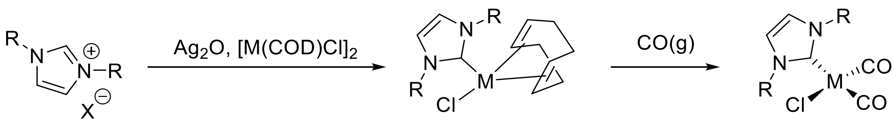
Ag$_2$O, [M(COD)Cl]$_2$
CO(g)
R
N
N–R
X
M
Cl
CO

Figure 39. Generalised route to dicarbonyl complexes. M = Rh or Ir.

Holmes *et al.* has reported the preparation of analogous Rh complexes using a *tert*-butyl substituted ligand (Figure 40).[8]

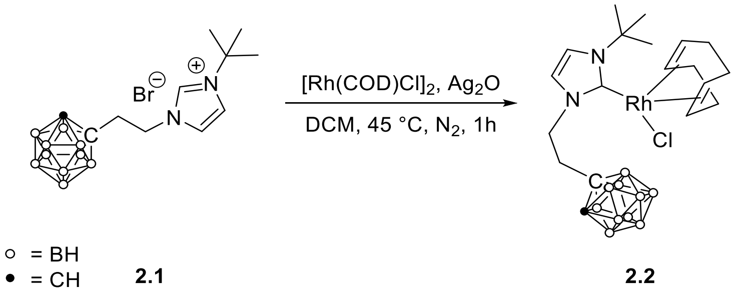
Br
N
C
[Rh(COD)Cl]$_2$, Ag$_2$O
DCM, 45 °C, N$_2$, 1h
Rh
Cl
○ = BH
● = CH

2.1 **2.2**

Figure 40. Route to Rh(COD) complex bearing NHC-carborane tethered ligand published by Holmes *et al.*[8]

The preparation of **L2** and precursors for **L1** has been described previously.[9] A slightly modified procedure was used for **L1** which is described later (section 2.2). The procedure reported by Holmes for the analogous Rh complexes was followed using **L1** and **L2** (Figure 41). Reaction in DCM at 45 °C produced **C1** in 19 hours and **C2** in 1.5 hours. The reactions can be monitored by HRMS, with the relevant ligand precursor peak disappearing almost entirely over the course of the reaction.

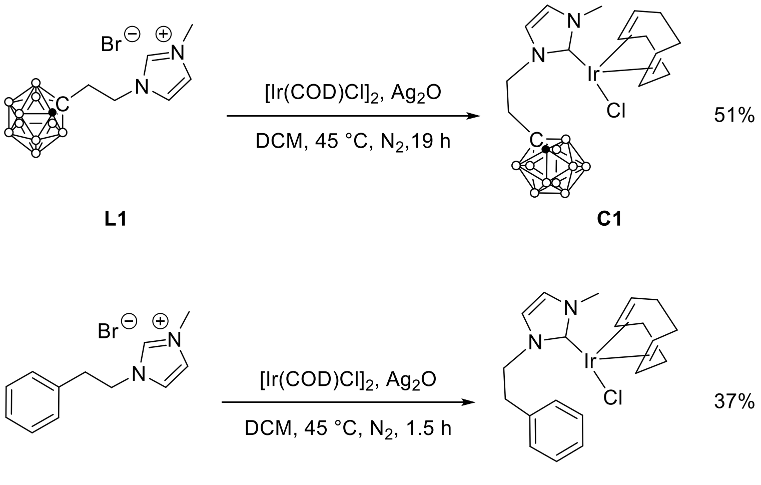
Br
N
C
[Ir(COD)Cl]$_2$, Ag$_2$O
DCM, 45 °C, N$_2$,19 h
Ir
Cl
51%
[Ir(COD)Cl]$_2$, Ag$_2$O
DCM, 45 °C, N$_2$, 1.5 h
37%

L1 **C1**

L2 **C2**

Figure 41. Synthesis of Ir complexes **C1** and **C2**.

NMR spectroscopy is a valuable tool in assessing the success of these reactions. For example, the ^{1}H NMR spectrum of **L2** as compared to that of **C2** is shown in Figure 42.

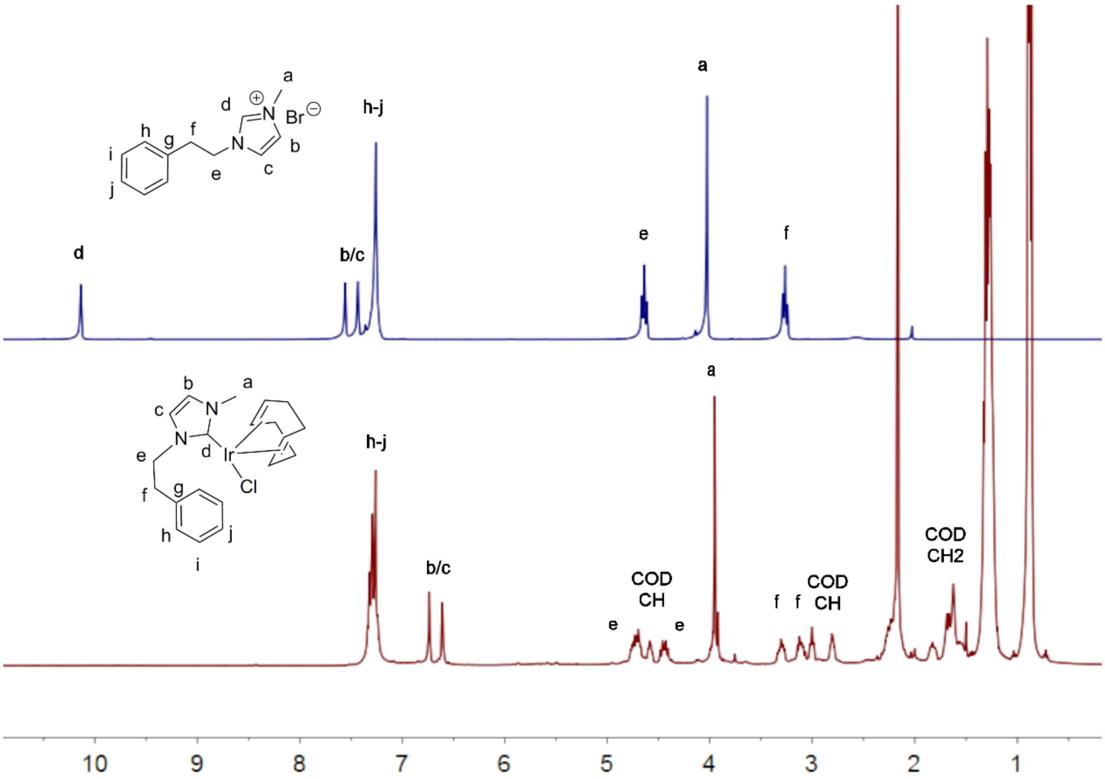

Figure 42. ^{1}H NMR spectra (400 MHz, $CDCl_3$). Top: **L2**. Bottom: **C2**.

The absence of the imidazolium signal (d) at 10.1 ppm is clear evidence of carbene formation. Additionally, upon complexation the ethyl link protons (e and f) become diastereotopic and appear as four individual signals, each with a relative integral of 1H. Analysis of the 2D HMQC demonstrates that in both cases a single carbon atom can be correlated to two proton signals. The diastereotopic nature of these protons has been observed by Holmes with the analogous Rh complex **2.1**. It was postulated that this could be due to restricted rotation about the carbene-metal bond due to steric crowding. The CH signals on the COD ligand also become inequivalent upon complexation, which lends weight to this theory. If the NHC ligand does not rotate then the CH protons on the COD ligand above the plane of the NHC ligand are magnetically inequivalent to those below. The N-methyl group signal (a) consists of two overlapping singlets in an approximate 0.2:0.8 ratio. This is a similar effect to that observed by Holmes when a species with mixed halides is obtained.[9]

The data obtained for **C1** is similar, as seen in Figure 43. Once again, the ethyl linker protons (e and f) become diastereoptopic on complexation and appear as four individual 1H signals. Similarly, there are 4 signals attributable to the COD CH protons. The carboranyl C-H signal at 4.02 ppm (h) is still present, indicating that cyclometallation *via* CH activation has not occurred. The 3 protons for the N-methyl signal (a) are again made up of two singlets, this time in a 0.15:0.85 ratio.

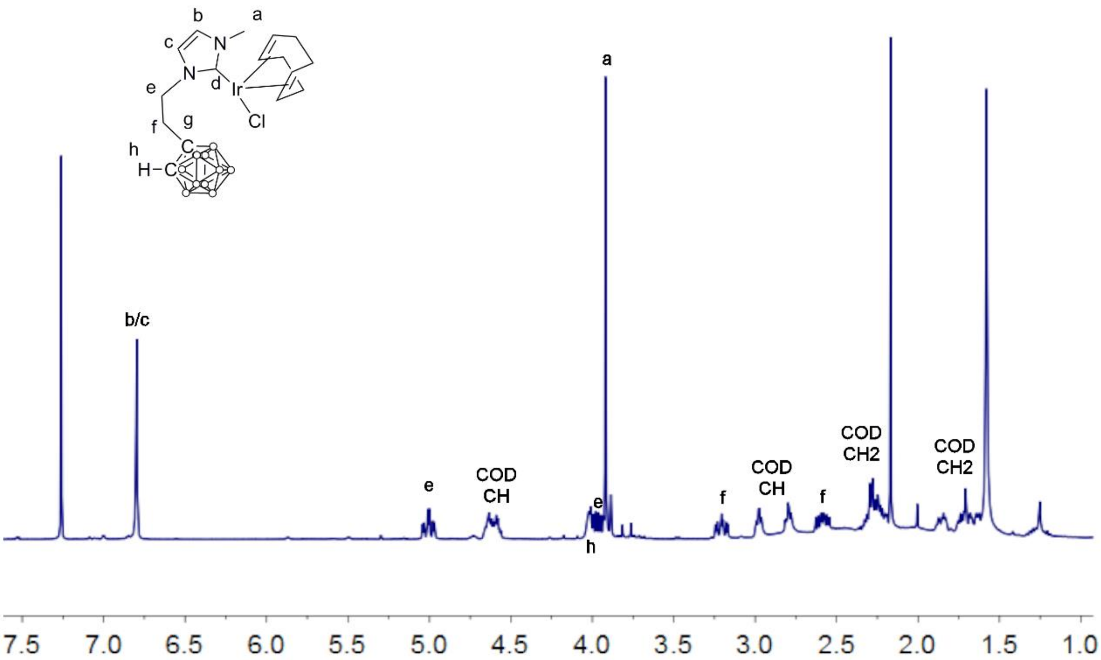

Figure 43. ^{1}H NMR spectrum (400 MHz, $CDCl_3$) of **C1**.

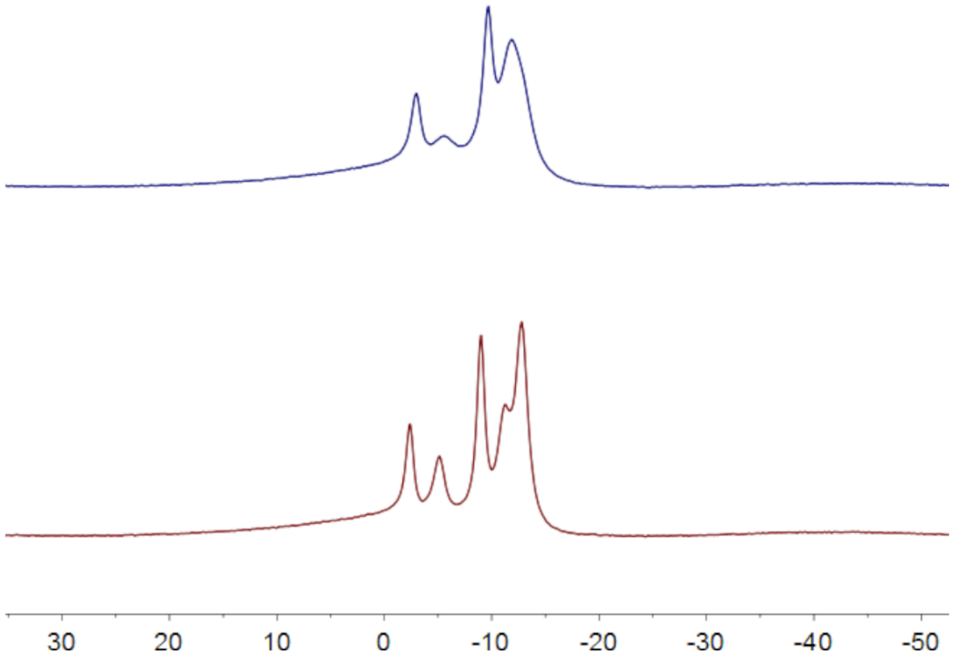

Figure 44. $^{11}B\{^1H\}$ NMR spectra (96 MHz, d_6-DMSO [above] and $CDCl_3$ [below]). Top: **L1**. Bottom: **C1**.

There is very little change in the $^{11}B\{^1H\}$ NMR spectra upon complexation of **L1** to form **C1b** (Figure 44). This is not unexpected as the boron environments are likely to be largely unaffected by complexation, being distant from the metal centre. This is also consistent with the data reported by Holmes for **2.2** (Figure 40).[8]

High resolution mass spectrometry (HRMS) also proves useful in determining the composition of these complexes. As is generally observed for complexes of this type, a peak corresponding to [M-Cl]$^+$ is observed.[10,11] In the case of **C2** the pattern of the molecular ion envelope is fairly simple, showing two major peaks separated by two mass units (Figure 45). These are due to the two stable isotopes of Ir: ^{191}Ir and ^{193}Ir which are 37.3% and 62.7% abundant, respectively.[12]

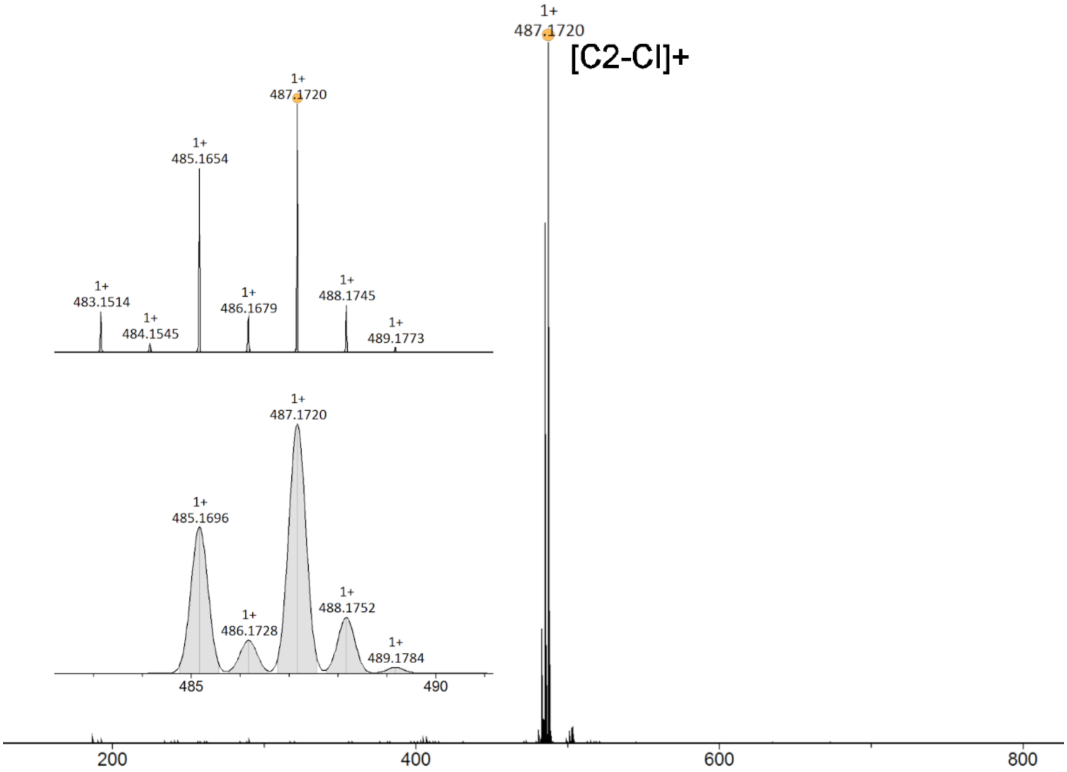

Figure 45. HRMS spectrum of **C2**. Inset: above: molecular ion peak [**C2**-Cl]$^+$, below: calculated molecular ion peak for [**C2**-Cl]$^+$.

The mass spectrum obtained for **C1** likewise shows an envelope that corresponds to [**C1**-Cl]$^+$ (Figure 46). In this case the shape of the envelope is dominated by the presence of the carborane cluster. As boron has two stable isotopes - ^{10}B and ^{11}B in a 19.9% and 80.1% relative abundance respectively – the presence of 10 boron atoms in the carborane cage results in a wide range of different molecular ion peaks that correspond to the various $[C_2{}^{10}B_n{}^{11}B_{10-n}H_{11}]$ combinations.[12]

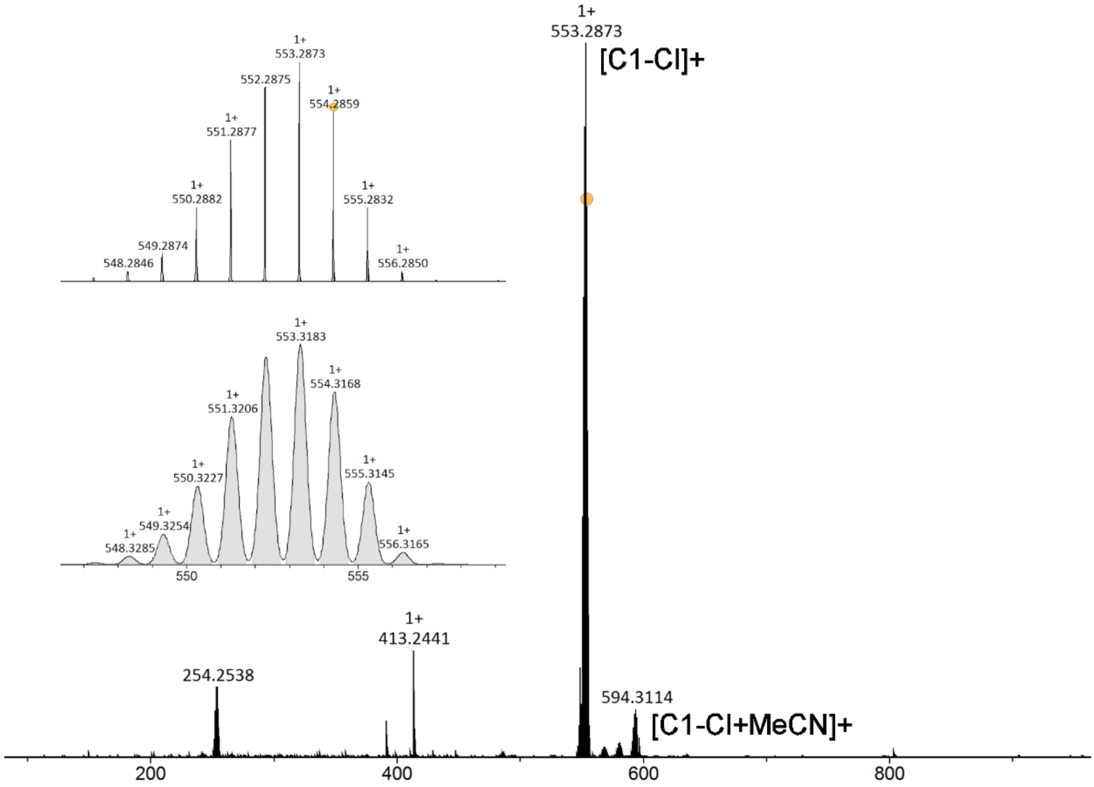

Figure 46. HRMS spectrum of **C1**. Inset: above: molecular ion peak [**C1**-Cl]$^+$, below: calculated molecular ion peak for [**C1**-Cl]$^+$.

Single crystals suitable for X-Ray diffraction analysis of **C1** and **C2** were grown by vapour diffusion of pentane into a concentrated solution of the complex in DCM. The asymmetric unit for **C1** contains four molecules of **C1** (Figure 47). Three of these feature a chloride ligand, however the fourth shows an excess of residual electron density which was modelled as a mixed chloride/bromide complex with 0.8/0.2% occupancy (Figure 48). The asymmetric unit for **C2** holds just one complex. In this case the crystal structure obtained shows a mixed halide complex, with an occupancy of 0.2% for the bromide and 0.8% for the chloride (Figure 49). This is backed up by SEM/EDX data which give a chloride:bromide ratio of 1:0.64 (calculated 1:0.56 for 0.8:0.2). Therefore it is likely that this is the reason for the duplicity of signals observed in the ^{1}H NMR spectrum of **C2**.

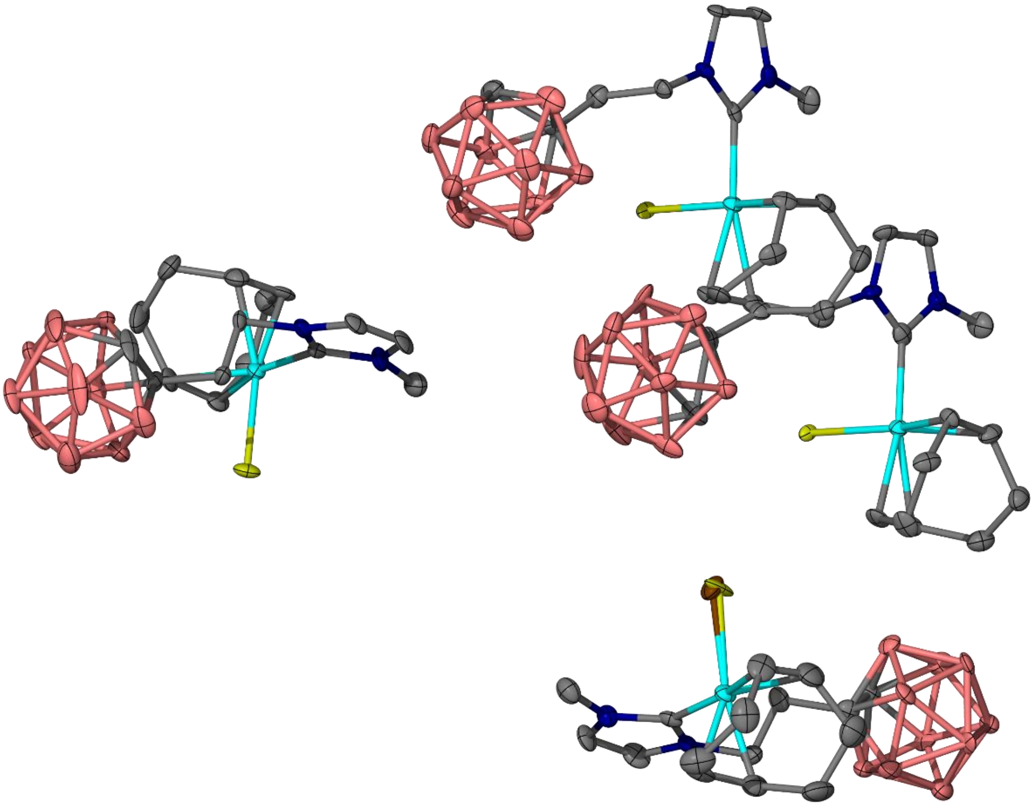

Figure 47. Molecular structure for the asymmetric unit of **C1**. Ellipsoids shown at the 50% probability level. Hydrogen atoms omitted for clarity.

There is a slight variation in the carbene-Ir bond lengths between the four molecules in the asymmetric unit of **C1**, showing distances in the range 2.004 - 2.045 Å. These lengths are at the shorter end of those reported in the literature.[3,13–15] Both **C1** and **C2** show a square planar geometry, as expected for complexes of this type. A comparison between the structures of the halide mixed complexes is given in Table 2. The bond lengths in **C1** are the same as in **C2**, when the errors in the data are taken into account. Both complexes show the expected trends, with larger Ir-C_{COD} distances *trans* to the NHC ligand than *trans* to the halide. This reflects the greater *trans*-influence of the NHC ligand, as a consequence of the strong σ-donor properties.

Due to the halide mixing observed with **C1** and **C2**, attempts were not made to synthesise the carbonyl analogues, as it was unclear what impact the mixed halides would have on the CO stretching frequencies obtained. Instead, efforts to determine the electron donating properties were undertaken computationally. Gusev has proposed the use of the model complex [Cp*Ir(CO)L] to computationally probe the electron donating effects of various ligands.[16,17] This is discussed in Chapter 3.

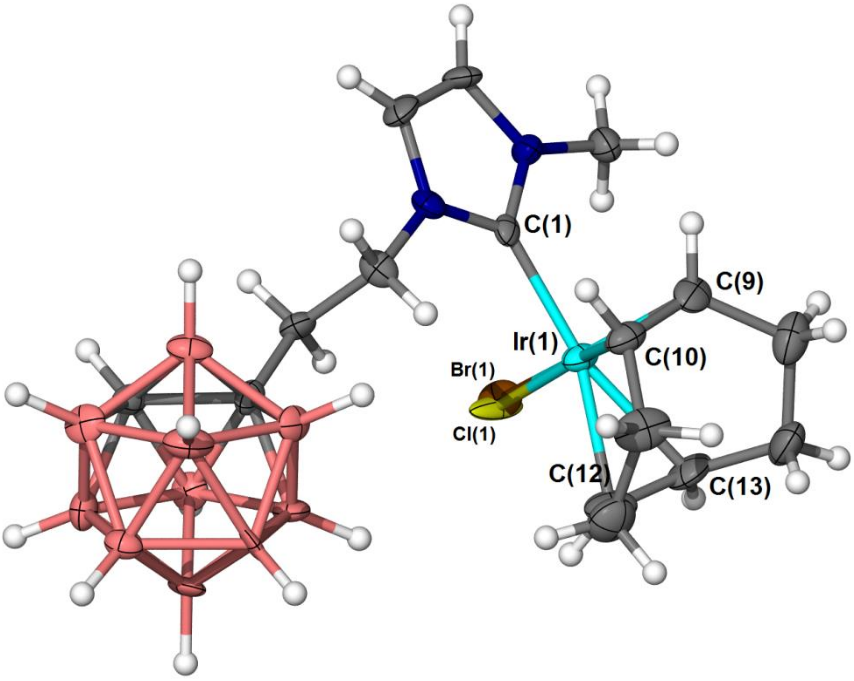
C(1)
C(9)
Ir(1)
C(10)
Br(1)
Cl(1)
C(12)
C(13)

Figure 48. Partial asymmetric unit of **C1**, showing halide mixing. Ellipsoids are shown at the 50% probability level.

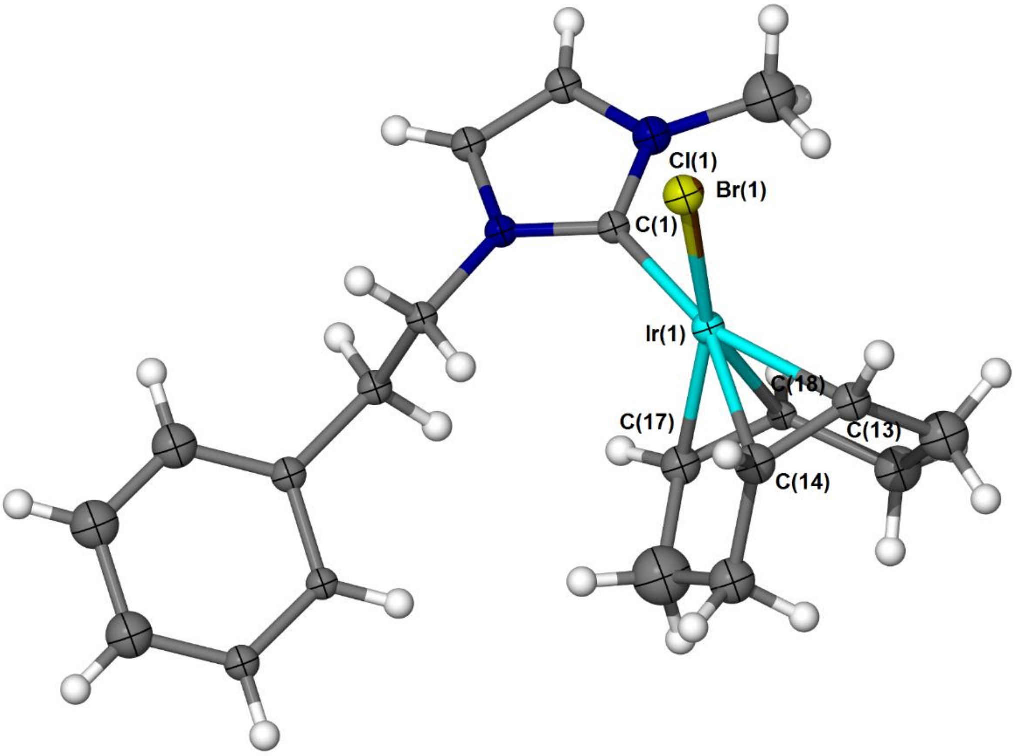
Cl(1)
Br(1)
C(1)
Ir(1)
C(18)
C(17)
C(13)
C(14)

Figure 49. Molecular structure of **C2**, showing halide mixing. Ellipsoids are shown at the 50% probability level.

Table 2. Selected bond lengths for the halide mixed molecular structures of **C1** and **C2**.

Bond	Length C1 / Å	Length C2 / Å	Literature range[3,13–15] / Å
Ir(1)-C(1)	2.026(9)	2.040(6)	1.99 – 2.09
Ir(1)-Cl/Br(1)	2.408(10)	2.404(9)	
Ir(1)-C(9)	2.088(9)		2.09 – 2.12
Ir(1)-C(18)		2.103(7)	
Ir(1)-C(10)	2.116(9)		
Ir(1)-C(17)		2.089(6)	
Ir(1)-C(12)	2.166(10)		2.16 – 2.18
Ir(1)-C(14)		2.173(6)	
Ir(1)-C(13)	2.188(9)		
Ir(1)-C(13)		2.167(6)	

2.2 Synthesis of Catalytically Active Iridium Complexes

Our group have previously prepared a range of Ir complexes and investigated their catalytic activity for the transfer hydrogenation of acetophenone (Chapter 1).[18] The key complexes of interest are those in which the carborane is cyclometallated (**C4/C5** and **C6**), as these gave the highest conversions (Figure 50). It is notable that these performed better than their non-cyclometallated counterpart **C3**, and especially interesting that this improvement upon cyclometallation was not replicated with phenyl analagoues (Figure 50). It is desirable to probe the reasons behind this effect, and determine what role the carborane plays in catalysis. This may lead to rational design of new catalysts in future.

The pendant carborane may cyclometallate through either a boron or a carbon atom. When the complex is prepared through the silver oxide route a mixture of boron and carbon cyclometallation is observed (**C4/C5**). Carbon only cyclometallation (**C6**) may be selected by deprotonation using *n*-BuLi. Although the mixture of **C4/C5** was found to be the most catalytically active, **C6** also has a good activity, and it was decided that reactions with a single species should make analysis more straightforward. For this reason efforts were initially focussed on the preparation of **C6**.

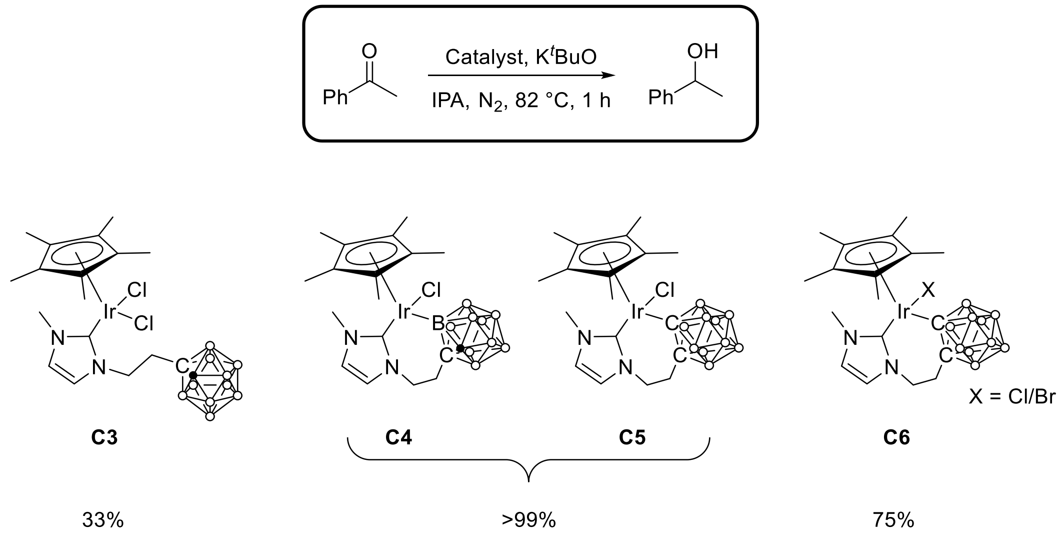
Catalyst, K^{t}BuO
IPA, N_2, 82 °C, 1 h
O
OH
Ph
Ph
Cl
Ir
Cl
N
N
C
B
X
X = Cl/Br
C3
C4
C5
C6
33%
>99%
75%

Figure 50. Complexes prepared by Holmes with conversions for the TH of acetophenone to 1-phenylethanol.[18]

The synthetic route to **C6** is shown in Figure 51. Although the synthesis has been published, it is not without its challenges. The first issues arise during the preparation of the ligand where coupling of the carborane with N-methylimidazole is a straightforward S_N2 reaction. However, carboranes often undergo deboronation in the presence of a base, such as an imidazole.[19] In order to reduce this possibility the reaction is carried out at a high concentration in toluene, with the aim of precipitating the product prior to deboronation. However, in many cases, a small quantity of the deboronated *nido* product was found to be present.

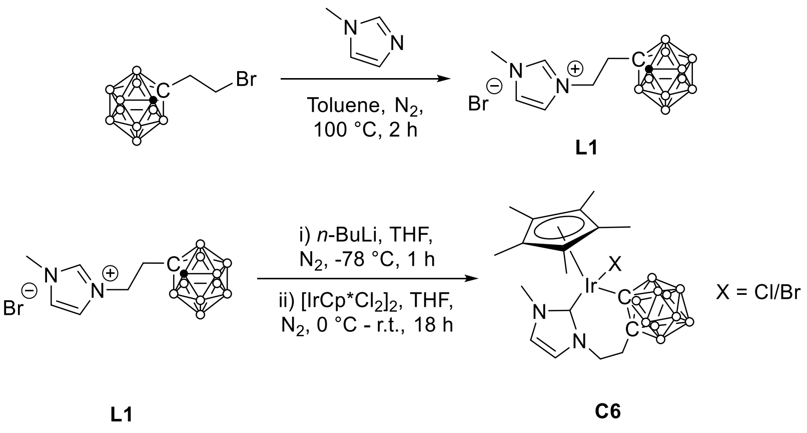
Br
N
N
Toluene, N_2,
100 °C, 2 h
Br
C
L1
i) *n*-BuLi, THF,
N_2, -78 °C, 1 h
ii) $[IrCp^*Cl_2]_2$, THF,
N_2, 0 °C - r.t., 18 h
Ir
X
X = Cl/Br
L1
C6

Figure 51. Synthetic route to **C6**. Use of *n*-BuLi allows for the selective deprotonation of a carbon atom in the carborane cage.

Once formed, separation of the zwitterionic *nido* species from the *closo* salt is challenging. The NMR spectra shown in Figure 52 are from a mixture of *closo*-**L1** and *nido* species, after attempted purification by hot-toluene washing, as described by Holmes.[9] It is however possible to separate the two species by trituration in MeOH. The *nido* species is mostly insoluble in MeOH, thus a mixed sample may be dissolved in a small quantity of MeOH and filtered through celite. It is often necessary to repeat the process at least twice to ensure complete removal of *nido* contaminants.

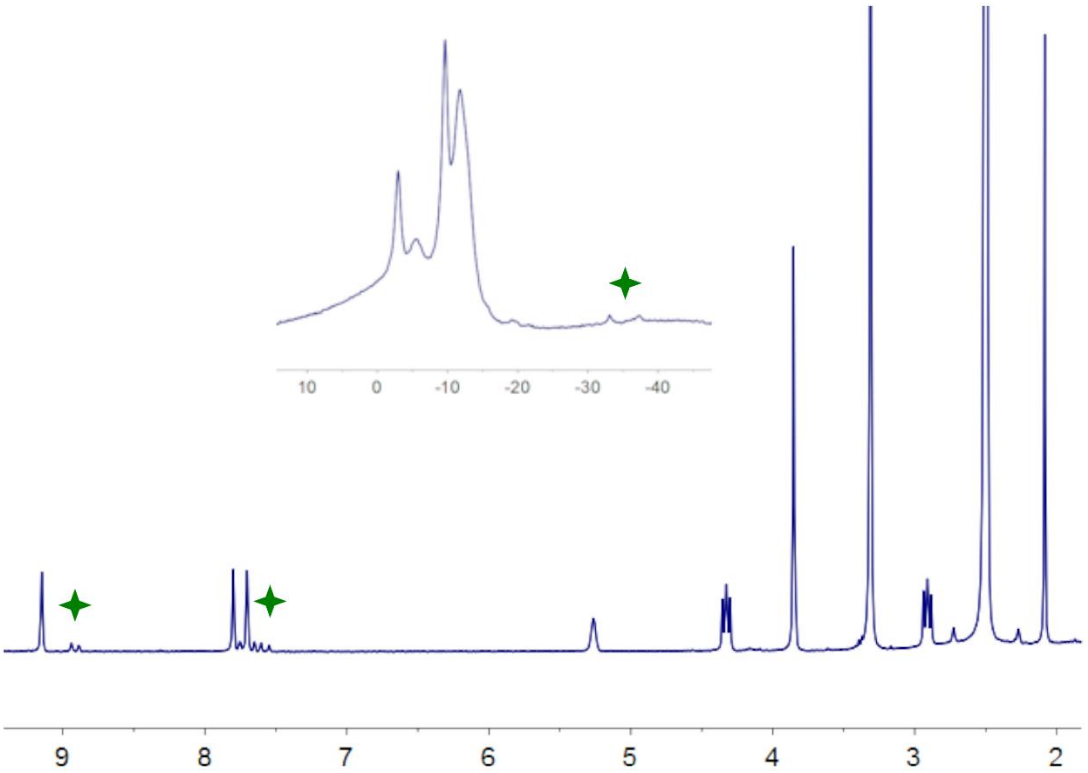

Figure 52. ^{1}H NMR spectrum (300 MHz, d_6-DMSO) of *nido* contaminated **L1**. Inset: ^{11}B{^{1}H} NMR spectrum (96 MHz, d_6-DMSO) showing characteristic signals of a *nido*-cage. Green stars denote *nido* product signals.

Synthesis of complex **C6** uses *n*-BuLi to generate the free carbene and also to selectively deprotonate the unsubstitued carbon atom on the carborane cage (Figure 51). The procedure was attempted using slightly more than two equivalents of *n*-BuLi, however, analysis of the product by HRMS and ^{1}H NMR spectroscopy frequently revealed incomplete cyclometallation and/or the presence of impurities (Figure 53 and Figure 54). It was found that addition of further portions of *n*-BuLi pushed the reaction to completion, (*cf.* Figure 55 and Figure 56) however a concomitant increase in impurities was sometimes observed (*cf*. Figure 56 and Figure 57).

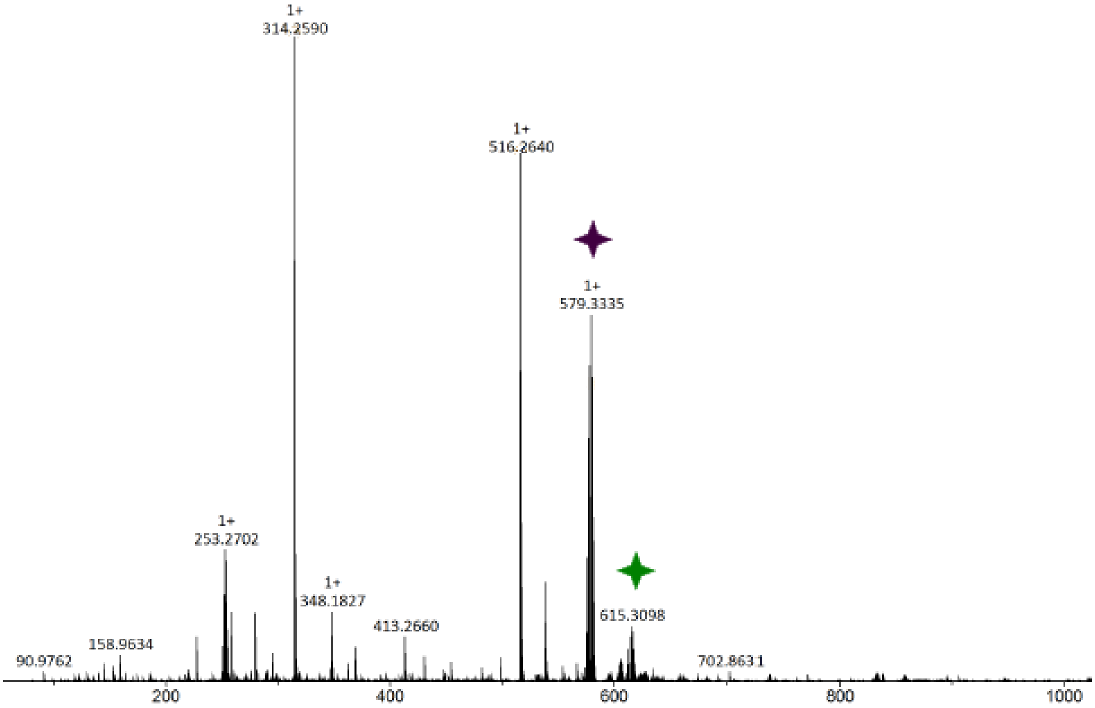

Figure 53. Example HRMS of impure product isolated during attempted synthesis of **C6** using the literature method. Green star denotes non-cyclometallated impurity (**C3**). Purple star denotes **C6**.

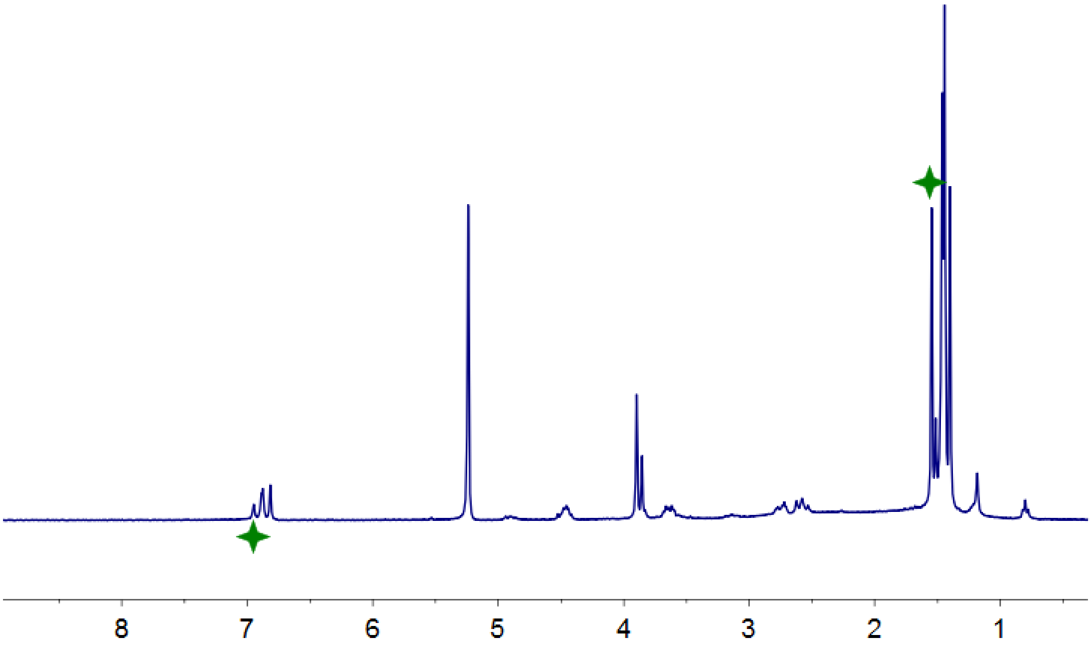

Figure 54. ^{1}H NMR spectrum (300 MHz, CD_2Cl_2) of impure product isolated during attempted synthesis of **C6** using the literature method. Green stars indicate impurities.

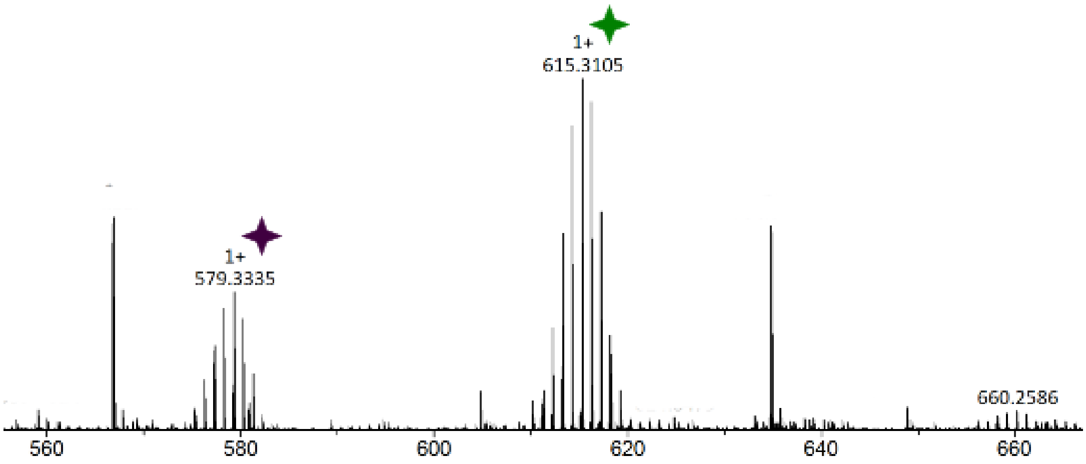

Figure 55. HRMS of reaction mixture during attempted synthesis of **C6**, after addition of 2.2 equivalents of *n*-BuLi. Purple star denotes **C6**, green star denotes **C3**.

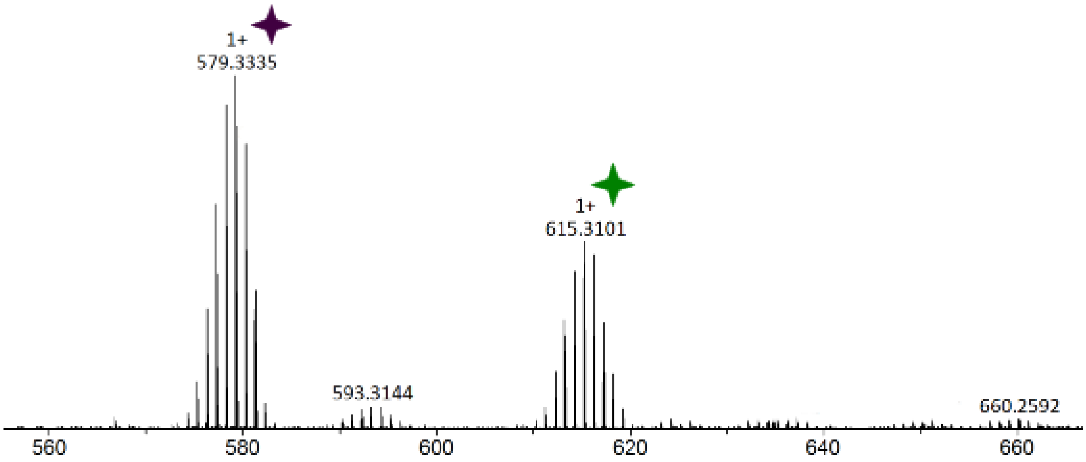

Figure 56. HRMS of reaction mixture during attempted synthesis of **C6**, after addition of 4.4 equivalents of *n*-BuLi. Purple star denotes **C6**, green star denotes **C3**.

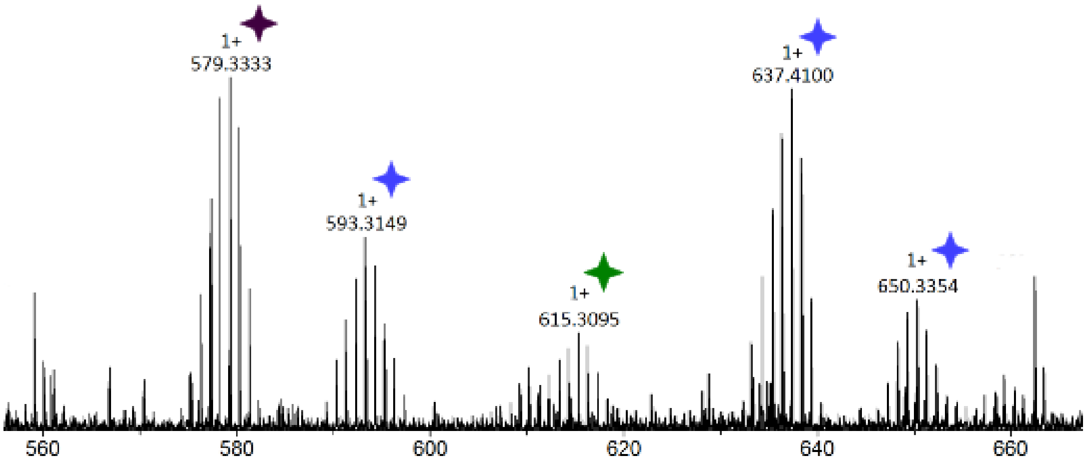

Figure 57. HRMS of reaction mixture during attempted synthesis of **C6**, after addition of 7.7 equivalents of *n*-BuLi. Purple star denotes **C6**, green star denotes **C3**, blue stars denote carborane containing side products.

In spite of the capricious nature of the chemistry, it was occasionally possible to prepare the desired compound, with analytical data in agreement with the literature (Figure 58 and Figure 59).[18] This was used to further probe the catalytic reaction.

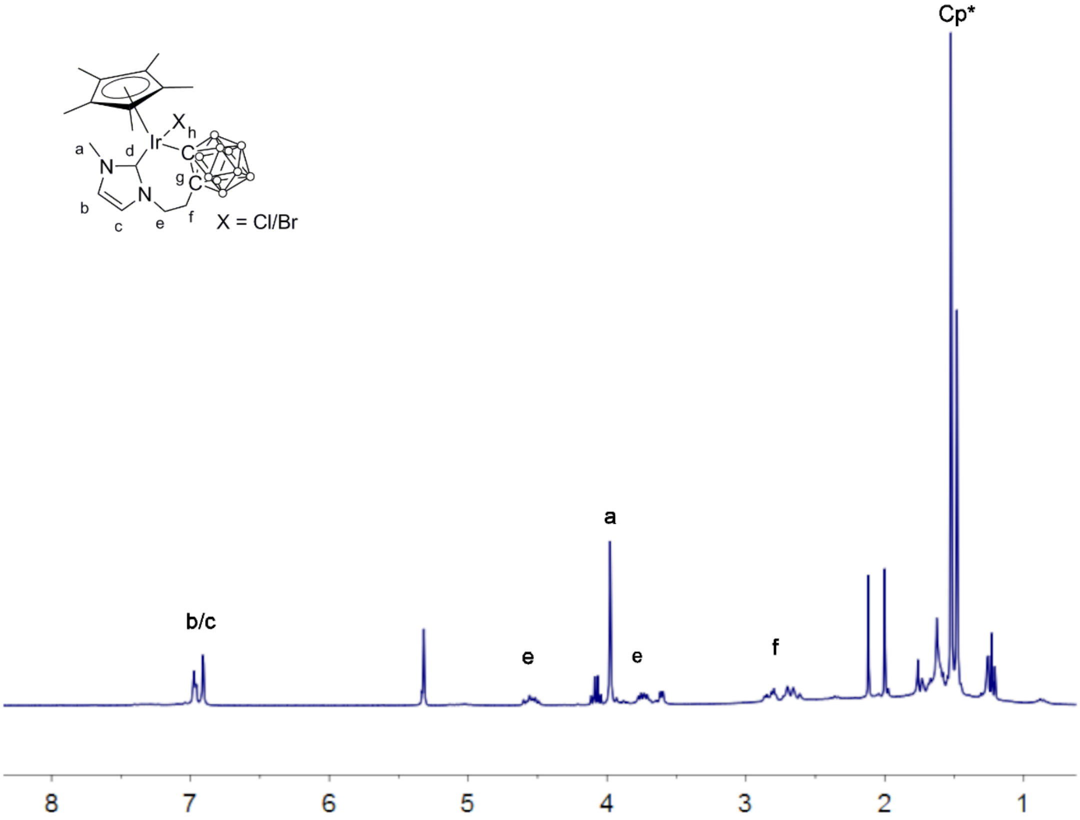

Figure 58. ^{1}H NMR spectrum (300 MHz, CD_2Cl_2) of **C6**.

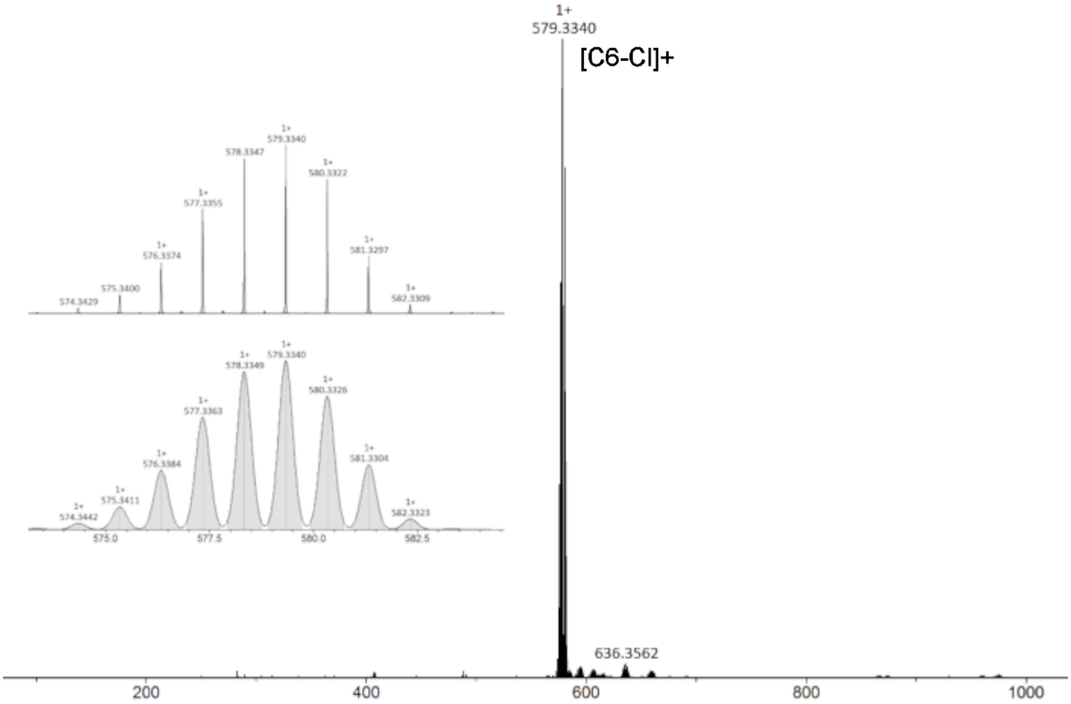

Figure 59. HRMS of **C6**. Inset: above: molecular ion peak [**C6**-Cl]$^+$, below: calculated molecular ion peak for [**C6**-Cl]$^+$.

Complexes **C3** and the mixture **C4**/**C5** were also prepared, with slight adaptions to the literature procedure. **C3** is prepared *via* the silver oxide route using **L1** and $[IrCp^{*}Cl_2]_2$ (Figure 60).

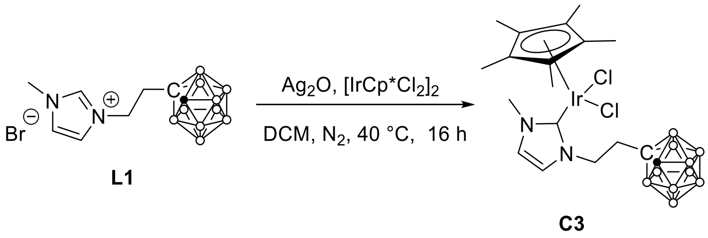

Figure 60. Literature synthesis of **C3** from **L1** *via* silver oxide route.[18]

The ^{1}H NMR spectrum of **C3** shows similar features to that of **C6** albeit with slightly differing chemical shifts; the major difference is the presence of a broad singlet corresponding to the carboranyl CH at 4.45 ppm. The data obtained for **C3** were comparable with that previously reported.[18] One difference however was the presence in the HRMS of a signal at *m/z* 660 that corresponds to $[C_{18}H_{35}B_{10}IrN_2Br]^+$, i.e. [**C3**-2Cl+Br]$^+$. Holmes did not observe halide mixing in **C3**, however it is possible that a longer reaction time has led to this effect.

With complex **C3** in hand, attempts were made to synthesise the mixture of **C4**/**C5** using the silver oxide route (Figure 61).

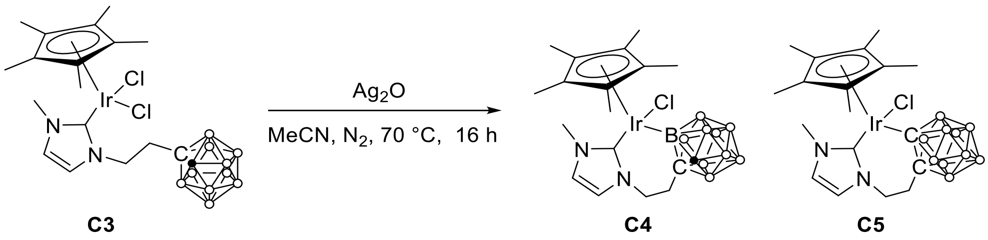

Figure 61. Literature synthesis of **C4**/**C5** from **C3** *via* silver oxide route.[18]

Reaction progress can be monitored by HRMS, which typically revealed incomplete cyclometallation after the prescribed 16 hour period. Attempts were made to drive reaction progress further by addition of more Ag_2O, however incomplete reaction was still observed. Silver oxide is only sparingly soluble in MeCN; for this reason reactions were performed with a large volume of solvent, in addition to a slight excess of silver oxide, in an attempt to increase the active quantity of the base in solution. When such reactions were monitored by HRMS the eventual disappearance of the *m/z* 615 peak attributed to **C3** was noted after 24-48 hours. The work-up was also modified, with filtration through celite, followed by recrystallization from acetone and pentane affording a cleaner product in higher yield.

Analysis of the product by ^{1}H NMR spectroscopy is challenging in the case of **C4**/**C5**, due to the mixture of products. In addition to the obvious mixture of boron and carbon cyclometallation, multiple forms of stereoisomerism also contribute. The Ir is itself a chiral centre, meaning that the signals for the CH_2 protons become diastereotopic. Additionally, in the case of boron cyclometallation, there are two chemically equivalent BH vertices that may be activated, leading to two different products (Figure 62).

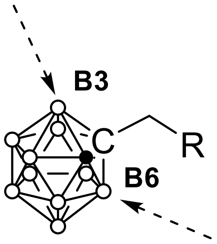

Figure 62. Schematic of substituted carborane showing possible sites of BH activation by a metal centre, B3 or B6.

The ^1H and $^{11}B\{^1H\}$ NMR spectra obtained for **C4**/**C5** were compared with those reported by Holmes and judged to be reasonably similar.

The HRMS is more informative. In spectra obtained for **C4**/**C5** no signal is observed at *m/z* 615, which would be indicative of **C3**. A peak at *m/z* 579 corresponding to $[M-Cl]^+$ demonstrates formation of the product. However, an additional peak at *m/z* 702 was always present. The envelope shape clearly identifies the species as carboranyl in nature, however an explanation of what compound is responsible for this impurity could not be realised.

The complexes **C3**, **C4**/**C5** and **C6** were used in a variety stoichiometric reactions, as well at catalytic screening and real-time reaction monitoring (see Chapter 4). Sometimes these complexes were supplemented by those previously prepared by Holmes.

2.3 Stoichiometric Reactions

Intermediates in catalytic reactions are, by their nature, often very short-lived. To enable them to be observed on a longer timescale, stoichiometric reactions that mimic catalytic conditions are often employed. Purported intermediates isolated by this method can be characterised, and then tested in a catalytic reaction. In this way, an insight into possible mechanisms for the catalysis can be gained. To this end, various stoichiometric reactions with relevant reagents were performed to gain insight into the transfer hydrogenation reaction catalysed by Ir-NHC-carborane complexes.

2.3.1 Reaction of Cyclometallated Complex C6 with HCl

Complex **C3** transforms into **C6** *via* formal loss of HCl (Figure 63). In order to probe possible routes between the cyclometallated and non-cyclometallated complexes, a stoichiometric reaction with HCl was carried out (Figure 63).

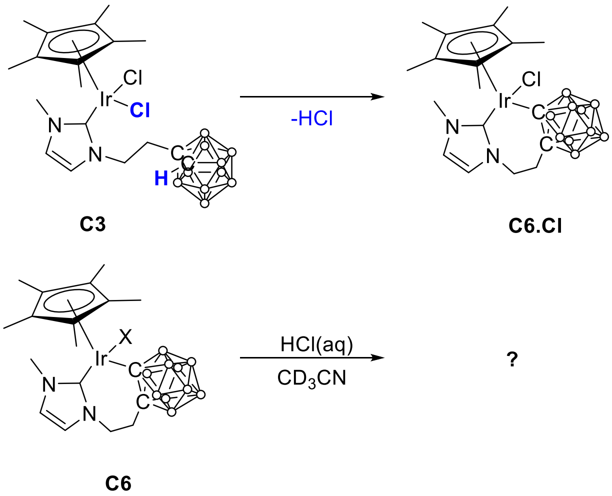

Figure 63. Top: Formal loss of HCl from **C3** generates **C6**. Bottom: Reaction of **C6** with HCl in a stoichiometric reaction in CD_3CN.

Complex **C6** was dissolved in CD_3CN in a Young's NMR tube and 0.9 equivalents of HCl was added, with any changes being monitored using ^1H NMR spectroscopy. No change was observed after standing at room temperature for 17 hours, or after heating to 80 °C for 24 hours. After the addition of 4 further equivalents of HCl combined with heating at 80 °C for 22 hours the ^1H NMR spectrum showed a mixture of starting material and a product (Figure 64). No further changes were observed in the spectrum after heating for a further 72 hours (Figure 64). The carboranyl CH signal can be seen at 4.61 ppm in the spectrum for **C3** (bottom spectrum, green star). A broad hump is observed in the product spectrum at 4.40 ppm (middle spectrum, green star). This signal is much broader than that seen for **C3**, however this could be an indication of a dynamic exchange process, between the protonated and deprotonated carborane. The product spectrum has 5 resonances in the NHC backbone region, with the peaks at 6.73 and 6.90 ppm being absent from the spectra of both **C6** and **C3**. The two doublets at 7.18 and 7.26 ppm (middle spectrum - purple star) have a chemical shift close to that of analogous signals in **C6**, however the peak shape matches more closely with those in the spectrum for **C3** (bottom spectra - purple star).

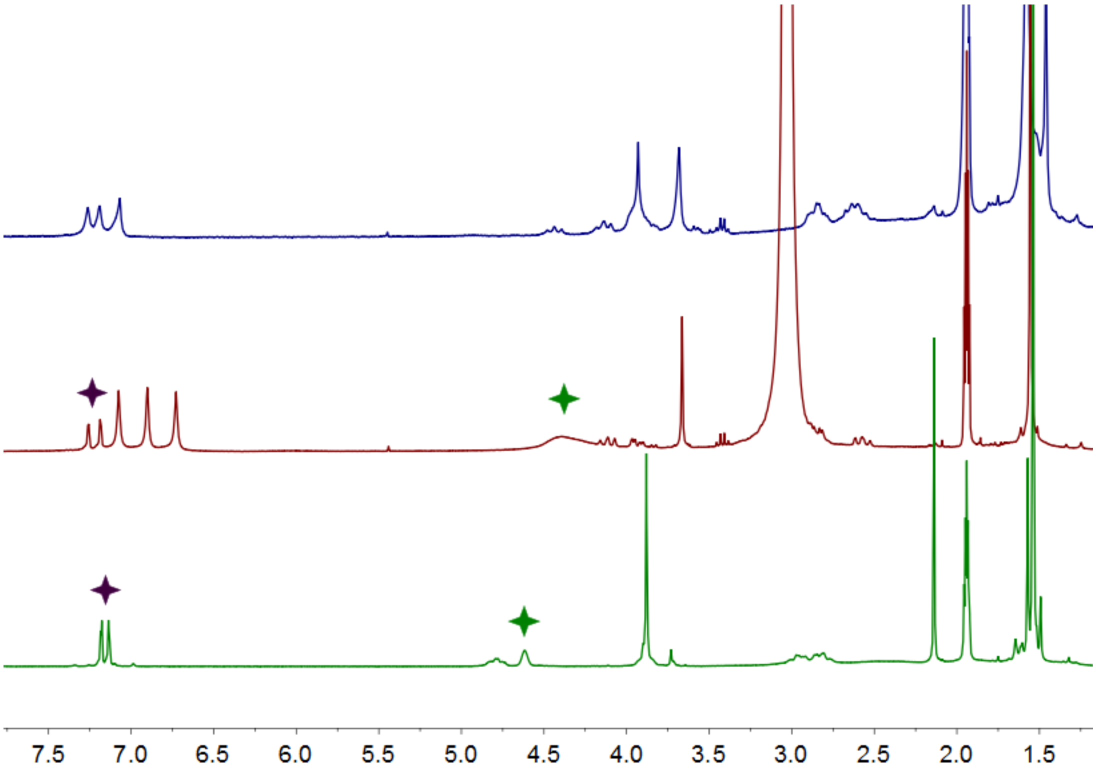

Figure 64. ^{1}H NMR spectra (300 MHz, CD$_3$CN). Top: **C6** Middle: **C6** + 5 equivalents HCl, heated for 72 hours. Bottom: **C3**.

The ^{11}B{^{1}H} NMR spectrum of the product of **C6** and 5 equivalents of HCl shows slight changes from the starting material (Figure 65). Comparison of the ^{11}B{^{1}H} NMR spectrum obtained with that for **C3** does not indicate that **C3** has been formed. A HRMS obtained of the products of this reaction revealed the presence of **C6** (*m/z* 579 for [M-Cl]$^+$) as the major peak (Figure 66). A very low intensity peak corresponding to **C3** at *m/z* 615 can also be seen. Overall, it is clear that the cyclometallated complex does not cleanly produce the non-cyclometallated complex upon action with acid.

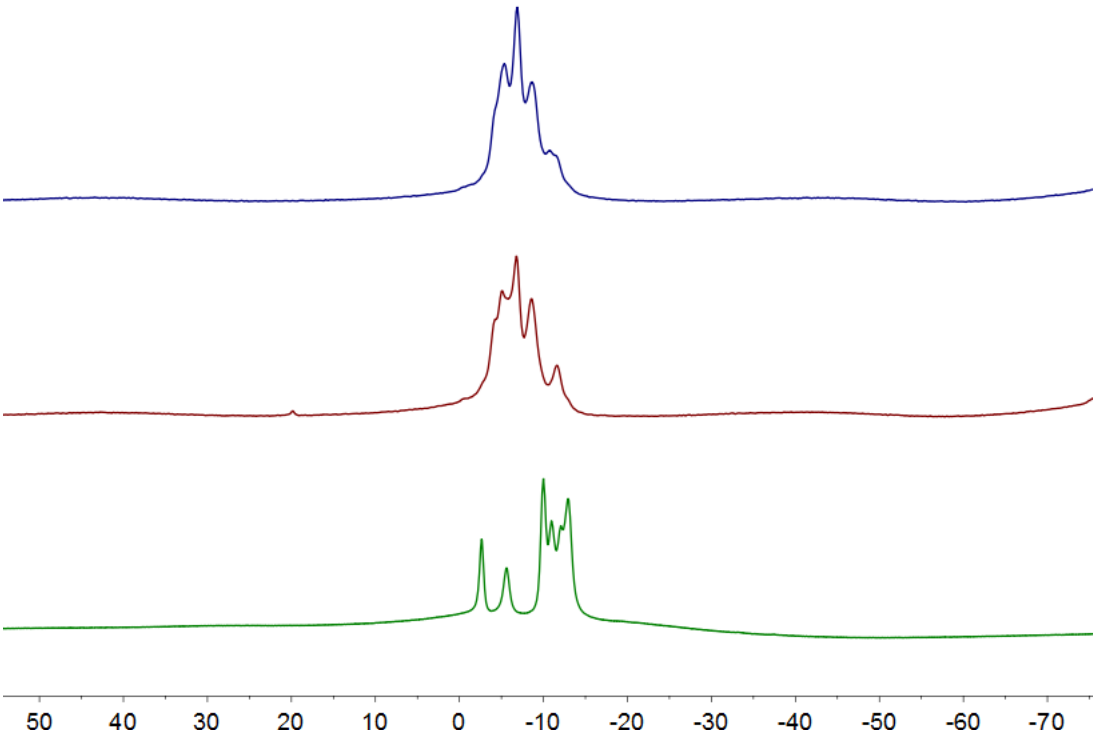

Figure 65. $^{11}B\{^{1}H\}$ NMR Spectra (96 MHz, CD_3CN). Top: **C6**. Middle: **C6** + 5 equivalents HCl, heated to 80 °C for 72 hours. Bottom: **C3**.

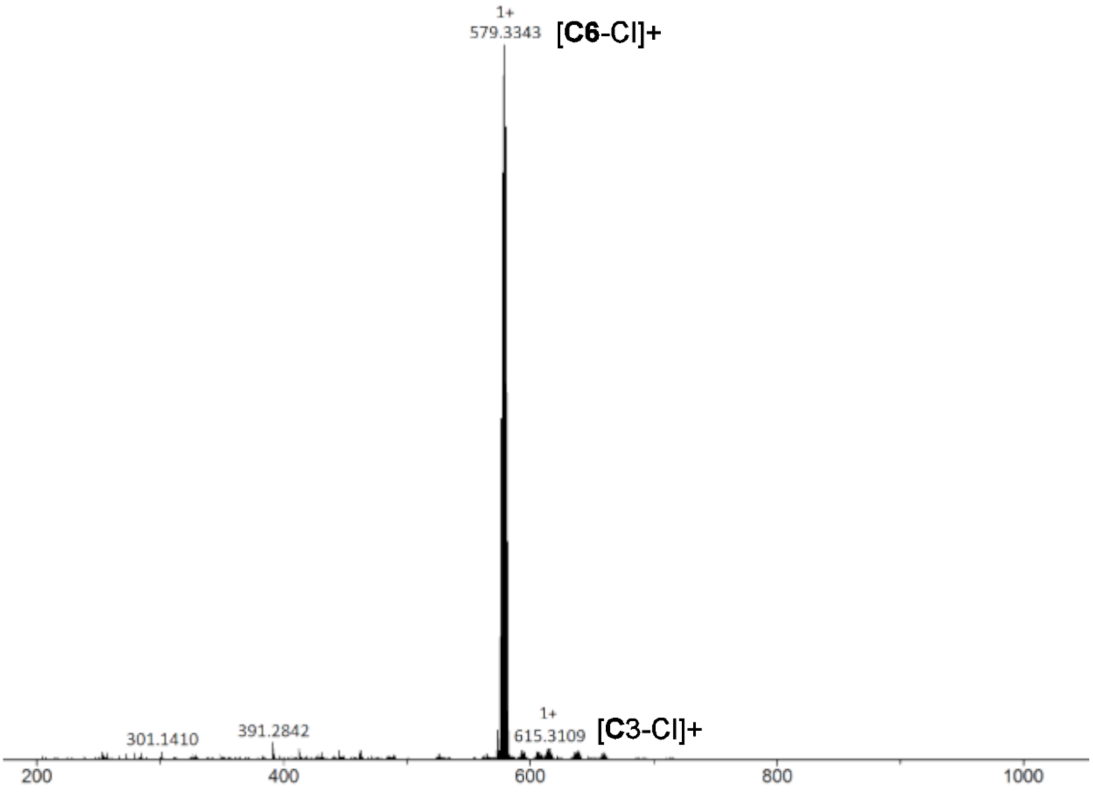

Figure 66. HRMS obtained following the reaction of **C6** + 5 equivalents of HCl, heated to 80 °C for 72 hours.

2.3.2 Reaction of Cyclometallated Complex C6 with IPA and K^{t}BuO

If the carborane moiety is involved in the transfer hydrogenation reaction as a proton shuttle, then there must be a proton source in the reaction with which to protonate the carborane. The IPA solvent seems the most likely option. Therefore, the reaction of **C6** with IPA was tested. As it was desirable to monitor the reaction by NMR, a substoichiometric quantity of IPA was added to a solution of **C6** in CD_3CN in a Young's NMR tube. No reaction was observed to take place, either at room temperature or after heating to 80 °C for 21 hours. This is probably to be expected given that no reaction is observed under catalytic conditions in the absence of a base.[18]

When 0.9 equivalents of K^{t}BuO in THF were added to the NMR tube containing **C6** and IPA an immediate colour change was observed, from yellow to red. Changes are visible in the ^{1}H NMR spectrum after 5 minutes of heating at 80 °C, with the reaction proceeding further after 1 hour, and appearing to be complete after heating for 18 hours (Figure 68). Curiously, the red colour reverted back to yellow by the end of the reaction. Possible products from the reaction would be an alkoxide complex (^{t}BuO or ^{i}PrO) or a hydride complex (if β-hydride elimination occurs), in which the halide has been replaced. In the case of the former, a resonance for coordinating alkoxide should be seen in the ^{1}H NMR spectrum, as distinct from that which is free in solution. In the case of hydride formation, the by-product acetone should be visible, given that the reaction was performed in a sealed Young's NMR tube.

Bergman *et al.* have reported a series of IrCp* alkoxide complexes along with the chemical shifts of the alkoxide protons (Figure 67).[20] In complex **2.3** a distinct downfield shift is seen on coordination of the alkoxide relative to the reported shifts of free ethanol. For complex **2.4** a downfield shift of the CH signal is seen, in addition to the two methyl groups becoming inequivalent.

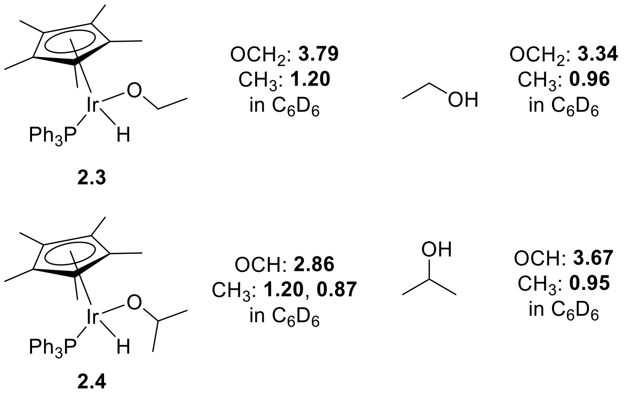

Figure 67. Comparison of ^{1}H NMR shifts for coordinated alkoxides versus parent alcohols (ppm).[20,21]

There is no indication of the presence of any signals due to a coordinated *iso*-propoxide in the ^{1}H NMR spectrum of **C6** with IPA and K^{t}BuO. The expected doublet at 1.09 ppm and septet at 3.86 ppm that correspond to free IPA in CD_3CN remain for the reaction duration (Figure 68). The peaks integrals decrease relative to the residual CD_2HCN peak during the final overnight heat, however no new peaks in the region reported by Bergman are observed.

Based on the data reported by Bergman it would be expected that a coordinated *tert*-butoxide group would appear at a different chemical shift to that of *tert*-butanol. A peak assigned as corresponding to ^{t}Bu protons is seen at 1.17 ppm in the ^{1}H NMR spectra (Figure 68). The signal remains at this shift throughout the reaction progress. The reported shift for butanol in CD_3CN is 1.16 ppm, and this has been confirmed by obtaining a ^{1}H NMR spectrum of K^{t}BuO solution in THF in CD_3CN.[21] Therefore it is unlikely that *tert*-butoxide coordination has occurred.

A peak corresponding to acetone can be seen for the duration of the reaction. The ratio of the peak integrals for acetone to residual CD_2HCN remains essentially constant throughout the reaction, even decreasing slightly towards the end. However, the differences are small <2%, and therefore within error. This data does not provide convincing evidence for formation of a hydride *via* β-hydride elimination from a coordinated propoxide.

Although signals for the suggested products of this reaction are not seen, there are clear changes to the ^{1}H NMR spectra during the course of the reaction. In the region around 7 ppm where signals for the NHC backbone are generally seen, the peak shapes change significantly, becoming more complex and appearing over a smaller range. The N-methyl group signal (3.93 ppm) appears to vanish completely upon addition of the base. A comparable signal appears concomitantly at 3.59 ppm. A change is also seen to the Cp* methyl group signal, appearing at the start of the reaction as two singlets (1.57 and 1.48 ppm). Upon addition of a base, these signals disappear with a new singlet at 1.49 ppm. The integral of this signal relative to the backbone signals is less than half what would be expected. The duality of signals observed for the Cp* and methyl groups in **C6** is believed to be a result of the presence of both chloride and bromide ligands (confirmed by SCXRD).[9] So, a simplification in this region would imply that the two halides in the complex have been replaced by one single ligand type, supporting the idea that an alkoxide has replaced the halide. However, as noted earlier, there is a distinct lack of other signals indicative of a coordinated alkoxide. Another explanation could be the selective removal of one type of halide ligand, leaving only **C6**.Cl or **C6**.Br intact.

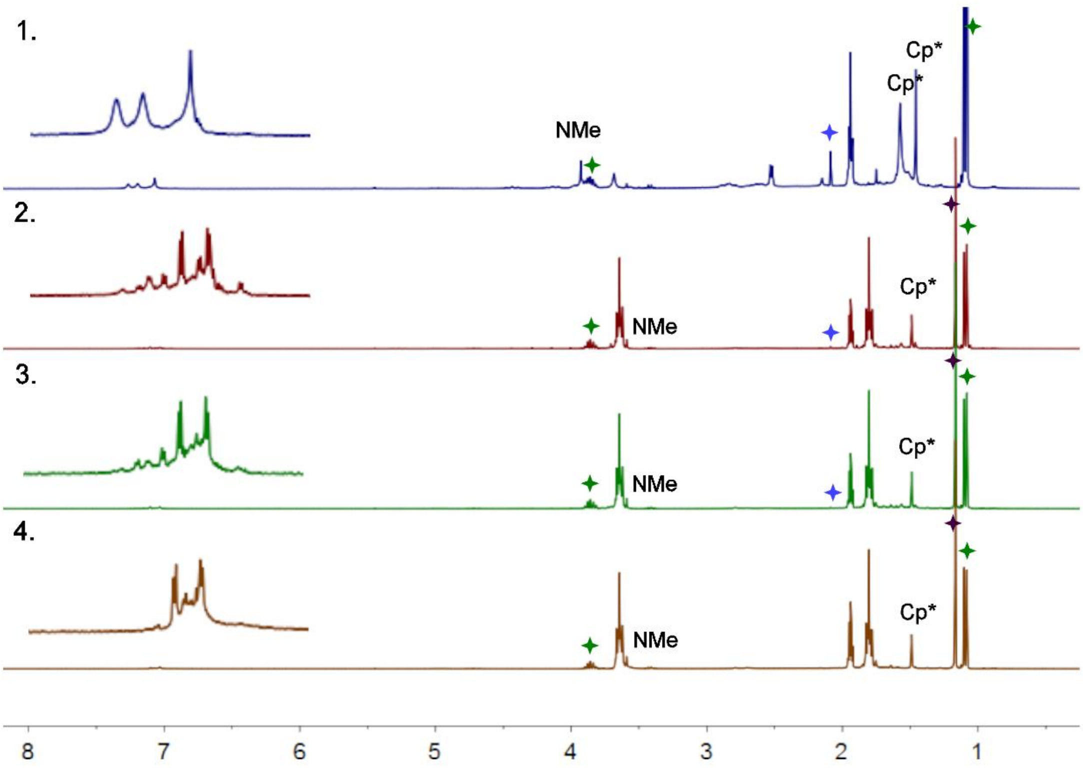

Figure 68. ^1H NMR spectra (CD_3CN, 300 MHz) recorded for reaction of **C6** with K^{t}BuO and IPA. Green stars denote IPA, purple stars denote K^{t}BuO, blue stars denote acetone. **1. C6** + IPA, **2.** 5 minutes after K^{t}BuO addition. **3.** 1 hour after K^{t}BuO addition. **4.** 18 hours after K^{t}BuO addition. Inset: enlarged images of NHC-backbone region.

There are also subtle changes in the $^{11}B\{^1H\}$ NMR spectra (Figure 69) during the course of the reaction of **C6** with IPA and K^{t}BuO. A peak at -10.9 ppm disappears and a new peak appears at -1.3 ppm. There is also evidence for the formation of a small amount of a *nido*-species with the appearance of signals at -32.9 and -37.1 ppm. This is not surprising, given the base-sensitive nature of carboranes.

The HRMS data obtained for the reaction product shows the starting material peak at *m/z* 579. Additionally there are two or more overlapping ion signals with highest intensity peaks at *m/z* 640.4039 and *m/z* 645.3615. One carborane containing species with a mass of less than the starting complex is seen at *m/z* 539.2487. None of these signals can be rationalised.

These results clearly indicate that **C6** reacts with K^{t}BuO in the presence of IPA or vice versa, however the identity of the product formed proves difficult to determine.

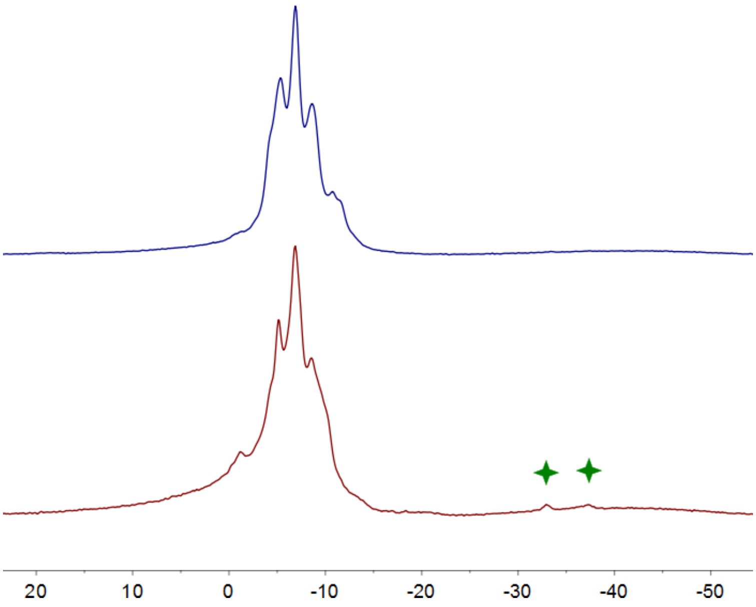

Figure 69. $^{11}B\{^{1}H\}$ NMR Spectra (96 MHz, CD_3CN). Top: **C4**. Bottom: **C4** + K^{t}BuO + IPA, heated 80 °C for 18 hours.

2.3.3 Stoichiometric Reaction of Cyclometallated Complex C6 with K^{t}BuO

A stoichiometric reaction was performed to investigate the reaction of base with **C6** in the absence of IPA. Upon addition of K^{t}BuO to a Young's NMR tube containing a solution of **C6** in CD_3CN a colour change was observed from yellow to red. Precipitation of a solid also occurred. Comparison of the ^{1}H and $^{11}B\{^{1}H\}$ NMR spectra obtained with those of the reaction of **C6**, K^{t}BuO and IPA indicate that the same product is formed in both cases. As with previous reactions, there is no evidence of butoxide coordination.

HRMS data from this reaction shows a peak corresponding to the starting complex at *m/z* 579. The only other signal that appears to correspond to a carboranyl species (based on broad *m/z* range) is at *m/z* 637.4931. One possibility at this mass would be [**C6**-Cl+acetone]$^{+}$. However, the predicted *m/z* is 637.3760 giving a large error of 184 ppm. Additionally, the predicted spectrum is not a good match with that obtained of the product. Therefore it is unclear what species gives rise to this signal.

2.4 Investigation of Hydride Complexes

The stoichiometric reactions described hitherto have aimed to characterise products formed under simulated catalytic conditions. Conclusive characterisation of these products has however, proved elusive. Formation of a metal hydride is considered to be an essential intermediate for transfer hydrogenation in both inner and outer-sphere mechanisms.[22] Therefore it is desirable to probe the circumstances under which a hydride species derived from the complexes under investigation may be formed. Isolation of a hydride species opens up the possibility of comparing the catalytic activity of such a species with the original complex. Efforts were therefore directed towards the preparation of hydridic species derived from complexes **C3** and **C6**.

2.4.1 Mechanism of Hydride Formation

In TH reactions, metal hydrides may be formed from propoxide complexes *via* β-hydride elimination, after which the formed acetone may be displaced by the substrate ketone.[22,23] However, in the initially proposed catalytic cycle, there is no vacant site adjacent to the propoxide at which β-hydride elimination can occur (Chapter 1 - Figure 26) Yamaguchi *et al.* have reported interesting results in this area, obtained by stoichiometric reactions of various Ir complexes with both Na^{i}PrO and NaBH$_4$.[24] They propose formation of hydride complex **2.6** from coordinatively saturated complex **2.5** *via* a cationic intermediate in which the chloride ligand dissociates and acts as a counter-ion (Figure 70). They describe the subsequent synthesis of a dihydride complex **2.7**, where the coordination site for β-hydride elimination is provided by a ring-slip of the Cp* ligand. Both these routes would provide a way for **C6** to transform into a hydride complex. Therefore attempts to prepare hydride complexes derived from **C3** and **C6** were made, using the methods described.

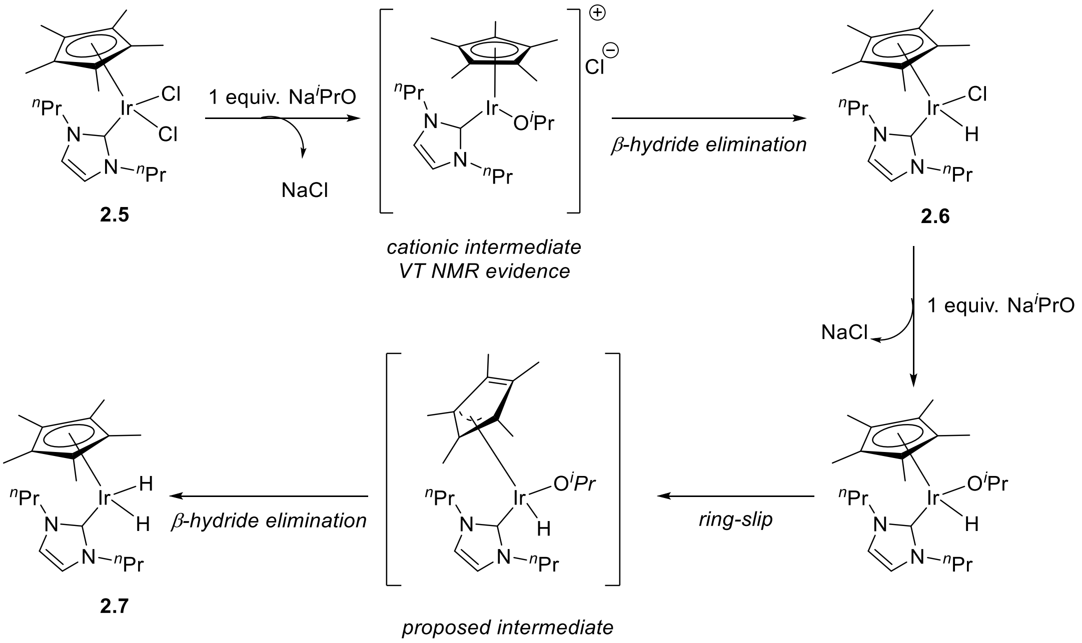

Figure 70. Hydride complexes and proposed formation mechanism reported by Yamaguchi.[24]

2.4.2 Comparison of Catalytic Activity with New Base

Before undertaking stoichiometric reactions, it was desirable to determine the effect of the base on the catalytic activity of the previously investigated Ir complexes. If similar behaviour is observed with Na^{i}PrO as with K^{t}BuO then the products of stoichiometric reactions with Na^{i}PrO can be considered a reasonable proxy for species present under catalytic conditions. Therefore a screen was carried out, using identical conditions to those used previously by Holmes for TH, replacing K^{t}BuO with Na^{i}PrO.[18] To investigate whether the cyclometallation effect is still observed, both **C3** and **C4/C5** were investigated. Both were samples obtained from a previous group member. The results for these complexes were compared with [IrCp*Cl$_2$]$_2$ as a benchmark as well as a run with no catalyst (Table 3).

Table 3. Comparison of conversions obtained with two alkoxide bases.

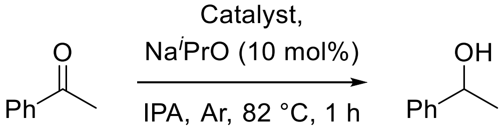

	Conversion				
Catalyst	Run 1	Run 2	Run 3	Average	With K^{t}BuO
-	7%	5%		6%	8%
[IrCp*Cl$_2$]$_2$	32%	42%	32%	32%	68%
C3	20%	19%		20%	33%
C4/C5	44%	49%		47%	>99%

Conversions calculated by comparing the ^{1}H NMR integral of the C*H* signal for 1,3,5-trimethoxybenzene to the C*H*OH signal for the product. Spectra were recorded by taking 0.1 mL of reaction mixture in 0.5 mL of CDCl$_3$. K^{t}BuO results are those previously obtained by Holmes.[18]

Conversion is reduced in all cases on switching from K^{t}BuO to Na^{i}PrO. The trends remain the same however: a decrease in activity is seen comparing [IrCp*Cl$_2$]$_2$ with **C3**, whilst the mixture of cyclometallated carborane complexes **C4/C5** provides the highest conversion.

The reaction mixture was analysed by HRMS for runs containing **C3** and **C4/C5**. In both cases a peak that corresponds to a cyclometallated complex having lost a halide ligand was observed at *m/z* 579. This is particularly surprising in the case of **C3**, as this peak is not observed in pure samples of the starting material. Other carborane containing species – identifiable by their distinctive isotope pattern – were also observed at *m/z* 595 and *m/z* 636. The data obtained for the run using **C3** are shown in Figure 71. The peak at *m/z* 595.3280 is a good match for [**C6**-Cl+O]$^+$ (Figure 71: 1). The peak at *m/z* 636.3545$^+$ is a good match for [**C6**-Cl+O+MeCN]$^+$ (Figure 71: 2). It is not clear what the likely site of oxidation in the complex is; one possibility is the formation of an imidazolone that is no longer coordinated to the Ir centre, but is held in place by the coordinated carborane tether (Figure 71 - left). Another possibility is the oxidation of the Cp* ring (Figure 71 - right). This effect has been observed in [Cp*IrTsDPEN] catalysts when used for the hydrogenation of O_2 (Figure 72).[25] Rauchfuss *et al.* observed that a peroxide species **2.8** may be formed from the hydridic catalyst derivative **2.9**. Attack of a Cp* methyl group ensues leading to the formation of a fulvene complex **2.10**.

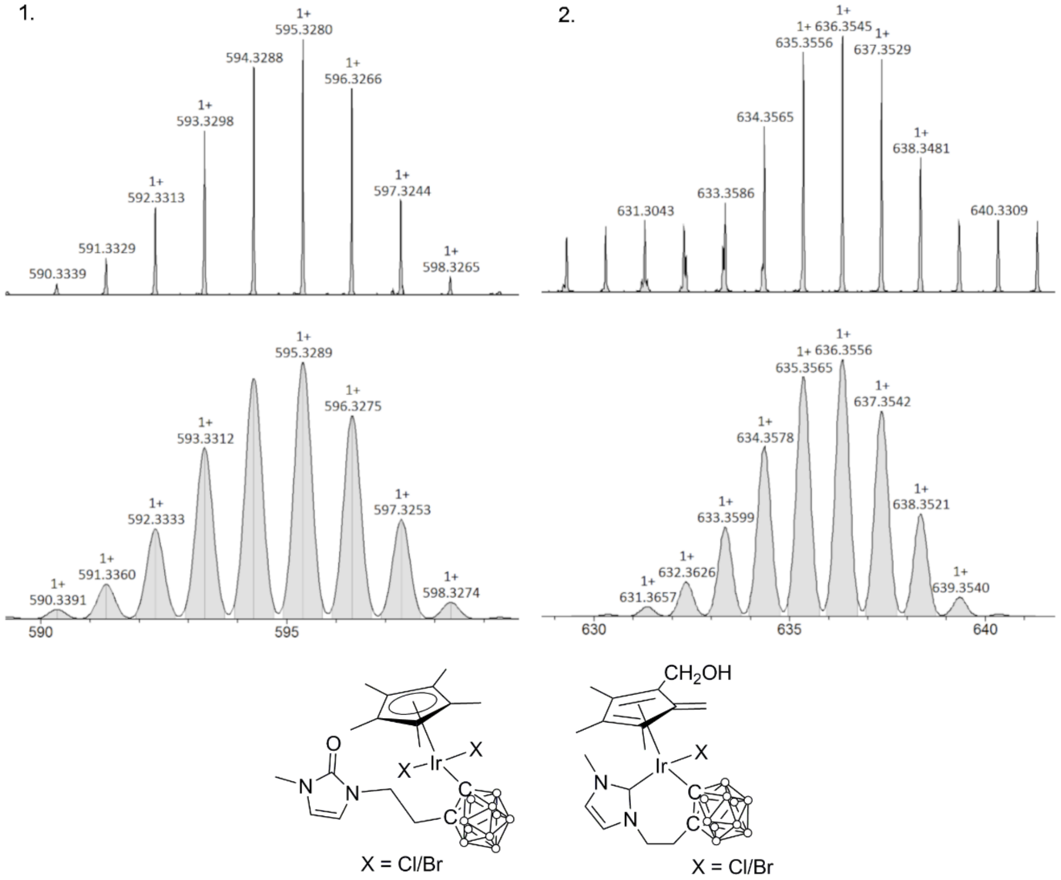

Figure 71. Above: HRMS data obtained from catalytic run using **C3**. Below: calculated values. (**1**) [**C6**–Cl+O]$^+$. (**2**) [**C6**–Cl+O+MeCN]$^+$. Structures indicate possible sites of oxygen incorporation.

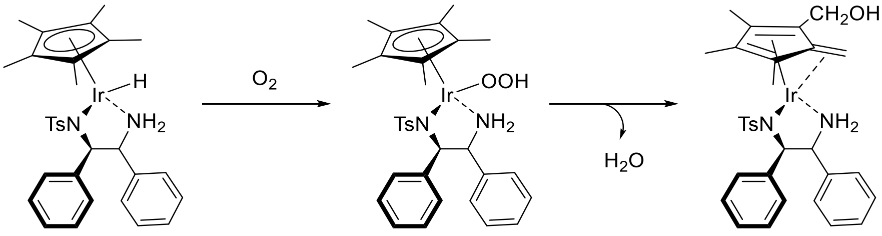

2.8 **2.9** **2.10**

Figure 72. Oxidation of a Cp* methyl group in the presence of oxygen as reported by Rauchfuss *et al.*[25]

As the HRMS data was obtained in aerobic conditions it is not clear whether the oxygen containing product is formed during catalysis or subsequent analysis. It is not therefore possible to draw definitive conclusions from these data.

The HRMS data for the catalytic run using **C4/C5** is similar to that for the run using **C3.** Good matches for the predicted spectra for [**C6**-Cl]$^+$ and [**C6**–Cl+O]$^+$ are again observed. The peak at *m/z* 636 can again be attributed to [**C4**–Cl+O+MeCN]$^+$ with an error of -4.4 ppm. However, there are many other peaks of a similar intensity which cannot be rationalised.

It is interesting that **C1** appears to become cyclometallated under catalytic conditions. This raises the question of why the activity for **C1** is lower than for **C4/C5**. One explanation is that the cyclometallation is slow enough to cause an induction period that leads to lower conversion after the 1 hour reaction time period. This could be investigated by kinetically profiling the catalytic reaction. Work in this area is described in Chapter 4.

2.4.3 Stoichiometric Reactions with $NaBH_4$

In addition to reactions using Na^{i}PrO, Yamaguchi *et al.* also report the preparation of hydride complexes using $NaBH_4$.[24] It would be expected for $NaBH_4$ to be more effective at producing hydride species than Na^{i}PrO. It is desirable to investigate not just **C6** due to its high catalytic activity, but also **C3** with relatively low activity to understand the differences. A stoichiometric reaction with $NaBH_4$ and **C3** was performed in which 1.8 equivalents of $NaBH_4$ were combined with a solution of **C3** in d_8-THF (Figure 73).

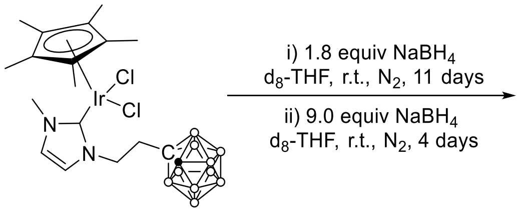

C3

Figure 73. Scheme showing conditions for the reaction of **C3** with $NaBH_4$.

The expected product of this reaction is the monohydride complex formed by displacement of one chloride ligand from **C3**. Upon combination, the solution was allowed to stand at room temperature for 5 hours. After this time a ^1H NMR spectrum was recorded and compared with that for **C3** in d_8-THF. Yamaguchi *et al.* report the hydride signals in the ^1H NMR spectrum between -13 and -17 ppm.[24] Consequently, spectra were recorded to -20 ppm to determine if hydridic signals are present. The signals in the positive region are nearly identical with those before addition of $NaBH_4$, and there are only a few signals in the hydride region of very low intensity. The biggest of these peaks appears at -16.22 ppm and integrates to just 0.02H relative to the 2H for the NHC backbone signals. The other three signals appear at -13.80, -14.03, and -15.43 ppm; these lie too close to the baseline for an adequate integration to be obtained. No further change was observed after standing at room temperature for 3 days. After an additional 7 days an excess of $NaBH_4$ was added causing the peak area of the signal at -16.22 ppm to increase slightly from 0.02 to 0.04. A visual inspection suggests an increase in the two more downfield hydride peaks, whilst the peak at -15.43 remains unchanged. The solution was allowed to stand at room temperature for 4 days after which time the relative peak area at -16.22 ppm was 0.06. A new broad peak at -13.32 ppm was also observed. In contrast to the stoichiometric reactions of **C6** with base (Sections 2.3.2 and 2.3.3), there are no changes observed for the Cp* or N-methyl signals. The $^{11}B\{^1H\}$ NMR spectrum obtained showed little change from that of the starting material.

A HRMS was also obtained for the product of this reaction. The major signal observed is at *m/z* 615 corresponding to [**C3**-Cl]$^+$ and/or the equivalent hydride complex having lost a hydride; likewise *m/z* 660 is observed for the [**C3**.Br-Cl]$^+$ (*vide supra* - 2.2). A minor peak that corresponds to a cyclometallated complex having lost a halide or hydride (i.e. **C6**-Cl) is also seen at *m/z* 579. There is also a peak at *m/z* 707.2456, however the origin of this could not be ascertained.

The results from this reaction indicate that under the conditions examined, formation of a hydride complex derived from **C3** is not facile. This could be an explanation for the low activity observed for this catalyst.

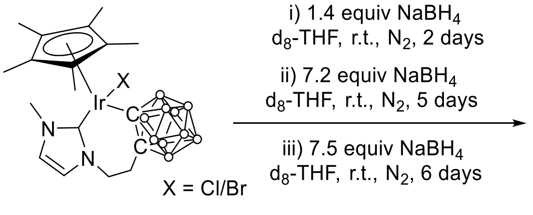

C6

Figure 74. Scheme showing conditions for the reaction of **C6** with $NaBH_4$.

A reaction between **C6** and $NaBH_4$ was also performed (Figure 74). A sample of **C6** in d_8-THF was placed in a Young's NMR tube, and 1.4 equivalents of $NaBH_4$ were added. In this case formation of a single hydride species at -15.57 ppm is evident after 3 hours of standing at room temperature (integral of 0.09), with the integral ratio increasing to 0.14 after 27 hours (Figure 75). As with the reaction with **C3**, the hydride integral was compared to that for the NHC backbone region. After 2 days excess $NaBH_4$ (total 8.6 equivalents) was added, which increased the main hydride integral to 0.38 after 4 further days at room temperature. The $NaBH_4$ loading was further increased (total 16.2 equivalents); this resulted after 3 days in a hydride integral of

0.42. After 27 hours minor peaks at -15.48 and -15.64 ppm were also present, appearing as 0.06 and 0.12 relative to an integral of 1 for the main signal at -15.57 ppm. After the addition of excess $NaBH_4$ the additional peaks are observed at -14.77, -15.60 and -15.64 ppm. At the end of the reaction the integral ratios as compared to the main hydridic signal are 0.02, 0.15 and 0.05 respectively.

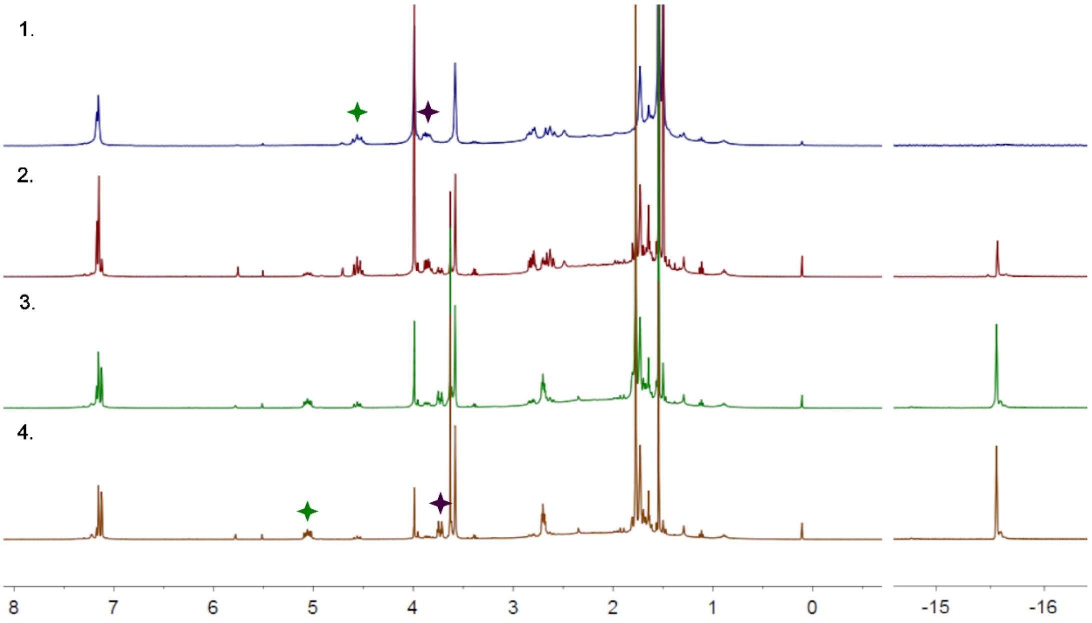

Figure 75. ^1H NMR Spectra (400 MHz, d_8-THF). **1**. **C6**. **2**. **C6** + 1.4 equivs $NaBH_4$ after 27 hours. **3**. **C6** + 8.6 equivs $NaBH_4$ after 7 days. **4**. **C6** + 16.2 equivs $NaBH_4$ after 13 days. Green and purple stars identify the shift in peak position for NCH_2 signals. Note: hydride region not to scale.

In addition to the presence of signals indicative of a metal-hydride species there are a number of features of note in the spectra obtained during the reaction. Firstly, the NHC backbone region sees a reduction of the signal in the range 7.17-7.19 ppm; there is a concomitant appearance of a broad doublet centred on 7.12 ppm (Figure 76 - left). Similarly, the NMe signal at 3.99 ppm decreases whilst a new peak at 3.64 ppm grows in (Figure 76 - centre). This pattern is repeated with the peaks associated with the Cp* methyl groups (Figure 76 - right). The initial peak positions are at 1.54 and 1.50 ppm, and during the reaction these decrease as a new signal at 1.77 ppm appears. Changes to the CH_2 signals are also apparent: the multiplet initially centred at 4.55 ppm shift downfield to 5.06 ppm (Figure 75 - green stars), whilst that 3.87 ppm shifts upfield slightly to 3.73 ppm (Figure 75 - purple stars). The complex set of peaks between 2.90 and 2.45 simplify somewhat to form a multiplet centred at 2.60 ppm.

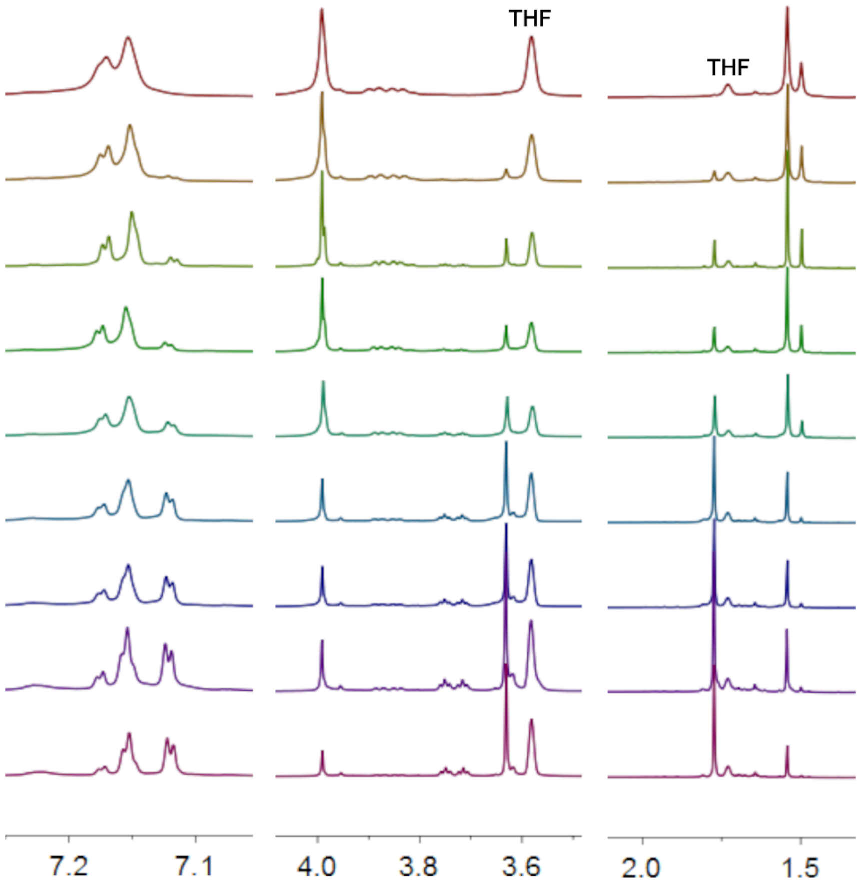

Figure 76. ^{1}H NMR Spectra (400 MHz, d_8-THF) taken throughout reaction of **C6** with $NaBH_4$ (top - prior to $NaBH_4$ addition, bottom -after 13 days), showing changes to the signals in the NHC-backbone region (left), NMe group (centre) and Cp* (right).

The main hydride integral may be compared with those attributed to new species. This gives a value of 0.55H (relative to 2H for the backbone protons), which may be indicative of a dimeric species, in which the ratio of hydride to NHC is 1:2 (Figure 77).

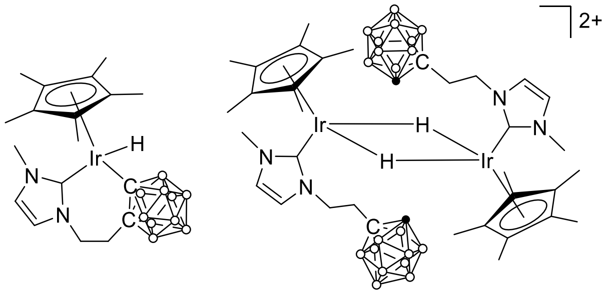

C6.H

[**C6**.H]$_2$

Figure 77. Possible structure for hydridic species derived from **C6**.

The $^{11}B\{^{1}H\}$ spectrum obtained of the reaction product showed an increase in the complexity of the spectrum, and a spreading out of the peaks, which could indicate a less symmetrical carborane species.

The HRMS data shows the major ion peak at *m/z* 579. As previously discussed, this is attributable to **C6** with either a halide or a hydride removed. This fact in combination with the ^{1}H NMR data seems to point toward the formation of a monohydride, which is further supported by the observation of a peak envelope at *m/z* 486.2306. This can be attributed to the MeCN adduct of **C6**.H in which the Cp* ring is absent (Figure 78). Given the +1 charge of the species, it is highly likely that this represents the direct observation of **C6**.H and not a fragment of **C6** in which the carborane has been protonated. However, it is unclear whether this adduct is extant in solution or if it is formed from **C6**.H within the mass spectrometer.

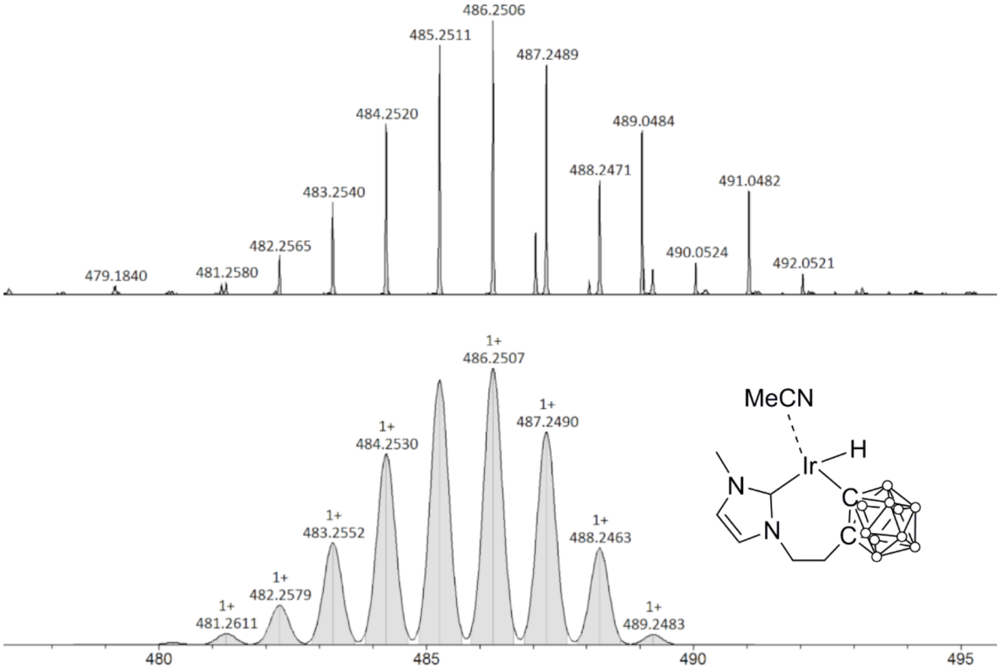

Figure 78. Above: HRMS data obtained from reaction of **C6** with NaBH$_4$. Below: Calculated molecular ion peak for [$C_8H_{20}B_{10}IrN_2$]$^+$ with structure inset.

Single crystals suitable for X-Ray diffraction were grown by layering anhydrous hexane over the crude reaction mixture in a Young's NMR tube. The structure shows an Ir centre coordinated by a Cp* ligand, and an NHC carborane tether which is cyclometallated through a carbon (Figure 79). There is an apparently vacant site, believed to be the location of a hydride ligand – however there was too much residual electron density about the Ir for it to be modelled as such. Were a hydride ligand not located at this site, the corresponding complex would feature Ir in the +2 oxidation state, which is rare.[26]

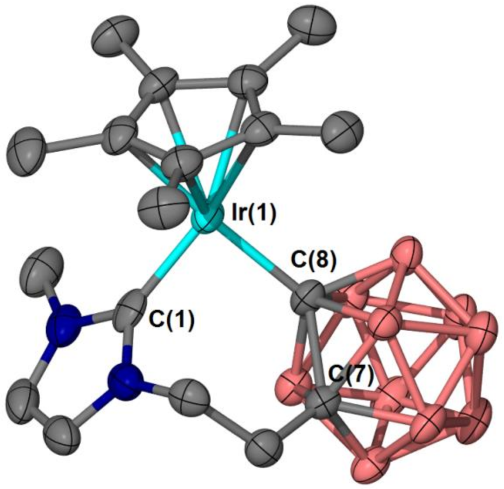

Figure 79. Molecular structure for **C6.H**. Ellipsoids shown at the 50% probability level, hydrogen atoms omitted for clarity.

Table 4. Comparison of selected structural parameters in **C6.H** and **C6**.[18]

Distance or angle	Complex	
	C6.H	**C6**
Ir(1)-C(1)	1.947(8) Å	2.041(5) Å
Ir(1)-C(8)	2.097(5) Å	2.149(6) Å
Cp*-Ir	1.901 Å	1.862 Å
C(1)-Ir(1)-C(8)	89.2(2) °	95.6(2) °

There are some differences between the structural parameters for **C6.H** and those reported for **C6** (Table 4). There is a contraction in the Ir-carbene bond length on going from **C6** to **C6.H**, with a slight reduction in the Ir-carborane distance also observed. By contrast the distance between the Ir centre and the plane defined by the inner Cp* carbon atoms has slightly increased. The NHC-carborane bite angle is also slightly reduced in **C6.H**, which is surprising given that the chloride/bromide ligand for **C6** is more bulky than a hydride. However, a non-covalent interaction between the N-methyl group of the NHC and bromide ligand in **C6**, may draw the NHC ligand away from the carborane, and account for the larger bond angle.

There are only four examples of [IrCp*(NHC)H] complexes listed in the Cambridge Crystallographic Database. The Ir-NHC bond length in **C6.H** is at the shorter end of the range of bond lengths recorded previously.[27–29]

2.4.4 Stoichiometric Reactions with Na^{i}PrO

Given that the results of the catalytic screen with Na^{i}PrO showed the same trends as that with K^{t}BuO, stoichiometric reactions using Na^{i}PrO were undertaken, with the aim of investigating the potential formation of a hydride species. It is desirable to learn whether the same hydride species will be generated from **C6** and Na^{i}PrO as with NaBH$_4$. Also whether Na^{i}PrO will prove more effective than NaBH$_4$ in the generation of a hydridic complex derived from **C3**.

Using conditions reported by Yamaguchi *et al.*, **C3** was reacted with a slight excess of Na^{i}PrO in anhydrous IPA. After stirring at room temperature for 18 hours the solvent was removed *in vacuo* and a crude ^{1}H NMR spectrum was obtained in C$_6$D$_6$, and compared with that for **C3** in C$_6$D$_6$. It is clear from the comparison that the reaction mixture contains both unreacted **C3** and a new product (Figure 80).

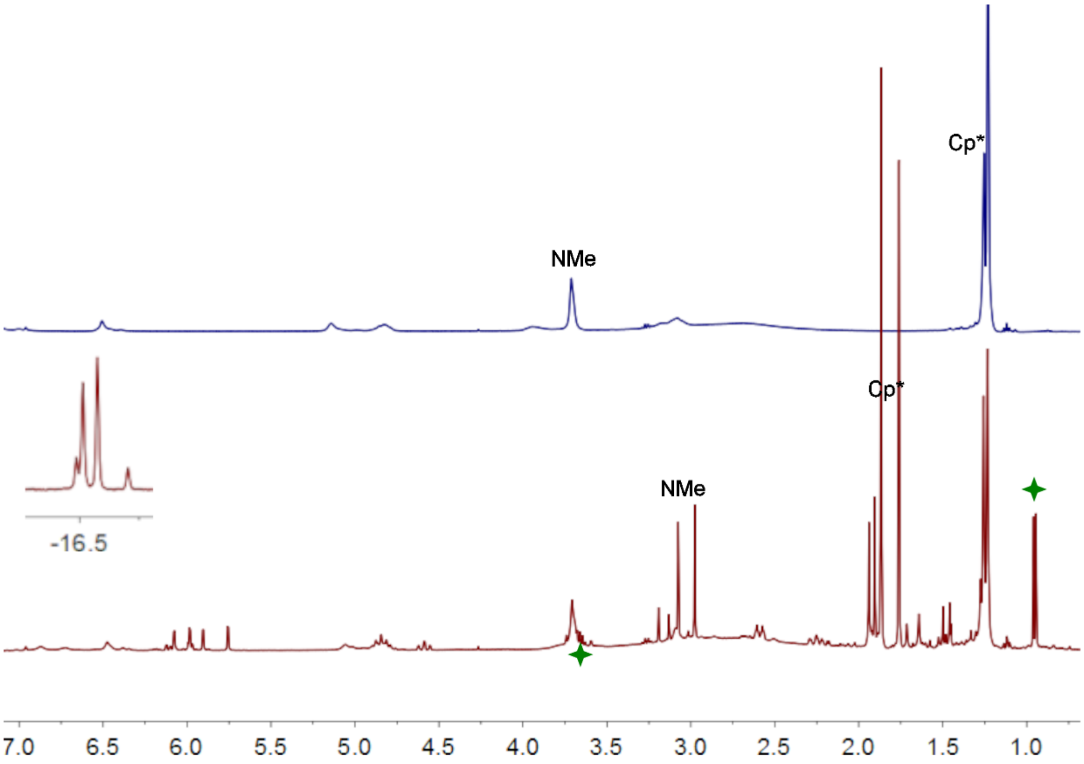

Figure 80. ^{1}H NMR spectra (400 MHz, C$_6$D$_6$). Top: **C3**. Bottom: crude product of **C3** and Na^{i}PrO, with partial hydride region inset. Green star denotes IPA.

Four major resonances are seen in the hydride region of the spectrum at -16.49, -16.51, -16.57, and -16.71 ppm. The total integral of this region as compared to a total of 2 for all NHC backbone resonances is 0.51. There are several more minor resonances at -13.40, -13.65, and -15.41. Use of 2D analysis (HMQC) allows for the suggested assignment of the new backbone, Cp*, and NMe signals, based on correlation of multiple ^{1}H signals to a single or similar ^{13}C environment (Figure 81).

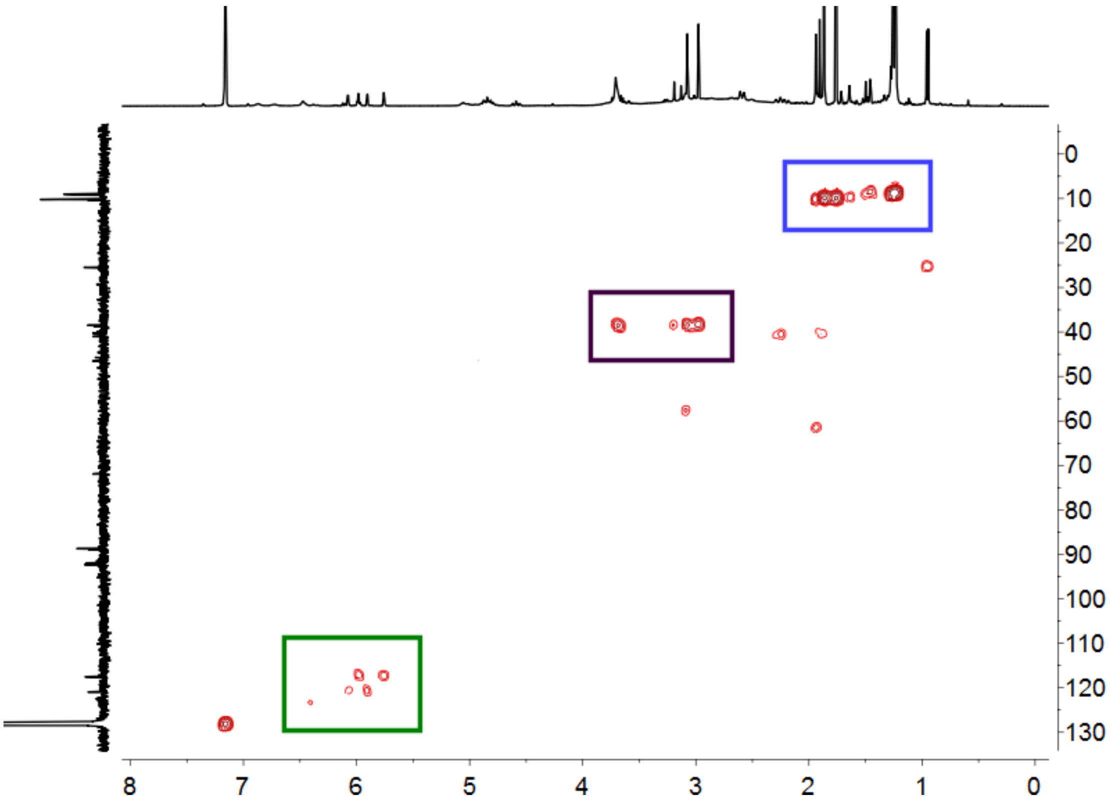

Figure 81. ^{1}H^{13}C HMQC spectrum (400 MHz, C_6D_6) of the product of **C3** and Na^{i}PrO. Green box – NHC backbone region, purple box – NMe region, blue box – Cp* region.

The backbone resonances of the crude product appear as a complex group of doublets, reminiscent of the product of cyclometallated **C6** and Na^{i}PrO (*vide infra*). The NMe signal appears as two singlets of approximately equal intensity at 2.97 and 3.07 ppm. The Cp* methyl signal also changes with two major peaks at 1.76 and 1.86 ppm. There are other possible signals at 1.90 and 1.94 ppm with integrations approximately 1/3 that of the major peaks. Residual IPA signals are seen at 0.96 ppm and 3.67 ppm (Figure 80 - green stars), with no evidence of propoxide coordination. There are peaks present in the baseline of the spectrum which correlate well with those for cyclometallated **C6** in C_6D_6, which is backed up by the HRMS data showing an ion of *m/z* 579 which corresponds to [**C6**–Cl]. A peak at *m/z* 615 for the starting material [**C3** – Cl] is present, again in agreement with the ^{1}H NMR data. The other major peak present in the HRMS comes at *m/z* 659.3336, which has not been rationalised.

Overall it is clear that **C3** reacts with Na^{i}PrO to form a new product or products which contain Ir hydrides. Given the multitude of apparent signals for the Cp* methyl groups and NMe groups, it seems likely that at least two products have formed. This also accounts for the large number of hydride signals observed.

The reaction of **C6** was also investigated under the same conditions. Compared to the ^{1}H NMR spectrum of **C6** in C_6D_6, the spectrum of the product is much more complex (Figure 82).

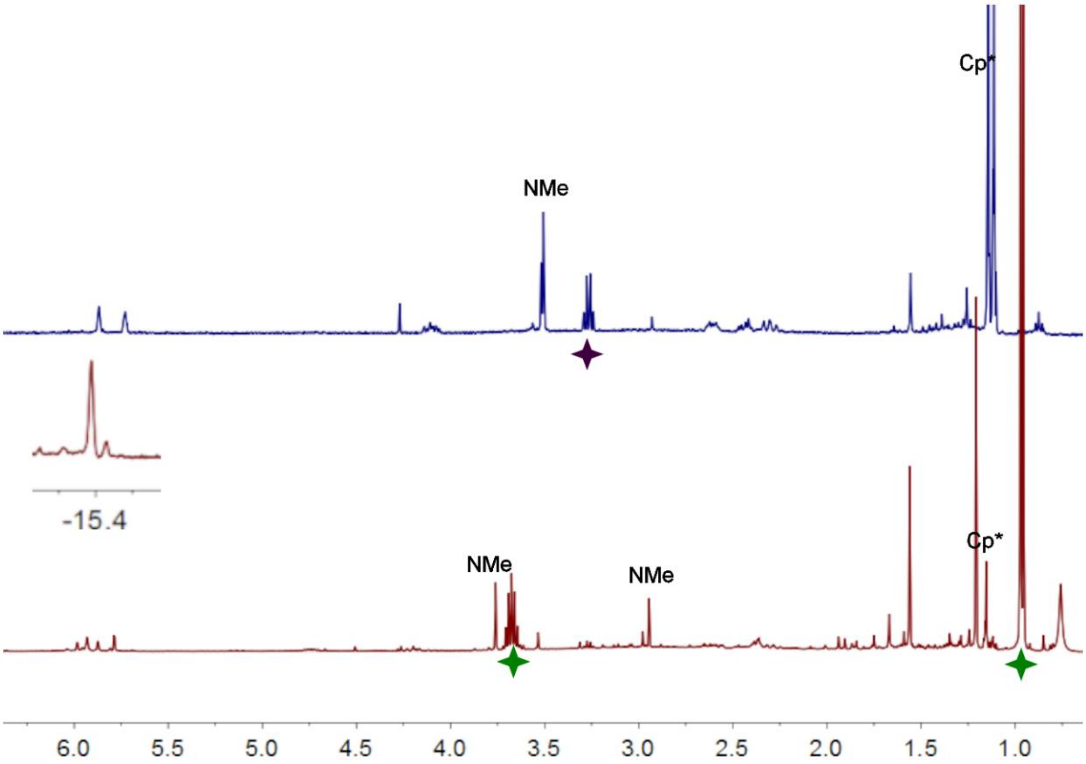

Figure 82. ^{1}H NMR spectra (400 MHz, C_6D_6). Above: **C6**. Below: crude product of **C6** and Na^{i}PrO, with partial hydride region inset. Green star denotes IPA, purple star denotes Et_2O.

Signals for residual IPA can be clearly seen at 0.96 and 3.67 ppm with no evidence of any coordination of a propoxide. A shift in the signals for the Cp* methyl groups is apparent, changing from a complex multiplet between 1.01-1.16 ppm in **C6** to two singlets at 1.21 and 1.15 ppm in the product. A shift is also observed for the N-methyl group from 3.50 ppm to two separate signals at 3.76 and 2.95 ppm. The NHC backbone region features more signals than the starting material. Two signals in the negative region are observed at -1.76 ppm, integrating to just over one relative to the 15 for the Cp* signals, and at -15.39 ppm, integrating to 0.3, which is likely due to partial hydride formation. This provides strong evidence that a hydride species or several hydride species are formed under catalytic conditions.

The major peak in the HRMS obtained from the product of the reaction of **C6** with Na^{i}PrO is at *m/z* 579, as for the reaction with $NaBH_4$ (*vide supra* - 2.4.3). Other peaks observed are the same as those obtained following the catalytic screens: *m/z* 595 and *m/z* 636, corresponding to [**C6**+O]$^+$ and [**C6**+O+MeCN]$^+$ (*vide supra* - 2.4.2). It should be noted however that in this case, although the envelope shapes are a good match with those predicted, the errors are both >40 ppm. Another signal at *m/z*

1156.6451 is observed, with the envelope shape and predicted mass matching reasonably (14 ppm error) with the formula $[C_{36}H_{67}B_{20}Ir_2N_4]^+$. $[C_{36}H_{\boldsymbol{68}}B_{20}Ir_2N_4]$ corresponds to two Ir centres coordinated by two Cp* ligands, and two NHC-carborane ligands. Figure 83 shows potential molecular structures that could lead to the displayed peak envelope. Given the *m/z* it seems clear that the carborane remains deprotonated and bound. One possible site of hydrogen loss could be a BH vertex, which could have been activated by a second Ir centre. The dimer of this (overall neutral) molecule + one hydrogen provides the required formula (Figure 83 - inset left). Alternatively, a hydride species in which one carborane has been doubly activated, observed without the hydride, is possible (Figure 83 - inset right). As previously, it is unclear whether such species are merely the result of the spectrometry, however the fact that they were not observed in any of the other reactions (*vide* supra - 2.4.2, 2.4.3) may be significant.

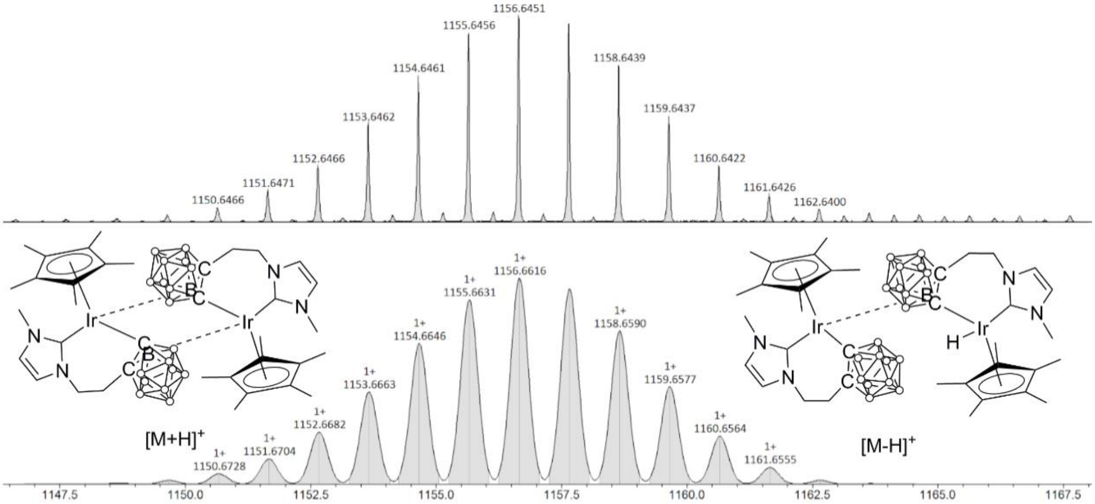

Figure 83. Above: HRMS data from the reaction of **C6** with $Na^{i}PrO$. Below: calculated data for $[C_{36}H_{67}B_{20}Ir_2N_4]^+$, with possible structures inset.

Single crystals suitable for X-Ray diffraction were grown by the vapour diffusion of hexane into a solution of the reaction mixture in THF, and were analysed at the Diamond Light Source. The overall structure observed in this case has near identical parameters to that seen for **C6.H** (2.4.3), albeit solving in the space group $P2_1/c$. Once again, there is an apparent vacant site, and it was not possible to model the presumed hydride ligand.

2.4.5 Summary

Comparisons between the analytical data following the different stoichiometric reactions are challenging, due to the different conditions and solvents used, however some hypotheses may be proposed (Table 5).

Firstly concerning the non-cyclometallated complex **C3**: reaction with $NaBH_4$ was sluggish when compared to both **C6** with $NaBH_4$ and reaction of **C3** with Na^iPrO. The hydride region of the spectra obtained for the reaction of **C3** with $NaBH_4$ is very different to that of **C3** with Na^iPrO. With $NaBH_4$ the major hydridic signal is observed at -16.22 ppm, whilst on reaction with Na^iPrO a cluster of 4 signals is observed in the region -16.49 to -16.71 ppm. Additionally, the reaction proceeds significantly further toward hydride species with Na^iPrO than with $NaBH_4$. It may be suggested that this is indicative of the formation of different hydride products.

Secondly concerning the cyclometallated complex **C6**: upon reaction with $NaBH_4$ or Na^iPrO, **C6** displays broadly similar hydridic signals, with a single major signal (-15.56 or -15.40 ppm respectively) with an associated smaller peak slightly upfield (-15.59 or -15.44 ppm respectively). Although the chemical shifts are different, due to the collection of spectra in different solvents it may be tentatively proposed that these are the result of the same complex. This is supported by the prevalence of the *m/z* 579 peak in the HRMS of both products, as this may be attributed to **C6** in which a hydride has substituted the chloride. This proposed complex (**C6.**H), also remains the only crystallographically characterised hydride species derived from these reactions. There were differences in the other signals seen in HRMS however. Reaction of **C6** with $NaBH_4$ allows for the direct observation of a hydridic species in the mass spectrum. The mass spectrum for reaction of **C6** with Na^iPrO shows the apparent presence of a dimer.

The question of whether the same species were formed by reaction of **C6** with K^tBuO is an open one. The lack of hydride data precludes comparison of this area, and the different solvents used for NMR acquisition make comparisons between the other signals challenging.

The products of the reactions with $NaBH_4$ appear to be different for **C3** and **C6**, with different signals observed for the hydrides and for the NMe and Cp* groups. The same is true for the reactions with Na^iPrO. If the product **C6**.H is responsible for the major hydride peak then this is logical, given that transformation of **C3** into **C6**.H would require cyclometallation of the carborane.

Table 5. Comparison of key signals in the ^{1}H NMR spectra for attempted synthesis of hydride complexes for **C3** and **C6**.

	Complex in d_8-THF		Complex in d_8-THF + $NaBH_4$		
	NMe	Cp*	NMe	Cp*	Hydride (major peaks only)
C3	3.91	1.62, 1.58	3.91	1.62, 1.58	-16.22
C6	3.99	1.54, 1.50	3.63	1.77, 1.54	-15.56
					-15.59 (d)

	Complex in d_6-benzene		Complex in d_6-benzene + Na^{i}PrO		
	NMe	Cp*	NMe	Cp*	Hydride
C3	3.72	1.23, 1.26	3.72	1.23, 1.26	-16.49
			2.97, 3.07	1.76, 1.86	-16.52
				1.90, 1.94	-16.58
					-16.70
C6	3.51, 3.52	1.16-1.10	3.76, 2.95	1.21, 1.15	-15.39
					-15.43

2.5 Conclusions and Future Work

Complexes of the type [Ir(COD)XL] (X= Cl/Br; L = NHC) were prepared from an imidazolium-carborane tethered ligand precursor and its phenyl analogue. These have been fully characterised; analysis indicated that the products obtained had been subject to halide scrambling during synthesis. For this reason, subsequent attempts to prepare dicarbonyl complexes were abandoned. However, in Chapter 3, computational efforts to analyse the relative basicity of the two ligands are described.

The synthesis of TH catalysts **C3**, **C4**/**C5** and **C6** was achieved by modifications to the literature procedures. The reactivity of these complexes was probed with a range of stoichiometric reactions relevant to TH conditions. It was established that the transformation of **C6** into **C3** is not facile in the presence of HCl. Reactions of **C6** with K^{t}BuO led to the formation of a new product, the identity of which could not be determined. Formation of a complex with a coordinated alkoxide was ruled out however.

Subsequent reactions aimed to prepare hydride complexes. Reaction of **C3** with $NaBH_4$ led to formation of trace quantities of a hydride species, whilst reaction of $NaBH_4$ with **C6** led to at least 50% conversion to a hydride species (although large excesses of $NaBH_4$ were required). The molecular structure obtained from crystals grown from the product of this reaction revealed a monohydride Ir(III) complex **C6**.H. The reaction of **C3** with Na^{i}PrO led to the partial formation of multiple hydridic species; the reaction with **C6** proceeded closer to completion, with one major hydride resonance observed. Once again, X-Ray crystallography revealed at least one of the products from the reaction with **C6** to be **C6**.H. Unfortunately, due to time constraints, further investigations on this species could not be performed.

Further and related work on this topic is discussed in Chapters 3 and 4. Chapter 3 describes efforts to analyse the system using computational methods. Chapter 4 describes on-line reaction monitoring of the TH reaction, allowing real-time observation of hydride species, and analysis of the kinetics of the reaction.

Isolation and purification of the various hydride species discussed in this chapter is highly desirable. In the case of **C3**, purification may enable determination of the structure. Once isolated, these hydride complexes could be used in a catalytic reaction, and compared to the parent complexes. This would provide valuable insight into their catalytic relevance.

2.6 Experimental

2.6.1. General Considerations

Where stated, reactions were carried out under an inert atmosphere of dry nitrogen or argon, using standard Schlenk line or glovebox techniques. Anhydrous solvents were dried by passing over activated alumina to remove water, copper catalyst to remove oxygen, and molecular sieves to remove any remaining water, *via* the Dow-Grubbs solvent system. Toluene, and DCM were freeze-pump-thaw degassed, while other solvents were degassed by purging with argon. Deuterated MeCN, IPA and acetophenone were dried by standing for 18 hours over activated 3 Å molecular sieves, followed by transfer to fresh activated 3 Å sieves, and then purged with argon prior to use. Deuterated benzene (99.6%) was purchased in a sealed ampoule and used directly. Decarborane was purchased from KatChem; all other chemicals were purchased from Sigma Aldrich, Alfa Aesar or Fluorochem and used without further purification. $[Ir(COD)Cl_2]_2$[30] and $[IrCp^*Cl_2]_2$[31] were prepared according to the standard literature methods. 6,9-Bis(acetonitrile)-decaborane was prepared by another group member according to the literature method.[32]

NMR spectra were recorded on either a Bruker AVneo 500 (CH dual cryoprobe), Bruker Ascend 400 or a Bruker DPX300 spectrometer. ^1H NMR and $^{13}C\{^1H\}$ chemical shifts were referenced against residual solvent peaks. Assignment of ^1H and $^{13}C\{^1H\}$ NMR spectra was aided by 2D $^1H^{13}C$ HMQC, and $^{13}C\{^1H\}$ DEPT 135 where relevant. Mass spectra were collected on a Bruker Daltonics (micro TOF) instrument operating in the electrospray mode. Elemental Analyses were performed by Mr Stephen Boyer at London Metropolitan University.

Single crystal X-ray diffraction data were collected at Diamond Light Source on Beamline I19 using syncrhotron radiation ($\lambda = 0.6889$ Å). Crystals were mounted under oil on Mitegen micromounts. Data sets were corrected for absorption using a multiscan method, and the structures were solved by direct methods using SHELXT and refined by full-matrix least squares on F2 using SHELXL-97, on the program Olex2.

2.6.2 Synthesis of Precursors and Ligands

1-Bromoethyl-1,2-dicarba-*closo*-dodecaborane

$B_{10}H_{12}(MeCN)_2$ (1.40 g, 7.03 mmol) was added to a Schlenk flask and placed under N_2. Anhydrous toluene (30 mL) was added followed by 4-bromo-1-butyne (0.66 mL, 7.03 mmol). The reaction mixture was slowly heated to 100 °C and held at this temperature for 4 hours. The solvent was removed *in vacuo* and the residue placed in a sonicator bath with portions of hexane (3 x 20 mL). The combined organic phase was transferred to a separating funnel and washed with 1 M NaOH (30 mL) followed by H_2O (2 x 20 mL). The organic phase was dried over $MgSO_4$ and the solvent removed *in vacuo* to yield the product as a white solid. Yield: 962 mg, 54%.

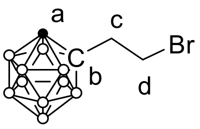

^{1}H NMR (400 MHz, DMSO) δ 5.19 (s, 1H, H_a), 3.58 – 3.45 (m, 2H, H_d), 2.82 (t, *J* = 8.0 Hz, 2H, H_c). ^{11}B{^{1}H} NMR (128 MHz, DMSO) δ -3.1, -5.8, -9.8, -11.8, -13.1. ^{13}C{^{1}H} NMR (101 MHz, DMSO) δ 74.2 (C_b), 62.7 (C_a), 38.8 (C_d), 28.8 (C_c). A mass spectrum could not be obtained for this compound. Consistent with literature data.[33]

L1

1-Bromoethyl-1,2-dicarba-*closo*-dodecaborane (400 mg, 1.59 mmol), anhydrous *N*-methyl imidazole (105 µL, 1.31 mmol) and anhydrous toluene (2 mL) were combined in an ampoule and held at reflux for 1.5 hours under nitrogen. The formed solid was isolated by filtration and washed with toluene. The solid was washed with a minimum quantity of MeOH into a fresh flask. Et_2O was added to the filtrate until precipitation of a white solid occurred. The solid was isolated *via* filtration, then dissolved in MeOH, and the insoluble matter removed by filtration through celite. Et_2O was added to the filtrate until precipitation of a white solid occurred. This solid was isolated by filtration and dried under suction. Yield: 168 mg, 38%.

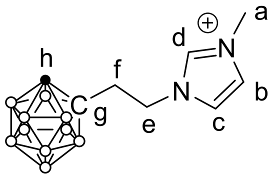

L1

^{1}H NMR (501 MHz, DMSO-d_6) δ 9.18 (s, 1H, H_d), 7.82 (s, 1H, $H_{b/c}$), 7.71 (s, 1H, $H_{b/c}$), 5.33 (s, 1H, H_h), 4.41 – 4.28 (m, 2H, H_e), 3.85 (s, 3H, H_a), 3.00 – 2.86 (m, 2H, H_f). ^{11}B{^{1}H} NMR (128 MHz, DMSO) δ -3.1, -5.8, -9.8, -12.2, -13.0. ^{13}C{^{1}H} NMR (126 MHz, DMSO) δ 137.0 (C_d), 123.6 ($C_{b/c}$), 122.3 ($C_{b/c}$), 72.5 (C_g), 63.2 (C_h), 46.9 (C_e), 35.9 (C_a), 35.4 (C_f).

HRMS (ESI$^+$): *m/z* $[C_8H_{21}B_{10}N_2]^+$ 253.2719, calcd for $[M\text{-}Br]^+$ 253.2706.
Consistent with literature data.[18]

L2

N-Methyl imidazole (500 µL, 6.27 mmol), 2-bromoethyl-benzene (860 µL, 6.27 mmol) and MeCN (2 mL) were added to a 3-neck round bottom flask and held at reflux for 24 hours. The solvent was removed *in vacuo* and the residue recrystallised from dichloromethane and Et_2O, to yield the product as a yellow solid. On grinding this became an off-white solid. Yield: 886 mg, 52%

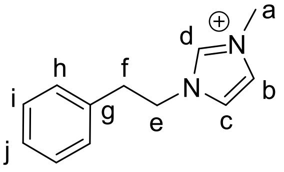

L2

^{1}H NMR (300 MHz, $CDCl_3$) δ 10.04 (s, 1H, H_d), 7.46 (s, 1H, $H_{b/c}$), 7.33 (s, 1H, $H_{b/c}$), 7.24 – 7.07 (m, 5H, $H_{h\text{-}j}$), 4.54 (t, *J* = 7.2 Hz, 2H, H_e), 3.93 (s, 3H, H_a), 3.17 (t, *J* = 7.2 Hz, 2H, H_f). ^{13}C{^{1}H} NMR (75 MHz, $CDCl_3$) δ 137.1 (C_d), 135.8 (C_g), 128.9 ($C_{h/i/j}$), 128.8 ($C_{h/i/j}$) , 127.3 ($C_{h/i/j}$), 123.3 ($C_{b/c}$), 122.5 ($C_{b/c}$), 50.9 (C_e), 36.6 (C_a), 36.4 (C_f).

HRMS (ESI$^+$): *m/z* $[C_{12}H_{15}N_2]^+$ 187.1244, calcd for $[M\text{-}Br]^+$ 187.1230
Consistent with literature data.[34]

2.6.3 Synthesis of Complexes

C1

L1 (29.6 mg, 0.0894 mmol), Ag_2O (10.6 mg, 0.0457 mmol), $[Ir(COD)Cl]_2$ (30.1 mg, 0.0448 mmol), activated 4 Å molecular sieves and DCM (5 mL) were combined in an ampoule and heated to 45 °C for 19 hours under nitrogen. The reaction mixture was filtered through cotton wool and twice through celite, and the filtrate reduced *in vacuo*. The residue was recrystallised from acetone and cold pentane to yield the produce as a yellow solid. Yield: 26.9 mg, 51%

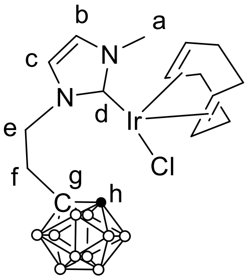

^{1}H NMR (400 MHz, $CDCl_3$) δ 6.82-6.78 (m, 2H, $H_{b/c}$), 5.01 (td, *J* = 12.7, 3.9 Hz, 1H, H_e), 4.69-4.54 (m, 2H, CODCH), 4.02 (s, 1H, H_h), 3.97 (ddd, *J* = 13.1, 11.7, 6.2 Hz, 1H, H_e), 3.92 (s, 3H, H_a), 3.27-3.15 (m, 1H, H_f), 3.02 – 2.93 (m, 1H, CODCH), 2.82 – 2.76 (m, 1H, CODCH), 2.59 (ddd, *J* = 14.7, 12.5, 6.2 Hz, 2H, C_f), 2.35 – 2.19 (m, 5H, $CODCH_2$), 1.89 – 1.81 (m, 1H, $CODCH_2$), 1.76 – 1.60 (m, 4H, $CODCH_2$). ^{11}B NMR (96 MHz, $CDCl_3$) δ -2.39, -5.13, -9.00, -11.27, -12.79 ^{13}C{^{1}H} NMR (101 MHz, $CDCl_3$) δ 181.5 (C_d), 122.2 ($C_{b/c}$), 120.4 ($C_{b/c}$), 86.3 (CODCH), 85.6 (CODCH), 72.2 (C_g), 63.4 (C_h), 52.7 (CODCH), 52.2 (CODCH), 49.2 (C_e), 38.2 (C_f), 37.6 (C_a), 34.0 ($CODCH_2$), 33.4 ($CODCH_2$), 30.0 ($CODCH_2$), 29.2 ($CODCH_2$).

HRMS (ESI$^+$): *m/z* $[C_{16}H_{32}B_{10}IrN_2]^+$ 553.3309, calcd for $[M\text{-}Cl]^+$ 553.3198.

Elemental analysis: Found: C, 25.18; H, 3.86; N, 4.24%, calcd for $C_{16}H_{32}B_{10}ClIrN_2$: C, 32.67, H, 5.48, N, 4.76%. Large error is attributed to the presence of both halide mixing and residual silver salts.

C2

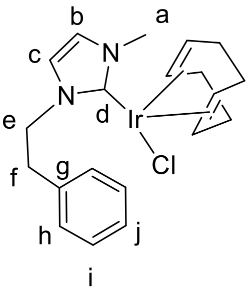

L2 (25.0 mg, 0.0937 mmol), Ag_2O (10.6 mg, 0.0457 mmol), $[Ir(COD)Cl]_2$ (32.2 mg, 0.0479 mmol), activated 4 Å molecular sieves and DCM (4 mL) were combined in an ampoule and heated to 45 °C for 1.5 hours under nitrogen. The reaction mixture was filtered through cotton wool and celite, and the filtrate reduced *in vacuo*. The residue was recrystallised from acetone and cold pentane to yield the produce as a yellow solid (17.5 mg, 37%).

^{1}H NMR (400 MHz, $CDCl_3$) δ 7.35-7.22 (m, 7H (includes $CHCl_3$), $H_{h\text{-}j}$), 6.74 (d, *J* = 1.0 Hz, 1H, $H_{b/c}$), 6.61 (d, *J* = 1.1 Hz, 1H, $H_{b/c}$), 4.80-4.6 (m, 2H, H_e/CODCH), 4.58 (td, *J* = 7.8, 3.7 Hz, 1H, CODCH), 4.45 (dt, *J* = 13.4, 8.2 Hz, 1H, H_e), 3.95 (s, 3H, H_a), 3.37-3.30 (m, 1H, H_f), 3.16-3.06 (m, 1H, H_f), 3.00 (t, *J* = 7.1 Hz, 1H, CODCH), 2.80 (td, *J* = 7.3, 3.4 Hz, 1H, CODCH), 1.90 – 1.51 (m, 8H, $CODCH_2$). $^{13}C\{^1H\}$ NMR (101 MHz, $CDCl_3$) δ 180.7 (C_d), 138.5 (C_g), 129.2 ($C_{h\text{-}j}$), 128.8 ($C_{h\text{-}j}$), 126.8 ($C_{h\text{-}j}$), 121.5 ($C_{b/c}$), 120.6 ($C_{b/c}$), 85.0 (COD*C*H), 84.2 (COD*C*H), 52.3 (C_e), 52.1 (COD*C*H), 51.2 (COD*C*H), 37.8 (C_f), 37.6 (C_a), 34.3 (COD*C*H_2), 33.2 (COD*C*H_2), 30.3 (COD*C*H_2), 29.2 (COD*C*H_2).

HRMS (ESI^+): *m/z* $[C_{20}H_{26}IrN_2]^+$ 487.1674, calcd for $[M\text{-}Cl]^+$ 487.1720

Elemental analysis: Found: C, 34.97; H, 3.69; N, 4.43%, calcd for $C_{20}H_{26}ClIrN_2$: C, 46.01, H, 5.02, N, 5.37%. Large error is attributed to the presence of both halide mixing and residual silver salts.

C3

L1 (99.9 mg, 0.300 mmol), $[IrCp^*Cl_2]_2$ (120 mg, 0.151 mmol), and Ag_2O (34.1 mg, 0.147 mmol) were combined in an ampoule with several activated 4 Å molecular sieves and placed under argon. Anhydrous DCM (10 mL) was added *via* syringe and the reaction mixture heated to 45 °C with light excluded for 72 hours. The reaction mixture was filtered through celite and washed with DCM (3 x 5 mL). The yellow filtrate was reduced *in vacuo* and the residue recrystallised from acetone and pentane to produce the product as a yellow solid. Yield: 117 mg, 61%.

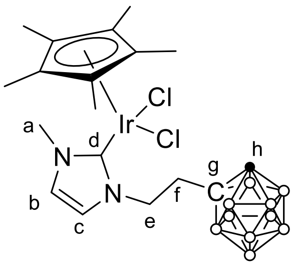

C3

^{1}H NMR (501 MHz, $CDCl_3$) δ 6.96 (d, *J* = 2.1 Hz, 1H, $H_{b/c}$), 6.89 (d, *J* = 2.1 Hz, 1H, $H_{b/c}$), 4.94 (td, *J* = 12.4, 4.8 Hz, 1H, H_e), 4.45 (s, 1H, H_h), 3.95 (s, 3H), H_a, 3.77 – 3.65 (m, 1H, H_e), 3.28 – 3.16 (m, 1H, H_f), 2.65 – 2.52 (m, 1H. H_f), 1.61 (s, 15H, Cp*). $^{11}B\{^1H\}$ NMR (128 MHz, $CDCl_3$) δ -1.8, -4.9, -9.3, -12.6. $^{13}C\{^1H\}$ NMR (126 MHz,

$CDCl_3$) δ 158.2 (C_d), 124.2 ($C_{b/c}$), 121.2 ($C_{b/c}$), 89.2 (Cp^*_{quat}) 60.9 (C_h), 49.7 (C_e), 39.1 (C_f), 38.8 (C_a), 9.5 (Cp*), 9.3 (Cp*).

HRMS (ESI^+): *m/z* $[C_{18}H_{35}B_{10}ClIrN_2]^+$ 615.3104, calcd for $[M\text{-}Cl]^+$ 615.3106; $[C_{18}H_{35}B_{10}BrIrN_2]^+$ 660.2568, calcd for $[M.Br\text{-}Cl]^+$ 660.2589.
Consistent with literature data.[18]

C4/C5 mixture

C3 (101 mg, 0.154 mmol) was added to an ampoule containing Ag_2O (61.8 0.267 mmol) and several activated 4 Å molecular sieves and placed under argon. Anhydrous MeCN (20 mL) was added and the ampoule sealed and heated to 70 °C with light excluded for 41 hours. The reaction mixture was filtered through celite and rinsed with MeCN (3 x 5 mL). The filtrate was reduced *in vacuo* and the residue recrystallised from acetone and pentane to yield a yellow solid. Yield: 27.4 mg, 29%.

^{11}B NMR (128 MHz, CD_3CN) δ -2.7, -5.4, -9.9, -12.1, -12.9.
HRMS (ESI^+): *m/z* $[C_{18}H_{34}B_{10}IrN_2]^+$ 579.3325, calcd for $[M\text{-}Cl]^+$: 579.3340. Also observed: *m/z* 702.4124.

C6

L1 (50.0 mg, 0.15 mmol) was added to a flame dried ampoule under nitrogen. Anhydrous THF (10 mL) was added and the solution cooled to -78 °C. n-BuLi (0.23 mL, 1.6 M, 0.37 mmol) was added dropwise and the solution held at -78 °C for 40 minutes. The reaction mixture was transferred to an ice bath and held at 0 °C for 1 hour. A suspension of $[IrCp^*Cl_2]_2$ (59.8 mg, 0.0751 mmol) in THF (15 mL) was added. The reaction orange/brown reaction mixture was allowed to warm to room temperature for 23 hours. Additional n-BuLi was added (0.12 mL, 1.6 M, 0.19 mmol) at -78 °C and the reaction mixture warmed to room temperature for 5 hours. The reaction mixture was again cooled to -78 °C and further n-BuLi (0.20 mL, 1.6 M, 0.32 mmol) added. The reaction mixture was allowed to warm to room temperature over 3 days. The solvent was removed *in vacuo* and the residue dissolved in DCM and passed through a silica plug. The plug was washed with DCM and small quantities of MeOH. The filtrate was then additionally passed through cotton wool and celite. The filtrate was reduced *in vacuo* and the residue recrystallised from DCM and pentane. The resulting yellow solid was isolated by filtration, and dried under suction. Yield: 81.6 mg, 88%

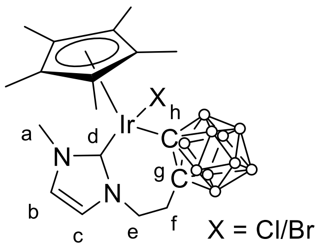

C6

^1H NMR (300 MHz, CD_2Cl_2) δ 6.97 (dd, *J* = 4.8, 1.9 Hz, 1H, $H_{b/c}$), 6.91 (d, *J* = 1.9 Hz, 1H, $H_{b/c}$), 4.64 – 4.46 (m, 1H, H_e), 3.98 (s, 2H, H_a), 3.81 – 3.67 (m, 1H, H_e), 2.90 – 2.75 (m, 3H, H_f), 2.76 – 2.59 (m, 2H, H_f), 1.52 (s, 6H), 1.48 (s, 4H). $^{11}B\{^1H\}$ NMR (96

MHz, CD_2Cl_2) δ -5.1, -6.9, -10.8. $^{13}C\{^1H\}$ NMR (75 MHz, CD_2Cl_2) δ 151.5 (C_d), 125.8 ($C_{b/c}$), 125.7 ($C_{b/c}$), 121.1 ($C_{b/c}$), 120.8 ($C_{b/c}$), 93.6 (Cp^*_{quat}), 93.3 (Cp^*_{quat}), 45.9 (C_e), 42.1 (C_a), 40.8 (C_a), 39.0 (C_a), 9.4 (Cp*), 9.1 (Cp*).
HRMS (ESI$^+$): *m/z*: $[C_{18}H_{34}B_{10}IrN_2]^+$ 579.3333, calcd: for $[M-Cl]^+$ 579.3340.
Consistent with literature data.[18]

2.6.4 Stoichimetric Reactions

Reaction of C6 with HCl

In a glovebox **C6** (12.3 mg, 0.020 mmol) was dissolved in CD_3CN (0.7 mL) and added to a Youngs NMR tube. Under a blanket of argon, HCl (18 µL, 0.97 M, 0.17 mmol) was added and the solution allowed to stand at room temperature for 16 hours. The reaction progress was monitored by NMR spectroscopy. The tube was heated to 80 °C for 24 hours. After this time HCl (aq) (80 µL, 0.97 M, 78 mmol) was added under a blanket of argon and the solution left to stand for 1 hour. The tube was heated to 80 °C for 19 hours.

Reaction of C6 with IPA

In a glovebox **C6** (12.3 mg, 0.020 mmol) was dissolved in CD_3CN (0.5 mL) and added to a Youngs NMR tube. Under a blanket of argon, IPA (1 µL, 0.13 mmol) was added. The reaction progress was monitored by NMR spectroscopy. The solution was allowed to stand at room temperature for 24 hours. The tube was held at 80 °C for 21 hours.

Reaction of C6 with IPA and K*ᵗ*BuO

K^{t}BuO (11 µL, 20% weight solution in THF, 0.018 mmol) was added under a blanket of argon to a Youngs NMR tube containing a solution of **C6** (12.3 mg, 0.0200 mmol) in CD_3CN (0.5 mL) and IPA (1 µL, 0.13 mmol). Upon addition a colour change from yellow to red was observed. The reaction progress was monitored by NMR spectroscopy. The mixture was allowed to stand and room temperature for 5 minutes. The tube was held at 80 °C for 18 hours.

Reaction of C6 with K^{t}BuO

K^{t}BuO (11 µL, 20% weight solution in THF, 0.018 mmol) was added under a blanket of argon to a Youngs NMR tube containing a solution of **C6** (12.3 mg, 0.020 mmol) in CD_3CN (0.5 mL). Upon tube agitation the solution changed from yellow to dark red and a precipitate formed. The reaction was observed by NMR spectroscopy.

Reaction of C3 with $NaBH_4$

C3 (19.2 mg, 0.0295 mmol) was dissolved in d_8-THF (0.5 mL) in a Young's NMR tube and ^1H and $^{11}B\{^1H\}$ were recorded. $NaBH_4$ (2.0 mg, 0.0529 mmol) was added along with further d_8-THF (0.2 mL). After 10 days of standing at room temperature further $NaBH_4$ (10.0 mg, 0.264 mmol) was added and the mixture allowed to stand for a further 3 days.

Reaction of C6 with $NaBH_4$

C6 (20.1 mg, 0.0327 mmol) dissolved in d_8-THF (0.5 mL) in a Young's NMR tube and ^1H and $^{11}B\{^1H\}$ NMR spectra recorded. $NaBH_4$ (1.7 mg, 0.045 mmol) was added and the mixture allowed to stand at room temperature for 2 days. After this time further $NaBH_4$ (9.0 mg, 0.24 mmol) was added and the mixture allowed to stand for another 5 days. A further portion of $NaBH_4$ (9.3 mg, 0.25 mmol) was added and the mixture stood for a further 5 days. Diffraction quality crystals were grown by layering anhydrous hexane over the reaction mixture.

Reaction of C3 with Na^iPrO

C3 (30.1 mg, 0.0464 mmol) and Na^iPrO (4.3 mg, 0.052 mmol) were combined in an ampoule with anhydrous IPA (2 mL) and stirred at room temperature under argon for 3 hours. After this time the ampoule was sealed and the reaction stirred at room temperature for a further 16 hours. The solvent was removed *in vacuo* and the yellow/orange residue analysed by NMR spectroscopy and HRMS.

Reaction of C6 with Na^iPrO

C4 (28.5 mg, 0.0464 mmol) and Na^iPrO (4.2 mg, 0.051 mmol) were combined in an ampoule and placed under nitrogen. Anhydrous IPA (2 mL) was added and the reaction mixture stirred under an atmosphere of nitrogen for 3 hours at room temperature. After this time the ampoule was sealed and the mixture stirred for a further 15 hours. The solvent was removed *in vacuo* and the crude residue analysed by NMR spectroscopy.

2.6.5 General Procedure for Catalytic Reactions Using Na^iPrO

Catalyst (1 mol% per Ir) and 1,3,5-trimethoxybenzene (55.5 mg, 0.33 mmol) were added to an ampoule and placed under argon. In a glovebox, Na^iPrO (8.2 mg, 0.1 mmol) and acetophenone (117 µL, 1.00 mmol) were added to the ampoule. The ampoule was sealed, taken out of the glovebox and connected to a schlenk line. Under an atmosphere of argon anhydrous IPA (2.3 mL) was added, the ampoule sealed, and the reaction mixture held at 82 °C for 1 hour. The reaction was quenched by cooling the ampoule in an ice-bath. An aliquot (0.1 mL) was added to an NMR tube with $CDCl_3$ (0.5 mL).

List of References

1 C. A. Tolman, *Chem. Rev.*, 1977, **77**, 313–348.

2 A. R. Chianese, A. Kovacevic, B. M. Zeglis, J. W. Faller and R. H. Crabtree, *Organometallics*, 2004, **23**, 2461–2468.

3 R. A. Kelly III, H. Clavier, S. Giudice, N. M. Scott, E. D. Stevens, J. Bordner, I. Samardjiev, C. D. Hoff, L. Cavallo and S. P. Nolan, *Organometallics*, 2008, **27**, 202–210.

4 D. J. Nelson and S. P. Nolan, *Chem. Soc. Rev.*, 2013, **42**, 6723–6753.

5 S. Ibáñez, M. Poyatos, L. N. Dawe, D. Gusev and E. Peris, *Organometallics*, 2016, **35**, 2747–2758.

6 S. C. Zinner, C. F. Rentzsch, E. Herdtweck, W. A. Herrmann and F. E. Kühn, *Dalton Trans.*, 2009, 7055–7062.

7 A. Chianese, X. Li, M. Janzen, J. Faller and R. Crabtree, *Organometallics*, 2003, **22**, 1663–1667.

8 J. Holmes, C. M. Pask, M. A. Fox and C. E. Willans, *Chem. Commun.*, 2016, **52**, 6443–6446.

9 J. Holmes, *Preparation of Brand New Ligand Architectures Incorporating N-Heterocyclic Carbene Complexes with Carboranyl Substituents: Coordination Chemistry, Catalytic Evaluation and Anticancer Properties,* University of Leeds, 2017.

10 Y. Gothe, T. Marzo, L. Messori and N. Metzler-Nolte, *Chem. Eur. J.*, 2016, **22**, 12487–12494.

11 M. V. Jiménez, J. Fernández-Tornos, J. J. Pérez-Torrente, F. J. Modrego, S. Winterle, C. Cunchillos, F. J. Lahoz and L. A. Oro, *Organometallics*, 2011, **30**, 5493–5508.

12 W. M. Haynes, *CRC Handbook of Chemistry and Physics 97th Edition*, CRC Press/Taylor & Francis, Boca Raton, FL., 97th edn., 2017.

13 C. Vicent, M. Viciano, E. Mas-Marzá, M. Sanaú and E. Peris, *Organometallics*, 2006, **25**, 3713–3720.

14 S. Gülcemal, A. G. Gökçe and B. Çetinkaya, *Inorg. Chem.*, 2013, **52**, 10601–10609.

15 J.-F. Sun, F. Chen, B. A. Dougan, H.-J. Xu, Y. Cheng, Y.-Z. Li, X.-T. Chen and Z.-L. Xue, *J. Organomet. Chem.*, 2009, **694**, 2096–2105.

16 D. G. Gusev, *Organometallics*, 2009, **28**, 763–770.

17 D. G. Gusev, *Organometallics*, 2009, **28**, 6458–6461.

18 J. Holmes, C. M. Pask and C. E. Willans, *Dalton Trans.*, 2016, **45**, 15818–15827.

19 L. I. Zakharkin and V. N. Kalinin, *Tetrahedron Lett.*, 1965, **6**, 407–409.

20 D. S. Glueck, L. J. N. Winslow and R. G. Bergman, *Organometallics*, 1991, **10**, 1462–1479.

21 G. R. Fulmer, A. J. M. Miller, N. H. Sherden, H. E. Gottlieb, A. Nudelman, B. M. Stoltz, J. E. Bercaw and K. I. Goldberg, *Organometallics*, 2010, **29**, 2176–2179.

22 D. Wang and D. Astruc, *Chem. Rev.*, 2015, **115**, 6621–6686.

23 J. S. M. Samec, J.-E. Bäckvall, P. G. Andersson and P. Brandt, *Chem. Soc. Rev.*, 2006, **35**, 237–348.

24 Y. Tanabe, F. Hanasaka, K. Fujita and R. Yamaguchi, *Organometallics*, 2007, **26**, 4618–4626.

25 Z. M. Heiden and T. B. Rauchfuss, *J. Am. Chem. Soc.*, 2007, **129**, 14303–14310.

26 C. E. Housecroft and A. G. Sharpe, *Inorganic Chemistry*, Pearson Education Limited,

Harlow, 1st edn., 2001.

27 H. Fumihiro, K. Fujita, R. Yamaguchi, Fumihiro Hanasaka, and Ken-ichi Fujita and R. Yamaguchi, *Organometallics*, 2005, **24**, 3422–3433.

28 M. C. Lehman, J. B. Gary, P. D. Boyle, M. S. Sanford and E. A. Ison, *ACS Catal.*, 2013, **3**, 2304–2310.

29 M. Prinz, M. Grosche, E. Herdtweck and W. A. Herrmann, *Organometallics*, 2000, **19**, 1692–1694.

30 J. Choudhury, S. Podder and S. Roy, *J. Am. Chem. Soc.*, 2005, **127**, 6162–6163.

31 C. White, A. Yates, P. M. Maitlis and D. M. Heinekey, in *Inorganic Syntheses*, ed. Russel N. Grimes, John Wiley & Sons, Ltd, New York, 29th edn., 2007, pp. 228–234.

32 M. F. Hawthorne, T. D. Andrews, P. M. Garrett, F. P. Olsen, M. Reintjes, F. N. Tebbe, L. F. Warren, P. A. Wegner, D. C. Young, R. P. Alexander, R. W. Blundon, H. A. Schroeder and T. L. Heying, in *Inorganic Syntheses*, John Wiley & Sons, Ltd, 2007, vol. 10, pp. 91–118.

33 K. Li, Y. Wang, G. Yang, S. Byun, G. Rao, C. Shoen, H. Yang, A. Gulati, D. C. Crick, M. Cynamon, G. Huang, R. Docampo, J. H. No and E. Oldfield, *ACS Infect. Dis.*, 2015, **1**, 215–221.

34 S. V. Dzyuba and R. A. Bartsch, *J. Heterocycl. Chem.*, 2001, **38**, 265–268.

Chapter 3

Computational Investigation into NHC-Carborane Complexes

This chapter describes a computational study performed on NHC-carborane ligands. The relative electron donor properties of NHC-carborane and NHC-phenyl ligands are calculated using a model carbonyl complex. Efforts to understand the effect of the carborane in the catalytic transfer hydrogenation reaction are described, including the geometry optimisation of intermediates and attempts to locate relevant transition states. An unusual Ir-fulvene complex, and it's possible relevance to catalysis, are discussed.

3.1 Introduction

3.1.1 Computational Chemistry

Computational chemistry encompasses a vast range of modelling methods, from *ab initio* calculations which attempt to solve the Schrödinger equation from first principles, to force-field calculations, which attempt to describe a system in terms of its intermolecular forces using classical mechanics. Density Functional Theory (DFT) lies somewhere between these, being a quantum-chemical method that uses functionals to describe electron density.[1]

The ground state energy of a given molecule is made up of the kinetic energy of the electrons, electron-electron interactions, and electron-nuclei interactions. The underlying theorem of DFT is that this energy can be expressed as a functional of the electron density of a system. Additionally, for the ground state of a molecule, the correct functional will correspond to the correct energy. Any other density will produce a higher energy result. Thus, theoretically, a "trial and error" approach of energy minimisation will ultimately yield the true ground state energy. This iterative optimisation procedure is known as the self-consistent field (SCF) method.[2]

This provides a good basis for the calculation of electronic energies if the geometry of a given species is already known. However, one of the strengths of DFT calculations lies in the ability to probe the structures of previously unknown species. In this case a geometry optimisation calculation is performed. After the energy minimisation cycle is complete, a calculation of the forces acting on each atom is performed, and the atoms are moved accordingly to minimise the energy (typically using gradient methods). The newly obtained geometry then undergoes the SCF cycle once more, and the process is repeated until a set of convergence criteria are met.[1,2]

Thus, species which cannot be characterised experimentally can have their geometry and electronic structure probed using computational methods. To understand chemical reactivity, the energy barriers between these species must also be investigated. The same approaches that locate a local minimum (i.e. equilibrium geometry) can be used to locate a locate maximum[1] (i.e. transition state). Therefore, the activation energy can be determined and thus the feasibility of a given mechanism.

3.1.2 Aims

Previous work found a difference in transfer hydrogenation (TH) activity between cyclometallated carboranyl complexes (**C4**/**C5**, **C6**) and their non-cyclometallated counterpart (**C3**), with the cyclometallated species being considerably more active (Figure 84). It was noted that when a complex was cyclometallated through a benzene ring instead of a carborane, the same increase in activity was not observed.

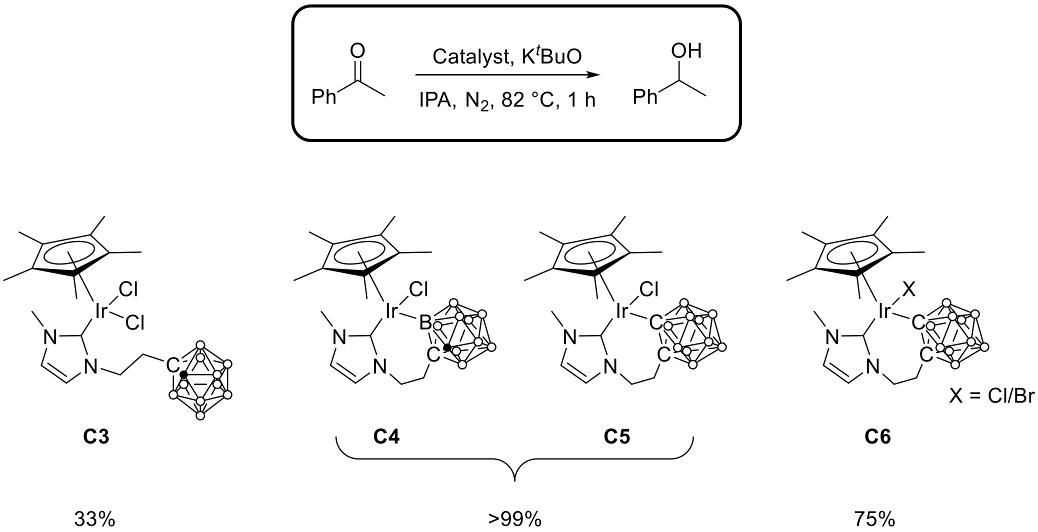

Figure 84. TH of acetophenone catalysed by NHC-carborane Ir complexes. Percentages show conversions to 1-phenyl ethanol determined by ^{1}H NMR spectroscopy.

Experimental work (Chapters 2 and 4) was performed to investigate the origin of this effect. A complementary computational study was envisaged, to provide an insight into the reaction mechanism and the role of the cyclometallated carborane in enhancing catalytic activity. The electronic differences between NHC ligands bearing carborane and phenyl substituents can be investigated using calculations of the carbonyl stretching frequencies of model complexes (Preface – *3.2* and Chapter 2 - *2.1*). This allows for the comparison of the donicity of these new ligands with already existing NHCs. Additionally, the effects of cyclometallation on the metal centre, and the differences between carbon and boron cyclometallation can be studied. The proposed mechanism (which envisions a bifunctional role for the NHC-carborane ligand) can also be investigated, by calculations on relevant intermediates and transition states.

---

[1] *Strictly speaking, a multidimensional hypersurface should be visualised when considering the energy landscape of a chemical reaction, rather than the traditional 2D reaction coordinate model. In this model, transition states are not maxima but saddle points - that is, they have a single negative second derivative, with all others being positive.*

3.2 Carbonyl complexes

As described earlier (Preface - *3.2* and Chapter 2 - *2.1*) Tolman Electronic Parameters (TEP) have been used to assess the relative donor/acceptor properties of phosphine ligands.[3] Latterly the scope of TEPs has been expanded to include other donor ligands including NHCs.[4] Due to the toxicity of $[Ni(CO)_4]$ - the precursor to the tested $[Ni(CO)_3L]$ complexes - investigations into carbonyl stretching frequencies have been carried out with different model complexes. In particular the $[Ir(CO)_2Cl(L)]$ system has been used widely.[5–8] As part of the investigation into the effects of carborane substituents on catalytic activity, attempts were made to assess the impact of the carborane substitutent on the relative donor strength of the appended NHC (**L1** vs **L2** - Figure 85). As previously discussed, synthesis of [Ir(COD)Cl(L)] complexes (which are precursors to the $[Ir(CO)_2Cl(L)]$ model complexes) resulted in the preparation of mixed halide species (Chapter 2 - *2.1*).

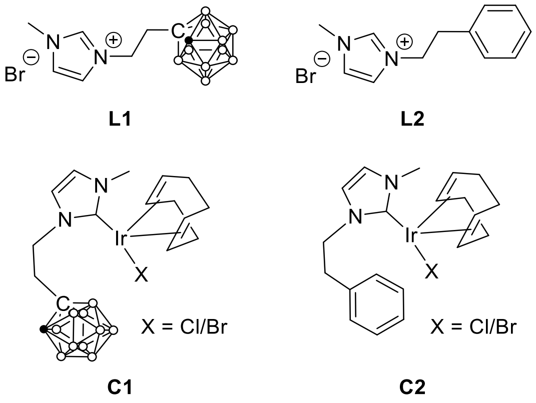

Figure 85. Ligands and complexes which are precursors to Ir carbonyl complexes.

Computational methods have been used to investigate the donor/acceptor properties of ligands using either $[Ni(CO)_3L]$ or $[Ir(CO)_2Cl(L)]$ complexes.[9,10] However, it was noted by Gusev *et al.*, that although a good correlation between TEP and calculated CO stretching frequency is observed, the correlation between CO stretching frequency and bond length for $[Ni(CO)_3L]$ complexes showed considerable scatter, especially when comparing different ligand classes.[11] A relatively poor correlation was also observed for calculated $[Ir(CO)_2Cl(L)]$ complexes. Given the intrinsic relationship between bond length and bond strength, a good correlation between these two values should be expected for a well-behaved system. Therefore, Gusev suggests the use of [Ir(CO)CpL] as a model complex in computational studies, as it fulfils a number of desirable criteria i) the presence of a single carbonyl ligand minimises complications due to vibronic coupling; ii) the low coordination number reduces steric effects due to ligand repulsion; iii) the ~90° degree angle between L and CO reduces the effects of *trans*-influence.

A series of ligands were investigated using this system. It has been previously noted that the use of the BP86 functional provides reasonable values for carbonyl stretching frequency, as long as a good correlation between frequency and bond length is observed.[12] Although the main aim was to investigate the relative donor/acceptor properties of **L1** vs **L2**, in order to validate the system, several other ligands were used for comparison (Figure 86).

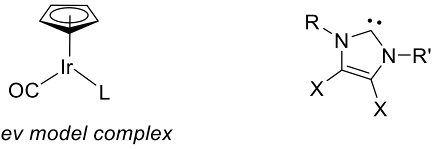

L=

L1: R = Me, R' = Et-C$_2$B$_{10}$H$_{11}$, X = H
L1.F: R = Me, R' = Et-C$_2$B$_{10}$F$_{11}$, X = H
L1.^{i}Pr: R = ^{i}Pr, R' = Et-C$_2$B$_{10}$H$_{11}$, X = H
L1.^{t}Bu: R = ^{t}Bu, R' = Et-C$_2$B$_{10}$H$_{11}$, X = H
L1.Cl: R = Me, R' = Et-C$_2$B$_{10}$H$_{11}$, X = Cl
L2: R = Me, R' = Et-Ph, X = H
L2.F: R = Me, R' = Et-C$_6$F$_5$, X = H
L2.^{i}Pr: R = ^{i}Pr, R' = Et-Ph, X = H
L2.^{t}Bu: R = ^{t}Bu, R' = Et-Ph, X = H
L2.Cl: R = Me, R' = Et-Ph, X = Cl
L3: R = Me, R' = Et
PCl$_3$, PMe$_3$, PPh$_3$

Figure 86. Model complex proposed by Gusev for CO stretching frequency calculation, and range of ligands investigated.

Combined geometry optimisation and frequency calculations were performed at the (RI-)BP86/SV(P) level. The carbonyl stretching frequencies were then correlated with the calculated CO bond length.

It was noted that for some of the carboranyl ligands, there was a close contact between the cluster CH proton and the oxygen of the carbonyl ligand. Given that this might have an impact on the bond length, the structures were modified in an attempt to remove this interaction. The results indicate that the arrangement of the ligand relative to the carbonyl can have a big impact on the stretching frequency/bond length with a large variation between different conformations observed. All the ligand conformations were correlated with the CO bond length, giving a poor fit for the line ($R^2 = 0.928$) (Figure 87). There are two clear outliers on this plot, which are for two conformations of **L1.F**. Removal of these structures from the plot gives an improved R^2 values of 0.987. The bond lengths and stretching frequencies for different conformers of the same ligand were averaged and the analysis was performed again (including the outliers). In this case, the fit is adequate (0.989) (Figure 88).

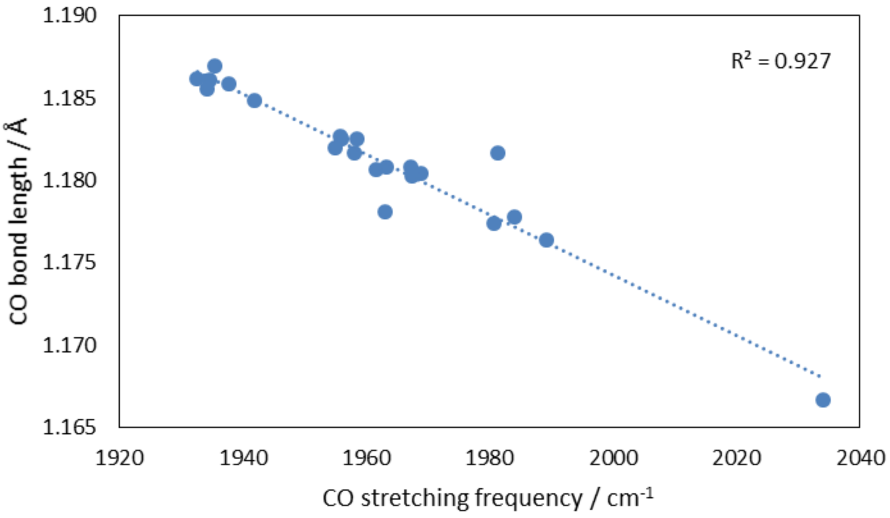

Figure 87. Correlation of calculated CO stretching frequency with CO bond length.

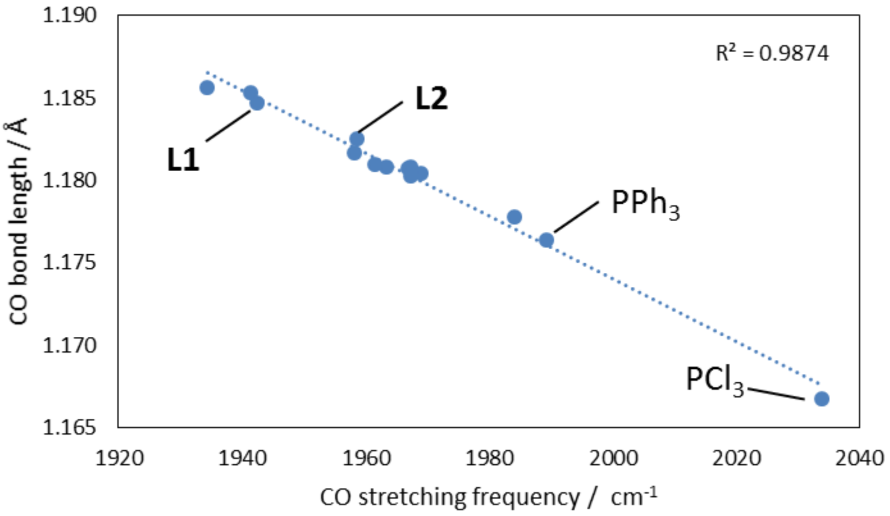

Figure 88. Correlation of calculated CO stretching frequency with CO bond length (averages).

The relative donor/acceptor properties of the various ligands can be examined by comparison of the CO stretching frequencies (Table 6). Within the carboranyl ligand class the trends seen are essentially as expected (entries 1-5). The addition of electron withdrawing chlorides to the NHC backbone causes an increase in CO stretching frequency, as is expected for a less electron rich metal centre (*cf*. entry 1 and 5). Changing from a methyl N-substituent to an ^{i}Pr has little effect, however a ^{t}Bu group causes a reduction in CO stretching frequency (*cf*. entry 1 and 3-4) (*vide infra*). A fluorinated carborane causes an increase in CO stretching frequency, even though the site of fluorination is remote (*cf*. 1 and 2). This appears to have a greater effect than the substitution of the NHC backbone (*cf*. 1, 2 and 5).

Table 6. Calculated carbonyl stretching frequencies and CO bond lengths.

Entry	Ligand	ν_{CO} / cm^{-1}	CO Bond Length
1	**L1**^{a}	1942	1.1847
2	**L1.F**^{a}	1967	1.1808
3	**L1.*ⁱ*Pr**^{a}	1941	1.1853
4	**L1.^{t}Bu**	1932	1.1860
5	**L1.Cl**^{a}	1962	1.1810
6	**L2**	1959	1.1825
7	**L2.F**	1967	1.1803
8	**L2.^{i}Pr**	1958	1.1817
9	**L2.^{t}Bu**	1962	1.1813
10	**L2.Cl**	1963	1.1808
11	**L3**	1969	1.1804
12	PCl_3	2034	1.1667
13	PMe_3	1984	1.1778
14	PPh_3	1989	1.1764

a. Values for these ligands are an average of three conformers.

For the phenyl-type ligands similar trends are observed (entries 6-10). The introduction of electron-withdrawing groups leads to an increase in CO stretching frequency as expected (*cf*. entries 6 and 7, 10). As with the carboranyl ligands, the impact of remote fluorination on an N-substituent is greater than the chlorination of the NHC backbone. The exchange of a methyl N-substituent for an ^{i}Pr results in a very small decrease in CO stretching frequency (*cf.* entry 6 and 8). Surprisingly, **L2.^{t}Bu** has a calculated stretching frequency higher than that of **L2** (*cf*. entry 6 and 9).

Comparison of the geometry obtained for **L2.^{t}Bu** with that for **L2** and **L2.^{i}Pr** gives some clues as to the reasons for this discrepancy. The NHC ligands examined typically display a twist relative to the plane described by the CO-Ir-C$_{carbene}$ atoms. In an "idealised" geometry the angle between this plane and that described by the NHC ring would be 90 °. However, angles <90 ° were observed in most cases (Figure 89). **L2** and **L2.^{i}Pr** display this effect with interplanar angles of 60 ° and 69 ° respectively. By contrast, in **L2.^{t}Bu** the planes are near perpendicular, with an angle of 86 ° (Table 7). This structural change may have an effect on the calculated stretching frequency.

Another difference in geometry is observed with the distance between the carbonyl ligand and one of the hydrogen atoms in the CH_2 linker. This distance is significantly longer in **L2.^{t}Bu** (0.2 Å), and it may be that non-covalent interactions between these two atoms influence the bond length or stretching frequency of the carbonyl ligand.

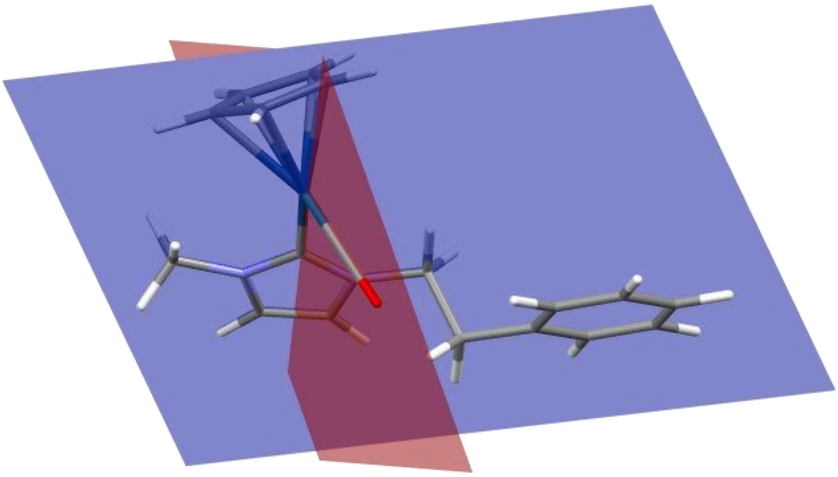

Figure 89. Optimised geometry for [IrCp(CO)**L2**] with NHC ring plane and CO-Ir-$C_{carbene}$ plane shown.

Table 7. Interplanar angles and CH-CO distances

Ligand	Interplanar angle / °	Closest CH contact / Å
L2	60.39	2.645
L2.^{i}Pr	68.60	2.685
L2.^{t}Bu	86.22	2.864

These interactions likely affect the observed CO bond length, however other than in the case described above there are no significant differences between the CH-CO distances between the carboranyl and phenyl ligands, and therefore a comparison is reasonable. This analysis suggests that carborane ligand **L1** is more electron donating than phenyl analogue **L2** (*cf*. entry 1 and 6), a trend which is replicated with the ^{i}Pr and ^{t}Bu substituted ligands (*cf*. entry 3 and 8, 4 and 9) - although as noted previously, the stretching frequency for **L2.^{t}Bu** is higher than expected. Indeed, all phenyl ligands are less electron donating than **L1**. However, there is no difference between the carborane and phenyl analogues when considering the fluorinated substituent and chlorinated backbone ligands (*cf*. entry 2 and 7, 5 and 10). This suggests that although the carborane may have an effect on electron donating properties, this can be surpassed by other changes to the ligand architecture.

This divergence in electronic properties between carborane and phenyl ligands is likely to have an effect on the catalytic performance of complexes with these two ligands. Ligands which are strong σ-donors may form more robust catalysts, and additionally may help to promote oxidative addition steps.[13]

3.3 Investigation of Cyclometallation Effect

Calculations were initially performed on the cyclometallated and non-cyclometallated Ru, Rh and Ir complexes bearing NHC-carborane ligands prepared by Holmes (Figure 90).[14] The cyclometallated Ru and Rh complexes which had not been successfully synthesised (**C4.Rh**, **C5.Rh**, **C4.Ru**, **C5.Ru**), were also modelled computationally. For all cyclometallated complexes, both CH and BH activated complexes were considered. Geometry optimisations were followed by vibrational frequency calculations at the (RI)BP86/SV(P) level, using crystal structures (where available) or modified crystal structures as input geometries. The structural parameters for the optimised structures can be compared with the parent crystal structure, to assess the validity of the method used (Table 8).

It is worth noting that crystal structures represent the packing of multiple molecules in the solid state, whilst calculations are performed for a single molecule in the gas phase, therefore absolute agreement is not expected.

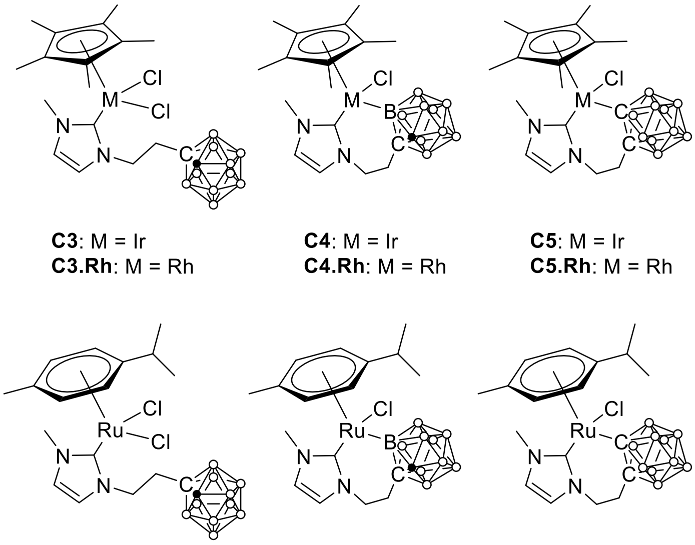

C3: M = Ir
C3.Rh: M = Rh

C4: M = Ir
C4.Rh: M = Rh

C5: M = Ir
C5.Rh: M = Rh

C3.Ru: M = Ru

C4.Ru: M = Ru

C5.Ru: M = Ru

Figure 90. Cyclometallated and non-cyclometallated complexes.

Table 8. Comparison of solid state bond lengths with calculated lengths at different levels of theory.[15]

	M-NHC	M-Cb	M-Cl	C-C carborane	M-arene centroid
Method	**C5**				
Solid State	2.041(5)	2.149(6)	2.5488(7)	1.741(7)	1.864
BP86/SVP	2.013	2.179	2.461	1.790	1.963
DFT-D3 BP86/SVP	2.003	2.155	2.453	1.777	1.943
BP86/def2-TZVPP	2.020	2.184	2.431	1.797	1.911
PBE0/SVP	2.014	2.173	2.430	1.720	1.922
	C3				
Solid State	1.88(3) - 1.97(4)	-	2.437(7) - 2.495(5)	1.64(4) - 1.70(3)	1.738 - 1.748
BP86/SVP	2.029		2.449 2.475	1.650	1.88
DFT-D3 BP86/SVP	2.017		2.443 2.465	1.648	1.867
BP86/def2-TZVPP	2.0370		2.4260 2.4448	1.6502	1.843
PBE0/SVP	2.030		2.445 2.421	1.629	1.847
	C3.Ru				
Solid State	2.064(7)	-	2.4145(18) - 2.435(2)	1.652(11)	1.682
BP86/SVP	2.049	-	2.443 2.422	1.651	1.730

For the M-carbene bond length, the computational results are in good to moderate agreement with the crystallographic data (0.02-0.12 Å difference). The lengths are both over- and underestimated which indicates there is not a systematic error. For the M-carborane bond length and C-C bond length within the carborane, the calculated lengths are accurate within 0.05 Å for all complexes. M-Cl distances are slightly overestimated (0.01-0.02 Å) for the non-cyclometallated complexes, whilst for the cyclometallated complex (**C5**) the length is underestimated (0.08 Å). The biggest difference is seen with the metal-arene bond lengths which are consistently overestimated by between 0.05 and 0.15 Å in the calculated structures. Although some differences in bond length would be expected between solid and gas phase structures, packing effects such as π-π stacking should lengthen bonds, rather than shorten them. The discrepancy seen is therefore likely to be a sign of the calculations not fully describing all the relevant interactions. Bonds between a metal and π-ligand have significant dispersive character; dispersive effects are often poorly described by DFT calculations, so this may be a source of the error. The calculations for **C3** and **C5** were re-run using the DFT-D3 correction, which attempts to account for these dispersive effects.[16] In fact this correction is likely to overestimate these effects, leading to the overbinding of atoms with highly dispersive interactions. The results of these calculations show a reduction in all bond distances, however the Ir-Cp* distance is still significantly overestimated (0.08-0.12 Å).

In an attempt to account for this, calculations were repeated at the (RI)BP86/def2-TZVPP and (RI)PBE0/SVP levels, to investigate the effect of changing the basis set and functional. The best agreement with the crystallographic data is obtained with the larger basis set, bringing the error on the M-arene distance to within 0.05 Å for **C5** and to within 0.10 Å for **C3**. The improvement is slight however, and the increased accuracy did not warrant the additional computational expense for all calculations

The geometry optimisation and frequency calculations allow for the calculation of enthalpies, entropies and hence Gibbs free energies for a given structure. The calculations were performed in the gas phase, but the COSMO solvation model (using the dielectric constant of DCM) was used to provide a solvation correction. A dispersion correction (DFT-D3) can also be applied to the energy to account for dispersive forces (Table 9). The absolute energies are of little value, however, comparison of the relative energies allows an assessment of the energy differences between isomers. For each metal, the complexes that are cyclometallated through a carbon atom have been set as the zero point. As the energy values are based on electronic energies, relative energies are only valid for species with identical numbers of electrons. Thus complexes which are cyclometallated through a boron may be compared directly. However, the non-cyclometallated complexes have one more atom of hydrogen and one of chlorine compared to their non-cyclometallated counterparts, which must be corrected for. The correction that has been applied here is the subtraction of E_{HCl} from E_M (M = non-cyclometallated complex).

Table 9. Relative energies for cyclometallated and non-cyclometallated complexes.

Complex	Relative H / kJ mol^{-1}			Relative S / J K^{-1} mol^{-1}			Relative G / kJ mol^{-1}		
C5	0	0	0	0	0	0	0	0	0
C4	-29	-26	-19	11	11	11	-33	-29	-22
C3 - HCl	-146	-132	-106	-105	-78	-78	-115	-108	-83
C5.Rh	0	0	0	0	0	0	0	0	0
C4.Rh	-23	-18	-12	8	8	8	-25	-20	-14
C3.Rh - HCl	-160	-148	125	-98	-71	-71	-131	-127	-104
C5.Ru	0	0	0	0	0	0	0	0	0
C4.Ru	-18	-16	-11	2	2	2	-18	-17	-12
C3.Ru - HCl	-181	-162	-139	-116	-89	-89	-147	-136	-112

Blue cells: gas phase, orange cells: COSMO (DCM) solvation, grey cells: DFT-D3 correction. Calculated at 298 K.

Comparison of carbon and boron cyclometallated isomers may be assumed to be reasonably accurate, as the conversion from one to the other is isogyric and virtually isodesmic (10 B-H bonds and one M-C bond, versus 9 B-H bonds, 1 C-H bond and one M-B bond). Therefore, the correlation energies of the two species may be considered very similar, and hence error cancellation makes this estimate reasonable.[1] For all metals studied, and at all levels of correction, the energy of the boron cyclometallated isomer is significantly lower than that of the carbon cyclometallated isomer. This effect is both enthalpic and entropic in nature. The higher entropy of the boron cyclometallated isomers can be explained by two equivalent available sites for cyclometallation (Chapter 1 - *1.1.5*). The enthalpy change is likely to be a reflection of the bond strengths.

The Gibbs free energy difference is consistently large enough that the thermodynamic product of the reaction would be predicted to be the boron cyclometallated isomer alone. Whilst the selective formation of the C-cyclometallated (mixed halide) complex **C6** is achieved through the relative acidities of B-H vs C-H bonds (a kinetic effect), a mixture of carbon and boron cyclometallation is seen when using the Ag_2O route (producing **C4**/**C5**). The computational results would therefore suggest that this reaction is not being performed under equilibrium conditions, which is in agreement with the experimental procedure, as cyclometallation is accompanied by the precipitation of AgCl - an irreversible process. Therefore, the main factor influencing the product ratio will be the relative energy barriers for the formation of the two isomers. It is likely that these are similar, and this is what leads to the formation of a mixed species. The mechanism of NHC deprotonation using Ag_2O has been investigated computationally, and was found to proceed *via* a barrierless initial deprotonation, followed by metalation.[17] If a similar mechanism is in operation in this case, the lack of energy barrier to deprotonation would explain the mixed complexes obtained. Investigation of the mechanism of carborane deprotonation in these reactions has not been considered in this study, but would be a relevant area of future research.

The calculated energies for the non-cyclometallated complexes are significantly lower in energy that the cyclometallated species. However, it is important to bear in mind that in this case the comparison is less realistic than for the two cyclometallated isomers. The enthalpy change calculated using HCl to balance electron numbers is likely to be overestimated due to the instability of this species in the gas phase. Additionally, the value of the entropic term will be artificially reduced because of the comparison of 2 species (**C4** and HCl) with 1 (**C3**). Although the absolute number is unlikely to be reflective of the true energy difference, these data do broadly agree with experimental evidence; spontaneous cyclometallation is not observed, and forcing conditions (strong bases or elevated temperatures and long reaction times - Chapter 2 - *2.2*) are required to effect it. The data also indicate that the non-cyclometallated Ru species is more stabilised than the Rh and Ir complexes; the Ru cyclometallated complex has never been successfully synthesised.

3.4 Investigation of the Proposed Catalytic Cycle

A bifunctional mechanism for the catalytic cycle was proposed; in this, the initially coordinated carborane is protonated by IPA, thus providing a vacant site for propoxide coordination. The coordinated propoxide eliminates as acetone to form a monohydride complex. Subsequently, the hydride is transferred to an incoming ketone, which coordinates as an alkoxide (effectively a reversal of the previous step). Finally, the alkoxide departs, deprotonating carborane, which then rapidly recoordinates to the metal centre, completing the cycle (Figure 91).[15]

To prove the validity of a proposed cycle using computational chemistry, it would be necessary to consider every possible mechanism. In practice, only a few likely possibilities are considered. The intermediates of these mechanisms, and the transition states that connect them are modelled, and thus the energy surface for the various reaction pathways can be determined. Pathways which are too high in energy to be feasible under the reaction conditions can be discounted, and it may be that there is a single pathway that appears most likely. This energy surface can also be used to generate kinetic parameters which is then directly comparable with experimental data. A number of techniques for achieving this have been described and reviewed recently.[18–20]

3.4.1 Geometry Optimisation of Potential Intermediates

The mechanism proposed was used as a starting point for this investigation, with the aim of investigating other possible pathways once an assessment of the suggested cycle had been made. The first step is to perform geometry optimisation calculations on the relevant intermediates. Also investigated were two potentially "off-cycle" intermediates in which propoxide coordination and hydride formation occur without decoordination of the carborane (Figure 91). As initial experimental work (Chapter 2) was conducted using the carbon cyclometallated complex, this was focussed on computationally. Geometry optimisation calculations were successful for all species except for **IVb**, for which all optimisations converged on structures with the ketone distant from the Ir centre (Figure 92).

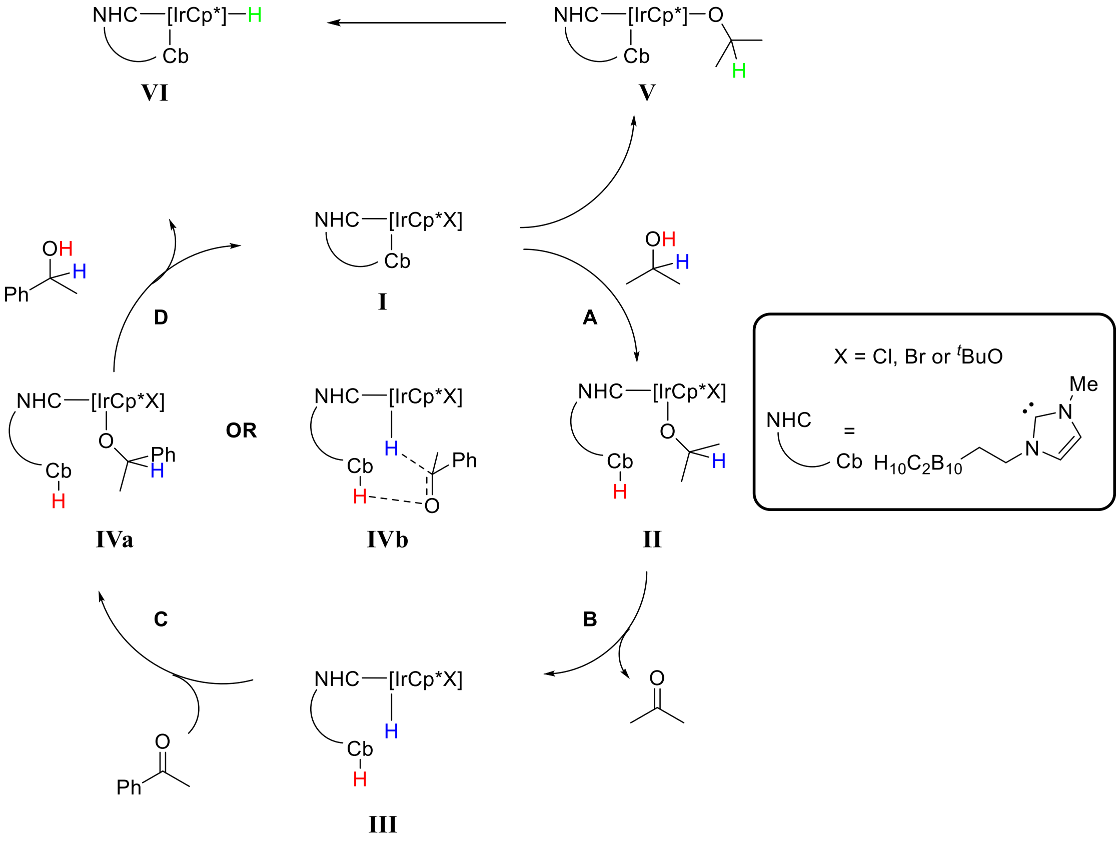
NHC—[IrCp*]—H
Cb
VI
NHC—[IrCp*]—O
Cb
H
V
OH
H
Ph
D
NHC—[IrCp*X]
Cb
I
OH
H
A
X = Cl, Br or ^{t}BuO
NHC = Cb $H_{10}C_2B_{10}$
Me
N
N
NHC—[IrCp*X]
O
Ph
H
Cb
H
IVa
OR
NHC—[IrCp*X]
H
Ph
Cb
H
O
IVb
NHC—[IrCp*X]
O
Cb
H
H
II
C
B
O
Ph
NHC—[IrCp*X]
H
Cb
H
III
O

Figure 91. Proposed cycle and intermediate species **I-VI** considered in initial optimisations.

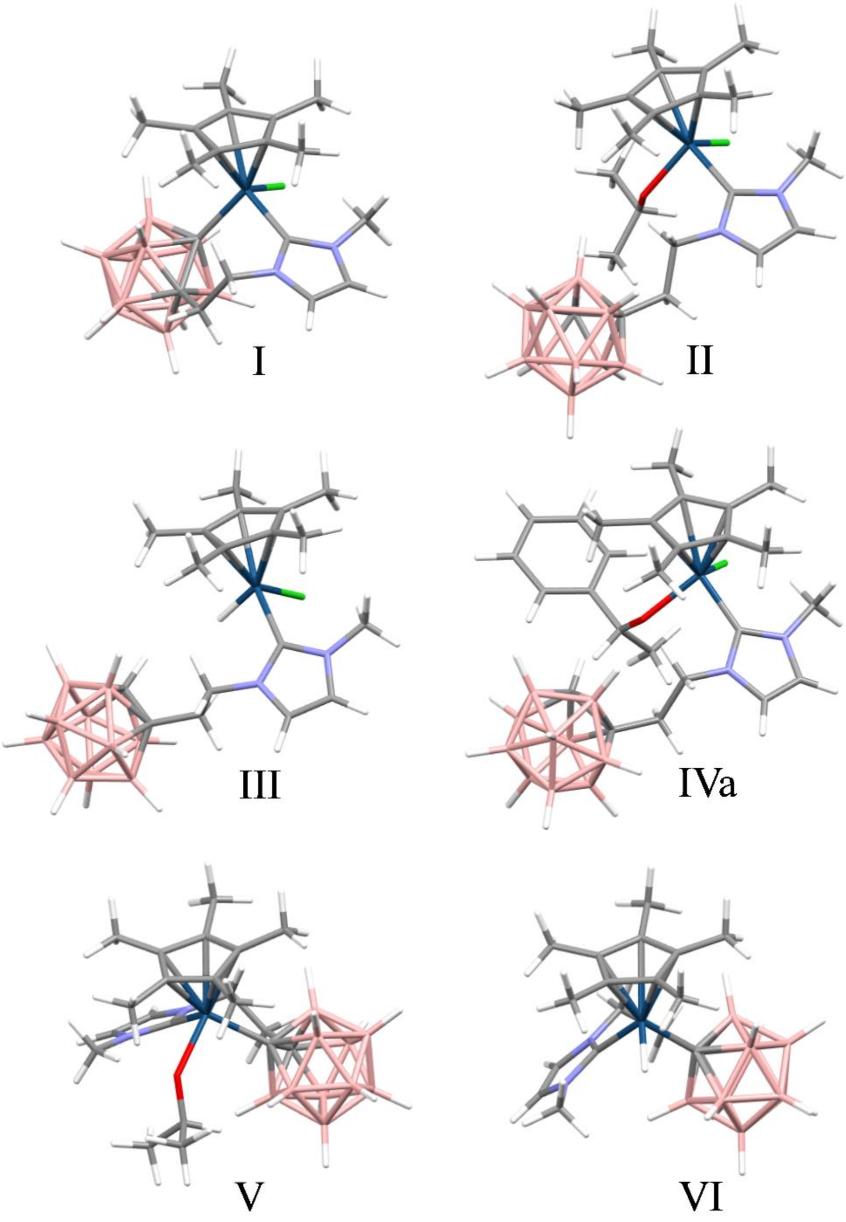

Figure 92. Optimised structures for intermediates **I**-**VI**.

As with the comparison between cyclometallated and non-cyclometallated complexes, it was necessary to correct the energies of each intermediate. This can be achieved by the addition of molecules relevant to the cycle: propanol, acetone, and acetophenone (HCl was used for the “off-cycle” species) (Table 10).

Table 10. Intermediates, molecules used for correction and relative Gibbs free energies.

Intermediate	Correctional Molecules	Relative Gibbs free energy		
I	Acetophenone, propanol	0	0	0
II	Acetophenone	+11	+40	+48
III	Acetophenone, acetone	-81	-65	-3
IVa	Acetone	+32	+61	+34
V	Acetophenone, HCl	+143	+164	+142
VI	Acetophenone, acetone, HCl	-10	0	+35

Blue cells: gas phase, orange cells: COSMO (DCM) solvation, grey cells: DFT-D3 correction.

For step **A** (**I**-**II**) there is an increase in Gibbs free energy at all levels of correction. The energy increase is higher when the COSMO and DFT-D3 corrections are applied. This is consistent because the uncoordinated propanol (present in the ground state energy) will be more stabilised in solution and in the presence of dispersive forces due to the polar OH group.

For intermediate **III** the Gibbs free energy is significantly lower than **II**, and somewhat lower than **I**. The effect is largest in the uncorrected gas phase calculation, which again may be attributable to the unfavourable gas-phase energy of propanol which is tempered by use of the solvation and dispersive corrections. There is an increase in entropy relative to **I** which is due to the inherent entropy in the free rotation of the uncoordinated carborane.

An energy increase is observed for the formation of **IVa**. This is partially due to the negative entropic effect of substrate coordination. As previously, the increase in relative energy of the solvated species compared to **I** may be artificially enhanced by use of propanol as a correction. The reduction that is seen when the dispersion correction is applied is surprising, and cannot be easily explained.

The energies of the two off-cycle species **V** and **VI** are likely to be artificially increased due to the use of HCl as a correction. A similar effect upon the addition of the DFT-D3 correction is seen for **V** as was seen for **IVa**. Once again, examination of the geometry of **V** reveals the presence of a weak interaction between the methyl group of the NHC and the oxygen of the alkoxide, which may account for the change. It is surprising that the energies of both **V** and **VI** increase upon application of the COSMO solvation correction, given that this ought to reduce the energetic penalty incurred by HCl.

In order to remove the need for use of HCl, an alternative correction system was used to compare **I** with **V** and **VI** (Table 11). In this case chloroethane/ethene was used to provide an "HCl" deficit.

Table 11. Relative Gibbs free energies using alternative corrections.

Intermediate	Correction	Relative Gibbs free energy		
I	Propanol, ethene	0	0	0
V	Chloroethane	105	119	86
VI	Acetone, chloroethane	-66	-55	-29

Blue cells: gas phase, orange cells: COSMO (DCM) solvation, grey cells: DFT-D3 correction.

The trends are the same using this correction, i.e. **V** unstable relative to **I**, **VI** more stable relative to **V**. In this case, with all corrections, **VI** is more stable than **I**. Although this correction removes the issue of modelling HCl in the gas phase, it does introduce the problem of gyricity. The bonding in ethene is different to that in chloroethane, and hence the computational model may perform more or less well in describing the two species. Overall these results indicate that **V** is more unstable than **I** and **VI**, whereas the relative stability of **VI** relative to **I** is unclear. This highlights the challenges associated with accurate energy comparisons for very different species in computational chemistry.

Each structure was also optimised featuring a bromide or *ᵗ*Bu ligand instead of a chloride.[2] The bromide species were higher in energy, and the *ᵗ*Bu species higher still, however energy gaps between intermediates followed the same trends. This therefore indicates that the identity of the X ligand may not impact the catalytic reaction.

An approximate assessment of reasonable energy barriers can be obtained using the Eyring equation; a barrier of ~100 kJ mol^{-1} would be in line with a reaction performed at 82 °C for 1 hour (calculation of rate constants for various barrier heights is provided in the appendix). All intermediate structures except **V** have calculated energies that are consistent with this. In the case of **V**, the energy of the intermediate is relatively high, and any transition state will necessarily be higher in energy. Thus the initially proposed mechanism is plausible, but the suggested off-cycle route to **VI** *via* **V** may be a high energy pathway that does not occur.

---

[2] *Calculations on species **II** with a ^{t}BuO$^-$ ligand replacing the chloride did not converge. Minima for all other species were successfully located.*

3.4.2 Transition States

Having obtained relative energies for the intermediates of interest, the next step is to locate transition states that link them. Energy minima structures are identified as such by the absence of any imaginary frequencies in the vibrational frequency calculation. A transition state is identifiable as a species with a single imaginary frequency which corresponds to a reaction coordinate. A number of techniques are available to attempt to locate transition states. Once a transition state has been identified, it is necessary to determine which two intermediate species are connected by it. This can be performed using direct reaction coordinate calculations, which follow the imaginary mode of the transition state to locate the energy minima on either side. If this analysis shows that the transition state links the two desired intermediates then the transition state energy can be compared with that of the initial geometry and hence the energy barrier determined.

3.4.2.1 Constrained Approaches

Initially, attempts were made in which a “guess” transition state structure was used as an input. The atoms which will undergo the greatest movement during the transition are fixed, and then a geometry optimisation was performed to allow the rest of the structure to undergo relaxation. A successful pre-transition state calculation results in a geometry with a single imaginary frequency that corresponds to the reaction coordinate. The transition state optimisation calculation is next carried out by removing the constraints on the atoms. An eigenvector following routine is used to follow the reaction coordinate to locate the energy maximum (Figure 93).

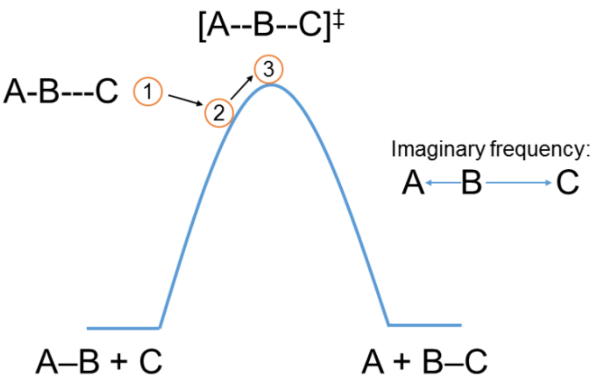

Figure 93. Schematic indicating transition state search process. Initial guess structure (1) is optimised (2). An eigenvector following routine follows the imaginary frequency to locate the energy maximum (3).

The first step (protonation of the carborane and coordination of a propoxide) and the second step (formation of a metal hydride) were both considered (Figure 94). It is likely that the third step will effectively be the reverse of the first.

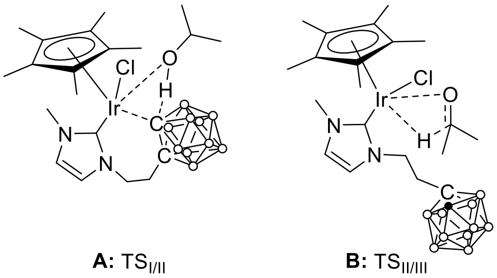

Figure 94. Proposed mechanisms for step **A** and **B** in the catalytic cycle.

For both steps, although some pre-transition state calculations resulted in location of promising imaginary frequencies, subsequent optimisations never resulted in the location of the desired transition states. In the case of the second step a transition state optimisation produced a geometry in which the hydride hydrogen sits between the Ir centre (1.98 Å) and the propoxide carbon (1.21 Å). One of the Cp* methyl group hydrogen atoms now also sits between the Cp* methyl carbon (1.37 Å) and the oxygen of the propoxide (1.27 Å). These bond distances are all outside of the expected range of these bond types – indicating that this represents a bond-breaking/bond forming step.[21] The vibrational frequency analysis revealed a single imaginary frequency at -1055 cm^{-1} which corresponds to the deprotonation of the Cp* methyl group by the propoxide (Figure 95).

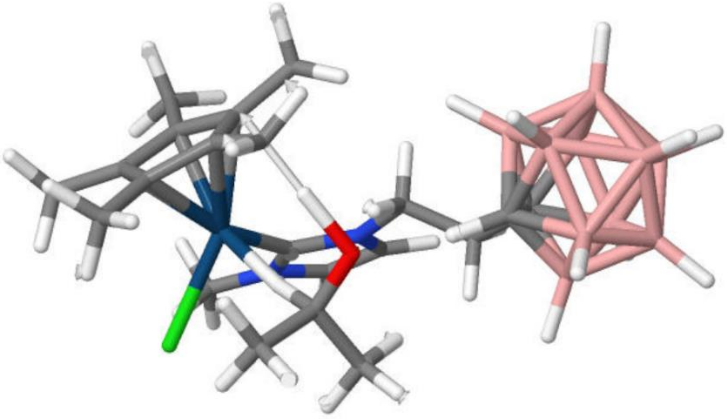

Figure 95. Imaginary vibrational mode (-1055 cm^{-1}) for transition state calculation.

The Gibbs free energy (DFT-D3) of this transition state relative to the starting complex is +85 kJ mol^{-1}. A Dynamic Reaction Coordinate (DRC) calculation confirmed the structure to be a transition state between the hydride complex with a closely associated ketone, and the coordinatively unsaturated fulvene complex with a closely held propanol (**IIIa**) (Figure 96). The geometry in the minus direction of the DRC calculation was optimised; after a slight modification to the geometry the calculation converged on a geometry near identical with that for **III** – with the new structure lying just 4 kJ mol^{-1} lower in energy. Optimisation of the geometry obtained in the plus direction generated structure **IIIa**.

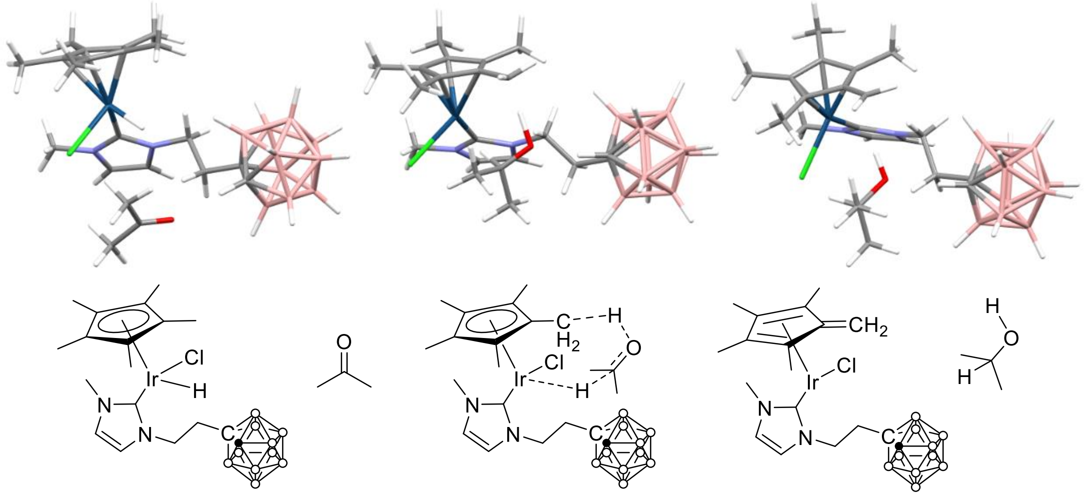

III **TS$_{III/IIIa}$** **IIIa**

Figure 96. Left: Geometry optimised structure for DRC calculation in the minus direction. Middle: Geometry optimised transition state structure. Right: Geometry optimised structure for DRC calculation in the plus direction.

Tetramethylfulvene complexes of Ir have previously been reported. These are structures in which the Ir centre is coordinated by a 1,3-cyclopentadiene ring with an exo-double bond (Figure 97). Coordination of the fulvene can be η-2, 4, or 6, although η^2 coordination is very rare.[22] **IIIa** differs from many reported fulvene complexes in that it results from a deprotonation, leaving a formal 2- charge on the former Cp* ligand, whereas literature examples are formed by hydride abstraction, or oxidation.[23–25] Bergman and Glueck however, reported the synthesis of **3.1**, resulting from an intramolecular deprotonation of the Cp* by an anilide counter-ion. In common with **3.1**, the CH_2 group in **IIIa** is bent away from the metal centre - indicating an η-4 coordination.[26]

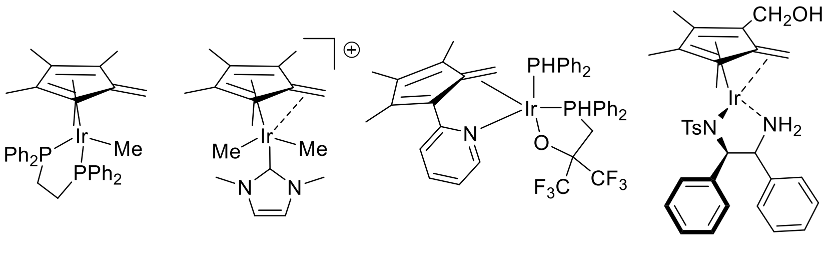

3.1 **3.2** **3.3** **3.4**

Figure 97. Example fulvene complexes.[22,23,25,26]

Compared to other Cp* complexes there is an elongation in the Ir-C bond length for the carbon adjacent to the site of deprotonation (2.597 Å vs. 2.212-2.377 Å for **III**). There is a clear contraction in the C$_{ring}$-C$_{exo}$ bond distance at the deprotonation site, with the distance indicating significant double bond character, as seen with other fulvene complexes. The bond lengths within in the ring are close enough to one another to indicate delocalisation, rather than an alternating structure of single and double bonds. However the lengths are all at the long end of the range expected for aromatic bonds (1.425-1.489 Å), which is in good agreement with those reported for the solid state structure of **3.1**.[26] **IIIa** lies at +51 kJ mol^{-1} relative to **I** and +54 kJ mol^{-1} relative to **III**.

In addition to species **IIIa** being structurally interesting, it is also worth noting that this unexpected reaction pathway constitutes a formal transfer of hydrogen from a metal complex to a substrate. It is easy to envisage how **IIIa** could revert to **III** by approach of an IPA molecule, thus this could be a catalytically relevant species. TH catalysts are generally considered to operate *via* a monohydride mechanism which may be either inner or outer-sphere (Chapter 1 - *1.2.3*).[27] Dihydride species are sometimes invoked, and more recently loss of the Cp* ligand to generate a polyhydride species has been suggested.[28–30] Formation of an Ir fulvene complex has been proposed as a deactivation pathway in the TH of dioxygen (Chapter 2 - *2.4.1*).[25] This potential mechanism is reminiscent of the Shvo catalyst described in Chapter 1 (Figure 98).[31] There are however, no examples previously reported that suggest the Cp* ligand acts as a hydrogen source itself. The energy barrier for this step of 85 kJ mol^{-1} is consistent with the experimentally observed reaction rate. Consideration of a catalytic cycle involving this transition is therefore a worthwhile future enterprise.

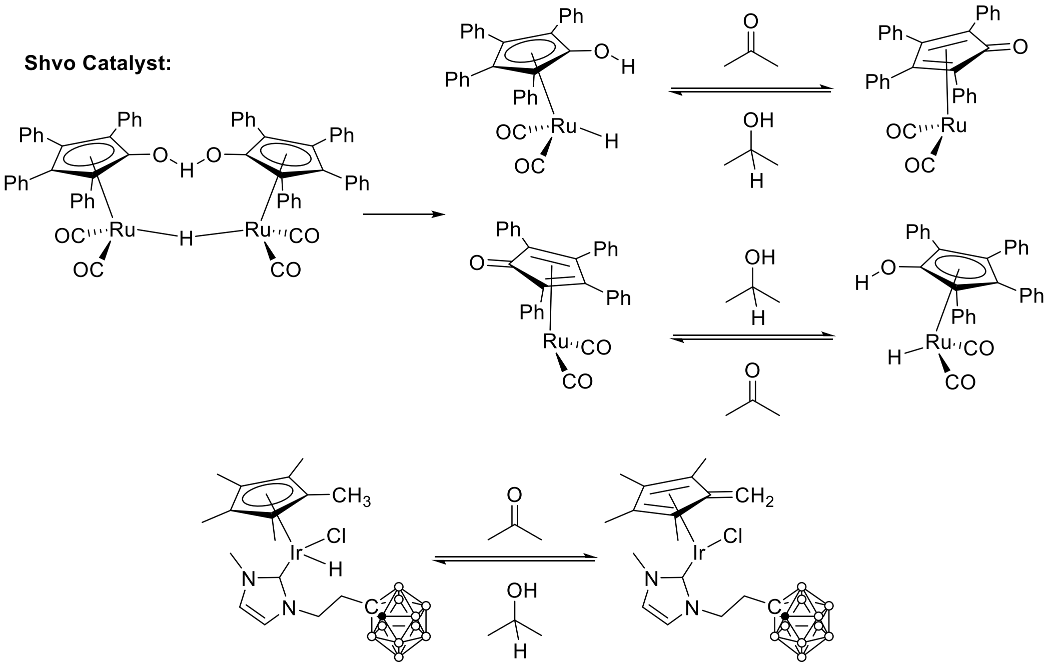

Figure 98. Top: Schematic showing mechanism for TH by Shvo catalyst. Bottom: Potential mechanistic pathway for TH observed computationally.

3.4.2.2 Manual Potential Energy Surface Scans

Another approach to locating transition states is to use a potential energy surface scan. This compares the relative energies of optimised structures that progress along a defined reaction coordinate, with the aim to locate a structure close to the maximum energy point. Such a structure can then be interrogated using the methods described above (3.4.2.1) (Figure 99).

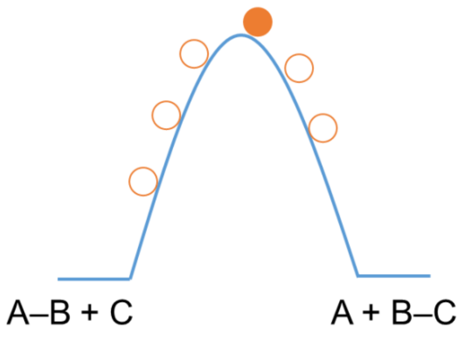

Figure 99. Schematic diagram of a potential energy surface scan. Input structures designed to be at various degrees of progress along the reaction coordinate are optimised (orange circles). The highest energy structure (filled circle) has the geometry closest to that at the energy maximum and can be used for subsequent transition state calculations.

For step **A**, the approach of propanol toward the Ir-$C_{carborane}$ bond was considered. A scan along the $C_{carborane}$-H_{OH} bond distance was performed using the programme Orca. The distance range 1.2-2.8 Å was investigated, as the CH bond lengths in carboranes were found to be ~1.11 Å in previous calculations. The calculated SCF energies for the various structures can be compared with the C-H distance (Figure 100). The energy profile revealed indicates a steady increase in energy followed by a sudden decline, as the C-H distance changes from 1.40 Å to 1.30 Å. As the C-H distance decreases there is a concomitant increase in O-H distance (Table 12). It can additionally be seen that progress towards the protonation of the carborane is accompanied by an increase in the C-C bond distance in the carborane cage beyond normal limits. In **C3** the bond length was calculated to be 1.65 Å. This is increased somewhat in the cyclometallated complex **C5** to 1.79 Å. The greatest distance between the carbon atoms during the scan was found to be 2.45 Å (Figure 101). It seems likely that this is a major contributing factor to the large increase in energy seen over the course of the scan. The bonding in carboranes is often described as being 3D-aromatic, and hence there is likely to be a large energetic penalty to distorting the structure in a way which disrupts this aromaticity.

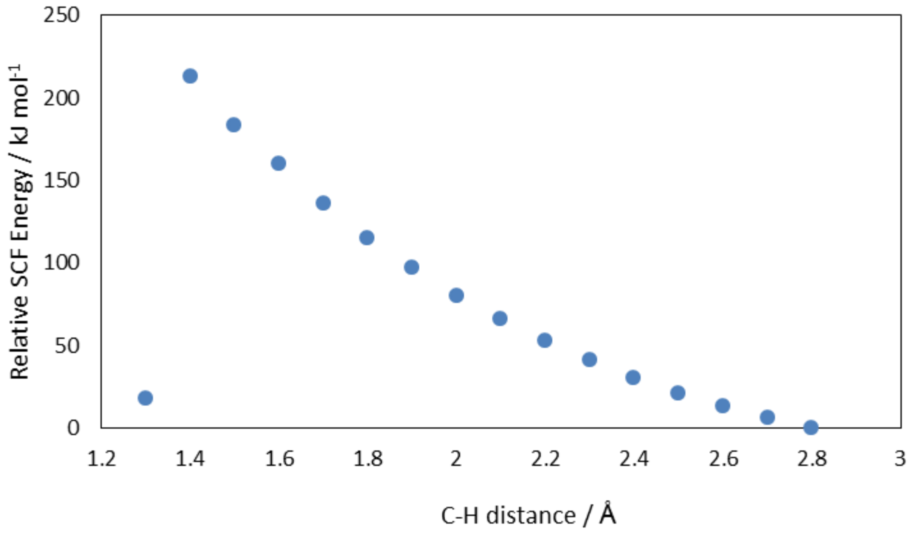

Figure 100. C-H distances versus calculated SCF energy.

The energy gap between the highest point (1.4 Å CH separation) and the next (1.3 Å CH separation) is 195 kJ mol^{-1} which is considerably higher than would be expected given the reaction conditions. It is worth noting that the energy gap is only the distance between the two geometries, and the actual energy barrier for the transition state that connects them could lie even higher in energy. Although this transition state is unlikely to represent the actual catalytic pathway, a transition state calculation was performed using the output geometry at the 1.4 Å distance. The imaginary frequency found from this calculation did not correspond to the desired reaction coordinate however.

Table 12. Bond distances at various PES scan optimised geometries.

Bond	Calculated length / Å	Interatomic distance / Å			
C-H	1.11	1.300	1.401	1.500	1.600
O-H	0.981	1.630	1.098	1.064	1.043
Ir-O	2.11	2.158	2.970	3.008	3.094
Ir-C	2.18	4.445	2.307	2.221	2.181
C-C	1.65	1.652	2.435	2.447	2.446

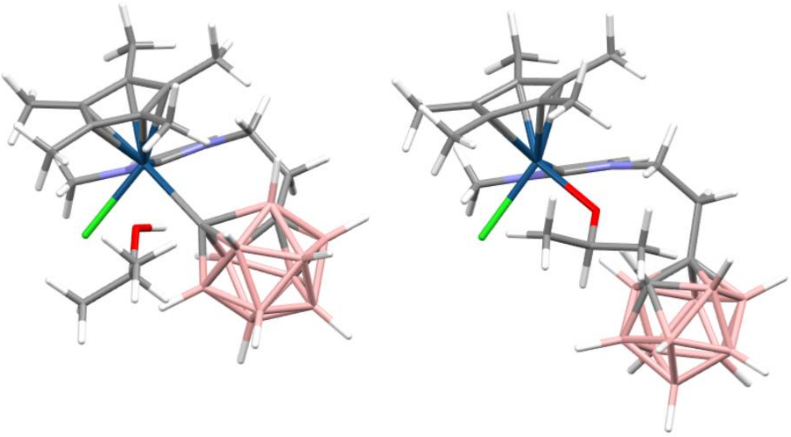

Figure 101. Left: Optimised constrained structure with a 1.4 Å C-H distance. structure. Right: Optimised constrained structure with a 1.3 Å C-H distance.

The same step was also investigated using a scan was also performed along the Ir-O distance, with distances between 3.0 and 2.1 Å (Figure 102). This shows a steady rise in energy with a gap of +84 kJ mol^{-1} between the lowest and highest point. When visualised the reaction coordinate followed is not the approach of the propanol coupled with carborane protonation. Instead, initially an interaction between the OH and Cl is observed, as the Ir-O distance decreases the chloride is pushed away, and the Cp* undergoes a slip from η^5 towards η^1 coordination. (Figure 103).

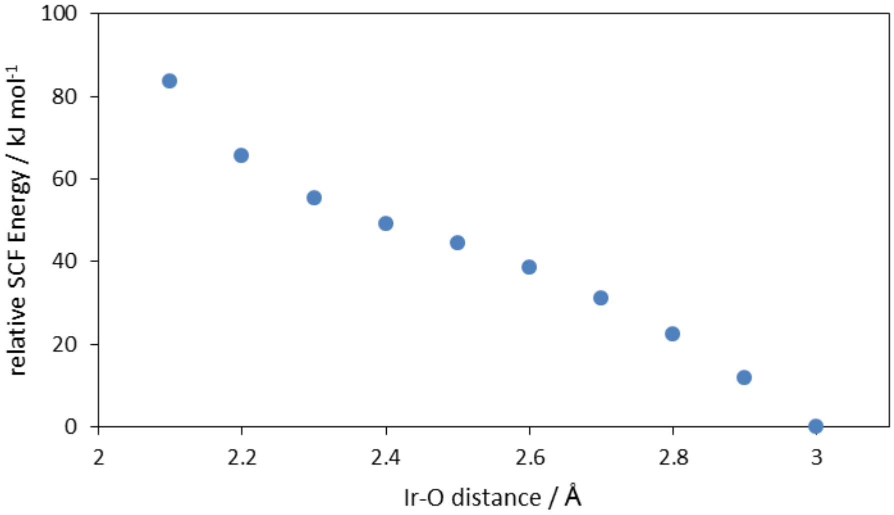

Figure 102. Ir-O distances versus calculated SCF energy.

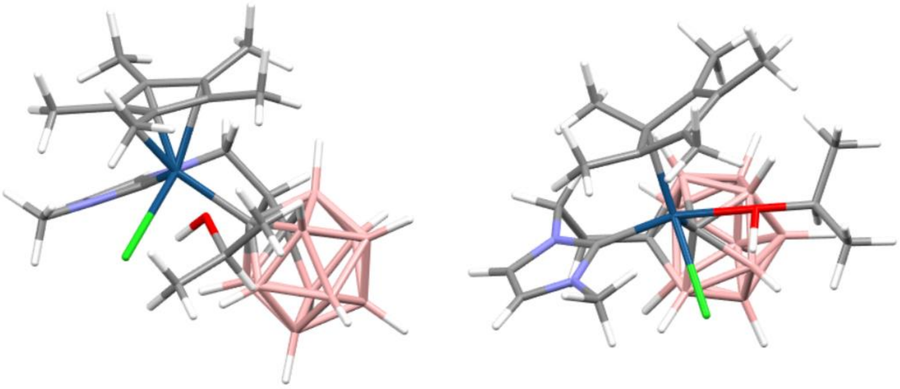

Figure 103. Left: Optimised constrained geometry structures for 3.0 Å Ir-O distance. Right: Optimised constrained geometry structures for 2.1 Å Ir-O distance.

The investigation of step **B** was continued using PES scans also run using Orca. In this case the Ir-$H_{propoxide}$ distance between 2.5 Å and 1.5 Å was investigated. The results give an unusual energy profile, with an initial large increase in energy between 2.5 Å and 2.4 Å, and a discontinuity between 1.98 Å and 1.93 Å (Figure 104). A discontinuity of this type is an indication that the scan has slipped from one energy pathway to another. This is reflected in the interatomic distances seen in the geometries before and after the discontinuity. Whilst the decreasing Ir-H distance does lead to small structural changes throughout, there is a large increase in the Ir-O distance between the 1.98 Å and 1.93 Å geometries. Likewise the $CH_{carborane}$-O distance increases significantly, as does the $C_{propanol}$-H distance. These values are reflective of a large movement away from the Ir centre by the outgoing ketone (Figure 105).

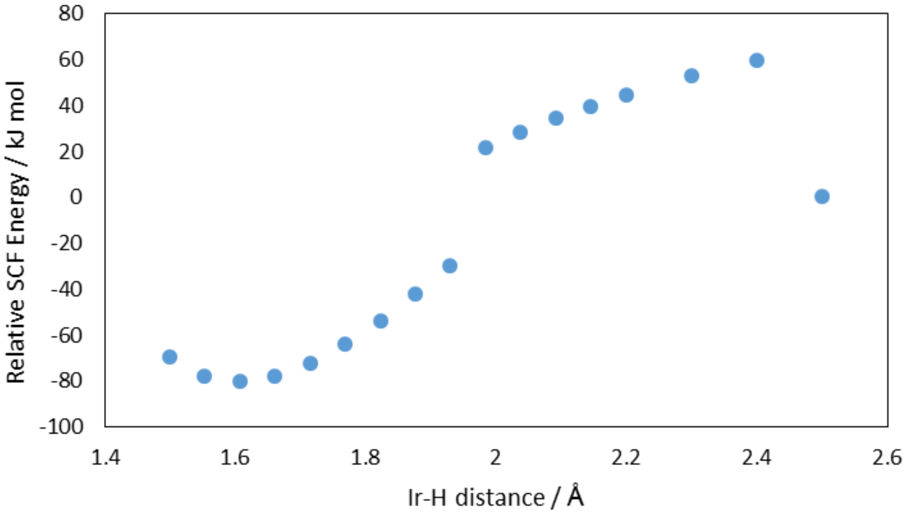

Figure 104. Ir-H distances versus calculated SCF energy.

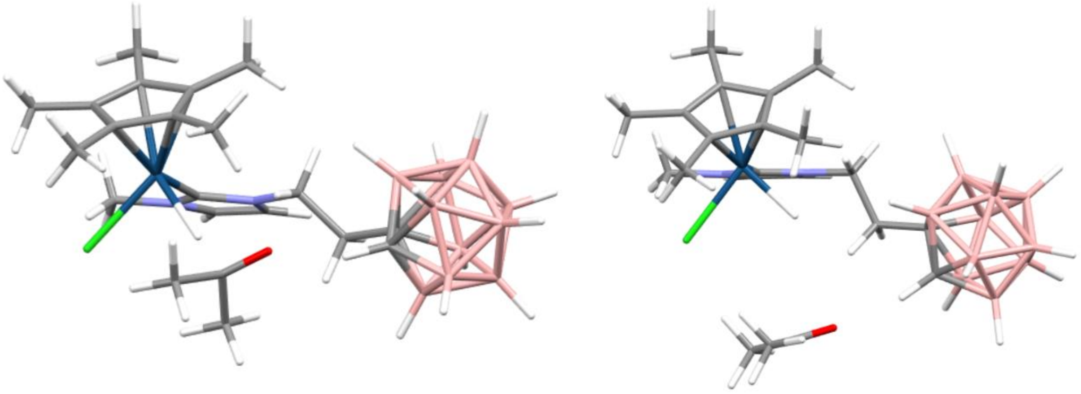

Figure 105. Optimised constrained geometry structures for 1.98 Å Ir-H distance (left) and 1.93 Å Ir-H distance (right).

The energy gap between the geometries at 2.5 Å and 2.4 Å is +59 kJ mol^{-1}, which is feasible for the reaction conditions used. Although the energy surface obtained is unlikely to be a true representation of the envisaged step, attempts were made to carry out a transition state calculation on the highest energy structure (2.4 Å Ir-H distance). The pre-transition state calculation converged on a structure with no imaginary frequencies, in which Cp* deprotonation had occurred as seen in **IIIa**. This structure was resubmitted to a full geometry optimisation calculation, and the resulting geometry was near identical to that previously calculated for **IIIa**, lying 4 kJ mol^{-1} higher in energy.

3.6 Conclusions and Future Work

The carbonyl stretching frequencies in [IrCp(CO)L] complexes have been calculated for a range of NHC ligands based on **L1** and **L2**. Analysis of the vibrational frequencies allows for an assessment of the relative donor strengths of these ligands. The values obtained lie within the expected range for NHC ligands, and mostly follow expected trends. The carboranyl-substituted ligands were found to be more electron donating than the phenyl analogues, in spite of the formal electron “deficiency” of the cluster species. This suggests that these ligands ought to perform better as supporting ligands for reactions where a high degree of electron density at the metal is required (e.g. oxidative addition).

Energy minima for a number of intermediates for the proposed cycle of TH using Ir-NHC complexes were located. The relative energies of the intermediates involved in the cycle (**I-IV**) were consistent with experimental reaction conditions, although it was not possible to locate transition states which connected these structures. For step **A**, a PES scan along the $C_{carborane}$-$HO_{propanol}$ bond length revealed a large energy difference (+195 kJ mol^{-1}) between structures before and after carborane protonation, which was attributed to severe deformation of the carborane cage. A scan along the Ir-O bond length did not locate an energy maximum, but had an energy gap of 84 kJ mol^{-1} between lowest and higher points. This reaction coordinate corresponded to the partial displacement of the Cp* ring by the incoming propanol. Taken together, these two scans suggest that the carborane protonation pathway is unlikely to be in operation in the catalytic reaction. For step **B** a PES scan provided a discontinuous energy pathway, which is unlikely to be reflective of a single reaction coordinate. Attempts to use the data to inform subsequent transition state searches were unsuccessful.

A transition state (**$TS_{III/IIIa}$**) was located between the intermediate **III** and the previously unconsidered fulvene complex **IIIa**. This pathway is particularly interesting as it offers a potential route to hydrogenation of substrates, although comparison with other possible mechanisms would be necessary to determine the viability of this pathway. Additionally, the route to intermediate **III** has not yet been located, though this offers fertile ground for further study.

There are many other avenues of investigation which would be worthwhile. Chief among these would be the investigation of other possible mechanistic routes, particularly in light of experimental results discussed in Chapters 2 and 4. The characterisation of the monohydride complex **C6.H**, warrants further investigation of the equivalent intermediate structure **VI**. An investigation into how this can be formed, both under catalytic conditions, and reaction conditions described in Chapter 2, may lead to further insights about the potential role of this species in catalysis. The results discussed in Chapter 4 suggest that dimeric species are formed under catalytic conditions, so consideration of these as potential intermediates would be apposite. Additionally, the observation of multiple hydride signals means that a mechanism involving a polyhydride species may be in operation.

Another point that has not been considered in detail is that of chirality. An investigation into the relative energies of different ketone coordination isomers could be considered, as this may give an insight into whether chirally resolved examples of these complexes would be competent asymmetric catalysts.

3.7 Experimental

Calculations were performed using the TURBOMOLE V6.40 package or the Orca 4.0.0.2 package.[32,33] Input coordinates were generated from crystallographic data (where available), modified crystallographic data, or chemical intuition. Structures were visualised and manipulated using either Avogadro 1.1.1, Facio 18.8.2, Mercury 3.0, or Molden. Imaginary frequencies were visualised using Jmol 14.8.0.

Geometry optimisations were performed at the (RI-)BP86/SVP, (RI)BP86/def2-TZVPP, or (RI-)PBE0/SVP level, followed by frequency calculations at the same level.[34–37] For all calculations a quasi-relativistic effective core potential replaced the core electrons of heavy atoms (Ir - 60 electrons; Rh/Ru - 28 electrons).[35,38] Energy minima were identified as such by the absence of imaginary frequencies; transition states were identified by the presence of a single imaginary frequency. Transition states were located by a constrained minimisation with atoms undergoing most change frozen, followed by a frequency calculation to identify the transition vector to follow during the transition state calculation. The transition state calculation used an eigenvector following routine along the imaginary frequency identified by the preceding calculation. This was followed by a frequency calculation on the optimised transition state. The minima adjacent to the transition state were identified using a DRC calculation. These calculations were performed in the DRC module of TURBOMOLE.

Solvation effects were modelled for DCM using the COSMO module of TURBOMOLE. A DFT-D3 correction to the energy of the computed structures was applied after the geometry optimisation.[16]

Coordinate and vibrational frequency files for calculated structures are provided in the electronic supplement.

Appendix

Table A1. Calculated rate constants for a given energy barrier at 82 °C.

$$k = \frac{k_b T}{h} e^{-\frac{\Delta G}{RT}}$$

ΔG^{TS} / kJ mol^{-1}	*k*
25	1.55×10^{9}
50	3.25×10^{5}
75	68.1
100	0.014
125	2.99×10^{-6}

Table A2. Relative Gibbs free energies for cycle intermediates.

Intermediate	Gibbs free energy		
I	0	0	0
I.Br	+9	+9	+1
I.^{t}BuO	+167	+184	+160
II	+11	+40	+48
II.Br	+15	+43	+44
III	-81	-65	-3
III.Br	-86	-64	-14
III.^{t}BuO	+24	+59	+98
IVa	+32	+61	+34
IVa.Br	+24	+49	+31
IVa.^{t}BuO	+154	+194	+145

Blue cells: gas phase, orange cells: COSMO (DCM) solvation, grey cells: DFT-D3 correction.

List of References

1 F. Jensen, *Introduction to Computational Chemistry*, John Wiley & Sons Ltd, Chichester, 2nd edn., 2007.

2 B. M. Rode, T. S. Hofer and M. D. Kugler, *The Basics of Theoretical and Computational Chemistry*, WILEY-VCH Verlag GmbH, Weinheim, 1st edn., 2007.

3 C. A. Tolman, *Chem. Rev.*, 1977, **77**, 313–348.

4 R. Dorta, E. D. Stevens, N. M. Scott, C. Costabile, L. Cavallo, C. D. Hoff and S. P. Nolan, *J. Am. Chem. Soc.*, 2005, **127**, 2485–2495.

5 R. A. Kelly III, H. Clavier, S. Giudice, N. M. Scott, E. D. Stevens, J. Bordner, I. Samardjiev, C. D. Hoff, L. Cavallo and S. P. Nolan, *Organometallics*, 2008, **27**, 202–210.

6 A. Chianese, X. Li, M. Janzen, J. Faller and R. Crabtree, *Organometallics*, 2003, **22**, 1663–1667.

7 S. C. Zinner, C. F. Rentzsch, E. Herdtweck, W. A. Herrmann and F. E. Kühn, *Dalton Trans.*, 2009, 7055–7062.

8 D. J. Nelson and S. P. Nolan, *Chem. Soc. Rev.*, 2013, **42**, 6723–6753.

9 L. Perrin, E. Clot, O. Eisenstein, J. Loch and R. H. Crabtree, *Inorg. Chem.*, 2001, **40**, 5806–5811.

10 D. G. Gusev, *Organometallics*, 2009, **28**, 6458–6461.

11 D. G. Gusev, *Organometallics*, 2009, **28**, 763–770.

12 Q. Shi, R. J. Thatcher, J. Slattery, P. S. Sauari, A. C. Whitwood, P. C. McGowan and R. E. Douthwaite, *Chem. Eur. J.*, 2009, **15**, 11346–11360.

13 S. Díez-González, N. Marion and S. P. Nolan, *Chem. Rev.*, 2009, **109**, 3612–3676.

14 J. Holmes, *Preparation of Brand New Ligand Architectures Incorporating N-Heterocyclic Carbene Complexes with Carboranyl Substituents: Coordination Chemistry, Catalytic Evaluation and Anticancer Properties,* University of Leeds, 2017.

15 J. Holmes, C. M. Pask and C. E. Willans, *Dalton Trans.*, 2016, **45**, 15818–15827.

16 S. Grimme, J. Antony, S. Ehrlich and H. Krieg, *J. Chem. Phys.*, 2010, **132**, 154104.

17 J. M. Hayes, M. Viciano, E. Peris, G. Ujaque and A. Lledós, *Organometallics*, 2007, **26**, 6170–6183.

18 S. Kozuch and S. Shaik, *Acc. Chem. Res.*, 2011, **44**, 101–110.

19 M. D. Wodrich, B. Sawatlon, E. Solel, S. Kozuch and C. Corminboeuf, *ACS Catal.*, 2019, **9**, 5716–5725.

20 A. Uhe, S. Kozuch and S. Shaik, *J. Comput. Chem.*, 2011, **32**, 978–985.

21 F. H. Allen, O. Kennard, D. G. Watson, L. Brammer, A. G. Orpen and R. Taylor, *J. Chem. Soc. Perkin Trans. 2*, 1987, S1–S19.

22 A. S. Ionkin and W. J. Marshall, *Inorg. Chem.*, 2005, **44**, 6244–6347.

23 J. M. Meredith, K. I. Goldberg, W. Kaminsky and D. M. Heinekey, *Organometallics*, 2012, **31**, 8459–8462.

24 D. V. Muratov, A. S. Romanov, M. Corsini, A. R. Kudinov, F. F. de Biani and W. Siebert, *Chem. Eur. J.*, 2017, **23**, 11935–11944.

25 Z. M. Heiden and T. B. Rauchfuss, *J. Am. Chem. Soc.*, 2007, **129**, 14303–14310.

26 D. S. Glueck and R. G. Bergman, *Organometallics*, 1990, **9**, 2862–2863.

27 J. S. M. Samec, J.-E. Bäckvall, P. G. Andersson and P. Brandt, *Chem. Soc. Rev.*, 2006, **35**, 237–348.

28 R. Corberán and E. Peris, *Organometallics*, 2008, **27**, 1954–1958.

29 U. Hintermair, J. Campos, T. P. Brewster, L. M. Pratt, N. D. Schley and R. H. Crabtree, *ACS Catal.*, 2014, **4**, 99–108.

30 J. Campos, U. Hintermair, T. P. Brewster, M. K. Takase and R. H. Crabtree, *ACS Catal.*, 2014, **4**, 973–985.

31 Y. Shvo, D. Czarkie, Y. Rahamim and D. F. Chodosh, *J. Am. Chem. Soc.*, 1986, **108**, 7400–7402.

32 R. Ahlrichs, M. Bär, M. Häser, H. Horn and C. Kölmel, *Chem. Phys. Lett.*, 1989, **162**, 165–169.

33 F. Neese, *Wiley Interdiscip. Rev. Comput. Mol. Sci.*, 2012, **2**, 73–78.

34 A. Schäfer, H. Horn and R. Ahlrichs, *J. Chem. Phys.*, 1992, **97**, 2571–2577.

35 K. Eichkorn, F. Weigend, O. Treutler and R. Ahlrichs, *Theor. Chem. Accounts Theory, Comput. Model. (Theoretica Chim. Acta)*, 1997, **97**, 119–124.

36 F. Weigend, M. Häser, H. Patzelt and R. Ahlrichs, *Chem. Phys. Lett.*, 1998, **294**, 143–152.

37 F. Weigend and R. Ahlrichs, *Phys. Chem. Chem. Phys.*, 2005, **7**, 3297–3305.

38 D. Andrae, U. Häußermann, M. Dolg, H. Stoll and H. Preuß, *Theor. Chim. Acta*, 1990, **77**, 123–141.

Chapter 4
On-line Monitoring of a Transfer Hydrogenation Reaction Catalysed by NHC-Carborane Iridium Complexes

4.1 Introduction

Monitoring the progress of a reaction is one of the most powerful ways a mechanism can be investigated. Information about both the reaction rate, and the identity of key intermediates can be obtained in this way. A multitude of techniques are available for reaction monitoring, including mass spectrometry, and IR, UV-vis, and NMR spectroscopies. There are a variety of approaches to reaction monitoring. Classically, reactions would be monitored “off-line”, by removing a sample from the reaction vessel and submitting this to an analytical technique of choice. More recently the ability to make direct measurements during a reaction has become available. These measurements may be “in-line”, with a spectroscopic probe inserted into the reaction vessel, or “on-line”, with tubing that leads to the required instrument inserted instead.[1] Monitoring of reactions enables reaction progress to be measured as a function of time, and hence kinetic analyses may be performed.

There are many benefits to in- or on-line reaction monitoring as it allows the monitoring of real reaction conditions, with minimal adaptations in set-up required. Classical kinetics often interrogates only the initial rates of a reaction, thereby ignoring how the reaction progress may vary over time. Modern reaction monitoring techniques enable the acquisition of data sets that encompass the full reaction duration. This can lead to a better understanding of the manifold complexities of reaction mechanisms.

4.1.1 DReaM Facility

The Dynamic Reaction Monitoring (DReaM) Facility at the University of Bath enables on-line monitoring of reactions using various techniques, chiefly NMR spectroscopy.[1–3] NMR spectroscopic analysis is achieved through use of an InsightMR flowprobe and related software (Bruker). The reaction set-up has continuous recirculation of reaction mixture between the reaction vessel and the InsightMR tube, which is located within a 500 MHz NMR spectrometer. The reaction mixture flows through thermally jacketed tubing to maintain the desired reaction temperature, with the flow-rate maintained by a standard HPLC pump. The return section of the tubing may be fitted to allow sampling for analysis by other techniques including: HRMS, HPLC, polarimetry and UV-vis spectroscopy. Reactions may be monitored using standard NMR nuclei: ^{1}H, ^{11}B, ^{13}C, ^{19}F and ^{31}P.

It is important to bear in mind the effect that flow will have on the NMR spectra recorded. Typical flow-rates used are 4 mL/min which corresponds to a residence time of 3 seconds within the magnet followed by 8 seconds in the detector. The 3 seconds spent within the magnet may be insufficient to build up complete magnetisation ($<5T_1$), dependant on the chemical environment of the nuclei. Therefore, signals for which 3 seconds is $<5T_1$ are often “under-integrated” when observed in flow compared to a static experiment which has a sufficient delay for full relaxation to occur. Additionally, signals with longer T_1 values will have a lower intensity than those with shorter T_1 values, which will affect the validity of quantification. It is however possible to apply a correction factor that accounts for the effects of flow. Two spectra are recorded, one flowing and one static, in which the signals would be identical, if flow had no effect. Dividing the integration value for the static experiment by that for the flowing experiment provides a flow correction factor (FCF) which is used to normalise integration values for all spectra recorded. One limitation of this approach is that all the signals which are to be quantified must be present in the static spectrum. This may present a problem for resonances corresponding to intermediates which are not present at the start or end of a reaction.

Whilst the InsightMR system is in general very versatile, there are a number of limitations. Firstly, the temperature range for reactions is -20 °C to 77 °C due to the tolerance of the NMR spectrometer. Additionally, because of the thinness of the tubing used, all reactions must be homogenous to prevent blockages. The minimum volume of solvent for a reaction is 10 mL, which presents a significant cost if deuterated solvents are used. The use of deuterated solvents may not be necessary, provided that the peaks of interest are suitably separated from solvent peaks, and also that a reasonable signal to noise ratio is still obtained for non-solvent peaks.

The utility of the DReaM set-up was recently demonstrated by Hall *et al.* in a fundamental study of deactivation pathways for the [Ru(arene)(TsDPEN)Cl] complexes developed by Noyori for transfer hydrogenation (TH).[3–5] The authors were able to demonstrate that reactions run with monitoring using the DReaM facility set-up did not differ in appearance over time, conversion or enantioselectivity compared to those monitored by off-line sampling. The kinetic data obtained from the reactions allowed for reaction progress kinetic analysis (RPKA - *vide infra*) to be performed, determining an order of 1 in the Ru catalyst. The presence of an active hydride species during catalysis (i.e. the catalyst resting state) was also confirmed. A signal at -5.47 ppm for a monohydride had been previously reported.[5] This signal was observed directly during the reaction, and EXSY NMR (Exchange Spectroscopy) experiments confirmed exchange between this hydride, the IPA and the 1-phenylethanol, thus demonstrating it to be an intermediate in the cycle. Two previously unconsidered deactivation pathways were also shown to be at work, one from the formation of a catalyst-base adduct and one due to arene loss from the hydride intermediate.

4.1.2 Kinetic Analysis

Determination of the rate law for a given reaction is a complex undertaking, but the rewards, in terms of mechanistic understanding, are significant. There are two key unknowns in the rate equation (1), the rate constant (k_r), and the order in each reagent (exponent values a, b). The classical approach is to determine a rate constant for each reagent by using the isolation method. In this method all reagents apart from one are used in a large excess, termed pseudo-1st order kinetics (2). The order in the reagent is determined from the initial rate of reaction, where the concentration of a reagent [A] may be approximated to the initial concentration $[A]_0$ (3).[6]

$$(1)\ rate = k_r[A]^a[B]^b$$

$$(2)\ rate = k_r'[A]^a\ and\ k_r' = k_r[B]_0$$

$$(3)\ rate = k_r'[A]^a\ and\ rate_0 = k_r'[A]_0$$

Although these methods are well-established, they are not without flaws. Applying pseudo-1st order conditions to a reaction often represents reaction conditions that bear little or no resemblance to those used in a genuine reaction. The analysis of kinetics under these conditions, therefore, may be of limited relevance. Likewise, by only studying the initial rate of a reaction, many secondary effects are ignored. The possibilities of catalyst deactivation, or of the product or intermediates being involved in the rate law, are not considered.

Modern reaction monitoring techniques can provide users with a superfluity of data points, which classic kinetic analysis cannot adequately process. Modern approaches to kinetic analysis have therefore been developed which make use of these large data sets. These approaches not only require fewer experiments to be performed, but can also provide insight into the whole profile of a reaction, including deactivation and product inhibition pathways.[7,8]

In 2005, Blackmond published one such method: Reaction Progress Kinetic Analysis (RPKA).[7] This approach builds on a method used to provide linear analysis for enzymatic reactions, first reported over 80 years ago.[9] RPKA requires a few key experiments with different reagent concentrations to be performed. Analysis can then be performed "by-eye" – mainly focussing on whether or not plots obtained from reactions performed under different conditions overlay with one another. This represents a breakthrough in kinetics, allowing simple data manipulations coupled with visual analysis to determine the order in catalyst and reagents, and the effects of catalyst deactivation and product inhibition. Since publication the method has been applied to a wide range of reactions by numerous groups.[10–14] In a particularly elegant example reported by Ruiz-Castillo *et al.*, RPKA is used to understand the mechanism of palladium catalysed amine arylation reactions. By analysing the kinetics of the reaction using phosphine ligand **4.1** it was determined that the oxidative addition and reductive elimination steps were both rate determining to some degree (Figure 106). This understanding led to the rational design of the electron rich and sterically bulky ligand **4.2**, which as predicted accelerated the reaction (Figure 106).[15]

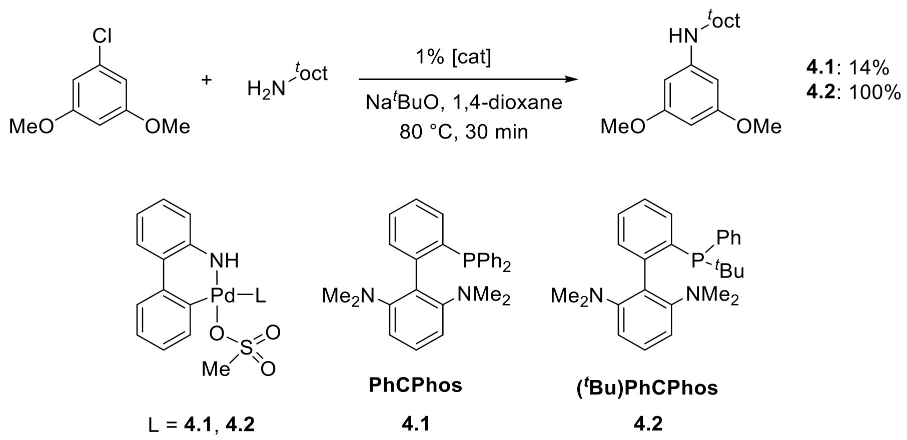

Figure 106. Palladium catalysed amine arylation reaction and structure of phosphine ligands **4.1** and **4.2**.[15]

A number of methods related to RPKA have since been published. These include the time adjusted method, also reported by Blackmond, which requires only two experiments to determine if product inhibition or catalyst deactivation are occurring.[16] Variable time normalisation analysis (VTNA) was described by Burés *et al.* and allows the determination of the order in all reagents using a series of simple experiments followed by visual analysis.[17] Graphs are plotted of the concentration of reactant or product against a normalised time-axis with the general form $\Sigma[X]^n\Delta t$, where t = time, X = reagent/catalyst, and n = any number. The calculation normalises the time axis relative to the concentration of the species in question, thereby removing any kinetic effect it has on the rest of the data. Experiments with two different initial concentrations of the species X are required (Figure 107). When the value of n equal to the order in that component is selected, the two concentration plots will overlay. With judicious planning, just 4 experiments are required to determine the order in catalyst and two reagents using this method. With the order in each reaction component determined, a plot of reactant/product against $\Sigma[X]^n[Y]^{n'}[cat]^{n''}\Delta t$ should yield a straight line, with the observed rate constant equivalent to the gradient (Figure 107 - d). Since the publication of this method 3 years ago, its utility has been demonstrated by various groups.[18–21]

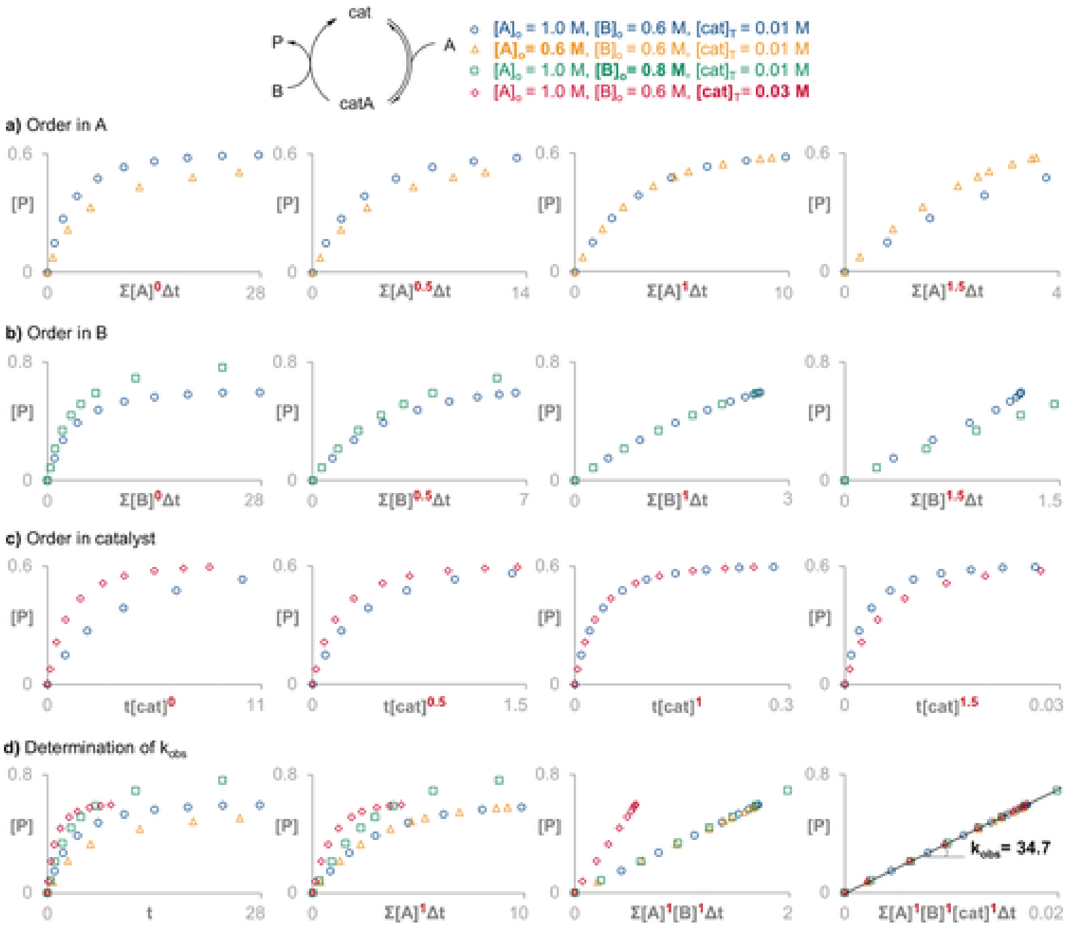

Figure 107. Variable time normalisation analysis enables the determination of the order in substrate A (a), substrate B (b), and catalyst (c). The sequential normalisation of the time scale in A, B, and catalyst leads to the overlay of all reaction profiles in a straight line with a slope that corresponds to k_{obs} (d). Figure reproduced with permission from John Wiley and Sons (License number: 4557830043329).[17]

A special case of VTNA was also reported by Burés, which allows for the straightforward determination of the order in catalyst for a given reaction.[22] The assumption is made that the concentration of the catalyst remains constant throughout the reaction – this allows for a simplification of the time normalisation axis to $t[cat]_0^n$. This approach means that by running reactions under identical conditions, other than the loading of the catalyst, should allow the determination of catalyst order. A graph is plotted of product/reactant concentration against the normalised time scale for various powers of n, until overlay of the two traces is achieved (Figure 108). The original paper has been cited over 50 times since publication 3 years ago, and applied to diverse fields of catalysis.[23–26]

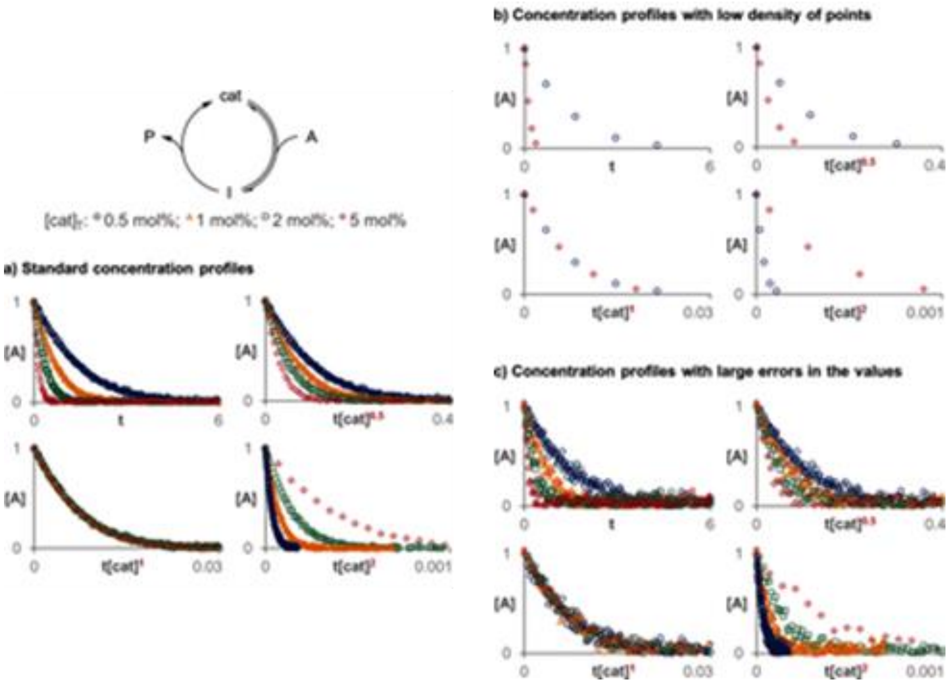

Figure 108. The correct order in catalyst is the one that causes all the curves to overlay (in this case first order). Figure reproduced under Creative Commons Licensing.[22]

4.1.3 Aims

Progress towards understanding the mechanism of TH catalysed by NHC-carborane catalysts **C3**, **C4**/**C5** and **C6** has been discussed in Chapters 2 and 3. Chapter 2 describes the use of stoichiometric reactions and catalyst screens to characterise potential intermediates. Chapter 3 discusses the insight gained by computational modelling of the reaction. On-line reaction monitoring should provide further information about the catalytic process, both in terms of the observation of intermediate species, and also in terms of potential kinetic analysis. Therefore, the aims of this body of work were to use the DReaM Facility to monitor the catalytic reaction in real time. It was envisioned that the direct observation of hydride species during the reaction would provide clues as to the nature of the active catalyst. Based on these results, further computational investigations on likely intermediates could be carried out, as well as the potential isolation of these species. Additionally, the large quantity of data obtained should allow for kinetic analysis, which may further provide insight into the mechanism. The primary aim in this regard is the determination of the order in catalyst, using the graphical method described by Burés.[22]

4.2 Preparation for use of the DReaM Facility

The aim of the DReaM facility is to allow for the monitoring of reactions under working conditions, however a few changes to previous reaction set-up were necessary. Due to the length of tubing used to recirculate the reaction mixture there is a minimum volume requirement of 10 mL, which is 4 times the volume used in previous catalytic reactions (Chapter 2). As a consequence of this larger scale, larger quantities of catalyst are required. Challenges associated with the syntheses of these catalysts, and the optimisation of reactions, has been described in Chapter 2 (2.2). There is a maximum operating temperature of 77 °C inside the spectrometer used at the DReaM Facility. As our original studies were performed at 82 °C, it is necessary to test the catalytic system at this lower temperature and compare these results to those obtained previously. It is also desirable to monitor the reaction over a longer period of time than the original 1 hour, so that suitable reaction lengths can be selected once at the facility. As the reaction mixture will be passed through narrow tubing it is vital that the sample is homogeneous, in order to prevent blockages. Therefore, initial tests were also carried out to determine the solubility of different reaction components at 77 °C.

The TH of acetophenone with IPA was performed using **C3** (non-cyclometallated) and **C4**/**C5** (cyclometallated) mixture under standard conditions, but at a reduced temperature (75 °C), in which a sample was taken every hour for 5 hours (Figure 109).

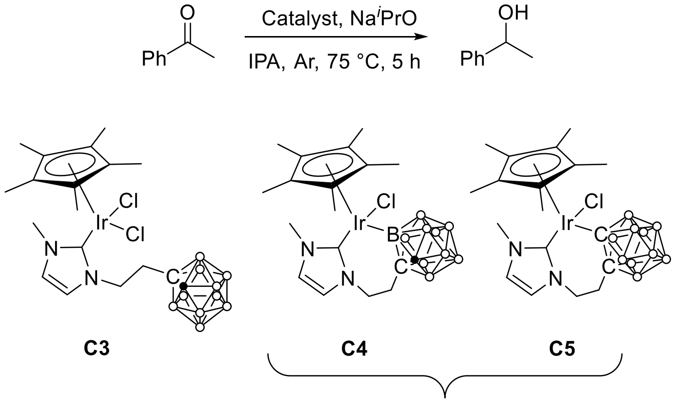

Figure 109. Reaction scheme for catalytic reaction with structures of catalysts **C3** and **C4**/**C5**. 1 mmol acetophenone, 1 mol% catalyst, 10 mol% Na^{i}PrO, 0.33 mmol 1,3,5-trimethyoxybenzene (internal standard), 2.3 mL IPA.

The conversions after 1 hour (21% - **C3**; 46% - **C4**/**C5**) are in excellent agreement with values obtained previously (Chapter 2) (20% - **C3**; 47% - **C4**/**C5**), indicating that the reduced temperature has little impact on observed reactivity (Figure 110). It is also noted that the cyclometallated catalyst outperforms the non-cyclometallated catalyst at all time-points measured. For both catalysts the highest rate of conversion is observed within the first hour. This indicates that any induction period (if present) occurs in a time period less than one hour. This highlights the usefulness of on-line reaction monitoring, as this will allow observation of the reaction more frequently and with better temporal resolution. The conversion for **C3** has reached a plateau after 2 hours, whilst for **C4**/**C5** this is reached after 3 hours. The cessation of reaction after these times could indicate catalyst decomposition, or product inhibition. These are again effects which may be probed using the DReaM facility.

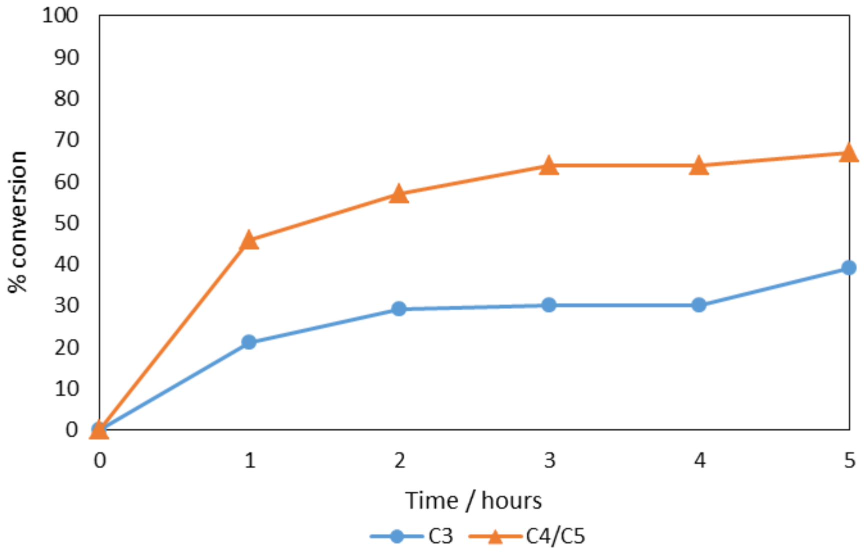

Figure 110. Reaction progress over time for TH catalysed by **C3** and **C4**/**C5**.

A number of solubility tests were conducted to check for homogeneity of the sample. The base, internal standard and IPA were combined in an ampoule and heated to 75 °C, using the same concentration as present in the catalytic reaction. It was observed that at room temperature some insoluble matter was present, but this was rapidly solubilised upon heating, and appeared to remain in solution on cooling (Figure 111).

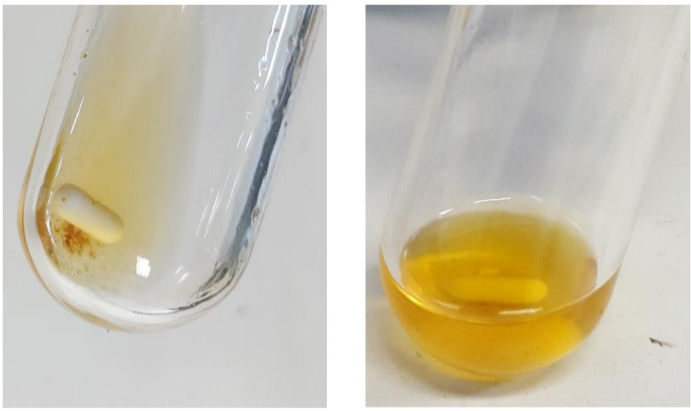

Figure 111. Mixture of Na^{i}PrO (0.10 mmol), and 1,3,5-trimethoxybenzene (0.33 mmol) in IPA (2.3 mL). Left: prior to heating. Right: after heating at 75 °C for 20 minutes and cooling to room temperature for 10 minutes.

Due to the success of this visual inspection, the mixture was prepared again and passed through tubing using a syringe pump to check for blockages. The thinnest tubing used in the DReaM Facility has an internal diameter of 0.125 mm. A piece of tubing was prepared made up of a section of wider tubing (0.79 mm inner diameter) connected to a section of thinner tubing (either 0.25 mm of 0.125 mm inner diameter) connected to another section of the wider tubing (Figure 112). The solution was passed through different sized tubing including fittings, to create a disturbance in the flow and better simulate future experimental conditions. Two thinner tube sizes were used so that an initial test using tubing with a larger diameter could be performed. The tubing sections were fitted with ferrules and nuts and then connected to one another using a union. One section of wider tubing was additionally fitted with a syringe adaptor for connection to a syringe pump.[27]

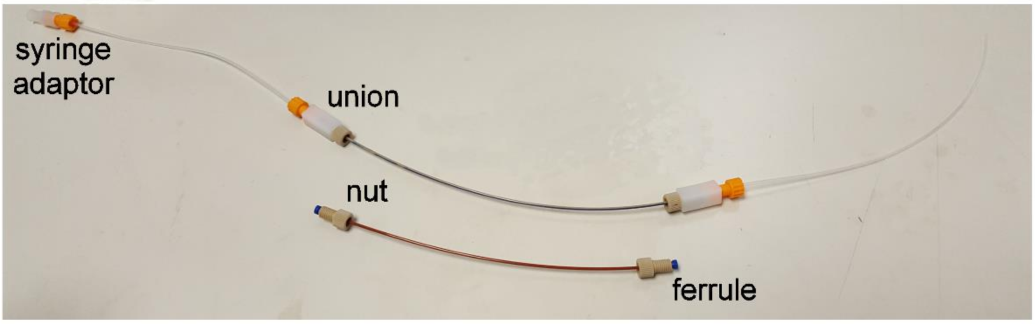

Figure 112. Labelled diagram of tubing used to check for blockages.

A sample (1 mL) of the heated mixture of Na^{i}PrO and 1,3,5-trimethoxybenzene in IPA was passed through the tubing at a rate of 0.5 mL/min. For both sizes of tubing fitted the syringe pump did not stall during pumping, indicating that no blockage had occurred.

Given the adequate solubility of the base and standard, a test was next performed using all reagents involved in the catalytic reaction, including **C3**. As observed previously, at room temperature some insoluble matter was present. It was additionally noted that the catalyst was not fully soluble at room temperature. Upon heating to 77 °C a visual inspection indicated that the sample appeared homogenous, however the presence of some very fine particles could not be ruled out. The stability was also investigated, and it was observed that the mixture underwent no obvious visual change after heating for 1 hour.

The reaction mixtures used for the catalytic reaction monitoring (*vide infra*) were passed through the tubing after the reaction had ceased. Once again, no blockage occurred with either tubing, indicating that the sample is sufficiently homogeneous.

4.3 Investigation into Transfer Hydrogenation using the DReaM Facility

4.3.1 Reaction Set-Up

The reaction was set-up as follows: a solution containing the relevant catalyst, acetophenone and 1,3,5-trimethoxybenzene (internal standard) in IPA was prepared in a round bottom flask fitted with a Young's adaptor and suba seal, and heated under nitrogen until it was sufficiently homogeneous for flow to start. The solution was then recirculated at a flow rate of 3 mL/min through the NMR spectrometer and initial spectra were recorded. The TH reaction was initiated by the addition of base in IPA solution. In general, it is preferable to add the catalyst to trigger a reaction, however due to the insolubility of the catalysts at room temperature this was not possible. A stock solution of standard in IPA was prepared and used for all experiments. A solution of base was prepared using the standard-doped IPA, thus ensuring that the concentration of standard was constant before and after base addition. The initial intent was to use Na^{i}PrO as with previous reactions discussed in Chapter 2. However, the supplied Na^{i}PrO was impure, hence K^{t}BuO was used instead as this was available.

4.3.2 Summary of Experiments

In total, 7 reactions were performed whilst at the DReaM Facility, encompassing a range of catalysts and catalyst loadings (Table 13). Reactions were run for a minimum of 3 hours, with some being allowed to continue overnight.

The first reaction performed (entry 1) corresponds to a direct scale-up of the conditions used in previous reactions. Subsequent examination of the temperature data for this reaction revealed that only 69 °C had been reached; for future experiments a higher external temperature was applied to maintain a 75 °C reaction temperature.

Two experiments at 75 °C were subsequently performed with **C3** using standard conditions, but varying the catalyst loading (entry 2: 2 mol% catalyst loading, entry 3: 1 mol% catalyst loading). Although the catalyst concentration was doubled in entry 2, the concentration of base was kept constant.

The reactions with **C4**/**C5** (entries 4 and 5) were more problematic due to issues adequately solubilising the catalyst. For this reason, these reactions were performed with the same relative catalyst:acetophenone:base ratio, but at half the concentration. Due to these solubility issues a lower catalyst loading of 0.5 mol% (entry 5) was used for the second experiment, instead of the 2 mol% used for **C3**.

Table 13. Summary of experiments performed using the DReaM Facility.

Entry	Catalyst	Catalyst loading[a] / mol%	Catalyst / mmol L^{-1}	Acetophenone / mol L^{-1}	Base / mol L^{-1}	T / °C
1	**C3**	1.0	4.0	4.00	0.04	69
2	**C3**	2.0	8.0	4.00	0.04	75
3	**C3**	1.0	4.0	4.00	0.04	75
4	**C4**/**C5**	1.0	2.0	2.00	0.02	75
5	**C4**/**C5**	0.50	1.0	2.00	0.02	75
6	$[IrCp^*Cl_2]_2$	0.50	0.50	2.00	0.02	75
7	$[IrCp^*Cl_2]_2$	0.25	0.25	2.00	0.02	75

a. Per Ir. Total reaction volume: 12.0 mL (IPA). Concentration of internal standard: 0.145 mol L^{-1}.

Reactions were performed with $[IrCp^*Cl_2]_2$ as a benchmark for comparison. Once again, solubility was a problem and thus these reactions were also performed at half concentration relative to those of **C3**. The loading of the catalyst was also decreased to 0.5 mol% (entry 6) and 0.25 mol% (entry 7).

4.3.3 Reaction Progress Over Time

Conversions for the catalytic reactions were determined by comparison of the aromatic region of the starting material (acetophenone) and the product (1-phenylethanol) with that of the C*H* signal of the internal standard (Figure 113). Integrals for multiple spectra were extracted by using a multiple integration command in TopSpin4.0. Once extracted the integral regions were corrected using calculated flow correction factors and hence plots of concentration vs time were obtained. In all experiments the formation of 1-phenylethanol corresponds directly to the consumption of acetophenone. This indicates that there are limited side-reactions occurring, a fact which is corroborated by no other signals being observed in the NMR spectra. Taking the example of the experiment using 2 mol% loading of **C3** (entry 2 - Table 13), a smooth reduction in the concentration of acetophenone is accompanied by an increase in 1-phenylethanol (Figure 114).

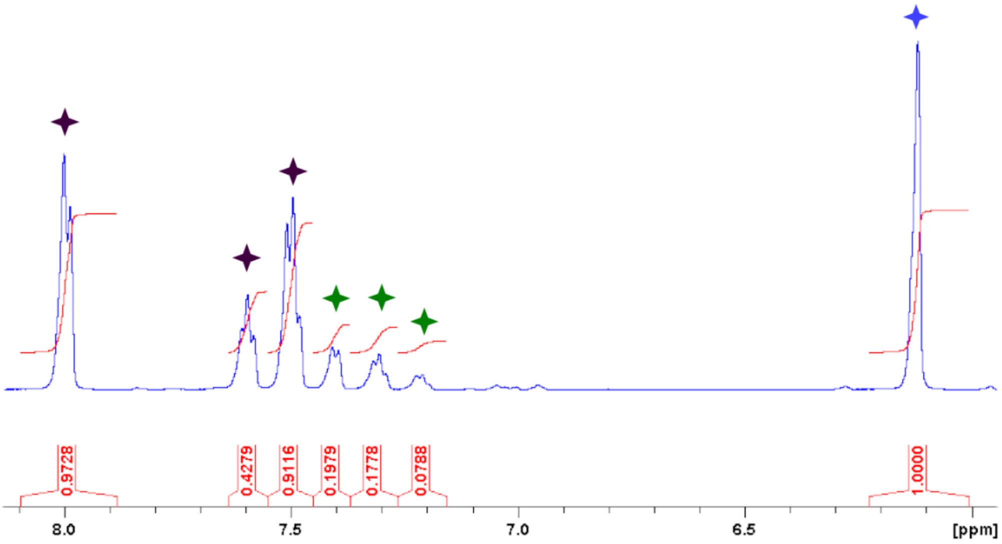

Figure 113. Example ^{1}H NMR spectrum (500 MHz, IPA) showing integral regions used for determination of conversion. Purple stars denote acetophenone, green stars denote 1-phenylethanol, blue star denotes internal standard.

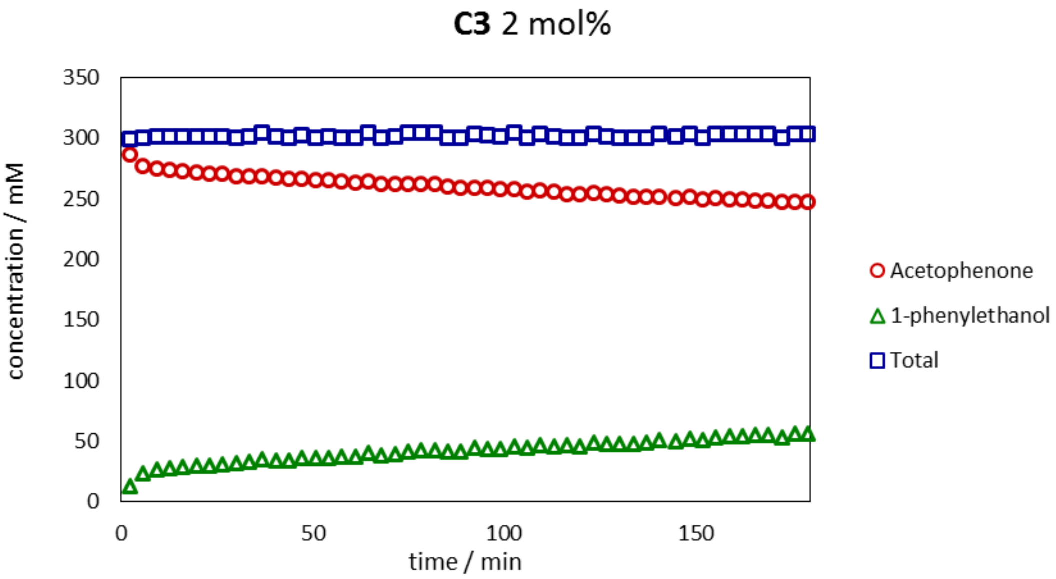

Figure 114. Plot of concentration versus time.

It can be seen that conversion of acetophenone to 1-phenylethanol is fairly low after 3 hours for all experiments except for the 1 mol% catalyst loading of **C4**/**C5** (Figure 115). It is noteworthy that conversion after 3 hours is very similar for both catalyst loadings tested when **C3** was used. For the **C4**/**C5** mixture and $[IrCp^{*}Cl_2]_2$, a higher catalyst loading leads to a significant increase in conversion after 3 hours; in both cases the increase is almost threefold.

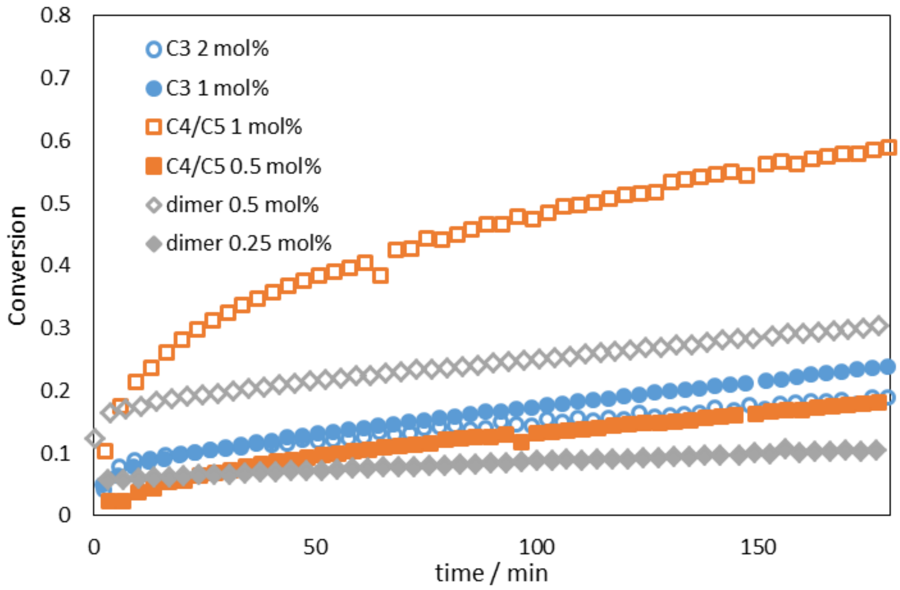

Figure 115. Plot of conversion versus time for all catalysts.

The results obtained may be compared with those previously reported by Holmes (Table 14).[28] Similar trends in activity between catalysts are retained, however conversions after 1 hour are considerably lower. It is important to note that the DReaM results were obtained at a lower temperature than those previously reported (75 °C *vs* 82 °C). However, results using Na^{i}PrO showed no decrease in conversion upon lowering of temperature (*vide supra* - 4.2). Although efforts were made to ensure that reagents were prepared in the same way, it is conceivable that differences in the water content of solvents or base purity may explain the different results obtained. At any given time during a reaction, 30% of the reaction mixture is in the flow system (3.7 mL of 12.5 mL); it is possible that this leads to a lower conversion, although previous results using this set-up have shown the system to replicate batch conditions well.[3] Nonetheless, the reagents and catalyst were added in a different sequence to previous batch reactions, in particular the catalyst and acetophenone being stirred for some time prior to base addition.

Table 14. Comparison of catalytic activity for batch and continuous flow reactions.

Entry	Catalyst[a.]	Batch		DReaM	
		Mol%	Conversion[b.]	Mol%	Conversion[c.]
1	**C3**	1	33%	1	14%
				2	11%
2	**C4**/**C5**	1	>99%	1	41%
				0.5	10%
3	$[IrCp^*Cl_2]_2$	1	68%	0.5	22%
				0.25	8%

a. Mol% catalyst values are per Ir centre. b. After 1 hour at 82 °C determined by ^1H NMR spectroscopy relative to internal standard, average of two runs. c. Reaction at 75 °C, conversion value at time-point closest to 60 min, determined by ^1H NMR spectroscopy (continuous flow) relative to internal standard.

The reaction with **C4**/**C5** at 1 mol% loading has the appearance of a 1st order decay over the whole course of the reaction (Figure 116). The decrease in rate over time may suggest that acetophenone is involved in the rate determining step of the catalytic reaction; as the concentration decreases collisions become less likely, and hence the reaction slows. To probe this further a log plot was used (Figure 117). The line in this case is not linear, indicating that the acetophenone is not exhibiting true 1st order decay. A graph of time vs 1/concentration was used to check if the decay was second order (Figure 118). In this case the line does appear to be linear. This may suggest that two molecules of acetophenone are involved in the rate determining step. However, it is also possible that the catalyst degrades over the reaction course. Analysis of the hydride region of the spectra may provide an insight into the veracity of this hypothesis (*vide infra* - 4.3.4).

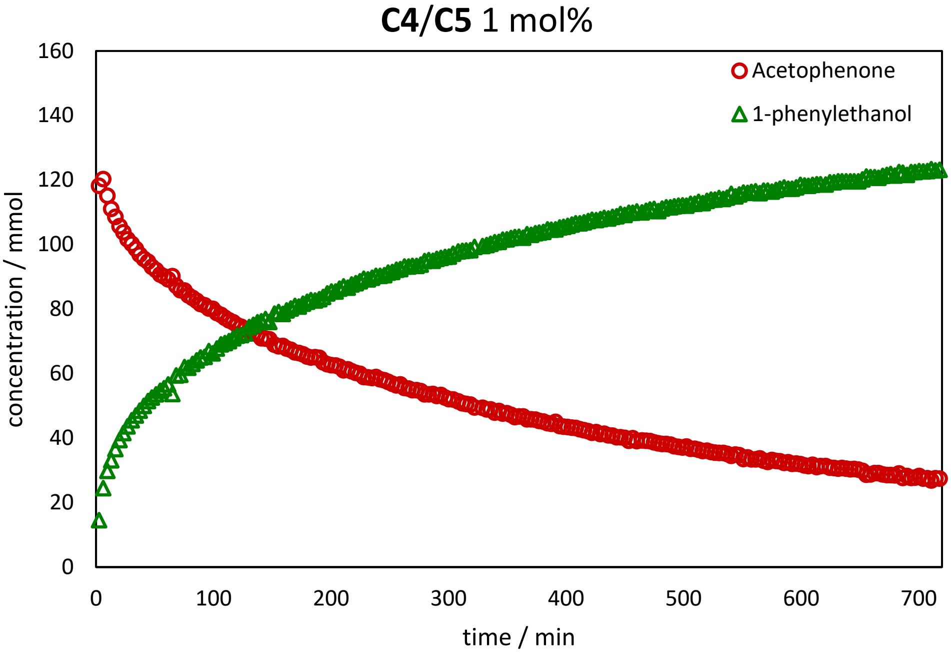

Figure 116. Reaction profile for **C4/C5** at 1 mol% catalyst loading. Change in concentration of acetophenone (red circle) and 1-phenylethanol (green triangle) over time

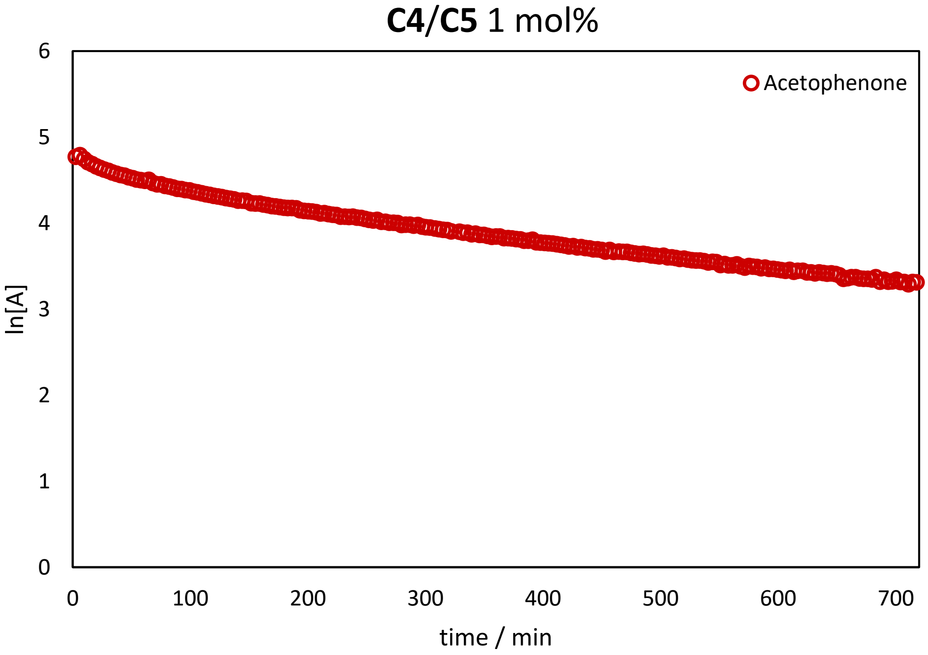

Figure 117. Graph showing time vs ln[acetophenone], for reaction catalysed by **C4/C5** at 1 mol% catalyst loading.

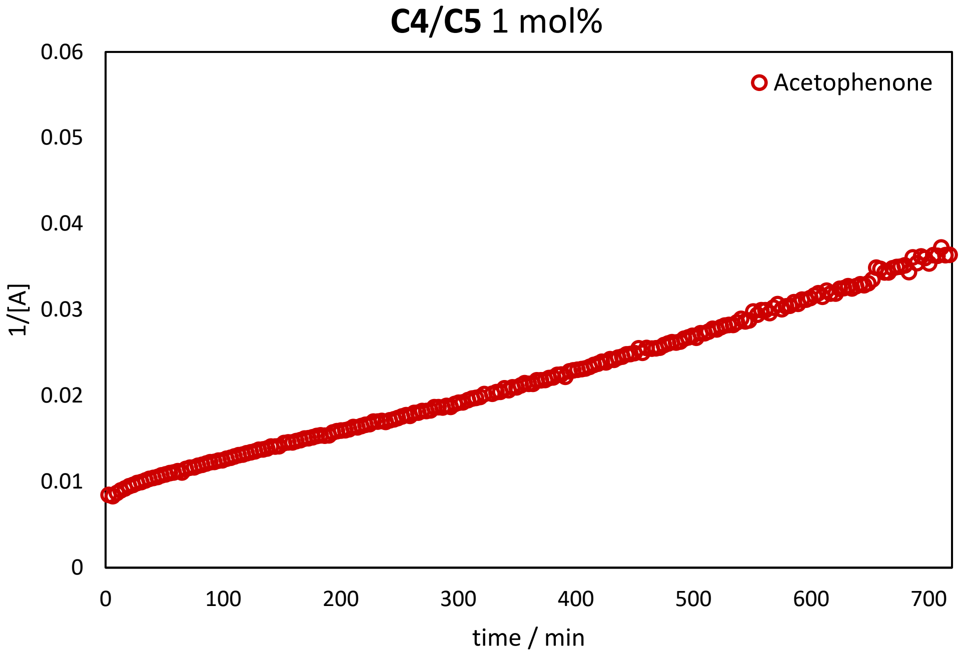

Figure 118. Graph showing time vs 1/[acetophenone] for reaction catalysed by **C4/C5** at 1 mol% catalyst loading.

By contrast, the reaction profile for **C3** at 1 mol% loading appears approximately linear, or to have a very shallow curve (Figure 119). The profile for $[IrCp^{*}Cl_2]_2$ at 0.5 mol% loading is also linear (Figure 120). A linear reaction profile indicates that acetophenone is not involved in the rate determining step, and hence the reaction rate does not decrease as the substrate is depleted. For example, it is possible that the coordination of acetophenone to the active catalyst is extremely fast in relation to the speed of turnover. In other words, the catalyst is rapidly saturated with substrate and turnover then proceeds at a steady rate, independent of acetophenone concentration. The steady reaction progress is an indication that the active species remains present throughout the reaction, with little or no decomposition occurring.

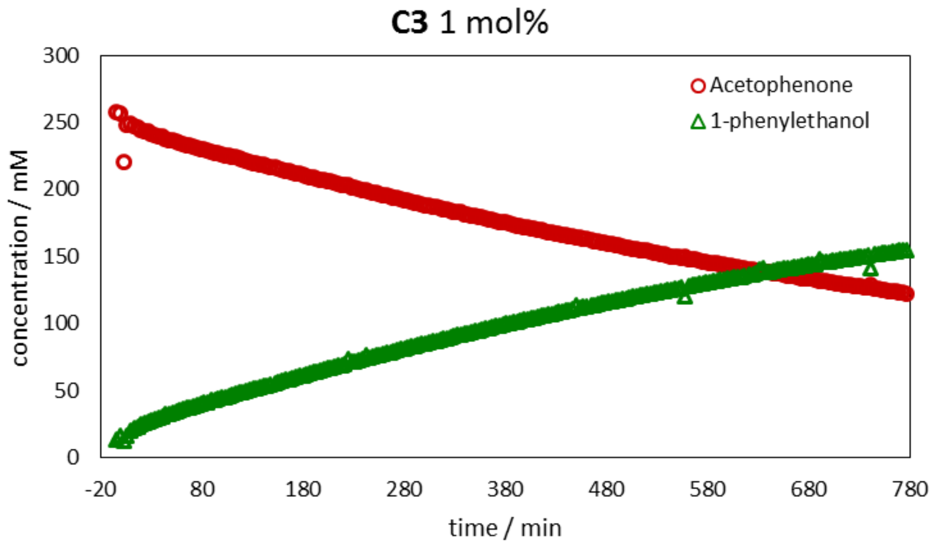

Figure 119. Reaction profile for **C3** at 1 mol% catalyst loading. Change in concentration of acetophenone (red circle) and 1-phenylethanol (green triangle) over time.

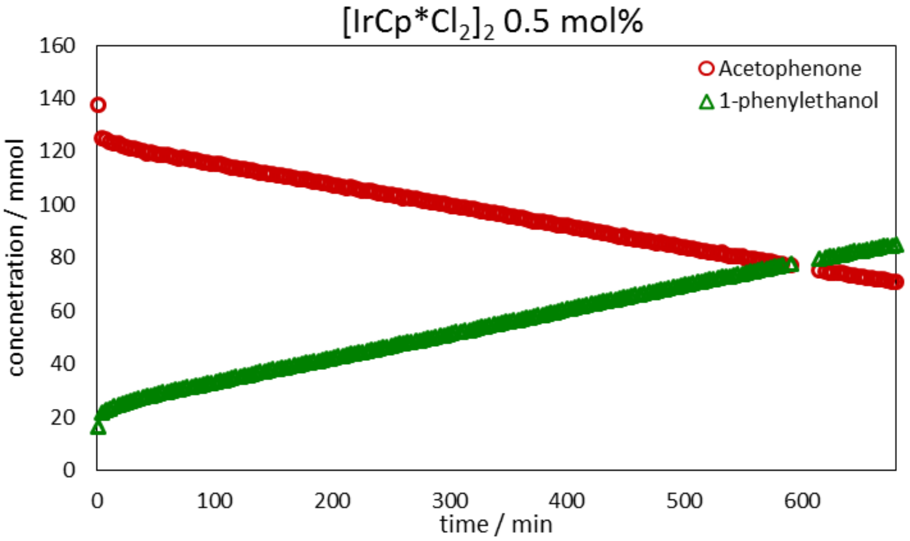

Figure 120. Reaction profile for [IrCp*Cl$_2$]$_2$ at 0.5 mol% catalyst loading. Change in concentration of acetophenone (red circle) and 1-phenylethanol (green triangle) over time.

4.3.4 Direct Observation of Hydride Species

In addition to the standard proton NMR spectra, the hydride region was also monitored using selective excitation. For all three complexes tested, hydride species were observed during the reaction. However, for each catalyst, different hydridic signals were noted.

Quantitative data may be obtained from the hydride spectra, however additional correction factors to account for the way the spectra were acquired need to be applied (4.5.7). Flow correction factors can be calculated by recording a static spectrum at the end of the reaction. One limitation of this is that accurate integration values can therefore only be obtained for species that are still present at the end of the reaction (4.1.1).

4.3.4.1 Reactions using C4/C5

For the reaction with **C4**/**C5** it was noted that a hydride signal is observed even prior to the addition of base. This signal, at -16.5 ppm, remains at an essentially constant concentration throughout the reaction, showing no signs of decay over time. This major signal, with a neighbouring minor signal further upfield, has an appearance reminiscent of the products of **C6** and both $NaBH_4$ and Na^iPrO (Chapter 2 - *2.4.3*, *2.4.4*) (Figure 121). Given that all spectra are recorded in different solvents it is not possible to say with any certainty that these species are the same. This signal was tentatively proposed to arise due the formation of **C6.H**, evidence of which was obtained crystallographically in from both reactions. The question of whether this is an active species is an interesting one. A reaction performed using **C4**/**C5** in the absence of base led to no conversion in the experiments reported by Holmes.[28] There are therefore, two possibilities. The first is that the observed hydride complex does represent an active species, but that the catalytic cycle cannot be completed without the presence of base. The second is that this hydride signal corresponds to an off-cycle inactive species, and that only those formed after the addition of base are involved in the catalytic reaction. However, it is worth noting that using the DReaM set-up a small amount of conversion (3%) of acetophenone into 1-phenylethanol was observed prior to base addition. This gives rise to the possibility that the catalysts are capable of turnover in the absence of base.

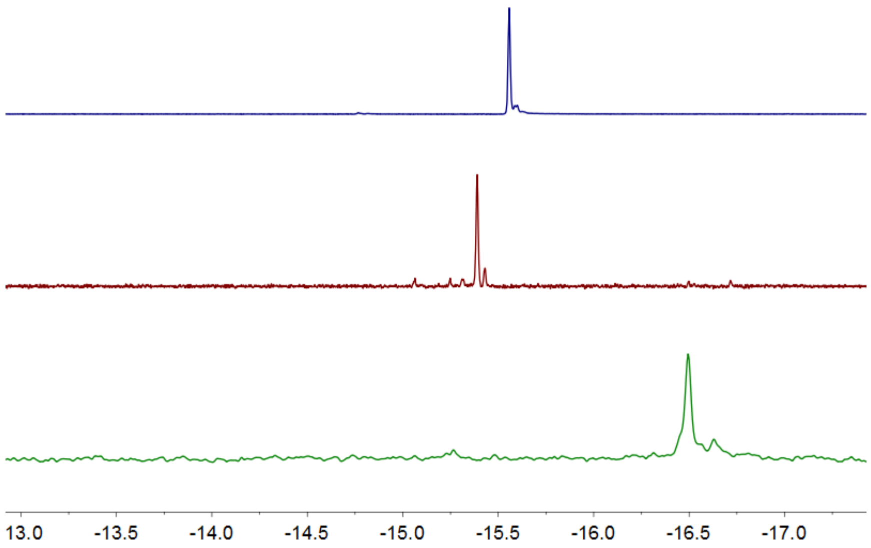

Figure 121. Top: ^1H NMR spectrum (400 MHz, d_8-THF) for product of **C6** and $NaBH_4$. Middle: ^1H NMR spectrum (400 MHz, d_6-benzene) for product of **C6** and Na^iPrO. Bottom: ^1H NMR spectrum (500 MHz, IPA) for reaction using **C4**/**C5** at 1 mol% catalyst loading prior to base addition (i.e. **C4**/**C5**, acetophenone, 1,3,5-trimethoxybenzene, IPA).

After the addition of base the hydride region increases in complexity (Figure 122). It must be recognised that, given a mixture of complexes is being used in the catalytic reaction (i.e. **C4** and **C5**), it is possible that this will lead to a mixture of hydridic products. For the most part the peaks formed initially remain at a relatively constant concentration for the reaction duration. The exception is the signal which appears initially at -15.85 ppm, which by the end of the reaction has been replaced by a signal at -15.79 ppm.

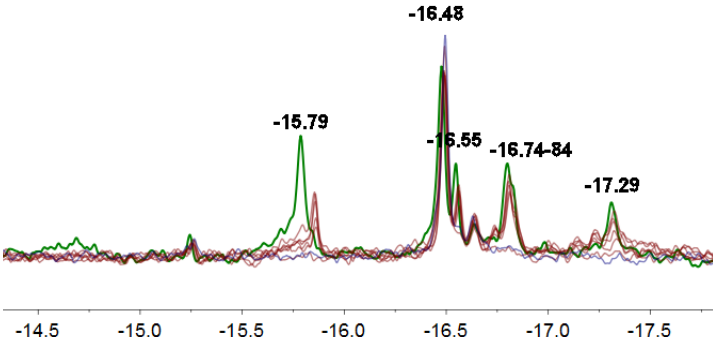

Figure 122. Superimposed ^{1}H NMR spectra (500 MHz, IPA) for reaction using **C4**/**C5** at 1 mol% loading. Blue spectra: prior to base addition, red spectra: evolution over first 20 min, green spectrum: final spectrum at 14.4 hours.

The concentration data are fairly scattered, which can make determining trends challenging (Figure 123). One solution to this is to examine the moving average for points in an attempt to smooth the data. The moving average converts each point into an average of a given number of preceding points. 10 points were used, as spectra were recorded approximately every 3 minutes, this means each moving average point shows the average concentration of that hydride signal in a 30 minute period. The moving average has been calculated and added as a trendline to each data set (Figure 124). Although the conversion data shows the reaction to be fastest at the start and then slows down, this trend is not obviously reflected in the hydride signals observed. The signals grow in at varying rates, but once present remain essentially constant for the duration of the reaction. The signal at -16.55 ppm (grey) appears by contrast to increase very slightly and slowly over the time course.

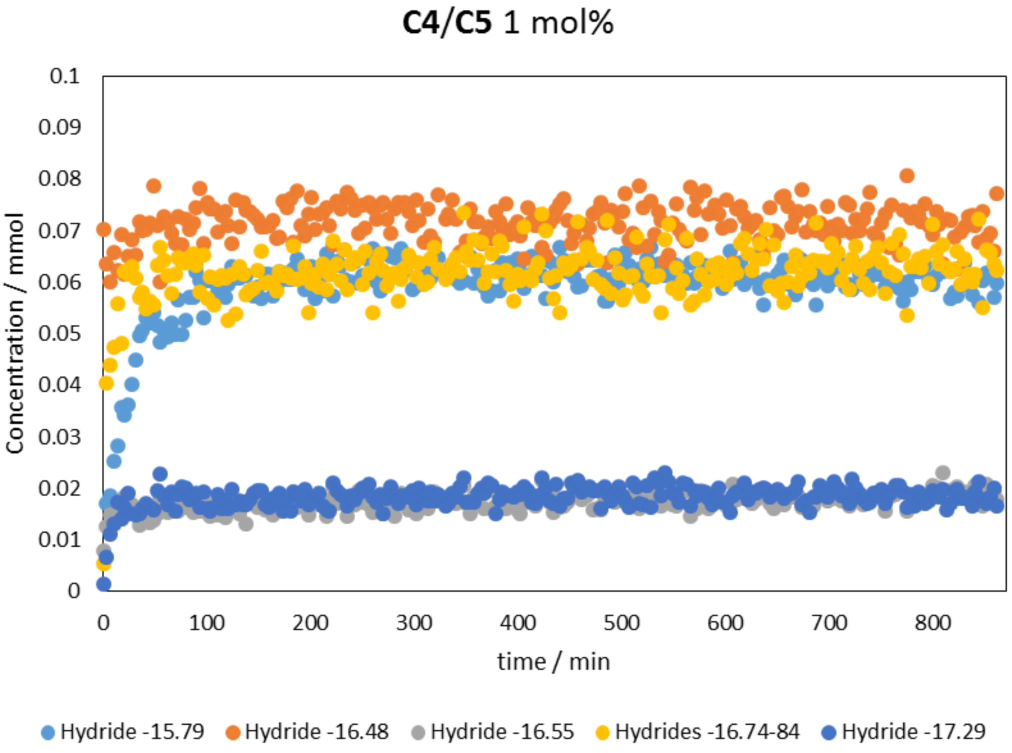

Figure 123. Raw data showing concentration of hydride signals over time.

It is possible to speculate on which of the hydride signals may be part of the same molecule by comparison of the concentration values. The concentration of the species giving rise to signals at -16.55 and -17.29 are very close to one another. Similarly, the signals at -15.79 and -16.74 have reasonably matched concentrations. The signal at -16.48 has a concentration that is different to the others. Under the assumption that all signals arise from a unique hydrogen, this analysis leads to the conclusion that there are three species present, giving a total hydride concentration of 0.16 mM, which is a small fraction of the 2 mM concentration of catalyst used. However, caution must be exercised, as it is entirely possible that these similarities in concentration are coincidental, and it is possible that polyhydride species with equivalent hydride environments give rise to some or all of the signals observed. It is expected that not all of the catalyst would convert to a hydridic species; Hall *et al.* report a starting concentration of just over half the total applied catalyst concentration, for Ru catalysed TH.[3]

There are no changes to the hydride spectra associated with the decreasing rate of reaction observed over time (*4.3.3* - Figure 116). The decrease in reaction rate may therefore indicate a pseudo first order dependence on acetophenone concentration.

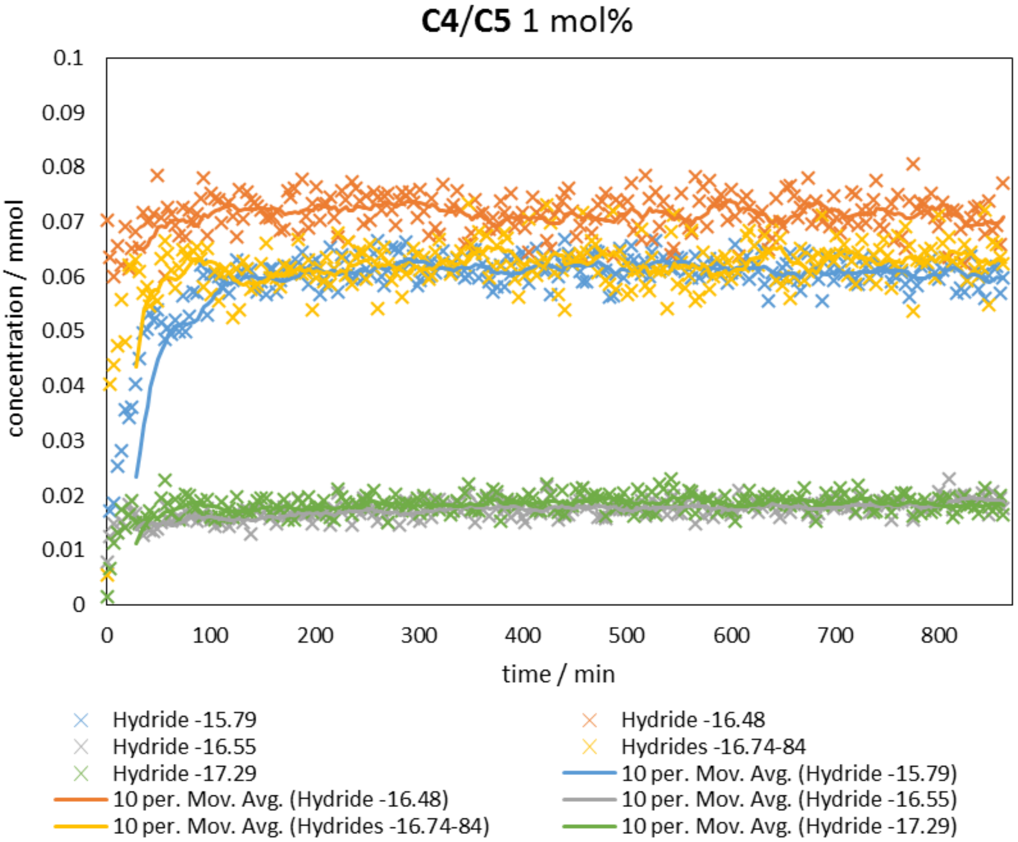

Figure 124. Concentration of hydride signals over time with moving average trendlines applied.

The spectra for the lower loading using **C4**/**C5** (0.5 mol%) have a low signal to noise ratio due to the low concentration used. However there are some similarities and some differences between the hydride spectra at the two catalyst loadings. No signal is observed prior to the addition of base at the lower catalyst loading. After base addition signals appear initially at -15.87 and -16.82 ppm, and after 3 hours additional signals at -15.22, -16.48 and -16.55 ppm are present. An overlay of the spectra from reactions at both catalyst loadings, taken at the same time point, is shown in Figure 125. Most signals that are present at the higher loading are also observed in the lower loading experiment, however the relative peak areas are significantly different. The signal at -16.48 ppm, which is present in near constant and relatively high concentration throughout the reaction at the higher loading, is a relatively weak signal in the lower loading reaction. The neighbouring peak at -16.55 ppm is broader, and appears less intense relative to the other signals observed. It is also notable that the signal at -17.29 ppm in the higher catalyst loading experiment is totally absent at the lower catalyst loading.

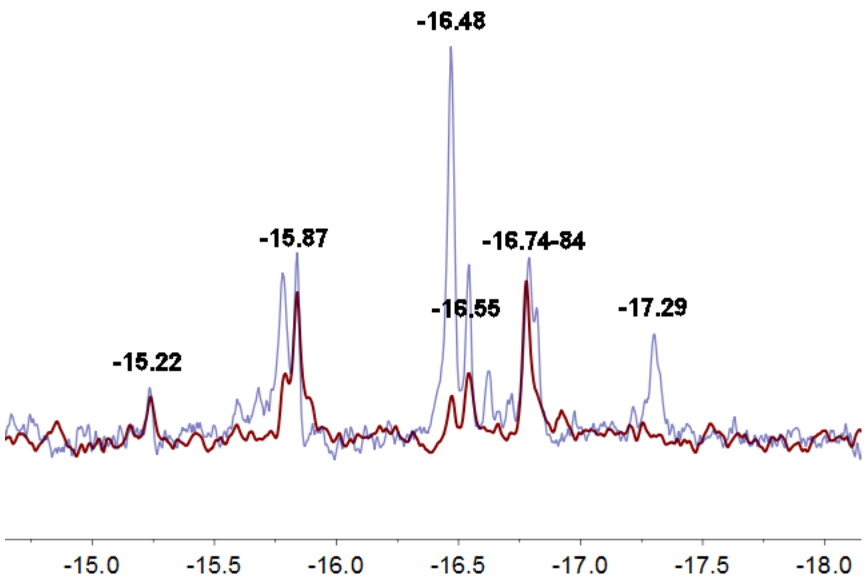

Figure 125. Superimposed ^{1}H NMR spectra (500 MHz, IPA). Blue trace: 1 mol% **C4**/**C5** after 297 min. Red trace: 0.5 mol% **C4**/**C5** after 297 min.

There are a number of possible reasons for the observed differences. A major difference between the two runs was the use of two different batches of catalyst, prepared by different experimentalists. As analysis of this product is challenging (Chapter 2 - *2.2*), it is possible that one batch contained impurities. Another reason for the differences could be due to the differing lengths of equilibration time prior to base addition. The higher loading reaction was stirred for several hours prior to base addition due to a blockage being created upon initial recirculation. As it is clear that acetophenone reacts with the catalyst in the absence of the base, it seems possible that this could lead to the formation of different products at different catalyst concentrations prior to the start of the reaction. It is clear that comparisons made between these two runs, particularly with regards to kinetic analysis, must be undertaken with caution.

4.3.4.2 Reactions using C3

The reactions using **C3** gave a much simpler picture of hydride species. In this case, three hydride signals were observed which appear rapidly and remain at a near constant concentration for the duration of the reaction.

As with **C4**/**C5** a hydride signal is seen even before addition of base, at -16.5 ppm, the same chemical shift as seen with **C4**/**C5**. It is likely that this signal is due to the same species, although its identity is uncertain. This signal does not seem to resemble those seen in stoichiometric reactions of **C3** with $NaBH_4$ and Na^{i}PrO (Chapter 2 – *2.4.3, 2.4.4*), where several hydridic signals were noted.

Although 3 hydride signals are formed quickly and remain present for the reaction duration, other signals are observed for the first 20 minutes of the reaction, which subsequently disappear (Figure 126).

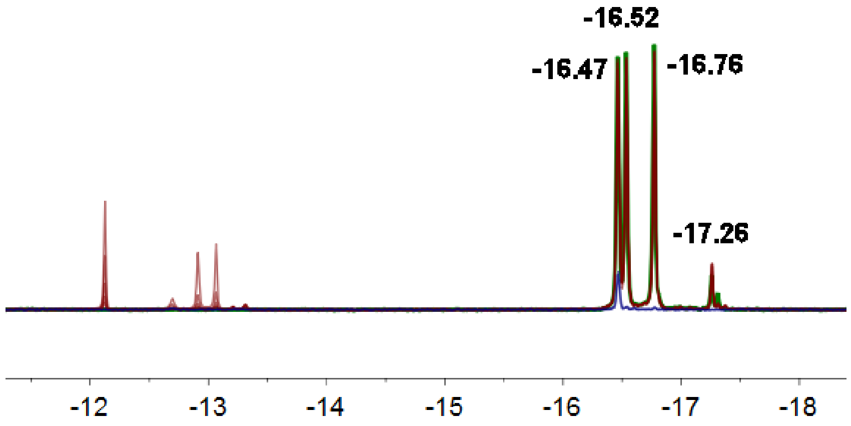

Figure 126. Superimposed ^{1}H NMR spectra (500 MHz, IPA) for reaction using **C3** at 2 mol% loading. Blue spectrum prior to base addition, red spectra: evolution over first 20 min, green spectrum: final spectrum at 3 hours.

It can be seen from these spectra that the signal observed prior to base addition (-16.47 ppm) increases in intensity after base addition, along with two other signals at -16.52 and -16.76 ppm. There is an additional minor peak at -17.26 ppm which is present throughout the reaction. Another small peak at -17.31 ppm is observed in the spectrum recorded after 3 hours. There are several peaks present in the more downfield region between -12.0 and -13.5 ppm immediately after base addition, however these decay rapidly during the first 20 minutes of reaction. This may represent an induction period, a hypothesis which fits well with the concentration values obtained, which show an increase in concentration of the major three hydride signals to a steady state after about 20 minutes (Figure 127). Examining the concentration changes as a function of time, it may be noted that the signals at -16.47 and -16.76 ppm grow rapidly then and remain constant throughout the reaction. The signal at -16.52 ppm undergoes a very slight increase in concentration over the course of the reaction. If all three hydride species are independent and monohydridic this would give a total hydride concentration of 7.62 mM for a reaction where the applied catalyst concentration is 8 mM. The signals at -16.52 and -16.76 ppm have very similar concentrations, and may therefore be attributable to one dihydride species. In this case, the total hydride concentration would be 5.14 mM, which is also reasonable.

Trihydride Ir(V) complexes bearing phosphine ligands have been reported previously, the formation of a trihydride species represents another possible interpretation of the data.[29,30]

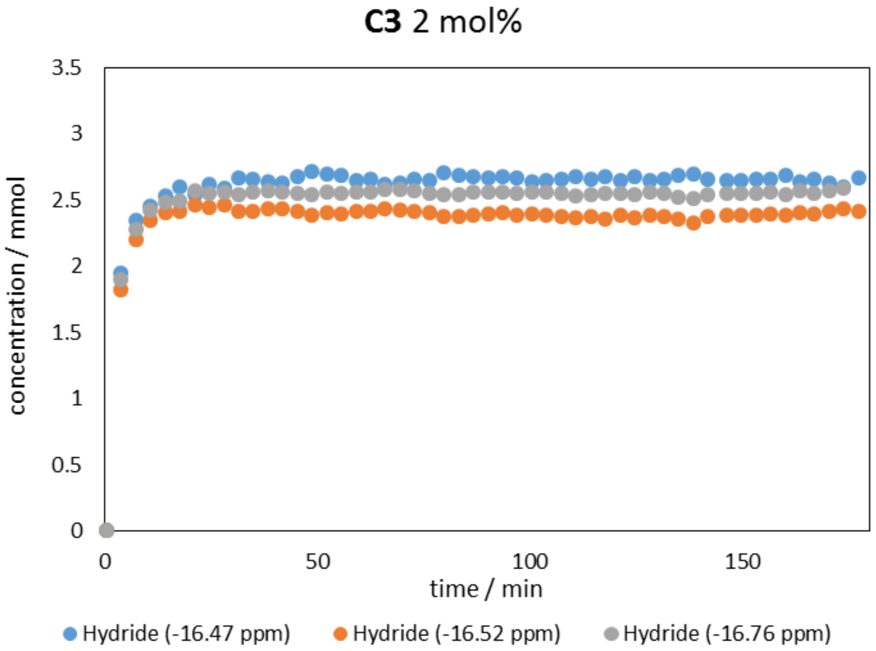

Figure 127. Concentration of hydride signals over time.

A similar induction period is observed with the 1 mol% catalyst reaction. This reaction was continued for 14 hours and the three major hydride signals appear broadly stable over this time period. There appears to be a slight decrease in the concentration of the species corresponding to the signal at -16.47 ppm, and as with the 2 mol% reaction, a very slight increase in the signal at -16.52 ppm throughout.

It is noteworthy that the reactions with both **C3** and **C4**/**C5** give rise to a signal at -16.47 ppm prior to the addition of base. In the case of **C3** this signal increases considerably after base addition, whilst for reactions using **C4**/**C5** the increase is slight. It seems likely that this signal arises due to the same species. The fact that this species is present in both catalytic runs with dramatically different conversions is interesting. The concentrations of the species are very different for the different catalysts, corresponding to 3.9% of the total catalyst used for **C4**/**C5** but 28% (1 mol%) or 33% (2 mol%) for **C3**. As **C4**/**C5** is much more active than **C3** this may indicate that the signal at -16.47 ppm represents an off-cycle species which does not play a role in catalysis.

4.3.4.3 Reaction using $[IrCp^*Cl_2]_2$

As was observed with the other catalysts investigated, hydride species were present prior to base addition with $[IrCp^*Cl_2]_2$. In this case a signal at -13.22 ppm was observed, which is considerably further downfield than the signal that was seen for **C3** or **C4**/**C5** at -16.47 ppm. Upon addition of base the spectrum increases in complexity considerably, with 8 major - and many minor - resonances present in the range -12.5 to -15.8 ppm. This is again more downfield than the range of resonances for **C3** and **C4**/**C5**. By the end of the reaction however the spectrum features just two peaks. During the first 20 minutes of the reaction many of the signals decrease considerably, whilst others increase (Figure 128). After approximately 4 hours of reaction time only 3 signals remain at -11.80, -13.79 and -13.93 ppm. Over the final 9 hours of the reaction the signal at -11.80 ppm gradually disappears (Figure 129).

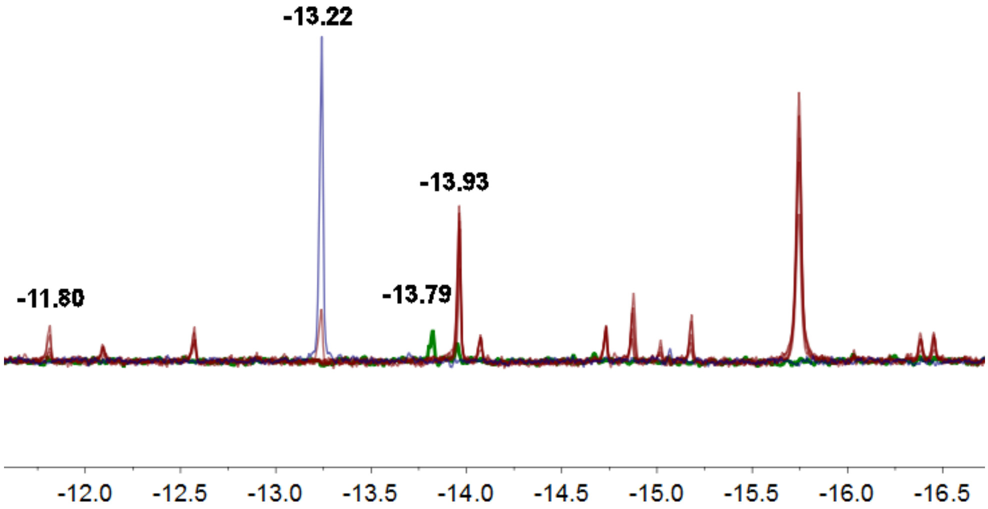

Figure 128. Superimposed ^{1}H NMR spectra (500 MHz, IPA) for reaction using $[IrCp^{*}Cl_2]_2$ at 0.5 mol% loading. Blue spectra: prior to base addition, red spectra: evolution over first 20 min, green spectrum: final spectrum at 13.7 hours

As only two signals remain at the end of the reaction, only these two can be integrated with flow correction factors applied. The plot of concentration against time for these two signals shows the higher field signal increasing in concentration rapidly in the first 20 minutes before undergoing an abrupt and then steady decay for the remainder of the reaction. By contrast the signal at -13.79 grows slowly, appearing to reach a maximum after about 7 hours, before slowly decreasing (Figure 130). It is clear that all hydride species present are decaying over the course of the reaction. This however appears to have no impact on the reaction rate (*4.3.3* - Figure 120). The reaction progress mapped in Figure 120 indicates that acetophenone is not involved in the rate determining step of the reaction, with the data obtained from the hydride spectra indicating that hydride species are not involved either.

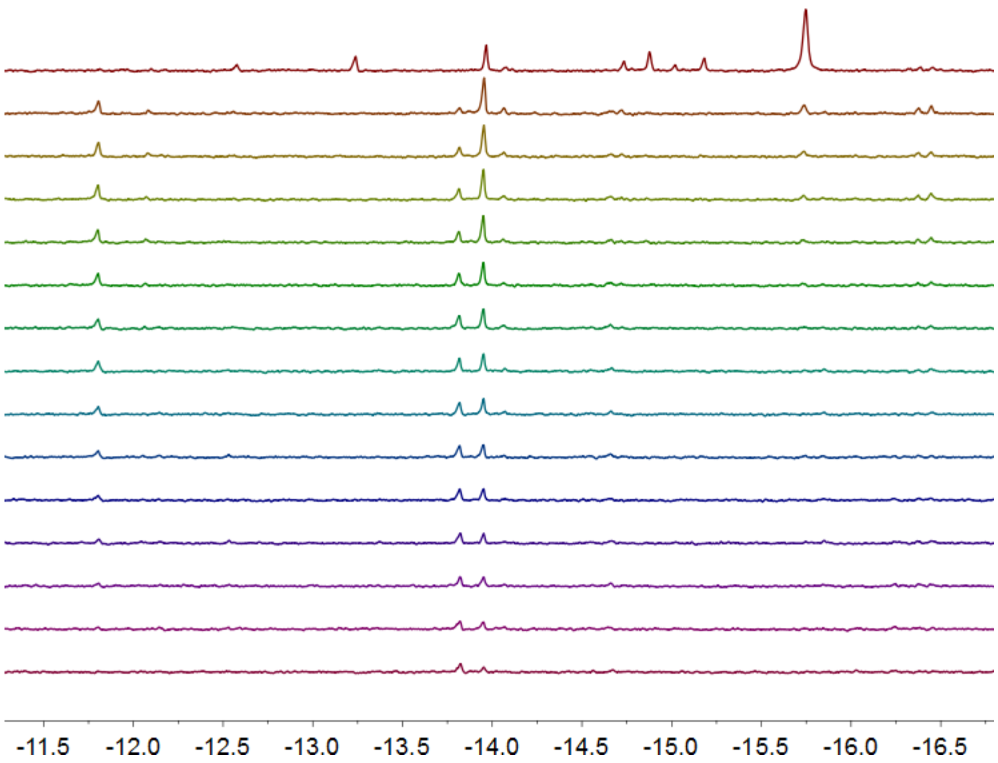

Figure 129. ^{1}H NMR spectra (500 MHz, IPA) for reaction using $[IrCp^*Cl_2]_2$ at 0.5 mol% loading. Top: After base addition. Middle spectra: approximate hourly intervals. Bottom: reaction end after 13.7 hours.

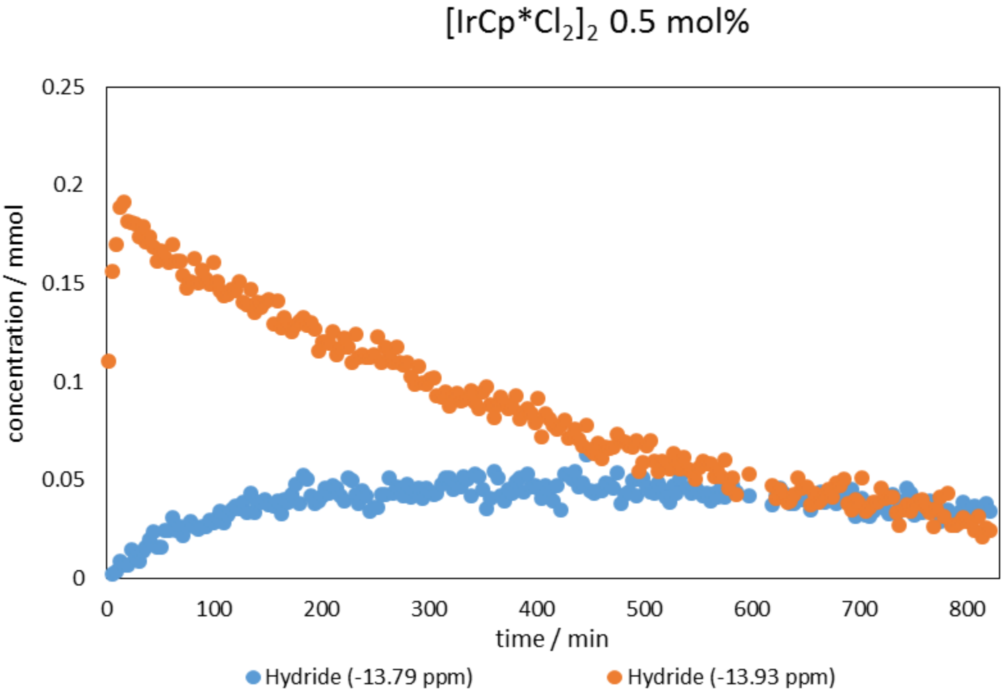

Figure 130. Plot of hydride concentration over time.

4.3.5 Static NMR Experiments

Following the experiment using **C3** at 2 mol% catalyst loading, a sample was taken and stored in a Young's NMR tube for further analysis. A variety of static NMR experiments were performed in an attempt to gain an insight into the nature of the hydride species observed. ^1H-^1H COSY and NOESY experiments were performed, but the signals were too weak to obtain any data of use. More useful data were obtained by running DOSY and HMBC experiments as well as measuring the T_1 relaxation times for the three hydride signals.

The DOSY experiment was performed to determine if the 3 hydride signals observed are due to different species. A similar diffusion constant was obtained for all three signals (Table 15), which indicates that either all three are on the same molecule, or that all three correspond to molecules of the same size. Because of the low sample concentration the errors on the measurements are quite large, hence the slight differences between the diffusion constants cannot be meaningfully discussed. The hydrodynamic radius can be calculated from the diffusion constant using the Stokes-Einstein equation (Table 15). The equation makes the assumption that the diffusing object is a perfect sphere that does not interact with any other molecules, an assumption which may be over-simplified in this case.[31,32] The radii obtained for the three signals were within 0.05 Å of one another (Table 15), and can be compared with crystal structure parameters for the complexes. If a centroid is applied to the crystal structure of **C6.H** then distances to the furthest atoms are in the range 4.1-4.7 Å, thus giving a moderate agreement with the calculated radii. The range for **C6** in the structure reported by Holmes is similar at 3.0-4.7 Å. For the non-cyclometallated complex **C3**, the distances are longer, being in the range 4.4-5.9 Å.[28] This may indicate that the hydrides are monomeric species, however, as noted previously the Stokes-Einstein equation is less valid in non-spherical molecules. Indeed, the non-cyclometallated complex **C3** deviates significantly from a spherical shape and a dimeric species is also unlikely to be spherical.[33]

The T_1 relaxation times for the three signals were also calculated (Table 16). As with the diffusion constants, the values for each hydride are similar, with errors large enough to make a discussion of differences meaningless.

Table 15. Stokes-Einstein equation, with calculated diffusion constants and hydrodynamic radii for 3 hydride signals observed at the end of 2 mol% **C3** reaction.

$$r = \frac{k_b T}{6\pi\eta D}$$

δ (static) / ppm	δ (in flow) / ppm	D / $m^2\ s^{-1}\ x10^{-10}$	Error / $x10^{-12}$	Hydrodynamic radius / Å
-16.60	-16.47	2.88	8.533	3.72
-16.68	-16.52	2.89	13.53	3.71
-16.91	-16.76	2.85	14.44	3.76

r = hydrodynamic radius (m), k_b = Boltzmann constant ($J\ K^{-1}$) η = solvent viscosity (Pa s), D = diffusion constant ($m^2\ s^{-1}$)

Table 16. T_1 values for the 3 hydride signals observed at the end of 2 mol% **C3** reaction.

δ (static) / ppm	δ (in flow) / ppm	T_1 / s	Error
-16.61	-16.47	1.14	0.05155
-16.68	-16.52	1.09	0.1688
-16.91	-16.76	1.06	0.07718

A number of factors contribute to the spin-lattice relaxation (T_1) of a given nucleus. Chief among these is dipolar relaxation, which occurs due to the nucleus in question being bonded to a second nucleus with a magnetic spin.[34] Thus the chemical environment of a hydride can lead to very different relaxation times. Relaxation times have been successfully used to distinguish between terminal hydrides and η-2 bound H_2; a short relaxation time (4-100 ms) is indicative of a non-classical hydride, whilst a long time (>350 ms) is indicative of a classical terminal hydride.[35,36] No examples of T_1 times for similar Ir-H complexes could be found - so identifying the signals as attributable to either terminal or bridging species is not possible. Ruthenium bridging hydrides have been reported to have long relaxation times (4-5 seconds), compared to terminal species (0.25 seconds), but it is not clear whether this effect would be replicated with Ir.[3] Nonetheless, all three hydrides have similar T_1 values, and thus it is likely that they are in similar chemical environments.

A ^1H-^{13}C HMBC NMR spectrum was also recorded, to gain structural insight into the hydride species. Although the spectrum obtained is very noisy in the positive proton region, clear cross-peaks associated with the hydride signals are apparent (Figure 131). The ^{13}C shifts of these signals correlate well with the expected range of a carbenic NHC carbon (161.1, 163.9, 164.2 ppm), and the range of the quaternary

Cp* carbon atoms (91.8, 90.9, 91.1 ppm).[28,37–39] This provides good evidence that the species that give rise to the hydride signals are complexes in which both the NHC and the Cp* remain bound to the Ir centre. It may further be tentatively proposed that the two further upfield hydride signals belong to the same molecule, based on their apparent correlation with a single carbenic ^{13}C signal.

Spectra were recorded using a sample from the **C4**/**C5** reaction at 1 mol% catalyst loading. However, due to the extremely low concentration of catalyst in the sample no spectra of adequate quality could be obtained.

Subsequent attempts were made upon return to Leeds. In this case a **C4**/**C5** mixture was combined in a Young's NMR tube with IPA and K^{t}BuO, and heated to 70 °C with monitoring by ^1H NMR spectroscopy. A broad signal focussed at -19.0 ppm was observed, but no 2D spectra could be obtained with the required resolution.

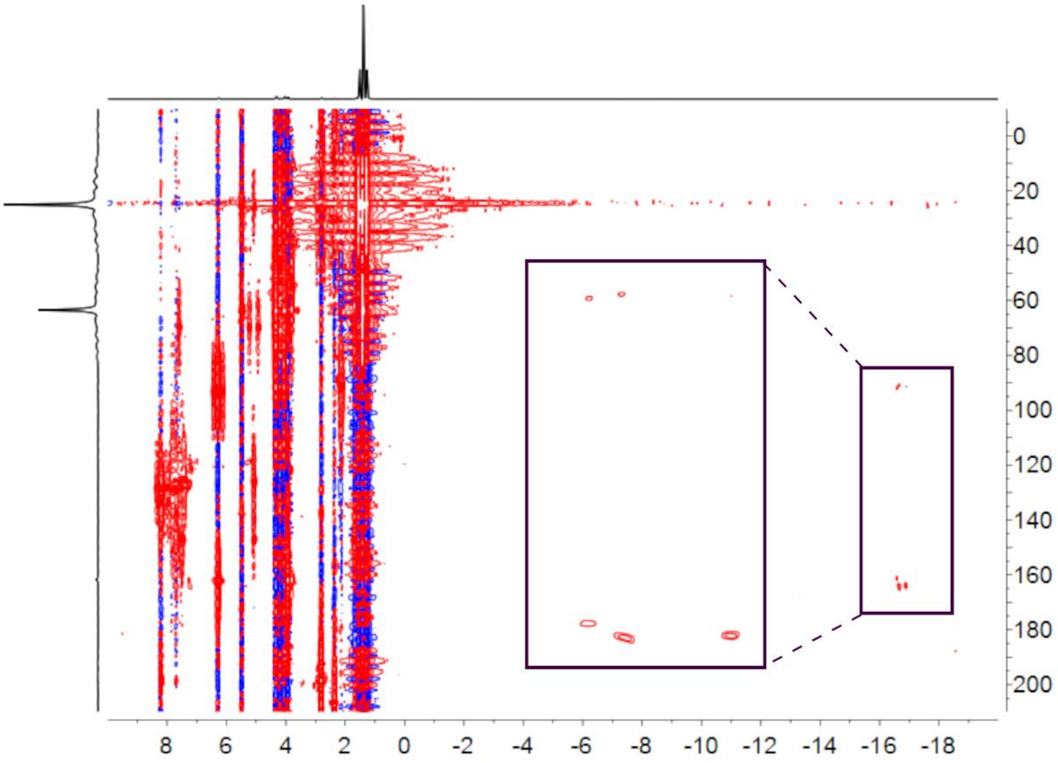

Figure 131. ^1H-^{13}C HMBC spectrum (500 MHz, IPA). Inset: enlarged region showing cross-peaks.

4.3.6 Mass spectrometry

Mass spectra were also recorded during each catalytic reaction. The reaction mixture was sampled after flowing through the NMR spectrometer, with samples being taken every 15 minutes for up to 4 hours. This on-line sampling provides additional information about catalyst speciation.

For all reactions the mass spectra obtained were complex, showing many ion peaks which changed over the reaction course. As described previously (Chapter 2 - *2.1*), the observation of carboranyl species in a mass spectrum is facile, due to the characteristic wide ion envelope.

For the reaction using **C4**/**C5** at 1 mol% loading, a mass spectrum recorded prior to base addition shows many signals attributable to carborane containing species. The most major of these appear at *m/z* 567, 607, 694, 1054, 1220, 1234 and 1250 (Figure 132). The molecular ion peak for **C4**/**C5** generally appears at *m/z* 579 corresponding to [**C4**/**C5**-Cl]$^{+}$. It is clear from these data that the higher mass peaks must be caused by some kind of dimeric species. These data do not change significantly in the spectra recorded 10 minutes after base addition.

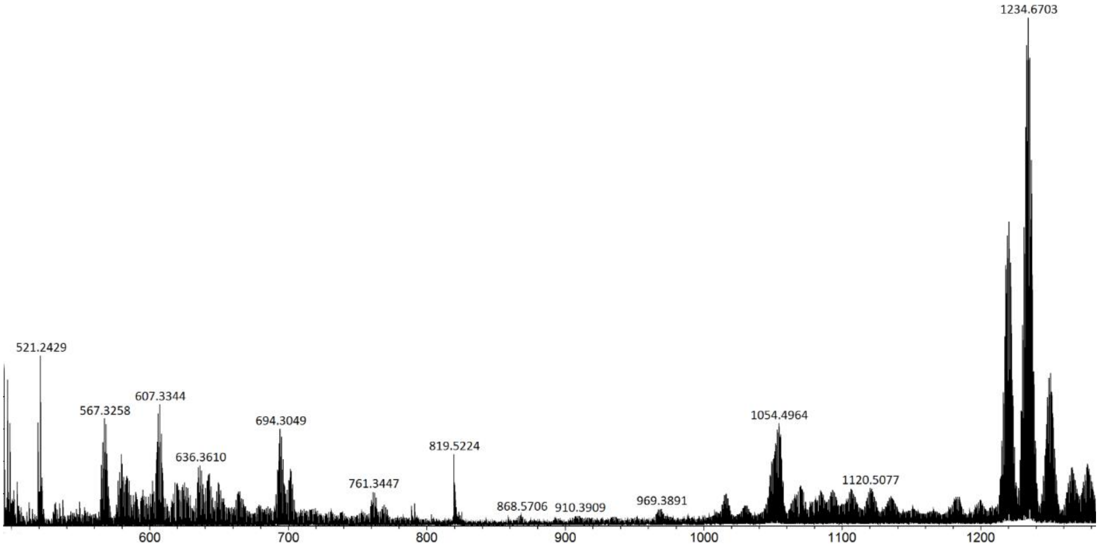

Figure 132. HRMS obtained for catalytic reaction using **C4**/**C5** (1 mol%) prior to base addition.

All mass spectra recorded after 25 minutes do not contain carboranyl signals. This is surprising, especially given the data for the hydride species indicates that, once formed, these species remain stable for the reaction duration. Spectra obtained at the lower catalyst loading were similar, showing some monomeric-type signals as well as higher mass dimeric signals, for the first 35 minutes of reaction. After this time no carboranyl signals were observed.

For **C3**, the mass spectrometry data obtained agree well with the NMR spectra recorded. There is a large range of carboranyl signals in the spectra recorded 2 minutes and 17 minutes after base addition, which can be correlated with the large number of hydride signals observed during this time (Figure 133). After 32 minutes the number of signals is greatly reduced and two major ion peaks at *m/z* 619 and 1198 are observed (Figure 134). These persist for the duration of the reaction with other minor peaks effaced. The signal at 1198 is clearly due to some form of dimer, possibly of featuring a mixture of chloride and hydride ligands, of which some are bridging (Figure 135). The origin of the peak at *m/z* 619 is not clear, being just 4 mass units heavier than the whole starting complex, and 2 mass units heavier than the monohydride substitied complex (Figure 136). No rational explanation for the presence of this structure that is within acceptable error limits could be found. Spectra obtained at the lower catalyst loading were near identical.

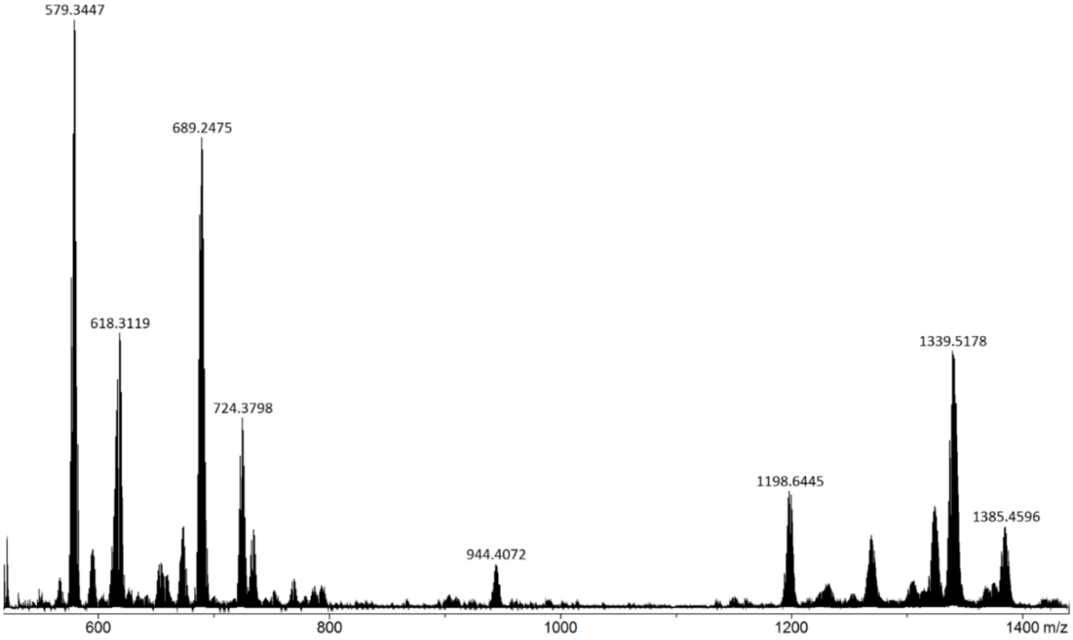

Figure 133. HRMS obtained for catalytic reaction using **C3** (2 mol%) after 17 minutes.

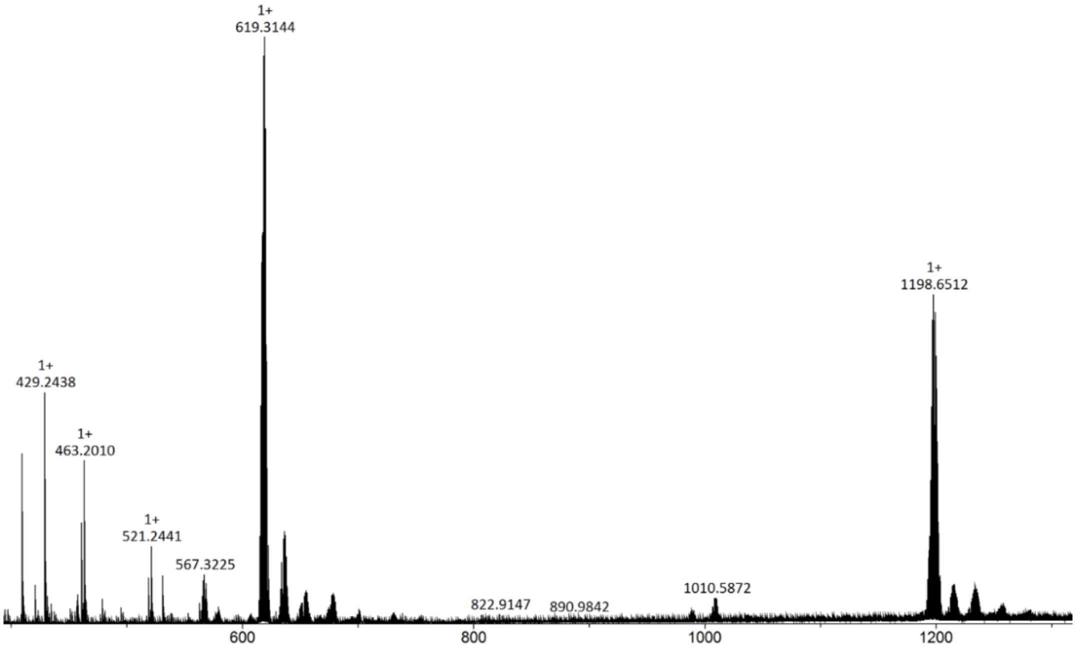

Figure 134. HRMS obtained for catalytic reaction using **C3** (2 mol%) after 32 minutes.

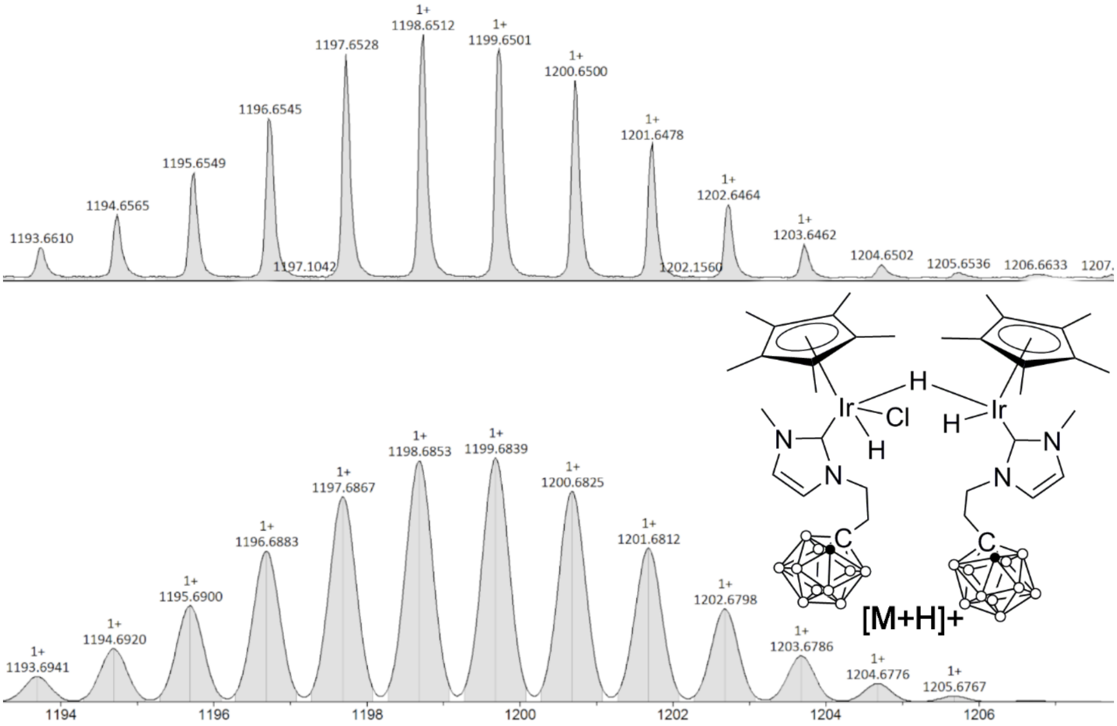

Figure 135. Top: Partial HRMS for reaction using **C3** (2 mol%). Bottom: Simulated pattern for $[C_{36}H_{73}B_{20}ClIr_2N_4+H]^+$. Inset: potential structure for dimer of this formula.

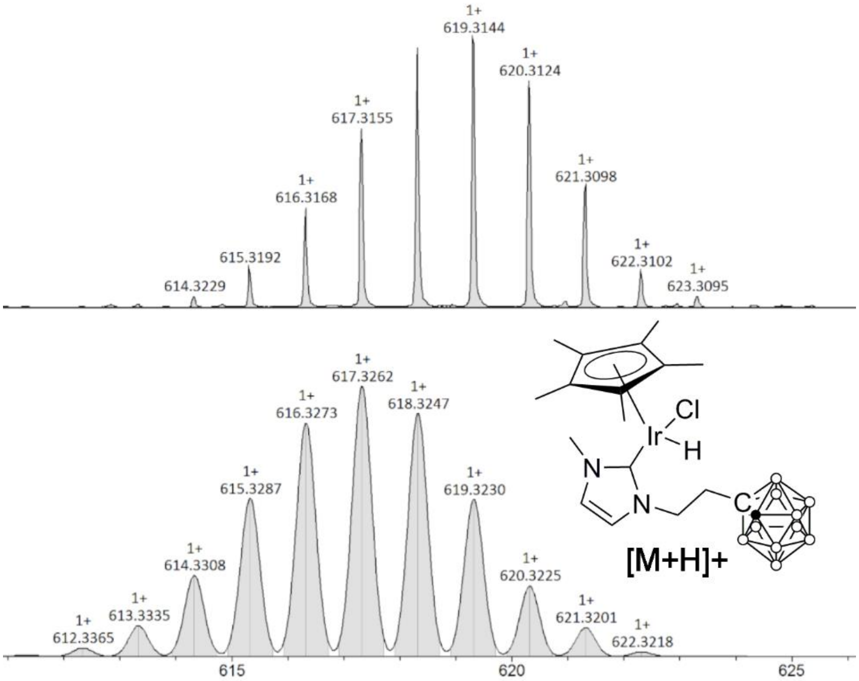

Figure 136. Top: Partial HRMS for reaction using **C3** (2 mol%). Bottom: Simulated pattern for $[C_{18}H_{36}B_{10}ClIrN_2+H]^+$. Inset: potential structure for complex of this formula.

The high *m/z* values 1220, 1234 and 1250 observed for the **C4**/**C5** reaction can be explained as Na^+, K^+ and $O+K^+$ adducts respectively of the *m/z* 1198 signal observed during the **C3** reaction. This indicates that some identical species are present in both reactions, which is in good agreement with the ^{1}H NMR data in which some hydridic species were observed to be the same in both reactions.

The spectra recorded for the experiments with $[IrCp^*Cl_2]_2$ also have two general regions in which ion peaks are observed. The exact mass of the dimer is 796.0360. For the first hour, signals are observed between *m/z* 650 and *m/z* 800, which are presumably due to some fragmentation of this complex. However, higher mass signals *m/z* >900 are also observed throughout the reaction. The highest of these emerges after 35 minutes of reaction at *m/z* 1421 and appears to correspond to a tetrameric species (Figure 137). After 1 hour, signals for the lower mass species are no longer apparent. For the lower loading reaction, initially similar signals are seen, however after 30 minutes no high mass number signals are observed.

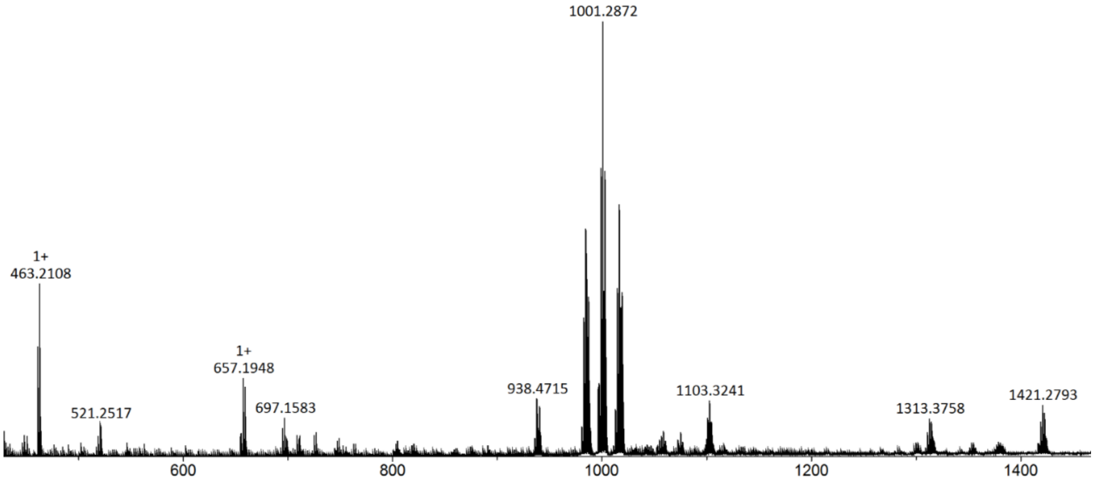

Figure 137. HRMS obtained for catalytic reaction using $[IrCp^*Cl_2]_2$ (0.5 mol%) after 35 minutes.

Unfortunately, as many of the signals observed cannot be explained this data does not shed light on likely catalyst speciation, beyond the supposition that dimers may be present.

4.3.7 Kinetic Analysis

Using the method described by Burés, attempts were made to determine the order in each catalyst.[22] This should be possible, as there is data for each catalyst at two different concentrations. All other conditions were kept the same, however it is important to note that there was some variation in the starting concentration of acetophenone as determined by NMR integration, which may have an impact on the results of the kinetic analysis.

The analysis was conducted by plotting the concentration of 1-phenylethanol vs $t[cat]_0^n$ for the two catalyst concentrations used in each case. Initial values of n were

0.5, 1.0 and 2.0, with other values investigated based on the appearance of the initial charts. For **C3**, none of these initially tested values of n gave a satisfactory overlay (Figure 138). For the first part of the reaction (~20 minutes of real reaction time), an order of 1 in **C3** seems to provide the closest match. However, after this the agreement of the data is poor, and no values in the range 0-2 provide a good overlay. This may point to an initial 1st order dependence on catalyst, after which the catalyst becomes deactivated in some way, possibly leading to a zero order dependence on catalyst. The reaction with **C4**/**C5** also does not appear to have an order in either 0.5, 1 or 2 . For these data the overlay improves at higher catalyst orders, becoming quite reasonable at n = 3, and even better at n = 4 (Figure 139). However, it is hard to envisage a situation where the order in catalyst is so high, so this seems unlikely. The data for the dimer also does not give a satisfactory overlay of points for n = 0.5, 1 or 2 (Figure 140). Better alignment could not be achieved with higher or lower values of n.

It is possible that the lack of convincing overlay achieved for these reactions is due to associated reactions not having exactly identical conditions (i.e. different starting acetophenone concentrations). However, it is also possible that the system is too complex to be modelled using this method. The method described by Burés is only effective in cases where the catalyst concentration remains constant throughout the experiment.[22] Other effects, like catalyst deactivation or product inhibition, are not adequately accounted for. These may be determined by other experiments, which due to time constraints could not be performed.

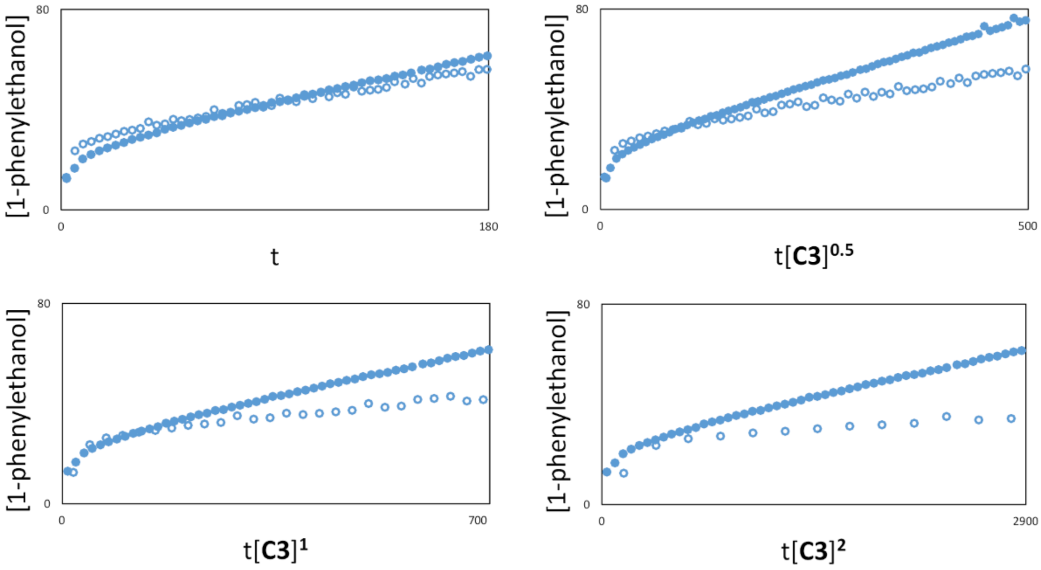

Figure 138. Analyses to determine order in catalyst for **C3**. Concentration of 1-phenylethanol vs. t[cat]^{n}.

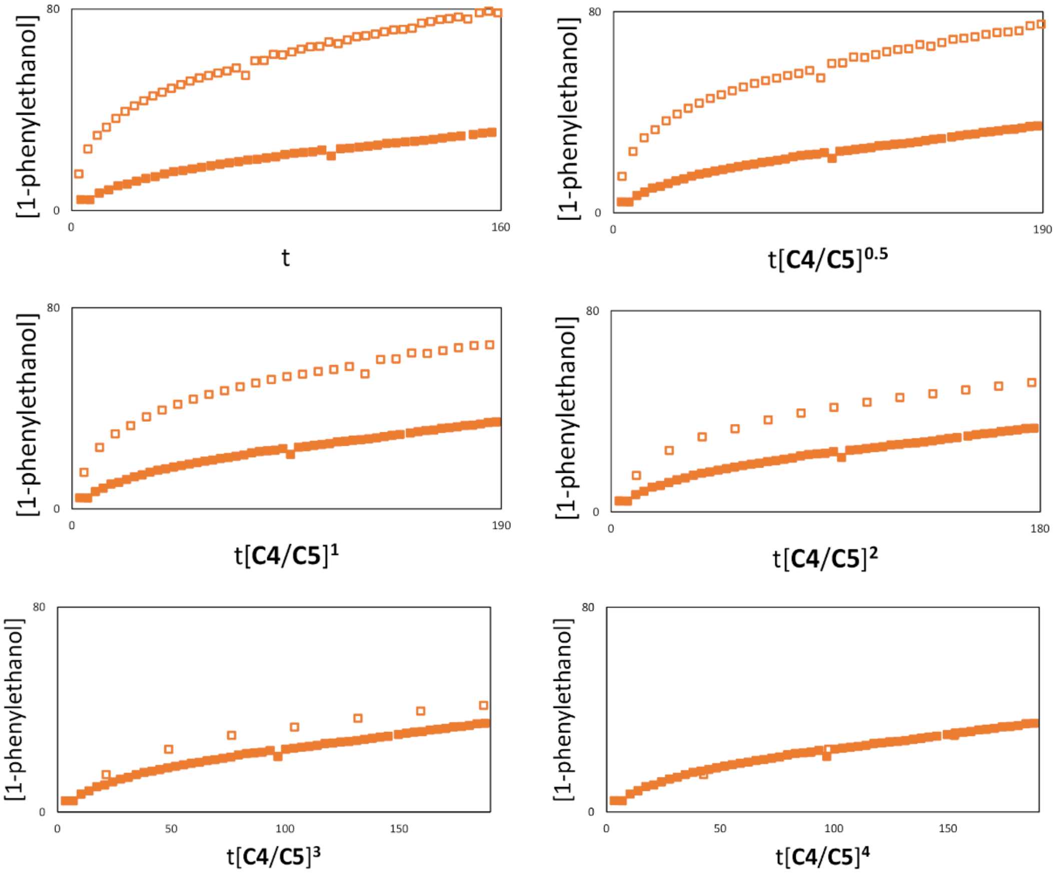

Figure 139. Analyses to determine order in catalyst for **C4/C5**. Concentration of 1-phenylethanol vs. t[cat]$^{n.}$

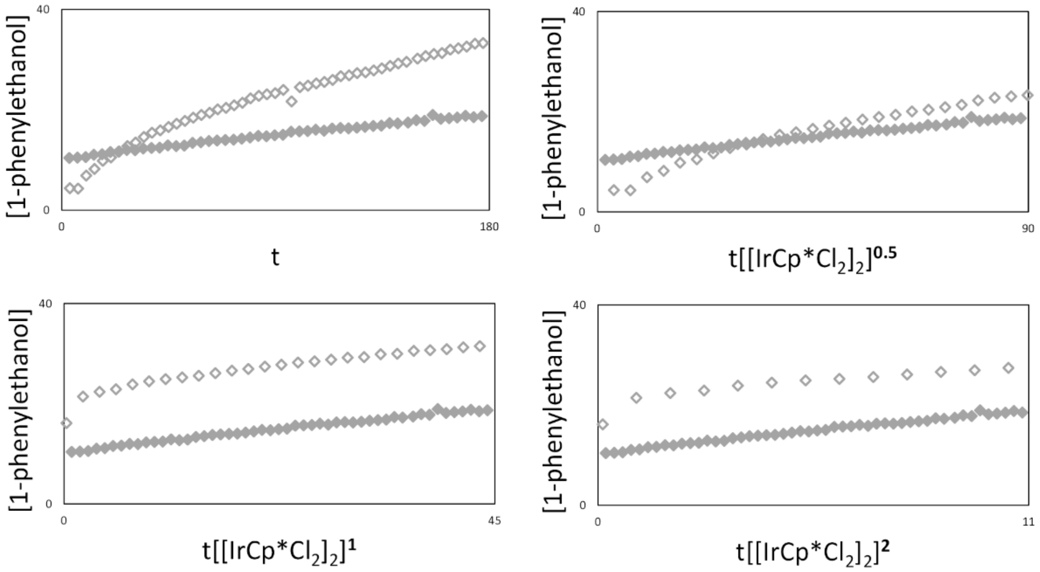

Figure 140. Analyses to determine order in catalyst for [IrCp*Cl$_2$]$_2$. Concentration of 1-phenylethanol vs. t[cat]$^{n.}$

4.4 Conclusions and Future Work

The mechanism of TH using Ir catalysts bearing NHC-carborane tethered ligands, as well as the parent complex [IrCp*Cl$_2$]$_2$, has been investigated using ^{1}H NMR spectroscopy and HRMS at the DReaM Facility. Prior to use of the facility, off-line reaction monitoring was used to check reaction progress over time. In this case, reaction progress appeared to cease after 2-3 hours. Solubility tests were also carried out which determined that the catalysts are relatively insoluble in IPA at room temperature, but that heating to 75 °C adequately solubilises both **C3** and **C4**/**C5**.

Using the DReaM Facility set-up, data sets were obtained for reactions using **C3**, **C4**/**C5** and [IrCp*Cl$_2$]$_2$ at two different catalyst loadings for each. ^{1}H NMR spectra were recorded between -25 ppm and 15 ppm, which were used to determine conversion values for all reactions. Using selective excitation, further spectra were recorded between -25 and -15 ppm which allowed for the observation of hydride species during the reaction.

Conversions achieved for reactions performed at the DReaM Facility were lower than comparable experiments in batch, however overall trends in catalyst reactivity were retained. The differences in conversion may be attributable to the differences in reaction set-up, and preparation of reagents.

In all cases, a hydride species was observed to form prior to the addition of any base - a phenomenon not previously noted in the literature. After base addition a range of hydride species could be observed, which differed dependent on catalyst. Three major hydride signals were observed in runs using the moderately inactive catalyst **C3**, after an induction period of approximately 20 minutes, during which time many signals are observed. The HRMS data obtained during these experiments show many carborane containing species until the spectrum obtained after half an hour, after which time two major signals are observed. One appears to correspond to a monomeric species, and the other to a dimer. The three hydride signals observed in reactions using **C3** were also seen in reactions with **C4**/**C5**; many other signals were also apparent. Mass spectral data from reactions with **C4**/**C5** pointed to the formation of monomeric and dimeric species. For the catalytic reactions with [IrCp*Cl$_2$]$_2$ there were initially more than 8 hydride signals, however over time these decayed to leave just two.

Attempts were made to use graphical methods to determine the order of the reaction in catalyst, however, no satisfactory overlay could be found for any catalysts. This may indicate a complex mechanism involving multiple cycles, catalyst deactivation, or product inhibition.

There is a wide scope for future work in this area. Other kinetic analyses could provide an insight into the mechanism, which could be obtained *via* on-line or off-line methods. In particular, the use of time adjustment could provide a valuable insight into whether catalyst deactivation is occurring.[16] This would also shed light on the results already obtained, as the graphical method only works for systems with a constant concentration of catalyst.

Determination of catalyst speciation during the reaction is desirable. If further access to the DReaM Facility was available, the use of EXSY NMR, as described by Hall *et al.* to demonstrate exchange between hydrides, IPA and acetophenone, could provide an insight into which hydride signals are responsible for catalytic activity[3]. As noted in Chapter 2, the isolation and full characterisation of **C6.H**, followed by application to catalysis should help identify whether or not this is an active intermediate. This may also be compared with the intermediates observed directly at the DReaM Facility. Attempts to synthesise the hydridic species observed during the reaction are worthwhile, as this may allow for further characterisation and hence structural elucidation. There are apparent similarities in speciation between **C3** and **C4**/**C5**, two catalysts with very different degrees of efficiency. Of particular interest is the hydridic species formed by reaction of $[IrCp^*Cl_2]_2$ with IPA and acetophenone. This has not been noted previously, and may lead to the possibility of catalysis under base-free conditions.

If any intermediates can be identified, these will feed back into the computational study, hopefully allowing for the determination of a plausible catalytic cycle.

4.6 Summary and Possible Mechanisms

Much of the evidence gathered does not allow for definite conclusions about what mechanism(s) may be in operation during the cycle. However, there are a number of key points which warrant further consideration.

It is clear from the stoichiometric reactions (Chapter 2 – *2.4.4*) that while **C6** undergoes reaction with Na^{i}PrO to form a single hydridic product, the reaction with **C3** is more complex leading to several hydrides. The formation of multiple products, not all of which may be catalytically competent, may contribute to lower activity. It is not possible to say with any certainty what these products are. It is possible that **C6** reacts with Na^{i}PrO to form **C6**.H, with the steric bulk of the carborane encouraging a rapid β-hydride elimination process. In the case of **C3** this bulk is not present, and thus react to form the hydride is slower. Additionally, with two halides present, more products can be formed. It is also possible that the lack of steric bulk at the metal centre allows for the formation of one or more dimeric species (Figure 141). Another possible explanation is the formation of polyhydride species *via* Cp* loss in the case of **C4**/**C5**, as suggested by Crabtree *et al.* (Chapter 1 – *1.2.3.2*).[40]

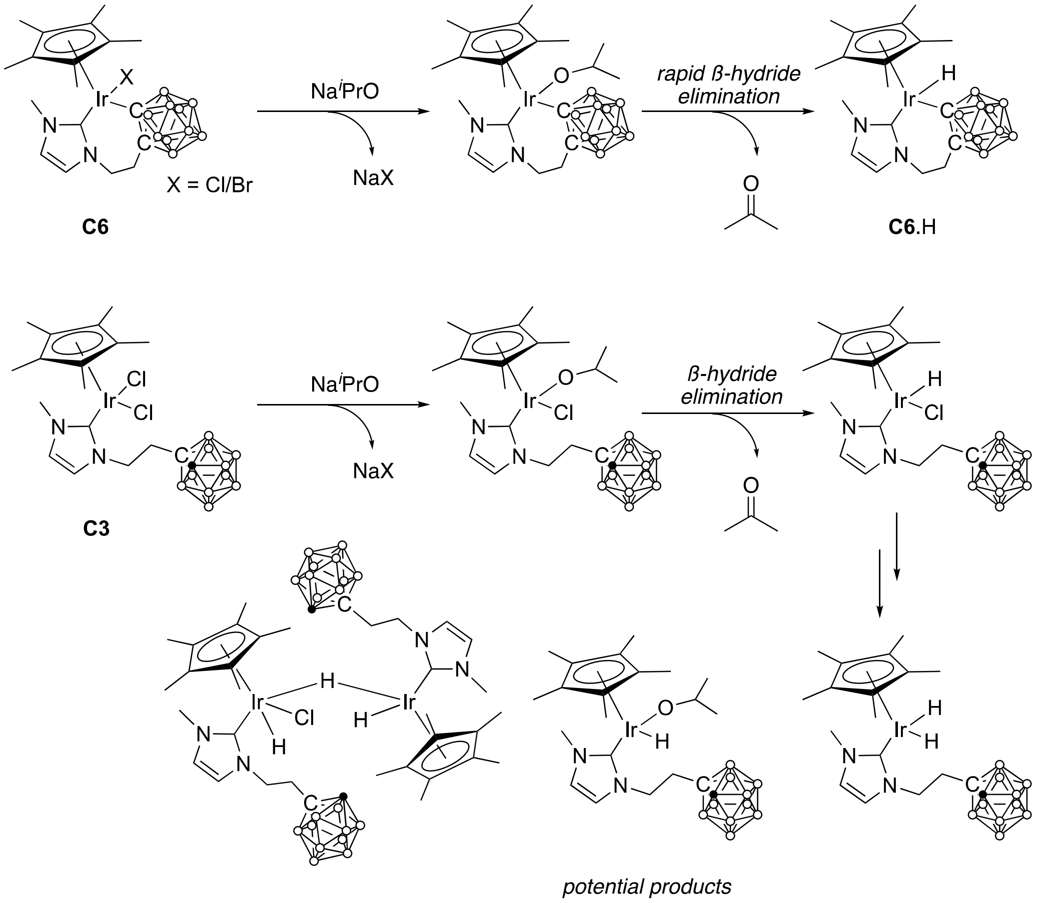
X = Cl/Br
Na^{i}PrO
NaX
rapid ß-hydride elimination
C6
C6.H
Na^{i}PrO
NaX
ß-hydride elimination
C3
potential products

Figure 141. Possible mechanistic scenario to explain difference in reactivity of **C3** and **C6**.

The possibility of Shvo-type mechanism was raised by the results of DFT calculations.[41] This could be envisaged as occurring for a monohydride derived from **C3** or **C6**. Were this to be the case, it is possible that the coordinated carborane would provide greater steric protection of the unsaturated iridium centre, than is present when the carborane is pendant (Figure 142).

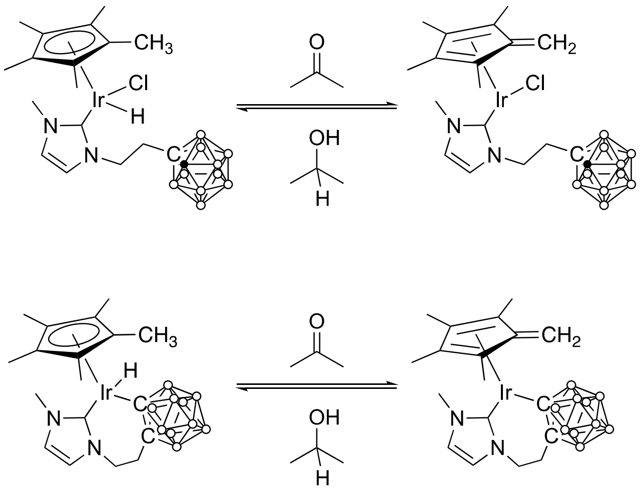

Figure 142. Possible Shvo-type equilibria for monohydride species derived from **C3** (top) and **C6** (bottom).

This suggested mechanism does not find solid agreement with the observation of multiple hydride signals using on-line NMR spectroscopy, or the observation of dimeric species using HRMS. However, although many hydridic signals were observed, it is possible that not all correspond to active catalytic species.

A few further experiments are suggested in order to test these hypotheses. Firstly, a mercury drop test should be carried out with each catalyst to rule out the involvement of nanoparticles. Secondly, the complex **C6**.H should be synthesised and tested for TH activity. The kinetics of **C6**.H could then be compared with **C6** thus giving an indicating of whether **C6**.H is a likely intermediate in the reaction. Finally, the possible Shvo-type mechanism should be probed further using DFT calculations, and energy barriers for relevant transition states compared (**A**, **B**, **C** - .Figure 143). If the barriers are significantly different then this may provide an explanation for the different activities of the different catalysts.

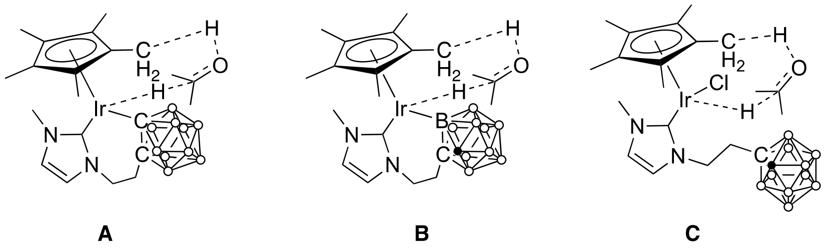

Figure 143. Transition states for Shvo-type mechanism for computational investigation.

4.5. Experimental

4.5.1 General Considerations

The synthesis of the complexes used in this chapter is described in Chapter 2. IPA and acetophenone were dried by standing for 18 hours over activated 3 Å molecular sieves, followed by transfer to new activated 3 Å sieves, and then purged with argon prior to use. Na^{i}PrO and 1,3,5-trimethoxybenzene were purchased from Alfa Aesar and Fluorochem respectively and used as received. K^{t}BuO was gifted by Dr Ulrich Hintermair (University of Bath).

NMR Spectra were recorded on a Bruker AVIII 300 MHz spectrometer (University of Leeds), a Jeol ECA 600 II spectrometer (University of Leeds), or a 500 MHz AVIII equipped with a nitrogen cooled Prodigy CryoProbe (DReaM Facility). ^{1}H NMR spectra were referenced to residual solvent peaks where relevant.

4.5.2 Off-line Catalytic Reaction Monitoring

Catalyst (1 mol% per Ir) and 1,3,5-trimethoxybenzene (55.5 mg, 0.33 mmol) were added to an ampoule and placed under argon. In a glovebox, Na^{i}PrO (8.2 mg, 0.1 mmol) and acetophenone (117 µL, 1.00 mmol) were added to the ampoule. The ampoule was sealed, taken out of the glovebox and connected to a Schlenk line. Under an atmosphere of argon, anhydrous IPA (2.3 mL) was added, the ampoule sealed, and the reaction mixture held at 75 °C for 5 hours. Aliquots (0.1 mL) were withdrawn every hour and added to an NMR tube with $CDCl_3$ (0.5 mL).

4.5.3 Attempted Preparation of Hydride Species

C4/**C5** (4.8 mg, 0.0078 mmol) was added to an ampoule, placed under argon, and anhydrous IPA added (3.0 mL). The mixture was heated to 77 °C to aid solubilisation. A sample (0.7 mL) was withdrawn and placed in a Young's NMR tube under an atmosphere of argon. K^{t}BuO (0.020 mL, 1.0 M solution in IPA, 0.020 mmol) and anhydrous acetophenone (0.020 mL, 0.24 mmol) were added, and the tube sealed. The sample was heated to 60 °C within a 600 MHz NMR spectrometer and spectra were recorded.

4.5.4 DReaM Facility Set-up

Reactions were carried out in a standard glass round-bottomed flask with Schlenk connections under an inert atmosphere of argon. A Vapourtec SF-10 peristaltic pump was used to circulate the mixture from the reaction vessel to an InsightMR flow tube (Bruker) located within the NMR spectrometer and back to the reaction vessel.

Tubing between the InsightMR flow tube and the reaction vessel was narrow diameter polyetheretherketone (PEEK) tubing (0.75 mm ID, Upchurch Scientific).

Tubing inside the InsightMR flow tube was PEEK (0.125 mm ID). All other connections were made using standard HPLC-type PEEK connectors (Upchurch Scientific), allowing the apparatus to be purged with argon as required.

Aliquots of reaction mixture were sampled for on-line MS from the flow pathway every 15 minutes (for up to 4 hours) on the return from the NMR spectrometer flow cell to the reaction vessel and diluted with IPA. This diluted reaction mixture was transferred directly to the mass spectrometer (Bruker MicroTOF-Q, ESI-TOF, positive ionisation mode) *via* stainless steel tubing (between flow pathway and pump; ID 0.18 mm, Thames Restek) and PEEK tubing (between pump and mass spectrometer)

4.5.5 General Procedure for Catalytic Reaction Monitoring (DReaM Facility)

Prior to the reaction the tubing was purged with anhydrous IPA followed by argon. Catalyst (0.25-2 mol%) was added to the reaction flask and placed under an atmosphere of argon. A solution of 1,3,5-trimethoxybenzene in IPA (145 mM) was added and the mixture stirred at 75 °C. Acetophenone (2.5 or 5.0 mmol) was added *via* microliter syringe. Once a satisfactory degree of homogeneity had been achieved, the sample was recirculated at 3 mL/min and ^{1}H NMR spectra recorded. Recirculation was paused and a solution of K^{t}BuO in 1,3,5-trimethoxybenzene/IPA stock solution (0.5 or 1.0 mL) was added. Recirculation was resumed once a satisfactory degree of homogeneity had been achieved, and ^{1}H NMR spectra were recorded.

Note: entries 4 and 6 (Table 13 - 4.3.2) were initially prepared at twice the concentration stated. In the case of entry 4, acetophenone was added and circulation of the sample led to blockage of the system. A sample from the reaction mixture (5.75 mL) was withdrawn, and diluted with fresh stock solution (6.25 mL), followed by addition of base solution (0.5 mL). In the case of entry 6, dilution was performed prior to acetophenone addition, when the insolubility of the catalyst was noted. A sample of reaction mixture was withdrawn (5.75 mL), which was diluted with fresh stock solution (6.25 mL), and then acetophenone (292 µL) was added followed by base solution (0.5 mL).

4.5.6 NMR Acquisition Parameters (DReaM Facility)

^{1}H (non-selective) spectra were acquired using a standard 30° pulse sequence, with a 1.64 second acquisition time and 1 second delay time, between -25 and 15 ppm using 8 scans.

^{1}H selective excitation spectra were acquired using the seldpfgse_calc.ptg pulse sequence, with a 2.0 second acquisition time and a 1 second delay time, between -25 and -15 ppm. The excitation was an 8 ppm window focussed at -15 ppm.

Static spectra for the calculation of flow correction factors were recorded at the end of a given experiment. For non-selective spectra the same parameters were applied, for the selective excitation spectra an additional static spectrum with a excitation focussed on the aromatic 1,3,5-trimethoxybenzene signal (5 ppm) was also recorded.

4.5.7 NMR Spectra Processing

Concentration data were obtained in the following manner. Integration values for the key peaks of interest (acetophenone - aromatic, CH_3; 1-phenylethanol - aromatic, CH, CH_3; 1,3,5-trimethoxybenzene - CH, CH_3; hydrides) were obtained by defining and saving the integral regions in a representative spectrum, and employing the “multi_integ3” command in TopSpin 4.0. A number of corrections were then applied to the raw integral data. For the non-excited signals these were as follows: flow correction factors, and number of protons relative to the standard. For the selective excitation spectra additional corrections were applied for: differences in receiver gain and non-linear response to receiver gain.

Appendix

Table A1. Centroid to furthest atom distances in solid state structures of NHC-carborane complexes.[28]

	Distance: centroid – functional group / Å			
Complex	Carborane	Cp*	NHC	Chloride
C3	5.918	5.598	4.943	4.377
C6	4.731	4.307	4.342	3.020
C6.H	4.611	4.298	4.172	N/A

Distances measured between centroid for whole molecule and the furthest ellipsoid for each type of each ligand.

List of References

1 A. M. R. Hall, J. C. Chouler, A. Codina, P. T. Gierth, J. P. Lowe and U. Hintermair, *Catal. Sci. Technol.*, 2016, **6**, 8406–8417.

2 A. M. R. Hall, R. Broomfield-Tagg, M. Camilleri, D. R. Carbery, A. Codina, D. T. E. Whittaker, S. Coombes, J. P. Lowe and U. Hintermair, *Chem. Commun.*, 2018, **54**, 30–33.

3 A. M. R. Hall, P. Dong, A. Codina, J. P. Lowe and U. Hintermair, *ACS Catal.*, 2019, **9**, 2079–2090.

4 S. Hashiguchi, A. Fujii, J. Takehara, T. Ikariya and R. Noyori, *J. Am. Chem. Soc.*, 1995, **117**, 7562–7563.

5 K.-J. Haack, S. Hashiguchi, A. Fujii, T. Ikariya and R. Noyori, *Angew. Chemie Int. Ed.*, 1997, **36**, 285–288.

6 P. Atkins and J. de Paula, *Atkins' Physical Chemistry*, Oxford University Press, Oxford, 9th edn., 2010.

7 D. G. Blackmond, *Angew. Chemie Int. Ed.*, 2005, **44**, 4302–4320.

8 C. D.-T. Nielsen and J. Burés, *Chem. Sci.*, 2019, **10**, 348–353.

9 H. Lineweaver and D. Burk, *J. Am. Chem. Soc.*, 1934, **56**, 658–666.

10 P. Dydio, R. J. Detz and J. N. H. Reek, *J. Am. Chem. Soc.*, 2013, **135**, 10817–10828.

11 L. Mesas-Sánchez and P. Dinér, *Chem. Eur. J.*, 2015, **21**, 5623–5631.

12 R. S. Klausen, C. R. Kennedy, A. M. Hyde and E. N. Jacobsen, *J. Am. Chem. Soc.*, 2017, **139**, 12299–12309.

13 D. Lehnherr, Y. Ji, A. J. Neel, R. D. Cohen, A. P. J. Brunskill, J. Yang and M. Reibarkh, *J. Am. Chem. Soc.*, 2018, **140**, 13843–13853.

14 C. S. Buettner, D. Willcox, B. G. N. Chappell and M. J. Gaunt, *Chem. Sci.*, 2018, **10**, 83–89.

15 P. Ruiz-Castillo, D. G. Blackmond and S. L. Buchwald, *J. Am. Chem. Soc.*, 2015, **137**, 3085–3092.

16 R. D. Baxter, D. Sale, K. M. Engle, J.-Q. Yu and D. G. Blackmond, *J. Am. Chem. Soc.*, 2012, **134**, 4600–4606.

17 J. Burés, *Angew. Chemie Int. Ed.*, 2016, **55**, 16084–16087.

18 T. C. Malig, D. Yu and J. E. Hein, *J. Am. Chem. Soc.*, 2018, **140**, 9167–9173.

19 H. Noda, F. Amemiya, K. Weidner, N. Kumagai and M. Shibasaki, *Chem. Sci.*, 2017, **8**, 3260–3269.

20 C. Colletto, A. Panigrahi, J. Fernández-Casado and I. Larrosa, *J. Am. Chem. Soc.*, 2018, **140**, 9638–9643.

21 H. Nagae, T. Hirai, D. Kato, S. Soma, S. Akebi and K. Mashima, *Chem. Sci.*, 2019, **10**, 2860–2868.

22 J. Burés, *Angew. Chemie Int. Ed.*, 2016, **55**, 2028–2031.

23 M. E. Fieser, M. J. Sanford, L. A. Mitchell, C. R. Dunbar, M. Mandal, N. J. Van Zee, D. M. Urness, C. J. Cramer, G. W. Coates and W. B. Tolman, *J. Am. Chem. Soc.*, 2017, **139**, 15222–15231.

24 D. Whitaker, J. Burés and I. Larrosa, *J. Am. Chem. Soc.*, 2016, **138**, 8384–8387.

25 C. Weatherly, J. M. Alderson, J. F. Berry, J. E. Hein and J. M. Schomaker, *Organometallics*, 2017, **36**, 1649–1661.

26 S. Arkhipenko, M. T. Sabatini, A. S. Batsanov, V. Karaluka, T. D. Sheppard, H. S.

Rzepa and A. Whiting, *Chem. Sci.*, 2018, **9**, 1058–1072.

27 J. H. Bannock, S. H. Krishnadasan, M. Heeney and J. C. de Mello, *Mater. Horizons*, 2014, **1**, 373–378.

28 J. Holmes, C. M. Pask and C. E. Willans, *Dalton Trans.*, 2016, **45**, 15818–15827.

29 D. M. Heinekey, J. M. Millar, T. F. Koetzle, N. G. Payne and K. W. Zilm, *J. Am. Chem. Soc.*, 1990, **112**, 909–919.

30 D. M. Heinekey, A. S. Hinkle and J. D. Close, *J. Am. Chem. Soc.*, 1996, **118**, 5353–5361.

31 C. Cruickshank Miller, *Proc. R. Soc. London. Ser. A, Contain. Pap. a Math. Phys. Character, Vol. 106, Issue 740, pp. 724-749*, 1924, 724–749.

32 J. T. Edward, *J. Chem. Educ.*, 1970, **47**, 261.

33 M. R. Churchill and S. A. Julis, *Inorg. Chem.*, 1977, **16**, 1488–1494.

34 R. J. Abraham, J. Fisher and P. Loftus, *Introduction to NMR Spectroscopy*, John Wiley & Sons Ltd, Chichester, 1st edn., 1988.

35 D. G. Hamilton and R. H. Crabtree, *J. Am. Chem. Soc.*, 1988, **110**, 4126–4133.

36 P. J. Desrosiers, L. Cai, Z. Lin, R. Richards and J. Halpern, *J. Am. Chem. Soc.*, 1991, **113**, 4173–4184.

37 H. Fumihiro, K. Fujita, R. Yamaguchi, Fumihiro Hanasaka, and Ken-ichi Fujita and R. Yamaguchi, *Organometallics*, 2005, **24**, 3422–3433.

38 U. Hintermair, J. Campos, T. P. Brewster, L. M. Pratt, N. D. Schley and R. H. Crabtree, *ACS Catal.*, 2014, **4**, 99–108.

39 S. Semwal, I. Mukkatt, R. Thenarukandiyil and J. Choudhury, *Chem. Eur. J.*, 2017, **23**, 13051–13057.

40 J. Campos, U. Hintermair, T. P. Brewster, M. K. Takase and R. H. Crabtree, *ACS Catal.*, 2014, **4**, 973–985.

41 Y. Shvo, D. Czarkie, Y. Rahamim and D. F. Chodosh, *J. Am. Chem. Soc.*, 1986, **108**, 7400–7402.

Part II

Electrochemical Synthesis of Copper N-Heterocyclic Carbene Complexes

Chapter 1
Introduction to Electrochemical Synthesis of NHC Complexes

This chapter introduces areas relevant to Part 2 of this thesis, which describes the electrochemical synthesis of copper-NHC complexes. This work primarily concerns NHCs which are derived from a triazolium salt. As NHCs have been discussed in the Preface, herein electrochemical synthesis and its application to inorganic chemistry is described, as well as specific information about the methods used in this work. A brief overview of NHCs with non-classical architectures is also provided.

1.1 Principals of Electrochemical Synthesis

An electrochemical reaction is one in which a current is passed through a solution using an external power supply, in order to cause an oxidative or reductive reaction at the electrodes. Organic electrochemical reactions are generally classified as either cathodic reduction, anodic oxidation, or combined - in which a redox reaction occurs. The general principle of an anodic oxidation reaction is to oxidise a molecule at the anode to form a radical or radical cation. The oxidised species is highly reactive, and will react with nucleophiles (Figure 144). Electron-rich molecules are suitable for this treatment, due to possessing a high energy HOMO (and hence a low oxidation potential). The reverse principles apply for cathodic reduction reactions.[1]

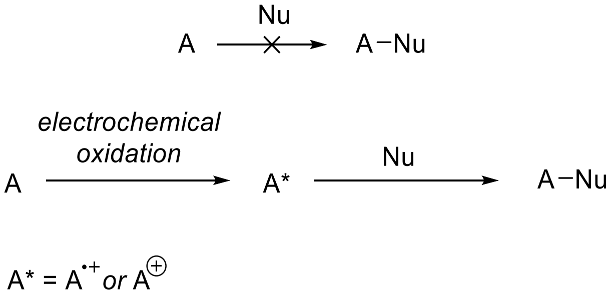

Figure 144. Generalised scheme for anodic oxidation followed by subsequent reaction.

Although the principles are the same, using electrochemistry to synthesise metal complexes is somewhat different. An anodic oxidation reaction occurs on the anode itself (termed a sacrificial anode), and metal ions are released into solution. The metal ions are then able to react with available ligands in the same solution, which may have been generated from ligand precursors in a reduction reaction at the cathode.

1.1.1 Inorganic Electrochemistry

The synthesis of metal complexes by electrochemical means has been known since the 1970s. Eisenbach and Lehmkuhl reported the preparation of acac and alkoxide complexes of Fe, Co and Ni in 1975.[2] In the same year Tuck *et al.* described the electrochemical synthesis of In complexes with halide and alkoxide ligands.[3] Three years later, the same group independently reported the preparation of acac complexes, extending the scope to include the entire 1st row of transition metals (excluding Sc).[4] Over the next two decades this group would describe a vast array of electrochemically prepared complexes. Cationic,[5,6] neutral,[4] and anionic[5,7] complexes have all been reported. The scope of metals used includes the 1st row transition metals,[4,8] main group elements from groups 13 and 14,[9,10] 2nd/3rd row transition metals from groups 4, 11 and 12,[4,6,9] and f-block elements.[5,11,12] Additionally, a wide variety of ligands have been reported to be compatible: halides,[3,8] acac,[2,4,5,11,13] alkoxide,[2,3] thiol,[9,10,14] carboxylate,[15] catechols,[15–17], amines,[18] and phosphides (Figure 145).[19]

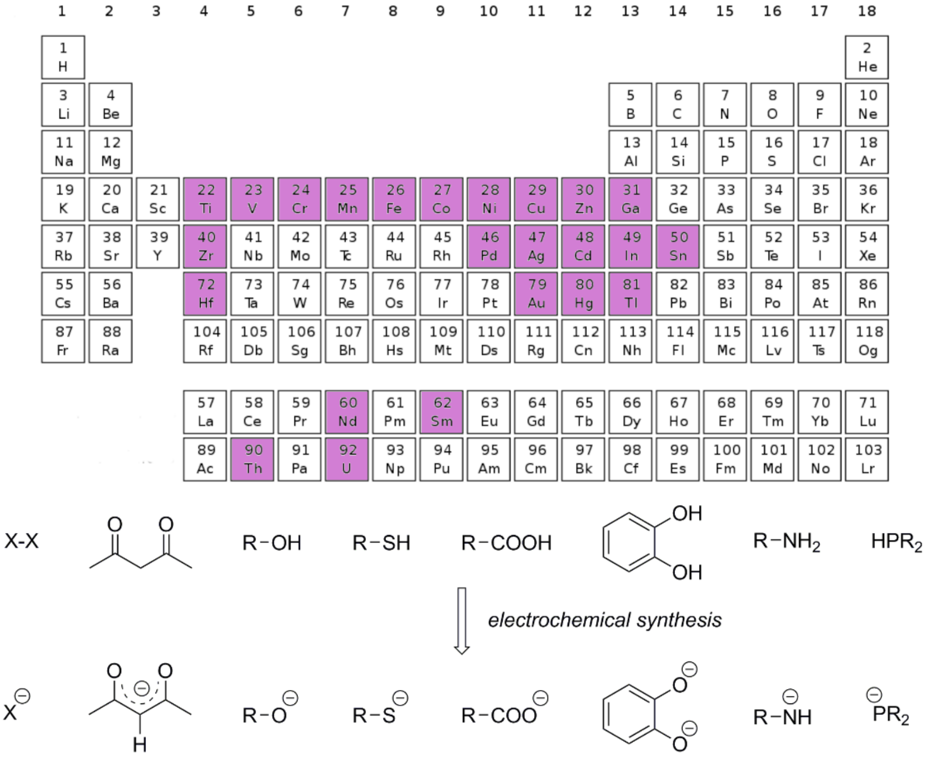
1 2 3 4 5 6 7 8 9 10 11 12 13 14 15 16 17 18
1 H
2 He
3 Li 4 Be 5 B 6 C 7 N 8 O 9 F 10 Ne
11 Na 12 Mg 13 Al 14 Si 15 P 16 S 17 Cl 18 Ar
19 K 20 Ca 21 Sc 22 Ti 23 V 24 Cr 25 Mn 26 Fe 27 Co 28 Ni 29 Cu 30 Zn 31 Ga 32 Ge 33 As 34 Se 35 Br 36 Kr
37 Rb 38 Sr 39 Y 40 Zr 41 Nb 42 Mo 43 Tc 44 Ru 45 Rh 46 Pd 47 Ag 48 Cd 49 In 50 Sn 51 Sb 52 Te 53 I 54 Xe
55 Cs 56 Ba 72 Hf 73 Ta 74 W 75 Re 76 Os 77 Ir 78 Pt 79 Au 80 Hg 81 Tl 82 Pb 83 Bi 84 Po 85 At 86 Rn
87 Fr 88 Ra 104 Rf 105 Db 106 Sg 107 Bh 108 Hs 109 Mt 110 Ds 111 Rg 112 Cn 113 Nh 114 Fl 115 Mc 116 Lv 117 Ts 118 Og
57 La 58 Ce 59 Pr 60 Nd 61 Pm 62 Sm 63 Eu 64 Gd 65 Tb 66 Dy 67 Ho 68 Er 69 Tm 70 Yb 71 Lu
89 Ac 90 Th 91 Pa 92 U 93 Np 94 Pu 95 Am 96 Cm 97 Bk 98 Cf 99 Es 100 Fm 101 Md 102 No 103 Lr
X-X
R-OH
R-SH
R-COOH
OH
OH
R-NH2
HPR2
electrochemical synthesis
X⊖
H
R-O⊖
R-S⊖
R-COO⊖
O⊖
O⊖
R-NH⊖
⊖PR2

Figure 145. Scope of inorganic electrochemical reactions described by Tuck *et al.* Top: Periodic table indicating elements used. Bottom: Ligand precursors and associated reduced products.

The preparation of organo halide complexes of a range of metals has also been described,[7] as has the preparation of a Cu acetylide complex.[20] These represent the first examples of the electrochemical preparation of organometallic complexes (*vide infra* – 1.1.2).

Many of these complexes require stabilisation from a supporting neutral ligand (commonly bpy or phen); Tuck *et al.* report that such a ligand may be added during electrolysis with no negative effects on reaction outcome.[7,13]

There have been contributions to this area from other groups, and several detailed review articles are available which provide a comprehensive list of electrochemically synthesised complexes.[21–24]

The common feature of all the ligands listed is that the $[L]^-$ ligand is derived from an LH precursor. It is the reduction of this species, and concomitant oxidation of the sacrificial metal anode, that allows for the generation of the metal complexes (Figure 146).

$$\text{cathode:}\quad n\mathrm{LH} + ne^{\ominus} \longrightarrow \mathrm{L}^{\ominus} + n/2\,\mathrm{H_2(g)}$$

$$\text{anode:}\quad \mathrm{M} \longrightarrow \mathrm{M}^{n+} + ne^{\ominus}$$

Figure 146. General scheme for electrochemical synthesis of metal complexes.

Ligands with more than one reducible site are also compatible with this method. For example, catechol-type ligand precursors have been successfully reduced to form bidentate $[O_2R]^{2-}$ ligands in combination with Zn and Cd (**1.1**, **1.2** - Figure 147).[17] This process has additionally been demonstrated recently for mixed reducing groups (i.e. NH and OH) with half-salen type ligands (**1.3** - Figure 147).[25] In some cases it is possible to reduce just one of multiple possible reduction sites, as with complex **1.4**, in which only one of the OH groups on the catechol ligand is reduced (Figure 147). The selectivity was in this case attributed to a stabilising hydrogen bond between the OH group on one ligand, and O^- group on another.[16]

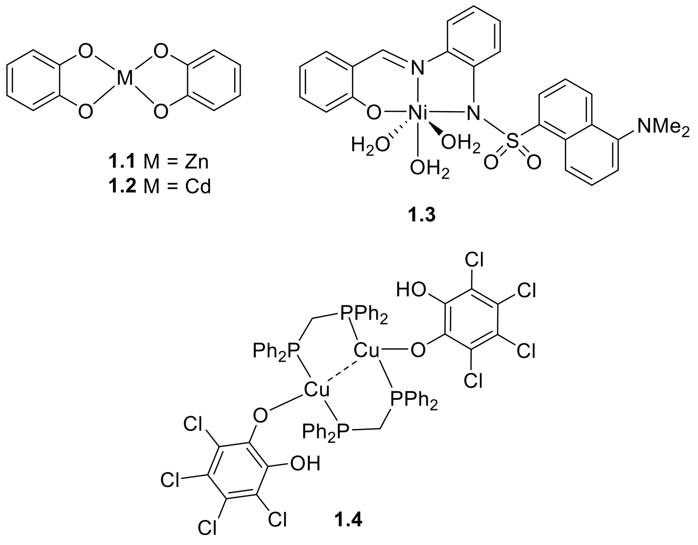

1.1 M = Zn
1.2 M = Cd

1.3

1.4

Figure 147. Complexes prepared electrochemically, showing full and partial reduction of reducible groups.

Tuck advocates the calculation of a reaction yield based on the quantity of metal consumed (calculated by pre-weighing the electrode). This allows the current efficiency to be calculated using equation 1.[4,24] The current efficiency (measured in units of mol F^{-1}) can give an insight into the oxidation processes occurring in the cell.

$$(1)\ current\ efficiency = \frac{moles\ of\ metal\ dissolved}{moles\ of\ electrons\ transfered}$$

For example when one mole of metal is released for each mole of electrons transferred (1 mol F^{-1}), a one electron oxidation is invoked. A value of 0.5 mol F^{-1} indicates that a 2 electron oxidation, generating M^{2+} ions, is in operation. Generally, the lowest stable oxidation state for the metal in question is formed. Although the products isolated are sometimes in higher oxidation states, this is believed to occur by oxidation processes in solution, rather than as a results of electrolysis.[9,10,15,24] Provided the low oxidation state is sufficiently stable, or stabilised by supporting ligands, it may be isolated. This is advantageous, as it provides the synthetic chemist with a route to otherwise inaccessible metal complexes.[14,16] There are a few examples of direct oxidation of metals to higher oxidation states, for example synthesis of a Mn(III) complex was found to have a current efficiency of 0.33 mol F^{-1}.[26] Similarly, a current efficiency of 0.47 mol F^{-1} for the formation of a Cu(II) species, suggests oxidation is solely electrochemically driven in this case.[27]

There are many benefits associated with using electrochemical synthesis to prepare inorganic compounds. The conditions used are mild, typically being conducted at room temperature, often in the fairly benign solvent MeCN and generate minimal by-products. In spite of the mild conditions, the reactions generally proceed quickly and this can be controlled to some extent by variation of the current.[24] Once the reaction is complete, the work-up procedure is generally facile, with products often precipitating directly from the reaction mixture.[21] In cases where the product remains in solution, addition of Et_2O will usually effect precipitation. A large range of structures have been shown to be accessible, of particular value are low oxidation state metal complexes which present a synthetic challenge using standard techniques.[16,22,24] Additionally, heteroleptic complexes bearing neutral donor ligands can be prepared by addition of such ligands to the reaction mixture, without a need to adapt the set-up.[9,10,17,19]

Electrochemical synthesis of metal species has challenges too. Chief among these is the need for the desired metal to be suitable for machining into an electrode (i.e. it must not be too brittle). Further to this, many of the examples above make use of $[Et_4N][ClO_4]$ as a supporting electrolyte. $[Et_4N][ClO_4]$ is well-suited as an electrolyte due to its excellent solubility properties, and the weak coordination of the perchlorate anion to metals. However perchlorate salts are highly hazardous.[24] The use of an electrolyte in general is something of a disadvantage. Although in many cases metal complexes precipitate from solution, if this does not occur then separation of the product from electrolyte can be extremely challenging.

In spite of the demonstrated utility of the electrochemical method, it has never really entered the mainstream. Review articles from the early 90s were assured that electrochemistry was being used for the preparation of otherwise inaccessible complexes, and that it was so successful in inorganic synthesis that application to other areas in future was certain.[21,22] And yet a review from 2015 discusses the vast potential of electrochemical synthesis, and urges its consideration as a valuable synthetic tool, rather than as a niche alternative, indicating that progress has been slow.[24] It may be that the method is still perceived as challenging, in spite of the relatively simple set-up required. In this case, synthetic chemists may take comfort in the words of Tuck: “an ignorance of the detailed electrochemistry, and even of such fundamental parameters as E_0, need be no bar to the use of electrochemical methods in non-aqueous solvents in preparative chemistry”.[28]

1.1.2 Electrochemical Synthesis of Organometallic Complexes

The earliest reported electrochemical synthesis of organometallics were organohalide complexes.[7,29,30] These can be prepared electrochemically by the oxidation of a sacrificial metal anode, and the reduction of the RX species, to generate $[R]^-$ and $[X]^-$. Cd complexes prepared from alkyl halides were reported in 1976. The formed complexes were found to be unstable, but could be isolated by the addition of a neutral donor ligand, as in complex **1.5** (Figure 148).[7] Not long after this, alkylhalide complexes of Sn were also prepared (e.g. **1.6** - Figure 148).[29] The first transition metal organometallics were reported in the same year, with aryl Ni and Pd complexes described (**1.7** - Figure 148). The preparation of these complexes electrochemically represented a significant improvement in terms of simplicity, safety and atom economy, as the usual route to such species involved reaction of a lithiated aryl species with the metal dihalide salt, or use of a Grignard reagent. Although effective in the synthesis of Ni and Pd complexes, the authors note that attempts to replicate the results with Pt were unsuccessful.[30] This may be due to the electrochemical inertness of Pt.[31]

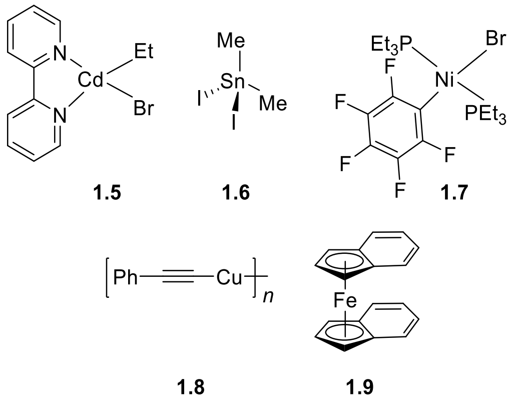

1.5 **1.6** **1.7** **1.8** **1.9**

Figure 148. Organometallic complexes prepared electrochemically.

Acetylide complexes of Cu, Ag, Au, Fe Ni, Co and Zn have also been prepared electrochemically. The first example was complex **1.8** reported by Tuck *et al.* in 1985 (Figure 148).[20] The complex was produced in a near quantitative yield (based on the mass of Cu), and improves on previous methods requiring lithiation or reaction with basic Cu salts. As with previous examples, complexes bearing neutral donor ligands in addition to the acetylide could also be obtained by addition of these to the reaction solution prior to electrolysis. Acetylide complexes of other transition metals were prepared electrochemically by Casey and Vecchio. The authors additionally describe the preparation of various metallocenes using Fe, Ni, Co, and Zn. Cp and Cp* complexes could be obtained by this method, as could more exotic MeCp, fluorenyl and indenyl complexes (e.g. **1.9**), thus showing the broad applicability of electrochemical synthesis (Figure 148).[32]

More recently, there have been few examples of electrochemical synthesis of organometallic complexes. There are reports that use an electrochemically generated reactive Ni(0) species to form aryl halide complexes (**1.10**, **1.11** - Figure 149). This method differs from previously discussed electrochemical syntheses in that the ligand is not reduced in the reaction, and the anode is not sacrificial. Rather, the metal is reduced, thus generating a reactive intermediate, which allows an otherwise challenging oxidative addition reaction to occur.[33,34]

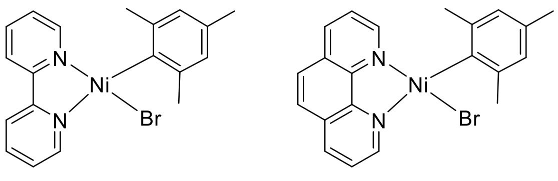

1.10 **1.11**

Figure 149. Organometallic Ni complexes prepared by generation of a reactive Ni(0) species.

1.1.3 Electrochemical Synthesis of NHC Complexes

Most of the electrochemical reactions described above rely on the reduction of an LH species to generate the $[L]^-$ ligand. Given that NHC ligands are also produced by a deprotonation reaction, it is easy to see how this method could be used to synthesise NHC complexes. In 2011, Chen *et al.* described how the passage of current through a solution of imidazolium salts in MeCN using metal plates could be used to prepare NHC complexes of the metal in question. Cationic complexes of Cu, Ni and Fe were reported, with yields ranging from 60-89% for Cu, 32-71% for Ni, and 24-34% for Fe (Figure 150). The method is particularly elegant in the case of NHC synthesis, as the imidazolium salt acts as an electrolyte.[35] Subsequently, an extension to this method was reported by Willans *et al.*, by demonstrating that both neutral and anionic Cu-NHC complexes can be prepared. Selectivity is achieved by choice of counter-ion; a non-coordinating anion will favour the formation of a cationic bis-NHC complex, whilst a coordinating anion will favour formation of a neutral mono-NHC complex. It was also shown that the method can be used to prepare NHC complexes bearing base-sensitive substituents, which would be challenging using traditional methods (e.g. **1.16** - Figure 150).[36]

The advantages of electrochemical synthesis (mild conditions, short reaction times, straightforward isolation procedure) can all be argued for NHC complex synthesis. In addition to this, the removal of the need for strong bases is a major advantage, as this makes the reactions safer and greener, as well as allowing access to previously challenging architectures bearing base sensitive groups.

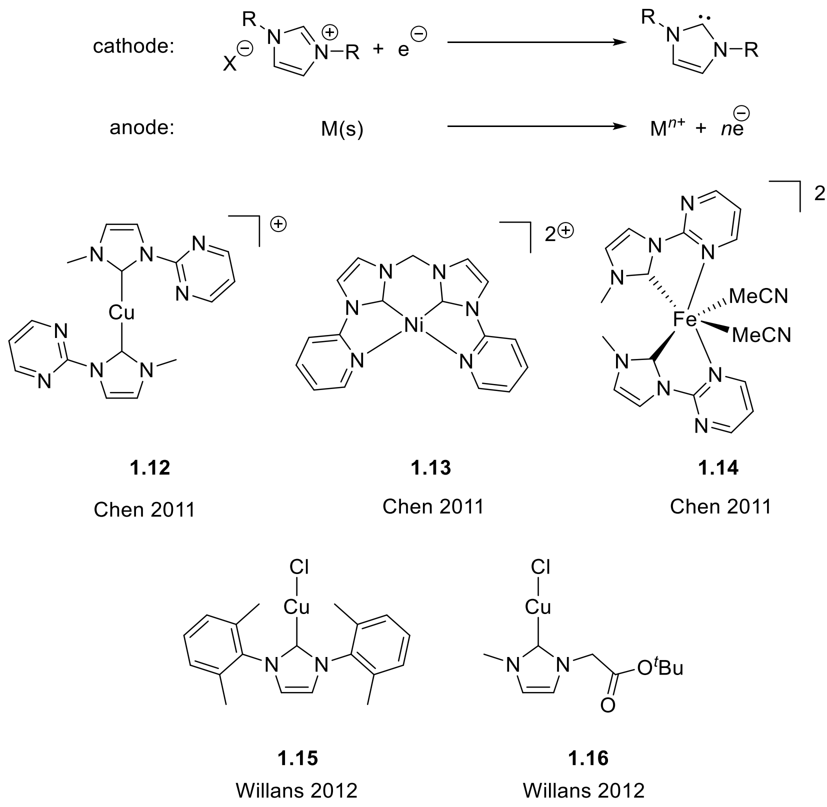

1.12 Chen 2011

1.13 Chen 2011

1.14 Chen 2011

1.15 Willans 2012

1.16 Willans 2012

Figure 150. NHC complexes prepared electrochemically reported by Chen and Willans.

1.2 Unusual NHC Architectures

The archetypal NHC is one that has been derived from an imidazolium salt, as in the first example reported by Arduengo (Preface - *1*).[37] This is the case, in spite of the fact that reports of NHCs with non-classical backbones began to be reported just a few years later. **1.17**, often called Enders carbene, was isolated as a stable crystalline substance in 1995, thus representing the first example of an NHC derived from a triazolium salt (Figure 151).[38] Enders carbene later became the first commercially available carbene.[39] The first example of an acyclic diamino carbene (**1.18**) was reported 1 year later, and 1 year after that the first NHC derived from a thiazolium salt was described (**1.19** - Figure 151).[40,41]

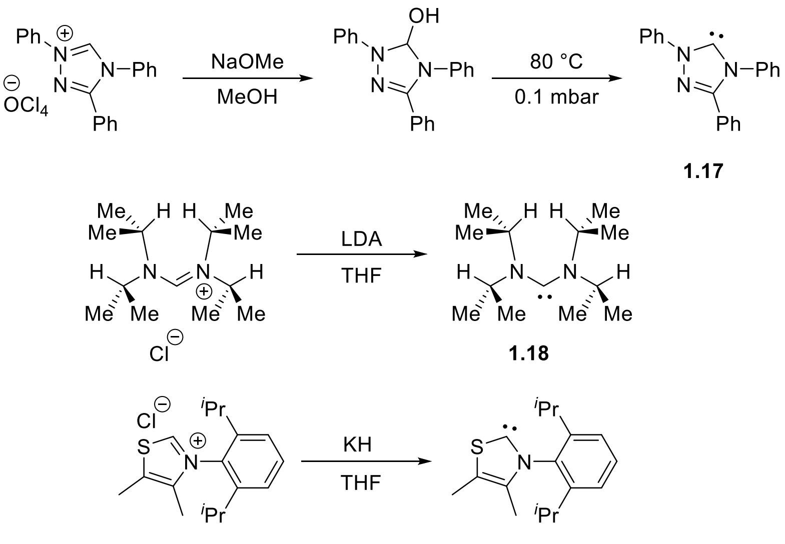

1.17

1.18

1.19

Figure 151. Synthesis of non-classical NHCs (**1.17**, and **1.18**) and acylic diamino carbene (**1.19**).[38,40,41]

These reports were followed by the serendipitous discovery of “abnormal” carbene binding, that is, the coordination of an imidazole ring through the C4/5 position, rather than the traditional C2 position (Figure 152). This binding was highly unexpected, and computational results suggested such a binding mode was more disfavoured than the expected C2 coordination.[42] However, it has proved possible to isolate a free abnormal carbene, by blocking the C2 position (Figure 152).[43] Abnormal carbenes have found numerous applications in catalytic reactions, with their success due in part at least to their strong σ-donor properties.[44,45]

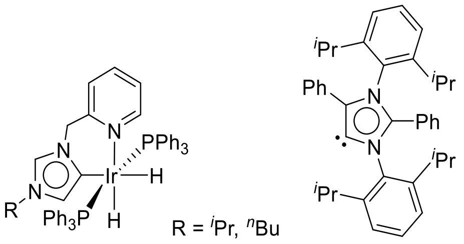

1.20

1.21

Figure 152. First example of abnormal carbene complex (**1.20**) and isolated free abnormal carbene (**1.21**).

Numerous NHC architectures have now been reported, with the synthesis and application of such species the subject of a number of recent reviews (Figure 153).[44–48] The main advantage of being able to vary the ring system of a carbene lies in the effect this has on the electronic behaviour of the system; the different classes of stable carbene have been found to have different donor properties. This has led to many examples of dramatic changes in catalytic activity, when differently structured, or differently coordinated NHCs are used.[44]

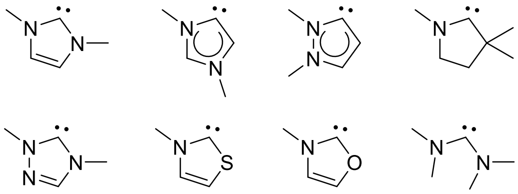

Figure 153. Examples of various NHCs.[44,49]

1.3 Methods for Electrochemical Synthesis

Two methods for the electrochemical synthesis of metal complexes have been used in the work described hence. Early reactions were carried out using a set-up established by previous group members, and used for all published examples of batch electrochemical synthesis by the Willans group.[36,50,51] During this study, an ElectraSyn 2.0 (IKA) was acquired, and this was also used for some reactions. A brief description of the two reaction set-ups is given below.

1.3.1 Power Supply

The basic requirement for an electrochemical reaction is the flow of current through a solution containing the necessary reagent and electrodes of the relevant metal. This was achieved by preparing a solution of the required ligand precursor in MeCN under an inert atmosphere in a 3-neck round bottom flask (Figure 154). The central neck of the 3-neck flask allows connection to a Schlenk line for supply of inert gas. The two side necks allow the electrodes to be inserted easily. Electrodes were cut from sheets of copper and were approximately 1 cm x 4 cm. The electrodes were attached to a benchtop power supply by crocodile clips, with the wire connection passing through a suba seal to allow for inert conditions. The flask was mounted over a stirrer plate to enable reaction mixing.

The power supply allows for the adjustment of the supplied voltage (up to 30 V), and provides a readout of the current generated. Reactions were generally run at 50 mA initially; adjustment of either the voltage or the distance between the electrodes was used to maintain this. Over time, it is generally observed in these reactions that the current falls, and reactions were stopped when a current no longer registered. The reactions can be monitored by removing aliquots of reaction mixture *via* syringe and submitting them to analysis by HRMS and/or ^{1}H NMR spectroscopy.

This method proved successful for the preparation of a range of Cu, Fe and Mn complexes, in spite of the lack of fine control afforded by the set-up.[36,51]

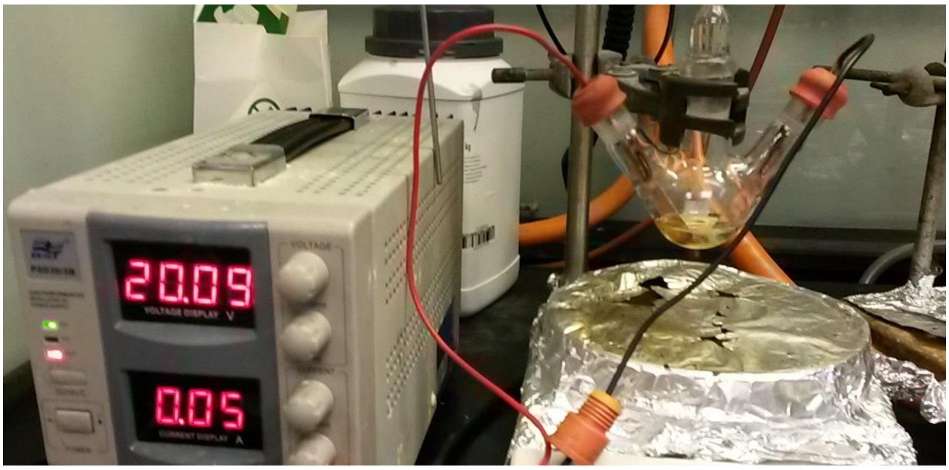

Figure 154. Power supply set-up for electrochemical reactions.

1.3.2 ElectraSyn

The ElectraSyn 2.0 is a piece of apparatus marketed by IKA. The device is made up of a base, which provides a stirring function and also supplies the electricity. The reactions are performed in vials (also supplied by IKA), with screw-caps into which the electrodes are fitted (Figure 155). The cap of the vial has external contacts which connect to the base and supply the electricity. At a base level this set-up is very similar to that used previously, however there are a number of key advantages. The screw-caps which the electrodes are attached to allow for 3 fixed interelectrodic distances (5, 10 and 15 mm). This means that if the same reaction is performed twice, the conditions can be replicated exactly; if the same concentration of electrolyte is used the resistance should be identical in both reactions. Additionally, the ElectraSyn allows reactions to be performed at a fixed voltage or current, again allowing better consistency between reactions. There is also the possibility of alternating the polarity of the electrodes during the reaction, a feature which can reduce electrode fouling.

The ElectraSyn has a maximum operating potential of 10 V, which is lower than that of the power supply, but still well over the potentials notionally required for electrochemical synthesis of NHC complexes.[52] It is possible to perform reactions under an inert atmosphere either by placing the whole apparatus in a glovebox, or by using a needle inserted through the septum at the top of the vial cap. This septum may also be used for sampling during the reaction.

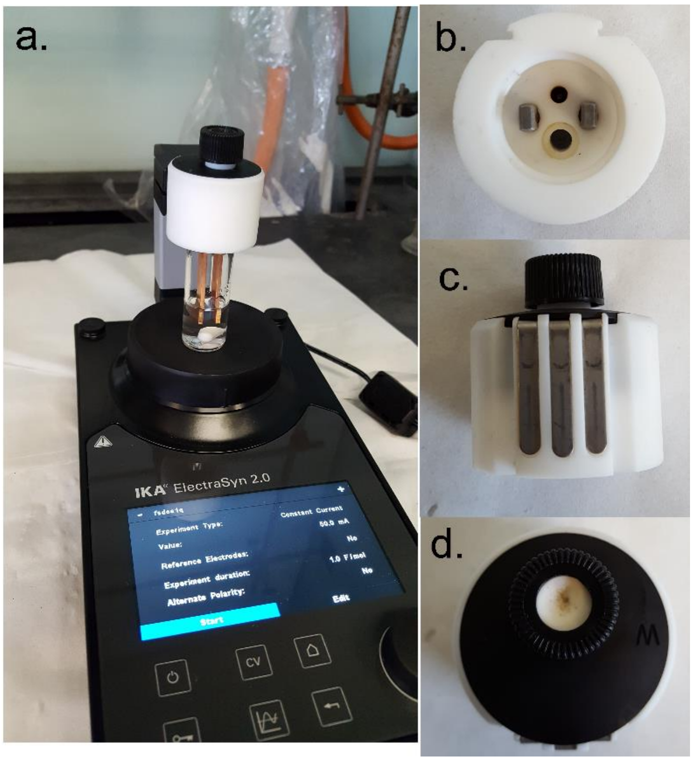
a.
b.
c.
d.
IKA ElectraSyn 2.0

Figure 155. a. ElectraSyn set-up for electrochemical reactions, b. electrode fittings in vial cap, c. electrical contacts on vial cap, d. septum on vial cap.

1.3.3 Electron Equivalents

Faraday's law can be used to calculate both the theoretical and actual quantity of charge needed for an electrochemical reaction. The theoretical value is dependent on the quantity of reducing species (i.e. ligand precursor), and the number of electrons transferred in this step (equation 2). Reduction of an imidazolium salt to form an NHC is a one-electron process, so *n*=1 for all reactions. The amount of charge that is used during a chemical reaction is the product of the current and the reaction time (equation 3). It is common practice within the group to discuss reactions in terms of number of "Q". In this case "Q" refers not to the quantity of charge used in an electrochemical reaction, but rather how many times more charge was passed than the theoretical required value (equation 4). Thus the number of Q reported for a reaction can be considered to be the number of equivalents of electrons. It is generally observed that an excess of charge is required to fully convert the starting material.

$(2)\ Q = nFN$

$(3)\ Q = It$

$Q = charge\ (C)$

$n = number\ of\ electrons$

$F = Faraday's\ constant\ (C\ mol^{-1})$

$N = number\ of\ moles\ (mol)$

$I = current\ (A)\ t = time\ (s)$

$(4)\ Q = \frac{Q_{actual}}{Q_{theoretical}}$

1.4 Aims

When considering applications of NHC complexes (in particular in catalysis), fine tuning of the ligand properties is of vital importance. Being able to prepare two ligands with identical steric properties, but different electronic properties is one of the abilities unique to the NHC-chemist. The utility of the electrochemical method for the preparation of NHC-complexes derived from imidazolium salts has been previously demonstrated. However, the application of the method to more structurally diverse NHC backbones has not been previously considered. Given the intrinsic variability in electronic and, potentially, steric properties, it is desirable to investigate the full extent of the reaction scope. This will create a toolbox, whereby a complex with ligands containing properties desirable for a certain application can be prepared electrochemically. This may be of particular value for ligand classes known to be more challenging to handle than traditional NHCs, such as thiazole and acyclic carbenes.[40,41]

The objective of this study was to expand the scope of the electrochemical method to include a diverse array of NHC architectures. Initial efforts will be directed towards 1,2,4-triazolium salts, with other ligand architectures (e.g. thiazolium, 1,2,3-triazolium, pyrazolium, ring-expanded nitrogen heterocycles, abnormal carbenes) to be considered subsequently. It was aimed to prepare a range of copper-NHC complexes derived from triazolium salts. Copper was selected as it is a low cost metal, and additionally should afford straightforward mono or bis-NHC products. Iron is also a low cost metal, however, in general NHCs with chelating substituents are used. Characterisation of iron complexes can also present a significant challenge as the presence of even a low concentration of paramagnetic impurities can lead to low quality NMR spectra. The prepared copper complexes will be isolated and characterised, to allow for confirmation of the effectiveness of the electrochemical method.

List of References

1 K. Chiba and Y. Okada, *Curr. Opin. Electrochem.*, 2017, **2**, 53–59.

2 H. Lehmkuhl and W. Eisenbach, *Justus Liebigs Ann. Chem.*, 1975, **1975**, 672–691.

3 J. J. Habeeb and D. G. Tuck, *J. Chem. Soc. Chem. Commun.*, 1975, **0**, 808–809.

4 J. J. Habeeb, D. G. Tuck and F. H. Walters, *J. Coord. Chem.*, 1978, **8**, 27–33.

5 N. Kumar and D. G. Tuck, *Can. J. Chem.*, 1982, **60**, 2579–2582.

6 J. J. Habeeb, F. F. Said and D. G. Tuck, *J. Chem. Soc. Dalton Trans.*, 1981, **0**, 118–120.

7 J. J. Habeeb, A. Osman and D. G. Tuck, *J. Chem. Soc. Chem. Commun.*, 1976, **0**, 379–380.

8 J. J. Habeeb, L. Neilson and D. G. Tuck, *Inorg. Chem.*, 1978, **17**, 306–310.

9 C. Geloso, R. Kumar, J. R. Lopez-Grado and D. G. Tuck, *Can. J. Chem.*, 1987, **65**, 928–932.

10 J. L. Hencher, M. Khan, F. F. Said, R. Sieler and D. G. Tuck, *Inorg. Chem.*, 1982, **21**, 2787–2791.

11 L. Matassa, N. Kumar and D. G. Tuck, *Inorganica Chim. Acta*, 1985, **109**, 19–21.

12 G. Jiansheng, Y. Yaxian, L. Baolong, Q. HuiFen and D. G. Tuck, *Synth. React. Inorg. Met. Chem.*, 1997, **27**, 1249–1259.

13 L. Bustos, J. H. Green, J. L. Hencher, M. A. Khan and D. G. Tuck, *Can. J. Chem.*, 1983, **61**, 2141–2146.

14 J. H. Green, R. Kumar, N. Seudeal and D. G. Tuck, *Inorg. Chem.*, 1989, **28**, 123–127.

15 T. A. Annan, C. Peppe and D. G. Tuck, *Can. J. Chem.*, 1990, **68**, 423–430.

16 T. A. Annan, J. E. Kickham and D. G. Tuck, *Can. J. Chem.*, 1991, **69**, 251–256.

17 H. E. Mabrouk, D. G. Tuck and M. A. Khan, *Inorganica Chim. Acta*, 1987, **129**, 75–80.

18 R. Kumar and D. G. Tuck, *Inorganica Chim. Acta*, 1989, **157**, 51–56.

19 T. A. Annan, R. Kumar and D. G. Tuck, *J. Chem. Soc., Chem. Commun.*, 1988, **0**, 446–448.

20 R. Kumar and D. G. Tuck, *J. Organomet. Chem.*, 1985, **281**, c47–c48.

21 A. M. Vecchio-Sadus, *J. Appl. Electrochem.*, 1993, **23**, 401–416.

22 M. C. Chakravorti and G. V. B. Subrahmanyam, *Coord. Chem. Rev.*, 1994, **135**–**136**, 65–92.

23 A. D. Garnovskii, L. M. Blanco, B. I. Kharisov, D. A. Garnovskii and A. S. Burlov, *J. Coord. Chem.*, 1999, **48**, 219–263.

24 A. Rodríguez and J. A. García-Vázquez, *Coord. Chem. Rev.*, 2015, **303**, 42–85.

25 M. J. Romero, R. Pedrido, A. M. González-Noya, M. Maneiro, M. I. Fernández-García, G. Zaragoza and M. R. Bermejo, *Dalton Trans.*, 2012, **41**, 10832–10844.

26 M. R. Bermejo, A. M. González, M. Fondo, A. García-Deibe, M. Maneiro, J. Sanmartín, O. L. Hoyos and M. Watkinson, *New J. Chem.*, 2000, **24**, 235–241.

27 M. R. Bermejo, R. Pedrido, A. M. González-Noya, M. J. Romero, M. Vázquez and L. Sorace, *New J. Chem.*, 2003, **27**, 1753–1759.

28 D. G. Tuck, *Pure Appl. Chem.*, 1979, **51**, 2005–2018.

29 J. J. Habeeb and D. G. Tuck, *J. Organomet. Chem.*, 1977, **134**, 363–379.

30 J. J. Habeeb and D. G. Tuck, *J. Organomet. Chem.*, 1977, **139**, C17–C20.

31 W. M. Haynes, *CRC Handbook of Chemistry and Physics 97th Edition*, CRC

Press/Taylor & Francis, Boca Raton, FL., 97th edn., 2017.

32 A. T. Casey and A. M. Vecchio, *Appl. Organomet. Chem.*, 1990, **4**, 513–522.

33 D. G. Yakhvarov, D. I. Tazeev, O. G. Sinyashin, G. Giambastiani, C. Bianchini, A. M. Segarra, P. Lönnecke and E. Hey-Hawkins, *Polyhedron*, 2006, **25**, 1607–1612.

34 D. G. Yakhvarov, A. Petr, V. Kataev, B. Büchner, S. Gómez-Ruiz, E. Hey-Hawkins, S. V. Kvashennikova, Y. S. Ganushevich, V. I. Morozov and O. G. Sinyashin, *J. Organomet. Chem.*, 2014, **750**, 59–64.

35 B. Liu, Y. Zhang, D. Xu and W. Chen, *Chem. Commun.*, 2011, **47**, 2883–2885.

36 B. R. M. Lake, E. K. Bullough, T. J. Williams, A. C. Whitwood, M. A. Little and C. E. Willans, *Chem. Commun.*, 2012, **48**, 4887–4889.

37 A. J. Arduengo, R. L. Harlow and M. Kline, *J. Am. Chem. Soc.*, 1991, **113**, 361–363.

38 D. Enders, K. Breuer, G. Raabe, J. Runsink, J. H. Teles, J.-P. Melder, K. Ebel and S. Brode, *Angew. Chemie Int. Ed.*, 1995, **34**, 1021–1023.

39 D. Bourissou, O. Guerret, F. P. Gabbaï and G. Bertrand, *Chem. Rev.*, 2000, **100**, 39–91.

40 R. W. Alder, P. R. Allen, M. Murray and A. G. Orpen, *Angew. Chemie Int. Ed.*, 1996, **35**, 1121–1123.

41 A. J. Arduengo, J. R. Goerlich and W. J. Marshall, *Liebigs Ann.*, 1997, **1997**, 365–374.

42 S. Gründemann, A. Kovacevic, M. Albrecht, J. W. Faller Robert and H. Crabtree, *Chem. Commun.*, 2001, **103**, 2274–2275.

43 E. Aldeco-Perez, A. J. Rosenthal, B. Donnadieu, P. Parameswaran, G. Frenking and G. Bertrand, *Science (80-.).*, 2009, **326**, 556–559.

44 O. Schuster, L. Yang, H. G. Raubenheimer and M. Albrecht, *Chem. Rev.*, 2009, **109**, 3445–3478.

45 R. H. Crabtree, *Coord. Chem. Rev.*, 2013, 257, 755–766.

46 J. Vignolle, X. Cattoën and D. Bourissou, *Chem. Rev.*, 2009, **109**, 3333–3384.

47 M. Soleilhavoup and G. Bertrand, *Acc. Chem. Res.*, 2015, **48**, 256–266.

48 Á. Vivancos, C. Segarra and M. Albrecht, *Chem. Rev.*, 2018, **118**, 9493–9586.

49 D. J. Nelson and S. P. Nolan, *Chem. Soc. Rev.*, 2013, **42**, 6723–6753.

50 E. K. Bullough, M. A. Little and C. E. Willans, *Organometallics*, 2013, **32**, 570–577.

51 M. R. Chapman, S. E. Henkelis, N. Kapur, B. N. Nguyen and C. E. Willans, *ChemistryOpen*, 2016, **5**, 351–356.

52 M. R. Chapman, *A Versatile Electrochemical Protocol for the Synthesis of Transition Metal Complexes*, University of Leeds, 2016.

Chapter 2

Investigation into the electrochemical synthesis of copper-NHC complexes derived from triazolium salts

This chapter describes electrochemical reactions using triazolium salts and copper electrodes, to prepare novel complexes. Chemical synthesis of novel copper complexes has also been performed. An unexpected ring-opening reaction leading to the formation of a diimine ligand was observed during electrochemical synthesis. The scope of this reaction was explored through the synthesis of a range of triazolium salts. Investigations into related ring-opening reactions have also been carried out.

2.1 Introduction

Electrochemical synthesis is an effective strategy for the preparation of a range of NHC complexes (Chapter 1 - *1.1.3*).[1,2] Thus far, NHCs which are derived from imidazolium salts have been prepared, but the method has not been demonstrated for non-classical NHC architectures. Given the scope of such architectures and their broad applicability to catalytic reactions, it is desirable to extend the method to include these structures.[3]

2.2 Reactions of Copper with Triazolium 1

Triazolium salts were selected as an initial target in the investigation into broadening the applicability of the electrochemical method. To this end **Tz1.BF$_4$**, and **Tz1.Cl** were obtained from Dr Andrew Smith (University of St Andrews) (Figure 156). Triazolium salts of this general structure, and in particular chiral derivatives thereof, are successful organocatalysts for Umpolung type reactions.[4] **Tz1.BF$_4$** and **Tz1.Cl** complement one another, in the sense that both mono and bis-NHC Cu complexes are expected to be accessible *via* the electrochemical method.

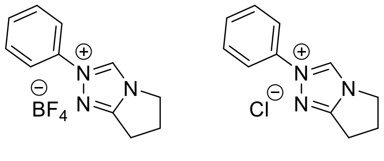
Tz1.BF$_4$ **Tz1.Cl**

Figure 156. Structure of triazolium salts **Tz1.BF$_4$** and **Tz1.Cl**.

2.2.1 Chemical Reaction of Copper with Triazolium 1

An electrochemical reaction using **Tz1.BF$_4$** is expected to produce bis-NHC complex **Cu1a.BF$_4$**, as the tetrafluoroborate counter-ion is non-coordinating (Figure 157).[2] As an initial test, efforts were made to synthesise **Cu1a.BF$_4$** by chemical means. This was achieved by reaction of **Tz1.BF$_4$** with K^{t}BuO in the presence of [Cu(MeCN)$_4$][BF$_4$] (Figure 157).

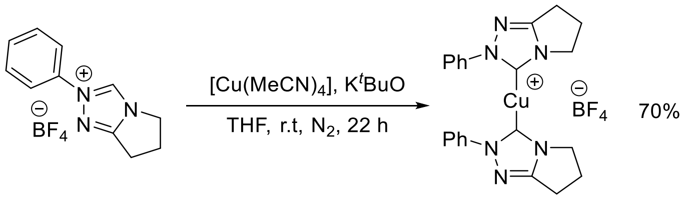

Tz1.BF$_4$ **Cu1a.BF$_4$**

Figure 157. Chemical synthesis of **Cu1a.BF$_4$** from **Tz1.BF$_4$**.

NMR spectroscopy can be used to determine the outcome of the reaction (Figure 158). The ^{1}H NMR spectrum of the product shows the clear absence of the NC*H*N proton signal, as well as a variation in the chemical shift for other resonances. This provides evidence that complexation has occurred, although whether a mono or bis-NHC complex has been formed cannot be determined by this method. Small signals corresponding to unreacted **Tz1.BF$_4$** are also apparent in the ^{1}H NMR spectrum, indicating incomplete conversion. A comparison of peak integrals suggests ~2% of the isolated material obtained is **Tz1.BF$_4$**.

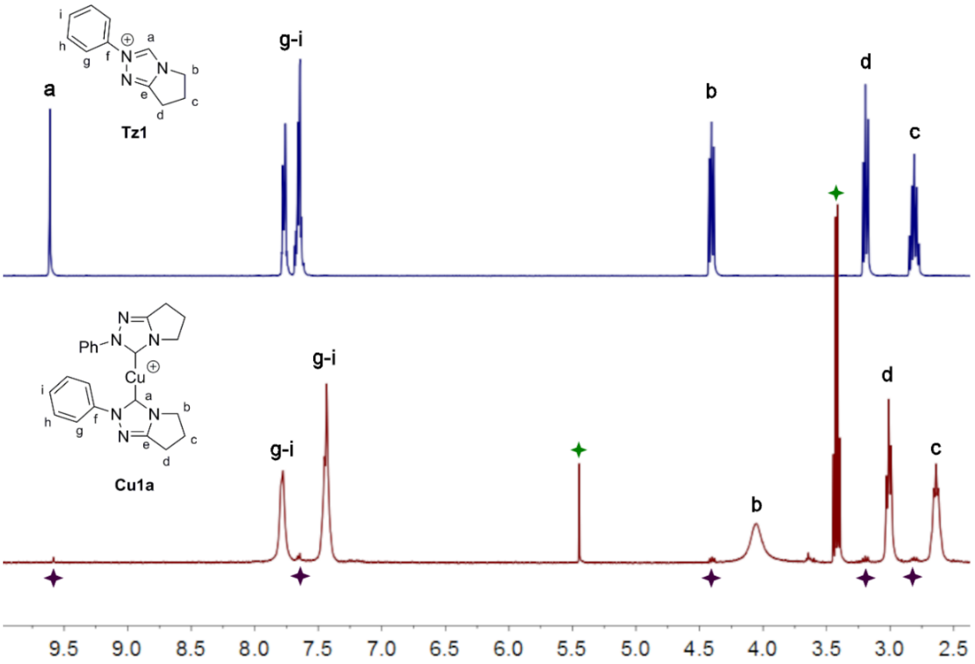

Figure 158. ^{1}H NMR spectra (400 MHz, CD$_3$CN). Top: **Tz1.BF$_4$**. Bottom: **Cu1a.BF$_4$**, purple stars denote presence of **Tz1.BF$_4$**, green stars denote residual solvent (DCM and Et$_2$O).

The HRMS data corroborate the ^{1}H NMR data, with a major ion peak at *m/z* 433, with an associated peak at *m/z* 435, corresponding to [M-BF$_4$]$^+$ for **Cu1a.BF$_4$**. Two major peaks are seen in the ion envelope due to the two stable isotopes of copper, ^{63}Cu and ^{65}Cu, which are 69.2% and 30.8% abundant respectively.[5] An ion peak at *m/z*

186 corresponds to $[M-BF_4]^+$ for **Tz1.BF₄**. Care must be taken when analysing HRMS data for Cu-NHC complexes as ligand scrambling between mono and bis NHC complexes is a known phenomenon.[6,7]

Attempts were made to purify **Cu1a.BF₄** by washing and recrystallisation, however these were unsuccessful. It is unsurprising that **Tz1.BF₄** and **Cu1a.BF₄** prove inseparable due to their similar polarities. The use of other separation techniques such as column chromatography or reverse-phase HPLC is precluded by the likely air and moisture sensitivity of **Cu1a.BF₄**. Separation could be achieved on a small scale by growth of single crystals - however this is an operationally impractical technique to procure a workable quantity of compound. Multiple attempts to drive the reaction to completion by modification of reaction stoichiometry were also unsuccessful.

Nonetheless, single crystals suitable for X-Ray diffraction of **Cu1a.BF₄** were grown by the slow diffusion of Et_2O into a concentrated solution of the product mixture in MeCN. The complex crystallised in the monoclinic crystal system and was solved in the *I*2/*a* space group. The structure reveals **Cu1a.BF₄** to be a 14 electron Cu(I) complex (Figure 159). The complex displays perfectly linear geometry at the Cu centre, revealed by the asymmetric unit containing half a complex. The unit cell contains four Cu centres.

The Cu(1)-C(1) bond length is within the range usually expected for bis-NHC Cu(I) complexes as has been found for triazolium-based NHC-Cu complexes previously (Table 17).[8,9] Likewise, the C-N bond lengths are similar to those found within standard NHCs. They are however significantly longer than for a non-metallated triazolium salt.[10] The N-N bond length indicates it is a true single bond, suggesting limited π-delocalisation about the ring.[11] The two fused 5-membered rings are co-planar, whilst the phenyl ring lies in a plane at an angle of 36.5 ° relative to the plane of the rest of the ligand. This may be derived from intermolecular π-π stacking interactions which are observed between the phenyl and triazole rings in the bulk crystal.

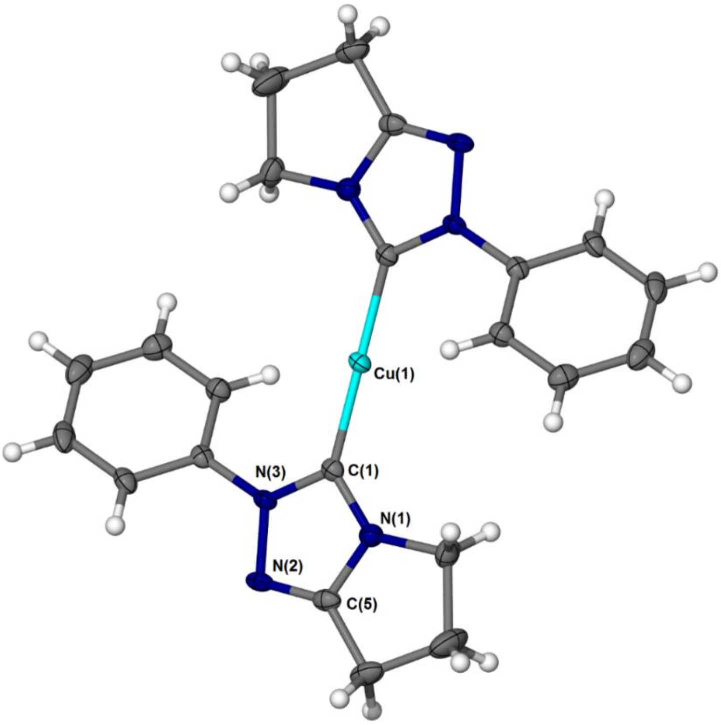

Figure 159. Molecular structure for **Cu1a.BF$_4$**. Ellipsoids are shown at the 50% probability level. One $[BF_4]^-$ counter-ion is omitted for clarity. Hydrogen atoms added in calculated positions and refined using the riding model.

Table 17. Selected bond lengths and angles for **Cu1a.BF$_4$**.

Bond	Distance / Å	Angle	/ °
Cu(1)-C(1)	1.8969(16)	N(1)-C(1)-Cu(1)	130.46 (12)
C(1)-N(1)	1.351 (2)	N(3)-C(1)-Cu(1)	127.97(12)
C(1)-N(3)	1.353 (2)	N(3)-C(1)-N(1)	101.44(13)
N(2)-N(3)	1.3968(18)		

2.2.2 Electrochemical Reaction with Triazolium 1

Given the promising results obtained for chemical synthesis using **Tz1.BF$_4$**, an electrochemical reaction was performed. This was performed in a 3-neck round-bottom flask, using Cu electrodes connected to a power pack. The reaction was performed in MeCN, at room temperature, with a current range of 10-50 mA maintained (Figure 160).

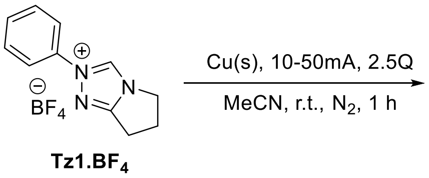

Tz1.BF$_4$

Figure 160. Scheme showing electrochemical reaction with **Tz1.BF$_4$**.

The reaction progress was monitored by HRMS, which indicated the formation of **Cu1a.BF₄**. Over time however the signal at *m/z* 433 (indicative of **Cu1a.BF₄**) decreased in comparison to signals at *m/z* 435 and 437. The isotope envelope of these signals clearly corresponds to a species containing one Cu centre. Attempts were made to drive the reaction to the formation of just one species, however these were curtailed by a loss of current in the reaction vessel over time. This potentially occurs due to a loss of electrolyte as the starting material is consumed.

The ^{1}H NMR spectrum of the product provides some insight into the nature of the product formed (Figure 161). The first key observation is the absence of a NC*H*N resonance, which is indicative of carbene formation. However, for each presumed proton environment, two resonances are observed. Half of these are attributable to **Cu1a.BF₄**. The peak area of the second set of signals (purple stars - Figure 161) corresponds to approximately half that of the resonances corresponding to **Cu1a.BF₄**. In addition to the presence of twice the number of expected CH_2 and aromatic resonances, there are two singlets observed at 8.49 and 8.08 ppm (blue stars - Figure 161), which have an integral ratio of 1 as compared to the secondary CH_2 signals. The origin of these is not immediately obvious, but the presence of two further proton environments does correlate well with the *m/z* 435 signal in the HRMS, which is two mass units heavier than the signal for **Cu1a.BF₄**.

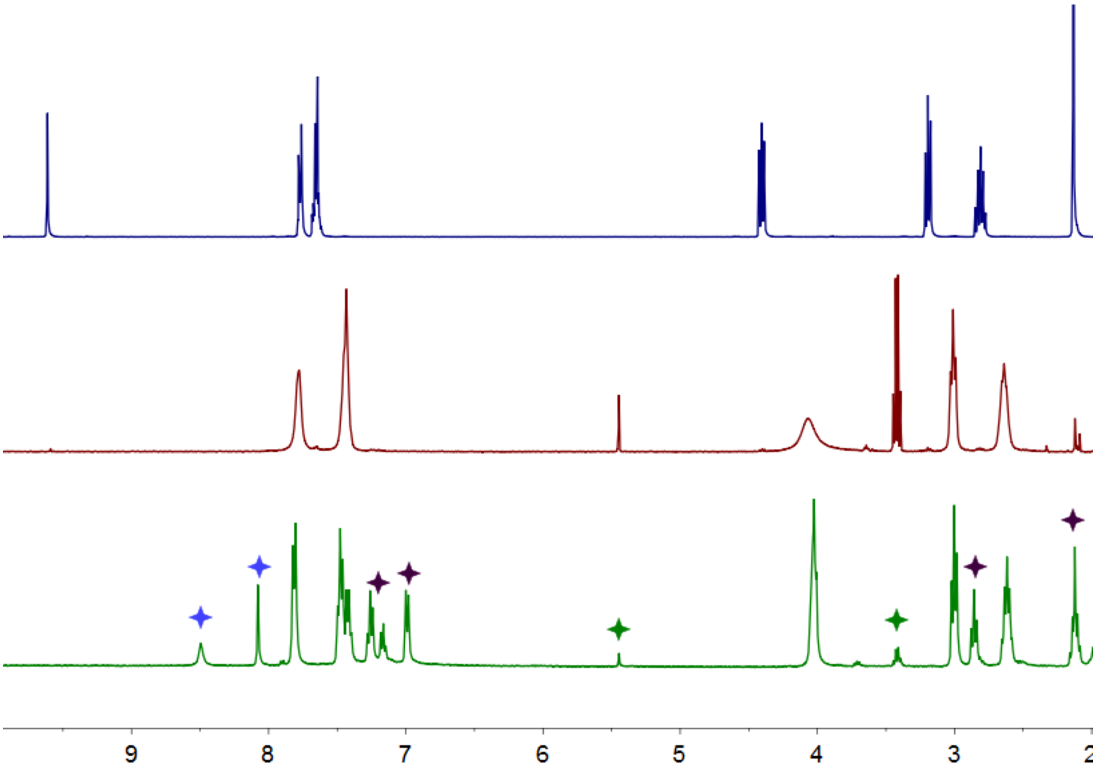

Figure 161. ^{1}H NMR spectra (400 MHz, CD_3CN). Top: **Tz1.BF₄**. Middle: **Cu1a.BF₄**. Bottom: product of electrochemical reaction using **Tz1.BF₄**. Purple stars denote new CH_2 and aromatic signals, blue stars denote new signals, green stars denote residual solvent (DCM and Et_2O).

The identity of the second species was determined by X-Ray crystallography. Single crystals were obtained by the vapour diffusion of Et_2O into a concentrated solution of the product mixture in MeCN. The structure of the second product, **Cu1b.BF$_4$**, is revealed to be an unusual Cu-NHC complex in which one of the ligands has undergone a ring-opening reaction, to produce a diimine ligand (Figure 162). **Cu1b.BF$_4$** crystallises in the triclinic crystal system and was solved in the $P\overline{1}$ space group. The structure is a 16 electron complex that displays a distorted trigonal planar coordination geometry. **Cu1a.BF$_4$** displays perfect planarity between both ligands, however, in **Cu1b.BF$_4$** the two ligands are almost perpendicular (85.8 °- interplanar angle) to one another. This distortion is presumably to avoid steric clashes between the phenyl and cyclopentyl rings. The Cu-NHC bond lengths are similar for **Cu1a.BF$_4$** and **Cu1b.BF$_4$** (Table 18). The C-N bond lengths in the ring-opened ligand (N(5)-C(16) and N(6)-C(12)) are indicative of double bond character, confirming the structure as a neutral donor.[11] The twist angle of the phenyl ring varies between **Cu1a.BF$_4$**, the NHC in **Cu1b.BF$_4$** and the diimine in **Cu1b.BF$_4$**. In **Cu1a.BF$_4$** the twist is 36.5 °, whilst the phenyl ring on the NHC of **Cu1b.BF$_4$** lies almost coplanar to the rest of the ligand, with a twist of just 4.5 °. In the diimine ligand, the angle is 24.1 °. Additionally, the cyclopentyl ring adopts an envelope conformation (31.5 ° out of plane), possibly derived from the absence of annulation to another ring system. This is in contrast to the planar geometry observed for the NHC ligands in both **Cu1a.BF$_4$** and **Cu1b.BF$_4$**.

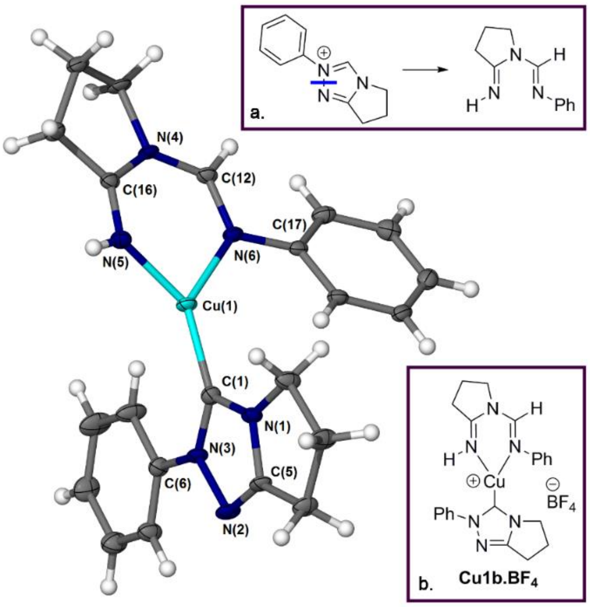

Figure 162. Molecular structure of **Cu1b.BF$_4$**. Ellipsoids are shown at the 50% probability level. One $[BF_4]^-$ counter-ion is omitted for clarity. Hydrogen atoms added in calculated positions and refined using the riding model. Inset: a. nitrogen-nitrogen bond cleavage resulting in diimine ligand; b. structure of **Cu1b.BF$_4$**.

Table 18. Selected bond lengths and angles for **Cu1b.BF$_4$**.

Bond	Distance / Å	Angle	/ °
Cu(1)-C(1)	1.886(2)	C(1)-Cu(1)-N(5)	137.86(10)
Cu(1)-N(5)	1.937(2)	C(1)-Cu(1)-N(6)	129.31(10)
Cu(1)-N(6)	2.046(2)	N(5)-Cu(1)-N(6)	92.64(9)
N(5)-C(16)	1.279(3)		
N(6)-C(12)	1.291(3)		

Upon exposure to air, the solution containing crystals of **Cu1b.BF$_4$** formed new crystals of a different species. **Cu1b'.BF$_4$** results from oxidation of **Cu1b.BF$_4$** from Cu(I) to Cu(II) with the replacement of the NHC ligand with a hydroxyl ligand (Figure 163). **Cu1b'.BF$_4$** crystallised in the tetragonal system and was solved in the *P*4$_2$/*n* space group.

The asymmetric unit shows an unusual "T-shaped" Cu(II) 15 electron complex. The unit cell however reveals a Cu$_4$O$_4$ distorted cube, in which the geometry at each Cu centre is a square based pyramid. Structures of this type are have been reported previously, and are of interest due to their magnetic properties.[12–14] The Cu-N distances remain similar on conversion from **Cu1b.BF$_4$** to **Cu1b'.BF$_4$**, with a slight decrease in the Cu-N(Ph) distance which is outside experimental error (Table 19). The Cu-OH distance of 1.955 Å is typical for Cu(II) complexes with bridging hydroxyl ligands.[15–18] The twist of the phenyl ring undergoes a dramatic change, now lying near perpendicular to the rest of the ligand (88 °). The envelope conformation of the cyclopentyl ring is retained.

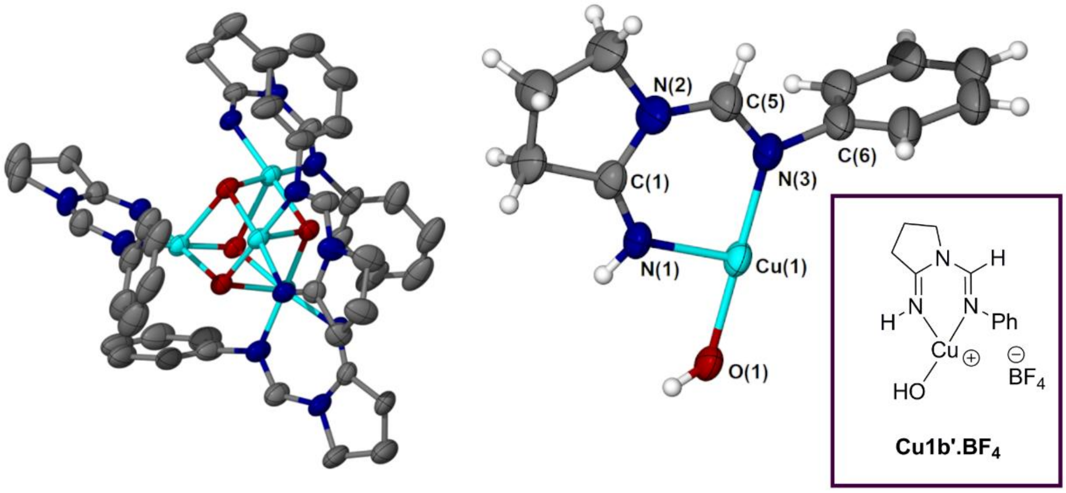

Figure 163. Molecular structure for **Cu1b'.BF$_4$**. Ellipsoids are shown at the 40% probability level. Left: Unit cell structure showing Cu$_4$O$_4$ cube. Hydrogen atoms and four [BF$_4$]$^-$ counter ions have been omitted for clarity. Right: Asymmetric unit. One [BF$_4$]$^-$ counter-ion omitted for clarity. Hydrogen atoms added in calculated positions and refined using the riding model.

Table 19. Selected bond lengths and angles for **Cu1b'.BF$_4$**

Bond	Distance / Å	Angle	/ °
Cu(1)-N(1)	1.944(3)	N(1)-Cu(1)-O(1)	90.92(14)
Cu(1)-N(3)	1.987(4)	O(1)-Cu(1)-N(3)	178.90(16)
Cu(1)-O(1)	1.955(3)	N(1)-Cu(1)-N(3)	89.76(15)
Cu(1)-O(1)^1	1.954(3)	O(1)-Cu(1)-O(1)^1	84.28(13)
Cu(1)-O(1)^2	2.359(3)	O(1)-Cu(1)-O(1)^2	84.14(13)
		O(1)^1-Cu(1)-O(1)^2	74.24(11)

1: 3/2-Y,+X,1/2-Z; 2: 3/2-X, 3/2-Y,+Z

When the packed structure of **Cu1b'.BF$_4$** is viewed down the crystallographic C-axis, channels can be observed (Figure 164). The channels are approximately 6 Å across. These channels contained cocrystallised MeCN, which could not be explicitly modelled during structure solution. For this reason the Squeeze routine from Platon was used. It was determined that there were 138 electrons unaccounted for by the complex per unit cell, corresponding to approximately 6 molecules of MeCN per molecule.

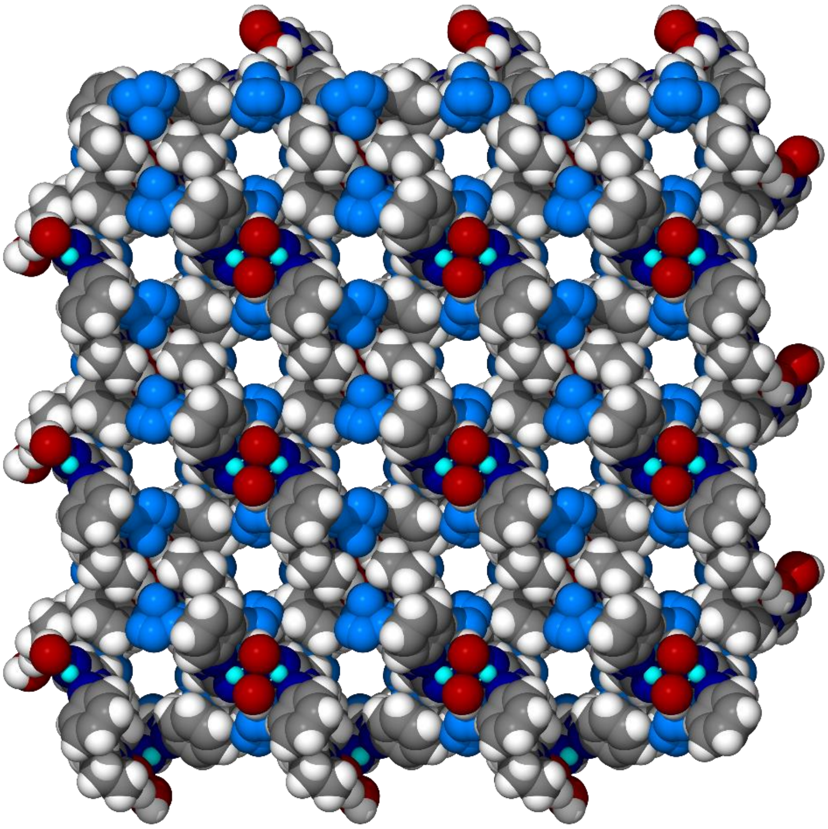

Figure 164. Space-filled model showing crystal packing of **Cu1b'.BF$_4$** viewed along the crystallographic C-axis.

The NMR and HRMS data for the product mixture from the electrochemical reaction of **Tz1.BF$_4$** may now be re-examined with the structure of **Cu1b.BF$_4$** in mind. The signal observed at *m/z* 435 in the HRMS corresponds to the molecular ion peak for [**Cu1b.BF$_4$**-BF$_4$]$^+$. The peak at *m/z* 437 (some of which is attributable to the ^{65}Cu isotope) could be due to the formation of **Cu1c.BF$_4$**, in the case of coordination by two imine ligands (Figure 165).

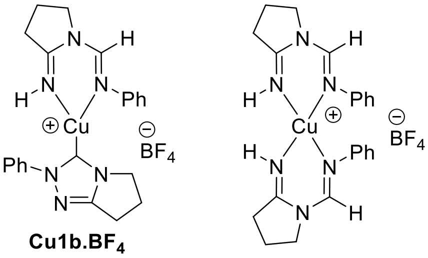

Cu1b.BF$_4$ **Cu1c.BF$_4$**

m/z 435 [M-BF$_4$]$^+$ *m/z* 437 [M-BF$_4$]$^+$

Figure 165. Structure of **Cu1b.BF$_4$** and complex **Cu1c.BF$_4$** with associated molecular ion peaks.

However, when direct injection HRMS was used to minimise ligand scrambling, there was no evidence for the presence of **Cu1c.BF$_4$** (2.7.5). This finding allows for the full analysis of the ^{1}H NMR spectrum (Figure 166). The ratio of integrals for NHC ligand peaks compared with imine ligand peaks is not 1 to 1, as would be expected for a pure sample of **Cu1b.BF$_4$**. Therefore it can be concluded that the sample contains a mixture of **Cu1a.BF$_4$** and **Cu1b.BF$_4$**. It is notable, and perhaps surprising that the NHC resonances for **Cu1a.BF$_4$** and **Cu1b.BF$_4$** appear at the same chemical shift. The NHC peak positions are shifted slightly relative to pure **Cu1a.BF$_4$**, and are also markedly sharper in the spectrum for **Cu1a.BF$_4$/Cu1b.BF$_4$** (Figure 161). The appearance of the NHC signals at the same chemical shift could be an indication that dynamic exchange occurs in solution, however, the peaks would be expected to be broader in this case.

The integral ratio of NHC signals to imine signals is approximately 2:1. This corresponds to a ratio of 1:2 for **Cu1a.BF$_4$** to **Cu1b.BF$_4$**. This ratio was found to be broadly replicable over two independent experiments.

It is worth noting that when the product mixture was allowed to crystallise, single crystals of **Cu1a.BF$_4$**, **Cu1b.BF$_4$**, and [Cu(MeCN)$_4$][BF$_4$] were all found. No crystals of proposed compound **Cu1c.BF$_4$** were ever observed.

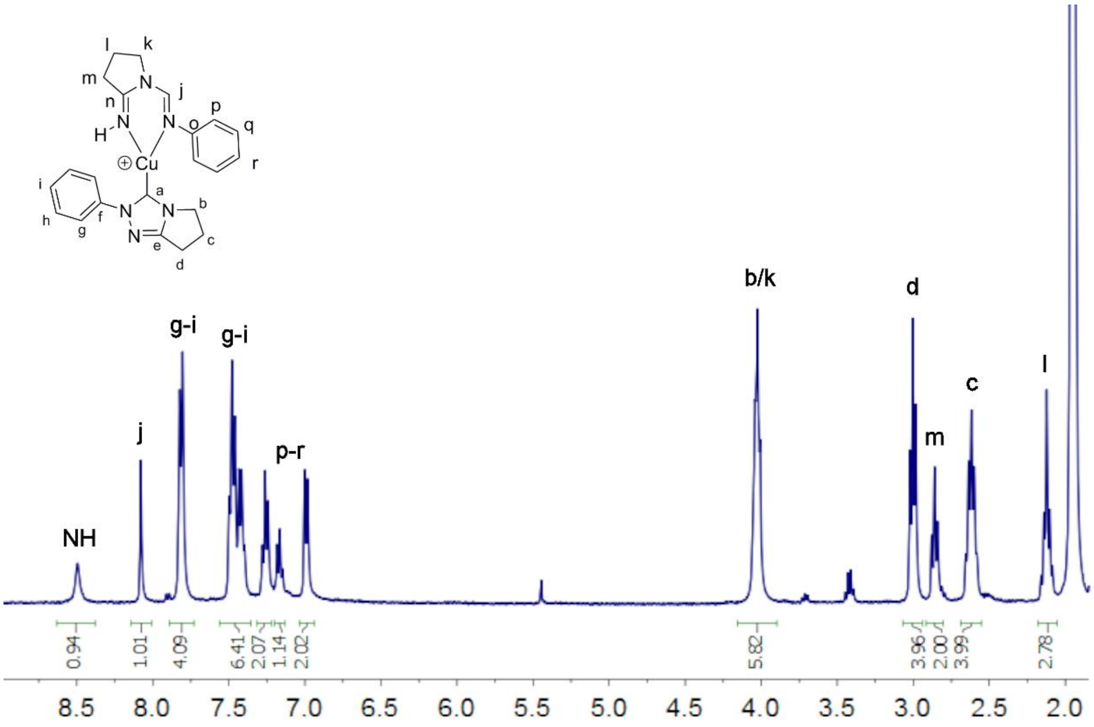

Figure 166. ^{1}H NMR spectrum (400 MHz, CD_3CN) for **Cu1a.BF$_4$/Cu1b.BF$_4$**. Integrals shown relative to 2 for CH_2 signal labelled “m”.

These findings were corroborated by the powder X-Ray diffraction data obtained on the bulk sample. Peaks were observed in the powder pattern that correlate well with those observed for both **Cu1a.BF$_4$** and **Cu1b.BF$_4$** (Figure 167).

The sum of the data therefore point toward the formation of a mixture of two Cu complexes **Cu1a.BF$_4$** and **Cu1b.BF$_4$** under electrochemical conditions.

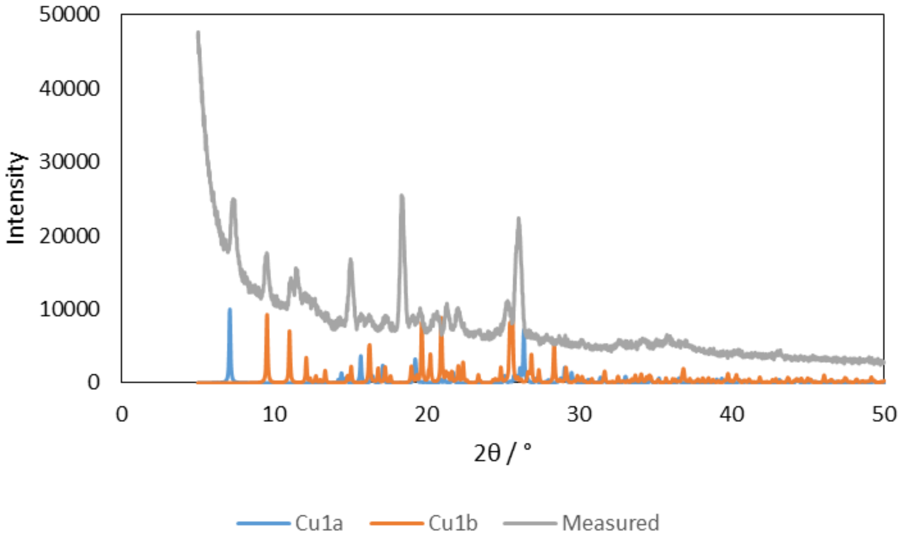

Figure 167. Comparison of simulated XRD powder pattern for **Cu1a.BF$_4$** and **Cu1b.BF$_4$** with measured sample of **Cu1a.BF$_4$/Cu1b.BF$_4$** mixture.

The formation of the diimine species is unexpected, and several key questions must be considered. Firstly, the question of why the ring-opening reaction occurs, and what is its mechanism. Given the successful synthesis of **Cu1a.BF₄** by chemical means, it is clear that the ring-opening is an electrochemical effect. A related question is what the scope of the ring-opening reaction is.

If the conversion of **Tz1.BF₄** into the diimine species is considered in isolation, a two electron reduction is required to form the product (Figure 168). Starting from **Tz1.BF₄** the transformation can be viewed as a formal addition of H^-, or alternatively, a two electron reduction and addition of H^+. If the NHC is formed prior to ring-opening then formal addition of H_2 is required. This still constitutes a two electron reduction however, completed by the supply of two protons. Given that the reaction occurs under electrochemical conditions, it is likely that a radical mechanism will be in operation.

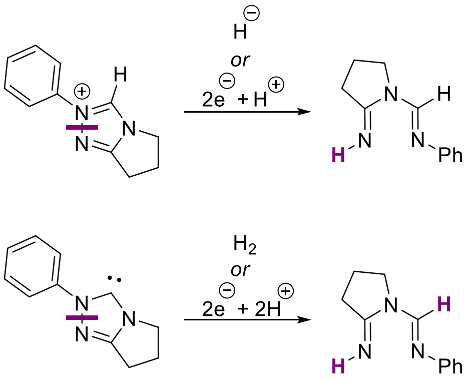

Figure 168. Schematic indicating formal reactivity of **Tz1.BF₄** or the NHC derived from **Tz1.BF₄** to form the diimine.

Whilst the reductive cleavage of N-N single bonds by chemical means is well-established, electrochemical reduction is less common (Figure 169).[19,20] The most common chemical method relies on dissolving metal conditions (e.g. sodium in liquid ammonia) to effect the reduction, combined with an aqueous proton source.[20–23] Other methods include hydrogenation using a metal catalyst such as Raney nickel or platinum, or the use of boron hydrides.[19–21,23,24]

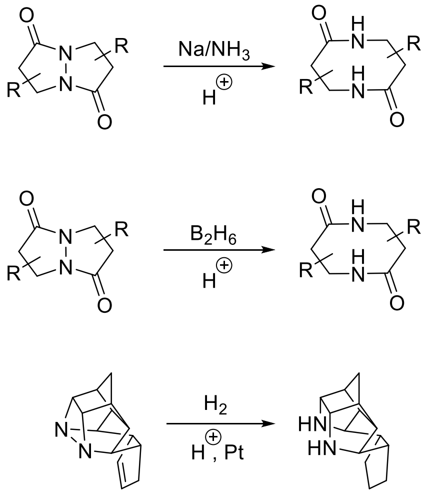
Na/NH$_3$
H$^\oplus$
B$_2$H$_6$
H$^\oplus$
H$_2$
H$^\oplus$, Pt
R
O
N
HN
HN

Figure 169. Examples of chemical reductive N-N bond cleavage.[21,24]

Hydrazides have been reduced to amides electrochemically, using a mercury pool or tin cathode (Figure 170).[23,25] Pyradizines can be electrochemically reduced, forming pyrroles after ring-contraction (Figure 170).[26] Although electrochemical cleavage of N-N bonds is known, the paucity of literature examples makes it difficult to draw comparisons with this work.

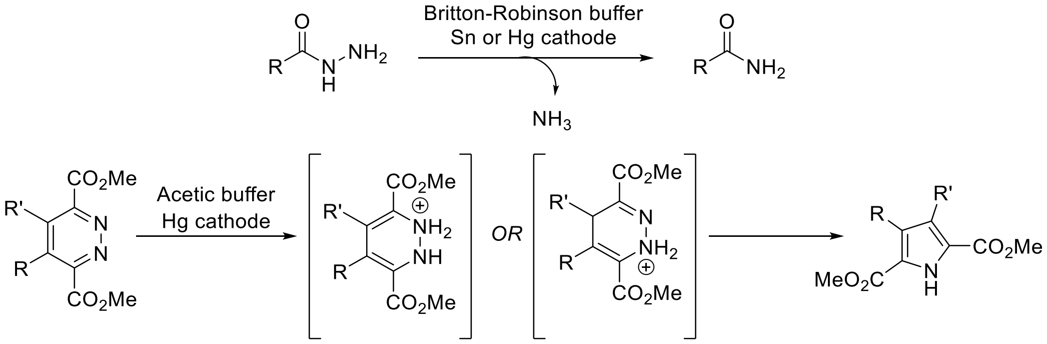
Britton-Robinson buffer
Sn or Hg cathode
NH$_3$
Acetic buffer
Hg cathode
OR
CO$_2$Me
MeO$_2$C
NH$_2$
R
R'

Figure 170. Examples of electrochemical reductive N-N bond cleavage.[23,25,26]

This chapter focusses on investigations into the scope of the observed ring-opening reaction, as well as synthetic preparation of complexes to allow mechanistic study. Known and related ring-opening reactions are also investigated. The bulk of the mechanistic investigation is described in Chapter 3.

2.3 Scope of the Ring-Opening Reaction

With a view to investigating the scope of the ring-opening reaction, a range of structurally diverse triazolium salts were prepared.

2.3.1 Synthesis of Triazolium 2

The structure of **Tz2.BF₄** is very different to that of **Tz1.BF₄**. As the nitrogen substituents of **Tz2.BF₄** bears non-conjugated aromatic groups. By contrast **Tz1.BF₄** features one conjugated aryl group and one fully aliphatic ring (Figure 171).

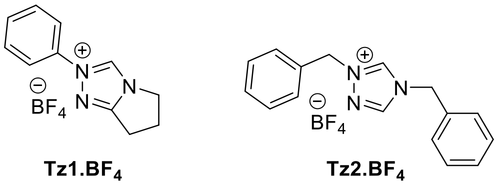

Figure 171. Structure of **Tz1.BF₄** and **Tz2.BF₄**.

This structural divergence is expected to provide very different electronic and steric properties, and hence prove a good probe for the generality of the ring-opening observed with **Tz1.BF₄**. The synthesis of **Tz2.BF₄** can be achieved in 3 steps (Figure 172). Reaction of benzyl bromide with 4-amino-triazole introduces the first benzyl group, in a one-pot procedure described by Scriven *et al.*[27] The presence of an amino group in the 4-position blocks this position from alkylation, whilst additionally activating the 1-position. The amino group can be removed *via* deamination using nitrous acid formed *in situ* from HCl and $NaNO_2$. A second benzyl substituent is introduced by reaction of the 1-benzyl-1,2-4-triazole with a slight excess of benzyl bromide in refluxing MeCN. The tetrafluoroborate salt can be prepared from the bromide salt using a salt metathesis reaction with excess NH_4BF_4 under aqueous conditions.

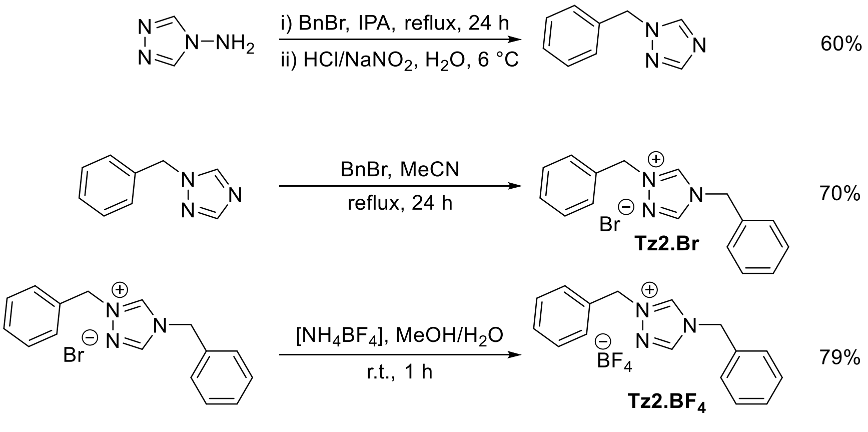

Figure 172. Synthetic route to **Tz2.BF₄**.

The NMR spectroscopic and HRMS data are as expected for the above compounds. There is a slight upfield shift observed for the two heterocyclic proton signals in the

^{1}H NMR from 10.32 and 9.33 ppm to 10.24 and 9.30 ppm upon salt metathesis. The observation of a peak in the ^{19}F{^{1}H} NMR spectrum confirms the presence of a $[BF_4]^-$ counter-ion.

Single crystals suitable for X-Ray diffraction analysis were grown by the vapour diffusion of Et_2O into a concentrated solution of **Tz2.BF$_4$** in MeCN. The structure obtained revealed the expected triazolium salt with a tetrafluoroborate counter-ion (Figure 173). The structural parameters are unremarkable, with the C-N and N-N bond lengths being in the expected range for a triazolium ring (Table 20).[11,28,29] Although the $[BF_4]^-$ counter-ion is located close to the cationic portion of the molecule, the distance between C(1)-H and F(2) of 2.76 Å is greater than the sum of the two van der Waals radii, and hence outside the range of a hydrogen bond.[30,31] Closer contact is observed between C(10)-H and F(2) (2.55 Å), and C(5)-H and F(3) (2.60 Å).

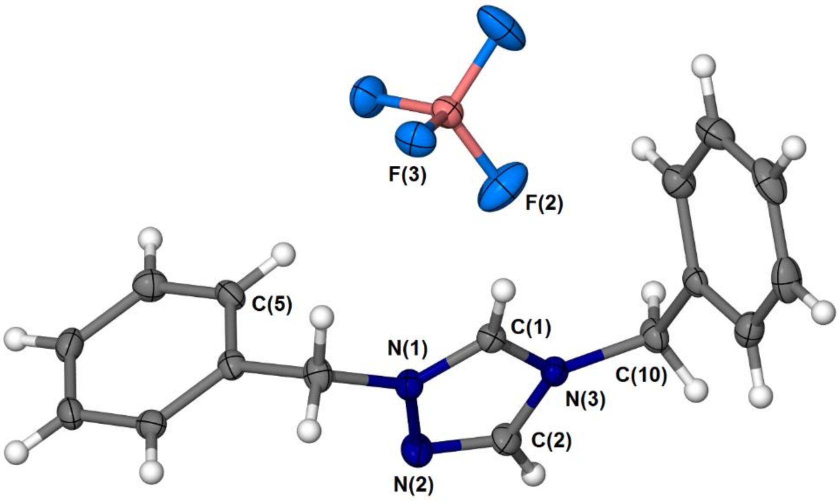

Figure 173. Molecular structure for **Tz2.BF$_4$**. Ellipsoids shown at the 50% probability level. Hydrogen atoms added in calculated positions and refined using the riding model.

Table 20. Selected bond lengths for the molecular structure of **Tz2.BF$_4$**.

Bond	Distance / Å	Bond	Distance / Å
C(1)-N(1)	1.317(3)	C(2)-N(3)	1.359(3)
C(1)-N(3)	1.335(3)	N(1)-N(2)	1.372(3)
C(2)-N(2)	1.302(3)		

2.3.2 Electrochemical Reaction of Triazolium 2

An electrochemical reaction was carried out using **Tz2.BF$_4$** and Cu electrodes (Figure 174), under the same conditions used in the reaction with **Tz1.BF$_4$**. After 30 minutes a sample was taken and analysed by HRMS. A variety of Cu containing species were observed, in addition to free **Tz2.BF$_4$**. Crucially however, no signals corresponding to formation of an imine-based complex were observed. The reaction was run for a further 30 minutes, after which time it was not possible to generate a current. The reaction product was isolated and purified, and submitted to analysis by NMR spectroscopy and HRMS.

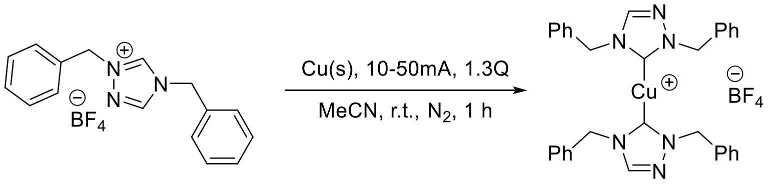

Tz2.BF$_4$ **Cu2a.BF$_4$**

Figure 174. Electrochemical reaction of **Tz2.BF$_4$**.

The HRMS displays a molecular ion peak at *m/z* 561 which corresponds to [**Cu2a**-BF$_4$]$^+$. Additionally, a signal corresponding to the mono-NHC Cu complex is observed at *m/z* 312 along with the associated MeCN adduct (*m/z* 353). A peak at *m/z* 471 can be attributed to a fragmentation of the bis-NHC Cu complex, in which one of the benzyl substituents is cleaved (Figure 175).

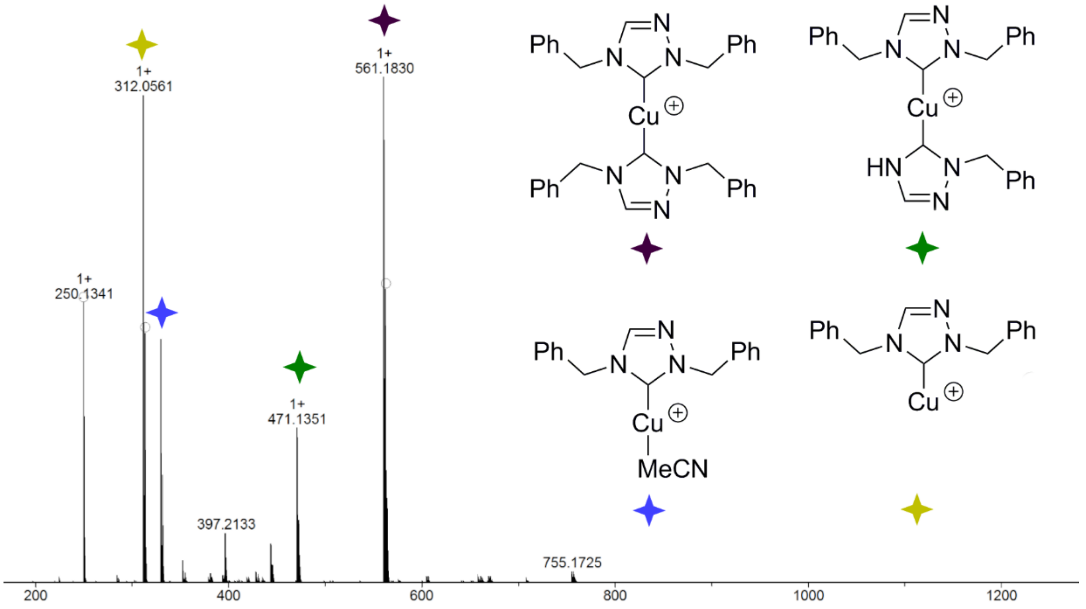

Figure 175. HRMS for the product of electrochemical reaction using **Tz2.BF$_4$**. Inset: structures corresponding to observed peaks.

Analysis by ^{1}H and ^{13}C{^{1}H} NMR spectroscopy however indicated the presence of just one product. It can therefore be assumed that many of the species observed in the HRMS are the result of fragmentation. The signals observed in the ^{1}H NMR are as expected for a complex of this type: the carbenic NC*H*N resonance disappears, and the other ligand signals shift slightly upon complexation. It is presumed that as with previous examples, the cationic bis-NHC species has been formed in this case (i.e. **Cu2a.BF$_4$**).

2.3.3 Narrowing of Scope

The electrochemical reaction using **Tz2.BF$_4$** shows that the ring-opening reaction is not universal for triazolium salts under these conditions. Therefore, two target ligands were identified to determine if conservation of certain structural features from **Tz1.BF$_4$** would promote ring-opening under electrochemical conditions (Figure 176).

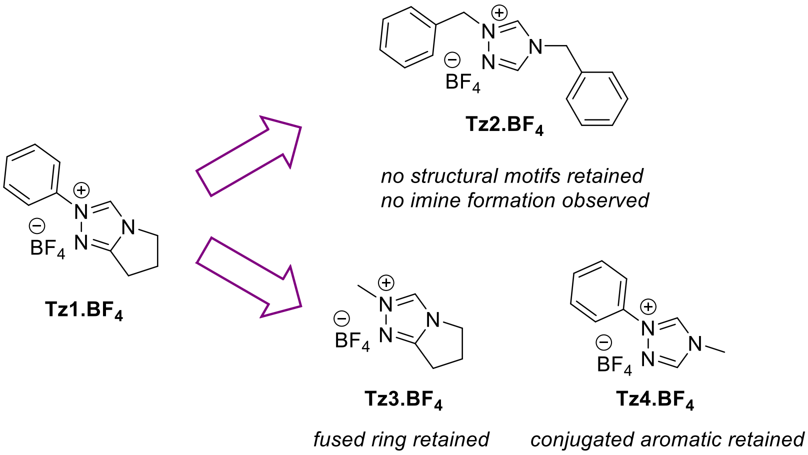
Tz2.BF4
no structural motifs retained
no imine formation observed
Tz1.BF4
Tz3.BF4
Tz4.BF4
fused ring retained
conjugated aromatic retained

Figure 176. Structural variation of triazolium salts **Tz1.BF$_4$**, **Tz2.BF$_4$** and new targets **Tz3.BF$_4$** and **Tz4.BF$_4$**.

2.3.4 Attempted Synthesis of Triazolium 3

The non-methylated triazole analogue of **Tz3.BF$_4$** is commercially available as a hydrochloride salt. Therefore attempts were made to prepare **Tz3.BF$_4$** from this precursor. The hydrochloride was neutralised by addition of NaOH, and the neutral product extracted into DCM. This was used directly in a methylation reaction with methyl iodide. The product was obtained in a moderate yield (55%), but analysis by ^{1}H NMR spectroscopy revealed it to be a mixture of the N1 and N2 methylated products in an approximate 1:1 ratio. This is perhaps not surprising, given the similar chemical environments of the two nitrogen atoms. Separation of these two products, either by recrystallisation or column chromatography, was not possible.

Triazolium salts featuring the fused ring motif are generally prepared in one-pot reactions using 2-pyrollidone to provide the 5-membered ring, and a hydrazine to supply the N-N bond.[32] Preparation of **Tz3.BF$_4$** in this way would require the handling of highly hazardous methylhydrazine. For this reason, efforts in this area were not pursued further.

2.3.5 Synthesis of Phenyl Triazoliums

Initially, attempts were made to prepare 1-phenyltriazole *via* an Ullman coupling. The reaction of bromobenzene and 1,2,4-triazole using D,L-proline as a supporting ligand and CuI lead to a conversion to product of ~11% as determined by ^{1}H NMR spectroscopy. Another attempt was made using a picolinamide ligand shown previously to be highly efficient for Ullman coupling reactions.[33] The results from this indicated that no reaction had occurred.

An alternative route to 1-phenyl-1,2,4-triazole is *via* a condensation reaction using phenylhydrazine and formamide (Figure 177).[34] This method proved to be successful, but in low yields (30%). The yield of the reaction could be improved (typically 60-84%) by the addition of acetic acid; the required imine condensation reactions are known to be acid catalysed.[35]

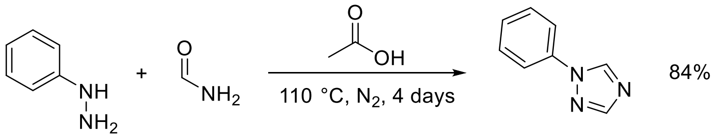

Figure 177. Reaction scheme for the synthesis of 1-phenyl-1,2,4-triazole.

Methylation of 1-phenyltriazole was achieved by reaction with methyl iodide, producing **Tz4.I** in a high yield. However, subsequent salt metathesis proved challenging. Attempts to produce **Tz4.BF$_4$** from **Tz4.I** using NH_4BF_4 were unsuccessful, with the isolated product containing a mixture of iodide and tetrafluorborate counter-ion (Figure 178). A signal in the ^{19}F{^{1}H} NMR spectrum (corresponding to the tetrafluoroborate ion) was observed, however, the crystal structure obtained was for **Tz4.I**.

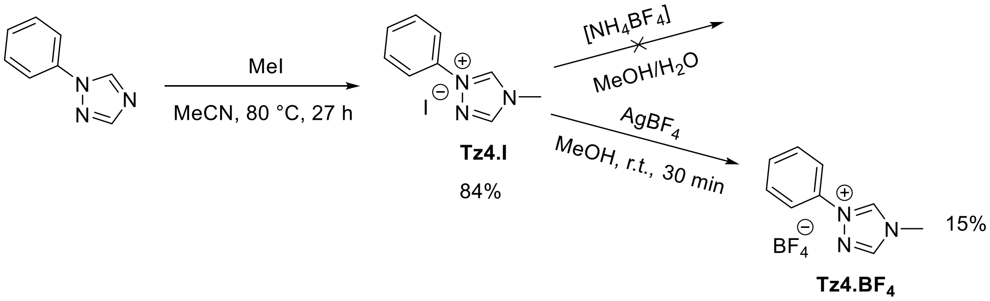

Figure 178. Reaction scheme for the synthesis of **Tz4.I** and **Tz4.BF$_4$**.

$AgBF_4$ was used as a stronger metathesis agent; the precipitation of highly insoluble AgI acts as a driving force in reactions of this kind. Unfortunately, although the reaction was successful, the product could not be easily separated from the large excess of unreacted $AgBF_4$ as it proved to be water soluble. An attempt was made using a stoichiometric quantity of $AgBF_4$, the product was in this case isolated but in a low yield (15%) (Figure 178). As with **Tz2.BF$_4$** a slight upfield shift of the two triazolium ring proton positions is observed: from 10.84 and 9.37 ppm (**Tz4.I**) to 10.80 and 9.34 ppm (**Tz4.BF$_4$**).

Single crystals suitable for X-Ray diffraction were grown from the slow diffusion of Et_2O into a concentrated solution of the sample in MeOH. Two types of crystals were obtained by this method: blocks and needles (Figure 179). The structure obtained from the blocks are of the expected product, with a $[BF_4]^+$ counter-ion. However, the structure obtained for the needle product showed a mixture of $[PF_6]^-$ and $[BF_4]^-$ counter-ions. Analysis of both the product and the $AgBF_4$ used by $^{31}P\{^1H\}$ NMR spectroscopy did not give any indication of phosphorus contamination however, thus the origin of the $[PF_6]^-$ ion is unclear. Other than this unusual observation, the solid state structure of **Tz4.BF$_4$** contains little of note - with structural parameters as expected, and in very good agreement with those of **Tz2.BF$_4$** (*vide infra* - 2.3.1).[11,28,29]

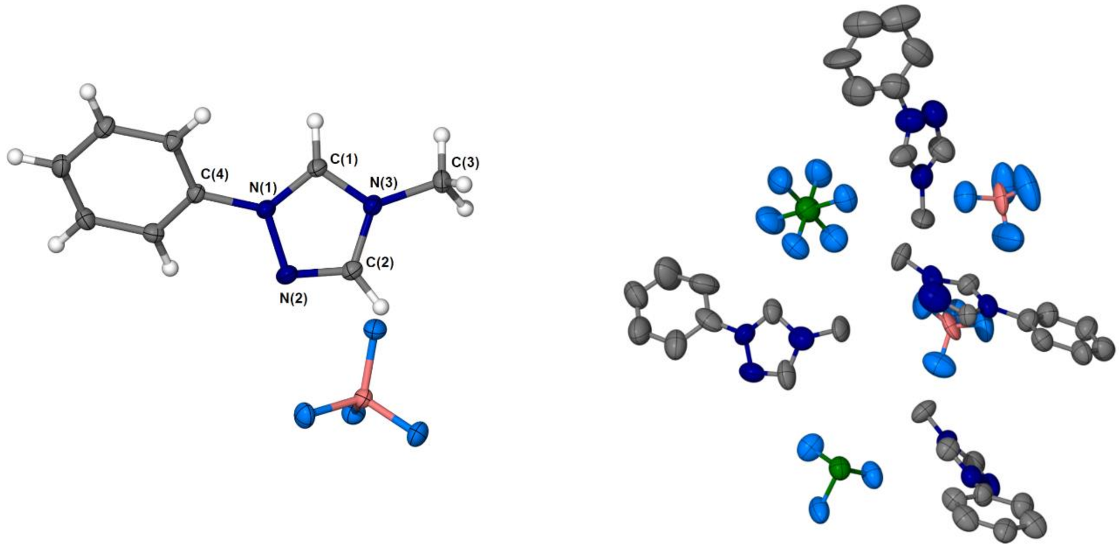

Figure 179. Left: molecular structure of **Tz4.BF$_4$** obtained from block crystal. Ellipsoids shown at the 50% probability level. Hydrogen atoms added in calculated positions and refined using the riding model. Right: asymmetric unit cell obtained from needle crystal. Ellipsoids shown at the 50% probability level, one triazolium cation, and all hydrogen atoms omitted for clarity.

Due to difficulties in the isolation of **Tz4.BF$_4$**, efforts were directed towards the synthesis of 1-phenyltriazolium salts with longer chain or bulkier substituents in the 4-position. It was anticipated that such groups would inhibit the water solubility of the products. An additional benefit is the possibility of preparing these from bromoalkanes which negates the need for the use of $AgBF_4$ and therefore avoids any potential issues with $[PF_6]^-$ contamination.

A range of alkylating agents were reacted with 1-phenyltriazole to furnish the triazolium bromide salts **Tz5.Br**, **Tz6.Br**, and **Tz7.Br** in low to moderate yields (Figure 180). In all cases the NMR spectroscopy and HRMS data confirm the expected structure.

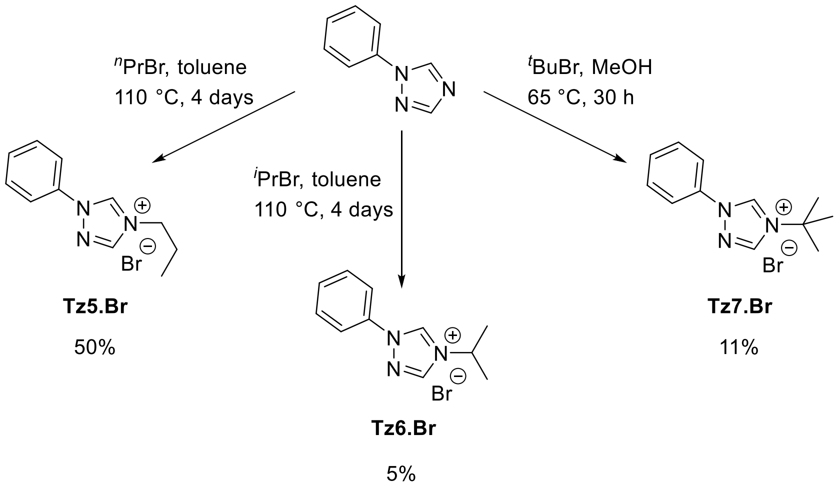

Figure 180. Preparation of triazolium bromide salts **Tz5.Br**, **Tz6.Br**, and **Tz7.Br** using bromoalkanes.

Crystal structures were obtained from the X-ray diffraction of single crystals of **Tz6.Br** and **Tz7.Br**, with bond lengths and angles as expected (Figure 181).[11,28,29]

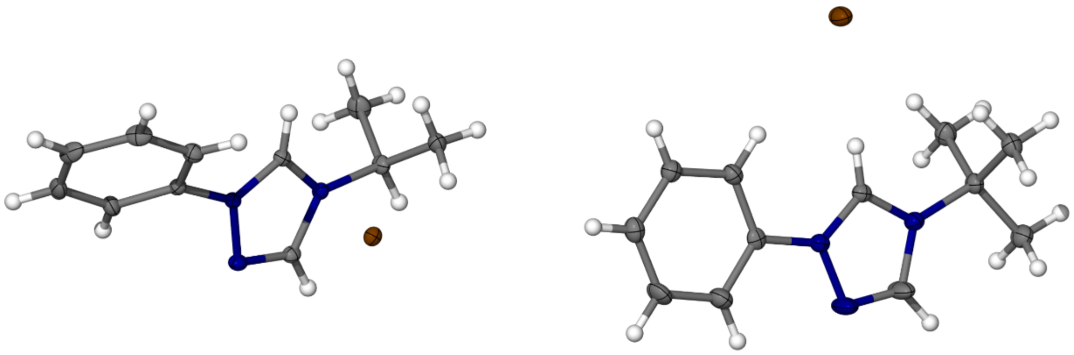

Figure 181. Left: molecular structure for **Tz6.Br**. Right: molecular structure for **Tz7.Br**.

A salt switch was achieved using $NaBF_4$ for **Tz5.Br**. The product proves to be partially soluble in water; when a small volume of water is used as the reaction medium the product precipitates from solution, though when large volumes are used no precipitation occurs. In these cases, the product can be recovered by removal of all solvent, trituration in MeCN followed by acetone, and then recrystallisation from acetone and Et_2O.

The structure of **Tz5.BF$_4$** is very similar to that of **Tz1.BF$_4$**, and therefore was selected for initial electrochemical testing, before expansion to other more structurally divergent triazolium salts.

2.3.6 Electrochemical Reaction of Triazolium 5

An electrochemical reaction using **Tz5.BF$_4$** and Cu electrodes was performed (Figure 182). The reaction was carried out in MeCN, at room temperature with a current of 50 mA maintained throughout the reaction. The product proved difficult to detect by

HRMS, both during the reaction and after isolation. However, analysis of the product by ^{1}H NMR spectroscopy indicated the formation of an NHC complex, presumed to be the bis-NHC complex **Cu5a.BF$_4$**. No resonances characteristic of an imine product were observed. The ^{1}H NMR spectrum is as expected, with the absence of the proto-carbenic CH signal, and a slight shift for other ligand peaks upon complexation. In spite of repeated efforts, it was not possible to obtain a satisfactory ^{13}C{^{1}H} NMR spectrum for this compound and proton spectra were always weak. One possible explanation is contamination with the reaction by-product [Cu(MeCN)$_4$][BF$_4$], which potentially was not removed during the work-up procedure. Attempts were made to remove this by trituration, which led to the isolation of a small quantity of solid. Analysis of this by ^{1}H NMR spectroscopy gave a spectrum of extremely poor quality, that may indicate decomposition. Subsequent elemental analysis gave values which were very low in carbon, hydrogen and nitrogen compared to the predicted values to **Cu5a.BF$_4$**. The values however also do not match with a mono-NHC complex. The poor agreement may be due to residual [Cu(MeCN)$_4$][BF$_4$], decomposition during attempted purification, and/or decomposition of the product in air prior to analysis.

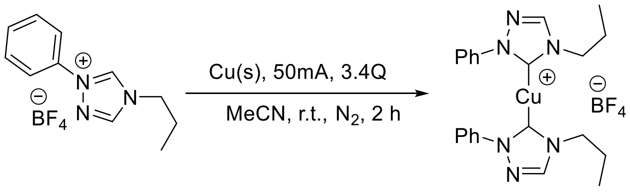

Tz5.BF$_4$ **Cu5a.BF$_4$**

Figure 182. Reaction scheme for the electrochemical synthesis of **Cu5a.BF$_4$**.

Although it was not possible to obtain complete data on this compound, the conclusion that ring-opening does not occur for this ligand may be adequately drawn on the basis of the ^{1}H NMR spectrum.

Tz5.BF$_4$ has a very similar structure to that of **Tz1.BF$_4$** and yet does not undergo the same ring-opening reaction under electrochemical synthetic conditions. The only other possible variant on **Tz1.BF$_4$** would be triazoliums featuring a substituted backbone (Figure 183).

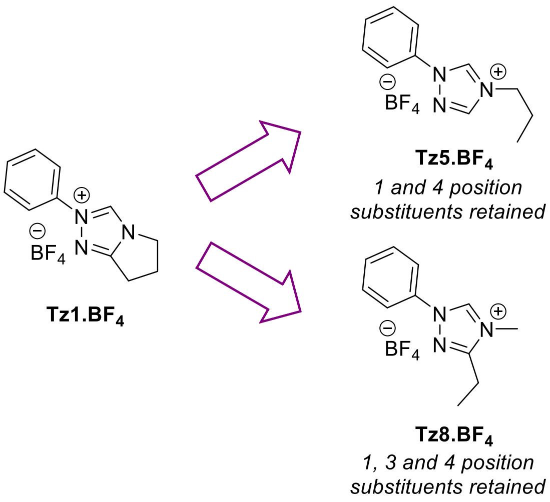
Tz1.BF$_4$
Tz5.BF$_4$
1 and 4 position substituents retained
Tz8.BF$_4$
1, 3 and 4 position substituents retained

Figure 183. Structural similarity between **Tz1.BF₄**, **Tz5.BF₄** and **Tz8.BF₄**.

2.3.7 Attempted Synthesis of Backbone Substituted Triazoliums

The retrosynthetic analysis for **Tz1.BF₄** is shown in Figure 184. It can be seen that by using a different amide, alternative groups may be delivered to the 3 and 4 positions in the triazolium ring. For this reason **Tz8.BF₄** was selected as a target for synthesis.

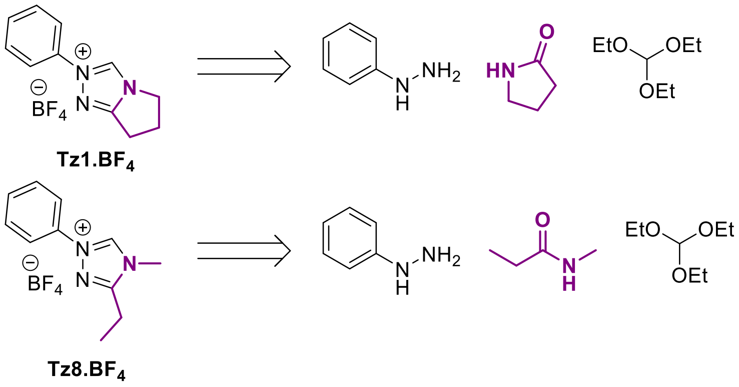
Tz1.BF$_4$
Tz8.BF$_4$

Figure 184. Products and starting materials for **Tz1.BF₄** and proposed target **Tz8.BF₄**.

Synthesis of **Tz8.BF₄** was attempted using slightly modified literature conditions for the preparation of **Tz1.BF₄** (Figure 185).[32] After reaction the product was isolated *via* phase separation followed by recrystallisation of the organic phase from MeCN and Et_2O.

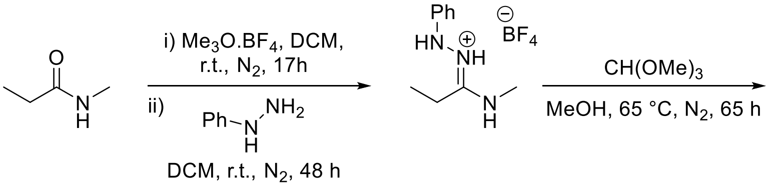
i) Me$_3$O.BF$_4$, DCM, r.t., N$_2$, 17h
ii) DCM, r.t., N$_2$, 48 h
CH(OMe)$_3$
MeOH, 65 °C, N$_2$, 65 h

Figure 185. Synthetic route used for attempted preparation of **Tz8.BF₄**.

The ^{1}H NMR spectrum was not as expected for the product, showing two sets of aromatic group resonances, and two highly downfield signals at 11.31 and 10.18 ppm. Additionally, although the expected ethyl backbone signal was apparent, there was no signal corresponding to a methyl group. The structure of the compound obtained was determined by X-ray crystallography to be **Tz8'.BF$_4$**, which is a triazolium ring, with an exo-nitrogen at the 4-position of the ring (Figure 186). Triazolium salts with this structural feature have been crystallographically characterised previously, and the parameters for **Tz8'.BF$_4$** agree well with the reported data.[36–38] This product arises from the elimination of either protonated or methylated [NH-Me] after initial imine formation. As both methylamine and dimethylamine are gaseous, this process would be irreversible. This pathway is not available in the formation of **Tz1.BF$_4$**, due to the amide in question being a lactam.

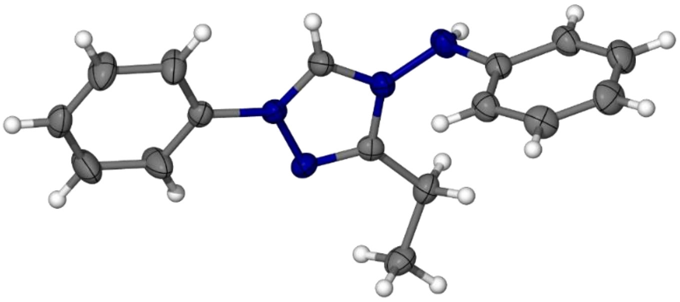

Figure 186. Molecular structure of **Tz8'.BF$_4$**. Ellipsoids shown at the 50% probability level. One [BF$_4$]$^-$ counter-ion omitted for clarity. Hydrogen atoms added in calculated positions and refined using the riding model.

The structure of **Tz8'.BF$_4$** is consistent with the ^{1}H NMR data; a D_2O shake leads to the disappearance of both downfield signals (Figure 187). It may be supposed that the proximity of the "carbenic" proton to so many electron withdrawing nitrogen atoms renders it more acidic than in standard triazoliums.

Due to this problematic elimination pathway, the known difficulties with isolation of imine species, and time constraints, attempts to prepare **Tz8.BF$_4$** or similar backbone substituted triazoliums were not pursued further.

A range of triazolium salts have been prepared and used to test the scope of the ring-opening reaction observed with **Tz1.BF$_4$**. Further mechanistic studies using **Tz2.BF$_4$** and **Tz5.BF$_4$** are discussed in Chapter 3.

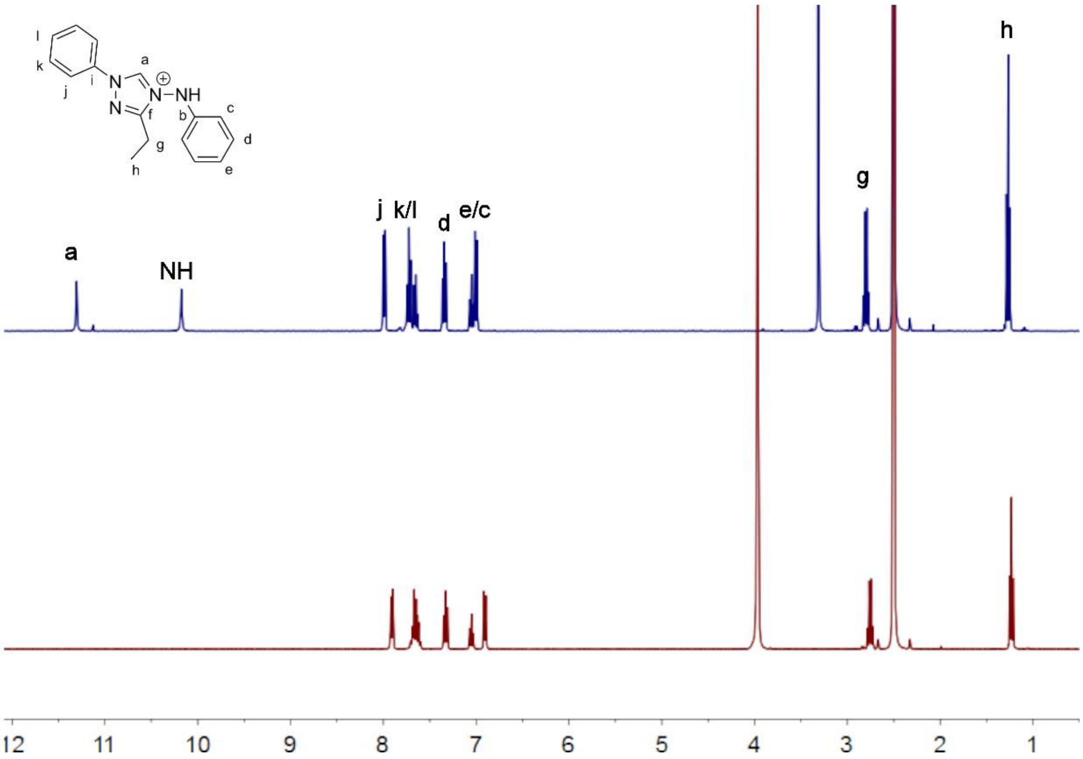

Figure 187. ^{1}H NMR spectra (400 MHz, d_6-DMSO). Top: **Tz8’.BF$_4$**. Bottom: D_2O shake on sample of **Tz8’.BF$_4$**, showing disappearance of NH and H_a signals.

2.4 Chemical Synthesis of bis-NHC Copper Complexes

It is desirable to prepare **Cu1a.BF$_4$** by chemical methods to monitor possible imine formation from the NHC. The complex may be electrolysed using Cu or graphite electrodes, in order to investigate whether the application of current drives ring-opening. The sample may also be heated, or reacted with reducing agents or hydrogen gas, to discover which conditions promote imine formation. The initial synthesis using K^{t}BuO established that the ring-opening reaction does not occur under chemical conditions (*2.2.1*). However, this synthesis resulted in the isolation of product that was contaminated with **Tz1.BF$_4$**, making it thus unsuitable for further testing.

2.4.1 Attempts to Prepare Copper Complexes using Triazolium 2

As attempts to prepare **Cu1a.BF$_4$** were initially unsuccessful, alternative methods for the chemical synthesis of bis-NHC Cu complexes from triazolium salts were sought. Due to the limited quantity of **Tz1.BF$_4$** available, **Tz2.BF$_4$** was used as a model ligand precursor in these reactions. A wide scope of reaction conditions were screened in attempts to prepare **Cu2a.BF$_4$** *via* chemical means, based on reactions reported in the literature.[39–42] These were all unsuccessful, and are summarised in the appendix (2.8 – Table A1).

Subsequent attempts used **Tz5.Br** in to ensure the synthetic challenges encountered using **Tz2.BF$_4$** were not due to the nature of the triazolium. The switch from a $[BF_4]^-$ counter-ion to a bromide should provide an additional driving force for these reactions.

2.4.2 Attempts to Prepare Copper Complexes using Triazolium 5

A literature method reported by Nolan *et al.* was next investigated.[43] This uses NaO^{t}Bu as the base, with $[Cu(MeCN)_4][BF_4]$ as a Cu(I) source in THF solvent. A reaction was initially performed using **Tz5.Br** to test the method (Figure 188).

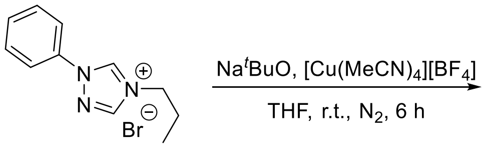

Tz5.Br

Figure 188. Reaction scheme for the chemical synthesis of **Cu5a**.

The product of the reaction was isolated as a white solid in a 45% yield. The HRMS data for the product indicated successful formation of bis-NHC Cu complex **Cu5a.BF$_4$**, with a peak at *m/z* 437 $[M-BF_4]^+$, as well as peaks at *m/z* 188 and 146 attributed to fragmentation. Analysis of the ^{1}H NMR spectrum suggests clean formation of **Cu5a.BF$_4$**, with no peaks corresponding to residual **Tz5.Br** being observed. However, the peak positions are shifted slightly by comparison with the ^{1}H NMR spectrum obtained for **Cu5a.BF$_4$** prepared electrochemically.

Although it is assumed that a bis-NHC complex is formed in these reactions, the change in chemical shifts in the NMR data may indicate the presence of some mono-NHC species. For this reason, attempts were made to prepare the mono-NHC analogue of **Cu5a***. The procedure for the synthesis of such complexes reported by Cazin *et al.* was adapted slightly (Figure 189).[44]

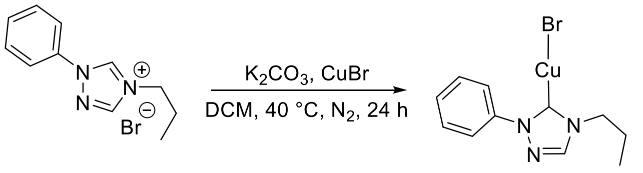

Tz5.Br

Cu5a*

Figure 189. Reaction scheme for the synthesis of **Cu5a***.

The HRMS data for the product of this reaction is identical to that for the product of the chemical reaction using **Tz5.Br** with a peak at *m/z* 437 indicative of the bis-NHC complex. There are differences however in the ^{1}H NMR data (Figure 190). The peak positions for this product do not match those for **Cu5a.BF$_4$** prepared electrochemically, or the product of the chemical reaction, although they are more similar to the electrochemical product. Elemental analysis confirmed the stoichiometry of the Cu complex prepared using this route to be the desired mono-NHC, **Cu5a***.

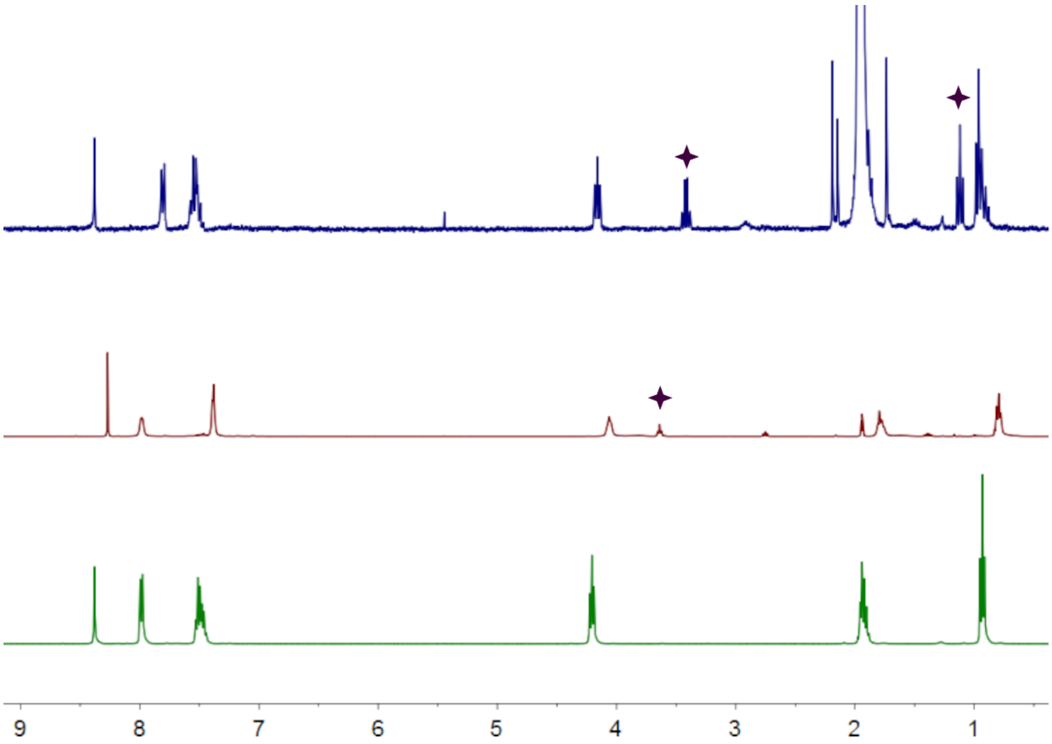

Figure 190. ^{1}H NMR spectra (400 MHz, CD_3CN). Top: **$Cu5a.BF_4$** prepared electrochemically. Middle: **Cu5a** prepared chemically. Bottom: **Cu5a*** prepared chemically. Purple stars denote solvent peaks (top: Et_2O, middle: THF).

Single crystals suitable for X-ray diffraction were grown from a concentrated solution of **Cu5a** (prepared chemically) in CD_3CN. The structure was solved in the $P2_1/c$ space group, and the asymmetric unit reveals a bis-NHC-Cu complex (Figure 191). However, the counter-ion is a bromide rather than the expected $[BF_4]^-$, in spite of the observation of a signal for the $[BF_4]^-$ moiety in the $^{19}F\{^1H\}$ NMR spectrum. The geometry at the Cu centre is distorted trigonal, with the Cu coordinated by two NHCs and a loosely associated bromide ion. The Cu-carbene distances are near identical for both NHC ligands, and in good agreement with other Cu-NHC complexes (Table 21).[8,9] The carbene-Cu-bromide angles are essentially the same for both ligands.

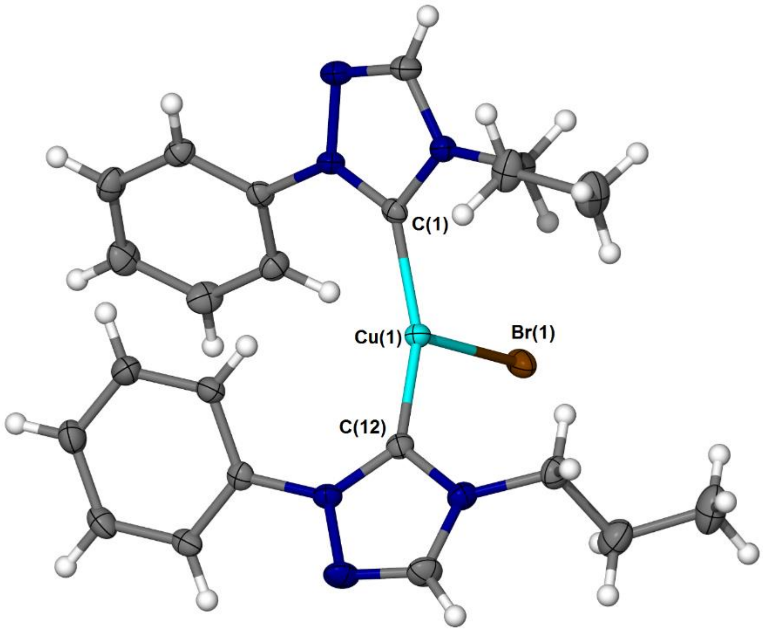

Figure 191. Molecular structure for **Cu5a.Br**. Ellipsoids shown at 50% probability level. Hydrogen atoms added in calculated positions and refined using the riding model.

Table 21. Selected bond lengths and angles for **Cu5a.Br**.

Bond	Distance / Å	Angle	/ °
Cu(1)-C(1)	1.9275(19)	C(1)-Cu(1)-C(12)	145.0
Cu(1)-C(12)	1.927(2)	C(1)-Cu(1)-Br(1)	107.6
Cu(1)-Br(1)	2.5087(4)	C(12)-Cu(1)-Br(1)	107.1

The angle between the NHC plane (C1) and that described by C(12), Cu(1) and Br(1) is 91.4 °, whilst the NHC containing C(12) has a different twist angle of 64.0 °. The phenyl rings are twisted to a similar degree relative to the NHC plane for each ligand (33.1 ° for C(1) and 36.7 ° for C(12)).

Elemental analysis of **Cu5a.Br** confirms the bis stoichiometry with a bromide rather than $[BF_4]^-$ counter-ion.

It therefore seems likely that the bis-NHC complex forms both chemically and electrochemically, and that the differences observed in the ^1H NMR spectrum are due to the different counter-ions.

2.4.3 Preparation of Copper Complex 1a using Triazolium 1

Given the success of the reaction with test ligand **Tz5.Br**, the synthesis was repeated with **Tz1.Cl** (Figure 192). It was hoped that the synthesis would prove replicable, and also that the presence of a chloride rather than a bromide counter-ion on the triazolium would favour the formation of the Cu-BF_4 complex.

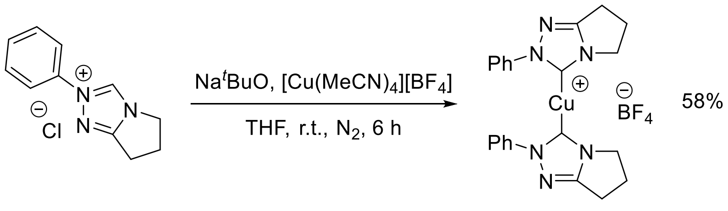

Tz1.Cl **Cu1a.BF4**

Figure 192. Reaction scheme for the chemical synthesis of **Cu1a.BF$_4$.**

The product was isolated as an off-white solid in a moderate 58% yield. The NMR spectroscopic and HRMS data were compared with **Cu1a.BF$_4$** prepared previously (2.2.1). As was seen with the preparation of **Cu5a.Br**, although the peaks in the ^{1}H NMR spectrum may be attributed to the expected complex, the chemical shift has changed slightly. It is possible that this is due to a change in counter-ion, as previously observed. Elemental analysis suggests a 5:1 ratio of [BF$_4$]$^-$ to chloride as counter-ion.

Single crystals suitable for X-Ray diffraction were grown by the vapour diffusion of Et$_2$O into a concentrated solution of the product in MeCN. The crystal structure was found to have structural parameters that were near identical to those found previously (*2.2.1* - Table 17). The only difference was that the new structure was solved in the *C*2/*c* space group, as opposed to the *I*2/*a* space group observed previously, however this is likely to be a simple crystallisation effect.

The successful preparation of **Cu1a.BF$_4$** allows for further reactivity studies to be performed, which are discussed in Chapter 3.

2.5 Investigation of Related Ring-opening Species

2.5.1 MTT

The transformation of MTT to formazan is a common example of reductive ring-opening in heterocycles (Figure 193). MTT is a tetrazolium dye used as a test for viable cells in the screening of antiproliferative drugs. The starting tetrazolium is yellow, but is reduced by NADH in living cells to the purple-coloured formazan.[45,46]

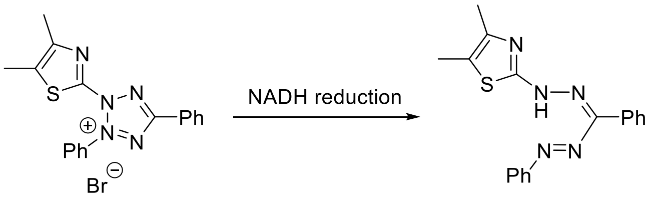

MTT **formazan**

Figure 193. Reduction of yellow coloured tetrazolium salt MTT to purple coloured formazan by NADH.

There is no site for carbene formation in MTT, however the formazan product could coordinate in a bidentate manner similar to the diimine ligand in **Cu1b.BF$_4$**.

2.5.1.1 Electrochemical Reaction of MTT with Copper

Whilst MTT to formazan is a well-documented reductive ring-opening process, performing this reaction electrochemically has not been previously reported. An electrochemical reaction was therefore performed: MTT was suspended in anhydrous MeCN and Cu electrodes inserted (Figure 194).

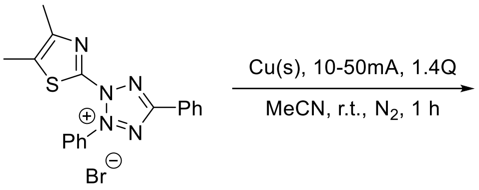

Figure 194. Reaction scheme for electrochemical reaction using MTT.

Upon contact of the electrodes with the yellow solution, a dark green colour was produced, in the absence of an applied potential. After standing the electrodes in the solution for 10 minutes the colour had changed completely, however HRMS data showed only an ion signal corresponding to [MTT-Br]$^+$ (Figure 195). A current was therefore applied for approximately 1.4 Q. At the end of the reaction, the HRMS showed a main ion peak indicating MTT, as well as two less intense signals corresponding to [Cu(MTT)]$^+$ [Cu(MTT)$_2$]$^+$. There was, however, no evidence of the ring-opened formazan product. The NMR data for the isolated product showed very subtle changes from that of MTT – but no evidence of an NH signal was apparent. IR spectra were also recorded, as if formazan has been generated, a diagnostic NH stretch signal should be observed in the range 3100-3500. As with the NMR data, there were differences between the spectrum for MTT and that for the reaction product, however, no NH stretch could be seen (Figure 196 and Figure 197).

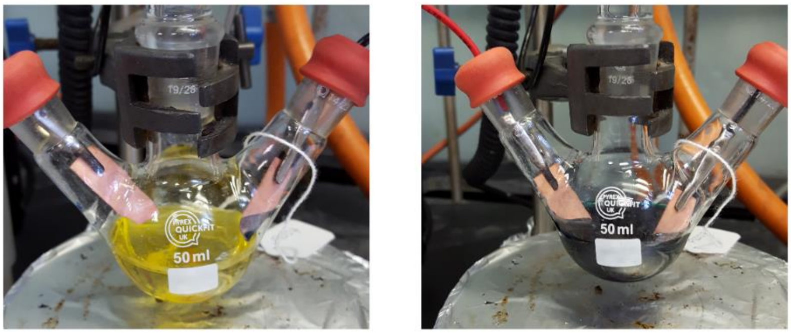

Figure 195. Left: solution of MTT in MeCN prior to electrode insertion. Right: solution of MTT in MeCN after 10 minutes in contact with Cu electrodes.

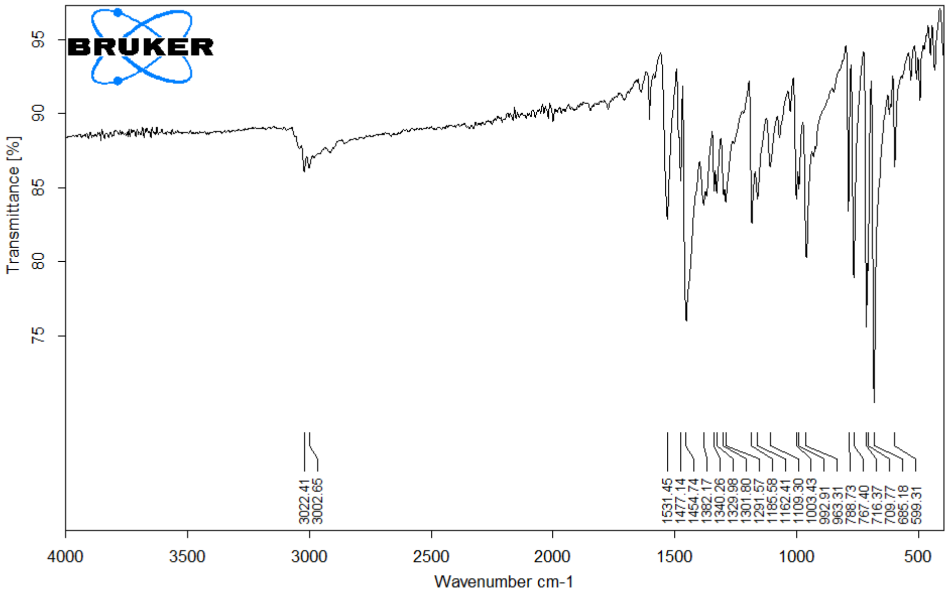

Figure 196. IR spectrum for MTT.

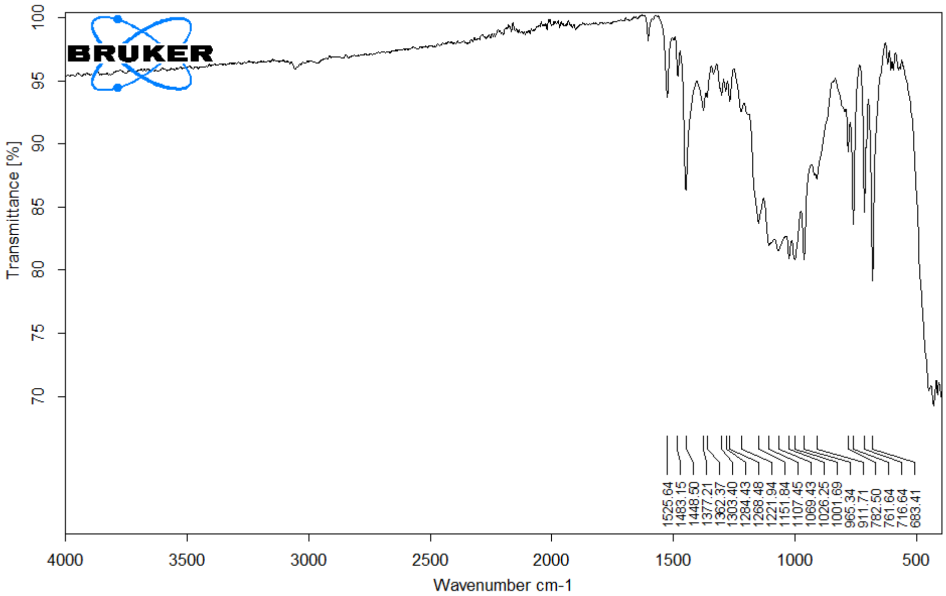

Figure 197. IR spectrum for product of electrochemical reaction of MTT with Cu electrodes.

Single crystals suitable for X-ray diffraction were grown by the vapour diffusion of Et_2O into a concentrated solution of the product in MeCN. The crystal structure obtained indicates that the Cu has reacted with MTT to replace the bromide counter-ion with a Cu dibromide counter-ion (Figure 198). The crystal structure of MTT has not been reported, so structural parameters of the product cannot be compared. However, none of the bond lengths or angles observed are unexpected. The XRD powder pattern obtained for the bulk sample matches well with that predicted for the crystal structure, providing good evidence that this is the sole product obtained from the reaction. This correlates well with the slight changes observed in the ^1H NMR spectra, as well as the differences seen in the fingerprint region of the IR spectra.

The formation of MTT.$CuBr_2$ requires two equivalents MTT to supply both bromide ions. This likely accounts for the low yield based on raw mass of material; the fate of the $[MTT\text{-}Br]^+$ by-product is unclear, but is likely removed during the work-up procedure.

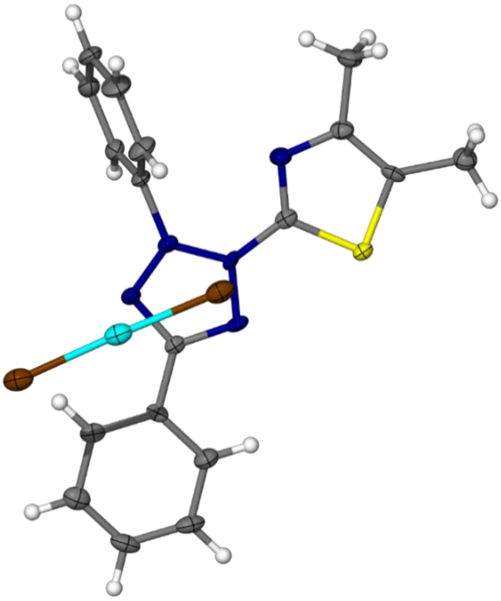

Figure 198. Molecular structure for MTT.$CuBr_2$. Ellipsoids shown at 50% probability level. Hydrogen atoms added in calculated positions and refined using the riding model.

2.5.1.2 Chemical Reaction of MTT with Copper

In order to determine the effect, if any, of the applied potential on the observed reactivity, a chemical reaction was carried out using MTT. Two reactions performed with MTT and Cu powder, one in MeCN and one in MeOH (Figure 199). The protic solvent MeOH was selected as a suitable solvent, as protonation is required to form formazan.

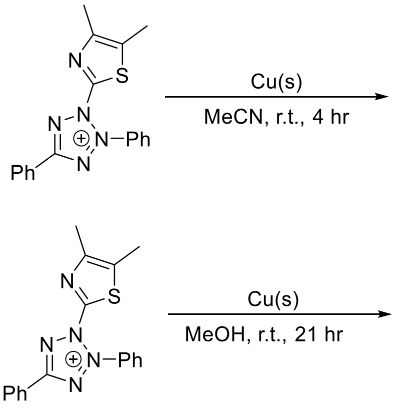

Figure 199. Reaction schemes for reaction of MTT with Cu powder.

The reaction in MeCN underwent colour changes as seen for the electrochemical reaction, becoming green rapidly, with the colour deepening over time. The colour change for the reaction in MeOH was slower, and hence the reaction time was increased.

The ^{1}H NMR data obtained for both reaction products were of poor quality, being broad and weak. The MeCN reaction product spectrum appears complex, with many new peaks, of which none are attributable to either starting material or the previously observed product. The MeOH reaction product spectrum shows peak regions similar to that for MTT; one signal for a CH_3 group and the 10 aromatic protons can be identified. There are several broad resonances at >9 ppm which could be indicative of an NH group. Apart from these downfield signals, the spectrum is similar to that of the MTT.$CuBr_2$ product obtained electrochemically. The broadness of the spectra for both products could be due to the presence of paramagnetic Cu species.

IR spectroscopy was also used to analyse the products. In the case of the MeCN product there are two signals in the NH stretching region (3509 and 3404 cm^{-1}) (Figure 200). The presence of two signals would generally indicate a primary amine, rather than the secondary amine expected for a formazan product. Additionally a weak and broad absorption band is observed at 1613 cm^{-1}. This could be attributed to a weak double bond (as in the aromatic rings of MTT) or an N-H bend (as in the NH group of the formazan product). The product obtained from MeOH does not show any bands in the NH stretching region (Figure 201). The IR spectrum shows similarities to that of both MTT and MTT.$CuBr_2$.

Powder XRD patterns were also collected for the two products (Figure 202). For the MeCN reaction only an XRD powder pattern of extremely low intensity could be obtained. While the diffraction pattern bears some similarity to that calculated for MTT.$CuBr_2$ most signals are barely above the baseline, so it is hard to draw a conclusion. The product from the MeOH reaction gave a slightly more lucid pattern, however agreement with the pattern for MTT.$CuBr_2$ is poor.

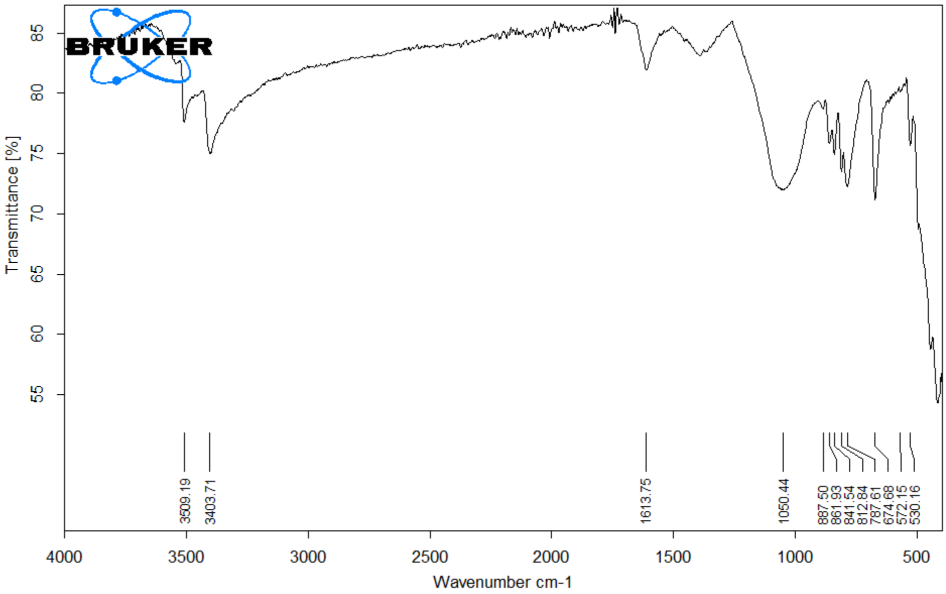

Figure 200. IR spectrum of product from chemical reaction of MTT with Cu powder in MeCN.

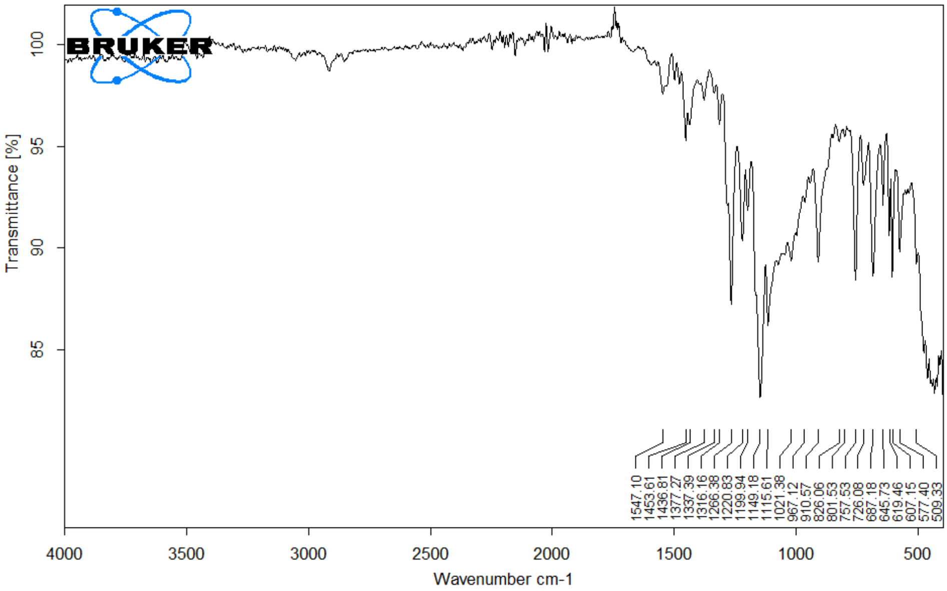

Figure 201. IR spectrum of product from chemical reaction of MTT with Cu powder in MeOH.

Given the challenging nature of the analysis of these reaction products, it has proved difficult to determine to what extent the formation of MTT.$CuBr_2$ is electrochemically driven. There is some evidence that the same reactivity is observed electrochemically as with the chemical reaction in MeOH. Nonetheless it is clear that Cu undergoes a chemical reaction with MTT, even if the products cannot be unambiguously identified. For this reason, further attempts to explore the potential electrochemical ring-opening of MTT were not made.

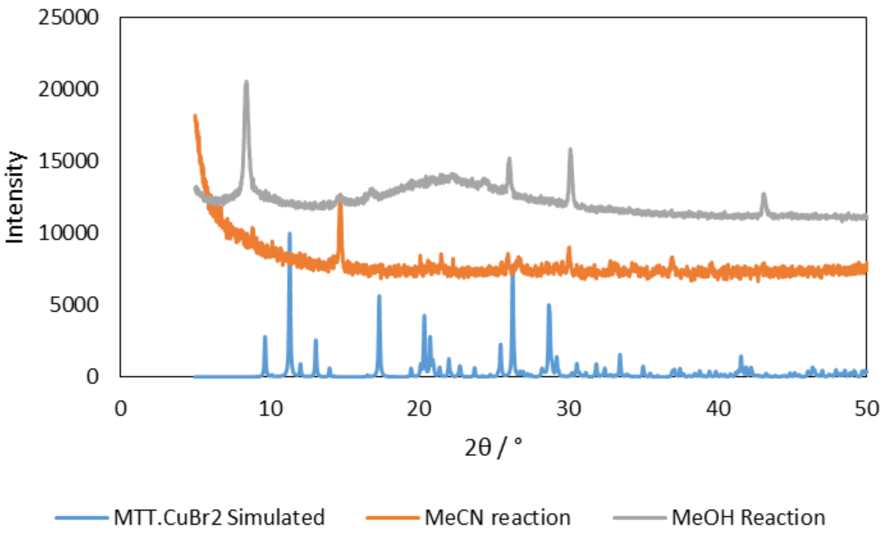

Figure 202. Comparison of simulated XRD powder pattern for MTT.$CuBr_2$ with measured sample of MeCN reaction product and MeOH reaction product.

2.5.2 Nitron

Nitron is a commercially available inexpensive compound featuring a 1,2,4-triazole motif. It has been used since the early 20th century as an analytical agent in the gravimetric analysis of nitrate ions.[47,48] Although it is generally considered to exist in the zwitterionic form, it can tautomerise to the carbenic form (Figure 203). Although the carbenic tautomer is not observable by NMR spectroscopy, the reactivity of nitron is strongly indicative of an equilibrium between the two forms.[49] Nitron reacts with elemental sulfur to form an adduct with a downfield carbon resonance characteristic of nucleophilic attack by a carbene in the ^{13}C NMR spectrum. Additionally, nitron reacts directly with $[Rh(COD)Cl]_2$ and $[Rh(CO)_2Cl]_2$ to form NHC complexes in quantitative yields. Analysis of carbonyl stretching frequencies indicate that the NHC derived from nitron is a donor of moderate strength.[49] The use of nitron as a “latent carbene source” has also been demonstrated with coinage metals.[50] Reaction of nitron with coinage metal salts cleanly forms either mono or bis-NHC complexes, depending on the stoichiometry used. Examples of both mono and bis-NHC complexes have been demonstrated with a range of Cu halide salts (**2.1**, **2.2**); examples using Ag have also featured non-coordinating anions (**2.3**) (Figure 203).

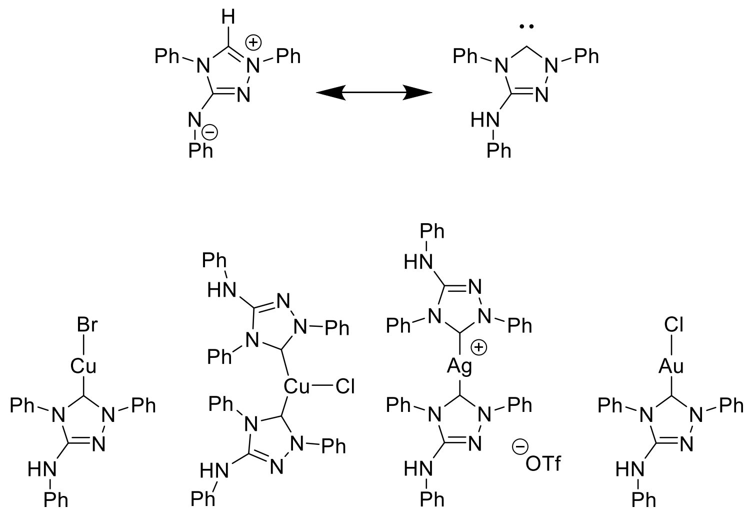

2.1 **2.2** **2.3** **2.4**

Figure 203. Tautomerism between zwitterion and carbenic forms displayed by nitron and example complexes reported by Siemeling *et al.*[50]

Nitron has been recently reported to undergo reaction to form a Blatter-type radical.[51] It was reported that the reaction proceeds *via* a ring-opening, ring-closing rearrangement upon standing in hydrous MeCN in aerobic conditions to form ring-expanded product **2.5**. (Figure 204).

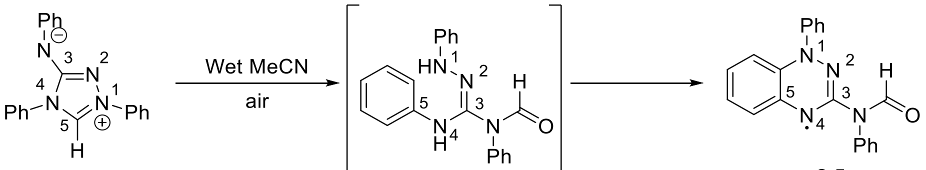

2.5

Figure 204. Rearrangement reaction of nitron reported by O'Donoghue *et al.*[51]

The formation of **2.5** proceeds *via* a C-N bond cleavage which opens the triazolium ring. Subsequent oxidative cyclisation allows access to the radical species. The ring-opening reaction was proposed to arise from attack of adventitious water on the carbenic carbon, followed by a ring-opening reaction. It is suggested that the exocyclic nitrogen atom present in nitron promotes the initial hydrolysis and additionally stabilises the formed radical; it was noted that 1,2,4-triphenyltriazolium does not undergo the same ring-opening reaction.[51]

It is interesting to investigate whether, under electrochemical conditions, nitron will undergo a ring-opening reaction, and if so whether this is *via* C-N or N-N bond cleavage. Additionally, investigation of reactions of the Cu complexes derived from nitron are of interest. It is also worth noting that the presence of adventitious water may provide an explanation for the ring-opening reaction observed with **Tz1.BF$_4$**.

2.5.2.1 Chemical Reaction of Nitron with Copper

Due to the overall neutrality of nitron, it was not possible to perform an electrochemical reaction in the absence of electrolyte. Therefore a chemical reaction between nitron and $[Cu(MeCN)_4][BF_4]$ was performed using conditions adapted from the literature (Figure 205).[50]

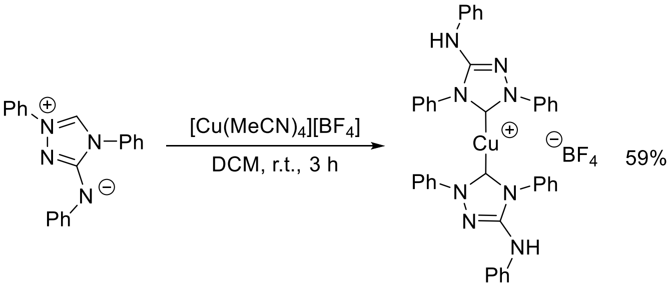

Cu9a.BF₄

Figure 205. Reaction scheme for the synthesis of **Cu9a.BF₄**.

Analysis of the product obtained gave some indication of the successful synthesis of **Cu9a.BF₄**. Namely, a dramatic increase in complexity of the $^{13}C\{^1H\}$ NMR spectrum was observed. This is in good agreement with the data reported for **2.2** which suggests coordination of two magnetically inequivalent NHCs. However, although changes from the ^1H NMR spectrum of nitron were apparent, the characteristic NH signal reported for previous products was not present.[50] HRMS data displayed a signal corresponding to protonated nitron, with no complex observed. However, elemental analysis indicated that a complex with the stoichiometry of the bis-NHC complex **Cu9a.BF₄** was formed.

Attempts were made to grow diffraction quality crystals of this product both under an inert atmosphere and in air. Crystals suitable for X-ray diffraction were obtained from the slow diffusion of Et_2O into a concentrated solution of **Cu9a.BF₄** in MeCN under an inert atmosphere. The structure was solved in the *C*2/*c* space group and shows the expected bis-NHC complex with a $[BF_4]^-$ counter-ion (Figure 206). As with **Cu1a.BF₄** the geometry at the Cu centre is perfectly linear, with the asymmetric unit containing one ligand and half a counter-ion. The Cu-NHC bond distance is in good agreement with other nitron complexes reported, as are the triazole ring distances (Table 22).[50]

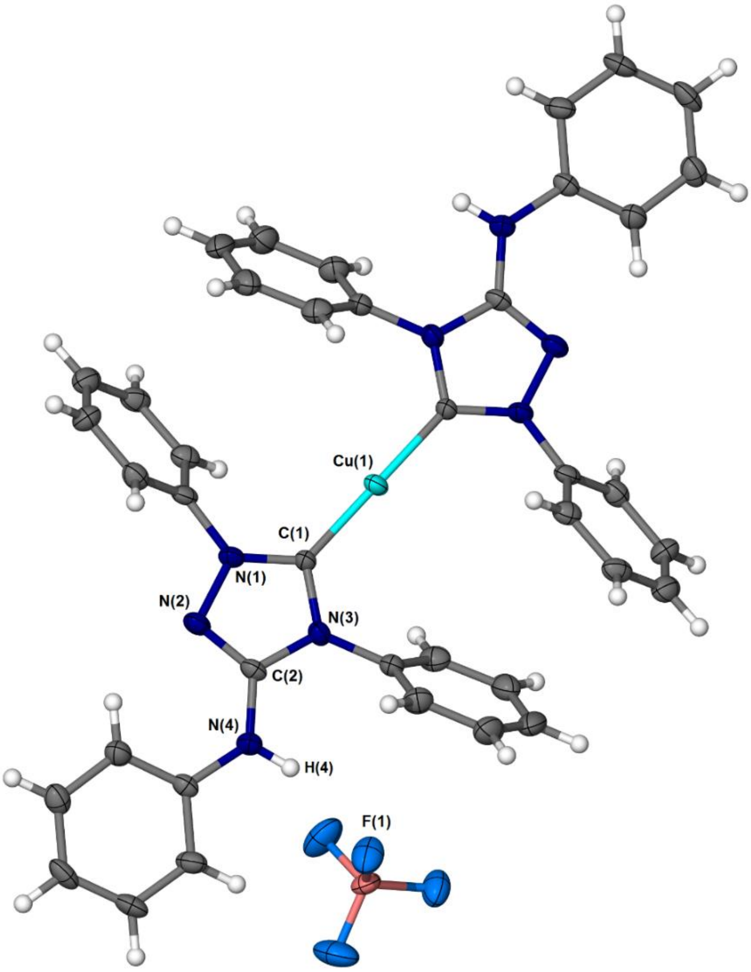

Figure 206. Molecular structure of **Cu9a.BF$_4$**. Ellipsoids shown at the 50% probability level. Hydrogen atoms added in calculated positions and refined using the riding model.

Table 22. Selected bond lengths for **Cu9a.BF$_4$**.

Bond	Distance / Å	Bond	Distance / Å
Cu(1)-C(1)	1.899(4)	C(2)-N(2)	1.322(6)
C(1)-N(1)	1.348(6)	C(2)-N(3)	1.388(6)
C(1)-N(3)	1.366(6)	C(2)-N(4)	1.357(6)
N(1)-N(2)	1.395(5)		

The major difference between **Cu9a.BF$_4$** and previously reported Cu complexes is the presence of a non-coordinating anion. This allows **Cu9a.BF$_4$** to adopt a linear geometry at the Cu centre, whilst the chloride and bromide complexes reported by Siemeling *et al.* are distorted trigonal.[50] This may contribute to the variability in the twist angle of the phenyl rings relative to the NHC rings that are observed. In **Cu9a.BF$_4$** the angles are almost identical for the N1 and N3 substituents, whilst in the chloride complex (**2.2** - Figure 203) all four rings show different angles, and the rings are rotated in different directions (Table 23). This is presumably to avoid steric clashes around a more congested Cu centre.

Table 23. Comparison of phenyl twist angles for **Cu9a.BF$_4$** and **2.2**.[50]

Twist Angle	**Cu9a.BF$_4$** / °	/ °
N(1)Ph - NHC	56.5	125.2 / - (disordered)
N(3)Ph - NHC	57.2	57.2 / 29.3
N(4)Ph - NHC	13.9	35.1 / 13.2

Solutions of the product in air became purple over time. Crystals suitable for X-Ray diffraction were obtained, and the structure solved. The solution obtained was not the expected Cu complex but rather a cationic form of nitron, **Tz9.BF$_4$**, in which both the NCN and amine nitrogen are protonated (Figure 207). The bond lengths are in broad agreement with those reported in the literature, and other triazolium salts discussed earlier.[11,28,29] The bond lengths within the triazolium ring are somewhat shorter than those found for **Cu9a.BF$_4$**, as would be expected. The large errors on many of the parameters limit truly meaningful discussion.

Although serendipitous, **Tz9.BF$_4$** is a potentially useful starting material for electrochemical reaction.

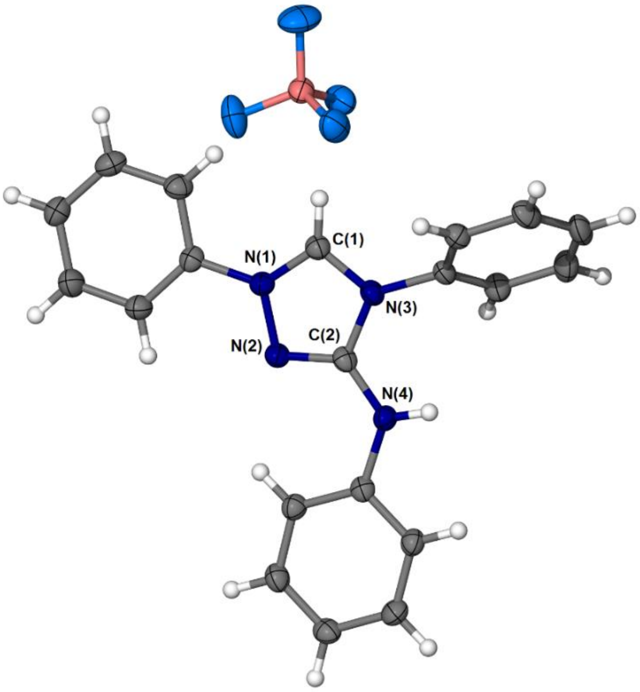

Figure 207. Molecular structure of **Tz9.BF$_4$**. Ellipsoids shown at 50% probability level. Hydrogen atoms added in calculated positions and refined using the riding model.

Table 24. Selected bond distances for **Tz9.BF₄**.

Bond	Distance / Å	Bond	Distance / Å
C(1)-N(1)	1.3018(19)	C(2)-N(2)	1.3164(19)
C(1)-N(3)	1.347(2)	C(2)-N(3)	1.3861(19)
N(1)-N(2)	1.3862(18)	C(2)-N(4)	1.349(2)

2.5.2.2 Preparation of a Cationic Nitron Derivative

Attempts to synthesise **Tz9.BF₄** directly, without the addition of a Cu source, were therefore undertaken. This was achieved using a mixed MeOH/water solvent system (to provide the necessary proton), and sodium tetrafluoroborate (to provide the $[BF_4]^-$ counter-ion). The ^{1}H NMR spectrum of the product proved to be diagnostic, with a new peak corresponding to the N-H proton appearing at 9.71 ppm. Its identity can be confirmed by use of a D_2O shake, upon which the signal disappears, with the others remaining unchanged.

2.5.2.3 Electrochemical Reaction of Triazolium 9

An electrochemical reaction was performed using **Tz9.BF₄** and Cu electrodes using the ElectraSyn. The reaction was performed in anhydrous MeCN under an inert atmosphere for 2.5Q (Figure 208).

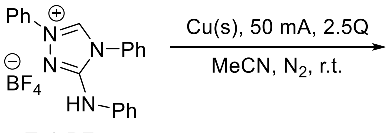

Tz9.BF₄

Figure 208. Reaction scheme for electrochemical reaction using **Tz9.BF₄.**

Analysis of the crude ^{1}H NMR spectrum showed similarities with that of **Cu9a.BF₄**, although the spectrum was far broader. The HRMS data had one peak corresponding to free ligand and another corresponding to the bis-NHC complex. After filtration and recrystallisation the NMR spectra obtained were of poor quality, in spite of an apparently concentrated sample. This is likely due to the co-precipitation of $[Cu(MeCN)_4][BF_4]$ during the work-up. The ^{1}H NMR spectrum obtained does not show any increase in the number of signals compared to that for **Cu9a.BF₄** or other nitron complexes previously reported, and hence there is no evidence that ring-opening has occurred. A powder X-ray diffraction pattern was obtained on the bulk sample and compared to that predicted for **Cu9a.BF₄** and $[Cu(MeCN)_4][BF_4]$ (Figure 209).[52] The major signals observed in the measured pattern agree well with those predicted for $[Cu(MeCN)_4][BF_4]$, with limited agreement with that for **Cu9a.BF4**. However, no signals that cannot be explained by the presence of either species are observed, and hence no evidence of ring-opening is found.

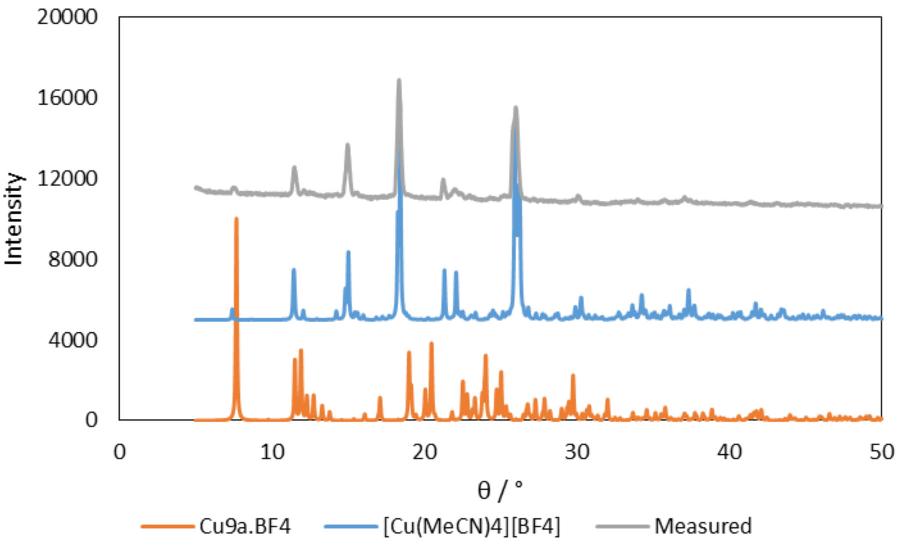

Figure 209. Comparison of simulated XRD powder pattern for **Cu9a.BF$_4$** and [Cu(MeCN)$_4$][BF$_4$] with that measured for the product of electrochemical reaction of **Tz9.BF$_4$** with Cu electrodes.[52]

2.6 Conclusions and Future Work

The electrochemical synthesis of bis-NHC Cu complexes derived from a range of triazolium salts has been demonstrated. In the case of **Tz1.BF$_4$** an unusual ring-opening reaction to form a diimine ligand was observed. The same reaction is not observed under chemical conditions, leading to the conclusion that the reaction is electrochemical in origin.

The scope of the ring-opening reaction was probed by the preparation of a range of triazolium salts. No alternative triazolium salts that have been investigated underwent electrochemical ring-opening. Some further structural modifications could be probed however (Figure 210). Preparation of backbone substituted triazolium salts should be undertaken; use of a longer chain or bulkier amide may prevent the problematic elimination pathway observed previously. Alternatively, other cyclic amides could be used to prepare 5,6 or 5,7 fused ring systems. Another avenue for investigation would be variation of the aryl group, to probe whether varying electronic properties impacts the ring-opening process.

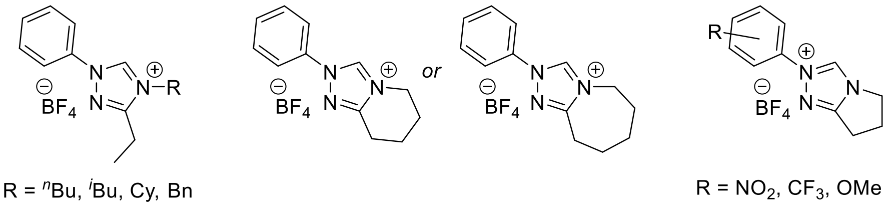

Figure 210. Possible alternative triazolium salts.

Synthesis of the bis-NHC Cu complexes **Cu1a.BF$_4$** and **Cu5a.Br** has been achieved by chemical means. In Chapter 3, investigations into the mechanism of the ring-opening reaction are discussed, using the ligand precursors and complexes prepared in this chapter.

2.7 Experimental

2.7.1 General Considerations

Where stated, reactions were carried out under an inert atmosphere of dry nitrogen or argon, using standard Schlenk line or glovebox techniques. Anhydrous solvents were dried by passing over activated alumina to remove water, copper catalyst to remove oxygen, and molecular sieves to remove any remaining water, *via* the Dow-Grubbs solvent system. MeOH, THF and DCM were freeze-pump-thaw degassed, while MeCN was degassed by purging with argon. Deuterated MeCN was dried by standing for 18 hours over activated 3 Å molecular sieves, followed by transfer to fresh activated 3 Å sieves, and then purged with argon prior to use. Chemicals were purchased from Sigma Aldrich, Alfa Aesar or Fluorochem and used without further purification. **Tz1.BF$_4$** and **Tz1.Cl** were gifted by Professor Andrew Smith (University of St Andrews) and used as received.

Electrochemical reactions were performed in either a 3-neck round bottom flask using copper electrodes made from sheet copper (99.9% purity) attached to a British Standard Tester PSD30/3B DC power supply *via* crocodile clips, or in an IKA ElectraSyn 2.0 using vials, caps and electrodes supplied by IKA. Copper electrodes were cleaned prior to use according to the following procedure: Electrodes were treated with HCl (~4M) in a sonicator bath for 5 – 10 minutes. The surfaces were cleaned with water, soap and a scouring pad, followed by acetone. Electrodes were dried in an oven prior to use.

NMR spectra were recorded on either a Bruker AV NEO 500, a Bruker AV3 HD 400, or a Bruker AV 300 spectrometer. ^{1}H NMR and ^{13}C{^{1}H} chemical shifts were referenced against residual solvent peaks. Assignment of ^{1}H and ^{13}C{^{1}H} NMR spectra was aided by 2D ^{1}H^{1}H COSY, ^{1}H^{13}C HMQC, ^{1}H^{13}C HMBC and ^{13}C{^{1}H} DEPT 135 where relevant. Mass spectra were collected on a Bruker Daltonics (micro TOF) instrument operating in the electrospray mode. Direct injection mass spectra were recorded on a Bruker Daltonics (micro TOF) by Dr Stuart Warriner. IR spectra were recorded on a Bruker Platinum ATR instrument. Elemental Analyses were performed by Mr Stephen Boyer at London Metropolitan University.

2.7.2 Synthesis of Precursors

1-Benzyl-1,2,4-triazole

Benzyl bromide (0.80 mL, 6.7 mmol), 4-amino-1,2,4-triazole (500 mg, 5.95 mmol) and IPA (15 mL) were heated at reflux for 24 hours. The solvent was removed *in vacuo* and replaced with water (20 mL) and cooled to 6 °C. Concentrated HCl

(1.0 mL, 12 M, 11.9 mmol) was added, followed by saturated aqueous $NaNO_2$ (499 mg, 7.23 mmol) dropwise. The reaction mixture was warmed to room temperature, and neutralised with K_2CO_3. The mixture was extracted with DCM (3 x 40 mL), and the combined organic phase dried over $MgSO_4$. The solvent was removed *in vacuo* and the residue purified by flash-column chromatography [33:67 pentane/ethyl acetate – 20:80 pentane/ethyl acetate. Rf: 0.26] to yield the product as a yellow oil. Yield: 572 mg, 60%.

^{1}H NMR (400 MHz, $CDCl_3$) δ 7.95 (s, 1H), 7.87 (s, 1H), 7.32 – 7.21 (m, 3H), 7.19 – 7.12 (m, 2H), 5.24 (s, 2H). ^{13}C{^{1}H} NMR (101 MHz, $CDCl_3$) δ 152.2, 143.1, 134.6, 129.2, 128.8, 128.1, 53.7.
HRMS (ESI$^+$): *m/z* $[C_9H_{10}N_3]^+$ 160.0867, calcd for $[M+H]^+$ 160.0869.
Consistent with literature data.[53]

1-Phenyl-1,2,4-triazole

Formamide (6.0 mL, 150 mmol) was added to an ampoule under nitrogen and heated to 80 °C. Phenyl hydrazine (2.0 mL, 20 mmol) was added and the mixture heated to 110 °C. Acetic acid (0.6 mL, 17 M, 10 mmol) was added dropwise and the mixture held at 110 °C for 4 days, over which time the colour changed from deep red to yellow. The mixture was cooled to room temperature and DCM (20 mL) added. The solution was washed with H_2O (3 x 25 mL), and the organic phase dried over $MgSO_4$ and the solvent removed *in vacuo*. The resulting yellow oil was cooled to -20 °C until it solidified. Yield: 2.048 g, 84%.

^{1}H NMR (300 MHz, $CDCl_3$) δ 8.55 (s, 1H), 8.10 (s, 1H), 7.70 – 7.63 (m, 2H), 7.54 – 7.45 (m, 2H), 7.43 – 7.35 (m, 1H). ^{13}C{^{1}H} NMR (75 MHz, $CDCl_3$) δ 152.7, 141.0, 129.9, 128.3, 120.2.
HRMS (ESI$^+$): *m/z* $[C_8H_7N_3]^+$ 146.0711, calcd for $[M+H]^+$ 146.0718.
Consistent with literature data.[34]

2.7.3 Synthesis of Triazolium Salts

Tz2.Br

Benzyl bromide (510 µL, 4.29 mmol), 1-benzyl-1,2,4-triazole (570 mg, 3.56 mmol) and MeCN (5 mL) were combined and heated at reflux for 21 hours. The solvent was removed *in vacuo* and the residue washed with Et_2O, then recrystallised from MeCN/acetone (1:10 v/v) to yield the product as a white solid. Yield: 823 mg, 70%.

^{1}H NMR (400 MHz, DMSO) δ 10.32 (s, 1H), 9.33 (s, 1H), 7.53 – 7.37 (m, 10H), 5.62 (s, 2H), 5.53 (s, 2H). ^{13}C{^{1}H} NMR (101 MHz, DMSO) δ 145.0, 142.7, 133.5, 133.1, 129.1, 128.9, 128.9, 128.8, 54.9, 50.6.
HRMS (ESI$^+$): *m/z* $[C_{16}H_{16}N_3]^+$ 250.1342, calcd for $[M-Br]^+$ 250.1339.

Consistent with literature data.[54]

Tz2.BF$_4$

1,4-Benzyl-1,2,4-triazolium bromide (500 mg, 1.50 mmol) was dissolved in MeOH (15 mL) and H_2O (5 mL) and a solution of NH_4BF_4 (789 mg, 7.52 mmol) in H_2O (10 mL) was added. The reaction mixture was stirred for 1 hour after which time a white precipitate had formed. The product was isolated by filtration and washed with Et_2O (10 mL). Yield: 402 mg, 79%.

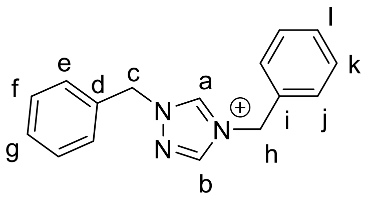

^{1}H NMR (400 MHz, DMSO) δ 10.24 (s, 1H, H$_a$), 9.30 (s, 1H, H$_b$), 7.52 – 7.38 (m, 10H, H$_{e\text{-}f/j\text{-}l}$), 5.60 (s, 2H, H$_c$), 5.50 (s, 2H, H$_h$). ^{13}C{^{1}H} NMR (101 MHz, DMSO) δ 145.0 (C$_b$), 142.7 (C$_a$), 133.5 (C$_{d/i}$), 133.1 (C$_{d/i}$), 129.1 (C$_{e\text{-}g/j\text{-}l}$), 129.0 (C$_{e\text{-}g/j\text{-}l}$), 128.9 (C$_{e\text{-}g/j\text{-}l}$), 128.9 (C$_{e\text{-}g/j\text{-}l}$), 128.8 (C$_{e\text{-}g/j\text{-}l}$), 54.9 (C$_c$), 50.7 (C$_h$). ^{19}F NMR (376 MHz, DMSO) δ -148.26, -148.31.

HRMS (ESI$^+$): *m/z* $[C_{16}H_{16}N_3]^+$ 250.1350, calcd for $[M\text{-}BF_4]^+$ 250.1339.

Single crystals suitable for X-ray diffraction analysis were grown by vapour diffusion of Et_2O into a concentrated solution of **Tz2.BF$_4$** in MeCN.

Tz4.I

1-Phenyl-1,2,4-triazole (435 mg, 2.99 mmol), MeI (375 µL, 6 mmol) and MeCN (7 mL) were combined in an ampoule and held at reflux for 27 hours. The solvent was removed *in vacuo* and the residue recrystallised from MeCN and Et_2O. Yield: 723 mg, 84%

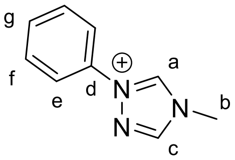

^{1}H NMR (300 MHz, DMSO) δ 10.84 (s, 1H, H$_a$), 9.37 (s, 1H, H$_c$), 7.95 – 7.84 (m, 2H, H$_{e\text{-}g}$), 7.77 – 7.59 (m, 3H, H$_{e\text{-}g}$), 3.99 (s, 3H, H$_b$). ^{13}C{^{1}H} NMR (75 MHz, DMSO) δ 145.8 (C$_c$), 142.2 (C$_a$), 134.9 (C$_d$), 130.5 (C$_{e\text{-}g}$), 130.3 (C$_{e\text{-}g}$), 120.6 (C$_{e\text{-}g}$), 34.4 (C$_b$).

HRMS (ESI$^+$): *m/z* $[C_9H_{10}N_3]^+$ 160.0867, calcd for $[M\text{-}I]^+$ 160.0869.

Tz4.BF$_4$

Tz4.I (198 mg, 0.690 mmol) and $AgBF_4$ (142 mg, 0.727 mmol) were combined in MeOH (15 mL) and stirred for 30 min. Upon combination a green/yellow solid formed immediately. The suspension was filtered through celite, and the filtrate reduced *in vacuo*. The residue was recrystallised from MeCN and Et_2O to yield the product as a brown solid. Yield: 25.6 mg, 15%.

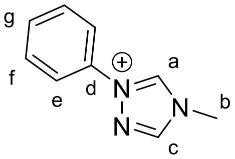

^{1}H NMR (300 MHz, DMSO) δ 10.81 (s, 1H, H$_a$), 9.35 (s, 1H, H$_c$), 8.09 – 7.39 (m, 5H, H$_{e\text{-}g}$), 3.98 (s, 3H, H$_b$). ^{13}C{^{1}H} NMR (75 MHz, DMSO) δ 145.8 (C$_c$), 142.2 (C$_a$), 134.9

(C_d), 130.5 (C_{e}-$_{g}$), 130.3 (C_{e}-$_{g}$), 120.6 (C_{e}-$_{g}$), 34.3 (C_b). $^{19}F\{^1H\}$ NMR (282 MHz, DMSO) δ -148.34.
HRMS (ESI$^+$): *m/z* $[C_9H_{10}N_3]^+$ 160.761, calcd for $[M\text{-}BF_4]^+$ 160.0869.

Tz5.Br

1-phenyl-1,2,4-triazole (1.500 g, 10.3 mmol) and 1-bromopropane (8.0 mL, 88.1 mmol) were combined in an ampoule with toluene (7 mL), sealed and held at reflux for 4 days. Over the course of the reaction an off-white precipitate formed in the flask. The reaction was cooled to room temperature and the precipitate isolated by filtration. The residue remaining in the reaction flask was recrystallised from MeCN and Et_2O, and isolated by filtration. The beige solids were combined and dried in an oven. Yield: 1.385 g, 50%.

^1H NMR (300 MHz, DMSO) δ 10.92 (s, 1H), 9.48 (s, 1H), 8.00 – 7.88 (m, 2H), 7.78 – 7.57 (m, 3H), 4.29 (t, *J* = 7.2 Hz, 2H), 1.96 (h, *J* = 7.3 Hz, 2H), 0.97 (t, *J* = 7.4 Hz, 3H). $^{13}C\{^1H\}$ NMR (75 MHz, DMSO) δ 145.0, 141.6, 135.1, 130.4, 130.2, 120.6, 49.4, 22.2, 10.5.
HRMS (ESI$^+$): *m/z* $[C_{11}H_{14}N_3]^+$ 188.1184, calcd for $[M\text{-}Br]^+$ 188.1182.
Consistent with literature data.[29]

Tz5.BF$_4$

Tz5.Br (500 mg, 1.86 mmol) was dissolved in a mixture of MeOH (5 mL) and H_2O (5 mL). A solution of $NaBF_4$ (1.028 g, 9.36 mmol) in H_2O (10 mL) was added, and the mixture stirred at room temperature for 1 hour. After 1 minute a white solid precipitated from solution. The solid was isolated by filtration, and washed with Et_2O. The filtrate was reduced *in vacuo*. The residue was triturated using MeCN (10 mL) and filtered through celite. The filtrate was reduced *in vacuo* and the residue triturated with acetone (10 mL) and filtered through celite twice. The filtrate was reduced *in vacuo* and the residue recrystallised from acetone and Et_2O. The solids from the initial filtration and the recrystallisation were combined. Yield: 378 mg, 74%

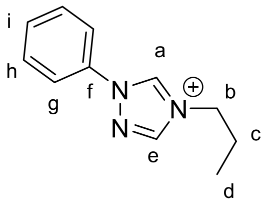

^1H NMR (300 MHz, DMSO) δ 10.87 (s, 1H, H_a), 9.45 (s, 1H, H_e), 7.92 (d, *J* = 7.5 Hz, 2H, $H_{g\text{-}i}$), 7.81 – 7.54 (m, 3H, $H_{g\text{-}i}$), 4.28 (t, *J* = 7.3 Hz, 2H, H_b), 1.96 (h, *J* = 7.2 Hz, 2H, H_c), 0.98 (t, *J* = 7.4 Hz, 3H, C_d). $^{13}C\{^1H\}$ NMR (75 MHz, DMSO) δ 145.1 (C_e), 141.5 (C_a), 135.1 (C_f), 130.5 (Cg-i), 130.2 ($C_{g\text{-}i}$), 120.7 ($C_{g\text{-}i}$), 49.5 (C_b), 22.2 (C_c), 10.5 (C_d). $^{19}F\{^1H\}$ NMR (282 MHz, DMSO) δ -148.28, -148.34.
HRMS (ESI$^+$): *m/z* $[C_{11}H_{14}N_3]^+$ 188.1180, calcd for $[M\text{-}BF_4]^+$ 188.1182.

Tz6.Br

1-Phenyl-1,2,4-triazole (998 mg, 6.87 mmol), 2-bromopropane (7.0 mL, 75 mmol) and toluene (10 mL) were combined in a sealed ampoule and held at reflux for 4 days. The formed grey solid was isolated by filtration and washed with Et_2O to yield the product. Yield: 94.5 mg, 5%.

The filtrate was reduced *in vacuo*, the residue dissolved in DCM (20 mL) and washed with H_2O (4 x 20 mL) followed by brine (1 x 20 mL). The organic phase was dried over $MgSO_4$, and reduced *in vacuo* to recover the unreacted starting material.

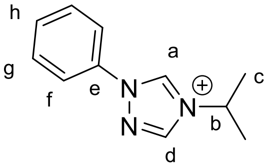

^1H NMR (300 MHz, DMSO) δ 10.94 (s, 1H, H_a), 9.58 (s, 1H, H_d), 8.09 – 7.87 (m, 2H, H_{f-h}), 7.79 – 7.54 (m, 3H, H_{f-h}), 4.80 (hept, *J* = 6.7 Hz, 1H, H_b), 1.61 (d, *J* = 6.7 Hz, 6H, H_c). $^{13}C\{^1H\}$ NMR (75 MHz, DMSO) δ 143.9 (C_d), 140.6 (C_a), 135.1 (C_e), 130.4 (C_{f-h}), 130.1 (C_{f-h}), 120.7 (C_{f-h}), 52.5 (C_b), 22.0 (C_c).

HRMS (ESI$^+$): *m/z* $[C_{11}H_{14}N_3]^+$ 188.1182, calcd for $[M-Br]^+$ 188.1182.

Single crystals suitable for X-Ray diffraction analysis were grown by vapour diffusion of Et_2O into a concentrated solution of **Tz6.Br** in MeCN.

Tz7.Br

1-Phenyl-1,2,4-triazole (500 mg, 3.43 mmol) was combined in an ampoule with 2-bromo-2-methylpropane (0.47 mL, 4.2 mmol) and MeCN (5 mL) and held at reflux for 30 hours. The formed precipitate was isolated by filtration, and further solid was obtained by recrystallisation of the reduced filtrate from MeCN and Et_2O. Analysis by ^1H NMR indicated that the reaction was incomplete. The reaction was restarted with additional 2-bromo-2-methylpropane (1.0 mL, 8.9 mmol) and MeCN (5 mL) and held at reflux for 48 hours. After work-up the NMR analysis still indicated an incomplete reaction. The reaction was restarted with additional 2-bromo-2-methylpropane (1.0 mL, 8.9 mmol) and MeOH (5 mL) and held at reflux for 30 hours. The reaction mixture was reduced *in vacuo* and the residue recrystallised from MeOH and Et_2O. Analysis of the product revealed a mixture of starting material and product. The solid was partitioned between H_2O (30 mL) and toluene (30 mL) and the aqueous phase extracted with toluene (2 x 30 mL). The aqueous phase was removed *in vacuo* and the residue crystallised by slow diffusion of Et_2O into MeCN to yield the product. Yield: 108 mg, 11%. The organic phase was reduced *in vacuo* to leave residual starting material.

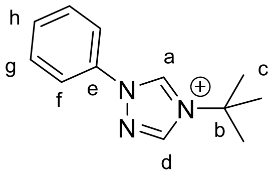

^1H NMR (300 MHz, DMSO) δ 10.92 (s, 1H, H_a), 9.74 (s, 1H, H_d), 8.02 (dt, *J* = 3.8, 2.3 Hz, 2H, H_{f-h}), 7.78 – 7.52 (m, 3H, H_{f-h}), 1.72 (s, 9H, H_c). $^{13}C\{^1H\}$ NMR (75 MHz, DMSO) δ 143.3 (C_d), 140.2 (C_a), 135.2 (C_e), 130.4 ($C_{f\text{-}h}$), 123.0 ($C_{f\text{-}h}$), 120.9 ($C_{f\text{-}h}$), 61.1 (C_b), 28.9 (C_c).

HRMS (ESI$^+$): *m/z* $[C_{12}H_{16}N_3]^+$ 202.1340, calcd for $[M\text{-}Br]^+$ 202.1339; $[C_8H_7N_3]^+$ 146.0714, calcd for $[M\text{-}Br\text{-}^tBu+H]^+$ 146.0718.

Single crystals suitable for X-Ray diffraction analysis were grown by vapour diffusion of Et_2O into a concentrated solution of **Tz7.Br** in MeCN.

Tz8’.BF_4

Trimethyloxonium tetrafluoroborate (1.777 g, 12.01 mmol) was added to a solution of N-methylpropionamide (0.94 mL, 10 mmol) in anhydrous DCM (10 mL) under nitrogen. The resulting solution was stirred at room temperature for 17 hours. Phenyl hydrazine (0.98 mL, 10 mmol) was added and the solution instantly became yellow, and a precipitate formed. The suspension was stirred at room temperature for 48 hours over which time the colour changed from yellow to dark red. The solvent was removed *in vacuo* and anhydrous MeOH (2 mL) was added followed by trimethylorthoformate (11 mL, 100 mmol). The red solution was heated to 85 °C for 24 hours. The solvent was removed *in vacuo* and attempts were made to recrystallise the residue from MeCN and Et_2O. When these failed, all residue and solids were combined and redissolved in anhydrous MeOH (2 mL) under nitrogen and trimethylorthoformate (11 mL) added, and the reaction mixture held at reflux for 41 hours. The mixture was cooled to room temperature and the solvent removed *in vacuo*. DCM was added to the residue and the insoluble matter removed by filtration. The filtrate was washed with water (1 x 30 mL) brine (1 x 40 mL) and water (2 x 40 mL), dried over $MgSO_4$ and reduced *in vacuo*. The residue was recrystallised from MeCN and Et_2O to yield a brown solid. Yield: 151 mg, 9%.

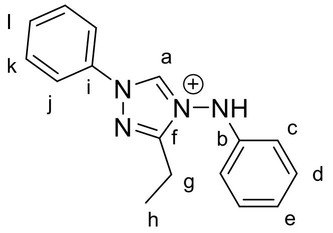

^{1}H NMR (501 MHz, DMSO) δ 11.31 (s, 1H, H_a), 10.18 (s, 1H, N*H*), 7.99 (d, *J* = 7.4 Hz, 2H, H_j), 7.72 (t, *J* = 7.8 Hz, 2H, H_k), 7.65 (t, *J* = 7.4 Hz, 1H, H_l), 7.41 – 7.29 (m, 2H, H_d), 7.05 (t, *J* = 7.4 Hz, 1H, H_e), 7.00 (d, *J* = 7.5 Hz, 1H, H_c), 2.80 (q, *J* = 7.5 Hz, 2H, H_g), 1.27 (t, *J* = 7.5 Hz, 3H, H_h). $^{13}C\{^1H\}$ NMR (126 MHz, DMSO) δ 158.1 (C_f), 144.6 (C_b), 144.1 (C_a), 135.1 (C_i), 130.5 (C_l), 130.1 (C_k), 129.6 (C_d), 122.6 (C_e), 120.5 (C_j), 113.8 (C_c), 16.9 (C_g), 9.9 (C_h). $^{19}F\{^1H\}$ NMR (376 MHz, DMSO) δ -148.16, -148.21.

HRMS (ESI$^+$): *m/z* $[C_{16}H_{17}N_4]^+$ 265.1449, calcd for $[M\text{-}BF_4]^+$ 265.1448.

Elemental Analysis: Found: C, 54.66; H, 4.81; N, 15.73. Calcd: C, 54.57; H, 4.87; N, 15.91.

Single crystals suitable for X-Ray diffraction analysis were grown by vapour diffusion of Et_2O into a concentrated solution of **Tz8’.BF_4** in MeCN.

Tz9.BF$_4$

Nitron (400 mg, 1.28 mmol) was suspended in MeOH (15 mL) and a solution of NaBF$_4$ (743 mg, 6.77 mmol) in water (25 mL) was added slowly. The resulting brown suspension was stirred at room tempterature for 18 hours. The MeOH was removed *in vacuo* and water (30 mL) added to the aqueous residue. The aqueous phase was extracted with DCM (3 x 25 mL), and the combined organic phase was then washed with water (1 x 50 mL), dried over MgSO$_4$ and reduced *in vacuo*. The residue was recrystallised from MeCN and Et$_2$O to yield the product as a beige solid. Yield: 128 mg, 25%.

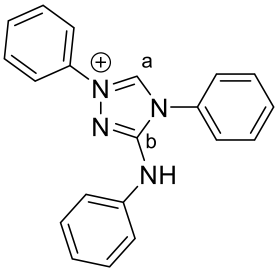

^{1}H NMR (501 MHz, DMSO) δ 10.84 (s, 1H, H$_a$), 9.71 (s, 1H, N*H*), 8.00 (dd, *J* = 7.7, 1.6 Hz, 2H), 7.89 – 7.81 (m, 2H), 7.79 – 7.68 (m, 5H), 7.63 (t, *J* = 8.2 Hz, 3H), 7.39 (t, *J* = 7.9 Hz, 2H), 7.10 (t, *J* = 7.4 Hz, 1H). ^{13}C{^{1}H} NMR (126 MHz, DMSO) δ 150.6 (C$_b$), 139.1 (C$_a$), 135.0 (C$_q$), 131.3, 130.7 (C$_q$), 130.2, 130.2, 130.1, 129.0, 126.8, 123.2, 119.9, 119.2. ^{19}F{^{1}H} NMR (376 MHz, DMSO) δ -148.19, -148.25.
HRMS (ESI$^+$): *m/z* [$C_{17}H_{20}N_4$]$^+$ 313.1303, calcd for [M-BF$_4$]$^+$ 313.1448.
Elemental Analysis: Found: C, 60.17; H, 4.19; N, 13.88. Calcd: C, 60.03; H, 4.28; N, 14.00.

2.7.4 Synthesis of Complexes:

Cu1a.BF$_4$

Tz1.Cl (134 mg, 0.606 mmol) was combined in an ampoule with Na^{t}BuO (64.1 mg, 0.667 mmol), [Cu(MeCN)$_4$][BF$_4$] (95.6 mg, 0.304 mmol) and anhydrous THF (7 mL) in a glovebox. The resulting brown suspension was stirred at room temperature for 6 hours, over which time the brown colour darkened. The reaction mixture was reduced *in vacuo* and the residue dissolved in MeCN and filtered through a Celite pipette in a glovebox. Et$_2$O was added to the filtrate, and the resulting off white solid was isolated *via* cannula filtration and washed with Et$_2$O (3 x 2 mL) before drying *in vacuo*. A second crop was obtained from the filtrate. Yield: 91.7 mg, 58%.

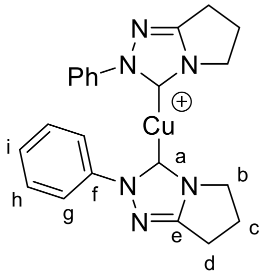

^{1}H NMR (400 MHz, CD$_3$CN) δ 7.67 (d, *J* = 5.1 Hz, 2H, H$_g$), 7.46 – 7.22 (m, 3H, H$_{h/i}$), 3.76 (br. s, 2H, H, H$_b$), 2.94 (t, *J* = 7.7 Hz, 2H, H$_d$), 2.55 (p, *J* = 7.4 Hz, 2H, H$_c$). ^{13}C{^{1}H} NMR (101 MHz, CD$_3$CN) δ 161.5 (C$_e$), 141.6 (C$_f$), 130.2 (C$_h$), 128.9 (C$_i$), 123.1 (C$_g$), 46.3 (C$_b$), 26.8 (C$_c$), 21.6 (C$_d$). ^{19}F{^{1}H} NMR (376 MHz, CD$_3$CN) δ -152.16, -152.21.
HRMS (ESI$^+$): *m/z* [$C_{22}H_{22}CuN_6$]$^+$ 433.1200, calcd for [**Cu1a.BF$_4$**-BF$_4$]$^+$ 433.1196.

Elemental Analysis: Found: C, 51.63; H, 4.42; N, 16.16. Calcd for [6 **Cu1a.BF_4**-BF_4+Cl]: C, 51.76; H, 4.34; N, 16.46.

Single crystals of this complex suitable for X-Ray diffraction analysis were obtained from a previous reaction with K^{t}BuO from the vapour diffusion of Et_2O into a concentrated solution of **Cu1a.BF_4** in MeCN.

Cu1a.BF_4/Cu1b.BF_4 mix

Tz1.BF_4 (99.8 mg, 0.366 mmol) was added to a three neck round bottom flask and placed under nitrogen. Anhydrous MeCN (5 mL) was added and Cu electrodes were inserted. A voltage was applied to maintain a current between 10 and 50 mA for 2.5Q. The reaction mixture was transferred to an ampoule with additional MeCN (10 mL). The mixture was filtered through cotton wool and celite in a glovebox. The filtrate was reduced *in vacuo* and the residue recrystallised from MeCN and Et_2O. The solids were isolated *via* cannula filtration and the filtrate was reduced *in vacuo*. The recrystallisation was repeated once on the residue. The solids were suspended in Et_2O, combined and dried *in vacuo* to yield the product as a brown solid. Yield: 41.3 mg.

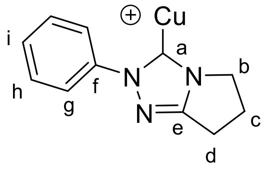

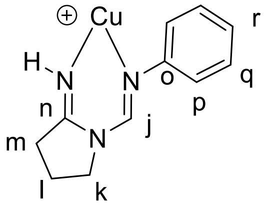

^{1}H NMR (400 MHz, CD_3CN) δ 8.49 (br. s, 1H, N*H*), 8.08 (s, 1H, H_j), 7.81 (d, *J* = 7.6 Hz, 4H, H_g), 7.53 – 7.38 (m, 6H, $H_{i/j}$), 7.26 (t, *J* = 7.6 Hz, 2H, H_q), 7.16 (t, *J* = 7.3 Hz, 1H, H_r), 6.99 (d, *J* = 7.6 Hz, 2H, H_p), 4.02 (d, *J* = 7.0 Hz, 6H, H_b and H_k), 3.00 (t, *J* = 7.6 Hz, 4H, H_d), 2.86 (t, *J* = 7.7 Hz, 2H, H_m), 2.68 – 2.55 (m, 4H, H_c), 2.12 (p, *J* = 7.3 Hz, 3H, H_l). ^{13}C{^{1}H} NMR (151 MHz,) δ 176.9 (C_a), 170.5, 161.8 (C_e), 152.9 (C_j), 150.5 (C_o), 141.6 (C_f), 130.3 (C_q), 130.2 (C_h), 129.1 (C_i), 126.9 (C_r), 123.4 (C_g), 122.9 (C_p), 53.7 (C_k), 46.7 (C_b), 34.8 (C_m), 26.8 (C_c), 21.8 (C_d), 21.1 (C_l). ^{19}F{^{1}H} NMR (376 MHz, CD_3CN) δ -151.87, -151.92.

HRMS (ESI$^+$): *m/z* $[C_{22}H_{22}CuN_6]^+$ 433.1205, calcd for [**Cu1a.BF_4**-BF_4]$^+$ 433.1196; $[C_{22}H_{24}CuN_6]^+$ 435.1361, calcd for [**Cu1b.BF_4**-BF_4]$^+$ 435.1353.

Single crystals suitable for X-ray diffraction analysis were grown by vapour diffusion of Et_2O into a concentrated solution of the product mixture in MeCN.

Elemental analysis was not obtained due to the mixture of species.

Cu2a.BF$_4$

Tz2.BF$_4$ (300 mg, 0.890 mmol) was dissolved in anhydrous MeCN (10 mL) under nitrogen. Cu electrodes were inserted into the solution and a voltage applied to maintain a current between 10 and 50 mA for 1 hour. The solution was transferred to an ampoule and filtered through celite in a glovebox. The filtrate was reduced *in vacuo* and the residue recrystallised from MeCN and Et$_2$O. The resulting white solid was isolated by cannula filtration, washed with Et$_2$O (3 x 3 mL) and dried *in vacuo*. A second crop was obtained by concentrating the filtrate *in vacuo* and recrystallising the residue. Yield: 250 mg, 87%.

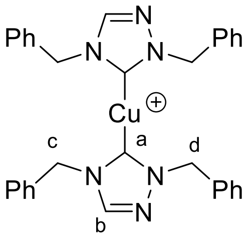

^{1}H NMR (300 MHz, CD$_3$CN) δ 8.25 (s, 1H, H$_b$), 7.38 – 7.28 (m, 6H, H$_{Ph}$), 7.27 – 7.18 (m, 4H, H$_{Ph}$), 5.33 (s, 2H, H$_{c/d}$), 5.21 (s, 2H, H$_{c/d}$). ^{19}F NMR (282 MHz, CD$_3$CN) δ -151.85, -151.90. ^{13}C{^{1}H} NMR (75 MHz, CD$_3$CN) δ 144.0 (C$_b$), 137.2 (C$_{Ph}$), 123.0 (C$_{Ph}$), 129.8 (C$_{Ph}$), 129.3 (C$_{Ph}$), 129.2 (C$_{Ph}$), 128.8 (C$_{Ph}$), 128.7 (C$_{Ph}$), 57.0 (C$_{c/d}$), 52.3 (C$_{c/d}$).

HRMS (ESI$^+$): *m/z* [$C_{32}H_{30}CuN_6$]$^+$ 561.1830, calcd for [M-BF$_4$]$^+$ 561.1822; [$C_{25}H_{24}CuN_6$]$^+$ 471.1351, calcd for [M-BF$_4$-Bn+H]$^+$ 471.1353; [$C_{16}H_{15}CuN_3$]$^+$ 312.0561, calcd for [M-BF$_4$-(NHC)]$^+$ 312.0557; [$C_{16}H_{16}N_3$]$^+$ 250.1341, calcd for [**Tz2**-BF$_4$]$^+$ 250.1339.

Elemental Analysis: Found: C, 50.38; H, 4.08; N, 12.63. Calcd for [**Cu2a.BF$_4$**]: C, 59.22; H, 4.66; N, 12.95. Large error attributed to residual [Cu(MeCN)$_4$BF$_4$] and air-sensitivity of product.

Cu5a.BF$_4$

A three neck round bottom flask was flame-dried and placed under nitrogen. **Tz5.BF$_4$** (300 mg, 1.09 mmol) was added followed by anhydrous MeCN (10 mL). Cu electrodes were inserted and a voltage applied to maintain a current of 50 mA for 3.4Q. Over the course of the reaction the colour changed from pale brown to dark brown. The reaction mixture was transferred to an ampoule *via* cannula and taken into a glovebox. The solution was filtered twice through celite and the filtrate reduced *in vacuo* to a volume of approximately 3 mL. Et$_2$O (7 mL) was added *via* cannula and the solution was stirred vigourously to induce precipitation. The off-white precipitate was isolated *via* cannula filtration, and washed with Et$_2$O (3 x 2 mL). The solid was dried *in vacuo* to yield the product. Yield: 224 mg, 78%.

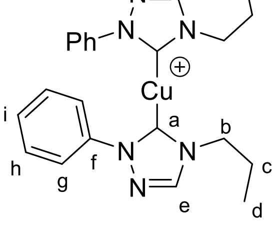

^{1}H NMR (300 MHz, CD_3CN) δ 8.38 (s, 1H, H_e), 7.86 – 7.76 (m, 2H, H_{g-i}), 7.61 – 7.47 (m, 3H, H_{g-i}), 4.16 (t, *J* = 7.2 Hz, 2H, H_b), 0.96 (t, *J* = 7.4 Hz, 3H, H_d) [H_c masked CD_2HCN signal].

It was not possible to obtain either a $^{13}C\{^1H\}$ NMR or HRMS for this compound.

Elemental Analysis: Found: C, 25.49; H, 3.44,; N, 13.62. Calcd: C, 50.35; H, 4.99; N, 16.01. Large error attributed to residual $[Cu(MeCN)_4][BF_4]$ and the air-sensitivity of the product.

Cu5a.Br

Tz5.Br (162 mg, 0.606 mmol) was combined in an ampoule with Na^{t}BuO (65.5 mg, 0.682 mmol), $[Cu(MeCN)_4][BF_4]$ (95.4 mg, 0.303 mmol) and anhydrous THF (7 mL) in a glovebox. The resulting yellow suspension was stirred at room temperature for 6 hours, over which time the colour changed to orange. The reaction mixture was reduced *in vacuo* and the residue redissolved in anhydrous THF and filtered through a Celite pipette in the glovebox. Anhydrous hexane was added to the filtrate to precipitate a white solid. The solid was isolated *via* cannula filtration and dried *in vacuo*. Yield: 72.3 mg, 45%.

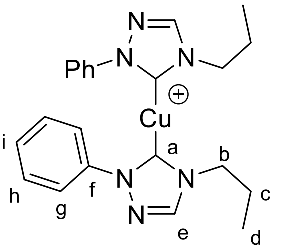

^{1}H NMR (400 MHz, CD_3CN) δ 8.26 (s, 1H, H_e), 8.06 – 7.93 (m, 2H, H_{g-i}), 7.39 (m, 3H, H_{g-i}), 4.10 – 3.98 (m, 2H, H_b), 1.81 – 1.74 (m, 2H, H_c), 0.80 (t, *J* = 7.7 Hz, 3H, H_d). $^{13}C\{^1H\}$ NMR (101 MHz, CD_3CN) δ 183.9 (C_a), 144.0 (C_e), 141.2 (C_f), 130.2 (C_{g-i}), 129.2 (C_{g-i}), 123.5 (C_{g-i}), 51.0 (C_b), 24.8 (C_c), 11.1 (C_d). $^{19}F\{^1H\}$ NMR (376 MHz, CD_3CN) δ -151.82, -151.88.

HRMS (ESI$^+$): *m/z* $[C_{22}H_{26}CuN_6]^+$ 437.1505, calcd for [**Cu5a.Br**-Br]$^+$ 437.1515.

Elemental Analysis: Found: C, 52.74; H, 5.84; N, 16.13. Calcd [**Cu5a.Br**]: C, 51.02; H, 5.06; N, 16.23. Calcd for [4 **Cu5a.Br**+C_6H_{14}+MeCN]: C, 52.44; H, 5.55; N, 15.92.

Cu5a*

Tz5.Br (100 mg, 0.373 mmol) and K_2CO_3 (104 mg, 0.752 mmol) were combined in an ampoule and taken into a glovebox. CuBr (59.1 mg, 0.412 mmol) and anhydrous DCM (3 mL) was added, the ampoule sealed and the reaction held at reflux for 24 hours. Over the course of the reaction the suspension changed from a pale purple colour to green. The reaction mixture was filtered through a silica pipette in the glovebox, the volume of the filtrate reduced to ~3 mL *in vacuo* and anhydrous hexane added. When no precipitation occurred the solvent was removed *in vacuo* and the black solid washed with anhydrous hexane (2 x 5 mL). The solid was dried *in vacuo*. Yield: 78.0 mg, 63%.

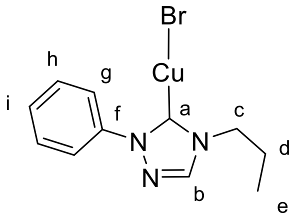

^{1}H NMR (400 MHz, CD_3CN) δ 8.38 (s, 1H, H$_b$), 7.99 (d, *J* = 7.7 Hz, 1H, H$_g$), 7.50 (m, 3H, H$_{h/i}$), 4.21 (t, *J* = 7.3 Hz, 2H, H$_c$), 0.93 (t, *J* = 7.3 Hz, 3H, H$_e$). H$_d$ signal masked by CD_2HCN. ^{13}C{^{1}H} NMR (101 MHz, CD_3CN) δ 180.6 (C$_a$), 144.3 (C$_b$), 140.8 (C$_f$), 130.3 (C$_h$), 129.6 (C$_i$), 123.5 (C$_g$), 51.2 (C$_c$), 25.1 (C$_d$), 11.1 (C$_e$).
HRMS (ESI$^+$): *m/z* [$C_{22}H_{26}CuN_6$]$^+$ 437.1517, calcd for [**Cu5a.Br**-Br]$^+$ 437.1515; [$C_{11}H_{14}N_3$]$^+$ 188.1193, calcd for [**Tz5**-Br]$^+$ 188.1182; [$C_8H_8N_3$]$^+$ 146.0710, calcd for [**Tz5**-^{n}Pr-Br+H]$^+$ 146.0713.
Elemental Analysis: Found: C, 39.85; H, 4.08; N, 12.62. Calcd: C, 39.95; H, 3.96; N, 12.71.

MTT.CuBr$_2$

MTT (207 mg, 0.500 mmol) was dissolved in anhydrous MeCN (20 mL) under nitrogen. Cu electrodes were inserted into the solution and allowed to stand for 10 minutes. A voltage was applied to maintain a current between 10 and 50 mA for 1 hour. The solution was transferred to an ampoule *via* cannula filter and then filtered *via* cannula two further times. The solvent volume was reduced *in vacuo* and the product precipitated by addition of Et_2O. The solid was isolated by cannula filtration, washed with Et_2O (4 x 5 mL), and dried *in vacuo*. A second crop was obtained by reducing the filtrate *in vacuo* and recrystallising the residue in air using hydrous solvents. Yield: 93.6 mg, 67%.

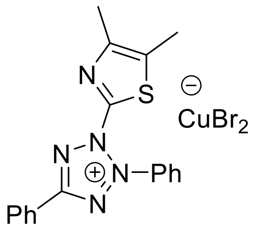

^{1}H NMR (300 MHz, CD_3CN) δ 8.43 – 8.21 (m, 2H, H$_{Ph}$), 7.98 – 7.62 (m, 8H, H$_{Ph}$), 2.49 (s, 3H, H$_{Me}$), 2.22 (s, 3H, H$_{Me}$). ^{13}C{^{1}H} NMR (75 MHz, CD_3CN) δ 135.6 (C$_{Ph}$), 135.0 (C$_{Ph}$), 131.4 (C$_{Ph}$), 131.1 (C$_{Ph}$), 128.7 (C$_{Ph}$), 127.3 (C$_{Ph}$), 14.9 (C$_{Me}$), 12.1 (C$_{Me}$).
HRMS (ESI$^+$): *m/z* [$C_{18}H_{16}N_5S$]$^+$ 334.1119, calcd for [MTT-Br]$^+$ 334.1121.
Elemental Analysis: Found C, 26.73; H, 1.62; N, 8.48. Calcd: C, 38.76; H, 2.89; N, 12.56

Cu9a.BF$_4$

Nitron (200 mg, 0.640 mmol), [Cu(MeCN)$_4$][BF$_4$] (94.8 mg, 0.301 mmol) and DCM (3 mL) were combined in an ampoule and stirred at room temperature for 3 hours, over which time a white precipitate formed. The solid was isolated *via* cannula filtration, and dried *in vacuo*. Yield: 123 mg, 59%.

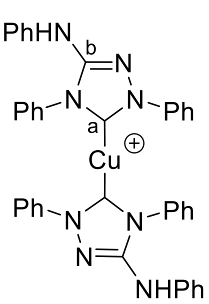

^{1}H NMR (400 MHz, CD_3CN) δ 7.78 – 7.70 (m, 7H), 7.64 – 7.52 (m, 16H), 7.52 – 7.26 (m, 30H), 7.18 – 7.03 (m, 8H), 6.96 (d, *J* = 7.2 Hz, 2H), 6.82 (s, 1H). ^{13}C{^{1}H} NMR (101 MHz, CD_3CN) δ 183.9 (C$_a$), 178.4 (C$_a$), 151.7 (C$_b$), 151.1 (C$_b$), 140.7 (C$_q$), 140.3 (C$_q$), 140.1, 135.5, 131.4, 131.3, 131.1, 131.0, 130.3, 130.0, 129.8, 129.3, 128.8, 128.6, 123.8, 123.6, 122.9, 119.3, 119.1. $^{19}F\{^1H\}$ NMR (376 MHz, CD_3CN) δ -151.87, -151.92.

HRMS (ESI^+): *m/z* $[C_{40}H_{32}CuN_8]^+$ 687.2038, calcd for $[M-BF_4]^+$ 687.2040.

Elemental Analysis: Found: C, 62.02; H, 4.10; N, 14.30. Calcd: C, 61.98; H, 4.16; N, 14.46.

2.7.5 Direct Injection HRMS on Cu1a.BF$_4$/Cu1b.BF$_4$ Mixture

Direct injection HRMS was performed on a sample of **Cu1a.BF$_4$/Cu1b.BF$_4$** to determine if bis-diimine complex **Cu1c.BF$_4$** (Figure 165) was present. Direct injection of the sample should reduce fragmentation and ligand scrambling.

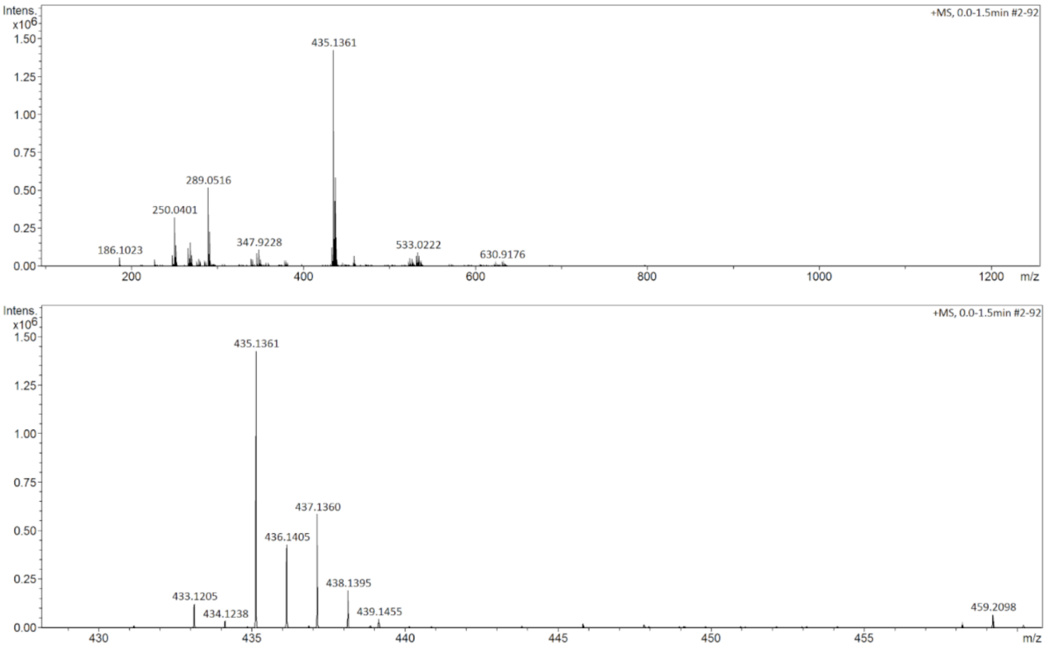

Top: Whole mass spectrum obtained by direct injection. Bottom: region of interest.

Table below describes the determination of presence of **Cu1c**. The relative measured intensities (column 2) were extracted using the DataAnalysis software on the region shown in the figure above.

	Measured intensity[a]	Scaled for **Cu1a**[b]	Remaining intensity[c]	Scaled for **Cu1b**[d]	Remaining intensity attributable to **Cu1c**[e]	Predicted intensity for pure sample[f]		
m/z	Mixed product					[**Cu1a**]$^+$	[**Cu1b**]$^+$	[**Cu1c**]$^+$
433	8.7	100	0			100		
434	2.3	26.9	0.7			26.2		
435	100	1149.7	1101.8	100	0	47.9	100	
436	30.1	346.1	334.1	30.3	4	12.0	26.3	
437	41	471.2	469.7	42.6	-5.3	1.5	47.9	100
438	13.4	153.6	153.5	13.9	1.9	0.1	12.0	26.3
439	3.1	35.1	35.1	3.2	1.7		1.5	47.9
440					-0.1		0.1	12.0
441								1.5
442								0.1

a. Relative intensity of signals obtained by direct injection of a sample of mixed product. b. Obtained by (observed intensity/8.7)*100. c. Obtained by [scaled for **Cu1a**]-[predicted for **Cu1a**] (removes part of signal at *m/z* 435 due to **Cu1a**). d. Obtained by (remaining intensity/1101.8)*100. e. Obtained by [scaled for **Cu1b**]-[predicted for **Cu1b**] (removes part of signal at *m/z* 437 due to **Cu1b**). Signal remaining can be attributed to **Cu1c**. Given the variation in results it is concluded that there is no evidence of the presence of **Cu1c**. *f.* Calculated based on isotope distribution for each complex.

2.7.6 X-ray Diffraction

Single crystal X-ray diffraction data were collected on an Agilent SuperNova diffractometer fitted with an Atlas CCD detector using either Mo Kα radiation (λ = 0.7107 Å) or Cu Kα radiation (λ = 1.5418 Å). Crystals were mounted under oil on nylon fibres. Data sets were corrected for absorption using a multiscan method, and the structures were solved by direct methods using SHELXT and refined by full-matrix least squares on F^2 using SHELXL-97, on the program Olex2. Images were generated using POV-RAY in the X-Seed program. Cif files and data tables are provided in the supplementary data.

Powder X-ray diffraction data were collected on a Bruker D2 Phaser diffractometer, using Cu Kα radiation (λ = 1.5418 Å). Simulated powder patterns were generated from single crystal XRD data using the Mercury 3.3 program.

2.8 Appendix

Table A1. Summary of reaction conditions used for attempted preparation of **Cu2a.BF$_4$** and related complexes.

Target Product	Conditions[a]	Outcome
Cu2a.BF$_4$ 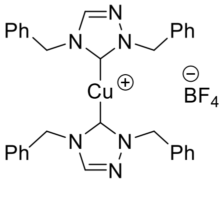 **Cu2a.BF$_4$**	1. Cu$_2$O (0.5 equiv), MeOH, 50 °C, 3 days 2. Cu$_2$O (0.5 equiv), MeOH, 50 °C, 4 days 3. Ag$_2$O (0.25 equiv), MeOH, 50 °C, 24 h 4. Ag$_2$O (0.5 equiv), MeOH, 50 °C, 2 days	Incomplete reaction
Cu2a.BF$_4$	Ag$_2$O (0.5 equiv), CuCl (1 equiv), MeCN, 82 °C, 75 h	Mixture of Cu and Ag complex
Cu2a.BF$_4$	1. NaH (2.1 equiv), THF, r.t., 18 h 2. [Cu(MeCN)$_4$][BF$_4$] (1.05 equiv), THF/MeCN, r.t., 5 days 3. THF/MeCN, 65 °C, 19 h 4. CuCl (1 equiv), THF/MeCN, r.t., 72 h	No reaction observed
Cu2a.BF$_4$	Cu(s) (2.5 equiv), MeCN, r.t., air, 24 h	Incomplete reaction[b]
Cu2a* 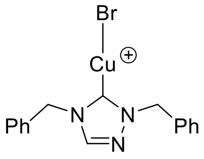 **Cu2a**	K$_2$CO$_3$ (2 equiv), CuBr (1 equiv), DCM, 40 °C, 24 h	Reaction successful
Cu2a.BF$_4$	AgBF$_4$ (2.2 equiv), CD$_3$CN	Reaction successful[c]
Cu2a.BF$_4$	1. K$_2$CO$_3$ (2 equiv), CuBr (0.5 equiv), DCM, 40 °C, 24 h 2. AgBF$_4$ (3 equiv), MeCN, r.t. 24 h	Intractable residue formed after step 1. Product decomposed after step 2.

Cu2a.BF$_4$	1. K_2CO_3 (2 equiv), CuBr (0.55 equiv), $AgBF_4$ (0.55 equiv) DCM, 40 °C, 24 h	Formation of **Cu2a**; Ag contamination
Cu2a.BF$_4$	1. K_2CO_3 (2 equiv), CuBr (0.5 equiv), $AgBF_4$ (1.2 equiv) DCM, 40 °C, 24 h	**Tz2.BF$_4$** isolated[d]

a. Equivalents given relative to **Tz2.BF$_4$**. *b.* Product additionally oxidised in air. *c*. Reaction performed in an NMR tube – product not isolated. This method was successful, but is wasteful, hence attempts to directly prepare the bis-NHC complex were pursued latterly. *d*. Multiple attempts were made to repeat this reaction, all resulted in isolation of ligand or product decomposition.

List of References

1 B. Liu, Y. Zhang, D. Xu and W. Chen, *Chem. Commun.*, 2011, **47**, 2883–2885.

2 B. R. M. Lake, E. K. Bullough, T. J. Williams, A. C. Whitwood, M. A. Little and C. E. Willans, *Chem. Commun.*, 2012, **48**, 4887–4889.

3 D. J. Nelson and S. P. Nolan, *Chem. Soc. Rev.*, 2013, **42**, 6723–6753.

4 J. Douglas, G. Churchill and A. Smith, *Synthesis*, 2012, **44**, 2295–2309.

5 W. M. Haynes, *CRC Handbook of Chemistry and Physics 97th Edition*, CRC Press/Taylor & Francis, Boca Raton, FL., 97th edn., 2017.

6 W. J. Youngs and J. C. Garrison, *Chem. Rev.*, 2005, **105**, 3978–4008.

7 B. R. M. Lake, *Copper N-Heterocyclic Carbenes: Novel Electrochemical Synthesis, Stabilisation of Variable Oxidation States and Unusual Carbene Reactivity,* University of Leeds, 2014.

8 S. Díez-González, E. D. Stevens, N. M. Scott, J. L. Petersen and S. P. Nolan, *Chem. Eur. J.*, 2008, **14**, 158–168.

9 J. Turek, I. Panov, P. Švec, Z. Růžičková and A. Růžička, *Dalton Trans.*, 2014, **43**, 15465–15474.

10 M. Bujak and J. Zaleski, *Zeitschrift für Naturforsch. B*, 2002, **57**, 157–164.

11 F. H. Allen, O. Kennard, D. G. Watson, L. Brammer, A. G. Orpen and R. Taylor, *J. Chem. Soc. Perkin Trans. 2*, 1987, S1–S19.

12 E. Ruiz, A. Rodríguez-Fortea, P. Alemany and S. Alvarez, *Polyhedron*, 2001, **20**, 1323–1327.

13 J. Tercero, E. Ruiz, S. Alvarez, A. Rodríguez-Fortea and P. Alemany, *J. Mater. Chem.*, 2006, **16**, 2729–2735.

14 D. Casanova, M. Llunell, P. Alemany and S. Alvarez, *Chem. Eur. J.*, 2005, **11**, 1479–1494.

15 H. Adams, N. A. Bailey, S. R. Collinson, D. E. Fenton, C. J. Harding and S. J. Kitchen, *Inorganica Chim. Acta*, 1996, **246**, 81–88.

16 S. Drumel, P. Janvier, M. Bujoli-Doeuff and B. Bujoli, *Inorg. Chem.*, 1996, **35**, 5786–5790.

17 M. Bichay, J. W. Fronabarger, R. Gilardi, R. J. Butcher, W. B. Sanborn, M. E. Sitzmann and M. D. Williams, *Tetrahedron Lett.*, 2006, **47**, 6663–6666.

18 R. T. Stibrany, *Cambridge Struct. Database*, 2014, 10.5517/cc11rsvf.

19 J. M. Mellor and N. M. Smith, *J. Chem. Soc., Perkin Trans. 1*, 1984, **0**, 2927–2931.

20 M. Yan, Y. Kawamata and P. S. Baran, *Chem. Rev.*, 2017, **117**, 13230–13319.

21 D. S. Kemp, M. D. Sidell and T. J. Shortridge, *J. Org. Chem.*, 1979, **44**, 4473–4476.

22 T. L. Gilchrist, D. Hughes and R. Wasson, *Tetrahedron Lett.*, 1987, **28**, 1573–1575.

23 M. Mentel, M. Beier and R. Breinbauer, *Synthesis*, 2009, **2009**, 1463–1468.

24 S. F. Nelsen and M. R. Willi, *J. Org. Chem.*, 1984, **49**, 1–6.

25 L. Horner and M. Jordan, *Justus Liebigs Ann. Chem.*, 1978, **1978**, 1505–1517.

26 H. Bakkali, C. Marie, A. Ly, C. Thobie-Gautier, J. Graton, M. Pipelier, S. Sengmany, E. Léonel, J.-Y. Nédélec, M. Evain and D. Dubreuil, *European J. Org. Chem.*, 2008, **2008**, 2156–2166.

27 B. A. Astleford, G. L. Goe, J. G. Keay and E. F. V. Scriven, *J. Org. Chem.*, 1989, **54**, 731–732.

28 M. A. Guino, M. O. Talbot, M. M. Slitts, T. N. Pham, M. C. Audi and D. E. Janzen, *Acta Crystallogr. Sect. E Crystallogr. Commun.*, 2015, **71**, 628–635.

29 D. Meyer and T. Strassner, *J. Org. Chem.*, 2011, **76**, 305–308.

30 K. Dong and S. Zhang, *Chem. Eur. J.*, 2012, **18**, 2748–2761.

31 A. Bondi, *J. Phys. Chem.*, 1964, **68**, 441–451.

32 J. E. Thomson, K. Rix and A. D. Smith, *Org. Lett.*, 2006, **8**, 3785–3788.

33 C. Sambiagio, *Investigations on the use of amidic ligands in copper-catalysed arylation reactions,* University of Leeds, 2015.

34 R. G. Micetich, P. Spevak, T. W. Hall and B. K. Bains, *Heterocycles*, 1985, **23**, 1645–1649.

35 J. Clayden, N. Greeves, S. Warren and P. Wothers, *Organic Chemistry*, Oxford University Press, Oxford, 5th edn., 2006.

36 L. Dupont, S. Englebert, O. Dideberg, B. Pirotte and J. Delarge, *Acta Crystallogr. Sect. C Cryst. Struct. Commun.*, 1991, **47**, 1756–1758.

37 L. Dupont, O. Dideberg, B. Pirotte and J. Delarge, *Acta Crystallogr. Sect. C Cryst. Struct. Commun.*, 1989, **45**, 1928–1930.

38 S. V. Voitekhovich, A. S. Lyakhov, L. S. Ivashkevich, V. E. Matulis, Y. V. Grigoriev, P. N. Gaponik and O. A. Ivashkevich, *Tetrahedron*, 2012, **68**, 4962–4966.

39 M. Pellei, V. Gandin, M. Marinelli, A. Orsetti, F. Del Bello, C. Santini and C. Marzano, *Dalton Trans.*, 2015, **44**, 21041–21052.

40 C. Dash, M. M. Shaikh and P. Ghosh, *J. Chem. Sci.* **|** *Indian Acad. Sci.*, 2011, **123**, 97–106.

41 J. J. Van Veldhuizen, J. E. Campbell, R. E. Giudici and A. H. Hoveyda, *J. Am. Chem. Soc.*, 2005, **127**, 6877–6882.

42 B. Liu, Q. Xia and W. Chen, *Angew. Chemie Int. Ed.*, 2009, **48**, 5513–5516.

43 Silvia Díez-González, A. Natalie M. Scott and S. P. Nolan, *Orgnaometallics*, 2006, **25**, 2355–2358.

44 O. Santoro, A. Collado, A. M. Z. Slawin, S. P. Nolan and C. S. J. Cazin, *Chem. Commun.*, 2013, **49**, 10483–10485.

45 M. V. Berridge, P. M. Herst and A. S. Tan, *Biotechnol. Annu. Rev.*, 2005, **11**, 127–152.

46 T. Mosmann, *J. Immunol. Methods*, 1983, **65**, 55–63.

47 M. Busch, *Berichte der Dtsch. Chem. Gesellschaft*, 1905, **38**, 861–866.

48 A. Hioki, T. Watanabe, K. Terajima, N. Fudagawa, M. Kubota and A. Kawase, *Anal. Sci.*, 1990, **6**, 757–762.

49 C. Färber, M. Leibold, C. Bruhn, M. Maurer and U. Siemeling, *Chem. Commun.*, 2012, **48**, 227–229.

50 C. Thie, S. Hitzel, L. Wallbaum, C. Bruhn and U. Siemeling, *J. Organomet. Chem.*, 2016, **821**, 112–121.

51 J. A. Grant, Z. Lu, D. E. Tucker, B. M. Hockin, D. S. Yufit, M. A. Fox, R. Kataky, V. Chechik and A. C. O'Donoghue, *Nat. Commun.*, 2017, **8**, 15088.

52 P. G. Jones and O. Crespo, *Acta Crystallogr. Sect. C Cryst. Struct. Commun.*, 1998, **54**, 18–20.

53 M. Serradeil-Albalat, C. Roussel, N. Vanthuyne, J.-C. Vallejos and D. Wilhelm, *Tetrahedron: Asymmetry*, 2008, **19**, 2682–2692.

54 J. Z. Vlahakis, C. Lazar, I. E. Crandall and W. A. Szarek, *Bioorg. Med. Chem.*, 2010, **18**, 6184–6196.

Chapter 3

Investigation into the mechanism of triazolium ring-opening reaction under standard conditions

Chapter 2 detailed the unexpected formation of an imine ligand during electrochemical synthesis, and attempts to understand this reactivity by investigating the scope and related reactions. This chapter describes the use of the ElectraSyn to probe the mechanism of imine formation. A series of control reactions have been carried out. The effect of current and voltage on reaction outcome has also been investigated. Deuteration studies are also used to gain an insight into the reaction mechanism.

3.1 Introduction

During electrochemical synthesis using **Tz1.BF$_4$** an unexpected ring-opening reaction was observed to take place. This resulted in the formation of a diimine ligand which formed part of the complex **Cu1b.BF$_4$**. This complex was obtained as an inseparable mixture with the expected bis-NHC product **Cu1a.BF$_4$** (Chapter 2 - *2.2.2*). When other triazolium salts were similarly tested, no imine formation was observed, indicating a narrow reaction scope (Chapter 2 - *2.3*). Chemical reactions using **Tz1.BF$_4$** yielded only **Cu1a.BF$_4$** indicating that the electrochemical method drives imine formation (Chapter 2 – *2.2.1, 2.4.3*). It is desirable to understand the reasons for imine formation, so that this pathway can be promoted or suppressed in future reactions. Using the ElectraSyn allows for more precise control of reaction conditions than was possible with the previous power supply set-up. Hence a detailed investigation of the various factors influencing imine formation can be undertaken.

3.2 Investigation into the Effect of Current on the Ring-Opening Reaction

The preparation of **Cu1a.BF$_4$** under chemical conditions, without the formation of **Cu1b.BF$_4$** clearly indicates that formation of **Cu1b.BF$_4$** is in some way a result of the electrochemical method. In an attempt to isolate the various confounding factors, a series of control experiments were designed and implemented.

3.2.1 Reaction of Triazolium 1 with Graphite Electrodes

An electrochemical reaction on **Tz1.BF$_4$** using glassy carbon electrodes was performed. The reaction was run for 2Q using the ElectraSyn apparatus at a fixed current of 50 mA. If the formation of any imine species was observed under these conditions, this would be an indication that **Tz1.BF$_4$** is unstable to the application of an electric current. The crude product was analysed by ^{1}H NMR spectroscopy. All the expected peaks for the **Tz1.BF$_4$** are still present after the electrochemical reaction (Figure 211). There are some additional signals present in the baseline, which may represent some form of decomposition, but due to the low intensity and broad signals it is not possible to assign them to any specific product. Crucially, CH and NH signals present in the imine ligand are not observed. The HRMS data also only show a signal at *m/z* 186 corresponding to [**Tz1.BF$_4$**-BF$_4$]$^+$. These data indicate that **Tz1.BF$_4$** does not spontaneously degrade to form the imine species under the application of current.

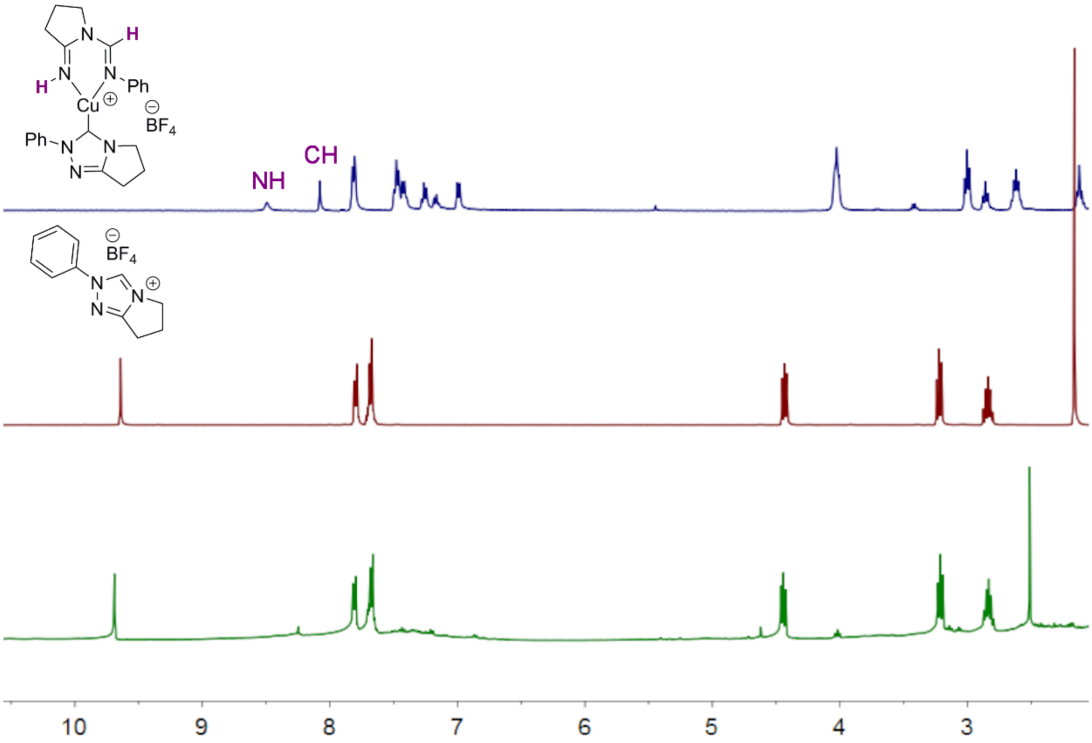

Figure 211. ^{1}H NMR spectra (400 MHz, CD_3CN). Top: **Cu1a**/**Cu1b** with NH and CH imine signals labelled. Middle: **Tz1.BF$_4$**. Bottom: product of electrolysis of **Tz1.BF$_4$** using glassy carbon electrodes.

3.2.2 Reaction of Cu1a.BF$_4$ with Copper Electrodes

A next question is whether **Cu1b.BF$_4$** is formed from **Cu1a.BF$_4$**. To answer this, an electrochemical reaction was performed in which a current was applied to **Cu1a.BF$_4$** using Cu electrodes. Formation of **Cu1b.BF$_4$** in this case would suggest that the mechanism for ring-opening goes *via* **Cu1a.BF$_4$**. No formation of **Cu1b.BF$_4$** would instead indicate that the complex may be formed directly from **Tz1.BF$_4$**, or that **Tz1.BF$_4$** plays a role in the mechanism. Once again, a fixed current of 50 mA was applied using Cu electrodes to a solution of **Cu1a.BF$_4$** in MeCN, and the crude reaction mixture analysed by ^{1}H NMR. In this case the picture is more complex. As seen with glassy carbon electrodes, there is a notable absence of the signals corresponding to either the CH or NH protons of the imine ligand. However, closer inspection of the data reveals that there has been a marked shift in peak position of the signals attributed to the NHC ligand. All signals now appear at the same chemical shift as those attributed to the NHC portion of **Cu1b.BF$_4$**.

The HRMS data does not provide any evidence for the formation of imine, showing simply signals attributable to **Cu1a.BF$_4$** and **Tz1.BF$_4$**. This is corroborated by the obtained powder x-ray diffraction pattern, which shows a good agreement with that predicted for **Cu1a.BF$_4$**, with no evidence of **Cu1b.BF$_4$** (Figure 212). This provides some evidence that ring-opening occurs directly from the ligand, rather than from the Cu complex.

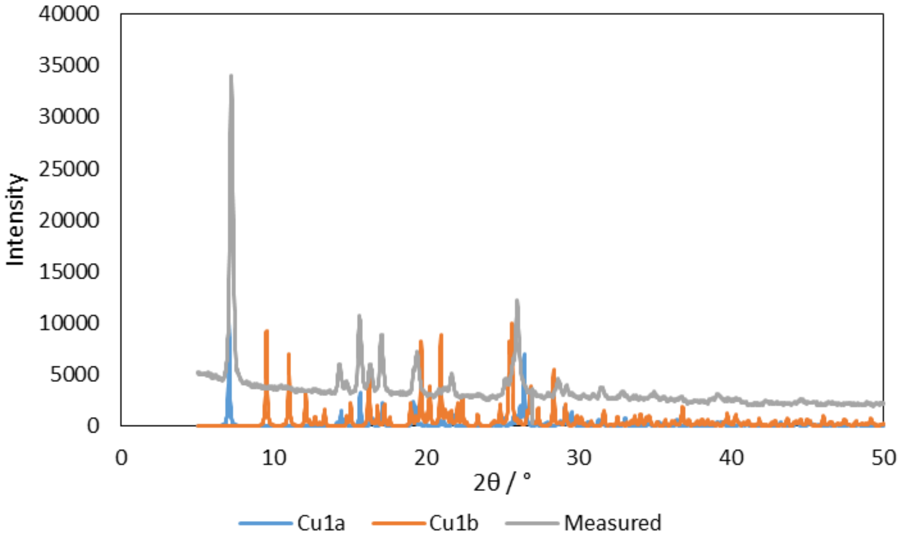

Figure 212. Comparison of simulated powder XRD pattern for **Cu1a.BF$_4$** and **Cu1b.BF$_4$** with that measured for reaction product.

3.2.3 Reaction of Triazolium 1 with Copper Powder

One other question is whether the ring-opening reaction is facilitated by the presence of metallic Cu. To investigate this, a reaction was performed using **Tz1.BF$_4$** and Cu powder under aerobic conditions. Such reactions have been reported to generate Cu NHC complexes.[1] The crude ^{1}H NMR spectrum showed some minor signals corresponding to residual **Tz1.BF$_4$**, along with two sets of signals indicating complexation of the ligand in an approximately 4:1 ratio. The major set corresponds well with those seen for **Cu1a.BF$_4$**. The minor set appears at a different chemical shift to those associated with the ring-opened product **Cu1b.BF$_4$**. Additionally, the characteristic C*H* and N*H* signals are not present. The HRMS data also has no indication of the formation of **Cu1b.BF$_4$**. The signals noted correspond to **Tz1.BF$_4$**, and **Cu1a.BF$_4$**. Additionally a signal at *m/z* 289 which corresponds to the monomeric complex solvated by one MeCN molecule. This may indicate that the additional signals in the ^{1}H NMR spectrum are due to the formation of a mixture of the mono and bis-NHC complexes. These data corroborate the theory that the formation of **Cu1b.BF$_4$** is driven by current.

3.3 Investigation into the Effect of Q on Reaction Progress

3.3.1 Varying Ligand and Q

In an attempt to learn more about the reaction progress, a series of reactions using varying Q were envisioned. This may provide further insight as to whether the ring-opening proceeds *via* the formation of the NHC-complex or whether it is a competing reaction occurring at the same time. To this end, reactions for a range of ligands were performed for 1 and 2Q. All reactions were performed using 0.3 mmol of the required ligand, in 5 mL of anhydrous degassed MeCN. A current of 50 mA was maintained, with voltages between 0 and 10 V being applied accordingly. After reaction the solvent was removed from the crude mixture and this was analysed by ^{1}H NMR spectroscopy (Table 25).

In spite of the standardisation of reaction conditions using the ElectraSyn, the results are not completely consistent. For example **Tz5.BF$_4$** showing near full conversion in the 1Q reaction, but only 70% for 2Q. Likewise, across the range of ligands a spread of conversion values is seen from 58-94% for 1Q and from 70-99% for 2Q. Although all reactions were performed under the same conditions, this highlights the difficulty of producing consistent results *via* the electrochemical method. A range of factors could contribute to differing results, for example, the differing conductivity of the ligands, the wear on the electrodes and different batches of solvent.

Table 25. Conversions obtained after 1 and 2Q for various triazoliums.

	1Q		2Q	
Ligand	Conversion^a	Ratio NHC to imine^b	Conversion after 2Q	Ratio NHC to imine
Tz1.BF$_4$	58%	1 : 0.61	92%	1 : 0.53
Tz1.Cl	68%	1 : 0.10	81%	1 : 0.13
Tz2.BF$_4$	65%	-	>99%	-
Tz5.BF$_4$	94%	-	70%	-

a. Conversions calculated relative to residual ligand peak where present. *b.* ratio given for peak integrals, not concentration of Cu complexes.

One conclusion that may be drawn is that the imine complex has begun to form already after 1Q. This is further evidence to support the theory that formation of **Cu1b.BF$_4$** proceeds directly from **Tz1.BF$_4$**. For both **Tz1.BF$_4$** and **Tz1.Cl**, the ratio of

NHC:imine peaks is relatively unchanged between the 1Q and 2Q reactions. There was no evidence of any ring opening with **Tz2.BF$_4$** and **Tz5.BF$_4$** after 2Q.

3.3.2 Multi-Q Reaction Monitoring

As formation of **Cu1b.BF$_4$** was already well underway after 1Q, a monitoring reaction was devised, to try to determine when this begins. An electrochemical reaction was performed using **Tz1.BF$_4$** with a small sample (0.25 mL) removed after various numbers of Q, for analysis by ^{1}H NMR (Figure 213). Consumption of ligand proceeds smoothly, being almost entirely complete after 2Q. After 0.1Q no **Cu1b.BF$_4$** was detectable by ^{1}H NMR, however given the low proportion of ligand converted (3%) it cannot be stated that this is due to no imine being present. The proportion of **Cu1a.BF$_4$** and **Cu1b.BF$_4$** products increase steadily, and remain relatively unchanged after 4Q. The slight decrease in the ratio of NHC signals seen from 2Q to 4Q is perhaps an indication that the imine product is being formed from the NHC complex. The differences in integral values (0.08 and 0.10) are fairly small and close to the error of measurement. As some ligand is still present after 2Q it is possible that this results either from the direct formation of **Cu1b.BF$_4$** from **Tz1.BF$_4$** or from the presence of **Tz1.BF$_4$** acting as a catalyst. However, it is clear that it is not possible to convert all the formed NHC complex into imine complex simply by applying a current.

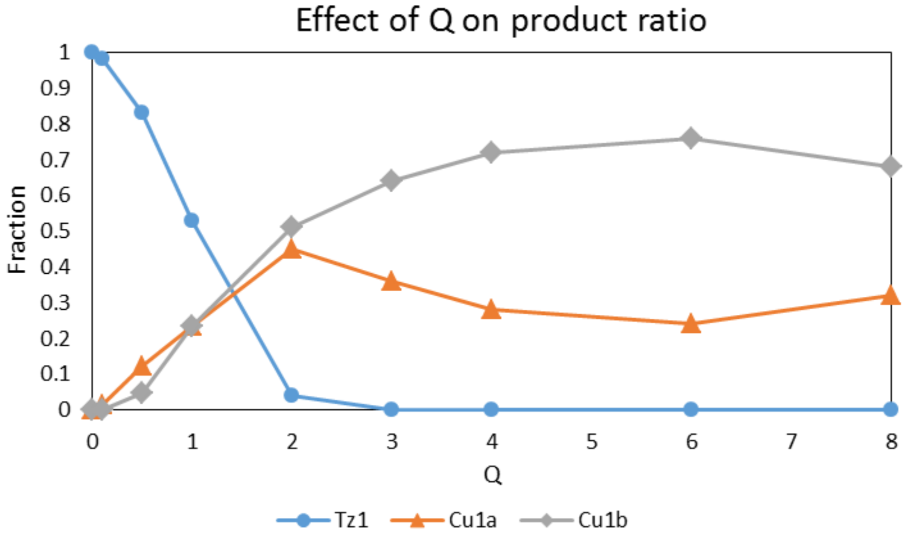

Figure 213. Reaction progress as a function of Q during the electrochemical synthesis of **Cu1a/Cu1b** mixture.

3.3.3 Summary of the Effect of Q:

A range of different ratios of the formation of imine and complex are seen at different Q values. The values for the sampling reaction can be compared with the 1 and 2Q reaction screen, as well as previous reactions performed using the power pack (in this case Q value is an estimate). When plotted as a chart it can be seen that there is no clear correlation (Figure 214). This, along with the fact that a reaction left running with multiple excesses of Q does not lead to full conversion is an indication that another factor may be at play in determining the product ratios.

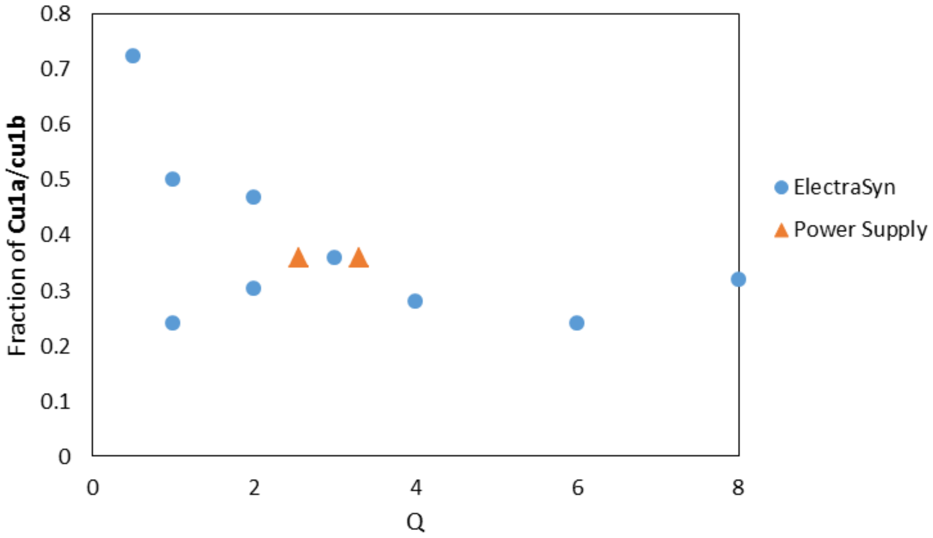

Figure 214. Scatter plot showing fraction **Cu1a**/**Cu1b** for all electrochemical reactions using **Tz1.BF$_4$** as a function of Q.

3.4 Effect of Voltage

Another avenue for investigation is the effect of the applied voltage on the product of an electrochemical reaction. Chapman *et al*. have reported the reduction potential of IMes.HCl to be -2.3 V relative to the ferrocene/ferrocinium couple determined by CV measurement. When reactions were performed in flow the optimum applied voltage was found to vary from 1.94-2.50 V depending on the reactor design. However, the Faradaic efficiency of the flow reactors is much greater than a batch system; it is therefore expected that a larger overpotential will be necessary to achieve full conversion for reactions using the ElectraSyn.[2] The reduction potential for triazolium salts is reported to be lower than for imidazolium salts, and is given as -1.8 V (relative to ferrocene/ferrocinium couple) for **Tz1.BF$_4$**.[3] This is in keeping with the lower pKa values reported for triazolium versus imidazolium salts.[4] Reactions that have been previously performed with a fixed current of 50 mA already generally apply an overpotential, with observed voltages typically being around 4 V at the start of the reaction. By the end of a reaction it is not uncommon to observe application of 10 V. However, in order to investigate whether the different reactivity is observed in different voltage windows, it is desirable to screen a range of voltages.

The ligand **Tz2.BF$_4$** was selected for a straightforward model reaction. An electrochemical reaction was run for 2Q at 2 V, 5 V and 10 V, with conversion being measured by ^{1}H NMR after reaction completion (Table 26).

Table 26. Results for electrochemical reactions run at a range of applied voltages.

Applied voltage / V	Reaction time / min	Observed current range / mA	Conversion[a]
2	97	5.8 - 12.5	16%
5	62	8.8 - 52.7	86%
10	16	43.9 - 100	>99%

Reaction conditions: A solution of 0.3 mmol in 5 mL of anhydrous MeCN was placed in a 10 mL ElectraSyn vial with Cu electrodes held 6 mm apart. Reactions were performed in a glovebox under an atmosphere of nitrogen.
a. Conversions calculated from a crude ^{1}H NMR spectrum as the ratio of product peak to residual ligand (if present).

A number of observations can be made from this data. Firstly, as expected, a lower applied voltage leads to a lower current and hence a longer reaction time. To maintain a given current the voltage for a fixed current reaction tends to increase over time, presumably due to decreased conductivity of the reaction mixture. This can be attributed to both a decrease in the concentration of the charged ligand species and an increase in electrode fouling. In the case of a fixed voltage reaction, naturally the reverse is true, with currents initially being high, but decreasing over the course of the reaction as conductivity decreases. It is notable that conversion is extremely low for the 2 V reaction, in spite of the fact that this should still represent application of an overpotential.[3] At 5 V the conversion is high, though it is still lower than the fixed current 2Q reaction performed using the same ligand (86% vs >99%). With a fixed voltage of 10 V full conversion is achieved within a short time period. Visual examination of the reaction mixtures also reveals some key differences between the voltages (Figure 215). A greater degree of electrode fouling is observed at higher voltages, whilst the reaction mixture is also darkest for the 10 V reaction. Given that the product from this reaction is colourless, this presumably indicates an increase in the formation of impurities. There is limited evidence in the ^{1}H NMR spectra for the formation of side-products, therefore it is likely that the dark colour of the reaction mixture is due to a greater concentration of metallic Cu species (Figure 216).

Although differences in reaction progress are seen over the range of voltages, no major differences are apparent in terms of product formation. In particular there is no evidence that imine formation begins to occur for this ligand once a given voltage threshold is reached. For **Tz1.BF$_4$** the higher voltage regions have already been explored through the fixed current experiments. Investigations with **Tz2.BF$_4$** have demonstrated that conversion is low and reaction time is long for lower voltages. Therefore, voltage scans with **Tz1.BF$_4$** were not considered to be expedient.

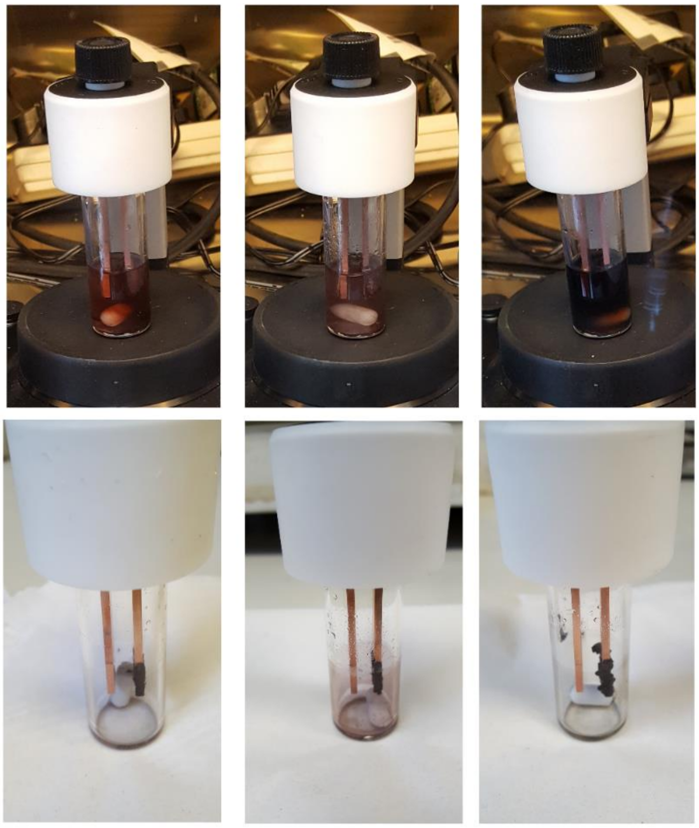

Figure 215. Above: Product mixture from the electrochemical reactions performed at 2, 5 and 10 V. Below: Electrodes after reactions performed at 2, 5 and 10 V showing differing degrees of fouling.

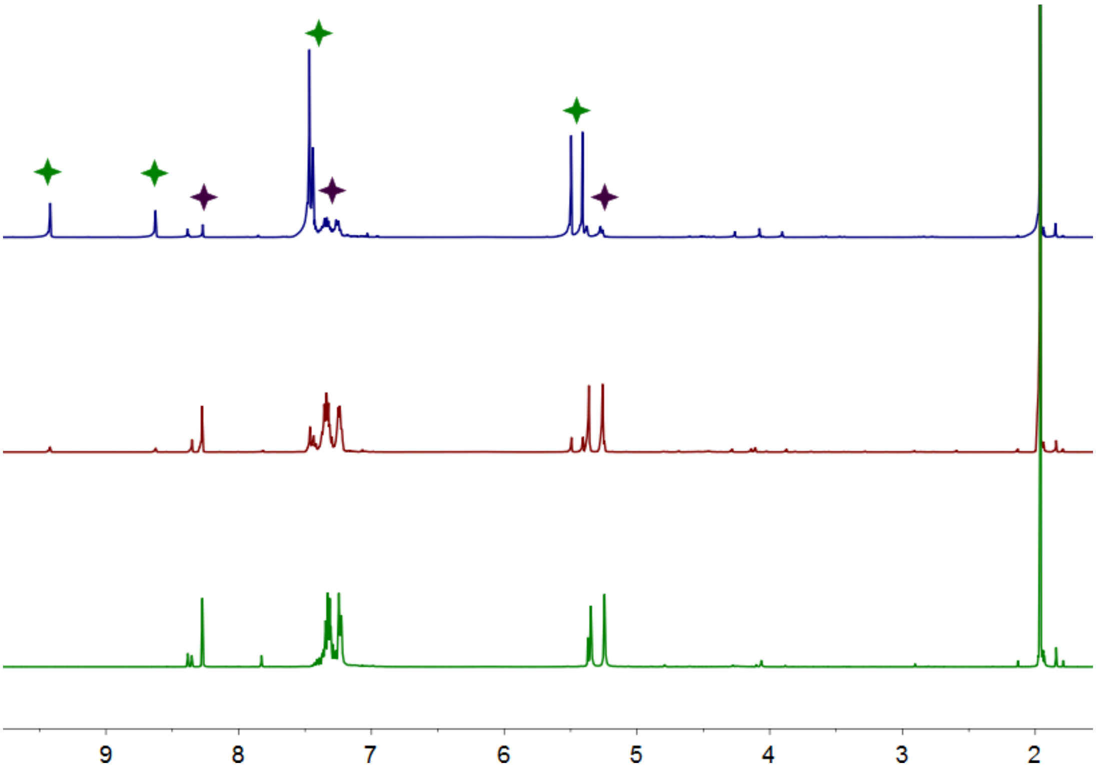

Figure 216. ^{1}H NMR spectra (400 MHz, CD_3CN) of crude product from electrochemical reactions at fixed voltages of: Top: 2 V; Middle: 5 V; bottom: 10 V. Green stars denote **Tz2.BF$_4$**, purple stars denote **Cu2a.BF$_4$**.

3.5 Deuterium Labelling Studies

3.5.1 Deuteration of Triazoliums

The question of where the "spare" hydrogen atoms in the imine product originate from is key to the determination of the mechanism of this reaction. One possibility is that the ligand itself supplies one or both of the hydrogen atoms (Figure 217). To determine this a labelling experiment was envisaged. Labelling the C5 position in **Tz1.BF$_4$** with deuterium would make it possible to determine whether either the CH or NH in the imine product come from the ligand. Therefore, efforts were undertaken to prepare **Tz1.D** (Figure 217).

Due to the limited availability of this ligand, test reactions were performed with **Tz5.BF$_4$**. Selective deuteration of this position has been reported for imidazoliums simply by heating in D_2O or CD_3OD.[5] Attempts were made with both D_2O and CD_3OD. The reaction with D_2O was found to be the more successful, achieving 95% deuterium incorporation, versus just 16% for CD_3OD (Figure 218). Problems were encountered however, as stirring the labelled triazolium in anhydrous MeCN for 2 hours under an atmosphere of nitrogen, resulted in significant deuterium-hydrogen exchange (25% deuterium remaining) (Figure 218). It is unclear whether this exchange arises due to adventitious water present in the MeCN, or occurs directly from the solvent itself. As the electrochemical reactions would need to be performed in MeCN, this fact presents a serious challenge. For this reason, other avenues of investigation were pursued.

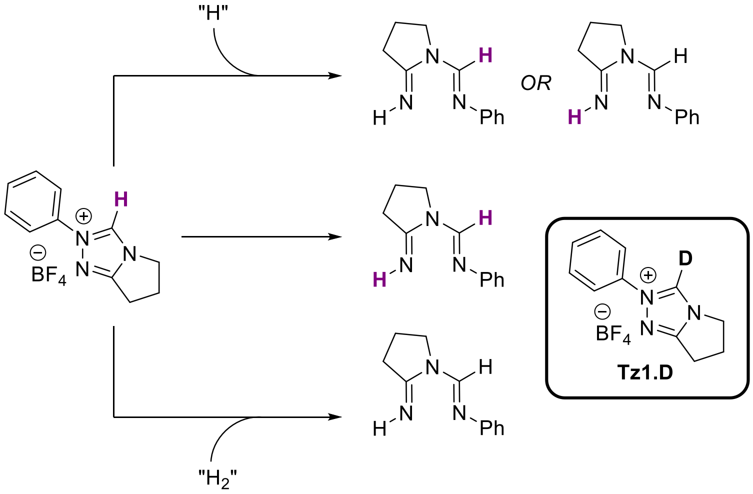

Figure 217. Possible sources of hydrogen atoms and their corresponding position in the imine product. Inset: structure of **Tz1.D**.

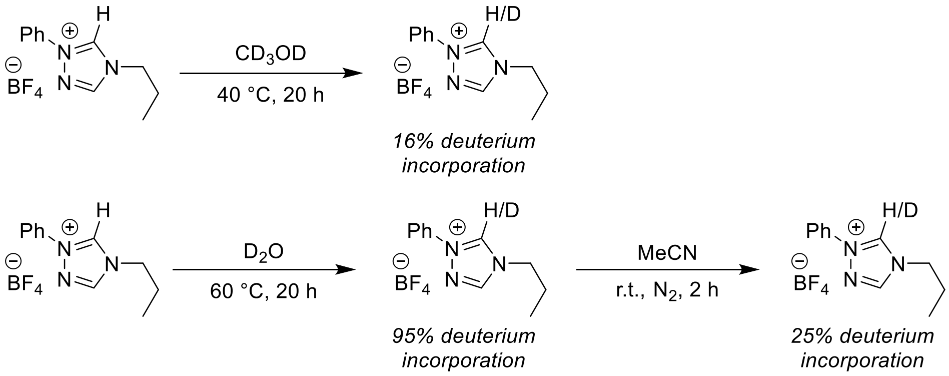
CD3OD
40 °C, 20 h
16% deuterium incorporation
D2O
60 °C, 20 h
95% deuterium incorporation
MeCN
r.t., N2, 2 h
25% deuterium incorporation
Ph
H
H/D
BF4

Figure 218. Reaction scheme showing preparation of deuterated triazoliums, and back-reaction.

3.5.2 Reaction in Deuterated Solvent

Another possible source of the hydrogen atoms is the MeCN solvent itself. The voltages typically applied in the electrochemical reactions are well outside the solvent window for MeCN, so degradation would be expected.[6] To this end, a reaction was performed in anhydrous deuterated MeCN under identical conditions to those performed previously. Analysis of the product by ^{1}H NMR did not show any deuterium incorporation at either the NH or CH imine positions. This provides good evidence that the MeCN solvent is not the source of these hydrogen atoms. This is an interesting observation in light of the results obtained with **Tz5.D** (*3.5.1*). The loss of deuterium incorporation observed in MeCN might be expected to be replicated in reverse in this reaction – leading to a deuterated triazolium salt prior to electrochemical reaction. There are a number of possibilities that explain the lack of deuterium incorporation into the product in this case. Firstly, that the triazolium does undergo H/D exchange, directly from the d_3-MeCN solvent, but that the additional hydrogen atoms observed in the product **Cu1b.BF$_4$** do not arise from the starting ligand. Secondly, that the triazolium does not undergo H/D exchange with d_3-MeCN, in which case, no further conclusions may be drawn. Thirdly, that the triazolium undergoes H/D exchange with adventitious water rather than the MeCN itself. In this case, it is unclear to what extent product deuteration would be expected.

It was additionally noted that the ratio of **Cu1a.BF$_4$** to **Cu1b.BF$_4$** was markedly different for this reaction than for most previous reactions. The proportion of **Cu1a.BF$_4$** was in this case 61%, which is much higher than for previous experiments at similar Q values (Figure 219). This would seem to indicate that changing the solvent *has* had an effect, but this is not due to the solvent itself being involved in the reaction.

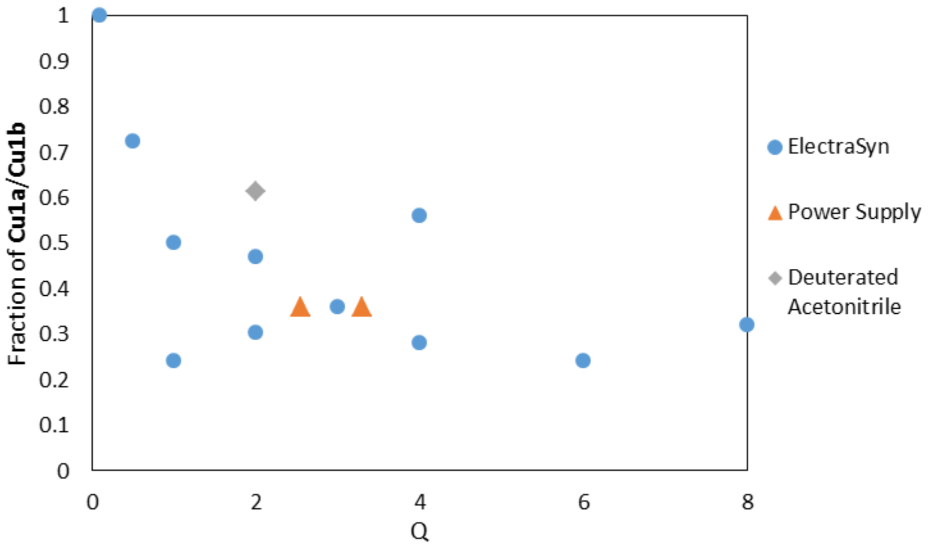

Figure 219. Scatter plot showing fraction **Cu1a**/**Cu1b** for all electrochemical reactions using **Tz1.BF$_4$** as a function of Q, including reaction using d$_3$-MeCN.

3.6 Effect of Water

Adventitious water could also be responsible for the ring-opening effect, as observed by O'Donoghue *et al.* in the related nitron system (Chapter 2 - *2.5.2*).[7] Although the MeCN use has been dried *via* a solvent purification system and then collected onto activated 4 Å molecular sieves, removal of *all* water cannot be guaranteed. Therefore, investigations in to the potential role water could play were carried out.

3.6.1 Addition of H_2O

A reaction was carried out in which 0.9 equivalents of degassed H_2O was added to the ElectraSyn vial prior to reaction. The reaction was run under the standard conditions used for previous reactions (2Q, 50 mA), and the crude product analysed by ^{1}H NMR spectroscopy. Analysis of the relative integrals for the products showed the product mixture to be 24% **Cu1a.BF$_4$**, the joint lowest proportion recorded thus far. The reaction was repeated with 1.3 equivalents of degassed H_2O as dopant. The product from this reaction was just 12% **Cu1a.BF$_4$**. An attempt was made to drive the reaction completely toward **Cu1b.BF$_4$** formation by addition of a ten-fold excess of H_2O. In this case however, the product mixture contained 36% **Cu1a.BF$_4$**. Impurities were observed in the ^{1}H NMR spectrum, however, not to a significantly greater extent than seen with other reactions. The water doped reactions did however show generally lower proportions of **Cu1a.BF$_4$** compared to reactions performed at a similar Q value (Figure 220).

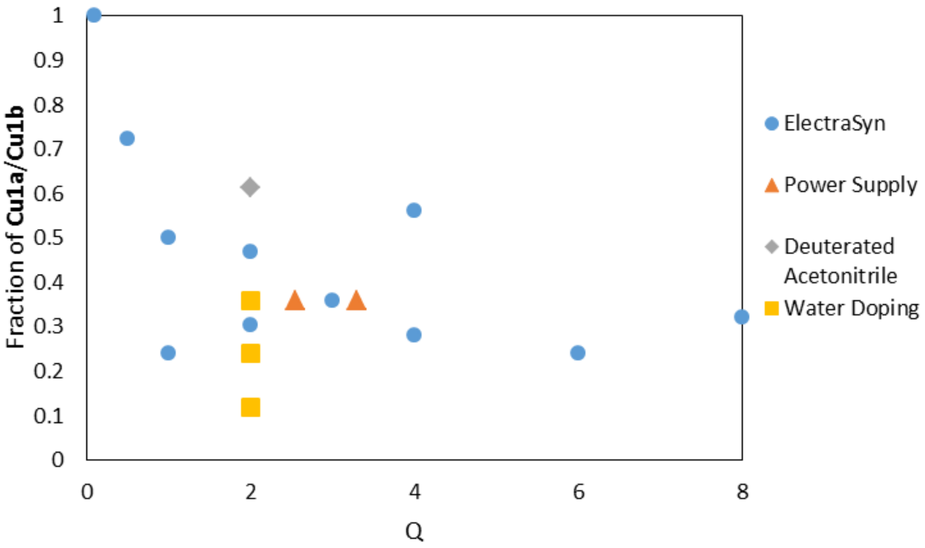

Figure 220. Scatter plot showing fraction **Cu1a**/**Cu1b** for all electrochemical reactions using **Tz1.BF$_4$** as a function of Q, including water doped reactions.

These data provide good evidence that water is responsible for the formation of the imine species; it is however unclear why a large excess of water hinders the reaction.

One obvious question is whether the action of water on **Cu1a.BF$_4$** is capable of generating **Cu1b.BF$_4$** in the absence of an electrical current. Degassed H_2O was added to a solution of **Cu1a.BF$_4$** in CD_3CN in a Young's NMR tube and the system was monitored by ^{1}H NMR (Figure 221). No formation of **Cu1b.BF$_4$** was observed even after standing for 8 days. Formation of a new product peaks not attributable to either **Tz1.BF$_4$** or **Cu1b.BF$_4$** was in evidence after 36 hours. These continued to grow in over the course of the reaction, reaching a relative ratio of 0.10 to 2 (for an aromatic signal in **Cu1a.BF$_4$**). The HRMS data for the product of this reaction shows signals attributable to [**Tz1.BF$_4$**-BF_4]$^+$ and [**Cu1a.BF$_4$**-BF_4]$^+$. There is no evidence that **Cu1b.BF$_4$** has been formed, and no indication of what the new product might be. This clearly demonstrates that any effect water is having on the formation of **Cu1b.BF$_4$** is current driven.

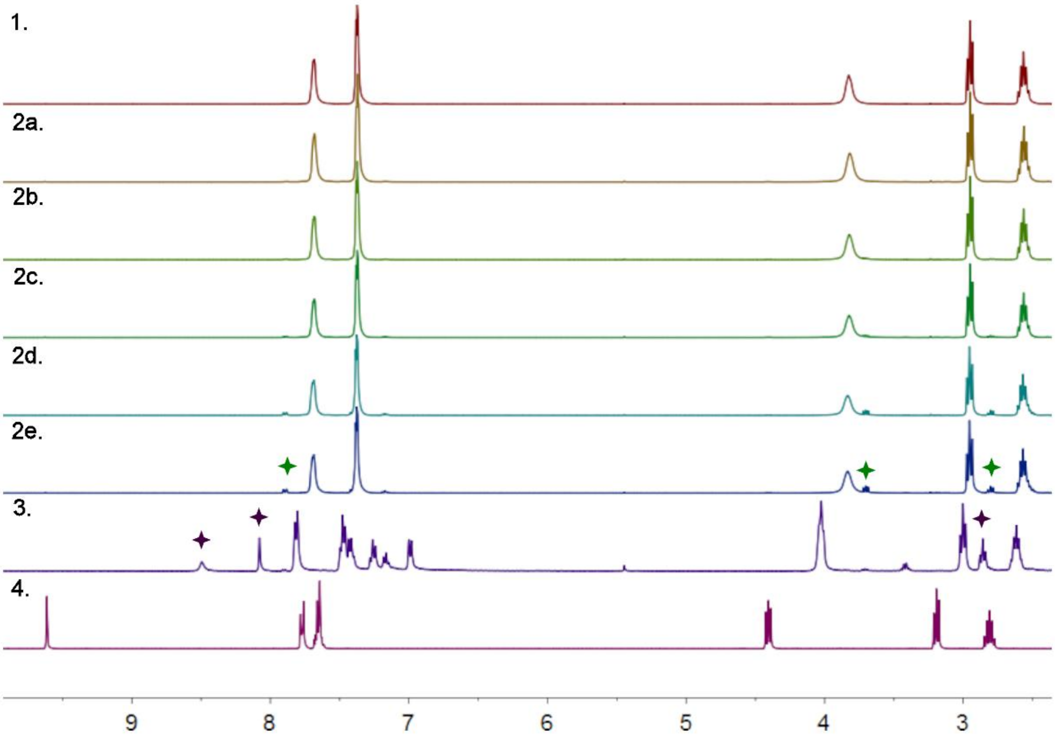

Figure 221. ^{1}H NMR spectra (400 MHz, CD_3CN). **1. Cu1a.BF$_4$**; **2a-e.** Reaction progress after addition of H_2O from 20 min – 8 days [green stars denote new product peaks]; **3. Cu1a**/**Cu1b** mixture [purple stars denote key peaks indicative of **Cu1b**]; **4. Tz1.BF$_4$**.

The electrolysis of water has a standard reduction potential of -1.23 V. Therefore, it would be expected that at the potentials applied the water present would have been electrolysed. So reactivity promoted by water could be due to a reaction with water or molecular oxygen or hydrogen.

3.6.2 Addition of D_2O

An electrochemical reaction was performed under identical conditions to those with water added, with degassed D_2O as the dopant (Figure 222 - top). The crude ^{1}H NMR spectrum was used to determine the degree of deuterium incorporation. Deuterium incorporation was found to be 60% for the CH position and 48% for the NH position, which would be expected to be more freely exchangeable (Figure 223). This results indicates that both hydrogen atoms are supplied by adventitious water. However, the NH in particular is expected to be liable to proton deuterium exchange in solution. For this reason a D_2O shake was performed on a sample of **Cu1a**/**Cu1b** mixture in anhydrous CD_3CN (Figure 222 - middle). This results in the complete disappearance of the NH signal, and no change to the CH signal. Another control experiment was performed in which degassed D_2O was added to a solution of **Tz1.BF$_4$** in CD_3CN, using the same concentration of water as used in previous doping experiments (Figure 222 - bottom). This results in 60% incorporation of deuterium at the C5 position.

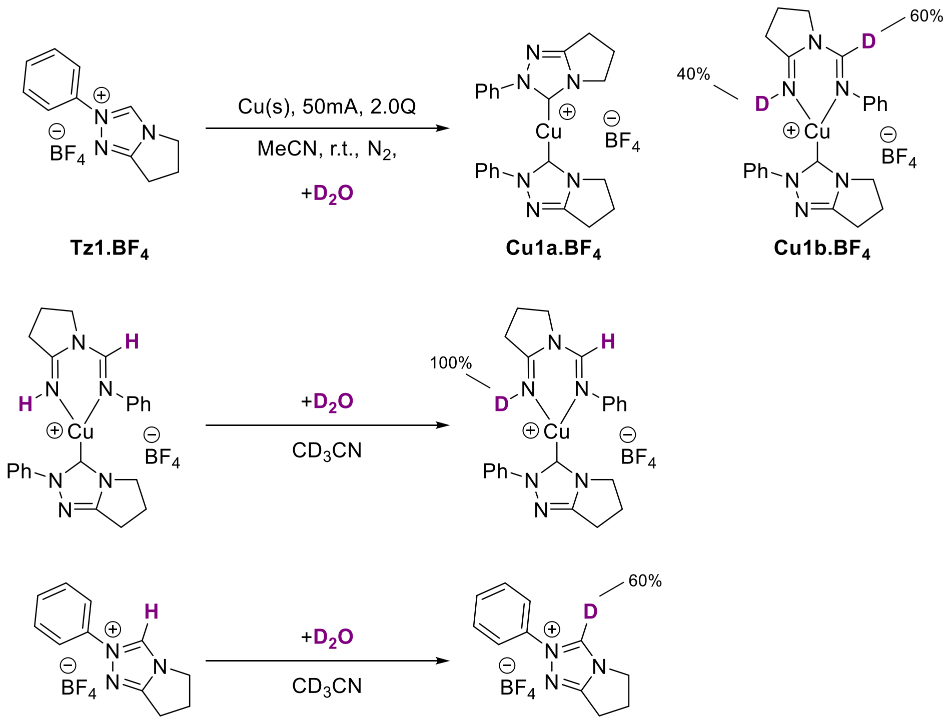

Figure 222. Reaction scheme showing deuteration experiments. Top: Electrochemical reaction doped with D_2O. Middle: D_2O shake on **Cu1a/Cu1b** mixture (**Cu1a** omitted for clarity). Bottom: D_2O shake on **Tz1.BF$_4$**.

Therefore the degree of deuterium incorporation seen in the reaction with D_2O doped can be explained as simply the action of D_2O on a solution of either **Tz1.BF$_4$** or **Cu1b.BF$_4$** in MeCN (Figure 224). The deuterated ligand precursor can be formed prior to the electrochemical reaction *via* deuterium hydrogen exchange. The subsequent electrochemical reaction would then generate **Cu1b.BF$_4$** with deuterium at the carbon position. Any residual D_2O in the reaction solution can then subsequently cause deuterium hydrogen exchange at the labile NH position.

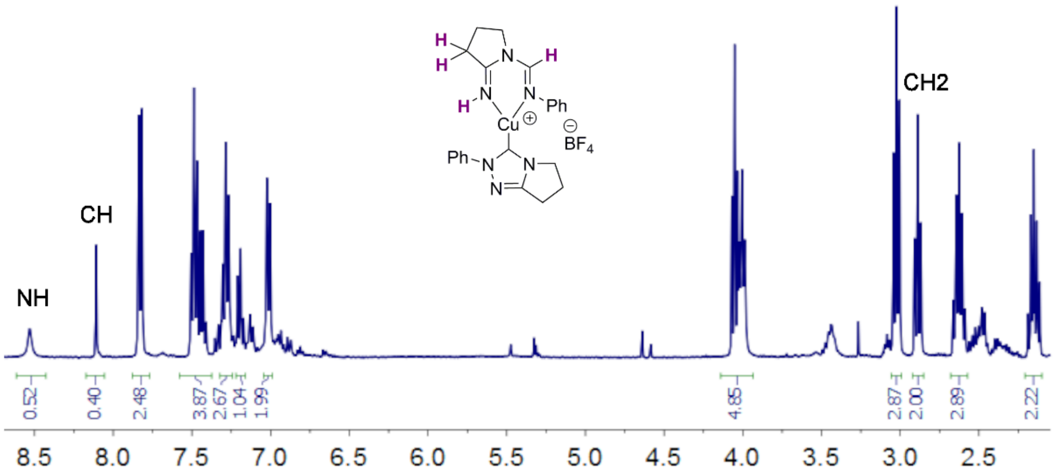

Figure 223. ^{1}H NMR (400 MHz, CD_3CN) spectrum obtained from the electrochemical reaction of **Tz1.BF$_4$** with Cu electrodes and D_2O dopant, with integral values shown below peaks. CH_2 peak used as reference, CH and NH peaks show lower integral values than predicted.

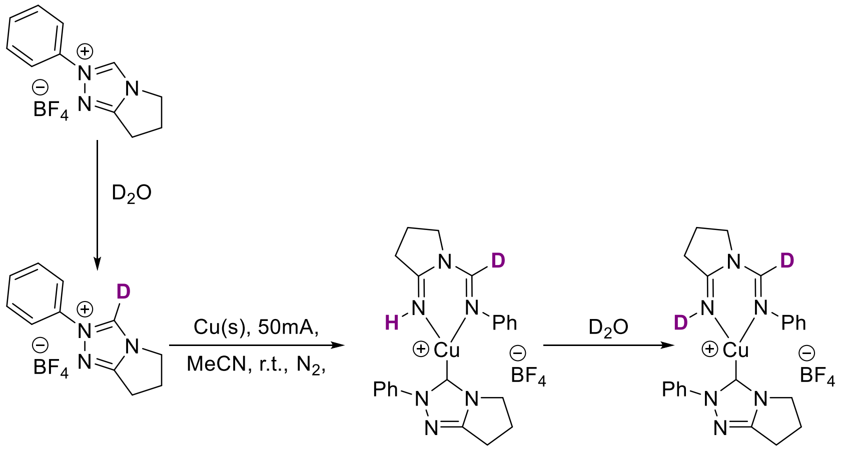

Figure 224. Possible route to deuterated **Cu1b.BF$_4$** *via* deuterium hydrogen exchange, before and after electrochemical reaction.

3.6.3 Effect of H_2O During Reaction

Given that experiments with D_2O do not provide conclusive proof that the formation of **Cu1b.BF$_4$** is driven by water, a further experiment was devised. In this case, an electrochemical reaction was run and monitored by ^{1}H NMR spectroscopy, as seen previously in the multi-Q experiment (3.3.2) (Figure 225). Once the ratio between **Cu1a.BF$_4$** and **Cu1b.BF$_4$** has plateaued, water may be doped in to see if this causes a change in the ratio. A positive result would indicate that **Cu1a.BF$_4$** is transformed into **Cu1b.BF$_4$** in the presence of water and an applied current. The reaction set-up was the same as for the multi-Q reaction, except for the reaction being performed outside the glovebox under an atmosphere of argon delivered *via* a syringe needle through the septum on the ElectraSyn vial. The reaction was judged to have plateaued after 8Q, at which point 5 µL of degassed water was added *via* microsyringe. After this point there is a slight increase in the proportion of **Cu1b.BF$_4$**. If the average of the three points prior to water addition is taken and compared with the average of the three points obtained after, the increase is 0.07. This is a small change that lies close to the error of the measurement. The graph does appear to show a clear trend however, so it may be significant that all three latter points show an increase in **Cu1b.BF$_4$** concentration. Therefore this experiment may point toward water playing a role in the formation of **Cu1b.BF$_4$** from **Cu1a.BF$_4$**.

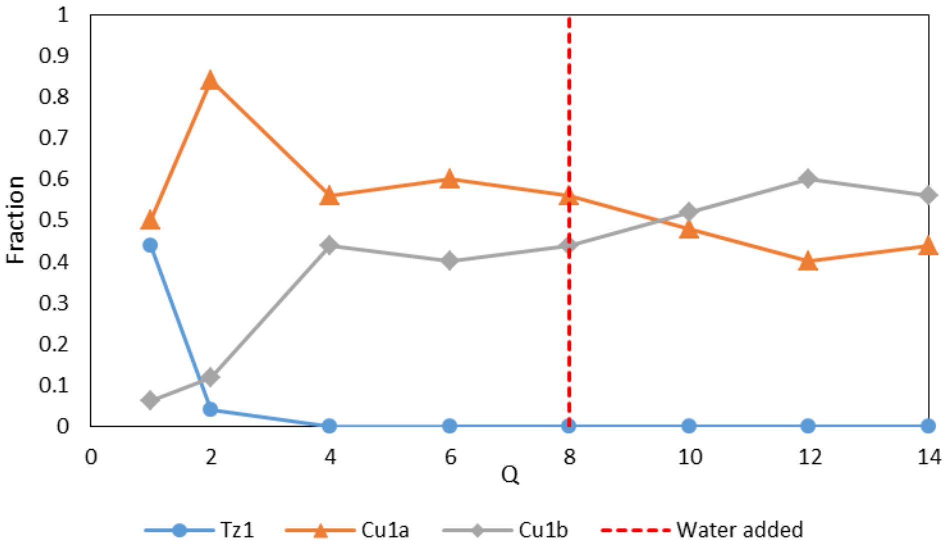

Figure 225. Reaction progress as a function of Q during the electrochemical synthesis of **Cu1a**/**Cu1b** mixture.

It is possible however, that water is responsible for the formation of **Cu1b.BF$_4$**, and also that **Cu1b.BF$_4$** is formed directly from **Tz1.BF$_4$**. In this case, the addition of water after consumption of **Tz1.BF$_4$** is complete would not cause an increase in the concentration of **Cu1b.BF$_4$**. Given the borderline nature of the results obtained in this experiment, it is not possible to entirely rule this scenario out.

The data obtained by doping water in at the start of a reaction may point toward this being the case, as a clear increase was seen in **Cu1b.BF$_4$** formation when more water was added (*3.6.1*).

3.7 Conclusions and Future Work

The effect of various reaction conditions on product outcome has been explored through a range of experiments. These were conducted to gain a better understanding of the electrochemical synthesis of NHC complexes in general, as well as to specifically probe the ring-opening reaction.

It was noted that variation of voltage had a dramatic effect on the efficiency of the reaction, although the product formed was unchanged in the voltage window studied. The lowest voltage used (2 V) led to a low conversion of just 16%, whilst the higher voltages (5 and 10 V) gave good conversions (86 and >99%). This indicates that it is necessary to use a significant overpotential to generate product under the conditions investigated.

It was noted that it is often necessary to supply greater than 1Q in order to achieve full conversion of the starting ligand. For most ligands, supplying 2Q is sufficient to achieve a good conversion.

The reactivity of both **Tz1.BF$_4$** and **Cu1a.BF$_4$** were investigated under a range of conditions. Electrolysis of a solution of **Cu1a.BF$_4$** did not form the ring-opened product **Cu1b.BF$_4$** thus appearing to rule out **Cu1a.BF$_4$** being an intermediate in this reaction. Evidence from reaction monitoring may point to formation **Cu1b.BF$_4$** after consumption of **Tz1.BF$_4$** was complete, thereby contradicting this. The reaction monitoring did however confirm that it is not possible to fully convert the product mixture to **Cu1b.BF$_4$**. This is in agreement with both the hypothesis that **Cu1a.BF$_4$** is not involved in the formation of **Cu1b.BF$_4$** and the hypothesis that adventitious water may promote the formation of **Cu1b.BF$_4$**.

The addition of varying quantities of water to reaction mixtures led to different proportions of species in the **Cu1a**/**Cu1b** product mixture. This is strong evidence that water plays a role in the reaction, however the mechanism by which this occurs is unclear. Although labelling experiments using D_2O were attempted, due to the lability of the key protons, the results were inconclusive. Addition of water to a mixture of **Cu1a**/**Cu1b** has no effect on product ratio when standing at room temperature. Addition of water to a mixture of **Cu1a**/**Cu1b** followed by electrolysis, appeared to lead to a slight increase in the concentration of **Cu1b.BF$_4$**, thus providing moderate support for the role of water in the reaction.

The data presented here do not provide sufficient information for a complete and definite determination of the reaction mechanism. There are however some conclusions that can be drawn. Control experiments established that the presence of both copper and a current are necessary to effect ring-opening. Furthermore, it seems clear that adventitious water is the key factor in determining the product ratio between **Cu1a.BF$_4$** and **Cu1b.BF$_4$**. Therefore two obvious pathways present themselves (**1** and **2** – Figure 226). The electrolysis of **Cu1a.BF$_4$** did not produce **Cu1b.BF$_4$**, in apparent contradiction with pathway **2**, although this may be due to poor conductivity in the solution. The multi-Q experiment indicated that conversion between **Cu1a.BF$_4$** and **Cu1b.BF$_4$** may be possible. Indeed, the fact that the conversion appeared to stall after a period of time is consistent with pathway **2** in which all the water has been consumed. Nonetheless, the presence of **Cu1b.BF$_4$** at early reaction stages gives credence to pathway **1**. The results presented in section 3.6.3 are unfortunately inconclusive, and thus do not lend particular weight to either proposal.

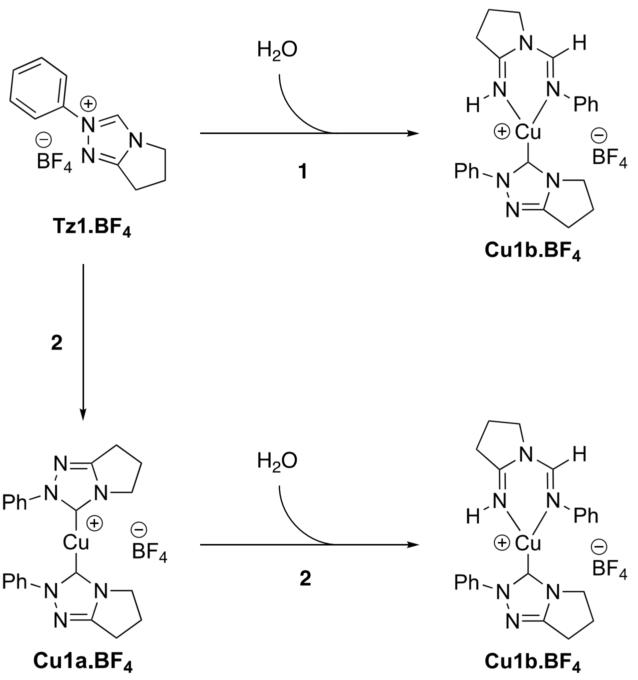

Figure 226. Two possible mechanistic pathways for the formation of **Cu1b.BF$_4$**.

If a further assessment of the mechanism was desired, three specific further experiments are suggested. First, electrolysis of **Cu1a.BF$_4$** (*3.2.2*) with a supporting electrolyte to ensure conductivity of the solution is maintained throughout. If this allows conversion to **Cu1b.BF$_4$** then this provides strong evidence for pathway **2**. A second experiment would repeat this with the addition of 1 equivalent of water at the start. Finally, the multi-Q monitoring experiment (*3.3.2*) should be performed with both an internal standard and a supporting electrolyte. The internal standard will allow for the determination of absolute concentrations, to give a clearer picture of how the product ratios change over time. The supporting electrolyte will ensure conductivity throughout. Once the adventitious water has been consumed, the ratio of **Cu1a.BF$_4$** to **Cu1b.BF$_4$** should stabilise. If pathway **1** is in operation then the addition of further water should not impact on this product ratio. If pathway **2** is occurring then this should provoke an increase in the concentration of **Cu1b.BF$_4$**. Thus a clear picture as to which of the two processes is occurring can be obtained.

The exact role that the water plays in the ring-opening reaction has not been determined. However, the two electron reduction of either **Tz1.BF$_4$** or the NHC derived thereof, requires a proton source, and thus it is easy to envisage how water could play this role (Figure 227).

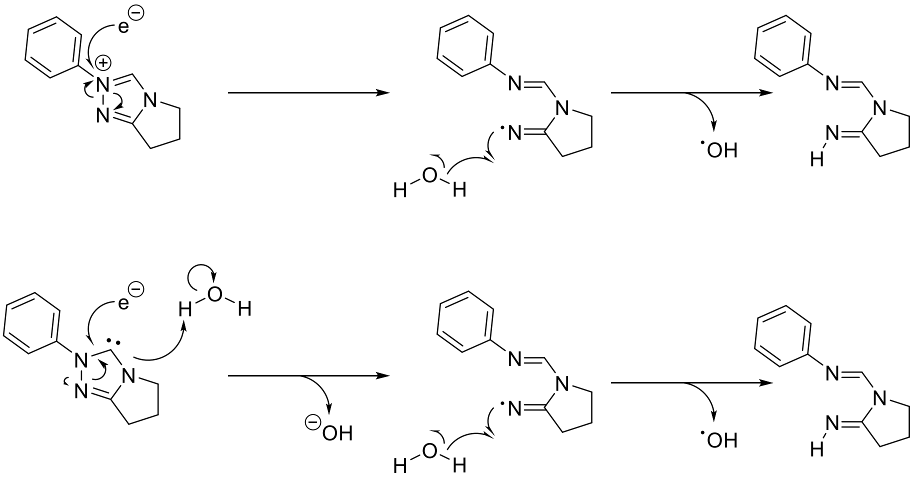

Figure 227. Possible route to the formation of the diimine ligand from either **Tz1.BF$_4$** (top) or NHC (bottom), assisted by adventitious water.

A reaction in which **Tz1.D** was used in conjunction with d$_3$-MeCN might provide further insight into the mechanism of the reaction. Assuming **Tz1.D** does not undergo reprotonation in d$_3$-MeCN then the location of deuterium incorporation into the product would determine whether the triazolium or adventitious water acts as a proton source.

A number of chemical reactions using **Cu1a.BF$_4$** could also be performed, for instance reaction with hydrogen gas or a reducing agent; this would probe the possibility of transforming **Cu1a.BF$_4$** into **Cu1b.BF$_4$**.

Investigations into the ligand scope of the ring-opening reaction are described in Chapter 2. Another interesting question is whether the same reaction would occur when a different metal is used - to probe this a range of electrochemically apposite metals could be tested. Silver or gold would be an appropriate starting point, as these should also produce complexes with a linear geometry, as seen with Cu. A reaction with Fe would also be interesting; successful electrochemical synthesis of Fe-NHC complexes has previously used imidazoliums with N-donor substituents, to better facilitate the preferred octahedral geometry of the resulting Fe(II) complexes.[8] Given this, and the known affinity of Fe for N-donor ligands, it is easy to envisage how formation of **Fe1b.BF$_4$** might be favoured over the formation of **Fe1a.BF$_4$** (Figure 228).

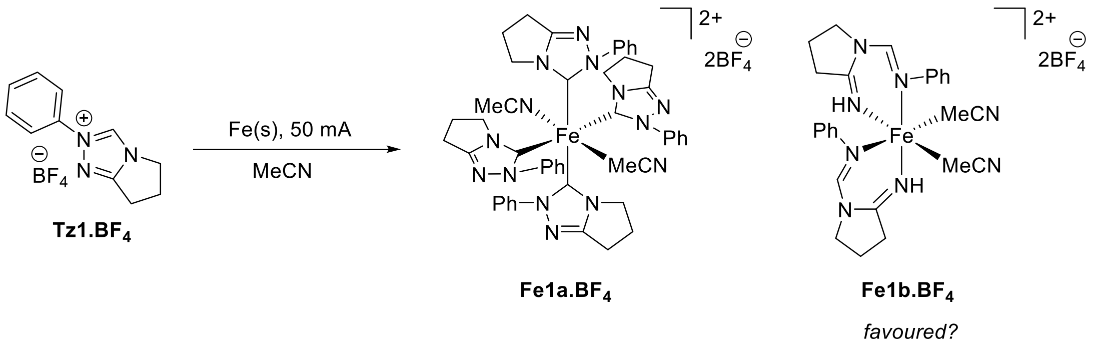
Tz1.BF$_4$
Fe(s), 50 mA
MeCN
Fe1a.BF$_4$
Fe1b.BF$_4$
favoured?
2+
2BF$_4^-$

Figure 228. Possible products from electrochemical reaction of **Tz1.BF$_4$** with Fe.

3.8 Experimental

3.8.1 General Considerations

Where stated all reactions were carried out under an inert atmosphere of dry nitrogen or argon, using standard Schlenk line or glovebox techniques. Anhydrous solvents were dried by passing over activated alumina to remove water, copper catalyst to remove oxygen, and molecular sieves to remove any remaining water, *via* the Dow-Grubbs solvent system. Deuterated MeCN was dried by standing for 18 hours over activated 3 Å molecular sieves, followed by transfer to fresh activated 3 Å sieves. MeCN, deuterated MeCN, water and D_2O were degassed by purging with argon.

Tz1.BF$_4$ and **Tz1.Cl** were gifted by Professor Andrew Smith (University of St. Andrews) and used as received. The synthesis, isolation and characterisation of all other triazolium salts and Cu complexes is described in Chapter 2.

All electrochemical reactions were performed using an ElectraSyn 2.0, using vials, caps and electrodes supplied by IKA. Cu electrodes were cleaned prior to use according to the following procedure: Electrodes were treated with HCl (~4M) in a sonicator bath for 5-10 minutes. The surfaces were cleaned with water, soap and a scouring pad, followed by acetone. Electrodes were dried in an oven prior to use.

NMR spectra were recorded on a Bruker Ascend 400 spectrometer. ^{1}H NMR and chemical shifts were referenced against residual solvent peaks. Mass spectra were collected on a Bruker Daltonics (micro TOF) instrument operating in the electrospray mode.

3.8.2 Standard Procedure for Electrochemical Reaction

Triazolium salt (0.3 mmol) was added to an oven dried 10 mL ElectraSyn vial in a glovebox. Anhydrous MeCN (5 mL) was added and the vial cap was fitted with electrodes (Cu or glassy carbon) held at a distance of 5 mm apart. The reaction was run for the given number of "Q" based upon a known quantity of ligand and a fixed value of either current or voltage. After the reaction was complete the mixture was transferred to an ampoule and the solvent removed on a Schlenk line. The flask was returned to a glovebox and a crude ^{1}H NMR obtained in anhydrous, degassed MeCN in a Young's NMR tube.

This procedure was followed for all reactions described in sections: 3.2.1, 3.3.1, 3.3.3.

This procedure was performed for the reaction described in section 3.2.2 using **Cu1a.BF$_4$** (46.2 mg, 0.089 mmol) and Cu electrodes. After reaction the product was isolated as follows: The crude reaction mixture residue was dissolved in MeCN and filtered through celite in the glovebox. The filtrate was recrystallised from MeCN and

Et_2O, and isolated *via* cannula filtration. The brown precipitate formed was washed with further portions of Et_2O (3 x 2 mL), isolated *via* cannula filtration and dried *in vacuo.* Yield: 20.4 mg.

This procedure was followed for the reaction described in section 3.5.2 using d_3-MeCN instead of MeCN.

3.8.3 Standard Procedure for Electrochemical Reaction with Dopant

Triazolium (0.3 mmol) was added to an oven dried 10 mL ElectraSyn vial fitted with Cu electrodes held at a distance of 6 mm apart and the vial purged with argon for 10 minutes. Degassed dopant (H_2O or D_2O) was added *via* microsyringe, followed by MeCN (5 mL). The reaction was run for 2Q at a fixed current of 50 mA. After the reaction was complete the mixture was transferred to an ampoule *via* syringe and the solvent removed on a Schlenk line. The flask was transferred to a glovebox and a crude ^1H NMR obtained in anhydrous, degassed MeCN in a Young's NMR tube.

This procedure was followed for reactions described in section 3.6.1 using H_2O, and 3.6.2 using D_2O.

3.8.4 Reaction Monitoring

Tz1.BF$_4$ (81.9 mg, 0.3 mmol) was added to a 20 mL ElectraSyn vial fitted with Cu electrodes held 6 mm apart under an inert atmosphere. Anhydrous MeCN (10 mL) was added and a current of 50 mA applied for a set number of Q. After the number of Q had elapsed an aliquot (0.25 mL) was withdrawn *via* syringe and transferred to a Young's NMR tube under an inert atmosphere. The sample was diluted with d_3-MeCN (0.3 mL) and a ^1H NMR spectrum recorded. The reaction was restarted with a current of 50 mA applied for a set number of Q (the number of Q was adjusted for sample removal).

This procedure was followed inside a glovebox under an inert atmosphere of nitrogen for the reaction described in section 3.3.2 (Table 27).

Table 27. Reaction progress as a function of Q

Q applied	Total Q	Mmol remaining	Proportion of species		
			Tz1	**Cu1a**	**Cu1b**
0.1	0.1	0.3	0.97	0.03	0
0.4	0.5	0.29	0.71	0.25	0.04
0.5	1	0.29	0.36	0.48	0.16
1.0	2	0.28	0.02	0.72	0.26
1.0	3	0.27	0	0.68	0.32
1.0	4	0.26	0	0.64	0.36
2.0	6	0.25	0	0.62	0.38
2.0	8	0.24	0	0.66	0.34

Relative concentration of species determined by comparison of NCH_2 signal for **Tz1**, NCH_2 signal for **Cu1a** and NC*H*N signal for **Cu1b**.

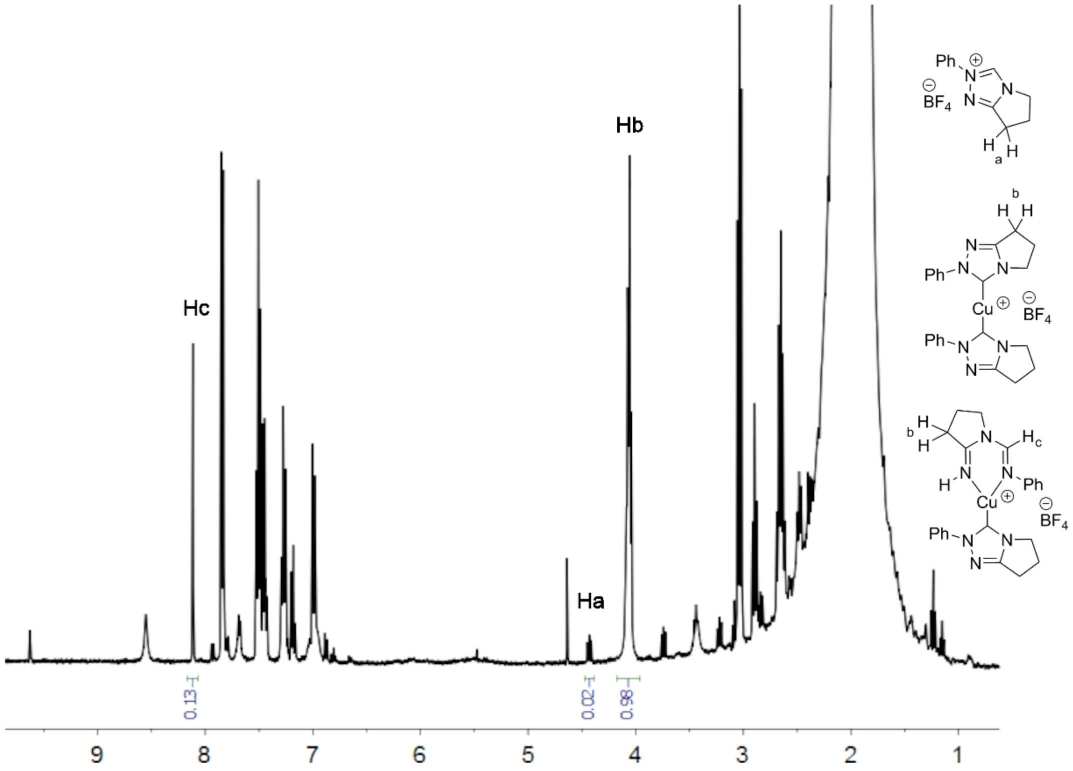

Example spectrum indicating peaks used to determine compound ratios.

This procedure was followed with the addition of water (5.0 µL, 0.28 mmol) after 8Q, using an ElectraSyn fitted with an argon inlet needle, for the reaction described in section 3.6.3 (Table 28).

Table 28. Reaction progress as a function of Q, with water added.

Q applied	Total Q	Mmol remaining	Proportion of species		
			Tz1	**Cu1a**	**Cu1b**
1.0	1.0	0.3	0.28	0.68	0.04
1.0	2.0	0.29	0.02	0.92	0.06
2.0	4.0	0.29	0	0.78	0.22
2.0	6.0	0.28	0	0.80	0.20
2.0	8.0	0.27	0	0.78	0.22
2.0	10.0	0.26	0	0.74	0.26
2.0	12.0	0.25	0	0.70	0.30
2.0	14.0	0.24	0	0.72	0.28

Relative concentration of species determined by comparison of NCH_2 signal for **Tz1**, NCH_2 signal for **Cu1a** and NC*H*N signal for **Cu1b**. Dashed line indicates water addition.

3.8.4 Synthesis of Tz1.D

Tz1.BF$_4$ (102 mg, 0.370 mmol) was combined in a sample vial with D$_2$O (2 mL), capped and heated to 60 °C for 20 hours. After cooling a further 2 mL of D$_2$O was added and the aqueous phase extracted with DCM (3 x 7 mL). The combined organic phase was dried over MgSO$_4$, and the solvent removed *in vacuo*. The residue was recrystallised from MeCN and Et$_2$O Yield: 30.7 mg, 30%, 95% deuterium incorporation.

^{1}H NMR (400 MHz, DMSO) δ 10.88 (s, 0.05H), 9.46 (s, 1H), 7.93 (d, J = 7.8 Hz, 2H), 7.72 (t, J = 7.6 Hz, 2H), 7.65 (t, J = 7.4 Hz, 1H), 4.29 (t, J = 7.2 Hz, 2H), 1.96 (h, J = 7.3 Hz, 2H), 0.98 (t, J = 7.4 Hz, 3H).

List of References

1 B. Liu, Q. Xia and W. Chen, *Angew. Chemie Int. Ed.*, 2009, **48**, 5513–5516.

2 M. R. Chapman, Y. M. Shafi, N. Kapur, B. N. Nguyen and C. E. Willans, *Chem. Commun.*, 2015, **51**, 1282–1284.

3 K. A. Ogawa and A. J. Boydston, *Chem. Lett.*, 2014, **43**, 907–909.

4 R. S. Massey, C. J. Collett, A. G. Lindsay, A. D. Smith and A. C. O'Donoghue, *J. Am. Chem. Soc.*, 2012, **134**, 20421–20432.

5 R. Giernoth and D. Bankmann, *European J. Org. Chem.*, 2008, **2008**, 2881–2886.

6 S. Pons and S. B. Khoo, *Electrochim. Acta*, 1982, **27**, 1161–1169.

7 J. A. Grant, Z. Lu, D. E. Tucker, B. M. Hockin, D. S. Yufit, M. A. Fox, R. Kataky, V. Chechik and A. C. O'Donoghue, *Nat. Commun.*, 2017, **8**, 15088.

8 M. R. Chapman, University of Leeds, 2016.